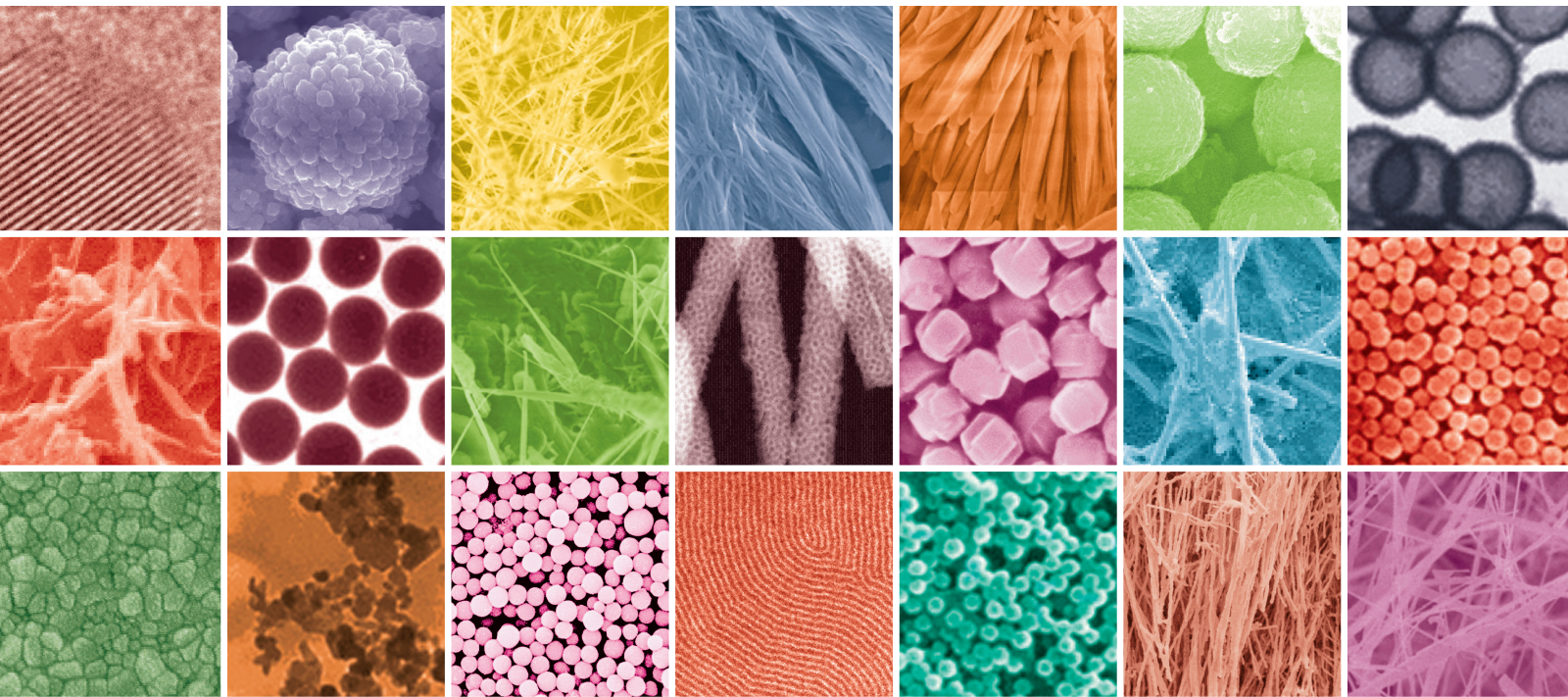


Nanomaterials for Environmental Applications

Guest Editors: Fan Dong, Ranjit T. Koodali, Haiqiang Wang,
and Wing-kei Ho





Nanomaterials for Environmental Applications

Journal of Nanomaterials

Nanomaterials for Environmental Applications

Guest Editors: Fan Dong, Ranjit T. Koodali, Haiqiang Wang,
and Wing-kei Ho



Copyright © 2014 Hindawi Publishing Corporation. All rights reserved.

This is a special issue published in "Journal of Nanomaterials." All articles are open access articles distributed under the Creative Commons Attribution License, which permits unrestricted use, distribution, and reproduction in any medium, provided the original work is properly cited.

Editorial Board

Katerina E. Aifantis, USA
Nageh K. Allam, USA
Margarida Amaral, Portugal
Xuedong Bai, China
Lavinia Balan, France
Enrico Bergamaschi, Italy
Theodorian Borca-Tasciuc, USA
C. Jeffrey Brinker, USA
Christian Brosseau, France
Xuebo Cao, China
Shafiq Chowdhury, USA
Kwang-Leong Choy, UK
Cui ChunXiang, China
Miguel A. Correa-Duarte, Spain
Shadi A. Dayeh, USA
Ali Eftekhari, USA
Claude Estournés, France
Alan Fuchs, USA
Lian Gao, China
Russell E. Gorga, USA
Hongchen Chen Gu, China
Mustafa O. Guler, Turkey
John Z. Guo, USA
Smrati Gupta, Germany
Michael Harris, USA
Zhongkui Hong, China
Michael Z. Hu, USA
David Hui, USA
Y.-K. Jeong, Republic of Korea
Sheng-Rui Jian, Taiwan
Wanqin Jin, China
Rakesh K. Joshi, UK
Zhenhui Kang, China
Fathallah Karimzadeh, Iran
Alireza Khataee, Iran

Do K. Kim, Korea
Alan K. T. Lau, Hong Kong
Burtrand Lee, USA
Jun Li, Singapore
Benxia Li, China
Xing-Jie Liang, China
Shijun Liao, China
Gong-Ru Lin, Taiwan
Tianxi Liu, China
Jun Liu, USA
Songwei Lu, USA
Daniel Lu, China
Jue Lu, USA
Ed Ma, USA
Gaurav Mago, USA
Santanu K. Maiti, India
Sanjay R. Mathur, Germany
Vikas Mittal, UAE
Weihai Ni, Germany
Sherine Obare, USA
Atsuto Okamoto, Japan
Abdelwahab Omri, Canada
Edward A. Payzant, USA
Kui-Qing Peng, China
Anukorn Phuruangrat, Thailand
Mahendra Rai, India
Suprakas Sinha Ray, South Africa
Ugur Serincan, Turkey
Huaiyu Shao, Japan
Donglu Shi, USA
Vladimir Sivakov, Germany
Marinella Striccoli, Italy
Bohua Sun, South Africa
Saikat Talapatra, USA
Nairong Tao, China

Titipun Thongtem, Thailand
Somchai Thongtem, Thailand
Alexander Tolmachev, Ukraine
Valeri P. Tolstoy, Russia
Tsung-Yen Tsai, Taiwan
Takuya Tsuzuki, Australia
Raquel Verdejo, Spain
Mat U. Wahit, Malaysia
Zhenbo Wang, China
Ruiping Wang, Canada
Shiren Wang, USA
Cheng Wang, China
Yong Wang, USA
Jinquan Wei, China
Ching-Ping Wong, Hong Kong
Xingcai Wu, China
Guodong Xia, Hong Kong
Ping Xiao, UK
Zhi Li Xiao, USA
Yangchuan Xing, USA
Shuangxi Xing, China
Nanping Xu, China
Doron Yadlovker, Israel
Yingkui Yang, China
Khaled Youssef, USA
Kui Yu, Canada
William W. Yu, USA
Haibo Zeng, China
Tianyou Zhai, China
Renyun Zhang, Sweden
Bin Zhang, China
Yanbao Zhao, China
Lianxi Zheng, Singapore
Chunyi Zhi, Hong Kong

Contents

Nanomaterials for Environmental Applications, Fan Dong, Ranjit T. Koodali, Haiqiang Wang, and Wing-kei Ho
Volume 2014, Article ID 276467, 4 pages

Removal of Hazardous Pollutants from Wastewaters: Applications of TiO₂-SiO₂ Mixed Oxide Materials, Shivatharsiny Rasalingam, Rui Peng, and Ranjit T. Koodali
Volume 2014, Article ID 617405, 42 pages

Phenol Removal by a Novel Non-Photo-Dependent Semiconductor Catalyst in a Pilot-Scaled Study: Effects of Initial Phenol Concentration, Light, and Catalyst Loading, Xiao Chen, Yan Liang, Xuefei Zhou, and Yanling Zhang
Volume 2014, Article ID 457485, 8 pages

Study of Modern Nano Enhanced Techniques for Removal of Dyes and Metals, Samavia Batool, Shatirah Akib, Mushtaq Ahmad, Khaled S. Balkhair, and Muhammad Aqeel Ashraf
Volume 2014, Article ID 864914, 20 pages

The Use of Biofloculant and Biofloculant-Producing *Bacillus mojavensis* Strain 32A to Synthesize Silver Nanoparticles, Sahar Zaki, Marwa Etarahony, Marwa Elkady, and Desouky Abd-El-Haleem
Volume 2014, Article ID 431089, 7 pages

Preparation and Characterization of Lecithin-Nano Ni/Fe for Effective Removal of PCB77, Shu Ding, Lin Zhao, Yun Qi, and Qian-qian Lv
Volume 2014, Article ID 678489, 7 pages

Quantitative Fractal Evaluation of Herbicide Effects on the Water-Absorbing Capacity of Superabsorbent Polymers, Renkuan Liao, Shumei Ren, and Peiling Yang
Volume 2014, Article ID 905630, 9 pages

Application of a Novel Semiconductor Catalyst, CT, in Degradation of Aromatic Pollutants in Wastewater: Phenol and Catechol, Xiao Chen, Yanling Zhang, Xuefei Zhou, Shoji Ichimura, Guoxiu Tong, Qiming Zhou, Xi Chen, Wenzhao Wang, and Yan Liang
Volume 2014, Article ID 524141, 10 pages

Chitosan and Its Derivatives Applied in Harvesting Microalgae for Biodiesel Production: An Outlook, Guanyi Chen, Liu Zhao, Yun Qi, and Yuan-Lu Cui
Volume 2014, Article ID 217537, 9 pages

Photodegradation of Methyl Orange Using Magnetically Recoverable AgBr@Ag₃PO₄/Fe₃O₄ Photocatalyst under Visible Light, Zhen Wang, Lu Yin, Ziwen Chen, Guowang Zhou, and Huixiang Shi
Volume 2014, Article ID 150150, 6 pages

A Novel Nanomodified Cellulose Insulation Paper for Power Transformer, Yuan Yuan and Ruijin Liao
Volume 2014, Article ID 510864, 6 pages

SO₂ Poisoning Behaviors of Ca-Mn/TiO₂ Catalysts for Selective Catalytic Reduction of NO with NH₃ at Low Temperature, Qingqing Tian, Hongfeng Liu, Weiyuan Yao, Yan Wang, Yue Liu, Zhongbiao Wu, Haiqiang Wang, and Xiaole Weng
Volume 2014, Article ID 904649, 6 pages

The Poisoning Effect of Na Doping over Mn-Ce/TiO₂ Catalyst for Low-Temperature Selective Catalytic Reduction of NO by NH₃, Liu Yang, Yue Tan, Zhongyi Sheng, and Aiyi Zhou
Volume 2014, Article ID 368583, 6 pages

The Research of Nanoparticle and Microparticle Hydroxyapatite Amendment in Multiple Heavy Metals Contaminated Soil Remediation, Zhangwei Li, Man-man Zhou, and Weidian Lin
Volume 2014, Article ID 168418, 8 pages

Effects of Surfactants on High Regularity of 3D Porous Nickel for Zn²⁺ Adsorption Application, Xiaogang Guo, Xueming Li, Yonghong Zheng, Chuan Lai, Wulin Li, Binbin Luo, and Daixiong Zhang
Volume 2014, Article ID 358312, 9 pages

Tuning the Morphological Structure and Photocatalytic Activity of Nitrogen-Doped (BiO)₂CO₃ by the Hydrothermal Temperature, Chongjun Wang, Zaiwang Zhao, Bin Luo, Min Fu, and Fan Dong
Volume 2014, Article ID 192797, 10 pages

Photocatalytic Degradation of 2-Chlorophenol Using Ag-Doped TiO₂ Nanofibers and a Near-UV Light-Emitting Diode System, Ju-Young Park and In-Hwa Lee
Volume 2014, Article ID 250803, 6 pages

The Key Role of pH Value in the Synthesis of Titanate Nanotubes-Loaded Manganese Oxides as a Superior Catalyst for the Selective Catalytic Reduction of NO with NH₃, Xiongbo Chen, Chaoping Cen, Zhixiong Tang, Wenhao Zeng, Dingsheng Chen, Ping Fang, and Zhihang Chen
Volume 2013, Article ID 871528, 7 pages

Mechanical and Morphological Properties of Poly-3-hydroxybutyrate/Poly(butyleneadipate-co-terephthalate)/Layered Double Hydroxide Nanocomposites, Yen Leng Pak, Mansor Bin Ahmad, Kamyar Shameli, Wan Md Zin Wan Yunus, Nor Azowa Ibrahim, and Norhazlin Zainuddin
Volume 2013, Article ID 621097, 8 pages

A Novel Synthesis Method of Porous Calcium Silicate Hydrate Based on the Calcium Oxide/Polyethylene Glycol Composites, Wei Guan, Fangying Ji, Yong Cheng, Zhuoyao Fang, Dexin Fang, Peng Yan, and Qingkong Chen
Volume 2013, Article ID 542109, 7 pages

Editorial

Nanomaterials for Environmental Applications

Fan Dong,¹ Ranjit T. Koodali,² Haiqiang Wang,³ and Wing-kei Ho⁴

¹Chongqing Key Laboratory of Catalysis and Functional Organic Molecules, College of Environmental and Biological Engineering, Chongqing Technology and Business University, Chongqing 400067, China

²Department of Chemistry, University of South Dakota, 414 E. Clark Street, Vermillion, SD 57069, USA

³Department of Environmental Engineering, Zhejiang University, Hangzhou 310027, China

⁴Department of Science and Environmental Studies, The Hong Kong Institute of Education, 10 Lo Ping Road, Tai Po, New Territories, Hong Kong

Correspondence should be addressed to Fan Dong; dfctbu@126.com

Received 11 June 2014; Accepted 11 June 2014; Published 25 June 2014

Copyright © 2014 Fan Dong et al. This is an open access article distributed under the Creative Commons Attribution License, which permits unrestricted use, distribution, and reproduction in any medium, provided the original work is properly cited.

Environmental pollution and energy shortage are two current major global challenges faced by human beings. In the past two decades, the evolution of nanotechnology represents an ever improving process in the design, discovery, creation, and novel utilization of artificial nanoscale materials. To meet the major challenges in environmental sustainability, these nanomaterials in various hierarchical fashions are stimulating various important practical applications in the environmental sector. The rapid development in materials and catalysis science has led to significant advances in understanding the controlled synthesis and structure-activity relationship of the nanomaterials. The design, synthesis, and modification of novel nanomaterials allow for enhanced performance for environmental related applications.

This special issue contains 19 papers, which are mainly related to environmental materials synthesis, photocatalysis, and pollutant removal. The purpose of this special issue is to provide readers with current advances in the use of nanomaterials for environmental applications and apprise them of the progress, challenges, and promises. Among them, 11 papers are related to organic pollutant degradation, heavy metal removal, and NO reduction with NH₃. One paper is about biodiesel production through harvesting microalgae. Furthermore, there are 4 papers devoted to morphological control of environmental materials, 2 papers related to adsorption optimization, and 1 paper dealing with power transformer with nanomodified cellulose insulation paper. We would like to express our sincere thanks to all the authors

for submitting their interesting works to this special issue. A brief summary of all 19 accepted papers is provided below.

The paper entitled “Removal of hazardous pollutants from wastewaters: applications of TiO₂-SiO₂ mixed oxide materials” reviewed the different removal techniques employed for wastewater treatment and the factors that influence the degradation efficiency. The application of TiO₂-SiO₂ binary mixed oxide materials for wastewater treatment is extensively covered. This literature survey indicated that these mixed oxide materials have enhanced abilities to remove a wide variety of pollutants. This paper also pointed out that even though these binary mixed oxides show better activity than pure TiO₂ materials in most instances, the utilization of these TiO₂-SiO₂ mixed oxides is limited for the mineralization of selected pollutants.

The review article entitled “Chitosan and its derivatives applied in harvesting microalgae for biodiesel production: an outlook” is aimed to describe and summarize current researches on the application of chitosan and chitosan-derived materials for harvesting microalgae. Biodiesel requires an efficient low-energy harvesting strategy so as to make biodiesel production economically attractive. Chitosan has emerged as a favorable flocculating agent in harvesting of microalgae. This offers a starting point for future studies able to invalidate, confirm, or complete the actual findings and to improve knowledge in this field.

In the review article entitled “Study of modern nano enhanced techniques for removal of dyes and metals,” a range

of wastewater treatment technologies have been introduced which can efficiently reduce both Cr(VI) and azo dyes simultaneously to less toxic form such as biodegradation, biosorption, adsorption, bioaccumulation, and nanotechnology. Rate of simultaneous reduction of Cr(VI) and azo dyes can be enhanced by combining different treatment techniques. As illustrated in this review, a range of nanomicrobiological techniques have been proposed or are under active development for treatment of polluted soil and wastewater, but many techniques are still at experimental or pilot stage. This review also evaluated the removal methods for simultaneous removal of Cr(VI) and azo dyes by surface engineered nanoparticles and nanophotocatalyst. Potential microbial strains capable of simultaneous removal of Cr(VI) and azo dyes have been summarized in some detail as well.

In the paper entitled “*The use of bioflocculant and bioflocculant-producing bacillus mojavensis strain 32A to synthesize silver nanoparticles*,” an organism was successfully used to produce more than one product at the same time. This study has investigated the ability of bioflocculant-producing *Bacillus mojavensis* strain 32A as a nanosilver synthesizer beside bioflocculant production. Three media, such as nutrient broth, bioflocculant-producing medium, and pure bioflocculant, were tested. The results emphasized that purified bioflocculant has the ability to produce anisotropy clusters of nanosilver ranging in size from 6 to 72 nm proving that the bioflocculant functioned as a reducing and stabilizing agent in nanosilver synthesis.

The paper entitled “*Preparation and characterization of lecithin-nano Ni/Fe for effective removal of PCB77*” described that a kind of combined material lecithin-nano-Ni/Fe is obtained by combining lecithin and nanoscale Ni/Fe bimetal via microemulsion method. The efficacy of such an original material was tested using PCB77 as target pollutant. A microemulsion system was optimized as template to prepare Ni/Fe nanoparticles, which was followed by an *in situ* loading process with the deposition of lecithin carrier. The Ni/Fe nanoparticles can be uniformly dispersed and closely combined with lecithin carrier. The constitution of lecithin-nano-Ni/Fe was a beneficial attempt to acquire the synergistic effect for intensified removal of environmental contaminants. It seems promising that the original system and the facile method described in this work will facilitate the development of the organic-inorganic hybrid materials.

The paper entitled “*Quantitative fractal evaluation of herbicide effects on the water-absorbing capacity of superabsorbent polymers*” introduced that 100-mesh sieves, electron microscopy, and fractal theory can be used to study swelling and water absorption in SAPs in the presence of three common herbicides (atrazine, alachlor, and tribenuron-methyl). 2.0 mg/L atrazine reduces the capacity by 9.64–23.3% at different swelling points and no significant diminution was observed for the other herbicides or for lower atrazine concentrations. They also found that the hydrogel membrane pore distributions have fractal characteristics in both deionized water and atrazine solution. A linear correlation was observed between the fractal analysis and the water-absorbing mass. Multifractal analysis characterized

the membrane pore distribution, which is superior to single-fractal analysis that uses the fractal dimension.

In the paper entitled “*Application of a novel semiconductor catalyst, CT, in degradation of aromatic pollutants in wastewater: phenol and catechol*,” a novel semiconductor catalyst, CT, was for the first time employed in the present study to degrade phenol and catechol. The phenolic compounds (initial concentration of 88 mg L⁻¹) were completely mineralized by the CT catalytic nanoparticles (1%) within 15 days under acidic condition and with the presence of mild UV radiation. The pollutants were adsorbed on the CT's surface and oxidized via charge-transfer and hydroxyl radical generation by CT. Given the low initial concentrations, a circumstance encountered in wastewater polishing, the current set-up should be an efficient and less energy- and chemical-consumptive treatment method.

The paper entitled “*Phenol removal by a novel non-photo-dependent semiconductor catalyst in a pilot-scaled study: effects of initial phenol concentration, light, and catalyst loading*” reported that a novel non-photo-dependent semiconductor catalyst (CT) was fabricated and employed to degrade phenol. The effect of operational parameters such as phenol initial concentration, light area, and catalyst loading on phenol degradation was investigated. CT catalyst exceeded titanium dioxide in treating and mineralizing low-level phenol, under both mild UV radiation and cloudy conditions. The results suggest that CT catalyst could be applied in circumstances when light is not easily accessible in pollutant-carrying media.

In the paper entitled “*A novel nanomodified cellulose insulation paper for power transformer*,” a novel cellulose insulation paper handsheet has successfully been modified with various contents of montmorillonite (MMT). Relative permittivity and breakdown strength were investigated. The microstructure of MMT in Kraft paper was investigated. The relative permittivity of the immersed oil Kraft-MMT handsheets (K-MMT) decreased with the increasing amount of MMT. For MMT concentration of 9 wt%, K-9% MMT possessed the lowest relative permittivity of approximately 2.3 at 50 Hz. The breakdown voltage of the paper-oil-paper composite insulation system increased from 50.3 kV to 56.9 kV.

In the paper entitled “*SO₂ poisoning behaviors of Ca-Mn/TiO₂ catalysts for selective catalytic reduction of NO with NH₃ at low temperature*,” the sulfur tolerance of Ca modified MnO_x/TiO₂ catalysts was investigated in low-temperature selective catalytic reaction (SCR) process. Experimental results revealed that the durability of developed catalysts in the presence of SO₂ could be improved by Ca modification. After being subjected to a range of analytical techniques, it was found that the surface Ca species could act as a SO₂ trap by preferentially reacting with SO₂ to form bulk-like CaSO₄, inhibiting the sulfation of active phase. Furthermore, the introduction of SO₂ had also preserved part of Lewis sites over the MnO_x. Both of these are conducive to NH₃ adsorption and activation at low temperature, hence improving the sulfur tolerance of Ca doped catalysts.

In the paper entitled “*The poisoning effect of Na doping over Mn-Ce/TiO₂ catalyst for low-temperature selective*

catalytic reduction of NO by NH₃,” sodium carbonate, sodium nitrate, and sodium chloride were chosen as the precursors to prepare the Na salts deposited Mn-Ce/TiO₂ catalysts through an impregnation method. The influence of Na doping on the performance of the Mn-Ce/TiO₂ catalyst for low-temperature selective catalytic reduction of NO_x by NH₃ was investigated. Experimental results showed that Na salts had negative effects on the activity of Mn-Ce/TiO₂ and the precursors of Na salts also affected the catalytic activity. Significant changes in physical and chemical properties of Mn-Ce/TiO₂ were observed after Na was doped on the catalysts. The decreases in surface areas and NH₃ adsorption amounts were observed after Na was doped on the catalysts, which could be considered as the main reasons for the deactivation of Na deposited Mn-Ce/TiO₂.

In the paper entitled “*The key role of pH value in the synthesis of titanate nanotubes-loaded manganese oxides as a superior catalyst for the selective catalytic reduction of NO with NH₃*,” alkaline titanate nanotubes TNTs (TNTs-AL), acidic TNTs (TNTs-AC), and neutral TNTs (TNTs-NE) were synthesized by controlling the washing pH value. When these TNTs were utilized as the catalyst supports for manganese oxides (Mn/TNTs-AL, Mn/TNTs-AC, and Mn/TNTs-NE), the key role of pH value was found. Titanate nanosheets, titanate nanorods, and titanate nanotubes were dominated in Mn/TNTs-AL, Mn/TNTs-AC, and Mn/TNTs-NE, respectively. MnO₂ crystal was observed when using TNTs-AC or TNTs-NE as the support. By contrast, Mn₃O₄ and NaNO₃ were observed when using TNTs-AL as the support. Mn/TNTs-NE showed the best selective catalytic reduction (SCR) of NO with ammonia due to the largest surface area, the best dispersion, and the most active redox property of manganese oxides.

The paper entitled “*The research of nanoparticle and microparticle hydroxyapatite amendment in multiple heavy metals contaminated soil remediation*” documented that a pot trial was conducted to evaluate the efficiency of two particle sizes of hydroxyapatite (HAP) induced metal immobilization in soils: nanometer particle size of HAP (nHAP) and micrometer particle size of HAP (mHAP). Both mHAP and nHAP were assessed for their ability to reduce lead (Pb), zinc (Zn), copper (Cu), and chromium (Cr) bioavailability in an artificially metal-contaminated soil. Furthermore, both mHAP and nHAP were efficient in covering Pb, Zn, Cu, and Cr from nonresidual into residual forms. The mHAP was superior to nHAP in the immobilization of Pb, Zn, Cu, and Cr in metal-contaminated soil and reducing the Pb, Zn, Cu, and Cr utilized by pakchoi. The results suggested that mHAP had the better effect on remediation of multiple metal-contaminated soils than nHAP and was more suitable for applying in *in situ* remediation technology.

In the paper entitled “*Effects of surfactants on high regularity of 3D porous nickel for Zn²⁺ adsorption application*,” three-dimensional porous nickel (3D-PN) film with large specific surface area (*A_s*) and high porosity has been successfully prepared by hydrogen bubble dynamic template method. This work presents the effects of PEG 10000 and 1,4-butanediol as new additive combination on surface morphology of

the PN film. Meanwhile, the application of 3D-PN in Zn²⁺ adsorption was investigated in the paper. The surface area is determined to be as large as 166.7 cm²/mg and the porosity is 0.762 cm³/g when the concentration of PEG 10000 and 1,4-butanediol was 0.3 g/100 mL and 0.1 g/100 mL, respectively. The adsorption capacity of PN for Zn²⁺ is observed to be 9.145 mg/g.

In the paper entitled “*Photodegradation of methyl orange using magnetically recoverable AgBr@Ag₃PO₄/Fe₃O₄ photocatalyst under visible light*,” a novel magnetically recoverable AgBr@Ag₃PO₄/Fe₃O₄ hybrid was prepared by a simple deposition-precipitation approach. The results revealed that the photocatalytic activity and stability of AgBr@Ag₃PO₄/Fe₃O₄ composite towards decomposition of methyl orange (MO) dye were superior to those of pure Ag₃PO₄ under visible light irradiation. The photocatalytic activity enhancement of AgBr@Ag₃PO₄/Fe₃O₄ is closely related to the efficient separation of electron-hole pairs derived from the matching band potentials between Ag₃PO₄ and AgBr, as well as the good conductivity of Fe₃O₄. Moreover, the photocatalyst could be easily separated by applying an external magnetic field due to its magnetic property. The quenching effects of different scavengers proved that active holes (h⁺) and superoxide species (·O₂⁻) played the major role for the MO degradation. This work would provide new insight for the construction of visible light responsible photocatalysts with high performance, good stability, and recoverability.

The paper entitled “*Tuning the morphological structure and photocatalytic activity of nitrogen-doped (BiO)₂CO₃ by the hydrothermal temperature*” described that various nitrogen-doped hierarchical (BiO)₂CO₃ nanosheets architectures were synthesized by a facile one-step template-free hydrothermal method through controlling the hydrothermal temperature (HT). It was found that HT acted as a crucial factor in determining the morphology of the samples. The *Rosa chinensis*-like, red camellia-like, and lamina-like of nitrogen-doped (BiO)₂CO₃ (N-BOC) micro-/nanostructures can be selectively fabricated under hydrothermal temperatures of 150, 180, and 210°C. The thickness of the nanosheets was in direct proportion to the increasing HT. The red camellia-like N-BOC-180, especially, exhibited the highest photocatalytic performance, superior to the well-known visible light photocatalyst C-doped TiO₂ and N-doped TiO₂.

The paper entitled “*Photocatalytic degradation of 2-chlorophenol using Ag-doped TiO₂ nanofibers and a near-UV light-emitting diode system*” reported the photocatalytic degradation of 2-chlorophenol using TiO₂ nanofibers and Ag-doped TiO₂ nanofibers synthesized using the sol-gel and electrospinning techniques. The crystallite size of the Ag-doped TiO₂ nanofibers was smaller than that of the TiO₂ nanofibers because silver retrained phase transformation not only controls the phase transformation but also inhibits the growth of anatase crystallites. The photocatalytic degradation rate followed a pseudo-first-order equation. The rate constants (*k*) of the TiO₂ nanofibers and the Ag-doped TiO₂ nanofibers were 0.056 and 0.144 min⁻¹, respectively.

In the paper entitled “*Mechanical and morphological properties of poly-3-hydroxybutyrate/poly(butyleneadipate-co-terephthalate)/layered double hydroxide nanocomposites*,” the nanocomposites of poly-3-hydroxybutyrate/poly(butyleneadipate-co-terephthalate)/layered double hydroxide (PHB/PBAT/LDH) were prepared from a binary blend of PHB/PBAT and stearate- Zn_3Al LDH via a solution casting method using chloroform as solvent. The pristine Zn_3Al LDH was synthesized from nitrate salts solution using coprecipitation technique and then was modified by stearate anions surfactant *via* ion exchange reaction. As a result, the basal spacing of the LDH was increased from 8.77 to 24.94°. The infrared spectrum of stearate- Zn_3Al LDH exhibited the existence of stearate anions in the synthesized Zn_3Al LDH. Mechanical properties with 2 wt% stearate- Zn_3Al LDH loading nanocomposites showed 56 wt% improvements in elongation at break compared to those of the blend.

In the paper entitled “*A novel synthesis method of porous calcium silicate hydrate based on the calcium oxide/polyethylene glycol composites*,” a novel method was developed to prepare porous calcium silicate hydrate (CSH) using the calcium oxide/polyethylene glycol (CaO/PEG_{2000}) composites as precursors. The reactivity of silica materials (SiO_2) was enhanced by increasing the pH value. Ca^{2+} could not sustain the release from CaO/PEG_{2000} and reacted with SiO_3^{2-} caused by silica to form CSH until the hydrothermal temperature reached 170°C, avoiding the hardly dissolved intermediates formation efficiently. The as-prepared CSH, due to the large specific surface areas, exhibited excellent release capability of Ca^{2+} and OH^- . This porous CSH has potential application in reducing the negative environmental effects of continual natural phosphate resource depletion.

We hope that these papers provide the reader with knowledge in this topical area and directions for future research.

Acknowledgment

We wish to express our sincere thanks to all the authors for submitting their interesting contributions to this special issue.

*Fan Dong
Ranjit T. Koodali
Haiqiang Wang
Wing-kei Ho*

Review Article

Removal of Hazardous Pollutants from Wastewaters: Applications of TiO_2 - SiO_2 Mixed Oxide Materials

Shivatharsiny Rasalingam, Rui Peng, and Ranjit T. Koodali

Department of Chemistry, University of South Dakota, Vermillion, SD 57069, USA

Correspondence should be addressed to Ranjit T. Koodali; ranjit.koodali@usd.edu

Received 6 February 2014; Accepted 26 March 2014; Published 16 June 2014

Academic Editor: Fan Dong

Copyright © 2014 Shivatharsiny Rasalingam et al. This is an open access article distributed under the Creative Commons Attribution License, which permits unrestricted use, distribution, and reproduction in any medium, provided the original work is properly cited.

The direct release of untreated wastewaters from various industries and households results in the release of toxic pollutants to the aquatic environment. Advanced oxidation processes (AOP) have gained wide attention owing to the prospect of complete mineralization of nonbiodegradable organic substances to environmentally innocuous products by chemical oxidation. In particular, heterogeneous photocatalysis has been demonstrated to have tremendous promise in water purification and treatment of several pollutant materials that include naturally occurring toxins, pesticides, and other deleterious contaminants. In this work, we have reviewed the different removal techniques that have been employed for water purification. In particular, the application of TiO_2 - SiO_2 binary mixed oxide materials for wastewater treatment is explained herein, and it is evident from the literature survey that these mixed oxide materials have enhanced abilities to remove a wide variety of pollutants.

1. Introduction

The energy demand is expected to be greater than 25 TW by the year 2050. This increase is expected to pose undue burden on natural resources and create challenges for sustaining our environment and quality of human life. In addition to energy, the demand for clean water is also expected to rise rapidly due to increasing global population. In addition, with the expeditious pace of industrialization, the disposal of industrial effluents poses threats to the environment and is becoming the biggest concern for the sustainable development of human society. Wastewater reclamation and recycling are essential goals to protect the global ecosystem and improve the quality of the environment. Several methods have been utilized for the removal of pollutants from contaminated water sources [1–9]. Among them, advanced oxidation processes (AOP) have emerged to be promising, efficient, economic, and reliable for the removal of pollutants from aquatic environments [4, 9, 10]. Among the various AOP methods, heterogeneous photocatalysis, using titanium dioxide (TiO_2) based photocatalysts, has emerged as a viable process for degrading a wide variety of pollutants [11–13].

Although TiO_2 has several important properties, such as ease of synthesis, excellent photostability, nontoxicity, and valence bands that are located at high positive potentials, there are several drawbacks that impair the performance of TiO_2 in photocatalytic processes. The absorbance of TiO_2 is limited to the UV region, and, thus, only a small fraction of the solar spectrum is utilized. The fast recombination of the photoinduced electron-hole pairs impedes the efficiency of the overall photocatalysis reaction. In addition, the relatively low surface area of TiO_2 limits the number of adsorptive sites of the target pollutant molecule. To overcome these aforementioned challenges, researchers have developed TiO_2 based mixed oxide materials that can provide large number of adsorptive sites by dispersion of TiO_2 species into a porous support with large surface area. Silica has been widely employed as a robust and stable mesoporous support for immobilizing photoactive TiO_2 species. The TiO_2 - SiO_2 mixed oxide photocatalysts have shown significantly enhanced activities compared to pure TiO_2 for a number of photocatalytic reactions for environmental remediation. The improved photocatalytic performance over TiO_2 - SiO_2 mixed oxide materials can be accredited to the presence of

highly dispersed TiO_2 species in the SiO_2 support, the better adsorption of the pollutant, and the presence of Ti-O-Si bonds that favor the activation of the organic pollutant [14].

In this review, we will first discuss the different types of aqueous pollutants followed by a discussion of selected removal techniques and their basic principles. Then, a brief overview of the synthesis methods of titania-silica (TiO_2 - SiO_2) mixed oxides is presented. This is followed by an extensive description of available characterization techniques of periodic and aperiodic titania-silica catalysts. Following this, the heterogeneous photocatalytic degradation of several pollutants, in particular, organic materials in aqueous phase, is discussed. Finally, the factors that influence the degradation reactions are critically reviewed.

1.1. Aquatic Pollution. Clean water is the most important and indispensable resource that maintains the demands for the daily activities of every aspect of human society, such as drinking, cleansing, industrial manufacture, and farm irrigation. However, the squandering of clean water at discretion and careless handling of wastewater to aquatic systems from households and industries severely contaminate the quality of natural aquatic environments. In general, the sources that result in water pollution can be classified as point and non-point sources [15]. The former one contains pollutants that are discharged from industries, septic materials, animal feedlots, mines and oil industries, and so forth into water sources [16]. The latter one includes runoffs from agriculture, sediment, animal wastes, and so forth [17]. Nonpoint sources, due to their irregularity, are more difficult to be tracked compared to point sources [18]. However, according to the Environmental Protection Agency (EPA), nonpoint sources are claimed to be the major cause of aqueous pollutants. The existence of these pollutants in water systems can cause serious environmental issues and pose threat to public hygiene and health. For instance, the contamination of groundwater by pesticides can endanger aquatic ecosystems. As the fertilizer is discharged into water sources, it can boost the multiplication of algae, which interrupts the oxygen level and upsets the ecological balance in the water system. Moreover, close contact or drinking of the contaminated water can cause skin rashes and other severe diseases like typhoid fever and stomach illness in humans. Waste inorganic and/or organic chemicals, in particular heavy metal ions, in the water may be ingested by fish and may also cause infection in humans, who catch and consume it. In the following section, the most commonly occurring hazardous pollutants along with their effects will be discussed.

1.2. Hazardous Pollutants. The most commonly observed hazardous wastes that threaten the global aquatic system can be divided into four groups according to the classification by the EPA: (i) hazardous wastes from nonspecific industrial processes, (ii) hazardous wastes from specific industrial sources, (iii) commercial chemical products, and (iv) toxic wastes. The EPA estimates that the above-mentioned pollutants have been increasingly detected during the past few decades in rivers, lakes, and oceans. In the following part, we

will discuss the some important inorganic and organic wastes in water.

1.2.1. Inorganic Wastes

Anionic Wastes. Phosphates (PO_4^{3-}) and nitrates (NO_3^-) are the most prevalent pollutants in contaminated surface water [19, 20]. Phosphorus (P) and nitrogen (N) are indispensable elements used in fertilizers for agriculture. Application of extensive amounts of P and N containing fertilizers on arable lands causes extensive accumulation of the phosphate (PO_4^{3-}) and nitrate (NO_3^-) in the soil. Due to the use of manual irrigation and/or natural rainfall, phosphates and nitrates can leach into ground and surface water sources, such as rivers and lakes. In addition to the P and N containing fertilizers, the manure from livestock is also a major source of phosphate and nitrate contaminants in water systems.

The contamination of water by nitrates poses a threat to the health of humans and other animals. Nitrate is found to be extremely toxic at high concentrations in water. It has been postulated to be the origin of methemoglobinemia in infants and it can cause toxic effects on livestock. Although phosphorus is not as toxic as nitrate in water, it can stimulate the growth of algae in water along with nitrate pollutants. Their excessive discharge to the surface water sources can lead to severe eutrophication in surface water sources. Eutrophication is the most widespread water contamination in global aquatic systems and it brings about numerous negative aftermaths to the environment and ecosystem. The most commonly observed consequence of eutrophication is that it causes the multiplication of algae and aquatic weeds, which give bad odor and taste of water in the aquatic systems, and prevents the use of such polluted systems as sources for clean water for industry, agriculture, and humans. In addition, eutrophication can induce the growth of phytoplankton and zooplankton in various aquatic environments. Besides, eutrophication is considered to be the cause for the disappearance of coral reefs and the extinction of several fish species.

Cyanides are another important class of anionic pollutants. Cyanides, which can be generated from either anthropogenic or natural sources, commonly exist in the form of cyanide salts, such as sodium cyanide and potassium cyanide, or in gaseous phase as hydrogen cyanide. Cyanides can be discharged into aquatic system from carelessly treated industry sewage, coal gasification, electroplating operations, and incomplete combustion of fuels. Cyanides cause severe threat to human life as the cyanide anion (CN^-) is recognized to be highly toxic. The ingestion and/or inhalation of cyanide anion (CN^-) by humans can lead to low vitamin B_{12} levels in the human body and can be lethal.

Cationic Wastes. The most commonly seen inorganic cationic wastes in aquatic systems are heavy metal ions, such as lead (Pb^{2+}) [21], arsenic ($\text{As}^{3+/5+}$) [22], mercury (Hg^{2+}) [23], chromium (Cr^{6+}) [24], nickel (Ni^{2+}) [25], barium (Ba^{2+}), cadmium (Cd^{2+}) [26], cobalt (Co^{3+}) [27], selenium (Se^{2+}) [28], and vanadium (V^{5+}) [25]. These above-mentioned heavy metal ions can be introduced into aquatic system via diverse

means [29]. For example, large amounts of heavy metal ions are produced from natural processes, such as weathering, volcano activities, and crustal movement. As in the modern society, the major sources of heavy metal pollutants are from human/industry activities, for instance, printed board and semiconductor manufacturing, metal finishing and plating, industrial dyeing processes, and so forth. Many heavy metal ions, for example, Fe^{3+} , Zn^{2+} , Cu^{2+} , Mn^{2+} , Co^{3+} , Ni^{2+} , and so forth, are actually essential trace elements (required in less than 100 mg per day) to maintain the daily metabolism of the human body. However, these heavy metal ions exhibit fatal toxicity and can poison humans and animals under excessive exposure and close contact. The indication of heavy metal poisoning in humans can be divided into acute and chronic symptoms. Acute symptoms include fatigue, hallucinations, headache, nausea, numbness, and abdominal pain. Chronic symptoms contain anxiety, dyslexia, lack of concentration, migraines, and so forth. Therefore, the removal of heavy metal ion pollutants from aquatic system is indispensable.

1.2.2. Organic Wastes. Organic pollutants are toxic molecular compounds and can cause significant diseases in humans, when exposed to high concentration levels. These organic compounds originate from a variety of industrial products such as detergents, petroleum hydrocarbons, plastics, organic solvents, pesticides, and dyes, and they can be found in diverse environments. In addition, these organic pollutants are a threat to wildlife and human, due to long-term deleterious effect and chemical complexity. In particular, thousands of persistent organic pollutants (POPs) are a family of chemicals consisting of a diverse group of organic substances, which are toxic, bioaccumulative, and prone to long range of transport [30–33]. It was reported elsewhere that POPs mainly differ in the level of chlorine substitutions and persist in the environment with long lives particularly in soils, sediments, and air [34]. They are released into the environment via municipal and industrial wastes, landfill effluents, agricultural practices, and so forth and undergo various reactions that validate their prevalence. There are a wide number of pollutants listed under the toxic and hazardous categories and some of the main types are detailed here.

Aliphatic organic compounds are mainly runoffs from the surface and are particularly seen in urban areas. In addition, the petroleum oils and the byproducts from the combustion of oil also are mostly aliphatic compounds. A variety of aliphatic organic compounds, that include alkenes, alkynes, dichlorodifluoromethane, 1,2-dichloroethane, 2-propanol, and tetramethylammonium ions, have been reported as toxic pollutants from aquatic environment mainly from surface runoffs. Polycyclic aromatic hydrocarbons (PAH) are another type of organic substances released to the environment from the incomplete combustion of organic substances including wood, carbon, and oil. They are neutral, nonpolar organic molecules consisting of two or more fused benzene rings and reported as a priority pollutant by the EPA [35]. The extensive use of polychlorinated biphenyls (PCBs) in numerous industrial processes, electrical transformers,

capacitors, carbonless copy paper, and plastics increases their penetration into the environment.

Surfactants are among the most versatile group of organic compounds utilized in industrial, household, personal care, and health products [36]. Owing to their existence in anionic, cationic, nonionic, and amphoteric forms, they have the ability to alter the physicochemical state of the natural habitat. At high concentrations, they can form complexes in water and cause harmful effects to microorganisms. Pesticides are another type of organics found in diverse chemical structures and are used for various agricultural and nonagricultural applications such as herbicides, insecticides, fungicides, and germicides. Dyes are colored substances that have strong affinity for the substrate to which it is being applied. Dyes are applied to numerous substrates such as textiles, leather, plastic, and paper. Dyes can be classified under different categories according to their application method, chemical structure, usage, or the type of chromophore present in them [37].

Phenol and phenolic compounds byproducts formed from many industrial processes, such as the manufacturing of herbicides, plastics, polymer precursors, photographic developers, dyes, drugs, and pulp and paper industry [38]. In addition, incomplete mineralization of the phenolic compounds ends up with natural organic byproducts that include humic substances, lignins, and tannins, which are prevalent in our environment. The toxicity of phenols and phenol derivatives is mainly attributed to the ease of donation of free electrons, forming phenoxy radicals and intermediates. These phenoxy radicals can penetrate the cell and damage membranes of endoplasmic reticulum, mitochondria, and nucleus and also their components like enzymes and nucleic acids. Furthermore, exposure to phenol may damage the skin through its reaction with amino acids in the epidermis [39].

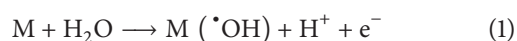
2. Removal Techniques

Continuous increase of pollutants in water bodies has necessitated the need to develop cost-effective methods for their removal. Destroying the pollutants to benign chemicals and/or removing these pollutants from contaminated water is imperative for a green environment. There are numerous treatment processes that have been applied for pollutant removal from wastewater, such as electrochemical oxidation [40], biodegradation [41, 42] membrane process [43], coagulation [44, 45], adsorption [46–49], precipitation [50], sonochemical degradation [51, 52], micellar enhanced ultrafiltration, and AOP [4, 9, 10]. Though these methods are considered as efficient methods for pollutant removal, each method has its own benefits and drawbacks. In this section, we will explain some of the most common methods that are frequently used for pollutant removal and their basic principles.

2.1. Electrochemical Oxidation. Electrochemical oxidation is an efficient and economic method, suitable when the wastewater contains nonbiodegradable organic pollutants. This method poses several advantages since it does not require

auxiliary chemicals, high pressures, or high temperatures. In addition, owing to its versatility and cost-effectiveness, electrochemical techniques have gained great attention for the removal of pollutants. The process of electrochemical oxidation mechanism is mainly based on the generation of the hydroxyl radicals at the electrode surface.

Two different types of mechanisms have been elaborated for electrochemical oxidation, such as direct and indirect oxidation methods [53]. In direct electrochemical oxidation, the degradation of organic compound occurs directly over the anode material, where the hydroxyl radical ($\cdot\text{OH}$) or the reactive oxygen species react with the organic compound. The pollutants are first adsorbed at the surface of the anode and are then degraded by an anodic electron transfer reaction as given by



In the indirect electrochemical oxidation, the organics are treated in the bulk solution by oxidants, such as $\cdot\text{OH}$, Cl_2 , hypochlorite (ClO^-), peroxodisulfate ($\text{S}_2\text{O}_8^{2-}$), and ozone (O_3), which are electrochemically generated at the electrode surface. Even though high removal efficiencies are achieved by both the direct and indirect electrochemical oxidation processes, their effectiveness strongly depends on the treatment conditions including pH, current density, types and concentration of pollutants, supporting electrolyte, flow rate, electrode preparation method, and nature of the electrode materials. Several electrode materials that include Pt, PbO_2 , Ti- SnO_2 , Ti/Pt, Ti/Pt-Ir, Ti/ PbO_2 , Ti/ $\text{PdO-Co}_3\text{O}_4$, Ti/ $\text{RhO}_x\text{-TiO}_2$, Ti coated oxides of Ru/Ir/Ta, IrO_2 , Ti/ RuO_2 , SnO_2 , PbO_2 , and so forth, and boron doped diamond (BDD) [6, 54–73] have been listed as efficient electrodes for the degradation of organics by electrochemical oxidation. Apart from these anode materials, graphite anodes are also considered as efficient materials for anodic oxidation of several organic pollutants [6, 62]. Particularly, the high oxygen overpotential, high electrocatalytic activity, chemical stability, long lifetime, and cost-effectiveness have been credited for the high efficiency of these graphite electrodes. In a recent publication, Govindaraj et al. investigated the electrochemical oxidation of bisphenol A (BPA) from aqueous solution using graphite electrodes [6]. The effect of the supporting electrolyte (type and concentration), initial pH, and applied current density on the performance was discussed in their work. The oxidation of polyhydroxybenzenes was conducted using a single-compartment electrochemical flow cell as illustrated in Figure 1 [56]. Diamond-based material was used as the anode and stainless steel was used as the cathode.

The effectiveness of this electrode was evaluated by monitoring the concentration of BPA. Chemical oxygen demand (COD) removal of 78.3% was obtained, when 0.05 M NaCl was used as the electrolyte at an initial pH of 5 and a current density of 12 mA/cm^2 . In a different study, the effect of different types of supporting electrolytes in the degradation of phenol using BDD electrode was studied by Alencar de Souza and coworkers [70]. The electrochemical performance was examined by measuring COD and the concentrations of all phenolic compounds formed during the electrolysis process.

The oxidation kinetic constants using different electrolytes were found to be in the following order: $k_{\text{Na}_2\text{SO}_4} \approx k_{\text{Na}_2\text{CO}_3} > k_{\text{H}_2\text{SO}_4} > k_{\text{H}_3\text{PO}_4}$. However, the addition of chloride ion to the electrolyte solution caused a major change in the reaction kinetics, and the rate constants were found to be in the following order: $k_{\text{H}_2\text{SO}_4} > k_{\text{Na}_2\text{SO}_4} > k_{\text{Na}_2\text{CO}_3}$. The difference in the reaction kinetics was explained by the oxidation mediated by the chloride ions, which was formed at low pH values. Though the concentration of chloride ions helped to rapidly increase the reaction rate, increment in the supporting electrolyte concentration also assisted to improve the reaction kinetics. Apart from the above-mentioned studies, there are several reports describing the utilization of BDD for oxidation of several organics such as salicylic acid [68], nitrophenol [73], nitrobenzene [72], and tetracycline [66]. A brief review regarding the application of BDD for incineration of synthetic dyes towards environmental application [67] and another review article by Martínez-Huitle and Ferro providing clarity for the electrochemical oxidation of organic pollutants are available [53].

2.2. Biological Process. In the 1990s, biological processes were used for the removal of heavy metal due to the reactive ability of microorganisms with a variety of pollutants that include organic and inorganic species. It was recognized that the microorganisms influence the mobility of the metal by modifying the chemical and physical characteristics of the metals [93]. Recently, Lu et al. investigated a novel biological filter with bacterial strain of *P. putida* immobilized in Calcium alginate granules for removal of formaldehyde in the gas phase [94]. The effects of inlet concentration, empty bed residence time, and nutrient feeding rate on the performance of the system were examined in their study. It was found that the removal efficiency of the dripping biofilter system increased from 68.6% to 93.5%, when the inlet formaldehyde concentration was in the range of 0.2 to 1.34 mg/m^3 . Among the various technologies, such as adsorption [95], chemisorption, photocatalytic oxidation [96], and botanical filtration [97], that have been tried for the removal of formaldehyde, the complete removal is still a challenging problem due to low kinetics, byproduct formation, and low efficiency using any of the above-mentioned methods. However, biological degradation technology with high removal efficiency has been successfully applied in industries for effluents and waste gas treatments. Even though biological processes have been used for several applications that include heavy metal ion removal and indoor air purification, its application has not been intensely investigated for numerous reasons. Thus, researchers have combined biological process with other techniques such as chemical processes [98, 99], photocatalysis [100], and AOP [74, 101, 102].

Combined biological and chemical degradation methods were carried out to evaluate the effectiveness of mature municipal landfill leachate in laboratory scale by Di Iaconi and coworkers. The biological treatment was followed by chemical oxidation for further removal of COD [98]. Higher removal efficiency was obtained due to the use of chemical treatment. In another study, a combined AOP and biological process was carried out to remove pesticides in aqueous

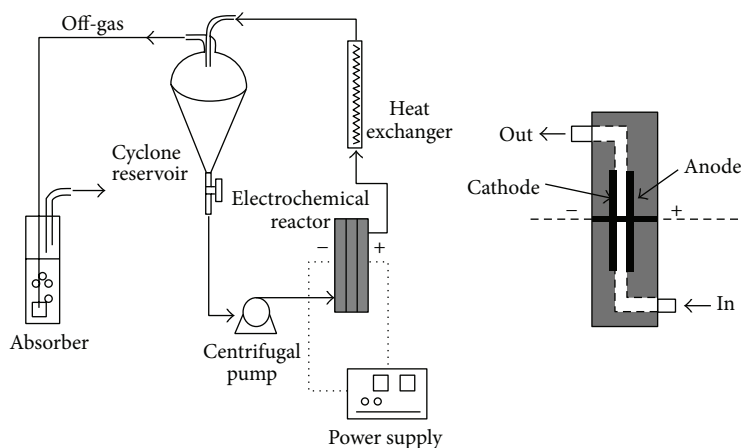


FIGURE 1: The pilot plant arrangement and illustration of electrochemical cell (reprinted with permission from [56]).

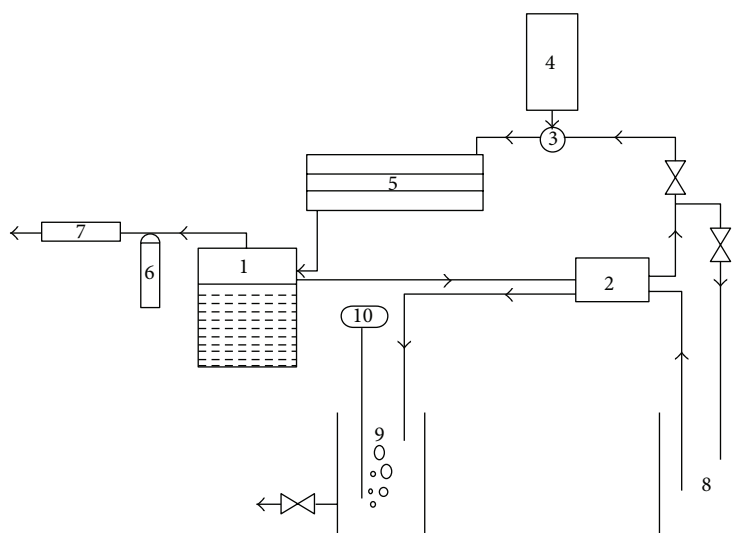


FIGURE 2: Experimental setup for combined chemical and biological degradation: (1) chemical oxidation tank, (2) peristaltic pump, (3) diffuser valve, (4) ozone generator, (5) UV emitting device, (6) excess KI trap, (7) ozone destruction device, (8) neutralizer, (9) biological treatment tank, and (10) air sparger (reprinted with permission from [74]).

solution [74]. The experimental setup for their study is illustrated in Figure 2. The chemical oxidation process was carried out in the tank labeled as 1. The UV emitting device (labeled as 5) consists of a stainless steel tube with a coaxial mercury vapor lamp. Ozone was produced from air by an ozone generator and was continuously fed into the oxidation tank. Finally, the pH of the system was adjusted to 7, and then the pollutant was fed to the biological treatment tank labeled as 9.

It was found that O_3 and O_3/UV oxidation treatment was able to achieve 90 and 100% removal of the pesticide deltamethrin, in a period of 210 min. Utilization of ozone with UV irradiation was found to enhance the degradation of pesticides. It has been well documented elsewhere that the rate of pesticide removal mainly depends on both the chemical nature of the pesticides being treated [103] and the treatment conditions [104]. In a different study, a sequential UV and biological degradation of a mixture of

4-chlorophenol, 2,4-dichlorophenol, 2,4,6-trichlorophenol, and pentachlorophenol were tested with an initial concentration of 50 mg/L [105]. Under their reaction conditions, pentachlorophenol degraded faster compared with other phenolic compounds and 4-chlorophenol degraded the slowest. A combined biological and chemical procedure was also used as an ecologically and economically favorable remediation technique for 2,4,6-trinitrotoluene (TNT) reduction in contaminated ground and surface water [106, 107]. It was observed that the anaerobic transformation process resulted in a faster reduction of TNT due to significant change in the redox potential of the solutions under both aerobic and anaerobic conditions. Biodegradation of organic pollutants by halophilic bacteria was carried out by Le Borgne and coworkers [108].

In a very recent study, wastewater from a pharmaceutical formulation facility in Israel was treated with a biological activated-sludge system followed by ozonation [101].

This work was aimed at reducing the concentrations of carbamazepine (CBZ) and venlafaxine (VLX), before their discharge into the municipal wastewater treatment plant, and they achieved efficient removal of the drugs by this collective method. The byproducts identified from the incomplete oxidation of ozonation were likely to be more biodegradable than the parent compounds; thus, a postozonation biological treatment was endorsed for the efficient removal of these toxic pharmaceuticals from the wastewater. A recent review has discussed the chemical and biological treatment technologies for leather tannery chemicals and wastewaters [109]. It was concluded from the review that there has not been a full scale application of emerging technologies using AOP to remove xenobiotics present in tannery wastewater, and, thus, there is an opportunity for researchers to explore this aspect. In addition, adsorption process has been widely used as an efficient technique for the removal of a variety of toxic pollutants and this is discussed in Section 2.3.

2.3. Adsorption. Adsorption is an effective and well-known process and has been widely explored as an alternate technique compared with the other waste removal methods due to the lower cost, flexibility and simplicity of design, and ease of operation. Moreover, adsorption does not result in production of any harmful substances. Discharge of several types of pollutants that include household wastes, phenolic wastes [46], dyes [110–112], pesticides [113], herbicides, and metal ions [114, 115] into the water body causes health issues not only for humans but also for aquatic life.

Dyes have been identified as a major contaminant in wastewater. Many industries, such as textile, leather, paper, plastics, food, and cosmetics, use several dyes as coloring materials [49]. Most of these dyes are very toxic, and when released into the environment, they can be transported over long distances in water sources resulting in their widespread dispersal. More than a million tonnes of dyes and coloring materials are produced annually, and the drinking water quality is greatly affected by the unsafe release of these dyes into the water body [44, 45]. In addition, the presence of even very small amounts (<1 ppm) of dyes, in particular the synthetic dyes, in water is undesirable. Therefore, the presence of dyes in wastewater is a major concern for toxicological and esthetical reasons.

Adsorption is a method that is capable of removing nondegradable waste pollutants. There are several adsorbents that include clay minerals [46, 116], activated carbon [82, 117], coal [111], wood, fly ash [118, 119], and biomaterials [108, 120–122] that have been listed for the removal of industrial wastes. However, due to the lack of effective adsorbate-adsorbent interactions, some of the above-mentioned materials are found to be noneffective for the adsorption of pollutants. Consequently, oxide materials, which are considered as an important class of adsorbents, have been explored for adsorption. In this regard, silica gels [123], zeolites [116, 124], Al_2O_3 [110], SiO_2 [81, 125, 126], and TiO_2 [14, 127] have been studied as adsorbents for removal of color effluents. The materials used and the factors influencing the adsorption will be extensively discussed in this section.

First, a brief discussion about the principle and equations related to some of the adsorption isotherms is made. Generally, the equilibrium adsorption capacity q_e (mol/g) is estimated by using

$$q_e = \frac{(C_o - C_e)V}{m}, \quad (2)$$

where C_o is the initial concentration of the pollutant (analyte); C_e is the equilibrium concentration of the pollutant (analyte); V is the volume of the analyte solution; m is the adsorbent mass.

A wide variety of equilibrium isotherm models that include Langmuir, Freundlich, Dubinin-Radushkevich, Temkin, Flory-Huggins, and Hill isotherms that have been classified under two parameter isotherms, and Redlich-Peterson, Sips, Toth, Koble-Corrigan, Khan, and Radke-Prausnitz isotherms grouped under three parameter categories [114, 128–130] are available. Among these, Langmuir, Freundlich, and Redlich-Peterson isotherms are the most commonly used models in adsorption studies and are detailed here.

The Langmuir isotherm has been applied to a variety of pollutant sorption processes, which involve homogeneous surfaces and negligible interaction between the adsorbed molecules. In addition, monolayer adsorption on the adsorptive site is the main assumption, in the Langmuir adsorption process, and the saturated monolayer adsorption capacity can be obtained using the following formula [128]:

$$q_e = \frac{q_m K_L C_e}{1 + K_L C_e}, \quad (3)$$

where q_e is the amount adsorbed per unit mass of adsorbent; q_m is the saturated monolayer sorption capacity; K_L is the sorption equilibrium constant (Langmuir constant); C_e is the equilibrium concentration of the solution. The above Langmuir isotherm equation can be arranged in four different linear forms which are named as Langmuir-1, Langmuir-2, Langmuir-3, and Langmuir-4. Among these, Langmuir-1 and Langmuir-2 are widely used to find the adsorption capacity [130]. The relevant equations are as follows:

$$\begin{aligned} \frac{C_e}{q_e} &= \left(\frac{1}{q_m} \right) C_e + \frac{1}{K_L q_m} && \text{Langmuir-1,} \\ \frac{1}{q_e} &= \left(\frac{1}{K_L q_m} \right) \frac{1}{C_e} + \frac{1}{q_m} && \text{Langmuir-2,} \\ q_e &= q_m - \left(\frac{1}{K_L} \right) \frac{q_e}{C_e} && \text{Langmuir-3,} \\ \frac{q_e}{C_e} &= K_L q_m - K_L q_e && \text{Langmuir-4.} \end{aligned} \quad (4)$$

Freundlich expressed an empirical equation, known as the Freundlich adsorption isotherm, in 1906. The relationship between the concentration of the solute in equilibrium, C_e , and the amount adsorbed, q_e , is a constant, K_F , and is expressed as follows:

$$q_e = K_F C_e^{1/n}. \quad (5)$$

The constants $1/n$ and K_F are calculated using the linearized form by taking the logarithm of the Freundlich isotherm as shown in the following equation:

$$\log q_e = \log K_F + \frac{1}{n} \log C_e. \quad (6)$$

The Freundlich isotherm can be applied for nonideal adsorption as well as multilayer adsorption processes.

The Redlich-Peterson equation is another popular model and has three different parameters commonly named as A , B , and g . The combination of the Langmuir and Freundlich models is given by the Redlich-Peterson isotherm, and the mechanism does not obey the monolayer adsorption. Several authors suggest that this model is appropriate for the sorption of metal ions over wide range of concentrations. At high concentration, the Redlich-Peterson approaches the Freundlich isotherm, and, at lower concentration, it follows the Langmuir model. The Redlich-Peterson model is given by the following equation:

$$q_e = \frac{AC_e}{1 + BC_e^g}. \quad (7)$$

By using the subsequent linearized form of the above equation, the constants A , B , and g can be obtained:

$$\frac{C_e}{q_e} = C_e^g \frac{B}{A} + \frac{1}{A}. \quad (8)$$

A large number of materials have been employed as adsorbents for removal of pollutants and they include natural materials, such as clays, coal, fly ash, zeolites and other siliceous materials, biomaterials, agricultural and industrial solid wastes, activated carbon, oxides, and mixed oxide materials.

Natural materials are well known as adsorbents from the beginning of recorded human development. In particular, clays have been utilized as an adsorbent and as an ion-exchange material for the removal of ions and organics due to their low cost, natural abundance, high adsorption capacity, and ion-exchangeable property [49, 131–134]. In the past decades, clay minerals such as bentonite, diatomite, and kaolin have garnered increasing interest due to their ability to adsorb both inorganic and organic materials. In particular, the adsorption of methylene blue (MB) dye molecule has been extensively studied over different clay minerals [131, 133, 135–138]. Apart from these clay minerals, zeolites and siliceous materials, such as silica, glass fibers, and perlite, deserve specific attention for wastewater treatment, as a result of their high availability and stability.

Fly ash is another type of natural material, which is relatively abundant and inexpensive and is currently being explored as an adsorbent for the removal of various organic pollutants that are present in wastewater, such as phenolic compounds, pesticides, and dyes. It has been documented elsewhere that these contaminants can be effectively removed by using fly ash as an adsorbent [49, 118, 119, 139]. In addition, the efficiency of fly ash is improved by converting the fly ash into zeolites [140] and mesoporous materials, such as MCM-41 and MCM-42 [141].

Biomaterials are another type of natural materials, which are mainly used for adsorption and degradation for water treatment applications. A few publications have discussed the adsorption of hazardous and toxic pollutants using biological materials [142–144]. The use of biomass for water treatment is gaining attention due to their availability in large quantities at low cost, in particular, for the removal of heavy metals [93, 142, 143], dyes [145–148], and phenols [149]. Srinivasan and Viraraghavan have examined various biosorbents including fungi, bacteria, algae, chitosan, and peat for decolorizing dye wastewaters and the mechanism(s) involved. In addition, the effects of various factors that influence dye wastewater decolorization and also the methods for increasing the biosorption capacity of the adsorbents are critically examined in this review [5]. The removal efficiency of pollutants by these biomaterials was enhanced by the attachment of polymers [150].

Activated carbon is another important, efficient, and commercially available material that consists of a wide variety of pores in it. Even though the adsorption process proceeds through a sequence of diffusion steps from the bulk phase into the mesopores followed by diffusion into the micropores, the major adsorption sites on activated carbon were reported to be located in the micropores [151, 152]. The studies on the adsorption of dyes using activated carbon and its derivatives have been widely discussed, and the ability of intake on the activated carbon was found to be increased, when adsorbates with relatively higher molar mass and lower water solubility were used [2, 151, 153, 154]. Annadurai and coworkers utilized activated carbon for the adsorption of rhodamine 6G (R6G) molecule [117]. The effects of particle size, temperature, and solution pH on the adsorption were examined in their study, and a maximum dye adsorption of 44.7 mg/g was obtained under their operating condition (temperature of 60°C, pH of 7, and particle size of 0.5 mm). It was observed that increasing the temperature and decreasing the particle size influenced the amount adsorbed, whereas little impact was noticed from changes in the solution pH towards adsorption. In addition, it has been noted that the intraparticle diffusion of dye molecules within the adsorbents was the rate limiting step in the adsorption process.

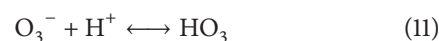
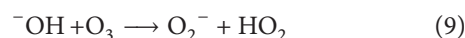
In a recent literature, Prola et al. used multiwalled carbon nanotubes (MWCNT) and powder activated carbon (PAC) for the adsorption of direct blue 53 dye from aqueous solution [155]. The isotherm model was best fit with the Sips isotherm model and the maximum adsorption capacities were found to be 409.4 and 135.2 mg/g for MWCNT and PAC, respectively. In addition to the dye molecules, adsorption of metal ions was also achieved by using activated carbon as an adsorbent. Adsorption of copper ions [156, 157] and chromium ions [158], from aqueous solutions by activated carbon, has been documented in recent publications. Furthermore, the influence of surface chemistry of activated carbon on the removal of nitrate ions from water was analyzed by Ota and coworkers [159]. Additionally, the removal of surfactants was also carried out over the activated carbon surface [36, 160]. Apart from the applications of pure activated carbons, modification methods and effects of activated carbon for water treatment have been extensively clarified in some

review articles suggesting the importance of activated carbon for the uptake of pollutants from the water environment [161, 162]. Even though the above-mentioned natural materials and activated carbon have been used as adsorbents, owing to the lack of effective adsorbate-adsorbent interactions, a number of the above-mentioned materials are found to be inactive for the adsorption of organics in the polluted water. Thus, only moderate adsorption capacity can be achieved by using some of these adsorbents.

Oxides constitute an important class of adsorbents, and, in this regard, zeolites [163], silica gels [123, 164], SiO₂ [92, 165], Al₂O₃ [110], and TiO₂ [166–170] have been established as effective adsorbents for the removal of several water pollutants. Microporous aluminosilicate materials (zeolites) are three-dimensional structures with negatively charged lattice. Owing to their high ion-exchange capability, relatively high surface area, and low cost, zeolite materials are good adsorbents and their usefulness has been reviewed by Ghobarkar et al. [171]. Another naturally abundant oxide material, silica, has earned much attention for pollutant removal due to the presence of silanol groups [172, 173]. In addition to high surface area and mechanical stability, the porous nature of silica makes it attractive for decontamination applications. However, due to its low resistivity towards the alkaline media, the application of silica is limited below pH level of 8 [173]. Furthermore, the acidic silanol groups provide strong and irreversible adsorption, in comparison with other surface functional groups. Even though the silica materials have this limitation, their high adsorption capacity for the removal of pollutants compared with other oxide materials, TiO₂, Al₂O₃ [14], and ZrO₂ [174] makes them attractive. Although adsorption is viewed as a promising water treatment method for industrial applications, it does not degrade the pollutant since the adsorption process merely removes pollutants from the aqueous phase and transfers them onto a solid matrix [175]. Thus, AOP have emerged as efficient methods for the mineralization of organic pollutants.

2.4. Advanced Oxidation Processes (AOP). AOP is an oxidation technique, which typically uses ambient conditions (room temperature and atmospheric pressure). Several AOP techniques such as ozonation, H₂O₂ photolysis, Fenton process, photo-Fenton process, and heterogeneous photocatalysis have been explored for the elimination of pollutants, particularly from water sources. These AOP techniques destroy the pollutants by chemical oxidation or reduction. In particular, AOP relies on the production of hydroxyl radicals ([•]OH), which are short-lived, extremely highly reactive species and attack most organic molecules with rate constants of 10⁻⁶ – 10⁻⁹ M⁻¹ s⁻¹. Moreover, the versatility of AOP is enhanced by different possible ways for the production of hydroxyl radicals. It is beyond the scope of this review to provide a review of all the AOP techniques in depth and the methods and materials used. Instead, we will cover the basic principles of selected AOP methods and their applications. Our focus is directed towards the use of TiO₂-SiO₂ materials for pollutant removal, in this review.

2.4.1. Ozonation. Ozone is unstable in water and the chemical properties of ozone rely on the experimental conditions. The molecular ozone can react as a dipole, electrophile, or nucleophile due to the two different resonance structures. In addition, depending on the pH, temperature, and concentration of organic and inorganic compounds in water, the half-life of ozone varies from a few seconds up to a few minutes. Ozone is a powerful oxidant and it can oxidize a large number of organic and inorganic materials. Ozone reacts either directly or indirectly with aqueous compounds. In the direct reaction, the molecular ozone directly reacts with the compounds, whereas the [•]OH radicals resulting from the decomposition of ozone (expressed in the following equations [12–15]) react with the compounds in the indirect reactions [176]:

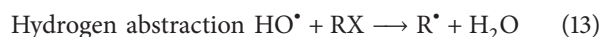


The direct reactions are very slow and solute selective, whereas the indirect radical reactions are fast and nonselective. Additionally, the direct reactions are dominant in acidic solutions, while the indirect reactions occur mostly at basic pH values. It was reported elsewhere that catalytic ozonation significantly enhanced the rate of oxidation more than noncatalytic ozonation [177], and, thus, catalytic ozonation has received much attention in wastewater treatment for removal of pollutants, such as phenolic compounds [177, 178]. Turhan and Uzman have reported the removal of phenol from water using ozone [179]. Ozonation of phenol gave catechol, hydroquinone, *p*-benzoquinone, *o*-benzoquinone, maleic acid, and oxalic acid as the ring cleavage intermediate products and it was noticed that some of the intermediates such as catechol, hydroquinone, and *p*-benzoquinone can be destroyed completely using ozone to CO₂ and H₂O. However, destruction requires long ozonation time and high dosage of ozone. It was reported by Hoigné and coworkers that the hydroxyl radicals are the active species in the decomposition of organics. Furthermore, they have reported that the amount of [•]OH radicals determined the ozonation efficiency and the effect of these [•]OH radicals in the reaction kinetics during ozonation was examined by utilizing [•]OH radical scavengers. However, studies towards the direct determination of the amount of [•]OH radical produced during the ozonation process are scarce [180].

Einaga and coworkers carried out catalytic oxidation of benzene with ozone over several support materials, such as Al₂O₃, SiO₂, TiO₂, and ZrO₂, and they found that the surface area of the catalysts is one of the important factors that affect the reaction. In addition, they carried out oxidation of benzene with ozone over several Mn ion-exchanged zeolite catalysts, such as Mn-Y, Mn-b, Mn-MOR, and Mn-ZSM-5 to investigate the effect of catalyst support on the reaction [181]. Mn-Y catalyst exhibited high activity for complete oxidation of benzene and formed CO_x without release of any organic

byproducts under moderate conditions. However, formic acid was formed with supported manganese oxide catalysts, Mn/SiO₂ and Mn/SiO₂-Al₂O₃ [182]. Recently, Einaga et al. have reported the effect of catalyst composition and preparation conditions on catalytic properties of Mn-based oxides for benzene oxidation with ozone. In their studies, they have compared the catalytic properties of several Mn oxides, from the standpoint of activity, product distribution, and efficiency of ozone utilization [183]. Even though chemical oxidation with ozone is considered as one of the effective techniques for treatment of wastewater, in some cases, ozone is used in combination with other treatments, particularly with biological treatment, to improve the degradation rate of pollutants [74, 101, 102, 104, 184, 185].

2.4.2. UV/H₂O₂ Treatment. H₂O₂ treatment in AOP also involves the formation of •OH radicals generated by the photolysis of H₂O₂ in the presence of UV irradiation and is very effective for the degradation of most of the organic pollutants. Owing to the higher molar absorption coefficient of the peroxide anion, the photolysis rate has been found to be pH dependent and increases at high pH values [186–188]. It was documented elsewhere [186] that the generated •OH radicals react with the organic substrate by three different mechanisms as listed below:



Owing to the commercial availability, thermal stability, infinite solubility in water, storage, and ease of formation of hydroxyl radical, the use of hydrogen peroxide as an oxidant has received significant attention for water purification. However, the rate of formation of hydroxyl radicals influences the oxidation of organic contaminants and this has been noted as the main disadvantage of the UV/H₂O₂ treatment process. Several studies have utilized the UV/H₂O₂ process for degrading organic compounds in aqueous media. Cater et al. used UV/H₂O₂ treatment to remove methyl *tert*-butyl ether (MTBE), a pollutant commonly found in gasoline contaminated in groundwater [187]. In their study, they have examined the effectiveness of UV/H₂O₂ treatment in the oxidation of MTBE. The degradation of MTBE was found to obey pseudo-first-order kinetics and showed good efficiency with the figure-of-merit electrical energy per order (E_{EO}) in the range of 0.2–7.5 kWh/m³/order. In another study, removal of naproxen, a nonsteroidal anti-inflammatory drug, was carried out by UV/H₂O₂ process by Felis et al. [189]. A 93% removal of naproxen was achieved after 3 min. of treatment with UV/H₂O₂ at pH = 6. In addition, they have obtained lower rate, when naproxen was subjected to aerobic or anaerobic treatment prior to the UV/H₂O₂ treatment. Wu et al. achieved a 100% removal of dimethyl sulfoxide (DMSO) when used with H₂O₂/UV treatment after 3 hours of degradation at pH = 3 [190]. In this study, the DMSO concentration was kept at 1,000 mg/L, and the H₂O₂

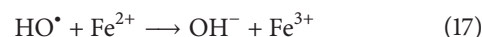
concentration was kept the same as that of DMSO with 5.5 mW/cm² UV irradiation intensity at a temperature of 25°C. In contrast, a lower decomposition (83%) was attained at a pH of 10, at the same temperature and the same period of time. According to this study, an acidic medium is more effective for the degradation of DMSO.

There are a large number of organic pollutants, such as phenols and phenolic compounds, benzene and substituted benzene, salicylic acid, proline, pyridine, and dyes [191], that have been degraded or mineralized using UV/H₂O₂ treatment. However, this treatment method is not the focus of this study. In addition to the UV/H₂O₂ treatment for oxidation of pollutants, another process involves the use of O₃/UV. Even though H₂O₂ increases the generation of •OH radicals in the ozone process, the cost of this process is too high due to the combination of two different processes, O₃/UV and O₃/H₂O₂. Shu and Chang utilized this combined process for the decoloration of textile dye C.I. Direct Black 22 [191, 192]. From their findings, it was noticed that the ozonation process took less time to remove the color than the H₂O₂/UV process. The H₂O₂/UV method removed 99% of total organic carbon (TOC) from the effluent. Consequently, a combination of both methods was proposed in order to achieve good efficiency. It has been noted that this combined method is mainly used for the removal of color effluents from wastewater due to its high efficiency for removal of both TOC and color [193].

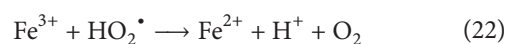
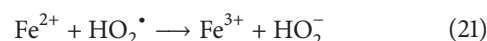
2.4.3. Fenton Reaction. Fenton reaction is a homogeneous catalytic oxidation process that uses a mixture of hydrogen peroxide (H₂O₂) and ferrous ions. Due to its simplicity and the availability of chemicals, this oxidation is considered as an advanced technique for waste removal. In acidic environment, H₂O₂ and Fe²⁺ ions in the contaminated solution produce hydroxyl radicals expressed as follows:



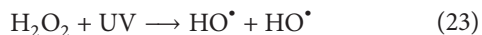
The decomposition of H₂O₂ is initiated by the ferrous ion and results in the formation of hydroxyl radical (HO•). These hydroxyl radicals, which are powerful oxidizing agents, then attack substrates and chemically decompose them. However, these hydroxyl radicals can be scavenged by reaction with Fe²⁺ and/or H₂O₂, by the following equations:



In addition, Fe³⁺, which is formed during the reaction, regenerates Fe²⁺ ions by reacting with H₂O₂ as per the following equations:



An extended Fenton reaction, named photo-Fenton reaction, takes advantage of UV irradiation for the formation of hydroxyl radicals in addition to the above-mentioned equations and is described by (23) and (24). Under these irradiation conditions, Fe^{2+} is regenerated by the photolysis of the Fe^{3+} ions/complex. Consider



There are several reports that have examined the applications of Fenton and photo-Fenton reactions. For example, Gutowska et al. studied the degradation mechanism of Reactive Orange 113 in aqueous solution by using $\text{H}_2\text{O}_2/\text{Fe}^{2+}$ [194]. In another report, a comparative study of Fenton and photo-Fenton oxidative decolorization was carried out against Reactive Black 5 (RB5). The pH, H_2O_2 , and Fe^{2+} dosage, dye concentration, and initial concentration ratios between $[\text{Fe}^{2+}]:[\text{H}_2\text{O}_2]:[\text{RB5}]$ were varied in their study. The optimal ratios were found to be $[\text{H}_2\text{O}_2]/[\text{RB5}]$ of 4.9:1 and $[\text{H}_2\text{O}_2]/[\text{Fe}^{2+}]$ of 9.6:1, with pH of 3. Even though both the Fenton and photo-Fenton reactions effectively decolorized the RB5 dye with 97.5 and 98% efficiency, the TOC removal rates were found to be significantly different. A significant removal (46.4%) was obtained with photo-Fenton reaction, whereas only 21.6% TOC removal was observed with the Fenton reaction. This result indicates that UV irradiation plays an important role in the mineralization of the RB5 dye. Elmolla and Chaudhuri degraded antibiotics amoxicillin, ampicillin, and cloxacillin in aqueous solution by the photo-Fenton process and examined the effects of UV irradiation, $\text{H}_2\text{O}_2/(\text{COD})$ and $\text{H}_2\text{O}_2/\text{Fe}^{2+}$ ratios, pH, and the initial concentration of antibiotics. They obtained complete degradation within 2 min., under the following optimal conditions: $\text{H}_2\text{O}_2/\text{COD}$ molar ratio of 1.5, $\text{H}_2\text{O}_2/\text{Fe}^{2+}$ molar ratio of 20, and pH of 3 [195]. Even though there are several reports that acknowledge the applicability of the Fenton and photo-Fenton oxidation for a variety of organics, large-scale industrial operations seem to be lacking; however, pilot plant studies show promise.

2.4.4. Heterogeneous Photocatalysis. Heterogeneous photocatalysis is a process, which embraces a large variety of reactions such as oxidation, dehydrogenation, metal deposition, organic synthesis, water splitting, photoreduction, hydrogen transfer, isotopic exchange, disinfection, anticancer therapy, water detoxification, and gaseous pollutant removal [196, 197]. Heterogeneous photocatalysis is considered as an effective AOP technique, particularly for air and water purification treatment. Heterogeneous photocatalysis can be carried out in gas or liquid phases, and the overall process can be explained by five different reactions: (i) transfer of the reactants in the fluid phase to the surface, (ii) adsorption of at least one of the reactants, (iii) reaction in the adsorbed phase, (iv) desorption of the product(s), and (v) removal of the products from the interface region [75]. Commonly, the heterogeneous photocatalysts are semiconductors, such as titanium dioxide (TiO_2), which can produce electron-hole

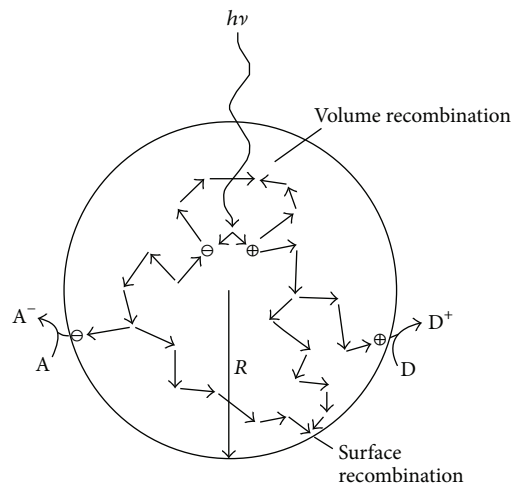
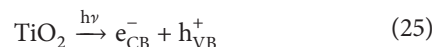


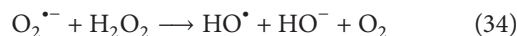
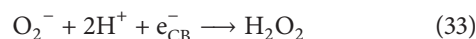
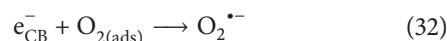
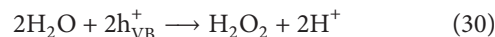
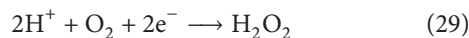
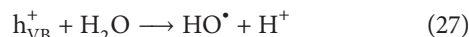
FIGURE 3: Recombination of electrons and holes within a semiconductor particle in the presence of acceptor (A) and donor (D) (reprinted with permission from [75]).

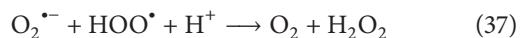
pairs by the illumination with photons whose energy is equal to or greater than the bandgap of the semiconductor as shown by



The electron-hole pairs then dissociate into free photoelectrons in the conduction band and holes in the valence band are produced [75, 196, 198, 199]. The photoefficiency can be reduced by the surface or volume recombination of the electron-hole pairs either in the bulk or at the surface as depicted in Figure 3. Thus, recombination is undesirable and is detrimental to the photocatalytic activity.

In this photocatalysis process, the contaminant molecule gradually breaks down by its reaction with highly reactive oxidative species (ROS), such as HO^\bullet , $\text{O}_2^{\bullet-}$, and HOO^\bullet , which can be generated during the illumination process by the following equations [197, 200–203]:





Among all these ROS, it has been widely noted that hydroxyl radicals are the most potent and important species responsible for the degradation of pollutants. Table 1 shows a comparison of the various removal techniques.

Frank and Bard have reported the heterogeneous photocatalytic oxidation of cyanide and sulfite in the presence of several semiconductors that include TiO_2 , ZnO , CdS , Fe_2O_3 , and WO_3 , in aqueous medium under sunlight [204]. It was noticed that TiO_2 , ZnO , and CdS showed good activity for cyanide oxidation, and no oxidation was seen using Fe_2O_3 and WO_3 . In addition, the rates of the photocatalytic oxidation were found to be greater for sulfite than cyanide. Among these oxides, titanium dioxide (TiO_2) is an effective semiconductor material that has been explored for numerous applications including adsorption [168, 169], heterogeneous photocatalysis for splitting of water [205, 206], solar cell applications [207], and degradation of pollutants.

The removal of inorganic anions that include cyanide [208–210], nitrite [211], and sulfite [204] has been studied in the presence of TiO_2 . In addition, the degradation of variety of pollutants that include several dye molecules [11, 13, 212–216], phenol and phenol derivatives [12, 46, 217, 218], and salicylic acid [219, 220] has also been researched.

Even though TiO_2 has been utilized as a photocatalyst for the degradation of a number of pollutants, its efficiency towards degradation is partly limited owing to its poor adsorptive property. In order to improve the efficiency of titania, researchers have prepared mixed oxide materials that can provide greater number of adsorptive sites; furthermore, by generating highly porous structures with large surface areas, effective dispersion of titania can also be achieved [221, 222]. Among the various mixed oxides, titania-silica has met the expectations of several researchers, due to the high surface area and the hydrophobic nature of silica [14].

3. Titania-Silica (TiO_2 - SiO_2) Mixed Oxides

As discussed in the previous section, the presence of various inorganic and organic hazardous pollutants in the aquatic system poses a huge threat to public hygiene and human health. Hence, effective and economic means of remediating the polluted water sources need to be developed. Several conventional methods for removal of hazardous materials from wastewater, such as physical adsorption, condensation, biofiltration, and catalytic destruction [7], show varying degree of efficiencies in wastewater treatment. However, these above-mentioned traditional wastewater treatment techniques face several drawbacks or limitations: (i) physical adsorption method only immobilizes the pollutants onto solid adsorbent instead of degrading them into harmless materials, (ii) the condensation and/or biofiltration methods show relatively low efficiency and only a limited number of pollutants can be treated in this manner, and (iii) catalytic

destruction processes are normally carried out under harsh conditions, such as extremely high temperatures (sometimes as high as 900°C). Therefore, an improved technique that presents high remediation efficiency that can be carried out under moderate conditions is desired. AOP, which are applicable at ambient temperature and pressure conditions, are recognized to be an ideal technique for environmental remediation. Extensive research interest has been devoted into heterogeneous photocatalysis and promising results have been obtained for the removal of highly toxic and nonbiodegradable pollutants that are commonly found in industrial wastewaters.

The following sections will briefly provide an overview of the synthesis of TiO_2 - SiO_2 mixed oxides and an extensive discussion about the applications of TiO_2 - SiO_2 mixed oxide materials towards the degradation of aquatic pollutants will also be carried out. A variety of synthetic methods have been reported for the preparation of periodic mesoporous materials, which are materials with uniform, regular, and well-arranged pores, and aperiodic TiO_2 - SiO_2 mixed oxide materials that have randomly arranged pores. Thus, some of the main preparation methods followed by the structural characterization of titania-silica are presented here. Finally, the photocatalytic activity of these TiO_2 - SiO_2 materials will be elaborated in great depth. Consequently, the factors that influence the photocatalytic activity such as the structural properties of the photocatalysts, pollution type and concentration, and pH will also be reviewed.

3.1. Periodic TiO_2 - SiO_2 Mixed Oxide Materials. Among numerous semiconductor materials, there has been considerable interest in the use of TiO_2 as a photocatalyst to degrade a variety of pollutants in water [196, 223–225]. However, the photocatalytic performance of TiO_2 is significantly constrained by the fast recombination of the photogenerated electron-hole pair. In addition, its large bandgap energy (3.2 eV in anatase), low adsorption efficiency, surface area, and porosity restrict the widespread application of TiO_2 photocatalysts.

In order to promote AOP in practical applications, TiO_2 based photocatalysts with large specific surface area and porosity that is conducive to adsorption of aquatic pollutants need to be developed. A common strategy is to incorporate TiO_2 into periodic mesoporous support materials such as SiO_2 . Periodic mesoporous SiO_2 materials possess high surface area, tunable pore size, and large pore volume that facilitate good dispersion of TiO_2 and adsorption of pollutant molecules as well.

In recent years, TiO_2 has been incorporated into highly ordered mesoporous siliceous materials such as SBA-15, MCM-41, and MCM-48. These periodic mesoporous siliceous supports with very high surface area and long-range ordered array of mesopores are recognized to be robust and stable supports for immobilizing TiO_2 species. In addition, the large surface area of mesoporous SiO_2 enables the high dispersion of TiO_2 species. With the above-mentioned merits, TiO_2 containing periodic mesoporous materials are expected to achieve markedly enhanced efficiencies for the

TABLE 1: Different removal techniques and its advantage(s) and disadvantage(s).

Removal techniques	Advantage(s)	Disadvantage(s)
Electrochemical oxidation	Does not require auxiliary chemicals, high pressures, or high temperatures.	Low selectivity and low reaction rates.
Biological process	Ecologically favorable process.	High capital and operational cost. Handling and disposing the secondary sludge pose problems.
Adsorption	Cost-effective method. Easy availability and operation. Most profitable process and more efficient than the conventional methods (i.e., precipitation, solvent extraction, membrane filtration, etc.).	Merely removes the pollutants from one phase (aqueous) to another (solid matrix). Expensive process for regeneration especially if the pollutants are strongly bound to the adsorbents.
Advanced oxidation processes (AOP)		
(i) Ozonation	Powerful oxidation technique oxidizes a large number of organic and inorganic materials.	More complex technology and requires high capital/operational cost. High electric consumption.
(ii) UV	An effective method that typically does not leave any byproducts which are harmful to the environment.	Less effective if the wastewater has high amounts of particulates which can absorb UV light.
(iii) UV/H ₂ O ₂	An effective technique in the oxidation and mineralization of most organic pollutants. Ease of formation of [•] OH radicals.	Less effective, when the wastewater has high absorbance. High operational cost.
(iv) O ₃ /UV/H ₂ O ₂	Most effective process due to the fast generation of [•] OH radicals. Can treat a wide variety of contaminants.	Needs to compete with high turbidity, solid particles, and heavy metal ions in the aqueous stream. High operational cost.
(v) Fenton reaction	Simple process. Easy availability of chemicals.	Production of sludge iron waste and handling the waste pose logistical problems.
(vi) Photo-Fenton reaction	Reduction of sludge iron waste compared to original Fenton reaction. Effective and fast degradation.	Needs a controlled pH medium for better performance.
(vii) Heterogeneous photocatalysis	Long-term stability at high temperature. Resistance to attrition. Low-cost and environmentally benign treatment technology.	Could form byproducts that can be harmful to the environment. Requires efficient catalysts that can absorb in the visible region.

photocatalytic degradation of aqueous wastes in comparison with nonsupported TiO₂.

In this section, the commonly conducted synthetic methods for the preparation of TiO₂ containing periodic SiO₂ mesoporous materials will be discussed. In addition, typical characterization techniques along with examples in which TiO₂ containing periodic SiO₂ mesoporous materials are used as photocatalysts for degradation of aqueous pollutants will also be covered.

3.1.1. Ti-SBA-15. SBA-15 is an important mesoporous material that is prepared by the using of triblock copolymers as structure directing agents. Because of its relatively large pore size (>6 nm) and thick pore walls, it has been used as a support to disperse TiO₂.

Synthesis. The synthetic methods for the incorporation of TiO₂ into SBA-15 mesoporous materials are mainly based on sol-gel reactions that include the hydrolysis, condensation, and precipitation of both titania and silica sols. A variety

of synthetic procedures have been designed and developed. Several experimental variables that include solvent, pH, temperature, nature of silica and titania precursor, and surfactant type have been varied with a purpose of obtaining TiO₂ species in different phases and/or immobilizing them in different locations in SBA-15 support. These are discussed in the following section.

(1) *Coprecipitation Method.* In this synthetic route, the titania and silica precursors are introduced to the synthesis pot and they undergo hydrolysis simultaneously. In a typical synthesis, desirable amounts of silica precursor, for instance, tetraethyl orthosilicate (TEOS) or trimethyl orthosilicate (TMOS) along with titania precursor, such as tetraethyl orthotitanate, tetrakispropyl orthotitanate, or tetrabutyl orthotitanate, are added to a solution containing a triblock copolymer such as Pluronic P-123 (poly(ethylene-oxide)₂₀-poly(propylene-oxide)₇₀-poly(ethylene-oxide)₂₀). After sufficient stirring, the suspension is transferred to a Teflon-lined autoclave and subjected to hydrothermal

reaction at temperatures ranging from 100 to 250°C for as long as 24 h. Compared to the synthesis procedures under ambient conditions, the use of higher temperature and pressure in the hydrothermal synthesis ensures the complete hydrolysis of both the silica and titania precursors as well as the successful formation of the hexagonal phased SBA-15 material. In addition, the hydrothermal synthesis also results in the homogeneous distribution of the titania species in the SBA-15 siliceous support and often leads to the establishment of Ti-O-Si heterolinkages that are reported to be highly active in various photocatalytic reactions. After the hydrothermal reaction, a washing procedure is necessary to remove any unreacted precursors. Eventually, the materials are calcined in order to eliminate the surfactant.

(2) *Postimpregnation Method.* Compared to coprecipitation, the postimpregnation method has been studied more frequently. The merits of utilizing the postimpregnation synthetic method for the preparation of titania incorporated SBA-15 can be summarized as follows. First, the hexagonal phase of SBA-15 is more robust to withstand the conditions utilized for the coprecipitation method. Second, by postimpregnation method, titania species can be grafted onto the pore wall or surface of the mesopores of the SBA-15 mesoporous materials rather than to the framework positions. The anchored titania species on the pore walls have a greater probability to interact with reactant molecules that infiltrate the pores of SBA-15. In addition, via the postimpregnation method, a relatively large amount of titania can be loaded in the preformed SBA-15 mesoporous support. Therefore, more available active sites can be generated with higher loadings of titania.

The synthesis of SBA-15 mesoporous materials has been established and well documented [226]. In a typical synthesis route, an appropriate amount of triblock copolymer Pluronic P-123 (poly(ethylene-oxide)₂₀-poly(propylene-oxide)₇₀-poly(ethylene-oxide)₂₀) is added and dissolved in a mixture solution of water and hydrochloric acid. After the addition of silica precursor, for instance, tetraethyl orthosilicate (TEOS), the mixed solution is transferred to Teflon-lined autoclave and subjected to hydrothermal synthesis. The solid product then undergoes filtration, washing, and drying steps and is finally calcined in air to decompose the triblock copolymer to obtain SBA-15. During the postimpregnation synthesis, a variety of titania precursors can be immobilized into the preformed SBA-15 hexagonal structured mesoporous material. A certain amount of preformed SBA-15 is sonicated in isopropanol and this is followed by the addition of the required amount of titania precursor with stirring. Water is then added slowly to the resulting mixture to initiate the hydrolysis of the titania precursor. After the completion of the hydrolysis of titania precursor, the solid is recovered by centrifugation and calcined in the presence of air to give Ti-SBA-15.

3.1.2. *Ti-MCM-41 and Ti-MCM-48.* MCM-41 and MCM-48 belong to the M41S series of mesoporous materials that were originally developed by Mobil research scientists.

These mesoporous materials have been widely employed as supports to disperse TiO₂.

Synthesis. Compared to Ti-SBA-15, the syntheses of titania incorporated into MCM-41 and MCM-48 periodic mesoporous materials require careful control of experimental conditions. The relatively small pore diameters (1.8 to 2.5 nm) and thin pore walls (1.2 to 2 nm) in MCM-41 and MCM-48 make the synthesis of these materials a little challenging. The successful formation of the hexagonal phased mesopores of MCM-41 and the cubic phased mesopores of MCM-48 is extremely sensitive to experimental conditions such as reaction temperature, time, surfactant concentration, precursor concentration, pH, and solvent used in the reaction. The syntheses of titania loaded MCM-41 and MCM-48 mesoporous materials are also based on sol-gel chemistry and can be mainly divided into two categories including coprecipitation and postimpregnation method.

(1) *Coprecipitation Method.* The coprecipitation method of synthesis of Ti-MCM-41 and Ti-MCM-48 is performed similar to Ti-SBA-15. However, instead of using triblock copolymer Pluronic 123, the structure directing agent used in the MCM-41 and MCM-48 synthesis is a cationic surfactant such as cetyltrimethyl ammonium bromide (CTAB). In a typical synthesis, a certain amount of CTAB is dissolved in a solution of water and alcohol. The synthesis gel contains titania and silica precursor, cationic surfactant, ethanol, and aqueous ammonia. Under basic conditions (pH > 8), the silica species exist as polyanions. The cooperative interaction between the silicate anionic species (I⁻) and the cationic surfactant (S⁺) induces a phase separation. With time, the silicate moieties undergo polymerization which decreases their charge density. Concurrently, the surfactant molecules undergo rearrangement to match the charge density at the surfactant-inorganic interface. The final mesophase formed is based on the structure having the lowest interface free energy or chemical potential. Meanwhile, the titania precursor undergoes hydrolysis and condensation to form either Ti-O-Ti or Ti-O-Si linkages. The gel is then transferred to a Teflon-lined autoclave and is typically held at 110°C to carry out the hydrothermal synthesis for as long as 48 h. After filtration, washing, and calcination to remove the surfactant, titania incorporated in MCM-41 or MCM-48 is obtained.

(2) *Postimpregnation Method.* Apart from the coprecipitation method, postimpregnation method is widely conducted for the synthesis of titania modified MCM-41 and MCM-48 mesoporous materials. The postimpregnation method is favored in the preparation of Ti-MCM-41 and Ti-MCM-48 photocatalysts for the ease of synthesis and the preservation of highly ordered hexagonal (MCM-41) or cubic (MCM-48) mesoporous structures. The method is similar to that discussed previously for Ti-SBA-15.

3.1.3. *Structural Characterizations.* The important techniques to characterize the titania containing mesoporous materials are discussed in this section.

Powder X-Ray Diffraction (XRD). Powder X-ray diffraction (XRD) is an informative technique to verify the periodic nature of the mesoporous structures in SBA-15, MCM-41, and MCM-48 materials and, additionally, the crystallinity and phases of the embedded titania species may also be inferred from powder XRD studies.

Figure 4 shows the low-angle XRD patterns of a series of titania loaded SBA-15 mesoporous materials [76]. In all of the XRD patterns for the $\text{TiO}_2/\text{SBA-15}$ samples, it can be observed that, in the range of 2θ between 0.8° and 2° , three well-resolved peaks are observed. These are ascribed to the reflections due to d_{100} , d_{110} , and d_{200} and demonstrate the characteristic hexagonal space group $P6mm$ in SBA-15 periodic mesoporous materials. With the addition of various amounts of titania, the intensity of the peaks due to intrinsic reflections in SBA-15 materials decreases subtly. This small decrease in the peak intensity in the titania loaded samples can be explained by the incorporation of titania in the mesopores of the SBA-15 that results in the less scattering contrast between the pores and pore walls. However, the relatively inappreciable change in the d_{100} , d_{110} , and d_{200} reflections indicates that the SBA-15 is a robust and stable support for immobilizing titania species.

Apart from the low-angle XRD, long-range XRD analysis was also carried out to investigate the nature of the titania species in the Ti-SBA-15 mesoporous materials. Figure 5 presents the wide-angle XRD patterns for a series of titania incorporated SBA-15 samples and a pure SBA-15 as reference [77]. It can be seen that the pure SBA-15 sample shows a broad peak at around $2\theta = 25^\circ$. This peak is due to the presence of amorphous silica that is the predominant phase in SBA-15. In addition, at relatively low loadings of titania (from 7% to 22%), as shown in Figures 5(b) to 5(e), the XRD patterns only show a broad peak at $2\theta = 25^\circ$ due to SBA-15. This phenomenon is most likely due to the high dispersion of the titania species in the large surface area SBA-15 mesoporous materials. Titania clusters are confined within the mesosized pores of SBA-15 and/or maybe amorphous in nature. However, with further increase of the titania loading (26% to 31%), peaks due to bulk TiO_2 can be perceived. This indicates that, in the materials at these two loadings, titania clusters have aggregated to form larger particles on the SBA-15 support.

Similar observations can also be found from the powder XRD analysis for titania incorporated into MCM-41 and MCM-48 mesoporous materials. Kasahara et al. performed powder XRD analysis for titania incorporated MCM-41 mesoporous materials [227]. Typical Bragg reflections of the MCM-41 mesoporous materials with $P6mm$ hexagonal symmetry were observed from the low-angle XRD patterns in all samples. In the wide-angle XRD plot, a characteristic peak due to only amorphous silica located at $2\theta = 25^\circ$ was found. This indicates the high dispersion of titania in the MCM-41 mesoporous support. Thus, low- and high-angle powder XRD experiments are useful in identifying the mesoporous and the titania phase (at high loadings).

Nitrogen Physisorption. In order to investigate the textural properties, such as surface area, pore volume, and pore size

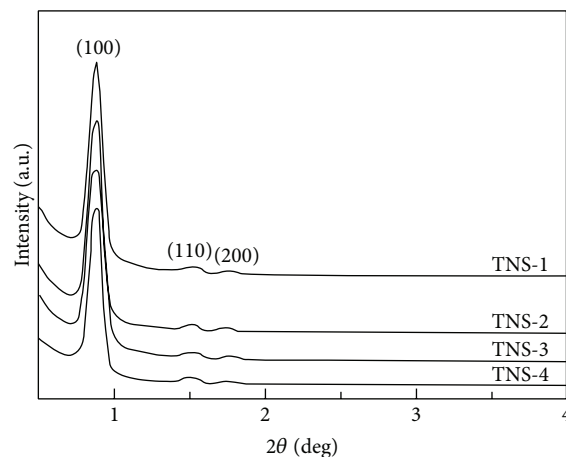


FIGURE 4: Small-angle XRD patterns of $\text{TiO}_2/\text{SBA-15}$ samples (reprinted with permission from [76]).

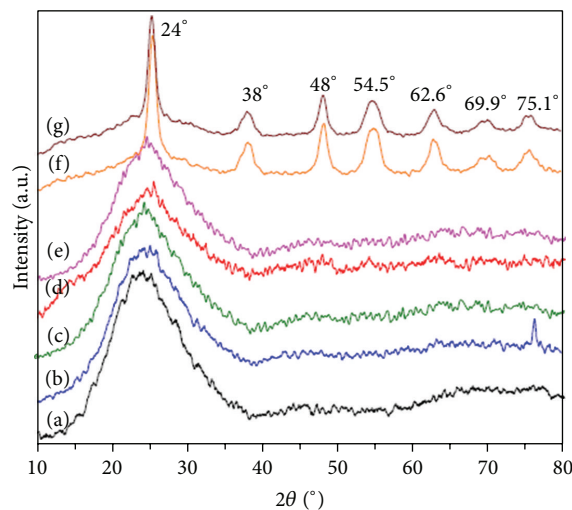


FIGURE 5: Wide-angle XRD patterns of $\text{TiO}_2/\text{SBA-15}$ mesoporous samples with different loadings of TiO_2 : (a) bare SBA-15, (b) 7% TiO_2 , (c) 12% TiO_2 , (d) 18% TiO_2 , (e) 22% TiO_2 , (f) 26% TiO_2 , and (g) 31% TiO_2 (reprinted with permission from [77]).

of titania incorporated into periodic mesoporous materials, nitrogen physisorption studies are carried out.

Figure 6(a) depicts the nitrogen adsorption-desorption isotherms for a series of titania containing MCM-41 mesoporous samples [78].

All the isotherms indicate type IV classification that is typical for mesoporous materials. In addition, a steep inflection that occurs at relative pressure values from 0.2 to 0.4 is an indication of the periodic array of the mesopores in the samples. Figure 6(b) presents the pore size distribution plots of the same batch of samples. The plots exhibit a very narrow pore size that is centered at around 28 \AA indicating their uniformity.

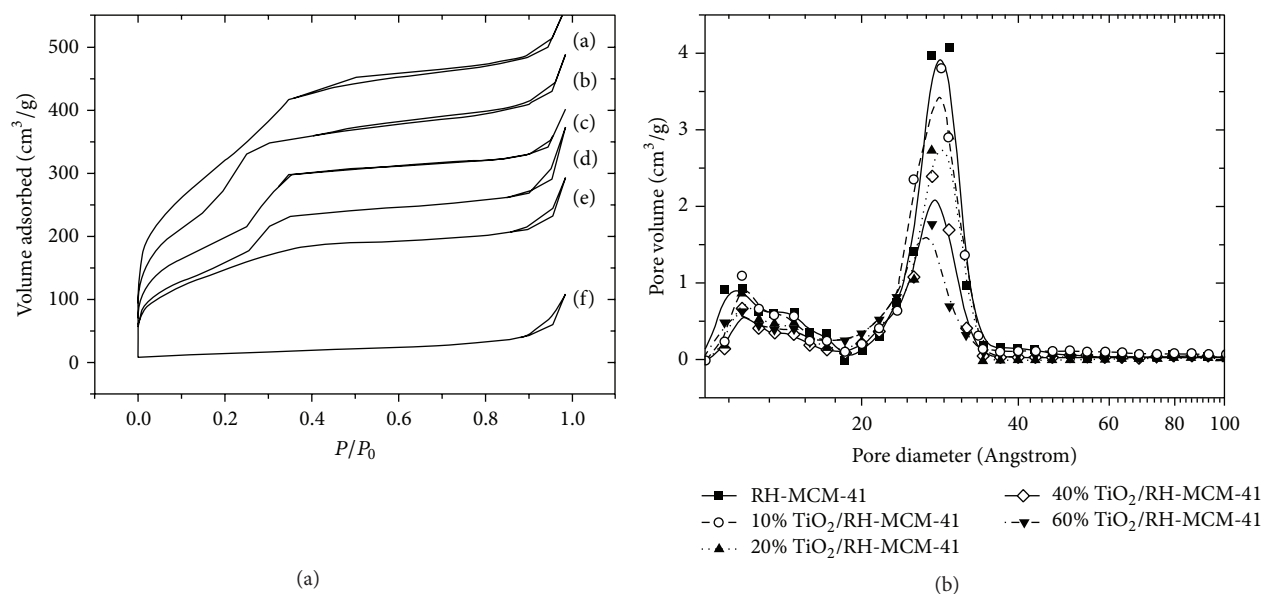


FIGURE 6: (a) N₂ adsorption-desorption isotherm: (a) RH-MCM-41, (b) 10% TiO₂/RH-MCM-41, (c) 20% TiO₂/RH-MCM-41, (d) 40% TiO₂/RH-MCM-41, (e) 60% TiO₂/RH-MCM-41, and (f) bare TiO₂. (b) Pore size distribution in RH-MCM-41 and TiO₂/RH-MCM-41 (reprinted with permission from [78]).

Inductively Coupled Plasma-Atomic Emission Spectrometry (ICP-AES). Depending on the various synthetic and processing methods, the amount of the titania species in the final mesoporous materials may be different from the amount added or expected. This may be due to some unreacted titania precursor or due to loss of weakly adsorbed titanyl species during the washing process. It is important to estimate the actual amount of titania retained in the final mesoporous material. ICP-AES is a commonly adopted analytical technique to accurately determine the actual contents of titania species in the final titania loaded periodic mesoporous materials. Tian et al. performed the ICP-AES analysis for a series of titania loaded MCM-41 samples with variable Ti concentrations [228]. The results indicate that only about one-tenth of the titania content was preserved in the final materials compared with the initially introduced Ti precursors in the synthesis gel. Since there can be significant differences between the amount of titania actually retained in the mesopore matrix and the amount added, it is crucial to estimate the real titania loading in the sample and ICP-AES analysis is an important technique in this regard. It should be pointed out that atomic absorption spectroscopy (AAS) is less useful in comparison to ICP method for determination of titania since refractory materials such as titania are difficult to be quantified by the AAS method.

UV-Vis Diffuse Reflectance Spectroscopy (DRS). DRS is a sensitive tool in understanding the optical properties and the local environment and coordination of Ti⁴⁺ ions in titania containing periodic mesoporous materials. Also, one can estimate the bandgap and particle sizes of TiO₂ by the DRS method. Figure 7 shows the DRS of a set of Ti-SBA-15 samples that contain different Ti amounts [79]. It can be seen that

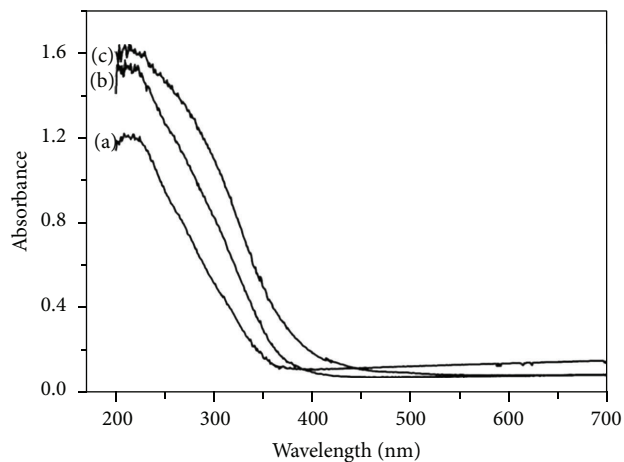


FIGURE 7: Diffuse reflectance UV-Vis spectra of Ti-SBA-(x) materials with varying titania loadings corresponding to (a) Ti-SBA-(6), (b) Ti-SBA-(9), and (c) Ti-SBA-(12) (reprinted with permission from [79]).

the Ti-SBA-15 samples exhibit absorption only in the UV region (<400 nm). Besides, the absorption onset shifts to higher wavelength with an increase of the titania content in the sample. This is due to the formation of the relative large clusters of titania at higher loadings. Apart from the absorption onset, there is an extra band near 214 nm in the sample with the least amount of TiO₂. This band is due to the ligand-to-metal charge-transfer (LMCT) from the O²⁻ to Ti⁴⁺ due to the presence of spatially isolated and tetrahedrally coordinated Ti⁴⁺ in the Ti-SBA-15 sample. With an increase of TiO₂ content in the sample, this band also displays a red

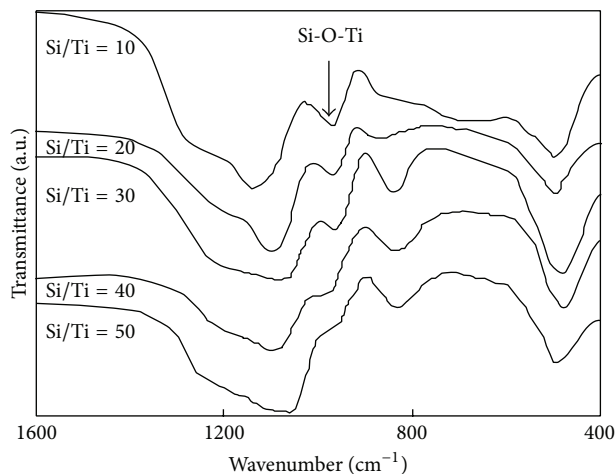


FIGURE 8: FT-IR spectra of Ti-MCM-41 with different Si/Ti ratios (reprinted with permission from [80]).

shift, which indicates that a portion of Ti^{4+} undergoes polymerization to form octahedrally coordinated Ti^{4+} . Hence, by conducting the DRS study, a better understanding of the optical properties and chemical environment of the titania species in the mesoporous materials can be obtained.

Fourier Transform-Infrared (FT-IR) Spectroscopy. FT-IR spectroscopy is widely applied to elucidate the surface environment of the titania containing periodic mesoporous materials. Figure 8 presents the FT-IR spectra of a series of Ti-MCM-41 samples with different Si/Ti ratios [80]. From the FT-IR spectra, an absorption peak appearing at 960 cm^{-1} is observed that may be assigned to the vibration of Ti-O-Si. With an increase of Ti content in the Ti-MCM-41 sample, the peak is observed to be more conspicuous. However, one should be careful in assigning this peak to Ti-O-Si since this vibration is also widely attributed to the presence of Si-O-H group. Thus, the use of FT-IR spectroscopy to infer the presence of Ti-O-Si bond is challenging. Other than this peak, three additional peaks at 440 , 800 , and 1060 cm^{-1} are due to the stretchings from the Si-O-Si support.

Raman Spectroscopy. The crystal phase of titania plays a critical role in photocatalytic reactions. Hence, Raman spectroscopy has been largely conducted to investigate the phase of titania in the periodic mesoporous materials. Figure 9 illustrates the Raman spectra of a series of Ti-SBA-15 samples [77]. In the samples with 26 and 31 wt.% of TiO_2 and pure TiO_2 , Raman bands at 640 , 520 , 400 , and 150 cm^{-1} with an additional shoulder at 200 cm^{-1} can be observed. The peaks at 640 , 200 , and 150 cm^{-1} can be assigned to E_g symmetric mode, the peak at 520 cm^{-1} is due to the combination of both B_{1g} and A_{1g} symmetry, and the peak at 400 cm^{-1} is due to B_{1g} symmetry. The Raman spectra indicate that titania exists in the anatase phase in these materials. For the Ti-SBA-15 samples with the TiO_2 loading lower than 22 wt.%, the peak intensities drop significantly indicating the presence of small sized and/or amorphous titania species. This is caused by the

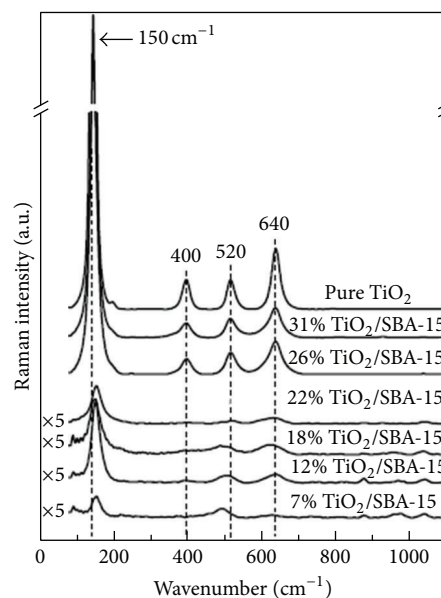


FIGURE 9: Raman spectra of $\text{TiO}_2/\text{SBA-15}$ mesoporous materials with different loadings of TiO_2 and pure TiO_2 samples (reprinted with permission from [77]).

high dispersion of the titania species in the high surface area SBA-15 support at relatively low TiO_2 content.

X-Ray Photoelectron Spectroscopy (XPS). XPS is a useful technique to elucidate the oxidation states of the titania and silica species and to also identify the presence of Ti-O-Si linkages from the peak positions of the binding energies. Figure 10 shows the XPS spectra of O 1s core-level of $\text{TiO}_2/\text{SBA-15}$ mesoporous samples [77]. As can be seen, all of the samples show a clear peak at a binding energy of 532.8 eV . This peak can be assigned to oxygen in bulk silica (Si-O-Si). Apart from the peak appearing at the binding energy of 532.8 eV , an extra peak in the range of $530.0\text{--}530.6\text{ eV}$ can also be observed in all studied samples. This peak can be ascribed to the presence of

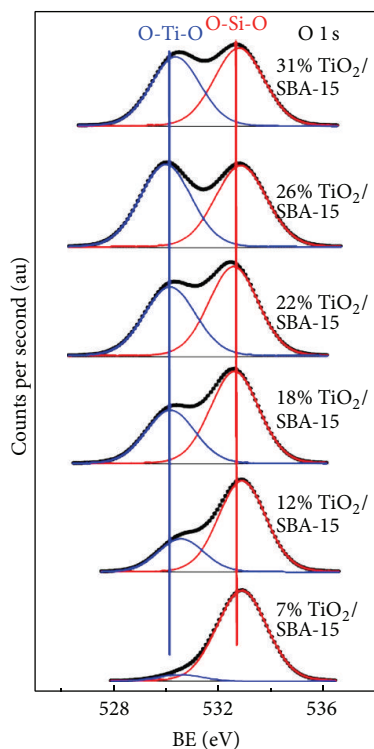


FIGURE 10: O 1s core-level spectra of $\text{TiO}_2/\text{SBA-15}$ mesoporous samples (reprinted with permission from [77]).

oxygen from Ti-O-Ti bonds. In addition, the intensity of the oxygen peak in the Ti-O-Ti species increases with the loading of titania in the samples.

Transmission Electron Microscope (TEM). TEM studies are widely conducted to illustrate the degree of the periodicity and morphologies of the mesoporous structures in various support materials, such as SBA-15, MCM-41, and MCM-48. Although powder XRD and nitrogen adsorption isotherms provide clues regarding the degree of periodicity of the pores, TEM studies can provide unequivocal evidence regarding the uniformity of the pores. Also, TEM can be used to identify the crystallinity and the phase of the titania species within the ordered mesoporous silica support. Figure 11 shows the TEM images of a representative Ti-SBA-15 mesoporous material [83]. Figures 11(a) and 11(b) indicate the highly periodic nature of the SBA-15 mesoporous materials indicating hexagonal phased pores in the materials after the incorporation of titania species. In order to elucidate the nature of titania species, high resolution transmission electron microscopy (HRTEM) and selected area electron diffraction (SAED) studies were carried and the results are shown in Figures 11(c) and 11(d). The d -spacings were determined to be 3.5122, 2.4000, 1.8947, and 1.7561 Å, which correspond to d_{101} , d_{103} , d_{200} , and d_{202} planes of anatase phase, respectively. Hence, the TEM results indicate that titania is in the form of anatase within the pores of SBA-15 periodic mesoporous materials.

Field Emission-Scanning Electron Microscope (FE-SEM). FE-SEM is an instructive instrument to understand the surface

morphologies of the titania loaded periodic mesoporous materials. Figure 12 presents the SEM images of a sequence of titania incorporated SBA-15 materials with two different morphologies [83]. As can be clearly seen from the SEM images, the sample labelled Rod-SBA-15 exhibits uniform rod shaped materials and the length of the rods is fairly similar ($\sim 1 \mu\text{m}$). However, the Normal-SBA-15 shows “wheat” like shape. After the incorporation of titania, both types of SBA-15 samples preserve their original morphologies. This indicates that SBA-15 is a very stable and robust support material for accommodating titania species.

3.1.4. Photocatalytic Reactions. In this section, we will discuss the photocatalytic reactions explored using titania incorporated into periodic mesoporous materials.

Photocatalytic Degradation of Dyes. Photocatalysis is an effective way to decompose dyes, which constitute an important class of pollutant. Among them, the degradation of MB dye has been explored extensively. During the photocatalytic processes, MB can be converted into gaseous CO_2 and inorganic ions such as SO_4^{2-} , NH_4^+ , and NO_3^- . Yang et al. investigated the photocatalytic performance of the Ti-SBA-15 mesoporous materials for the degradation of MB [229]. The removal efficiency of MB was correlated with their adsorption on $\text{TiO}_2/\text{SBA-15}$ mesoporous materials. The dark adsorption study indicated that the uptake amount of MB increased with the surface area of $\text{TiO}_2/\text{SBA-15}$ materials. In addition, the sample with higher surface area presented better photocatalytic performance in the degradation of MB. It is well known that, besides the surface area of the catalyst, other factors, such as crystal phase, crystallite size, and crystallinity of the titania species, also impact the photocatalytic activity. However, the photocatalytic activity is a balance between the surface area and crystallinity. Thus, the $\text{TiO}_2/\text{SBA-15}$ sample with 30% loading of TiO_2 showed the highest photocatalytic activity among all samples due to the high surface area without sacrificing too much crystallinity of TiO_2 . Similar observations can be seen from the works reported by Sahu et al. [226], Zhu et al. [79], and Acosta-Silva et al. [77], in which the anatase TiO_2 nanospecies were incorporated in SBA-15 mesoporous materials to realize the photocatalytic decomposition of MB. The photocatalytic activity of $\text{TiO}_2/\text{SBA-15}$ was shown to be significantly higher than that of pure TiO_2 .

In addition to the structural properties of the photocatalysts, the experimental conditions also had a dramatic influence on the photocatalytic decolorization of MB. Suraja et al. investigated the effect of the reaction time, concentration of MB, and the pH environment over the photocatalysis process [8]. With time, the photocatalytic degradation rate of MB increased due to the larger exposure under the light source. Regarding the concentration of MB, the photocatalytic degradation capacity stayed more or less identical at relatively low ($< 25 \text{ mg/L}$) initial dye concentration. However, after the initial concentration of MB exceeded 25 mg/L , a sudden decrease in the activity was noticed. This can be explained by the fact that, at high concentrations of

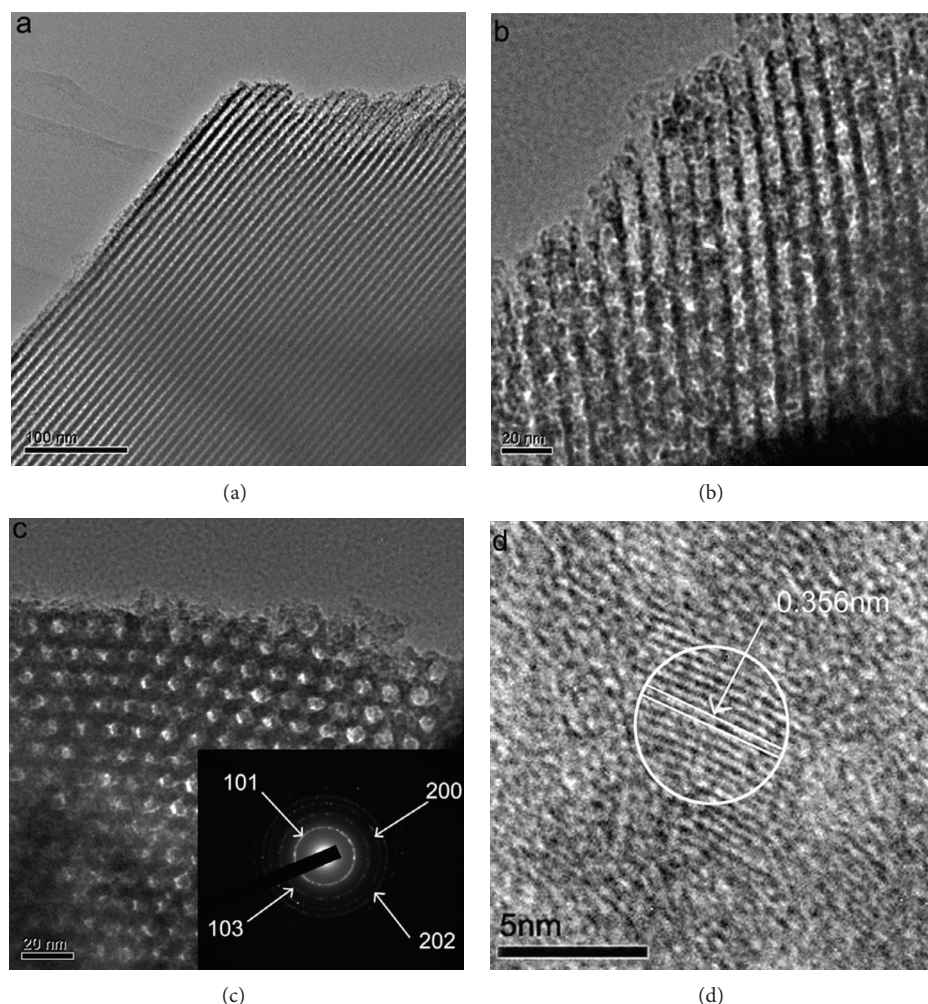


FIGURE 11: TEM images of (a) SBA-15 along [81] direction, ((b) and (c)) TiO₂/SBA-15 along [81, 82] direction (inset shows the SAED pattern), and (d) a typical HRTEM image of TiO₂ nanoparticle encapsulated in the channel of SBA-15 (reprinted with permission from [83]).

MB, irreversible adsorption of MB takes place. The lack of desorption of MB molecules from the surface prevents MB molecules in solution to adsorb at the surface and, thus, the degradation is low at high concentrations of MB. The pH of the solution in the photocatalytic reaction showed a significant impact on the MB degradation efficiency. Either acidic or basic conditions were proven to be detrimental for the MB degradation. The highest efficiency was achieved under neutral conditions.

Besides the hexagonal SBA-15 mesoporous materials, TiO₂ containing cubic MCM-48 mesoporous materials have also been studied for MB photodegradation. Liou and Lai developed TiO₂/MCM-48 composite materials and evaluated their performance for photocatalytic decomposition of MB [230]. Their results indicate that lower loadings of TiO₂ enhanced both adsorption of MB and photocatalytic activities. This was mainly due to the fact that, at high loadings, aggregation of TiO₂ caused clogging of the pores in MCM-48 and brought down their uptake of MB molecules.

At lower TiO₂ contents, high dispersion of titania in the MCM-48 mesoporous materials enabled more efficient contact and reaction with MB molecules.

Rhodamine dyes (R6G and B (RhB)) are also commonly seen as pollutants in the aquatic environment and they can be decomposed by titania incorporated into periodic mesoporous materials. De Witte et al. tested the photocatalytic performance of titania loaded SBA-15 for the photodecomposition of R6G [231]. The TiO₂/SBA-15 sample with larger pore diameters presented superior photocatalytic activity compared to the rest of the samples. This can be explained by the fact that the larger pore sized material facilitated better diffusion of R6G molecules and ensured good contact with TiO₂. Beyers et al. also confirmed the observation that large pore sizes in TiO₂/SBA-15 sample are conducive for the photocatalytic degradation of R6G [232]. In addition, the location (inside or outside of the SBA-15 channels) of the TiO₂ species in the TiO₂/SBA-15 samples and its influence on the photocatalytic activity were studied as well. Tian

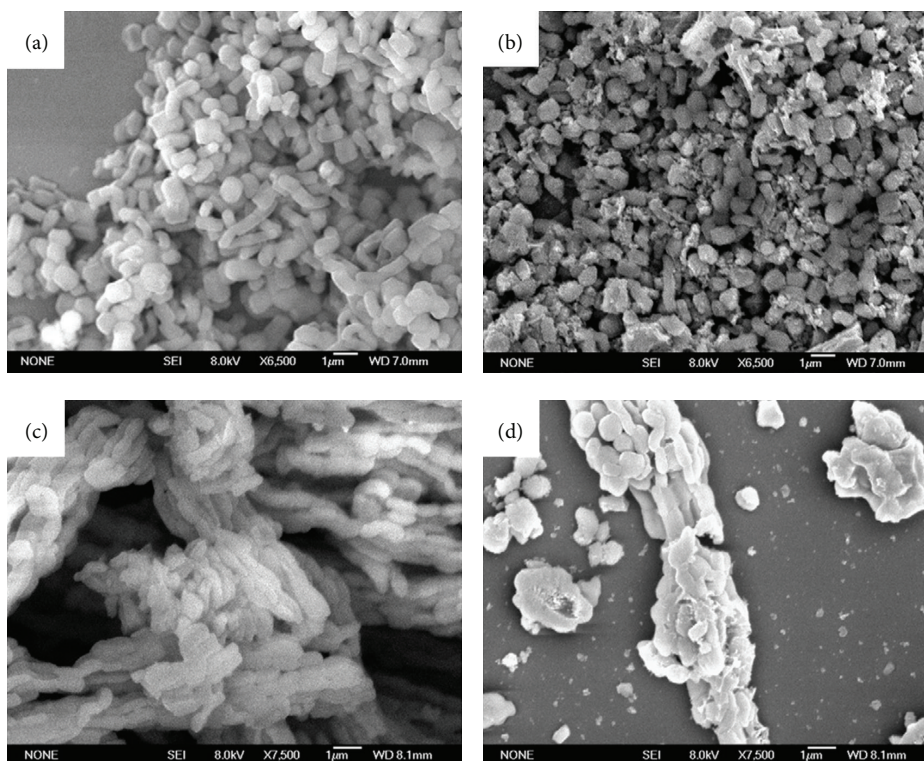


FIGURE 12: SEM images of (a) Rod-SBA-15, (b) $\text{TiO}_2/\text{Rod-SBA-15}$, (c) Normal-SBA-15, and (d) $\text{TiO}_2/\text{Normal-SBA-15}$ (reprinted with permission from [83]).

et al. examined the photocatalytic degradation of RhB by using titania loaded MCM-41 mesoporous materials [228]. It was suggested that the photocatalytic performance was based on both the loading and the position of the titania species. Compared with the pure TiO_2 sample, $\text{TiO}_2/\text{MCM-41}$ exhibited marked enhanced photocatalytic activity for RhB degradation.

Li et al. investigated the photocatalytic properties for methyl orange (MO) degradation over the $\text{TiO}_2/\text{SBA-15}$ mesoporous materials with different morphologies [83]. The rod-like SBA-15 supported sample presented higher photocatalytic activity than that of regular $\text{TiO}_2/\text{SBA-15}$. It was proposed that the rod-like SBA-15 mesoporous materials possessed smaller particle size and shorter channel than the regular SBA-15. In addition, the rod-like SBA-15 particles were arrayed in an ordered manner compared to the random distribution in the regular SBA-15 particles. All these properties in the rod-like SBA-15 materials facilitated the high dispersion of small particles of TiO_2 . Hence, the $\text{TiO}_2/\text{SBA-15}$ with rod-like structure exhibited better photocatalytic activity for MO degradation.

Anandan conducted the photocatalytic degradation of MO by using titania incorporated MCM-41 mesoporous materials and the role of peroxomonosulphate (PMS), peroxodisulphate (PDS), and H_2O_2 as electron accepters was examined in the photocatalytic reaction [233]. Ti-MCM-41 photocatalysts presented dramatically higher activity for MO degradation compared with bare TiO_2 . The enhanced efficiency can be ascribed to the large surface area of MCM-41

support that realized the high dispersion of TiO_2 photoactive species and facilitated the adsorption of MO. Among the electron accepters, PMS displayed the best performance in photodegradation of MO. It was proposed that the presence of PMS effectively brought down the photoinduced electron-hole recombination in TiO_2 and realized the enhanced formation of hydroxyl radicals (OH^*) for the decomposition of MO. PDS showed lower activity due to its limited reactivity with only photogenerated electrons on TiO_2 . H_2O_2 was found to be inert in the photocatalytic process for MO degradation due to its scavenging of hydroxyl radicals (OH^*).

Ding et al. observed that Ti-SBA-15 exhibited enhanced photocatalytic activity for the degradation of indigo carmine (IC) than anatase titania [234]. The enhanced photocatalytic activity in Ti-SBA-15 sample was mostly due to its high porosity and specific surface area and presence of more accessible photooxidative sites. Jyothi et al. developed titania incorporated into hexagonal MCM-41 and cubic MCM-48 mesoporous materials as photocatalysts for the photodecoloration of IC [235]. It was found that the hexagonal Ti-MCM-41 sample showed higher activity for the photodegradation of IC than that over the Ti-MCM-48 sample. This was ascribed to the smaller pore size (2.3 nm) in the MCM-41 mesoporous materials that confined the titania species into relatively small sizes. In contrast, the larger pore size (4.1 nm) of the MCM-48 support resulted in the growth of relatively large titania species. Hence, the MCM-41 sample with smaller titania clusters possessed higher dispersion of titania, which resulted in better photocatalytic performance.

Bhattacharyya et al. applied Ti-MCM-41 materials for the photocatalytic decoloration of Orange II dye [236]. The optimal loading of titania was determined to be 50 wt.%, at which the best adsorption capacity for Orange II dye and appropriate crystallinity and particle size of TiO_2 can be reached. Tseng et al. evaluated the activity of $\text{TiO}_2/\text{SBA-15}$ for the photodecomposition of Acid Red 1 (ARI) dye [237]. The photocatalytic results indicated that $\text{TiO}_2/\text{SBA-15}$ was an effective catalyst for the photodegradation of ARI and improved overall photocatalytic efficiency can be found over $\text{TiO}_2/\text{SBA-15}$ compared with pure TiO_2 . The highest activity was achieved from the sample with 30 wt.% loading of TiO_2 . The nanoscale sized TiO_2 clusters that were confined by the pores of SBA-15, the Ti-O-Si linkages, and the strong surface acidity of SBA-15 were considered to be the three main factors for an enhancement in the photocatalytic decolorization of ARI.

Photocatalytic Degradation of Phenolic Compounds. Phenols constitute another important class of pollutants. Alvaro et al. compared the photocatalytic activity of $\text{TiO}_2/\text{MCM-41}$ and $\text{TiO}_2/\text{SBA-15}$ for phenol degradation [238]. In the $\text{TiO}_2/\text{MCM-41}$ series of materials, the photocatalytic activity increased with increasing content of titania in the samples. However, in the SBA-15 based samples, the photocatalytic activity was maximum at an optimal concentration of titania and then decreased with an increase in titania loading. Comparing the phenol degradation efficiencies between $\text{TiO}_2/\text{MCM-41}$ and $\text{TiO}_2/\text{SBA-15}$ sample, it was observed that, in general, MCM-41 based samples showed higher activities than the SBA-15 based samples for the same loadings of titania. This can be attributed to the higher surface area of the MCM-41 support that enabled efficient dispersion of titania species when compared to SBA-15. Wang et al. assessed the phenol degradation efficiency by using $\text{TiO}_2/\text{SBA-15}$ mesoporous materials [76]. It was found that the photocatalytic efficiency improved with the loading of TiO_2 in the sample. The higher activity of the $\text{TiO}_2/\text{SBA-15}$ sample than that of commercial TiO_2 was attributed to the high specific surface area of the SBA-15 support that favored the diffusion of phenol as well as its good contact with the catalyst.

Adams et al. designed $\text{TiO}_2/\text{SBA-15}$ catalysts in different morphologies (thin film and powder form) to study their activity for the photodegradation of 2,4-dichlorophenol (2,4-DCP) [239]. Under identical experimental conditions, the thin films were able to degrade 2,4-DCP approximately half as fast as compared to the suspension form. The lower activity from the thin film sample was rationalized by its lower absorption of light compared to the powder sample. Despite inefficient photon capture, the thin film sample presented a promising prototype for the design for highly active photocatalysts. Orlov et al. tested the activity of a series of $\text{TiO}_2/\text{SBA-15}$ samples for *p*-chlorophenol photodegradation [240]. Among all of the catalysts, the one containing the highest concentration of spatially isolated, tetrahedrally coordinated Ti^{4+} ions showed the best activity for *p*-chlorophenol degradation. This can be explained by the generation of long-lived photoinduced electron-hole pairs in

the tetrahedrally coordinated Ti^{4+} ions that enhanced the overall photocatalytic efficiency.

Do et al. developed a set of Ti-MCM-41 samples with variable TiO_2 loading for the photodegradation of 4-nitrophenol (4-NP) [80]. It was observed that, initially, the photocatalytic activity increased with an increase of the TiO_2 loading in the Ti-MCM-41 sample. The highest activity was achieved from the sample with Si/Ti ratio of 20. Further increase in the TiO_2 loading in the sample caused a drop in the activity. The decrease in the activity was attributed to the aggregation of TiO_2 in nonframework positions of the MCM-41 support.

Artkla assessed the photocatalytic degradation of polyphenols (gallic acid) by using $\text{TiO}_2/\text{MCM-41}$ catalysts [78]. Several parameters, such as the loading of TiO_2 and the pH, were investigated to establish a structure-activity relationship. It was observed that using MCM-41 as support for titania significantly enhanced the photocatalytic activity for gallic acid degradation. Increase of the TiO_2 loading (>10 wt.%) was found to be detrimental for the photocatalytic reaction. This was explained by the formation of bulk TiO_2 (anatase) that caused pore clogging and precluded efficient contact between reactants and active sites in the MCM-41 mesoporous materials.

Photocatalytic Removal of Inorganic and Minor Organic Wastes. Aguado et al. prepared titania incorporated MCM-41 and SBA-15 mesoporous materials for photooxidation of free cyanides and iron (III) cyanocomplexes [241]. The $\text{TiO}_2/\text{MCM-41}$ and $\text{TiO}_2/\text{SBA-15}$ samples presented higher activity than that of pure TiO_2 (anatase) for photooxidation of CN^- . $\text{TiO}_2/\text{SBA-15}$ was found to be almost as active as commercial Degussa P25, which exhibited the highest activity. $\text{TiO}_2/\text{SBA-15}$ was further adopted and studied for photooxidation of iron (III) cyanocomplexes. The efficient photocatalytic performance from $\text{TiO}_2/\text{SBA-15}$ can be rationalized by reduction of screening effect compared to bare titania particles, the prevention of the formation of $\text{Fe}(\text{OH})_3$, and the presence of silica support that provided adsorption sites for the iron species resulting from the breakage and reaction of the complex. A similar observation can also be found from a work reported by López-Muñoz et al., who developed a series of $\text{TiO}_2/\text{SBA-15}$ for photooxidation of free cyanide and hexacyanoferrate (III) [242].

Artkla et al. assessed the activity for photocatalytic degradation of tetramethylammonium (TMA) ions over $\text{TiO}_2/\text{MCM-41}$ mesoporous materials [243]. $\text{TiO}_2/\text{MCM-41}$ presented enhanced activity for photodegradation of TMA compared to bare TiO_2 sample. Among all of the $\text{TiO}_2/\text{MCM-41}$ with various TiO_2 contents, the sample with 10 wt.% of TiO_2 exhibited the highest activity. In addition, the optimal photocatalytic efficiency was attained under neutral pH environment. Xu and Langford incorporated titania into MCM-41 mesoporous support to study the photocatalytic degradation of acetophenone [244]. It was established that the preparation method used for immobilizing titania species into MCM-41 support had a significant impact on the performance of the catalysts. The crystallinity of TiO_2 was an overriding factor that governed the photocatalytic activity of $\text{TiO}_2/\text{MCM-41}$ in

this study. The sample with more crystalline titania species showed higher activity.

3.2. Aperiodic TiO_2 - SiO_2 Mixed Oxide Materials. Aperiodic titania-silica binary mixed oxides are commonly synthesized using the sol-gel method. Aperiodic mesoporous materials do not possess uniform and periodic arrangement of pores. Several reported methods of preparation that include coprecipitation, impregnation, hydrothermal, flame hydrolysis, and chemical vapor deposition (CVD) have been implemented to tune the structural features of the mixed oxides by optimizing the synthetic procedures. In a recent review article, we have successfully discussed the different synthetic methodologies to prepare TiO_2 - SiO_2 mixed oxide materials [245]. To provide better transition and clarity to the readers, a brief discussion of the synthesis methods and the characterization techniques is elaborated herein.

3.2.1. Synthesis of Aperiodic TiO_2 - SiO_2 Mixed Oxides. The sol-gel synthesis of TiO_2 - SiO_2 materials usually involves the hydrolysis and condensation of titanium and silicon alkoxide precursors that lead to the formation of polymeric gels. By changing the experimental conditions, that include the amounts and types of precursors and solvents, water, pH, and temperature, the structural properties of the materials can be tailored. Furthermore, the porosities of the materials can be tuned by using an appropriate drying method. In a typical synthesis of xerogels materials, appropriate amounts of silica precursors and titania precursors are mixed with an alcoholic solvent, that include ethanol, methanol, or isopropanol, under vigorous stirring at ambient conditions. The sol is allowed to gel at ambient conditions and the solvent is allowed to evaporate. The dry powder obtained is then calcined. Generation of homogeneous gel is critical due to the unequal hydrolysis and condensation rates of the two different titanium and silicon alkoxide precursors. The unequal hydrolysis rates of these two alkoxide precursors can be explained by the differences in the partial charge of Si (+ 0.32) and Ti (+ 0.61). Due to their higher partial charge, titanium alkoxides undergo more rapid hydrolysis than silicon alkoxides, and this may lead to inhomogeneous distribution of titania in the mixed oxide materials. Thus, prehydrolysis of silicon alkoxides is necessary [246].

Preparation of $\text{TiO}_2/\text{SiO}_2$ nanomaterials was attained from the hydrolysis and polycondensation of tetrabutyl orthotitanate and tetraethyl orthosilicate via a sol-gel process by Cheng et al. [165]. Various amounts of silica doped with nanocrystalline titania powders were prepared and the influence of dopant concentration on the phase transition and grain growth was analyzed in their work. In addition, a constant dopant concentration of the sample was utilized to investigate the effect of calcination temperature on the photoactivity of titania. Spherical titania/silica particles with higher surface area, ranging from 400 to 700 m^2/g , and pore volume of 0.9–1.4 cm^3/g were prepared via the combination of emulsion and gelation of mixed sols [247]. The emulsion and gelation processes were carried out in the presence of dodecanol or hexane to the acid mixed sols prepared by mixing the prehydrolyzed silicon and the titanium alkoxides.

The polar nature of dodecanol provides suitable equilibrium composition of the biphasic system and controls the hydrolysis rate, whereas direct emulsion formation took place in the presence of hexane.

Homogeneous hydrolysis and condensation can also be achieved as discussed thereafter. The silicon alkoxide is hydrolyzed in an alcohol solution in the presence of concentrated acid, for example, HNO_3 , HCl , or H_2SO_4 , and water with vigorous stirring to create silanol groups [248–251], or the silicon alkoxide can be refluxed at 80°C in the presence of HCl or acetic acid [252, 253]. Then, these silanol groups undergo condensation process with the titanium alkoxide in the presence of water and form the active Ti-O-Si heterolinkages. Furthermore, acetic acid (AcOH) is utilized as a modifying agent to decrease the hydrolysis of titanium alkoxide in aqueous solutions via bridging of the acetate ligand with the terminal isopropoxyl groups present on the titanium alkoxide precursor [254, 255]. Acetylacetone (acac) has also been utilized to modify titanium alkoxides in several studies. acac can form chelated titanate species and decreases the hydrolysis rate of titanium alkoxide by increasing the coordination of titania from four to five [256–260]. 2-Methoxyethanol, a polar protic alcoholic solvent, was used as solution medium by Pirson et al. and can serve as a stabilizer of the titanium alkoxide towards the hydrolysis and condensation reactions [261]. In another study, isoamyl alcohol was used as a stabilizer for tetraisopropyl orthotitanate to reduce its rate of hydrolysis. Even though enhanced homogeneity of the gel was achieved by prehydrolysis of silicon alkoxides, the hydrolysis and condensation reactions were found to be slow and incomplete under ambient conditions. In addition, the ambient procedure requires long processing time to form a gel (a week to a month period of time) [91, 262]. Hence, reaction conditions, such as temperature and pressure, have been modified to overcome these challenges.

The hydrothermal treatment has been utilized by several researchers to achieve complete hydrolysis and condensation of the silica and titania precursors in a short period of time [263]. In this method, the reaction mixture containing the silica and titania precursors is placed in an autoclave reactor and heated to temperatures typically in the range of 100 to 200°C for a period of up to 24 h. Even though the hydrothermal synthesis method has been found to be a facile synthetic method to prepare crystalline and relatively stable materials, additional steps of washing, filtering, and drying are unavoidable. These additional steps can be avoided by the use of a supercritical drying method. Supercritical drying has been attempted to produce aerogels materials with enhanced porosities and high surface areas [263, 264]. Although these hydrothermal and supercritical drying methods result in materials with high crystallinity of the titania phase and high surface area, these are energy-intensive methods that require either extra processing steps or the use of expensive high-pressure equipment.

Different synthetic recipes have been attempted for the preparation of TiO_2 - SiO_2 materials in order to attain desirable structural properties that are responsible for enhanced photocatalytic activity. Use of appropriate solvents, acids, or bases, and effective metal precursors in the synthesis

procedure leads to the formation of materials with enhanced porosities and surface area. TiO_2 - SiO_2 xerogel materials with different pore sizes and surface areas have been prepared with a constant 1:4 molar composition of Ti:Si by simply changing the amounts of water, acids, or bases and hydrolysis procedure [265]. Gels formed in basic conditions possessed larger mesopores and lower surface area in comparison to the gel prepared in acid conditions due to lower pore collapse during drying. The partial hydrolysis of the silicon alkoxide in basic medium followed by the mixing of titanium alkoxide produced microporous xerogels owing to the high collapse of pores. However, even after the treatment in air at 600°C , the titania phase was amorphous. Pirson and coworkers have reported the synthesis of SiO_2 - TiO_2 xerogels by a sol-gel method in the presence of polar protic solvents [261]. It was noticed that the alcoholic solvents act as stabilizers for titania and control the reactivity of the titania precursor. The gels were found to be microporous, and calcination at temperatures above 350°C diminished the pores in these materials.

Avendaño and coworkers developed an experimental strategy to obtain mesoporous ZrO_2 - SiO_2 and TiO_2 - SiO_2 mixed oxides via the sol-gel process [174]. The surface acidity was examined by adsorbing pyridine. A simple acid-catalyzed sol-gel process without the addition of any chelating agents or prehydrolysis step was utilized to synthesize microporous titania-silica mixed oxides [266, 267]. The materials showed a narrow unimodal pore size distribution centred near 0.7 nm. A high dispersion of titania in the silica matrix was obtained by first mixing titanium alkoxide with TEOS in alcoholic solution and aqueous hydrochloric acid followed by calcination of the resulting solid material. However, the resulting materials were found to be amorphous. The surface area varied as a function of Si/Ti ratio. Budhi et al. synthesized a series of TiO_2 - SiO_2 xerogels [268]. Addition of nonpolar cosolvents, such as toluene, *p*-xylene, and mesitylene, resulted in materials with enhanced gelation rates and enlarged pores. The resulting materials have been utilized for phenol degradation and the TiO_2 - SiO_2 xerogels showed higher activity in comparison to a sample prepared by the hydrothermal method due to better adsorptive and highly reactive TiO_2 sites.

It has been postulated that, by improving the hydrophobic nature of titania-silica, one can enhance the adsorption of organic compounds on them compared to bare TiO_2 . Larsen and coworkers tried to enhance the hydrophobicity of titania-silica materials using noncyclic silicon precursors [269]. These materials were prepared by acid prehydrolysis of TEOS and dimethyldimethoxysilane in ethanol medium, followed by the addition of TiCl_4 in isopropanol [270]. In another study, Mariscal et al. enhanced the hydrophobic nature of TiO_2 - SiO_2 xerogels by mixing the titanium and silicon alkoxides with a hexane solution of trimethylchlorosilane (TMCS) in N_2 atmosphere [271]. Dagan and coworkers modified silica with methyl and phenyl moieties to control the polarity, hydrophobicity, ion-exchange capacity, and concentration of silanol groups on the surface of TiO_2 - SiO_2 xerogels [272]. The resultant modified silica sols were mixed with ethanol and addition of titanium alkoxide formed mixed oxide gels. These

methyl and phenyl moieties provide better adsorptive sites on the TiO_2 - SiO_2 mixed oxide materials.

TiO_2 / SiO_2 composite nanoparticles were prepared directly from the acidic precursor solutions of TiOSO_4 and TEOS by hydrolysis under hydrothermal conditions by Hirano et al. [273]. An increasing surface area with increasing silica content was attained with the materials prepared in their study. Enhanced photocatalytic activity was obtained with these materials in comparison to pure TiO_2 for the removal of NO gas. In another study, nanophase silica-titania particles were prepared by sol-gel and hydrothermal processing [250]. The textural properties of these materials such as surface area, particle size, crystallinity, and crystallographic phases were controlled by varying the calcination temperature and the molar ratio of Si and Ti. It was noticed that the crystallite sizes of SiO_2 - TiO_2 decreased when the mole fraction of silica increased and this behaviour was explained by the fact that the silica suppresses the growth of titania [89, 274]. In a following study, a similar method has been utilized by the same group, for the preparation of silica embedded nanocrystalline TiO_2 powders [89]. The crystal phase of titania was found to be strongly dependent on the silica content and the solvent composition. In addition, the silica embedded titania materials exhibit a strong inhibition for the formation of rutile phase. Thus, these materials show efficient photocatalytic activity, about 1.2 times better than the commercially available Degussa P25. The role of crystallinity of the titania phase in TiO_2 - SiO_2 prepared by a cosolvent induced gelation method was examined towards the degradation of phenol by our group [84]. It was found that addition of cosolvents enhanced the gelation process and the crystallinity of the titania phase, resulting in the formation of mesoporous TiO_2 - SiO_2 with higher photocatalytic activities for the degradation of phenol.

Li and coworkers synthesized silica-modified TiO_2 by utilizing hydrothermal methods [275]. Formation of Ti-O-Si bond with strong interaction between SiO_2 and TiO_2 in the materials was proven by XPS and FT-IR analysis. The silica content in the materials affected the crystallinity and the nature of the titania phase. Furthermore, these mixed oxide materials showed better photocatalytic activity in comparison to pure TiO_2 .

Another approach to significantly enhance the porosities and surface area is preparation of aerogels under supercritical conditions. In this method, the wet gel prepared by the same procedures explained above is slowly heated to critical temperature (T_c) and critical pressure (P_c) of the solvent employed. The solvent is then removed once the appropriate supercritical conditions of temperature and pressure are attained. Removal of solvent under such conditions prevents the formation of both the liquid-vapor meniscus and capillary pressure in the pores. Thus, pore collapse is prevented and the final materials possess relatively large pores.

Dutoit et al. synthesized mesoporous titania-silica aerogels with highly dispersed titania by a sol-gel process [276, 277]. An acidic hydrolysant (doubly distilled water and hydrochloric acid, 37 wt.%) was added to the solution of acetylacetonate modified tetraisopropyl orthotitanate and

tetramethyl orthosilicate in isopropanol solvent. The gel formed was subjected to different drying conditions including conventional drying, high-temperature supercritical drying, and supercritical CO₂ drying. It was noticed that the textural properties were affected by the drying conditions employed and the pH used for initiating the hydrolysis reactions [278]. A drop in mesoporosity and surface area was noticed in the materials, which contained low amounts of titania. In addition, it has been noted that the use of acidic conditions for sol-gel method leads to materials with substantial amounts of micropores [279].

Deng et al. synthesised TiO₂-SiO₂ aerogel materials with different TiO₂ contents [263]. Anatase microcrystallites were obtained after supercritical drying in ethanol. In addition, the photocatalytic degradation of phenol using these aerogels was examined and maximum activity was observed at molar ratio of TiO₂/SiO₂ = 1. Crack-free titania-silica aerogels with high titanium content, Ti/Si = 1, were successfully prepared by Cao and coworkers by simply adjusting the hydrolysis rate of the titanium and silicon alkoxide precursors [280]. Tailoring the interconnectivity of the pore network in the aerogel materials was found to improve the physicochemical characteristics of these materials. In their work, well-dispersed, nanometer-sized anatase crystal domains were crystallized by high-temperature supercritical drying in ethanol medium. In addition, the crystalline domains contained Ti-O-Si bonds.

Kim et al. synthesized titania-silica binary aerogel with 1:1 molar ratio of Ti to Si by first modifying tetrabutylorthotitanate (TBOT) with acetylacetone in methanol solution followed by the addition of TEOS [281]. In addition, a nonalkoxide sol-gel route for the synthesis of TiO₂-SiO₂ aerogel materials was also done by addition of TiCl₄ and SiCl₄ in a methanol medium. High surface area titania and titania-silica aerogels were obtained by the nonalkoxide sol-gel route and by a subsequent carbon dioxide supercritical drying step. However, the surface area of the resulting aerogel was found to be similar to that of the aerogel prepared by alkoxide sol-gel route.

The influence of the preparation method on the physicochemical properties of titania-silica aerogel materials was assessed by Brodzik and coworkers [222] using four different synthesis procedures: (i) modified titania precursor, (ii) fully hydrolyzed silica precursor, (iii) titanium and silicon precursors that were hydrolyzed and gelled without any modification, and (iv) impregnation of a preformed silica gel by a modified titania precursor. Anhydrous ethanol and methanol were used as solvents and the gel formation was induced by adjusting the pH of the system with ammonia. Finally, highly porous aerogels were obtained and the presence of anatase crystallites was inferred from XRD studies. In addition, the amount of water present in the reaction mixture was found to play a key role in formation of titania-silica lattice and strongly influenced the resulting photocatalytic activity. Furthermore, the impregnation and simultaneous hydrolysis methods resulted in highly active photocatalysts.

In summary, the synthetic routes for preparation of the binary aperiodic mixed oxide materials significantly influence the structural properties of the materials, which ultimately affect their photocatalytic activity. The following

section will provide a brief discussion of several characterization techniques.

3.2.2. Characterization of Aperiodic TiO₂-SiO₂ Mixed Oxides

Powder X-Ray Diffraction. X-ray diffraction (XRD) is a nondestructive analytical technique that is routinely used for the structural characterization of titania-silica materials. A typical peak near $2\theta = 25^\circ$ in the wide range XRD profile indicates the presence of TiO₂ anatase phase in the mixed oxide materials due to d_{101} crystallographic plane. In addition, peaks at 2θ near $36^\circ, 37^\circ, 39^\circ, 48^\circ, 54^\circ, 55^\circ, 63^\circ, 69^\circ, 70^\circ, 75^\circ,$ and 76° that corresponded to d -spacings of $d_{103}, d_{004}, d_{112}, d_{200}, d_{105}, d_{211}, d_{204}, d_{116}, d_{220}, d_{215},$ and d_{301} , respectively, are due to anatase phase of TiO₂ and peaks at $2\theta = 27^\circ, 37^\circ, 39^\circ, 41^\circ, 54^\circ, 55^\circ, 63^\circ, 68^\circ, 70^\circ, 75^\circ,$ and 76° correspond to d -spacings of $d_{110}, d_{101}, d_{200}, d_{111}, d_{211}, d_{220}, d_{002}, d_{301}, d_{112}, d_{320},$ and d_{202} , respectively, for the rutile phase of TiO₂. However, addition of silica prevents the formation of rutile peaks [165].

In most of these TiO₂-SiO₂ mixed oxide materials the X-ray patterns show a broad amorphous peak due to the presence of silica. However, with an increase in the calcination temperature and/or use of cosolvents, the crystallinity can be modulated as depicted in Figure 13. It can be clearly seen that the crystallinity of the peaks is improved either by the addition of aromatic cosolvents or by the increase in the calcination temperature. Furthermore, different phases of TiO₂ may be obtained by adjusting the pH of system or by changing the ethanol (solvent) to water ratio [89].

Raman Spectroscopy. Raman spectroscopy is widely used to identify the phase of titania along with XRD. The Raman study of a TiO₂-SiO₂ mixed oxide showed peaks near 638, 519, 399, 197, and 144 cm⁻¹ corresponding to E_{1g}, B_{1g}, B_{1g}, E_{1g}, and E_g symmetry modes, respectively [282]. A_{1g}, B_{1g}, and E_g modes are the active modes for anatase crystals [267].

Fourier Transform-Infrared (FT-IR) Spectroscopy. FT-IR technique is utilized for analyzing the stretching and bending vibration frequencies in the mixed oxide materials. In addition, this technique provides information regarding the presence of surface hydroxyl groups. The FT-IR spectrum of the titania-silica composites shows mainly four peaks with the wavenumbers of 780, 970, 1090, and 1200 cm⁻¹ as depicted in Figure 14 [85]. The peaks at the wavenumbers of 1090 and 780 cm⁻¹ are assigned to the symmetric and asymmetric stretching vibration of Si-O-Si in silica, respectively. The peak in the range of 920–970 cm⁻¹ is commonly attributed to Ti-O-Si vibrations [257]. However, these bands also overlap with vibration involving Si-O-H bonds. Thus, FT-IR cannot be used to infer the presence of Ti-O-Si linkages and other techniques such as XPS spectroscopy need to be performed for the quantitative calculation of Ti-O-Si linkages. The peak near 400 cm⁻¹ is commonly assigned for Ti-O-Ti bending.

N₂ Physisorption. Textural properties that include surface area, pore volume, and pore diameter of the mixed oxide materials are commonly investigated using nitrogen

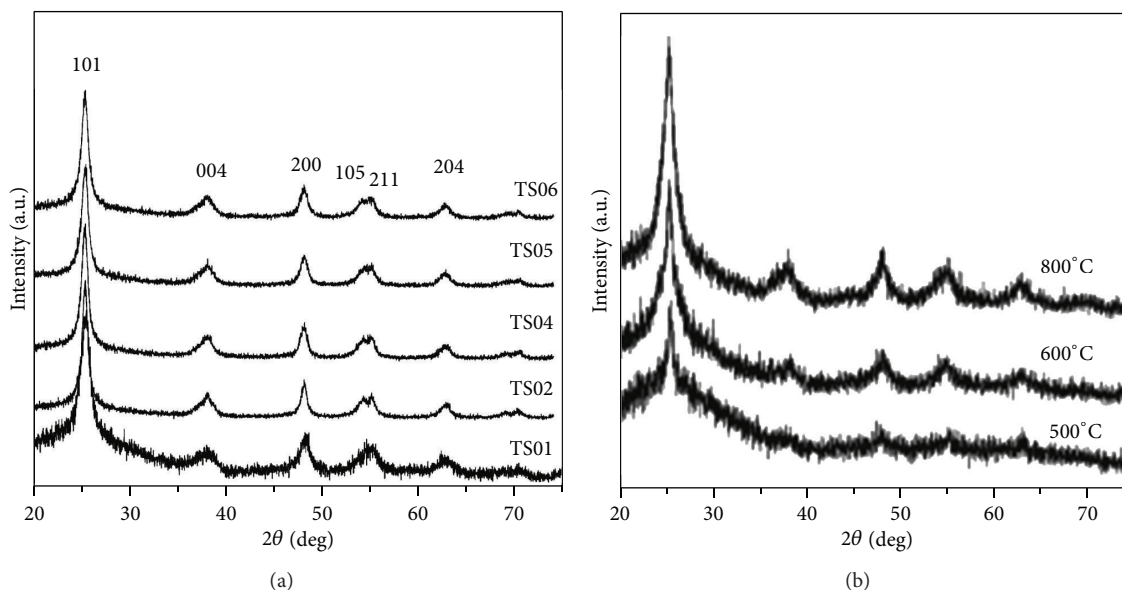


FIGURE 13: The wide-angle XRD patterns of TiO_2 - SiO_2 materials: (a) prepared in the ratio of solvent: cosolvent = 1 : 1, in which the cosolvents for TS01, TS02, TS03, TS04, TS05, and TS06 are ethanol, hexane, toluene, *p*-xylene, and mesitylene, respectively, and (b) prepared under the same condition with the same catalyst composition, but calcined at 500°C, 600°C, and 800°C (reprinted with permission from [84]).

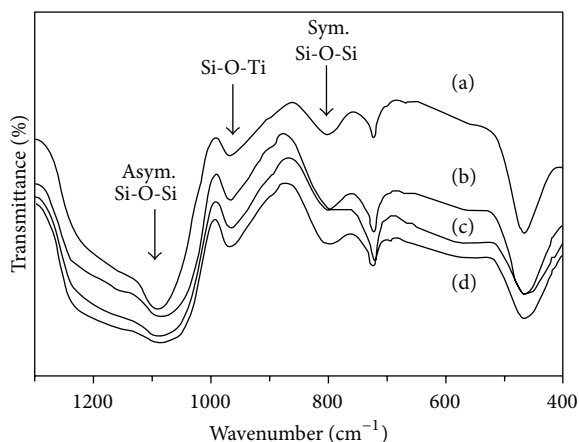


FIGURE 14: The FT-IR spectra of (a) calcined mesoporous silica, (b) titania modified silica with $\text{Ti}/\text{Si} = 10$, (c) $\text{Ti}/\text{Si} = 2.5$, and (d) $\text{Ti}/\text{Si} = 5$ (reprinted with permission from [85]).

physorption studies. The typical isotherms show a slow increase with the amount of N_2 adsorbed at low relative pressure values due to monolayer adsorption. As the relative pressure value increases, multilayer adsorption occurs and this is followed by capillary condensation. The mesoporous materials show type IV isotherms as evidenced by a hysteresis loop [283].

The nitrogen physisorption patterns of a series of materials with different Ti/Si amount are illustrated in Figure 15 and are compared with the isotherms of pure titania and silica synthesized under similar conditions. The materials labelled as X-Ti-01 and X-Si-06 contain only titania or silica, respectively, and show H2 type hysteresis loops, which are usually found in materials with a cross-linked porous system.

The isotherm of the titania-silica mixed oxide material with Ti/Si ratio of 1 (X-Ti-02) also shows H2 type of hysteresis with a relatively low surface area and pore volume in comparison with the rest of the mixed metal oxides.

On the other hand, the mixed oxide xerogels with higher silica contents, such as 1 : 2, 1 : 3, and 1 : 4 ratios of $\text{Ti} : \text{Si}$ (X-TiSi-03, X-TiSi-04, and X-TiSi-05), exhibit H3 type loops that are not leveled off at relative pressure that are very close to that of saturation vapor pressure. The pore size distribution plots for the corresponding mixed oxide materials are shown in Figure 16. The pure silica material shows a broader pore size distribution than pure titania. In addition, a narrow unimodal distribution of pore sizes is observed with the mixed oxide materials that contain lower amounts of silica.

UV-Vis Diffuse Reflectance Spectroscopy (DRS). DRS has been widely employed in the characterization of aperiodic titania-silica mixed oxide materials. Bandgap estimates of the mixed oxides are derived from DRS studies. The electron transition from valence band to conduction band is mainly attributed to the absorption of the materials below the wavelength of 400 nm and it is well documented that the absorption near the band edge follows the expression of $\alpha h\nu = A(h\nu - E_g)^{n/2}$, where α , h , ν , A , E_g , and n are the absorption coefficient, Planck's constant, light frequency, constant, bandgap energy, and integer, respectively [284]. The bandgap values reported for TiO_2 anatase in TiO_2 - SiO_2 mixed oxide materials differ due to use of different preparation methods, the presence of trace amounts of impurities or dopants in the crystalline network, or the particle size of TiO_2 . The bandgap energies are commonly calculated from the plot of Kubelka-Munk function versus the energy as illustrated in Figure 17. However, some reports also determine the bandgap energies from the Tauc plot, which is the derivation of the Kubelka-Munk

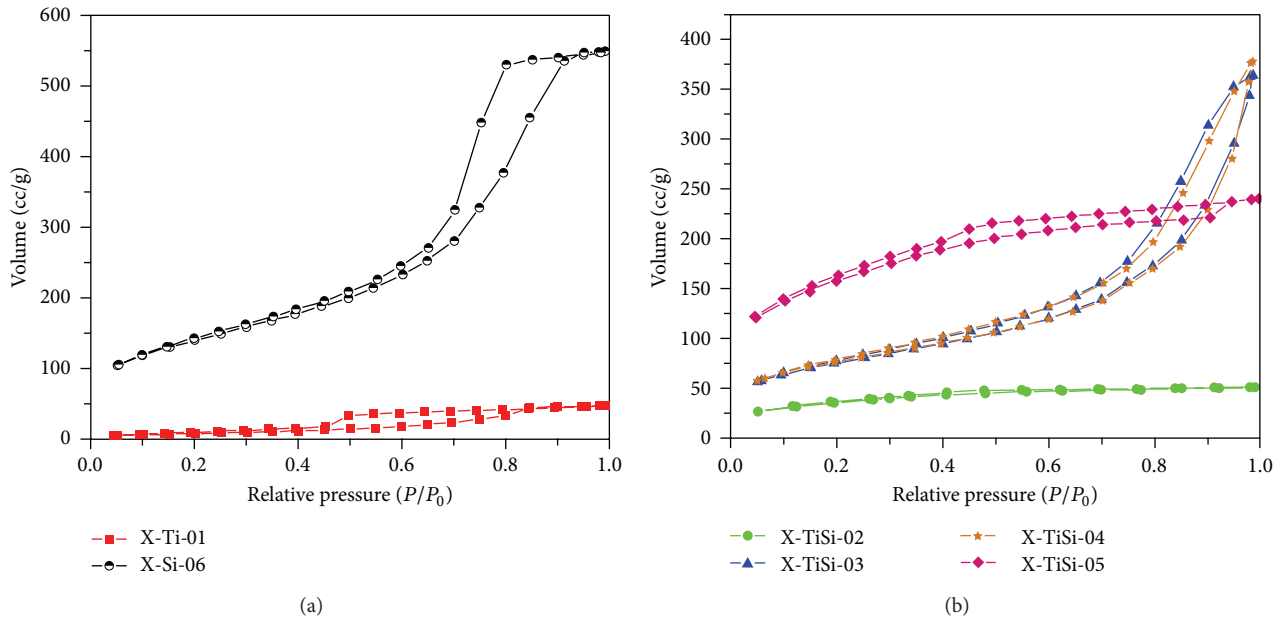


FIGURE 15: Nitrogen physisorption properties of TiO_2 - SiO_2 xerogel materials: (a) pure titania (X-Ti-01) and pure silica (X-Si-06) and (b) TiO_2 - SiO_2 mixed oxides with Ti/Si ratio of 1:1 (X-Ti-02), 1:2 (X-Ti-03), 1:3 (X-Ti-04), and 1:4 (X-Ti-05) prepared in ethanol-toluene solvent system (reprinted with permission from [86]).

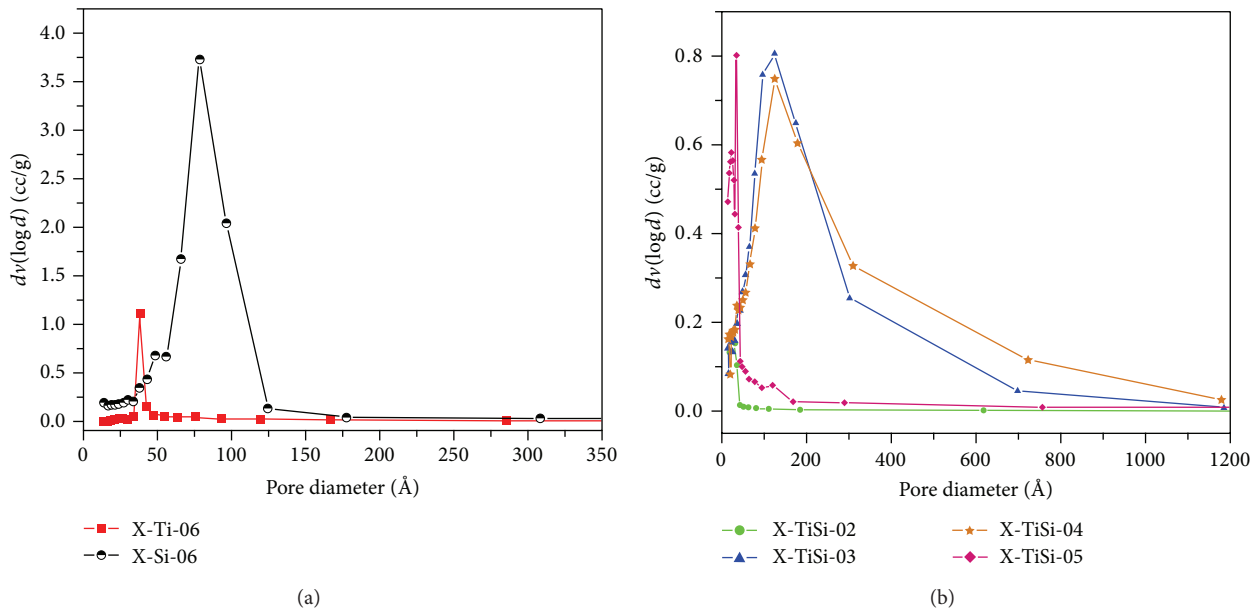


FIGURE 16: Pore size distribution of TiO_2 - SiO_2 xerogel materials: (a) pure titania (X-Ti-01) and pure silica (X-Si-06) and (b) TiO_2 - SiO_2 mixed oxides with Ti/Si ratio of 1:1 (X-Ti-02), 1:2 (X-Ti-03), 1:3 (X-Ti-04), and 1:4 (X-Ti-05) prepared in ethanol-toluene solvent system (reprinted with permission from [86]).

function. Aguado et al. used the Kubelka-Munk function (Figure 17) to calculate the bandgap energy of titania in their mixed oxide materials [87].

As the content of Si in the mixed oxides increases, the UV absorption edge shifts to higher energies. Furthermore, a blue shift was observed in the titania-silica mixed oxides prepared using different cosolvents and this shift was explained by

changes in the crystallite size of the anatase TiO_2 [84]. In addition to the bandgap the particle size of TiO_2 can also be determined by DRS studies using the Brus equation.

Scanning Electron Microscopy (SEM). The information regarding the morphology of the materials can be obtained from SEM studies. Due to the irregular arrangements of

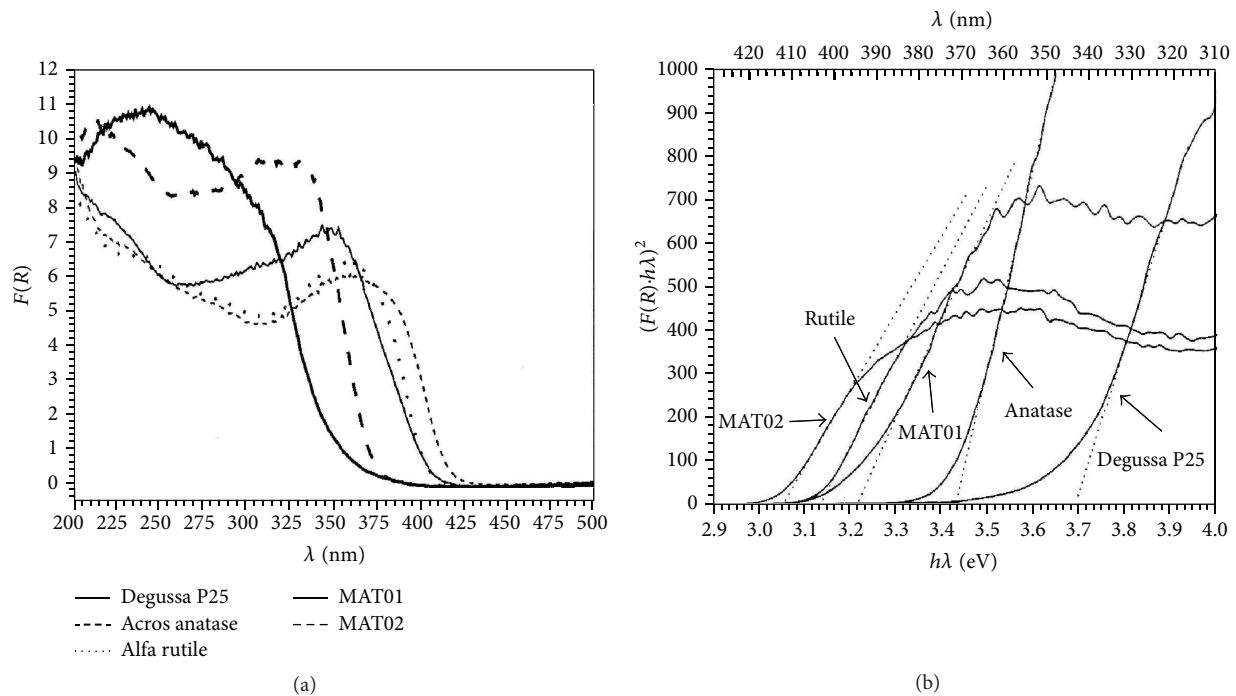


FIGURE 17: (a) UV-Vis DRS spectra of the mixed oxide materials MAT01, MAT02 along with Degussa P25, Acros anatase, and Alfa rutile materials and (b) the corresponding Kubelka-Munk function plot (reprinted with permission from [87]).

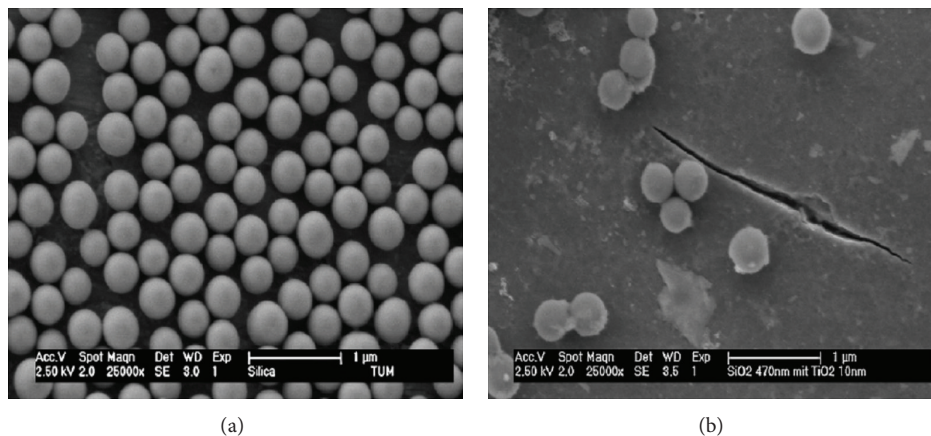


FIGURE 18: Typical scanning electron micrographs of (a) silica particles and (b) titania coated silica particles (reprinted with permission from [88]).

the pores in the aperiodic mixed oxide materials, the differences in the size and the morphologies are best obtained from SEM studies rather than TEM. Alaoui et al. and Cetinkaya et al. prepared TiO_2 - SiO_2 particles with different sizes respectively [285, 286]. SEM studies indicate that TiO_2 powder is randomly distributed in the silica matrix. Wilhelm and Stephan utilized SEM technique to characterize silica spheres that were coated with titania as illustrated in Figure 18 [88].

The SEM image illustrates that the silica particles have spherical shape and smooth surface. The coating was carried out by the gradual addition of titania sol into the aqueous

dispersion of silica which resulted in the attachment of small titania particles on the silica surface. The SEM image illustrates that, after coating, there is a loss in the smoothness of the silica surface.

Transmission Electron Microscopy (TEM). TEM is a powerful technique for structural characterization. The TEM image of TiO_2 - SiO_2 mixed oxide materials prepared with 20 mole% silica embedded with TiO_2 is illustrated in Figure 19. The size of the silica embedded TiO_2 particle prepared in the ethanol-rich solvent was found to be 7 nm and the high resolution TEM image shows the lattice fringes of TiO_2 [89]. The high

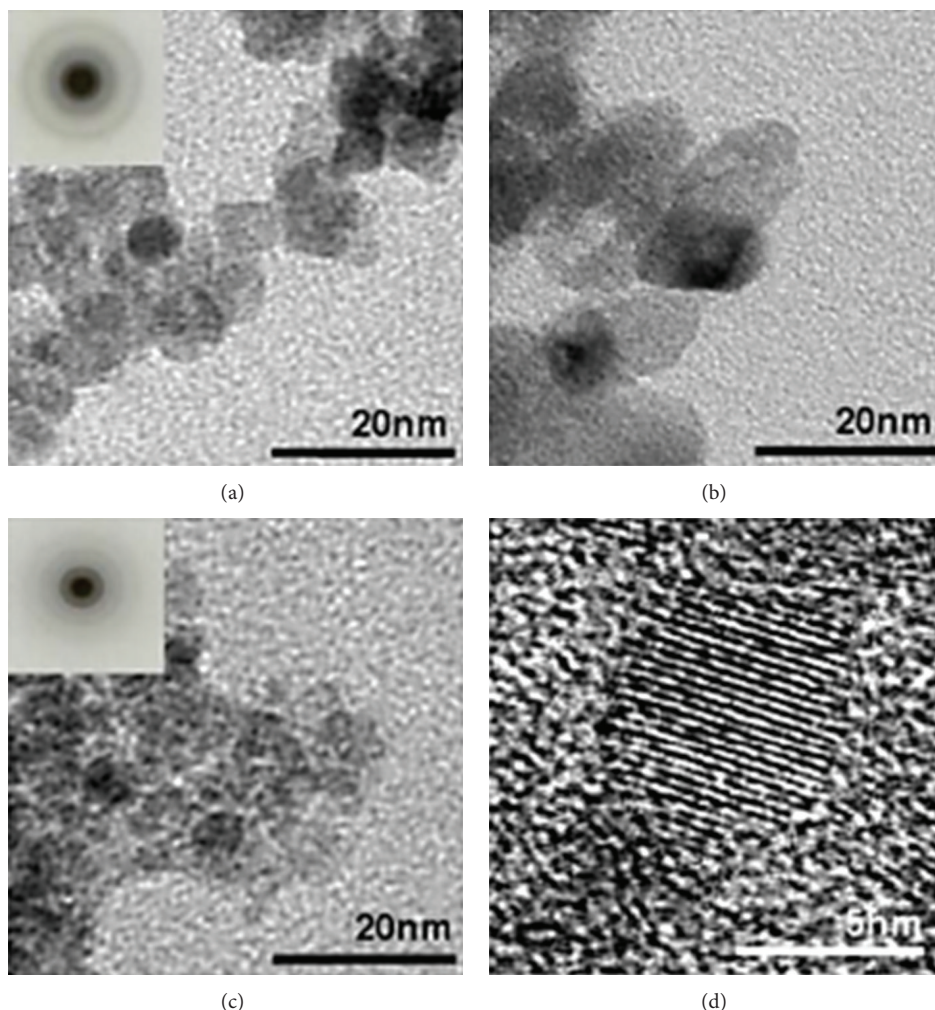


FIGURE 19: TEM images of TiO_2 nanoparticles prepared with different silica content and solvent composition: (a) pure TiO_2 (ethanol to water = 4 : 1), (b) pure TiO_2 (ethanol to water = 1 : 8), (c) 0.2 SiO_2 -0.8 TiO_2 (ethanol to water = 4 : 1), and (d) high resolution TEM (HRTEM) image of (c) (reprinted with permission from [89]).

resolution TEM analysis offers information regarding the phase of titania via providing the d -spacing values from the presence of lattice fringes in the mixed oxide materials. However, it was noted that it is very challenging to obtain the TiO_2 lattice fringes in the materials with higher silica loadings.

X-Ray Photoelectron Spectroscopy (XPS). XPS studies provide information on the binding energies of the titania and silica species in the mixed oxide materials. In addition, the interaction between SiO_2 and TiO_2 species can also be understood by comparing the peak positions of Si and Ti in the TiO_2 - SiO_2 mixed oxide with pure titania and silica. The XPS spectra obtained for the mixed oxides prepared with different Ti : Si ratios show a peak at the binding energy of 459.2 eV due to Ti (2p_{3/2}), which is slightly higher than that observed in TiO_2 anatase (458.8 eV). In addition, a shift in the Ti (2p_{3/2}) peak positions towards lower binding energies

was observed, when the silica amount increases in the mixed oxide (Figure 20) [90].

In a different study, the O 1s peak was found to be shifted to the lower binding energy with an increase in the TiO_2 content (Figure 21) in a TiO_2 - SiO_2 material. At higher TiO_2 contents, two O 1s bands were observed at around 530.5 and 532.5 eV indicating phase separation with titania-rich regions (Ti-O-Ti) and silica-rich regions (Si-O-Si) [91]. A further study evaluated the effect of calcination temperature to better understand the interaction between silica and titania species in the mixed oxide materials [287]. Li et al. experimentally found that the binding energies of Ti (2p_{1/2}), Ti (2p_{3/2}), and O 1s of titania-silica mixed oxide were shifted to higher values in the mixed oxide materials in comparison to pure TiO_2 [275]. This behavior was attributed to a decrease in the coordination number of Ti and a shortening of the Ti-O bond. The bond shortening resulted in the insertion of Ti^{4+} cations into the tetrahedral sites of the silica network to form Ti-O-Si linkages.

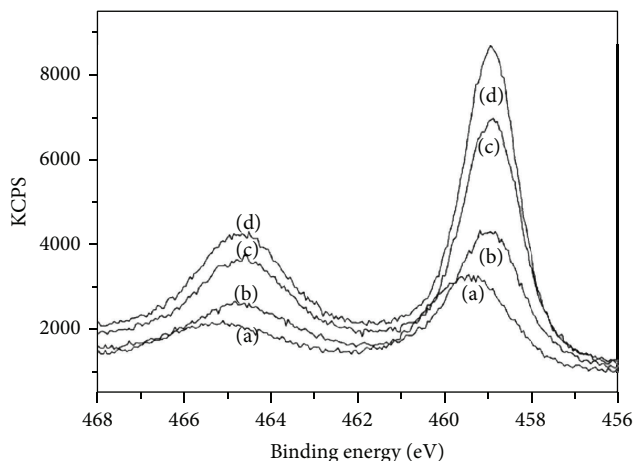


FIGURE 20: Ti (2p) peaks of TiO_2 - SiO_2 mixed oxides prepared with different Ti:Si ratios: (a) Ti:Si = 1:10, (b) Ti:Si = 3:7, (c) Ti:Si = 7:5, and (d) Ti:Si = 7:3 (reprinted with permission from [90]).

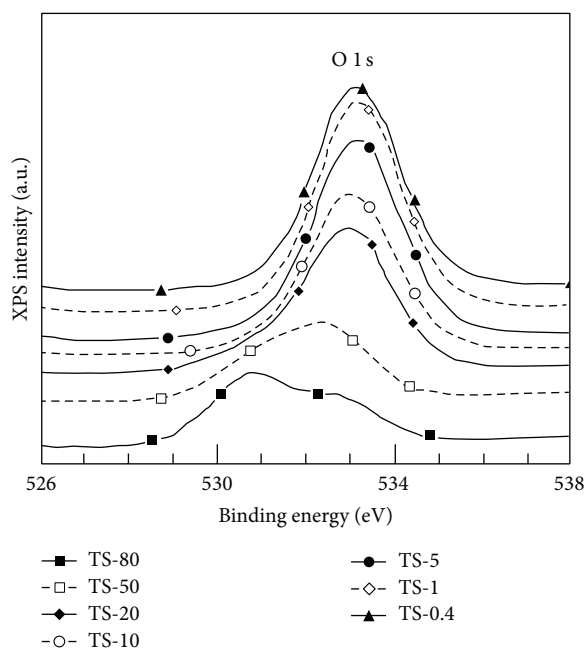


FIGURE 21: X-Ray photoelectron spectra of the O 1s level for Ti-Si binary oxides. The Ti weight % was in the range of 0.4–80 in the mixed oxide (reprinted with permission from [91]).

3.2.3. *Photocatalysis.* Semiconductor binary mixed oxides have emerged as promising materials for photocatalytic degradation of pollutants and photosplitting of water and, among them, TiO_2 - SiO_2 has been quite well studied.

Various types of aquatic pollutants that include inorganic ions, aliphatic hydrocarbons, such as alkanes and alkenes and their substituted derivatives, benzyl compounds, dyes, phenolic compounds, and pesticides were experimented using advanced oxidation process. This section will review the

various photocatalytic reactions that have utilized aperiodic TiO_2 - SiO_2 materials.

Photocatalytic Degradation of Inorganics. A comparative study using titania-silica xerogels and aerogels was carried out for the photocatalytic degradation of cyanides from the wastewater by Ibrahim and coworkers [288]. A decrease in the cyanide removal efficiency from 80% to 70% was obtained with an increase in the calcination temperature from 100 to 400°C. A removal of 82% was achieved at the calcination temperature of 500°C. Further increase in the calcination temperature reduced the removal efficiency. The decrease in activity was explained by the formation of greater amounts of rutile phase. In contrast, higher removal efficiency (~98%) was attained with the aerogel materials and the efficiency has been credited to the larger surface area of aerogel materials. In addition, the supercritical drying time was not found to be a major factor in the photocatalytic performance of the aerogel materials since all the materials showed similar activity when subjected to different drying times. However, the heating time in the drying process was found to affect the photoactivity, since the crystallinity of the titania phase in the aerogel materials was found to vary.

Removal of cyanide ions using TiO_2 - SiO_2 aerogel as photocatalysts has been examined in a separate study by Ismail et al. [289]. The molar ratio of Ti:Si was varied to find the optimum removal efficiency and the best degradation efficiency of 98% was achieved for the catalyst with the molar ratio of Ti:Si equivalent to 6:1. The higher efficiency of this material was explained by the larger specific surface area value of 850 m^2/g that allowed for effective dispersion of the photoactive titania species. Even though the cyanide removal in the wastewater has been carried out for water treatment, a survey of the literature indicates no reports for removal of other inorganic ions using TiO_2 - SiO_2 aerogels.

Photocatalytic Degradation of Aliphatic Compounds. Photocatalytic reactions of alkenes and alkynes in water were investigated by Anpo et al. over titania-silica oxides photocatalysts. The photocatalytic activity in the mixed oxide system was found to be higher at low TiO_2 content due to a decrease in the radiationless energy transfer between titania and silica [290]. In a different study, the photocatalytic decomposition of dichlorodifluoromethane was carried out on various metal oxides that include CaO, zeolite, silica-alumina, and titania-silica [252]. Among these, titania-silica exhibited the best performance due to the presence of strong acid sites which enhanced the decomposition of dichlorodifluoromethane. It was found that deactivation of the catalyst occurred rapidly due to the attack of fluorine on silicon in titania-silica. In addition, a combined mixture of titania-silica and CaO reacted with fluorine more readily in comparison to silica and protected the titania-silica catalyst from corrosion by fluorine, and it was found that the lifetime of this catalyst was longer than that of the bare titania-silica. The presence of acidic sites on titania-silica mixed oxide was found to be favorable for the decomposition of 1,2-dichloroethane [291]. Titania coatings have been deposited on silica by hydrolysis of titanium alkoxide precursors and examined as photocatalysts

for the dehydration of 2-propanol [292]. Preformed silica was used as the support for titania and the nature of titania coating was controlled by the ratio of titanium alkoxide to water. 2-Propanol dehydration was used as a probe reaction. Propene formation was found to be directly correlated with the anatase surface area. However, when the titania-silica samples were heated to temperatures less than 400°C, no correlation was obtained between the surface area and propene formation. This may be due to the presence of amorphous titania.

Photocatalytic degradation of tetramethylammonium (TMA) ions in water was studied with pure TiO₂ and silica-loaded TiO₂ [293]. An improved activity was attained with the catalyst of Si/Ti atomic ratio of 18%. In addition, the calcination temperature was noted as one of the factors affecting the degradation. The increased thermal stability of TiO₂ in the mixed oxide prevents the formation of the less active rutile phase, and this may be the reason for the higher photoactivity of silica-loaded TiO₂. Loading silica onto titania created a highly negative surface and this enhanced the adsorption of cations such as TMA and, as a result, its degradation was enhanced.

Catalytic reactions that include epoxidation of olefins and selective oxidation of saturated hydrocarbons have been carried out by utilizing amorphous microporous titania-silica mixed oxide materials by Klein and coworkers [266]. The materials show catalytic activity for selective oxidation reactions and also for selective epoxidation of olefins due to their distinct microporosity. A decrease in epoxidation activity was observed with an increase of TiO₂ in the materials. However, the hydrophilicity of these amorphous binary oxides was found to be different in comparison to their zeolitic analogues. This was proven by adsorption experiments of water and octane.

Photocatalytic Degradation of Benzyl Compounds. Photocatalytic decomposition of 1,4-dichlorobenzene was monitored using TiO₂/SiO₂ nanoparticles [89, 250]. The rate constant for the degradation reaction was found to be higher for TiO₂/SiO₂ than that of Degussa P25. However, it was found that 20 mol% of silica was the optimum loading. Various adsorbent supports were evaluated for the mineralization of 3,5-dichloro-N-(3-methyl-1-butyn-3-yl)benzamide (propylamide) in aqueous solution [294]. Zeolite, silica, and activated carbon were used as adsorbent supports for dispersing TiO₂. It was found that the TiO₂/SiO₂ system showed better adsorptive properties and increased the mineralization of propylamide in comparison with bare TiO₂.

Decomposition of benzyl trimethyl ammonium chloride (BTMA) and propionic acid was carried out over SiO₂ loaded TiO₂ under UV irradiation. Propionic acid showed lower degradation rate due to the presence of more negative charge on the surface of TiO₂-SiO₂ at pH 6 [295]. The influence of pH on the surface charge of silica-loaded TiO₂ materials was studied by Vohra and Tanaka for the photocatalytic activity of cationic, neutral, and anionic pollutants [296]. An enhanced photocatalytic activity was achieved with the cationic pollutants due to the presence of silica that increased the surface area and introduced Si-O⁻ groups, which facilitated the adsorption of the cationic pollutant species on the

surface of the catalyst. However, due to the occlusion of the active sites, the efficiency of the supported catalysts was found to decrease with an increase in the substrate concentration. Furthermore, it was interesting to note that anionic and nonionic compounds such as acetate and phenol remained unaffected during the degradation process.

Photocatalytic Degradation of Phenols. Phenols and phenolic compounds are released into the aquatic environment along with several industrial wastes and have gained attention from researchers for their removal from water bodies. Photocatalytic degradation of phenol over silica supported titania catalysts was carried out by Alemany et al. and the intermediates and products formed during the process were also identified in their study [297]. Hydroquinone and maleic acid were found to be the two major intermediates that were later oxidized to acetic acid and formic acid on prolonged irradiation. A high selectivity to the partial oxidation products was observed for the catalysts containing 0.5 and 1.0 monolayers of titania which were formed by the homogeneous precipitation of titania on the silica support. CO₂ was found to be the dominant final product for all the catalysts. The study also focused on finding the optimal titanium content, and it was found that there should be an optimal particle size for the effective photodegradation of phenol. Higher loadings greater than 30% of titania on the silica materials limit the photoefficiency due to the presence of larger sized titania particles.

The utilization of TiO₂-SiO₂ aerogels for the photocatalytic degradation of phenol pollutant was investigated by Deng and coworkers and it was noticed that the aerogels contained anatase microcrystallites after supercritical drying in ethanol [263]. These binary aerogel materials showed more superior activity than the commercial TiO₂ and the pure TiO₂ aerogels. The aerogel with 1:1 molar ratio of TiO₂ and SiO₂ showed optimum photocatalytic performance. The photocatalytic activity of the aerogels increased with the SiO₂ content at first and came to a maximum at molar ratio = 1:1.

Malinowska and coworkers chose three different phenol *para*-derivatives, such as *p*-chlorophenol, *p*-nitrophenol, and 4-hydroxybenzoic acid, as model compounds for the photodegradation processes over TiO₂-SiO₂ aerogel materials synthesized by a sol-gel technique [298]. Even though the aerogels prepared in their studies showed reasonable photocatalytic activity, it was comparatively less than that of TiO₂ aerogels. This was explained by the segregation of titania and silica phases and their poor contact that hindered the photocatalytic activity. The photocatalytic degradation of phenol over a series of TiO₂-SiO₂ mixed oxide materials prepared by sol-gel hydrothermal treatment has been reported recently [299]. The higher photocatalytic activities of the binary mixed oxide materials prepared using nonpolar solvents were attributed to a combination of factors such as higher apparent surface coverage of Ti-O-Si heterolinkages, larger pore sizes, and higher crystallinities of the titania phase. In particular, high crystallinity of the titania phase seemed to be critical for the complete mineralization of phenol in this study. Larger pore sizes permitted better transport of phenol and photodegradation products that were

formed during the mineralization to and from the active sites and higher crystallinity of TiO_2 enhanced the degradation efficiency by minimizing the electron-hole recombination in these photocatalysts.

Photocatalytic Degradation of Dyes. The runoffs from several industries such as textile, leather, and paper are a major contributor to this type of pollutants in the water body. In particular, removal of dyes from several colored effluents involves processes that produce compounds that are very toxic to the environment [285]. Thus, it is necessary to remove these colored pollutants from the environment. Anderson and Bard have studied the effect of incorporation of SiO_2 on TiO_2 photocatalyst prepared by a sol-gel technique [14]. It has been well documented that the efficiency of TiO_2 can be improved by preventing the recombination of the photo-generated electrons (e^-) and holes (h^+) pairs by the addition of charge-transfer catalysts on the TiO_2 surface. Alternately, one can increase the photocatalytic activity by incorporation of effective adsorption sites on the photocatalyst surface. The second approach has been espoused in their studies in the preparation of $\text{TiO}_2/\text{SiO}_2$ composites with different ratios of Ti/Si.

The application of photocatalysts with different Ti/Si ratios for the photodecomposition of R6G has been investigated and it has been noted that a Ti/Si ratio of 30/70 produces a catalyst about three times more active than commercially available Degussa P25 due to the enhanced adsorption of the dye. However, it has been noticed that the presence of larger amounts of SiO_2 decreases the activity. In a following study, Anderson and Bard have utilized two different binary mixed oxides $\text{TiO}_2/\text{SiO}_2$ and $\text{TiO}_2/\text{Al}_2\text{O}_3$ for the photodecomposition of salicylic acid and phenol [92]. It was observed that the $\text{TiO}_2/\text{Al}_2\text{O}_3$ system gave improved activity for the decomposition of salicylic acid relative to bare TiO_2 . Moreover, $\text{TiO}_2/\text{SiO}_2$ materials show higher activity than $\text{TiO}_2/\text{Al}_2\text{O}_3$ and TiO_2 towards the photocatalytic decomposition of phenol. The schematic diagram in Figure 22 illustrates the photocatalysis mechanism of the two mixed oxide catalysts $\text{TiO}_2/\text{Al}_2\text{O}_3$ and $\text{TiO}_2/\text{SiO}_2$ that have been utilized in their study.

It was noticed by Cheng and coworkers that the addition of silica in the titania-silica mixed oxides increases the photoactivity by suppressing the phase transformation of titania from anatase to rutile, and this has been also reported by several other researchers [165, 300, 301]. Also, the addition of silica facilitates the formation of oxygen vacancies in titania [165]. Yang and coworkers investigated the effect of addition of silica to titania, on the crystalline growth and the transformation of anatase to rutile phase [300]. It has been observed that the suppression in the crystallite size enhanced the surface area and resulted in a blue shift in the onset of absorption edge in the mixed oxide materials compared to pure titania. The photocatalytic activity of these silica-modified materials was evaluated by decolorization of MO solutions under UV-visible light irradiation and it was found that the silica content, calcination temperature, H_2SO_4 , and presence of oxidants such as KIO_4 , $(\text{NH}_4)_2\text{S}_2\text{O}_8$, and H_2O_2 greatly influenced the decolorizing process.

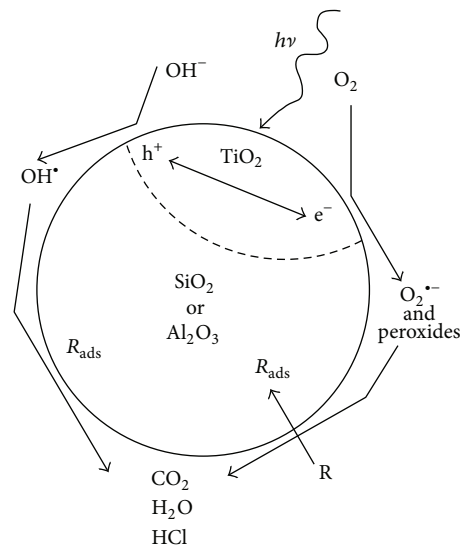


FIGURE 22: Schematic representation of the $\text{TiO}_2/\text{SiO}_2$ and $\text{TiO}_2/\text{Al}_2\text{O}_3$ photocatalysts with no interaction between the TiO_2 and SiO_2 or Al_2O_3 phases (reprinted with permission from [92]).

Photodegradation of two different dyes, reactive 15 (R15) and cationic blue X-GRL (CBX), was carried out over different surface bond conjugated $\text{TiO}_2/\text{SiO}_2$ materials prepared by impregnation method [302]. The material with 30 wt.% of $\text{TiO}_2/\text{SiO}_2$ shows higher activity due to the smaller particle size of TiO_2 on the sample. It was found that silica gel plays a key role in dispersion of TiO_2 . In another study, photocatalysts were prepared by surface functionalization with thiol, cyano, and thiocyno groups on silica and silica-titania catalysts and these were investigated for the photocatalytic degradation of MB [81]. The adsorption of MB on these catalysts is significantly altered due to the surface modification and varies with the type of functional group bound to the surface. In addition, all these functional groups are very stable to UV and the surface bond $\text{TiO}_2/\text{SiO}_2$ materials provide good photocatalytic activity for the decomposition of MB.

The photocatalytic degradation of a RhB with TiO_2 [303] and $\text{TiO}_2/\text{SiO}_2$ in aqueous dispersion was investigated by several researchers under visible and UV irradiation [303–305]. Rasalingam et al. studied the deethylation of RhB dye molecule in the presence of both TiO_2 and $\text{TiO}_2/\text{SiO}_2$ under visible and UV irradiation. The detailed mechanism for the deethylation process of RhB was investigated by high performance liquid chromatograph (HPLC) and liquid chromatograph-mass spectrometry (LC-MS) techniques. It was reported that RhB adsorbs on the surface of $\text{TiO}_2/\text{SiO}_2$ particles by the positively charged diethylamino group, whereas adsorption was achieved through the negatively charged carboxyl group on TiO_2 at pH of 4.3. Similar adsorption behavior of RhB dye molecule over TiO_2 - SiO_2 mixed oxide materials prepared under ambient conditions was recently studied by our group and it was concluded that, apart from the surface charge of the mixed oxide materials, the pore volume of the material also plays a key role in the adsorption of the dye molecule over the catalytic surface [86].

In addition, our group has investigated the influence of Ti-O-Si heterolinkages on the TiO₂-SiO₂ xerogel materials for the degradation of RhB dye [305]. The active heterolinkages (Ti-O-Si) were credited for the higher rate of degradation. The effect of cosolvent in increasing the surface area of these photocatalysts was reported by Budhi et al. [268]. Titania coated silica spheres prepared by heterocoagulation method were utilized as catalyst in the photodegradation of RhB dye in aqueous solution [88]. The experiments showed complete degradation of RhB without any photobleaching.

In another recent study, a series of aperiodic titania-silica photocatalysts was prepared in ethanolic solutions of polar aprotic cosolvents such as ethyl acetate (EtOAc), acetonitrile (ACN), acetone (ACT), and N,N-dimethylformamide (DMF) using sol-gel procedure by our group [304]. The use of polar aprotic solvents was found to be a feasible approach to modify the textural properties of the materials, such as surface areas and pore sizes, without the need to use expensive templates. Dark adsorption and degradation of RhB dye molecules on these titania-silica materials revealed that the pore volume of the mixed oxide mainly influenced the adsorption, while pore diameters enhanced the initial degradation rate. The larger pores permit the organics to diffuse in and out of the mesostructure to enhance their effective photocatalytic degradation under visible light irradiation.

Degradation of acid orange 7 (AO7) using TiO₂/SiO₂ composites, which were prepared by coating the SiO₂ surface with nano-TiO₂ by hydrolysis of TiCl₄, was examined by Cetinkaya and coworkers [286]. An improved adsorption of AO7 was attained with nano-TiO₂ on the surface of SiO₂ under UV light. Furthermore, the effect of calcination temperature on the photocatalytic degradation was also examined. A degradation efficiency of 40% was achieved with the sample calcined at 600°C. The high activity of this material was explained by the presence of a mixture of rutile and anatase phase in the structure that minimized electron-hole recombination.

Photocatalytic Degradation of Pesticides. Photocatalytic degradation of organophosphorous pesticides that include dichlorvos, monocrotophos, parathion, and phorate was investigated by using floating TiO₂/SiO₂ photocatalyst beads prepared by dip coating method [306]. Complete degradation was attained after 420 min. of sunlight irradiation. They have found that the addition of small amount of electron scavenger, Cu²⁺, escalates the photodegradation efficiency of organophosphorus pesticides via reduced electron-hole recombination and increased formation of hydroxyl radicals. The formation of these hydroxyl radicals on the TiO₂ surface is favored in acidic and alkaline solutions. Furthermore, an effective conversion of phosphate ester into trimethyl phosphate ester, formic acid, and acetic acid was achieved in the presence of acids and bases. The trimethyl phosphate ester is then photocatalytically degraded into PO₄³⁻ and formic acid. Even though Cu²⁺ increases the degradation efficiency, higher concentrations of Cu²⁺ lead to the formation of [Cu(H₂O)₄]²⁺ complex ions that absorb UV light and reduce the photoefficiency. Phanikrishna Sharma and coworkers

utilized titania-silica composite materials prepared using a styrene-acrylic acid emulsion as a latex polymer template, for the degradation of isoproturon (*N,N*-dimethyl-*N*-[4-(1-methylethyl)phenyl]), identified as a hazardous class III herbicide. Effective degradation was obtained at an optimal loading of 5 wt.% TiO₂ under solar light. Furthermore, a similar approach was successfully used for the degradation of commercially available pesticides such as imidacloprid and phosphadum [307, 308]. In a recent study, remediation of dimethyl phthalate, which is used in pesticides, plastics, safety glasses, rubber coating agents, and insect repellants, using hollow glass microsphere (HGM) coated with photocatalytic TiO₂ has been carried out by Jiang and coworkers [309]. In their study, they have optimized the condition for the formation of hydroxyl radicals by using terephthalic acid as hydroxyl radical trapper. Three different variables, such as the loading of HGM-TiO₂, concentration of terephthalic acid, and irradiation time, were investigated on the photocatalysis. It is worth mentioning here that the HGM-TiO₂ catalyst is available in market for the removal of aqueous pollutants as well as gaseous pollutants.

4. Factors Influencing Photocatalytic Degradation Using TiO₂-SiO₂ Mixed Oxides

It is noted that the photocatalytic activity of TiO₂-SiO₂ mixed oxides is closely related to their structural properties, such as crystallinity and crystallite size of titania, crystal composition, surface area, particle size distribution, porosity, bandgap, surface hydroxyl density, dispersion of TiO₂, and Ti-O-Si linkages. The use of a high surface area silica support provides good dispersion of titania. Also, the silica support increases the hydrophobic nature of the mixed oxide. This helps to adsorb a wide variety of organic pollutants and concentrate them close to the reactive TiO₂ centre [272]. The crystallite or particle size of titania plays a key role in degradation. Silica support confines the TiO₂ particles in the nanosize range due to quantum size effect, and the smaller titania particles in general show enhanced photocatalytic activity. This is explained by a decrease in the rate of volume charge carrier recombination of the electron-hole pairs in smaller sized titania particles. The photocatalytic activity is maximum at an optimal particle size at which the volume and surface charge carrier recombination of the electron-hole pairs is minimized. However, at very small particle sizes, surface charge carrier recombination is enhanced, and, thus, the resulting photocatalytic activity will decrease. In addition to the particle size, the photocatalytic activity also depends on the amount of titania. The photocatalytic activity is usually maximum at an optimal loading of titania. At higher loadings of titania, larger aggregates of titania are formed that occlude the pores and limit the diffusion of the reactant molecules, and, thus, the photocatalytic activity is lowered. Also, the crystallinity and the nature (phase) of titania are important factors that profoundly affect the photocatalytic activity. Mixed oxide materials that contain highly crystalline titania show enhanced activities. This is because amorphous materials in general contain larger number of defects that enhance electron-hole recombination. In the mixed oxide

material, the silica support prevents the phase transformation of the more active anatase phase to rutile on calcination. In addition to these factors, the chemical property of the TiO₂-SiO₂ binary oxide materials is modulated by the addition of SiO₂ into the TiO₂ network, and the formation of Ti-O-Si heterolinkages has been implicated to play an important role in the photocatalytic activity.

The porous properties such as pore volume and pore size of the mixed oxide materials influence the adsorption of the pollutant. In particular, larger pore sized materials provide better transport (molecular trafficking) of the pollutants and the product(s), in and out from the active sites, and contribute to enhanced degradation. It is generally observed that the rate of degradation increases with an increase in the pollutant concentration to a certain level. However, further increase in the pollutant concentration results in a decrease in the degradation rate. Among the various ROS, [•]OH radical is an important species in the degradation processes and the rate of degradation depends on both the probability of the formation of [•]OH radicals on the catalyst surface and the reactivity of [•]OH radicals with the pollutants. Thus, the enhancement in activity will rely on the probability of the reaction between the pollutant and these oxidizing species. However, the degradation efficiency decreases beyond a particular level of pollutant concentration. This is due to the inhibition of [•]OH radical generation via the coverage of active sites on the catalysts by the pollutant molecules/ions. In addition, another reason that was reported for the low activity particularly for dye pollutants was the UV-screening effect by the dyes. At high dye concentrations, a significant amount of UV light may be absorbed by the dye molecules rather than by the semiconductor particles and this reduces the efficiency of the catalytic reaction by reducing the generation of [•]OH radical and superoxide radical (O₂^{•-}).

The characteristic features of the pollutant in the wastewater differ with the variation in the solution pH [310]. The pH of the medium may lead to changes in solubility, stability, hydrophobicity, and also the color of the substance (applicable to dyes). In addition, the pH of the medium can also change the surface charge of the photocatalysts and degree of ionization of the organics. An organic compound remains in the neutral state at pH below its pK_a value and is negatively charged when the pH exceeds the pK_a value. Furthermore, electrostatic interactions between the semiconductor surface, solvent molecules, pollutant substrate, and the ROS formed during photocatalytic oxidation vary with solution pH. Thus, these variations in the pH play a vital role in the photocatalytic degradation efficiency.

A comparative table is provided in the supplementary section (in the Supplementary Material available online at <http://dx.doi.org/10.1155/2014/617405>) to indicate the various classes of compounds that have been examined for removal for contaminants.

5. Conclusions

This review has attempted to cover a wide range of wastewater effluent removal techniques for water treatment. The reader can get an idea about the various types of removal methods

and the basic principles behind each technique. Heterogeneous photocatalytic oxidation (HPO) has garnered extensive attention due to its effective removal of toxic compounds from waste effluents. The HPO process employs several oxide and mixed oxide catalysts, mainly for water purification. Among these materials, TiO₂-SiO₂ mixed oxides have been found to be more active than the other mixed oxides for the degradation of organics. In this work, we have covered the degradation of organics by utilizing TiO₂-SiO₂ binary mixed oxide materials and the factors that influence the degradation have been discussed. Furthermore, this review briefly explains the synthetic procedures and the main characterization techniques of the two main types of TiO₂-SiO₂ binary mixed oxides, periodic and aperiodic oxides. Even though these binary mixed oxides show better activity than pure TiO₂ materials in most instances, the utilization of these TiO₂-SiO₂ mixed oxides is limited for the mineralization of selected pollutants.

Conflict of Interests

The authors declare no conflict of interests.

Acknowledgments

Thanks are due to the National Science Foundation Grants NSF-CHE-0722632 and NSF-EPS-0903804 and the Department of Energy Grant DE-EE0000270.

References

- [1] L. G. da Silva, R. Ruggiero, P. D. M. Gontijo et al., "Adsorption of Brilliant Red 2BE dye from water solutions by a chemically modified sugarcane bagasse lignin," *Chemical Engineering Journal*, vol. 168, no. 2, pp. 620–628, 2011.
- [2] A. Dębrowski, P. Podkościelny, Z. Hubicki, and M. Barczak, "Adsorption of phenolic compounds by activated carbon: a critical review," *Chemosphere*, vol. 58, no. 8, pp. 1049–1070, 2005.
- [3] Y. Fu and T. Viraraghavan, "Fungal decolorization of dye wastewaters: a review," *Bioresource Technology*, vol. 79, no. 3, pp. 251–262, 2001.
- [4] A. K. Biń and S. Sobera-Madej, "Comparison of the advanced oxidation processes (UV, UV/H₂O₂ and O₃) for the removal of antibiotic substances during wastewater treatment," *Ozone: Science and Engineering*, vol. 34, no. 2, pp. 136–139, 2012.
- [5] A. Srinivasan and T. Viraraghavan, "Decolorization of dye wastewaters by biosorbents: a review," *Journal of Environmental Management*, vol. 91, no. 10, pp. 1915–1929, 2010.
- [6] M. Govindaraj, R. Rathinam, C. Sukumar, M. Uthayasankar, and S. Pattabhi, "Electrochemical oxidation of bisphenol-A from aqueous solution using graphite electrodes," *Environmental Technology*, vol. 34, no. 4, pp. 503–511, 2013.
- [7] K. Pirkanniemi and M. Sillanpää, "Heterogeneous water phase catalysis as an environmental application: a review," *Chemosphere*, vol. 48, no. 10, pp. 1047–1060, 2002.
- [8] P. V. Suraja, Z. Yaakob, N. N. Binitha, M. R. Resmi, and P. P. Silija, "Photocatalytic degradation of dye pollutant over Ti and Co doped SBA-15: comparison of activities under visible light," *Chemical Engineering Journal*, vol. 176–177, pp. 265–271, 2011.

- [9] R. Andreozzi, V. Caprio, A. Insola, and R. Marotta, "Advanced oxidation processes (AOP) for water purification and recovery," *Catalysis Today*, vol. 53, no. 1, pp. 51–59, 1999.
- [10] B. Ning, N. Graham, Y. Zhang, M. Nakonechny, and M. G. El-Din, "Degradation of endocrine disrupting chemicals by ozone/AOPs," *Ozone: Science and Engineering*, vol. 29, no. 3, pp. 153–176, 2007.
- [11] R. Thapa, S. Maiti, T. H. Rana, U. N. Maiti, and K. K. Chattopadhyay, "Anatase TiO₂ nanoparticles synthesis via simple hydrothermal route: degradation of orange II, methyl orange and rhodamine B," *Journal of Molecular Catalysis A: Chemical*, vol. 363, pp. 223–229, 2012.
- [12] Z. Guo, R. Ma, and G. Li, "Degradation of phenol by nanomaterial TiO₂ in wastewater," *Chemical Engineering Journal*, vol. 119, no. 1, pp. 55–59, 2006.
- [13] J. Yang, C. Chen, H. Ji, W. Ma, and J. Zhao, "Mechanism of TiO₂-assisted photocatalytic degradation of dyes under visible irradiation: photoelectrocatalytic study by TiO₂-film electrodes," *Journal of Physical Chemistry B*, vol. 109, no. 46, pp. 21900–21907, 2005.
- [14] C. Anderson and A. J. Bard, "An improved photocatalyst of TiO₂/SiO₂ prepared by a sol-gel synthesis," *Journal of Physical Chemistry*, vol. 99, no. 24, pp. 9882–9885, 1995.
- [15] A. S. Malik, D. Letson, and S. R. Crutchfield, "Point non-point-source trading of pollution-abatement: choosing the right trading ratio," *The American Journal of Agricultural Economics*, vol. 75, no. 4, pp. 959–967, 1993.
- [16] Y. Yuhong, Y. Baixing, and S. Wanbin, "Assessment of point and nonpoint sources pollution in Songhua River Basin, Northeast China by using revised water quality model," *Chinese Geographical Science*, vol. 20, no. 1, pp. 30–36, 2010.
- [17] S. R. Carpenter, N. F. Caraco, D. L. Correll, R. W. Howarth, A. N. Sharpley, and V. H. Smith, "Nonpoint pollution of surface waters with phosphorus and nitrogen," *Ecological Applications*, vol. 8, no. 3, pp. 559–568, 1998.
- [18] C.-G. Tang and C.-Q. Liu, "Nonpoint source pollution assessment of wujiang river watershed in Guizhou Province, SW China," *Environmental Modeling and Assessment*, vol. 13, no. 1, pp. 155–167, 2008.
- [19] N. Štambuk-Giljanović, "The pollution load by nitrogen and phosphorus in the Jadro River," *Environmental Monitoring and Assessment*, vol. 123, no. 1–3, pp. 13–30, 2006.
- [20] W. Ouyang, H. B. Huang, F. H. Hao, Y. S. Shan, and B. B. Guo, "Evaluating spatial interaction of soil property with non-point source pollution at watershed scale: the phosphorus indicator in Northeast China," *Science of the Total Environment*, vol. 432, pp. 412–421, 2012.
- [21] V. Kertész, G. Bakonyi, and B. Farkas, "Water pollution by Cu and Pb can adversely affect mallard embryonic development," *Ecotoxicology and Environmental Safety*, vol. 65, no. 1, pp. 67–73, 2006.
- [22] I. Razo, L. Carrizales, J. Castro, F. Díaz-Barriga, and M. Monroy, "Arsenic and heavy metal pollution of soil, water and sediments in a semi-arid climate mining area in Mexico," *Water, Air, and Soil Pollution*, vol. 152, no. 1–4, pp. 129–152, 2004.
- [23] J. Cheng, T. Yuan, W. Wang et al., "Mercury pollution in two typical areas in Guizhou province, China and its neurotoxic effects in the brains of rats fed with local polluted rice," *Environmental Geochemistry and Health*, vol. 28, no. 6, pp. 499–507, 2006.
- [24] R. Mu, Z. Xu, L. Li, Y. Shao, H. Wan, and S. Zheng, "On the photocatalytic properties of elongated TiO₂ nanoparticles for phenol degradation and Cr(VI) reduction," *Journal of Hazardous Materials*, vol. 176, no. 1–3, pp. 495–502, 2010.
- [25] B. Haidari, A. R. Bakhtiari, V. Yavari, A. Kazemi, and G. Shirneshan, "Biomonitoring of Ni and V contamination using oysters (*Saccostrea cucullata*) at Lengeh Port, Persian Gulf, Iran," *Clean: Soil, Air, Water*, vol. 41, no. 2, pp. 166–173, 2013.
- [26] S. T. Ingvertsen, H. Marcussen, and P. E. Holm, "Pollution and potential mobility of Cd, Ni and Pb in the sediments of a wastewater-receiving river in Hanoi, Vietnam," *Environmental Monitoring and Assessment*, vol. 185, no. 11, pp. 9531–9548, 2013.
- [27] M. Zeiner, T. Rezić, B. Santek, I. Rezić, S. Hann, and G. Stinger, "Removal of Cr, Mn, and Co from textile wastewater by horizontal rotating tubular bioreactor," *Environmental Science and Technology*, vol. 46, no. 19, pp. 10690–10696, 2012.
- [28] Š. Mechora, P. Cuderman, V. Stibilj, and M. Germ, "Distribution of Se and its species in *Myriophyllum spicatum* and *Ceratophyllum demersum* growing in water containing se (VI)," *Chemosphere*, vol. 84, no. 11, pp. 1636–1641, 2011.
- [29] D. Purushotham, M. Rashid, M. A. Lone et al., "Environmental impact assessment of air and heavy metal concentration in groundwater of Maheshwaram watershed, Ranga Reddy district, Andhra Pradesh," *Journal of the Geological Society of India*, vol. 81, no. 3, pp. 385–396, 2013.
- [30] R. Lohmann, K. Breivik, J. Dachs, and D. Muir, "Global fate of POPs: current and future research directions," *Environmental Pollution*, vol. 150, no. 1, pp. 150–165, 2007.
- [31] K. Breivik, R. Alcock, Y.-F. Li, R. E. Bailey, H. Fiedler, and J. M. Pacyna, "Primary sources of selected POPs: regional and global scale emission inventories," *Environmental Pollution*, vol. 128, no. 1–2, pp. 3–16, 2004.
- [32] M. S. El-Shahawi, A. Hamza, A. S. Bashammakh, and W. T. Al-Saggaf, "An overview on the accumulation, distribution, transformations, toxicity and analytical methods for the monitoring of persistent organic pollutants," *Talanta*, vol. 80, no. 5, pp. 1587–1597, 2010.
- [33] H. W. Vallack, D. J. Bakker, I. Brandt et al., "Controlling persistent organic pollutants-what next?" *Environmental Toxicology and Pharmacology*, vol. 6, no. 3, pp. 143–175, 1998.
- [34] K. C. Jones and P. De Voogt, "Persistent organic pollutants (POPs): state of the science," *Environmental Pollution*, vol. 100, no. 1–3, pp. 209–221, 1998.
- [35] L. H. Keith and W. A. Telliard, "Priority pollutants. I. A perspective view," *Environmental Science and Technology*, vol. 13, no. 4, pp. 416–423, 1979.
- [36] C. A. Basar, A. Karagunduz, A. Cakici, and B. Keskinler, "Removal of surfactants by powdered activated carbon and microfiltration," *Water Research*, vol. 38, no. 8, pp. 2117–2124, 2004.
- [37] K. Hunger, *Industrial Dyes: Chemistry, Properties, Applications*, Wiley VCH, Weinheim, Germany, 2003.
- [38] J. Michałowicz and W. Duda, "Phenols: sources and toxicity," *Polish Journal of Environmental Studies*, vol. 16, no. 3, pp. 347–362, 2007.
- [39] M. Hayashi, Y. Nakamura, K. Higashi, H. Kato, F. Kishida, and H. Kaneko, "A quantitative structure-activity relationship study of the skin irritation potential of phenols," *Toxicology in Vitro*, vol. 13, no. 6, pp. 915–922, 1999.
- [40] A. Dominguez-Ramos and A. Irabien, "Analysis and modeling of the continuous electro-oxidation process for organic matter removal in urban wastewater treatment," *Industrial and Engineering Chemistry Research*, vol. 52, no. 22, pp. 7534–7540, 2013.

- [41] Y. M. Slokar and A. Majcen Le Marechal, "Methods of decoloration of textile wastewaters," *Dyes and Pigments*, vol. 37, no. 4, pp. 335–356, 1998.
- [42] G. Odukkathil and N. Vasudevan, "Toxicity and bioremediation of pesticides in agricultural soil," *Reviews in Environmental Science and Bio/Technology*, vol. 12, no. 4, pp. 421–444, 2013.
- [43] J. M. Prodanovic and V. M. Vasic, "Application of membrane processes for distillery wastewater purification: a review," *Desalination and Water Treatment*, vol. 51, no. 16–18, pp. 3325–3334, 2013.
- [44] S. Papić, N. Koprivanac, A. Lončarić Božić, and A. Meteš, "Removal of some reactive dyes from synthetic wastewater by combined Al(III) coagulation/carbon adsorption process," *Dyes and Pigments*, vol. 62, no. 3, pp. 291–298, 2004.
- [45] J.-W. Lee, S.-P. Choi, R. Thiruvenkatachari, W.-G. Shim, and H. Moon, "Evaluation of the performance of adsorption and coagulation processes for the maximum removal of reactive dyes," *Dyes and Pigments*, vol. 69, no. 3, pp. 196–203, 2006.
- [46] I. Ilisz, A. Dombi, K. Mogyorósi, A. Farkas, and I. Dékány, "Removal of 2-chlorophenol from water by adsorption combined with TiO₂ photocatalysis," *Applied Catalysis B: Environmental*, vol. 39, no. 3, pp. 247–256, 2002.
- [47] P. V. Messina and P. C. Schulz, "Adsorption of reactive dyes on titania-silica mesoporous materials," *Journal of Colloid and Interface Science*, vol. 299, no. 1, pp. 305–320, 2006.
- [48] R. Jain, M. Mathur, S. Sikarwar, and A. Mittal, "Removal of the hazardous dye rhodamine B through photocatalytic and adsorption treatments," *Journal of Environmental Management*, vol. 85, no. 4, pp. 956–964, 2007.
- [49] M. Rafatullah, O. Sulaiman, R. Hashim, and A. Ahmad, "Adsorption of methylene blue on low-cost adsorbents: a review," *Journal of Hazardous Materials*, vol. 177, no. 1–3, pp. 70–80, 2010.
- [50] M.-X. Zhu, L. Lee, H.-H. Wang, and Z. Wang, "Removal of an anionic dye by adsorption/precipitation processes using alkaline white mud," *Journal of Hazardous Materials*, vol. 149, no. 3, pp. 735–741, 2007.
- [51] C. D. Vecitis, Y. Wang, J. Cheng, H. Park, B. T. Mader, and M. R. Hoffmann, "Sonochemical degradation of perfluorooctanesulfonate in aqueous film-forming foams," *Environmental Science and Technology*, vol. 44, no. 1, pp. 432–438, 2010.
- [52] N. L. Stock, J. Peller, K. Vinodgopal, and P. V. Kamat, "Combinative sonolysis and photocatalysis for textile dye degradation," *Environmental Science and Technology*, vol. 34, no. 9, pp. 1747–1750, 2000.
- [53] C. A. Martínez-Huitle and S. Ferro, "Electrochemical oxidation of organic pollutants for the wastewater treatment: direct and indirect processes," *Chemical Society Reviews*, vol. 35, no. 12, pp. 1324–1340, 2006.
- [54] S. Tanaka, Y. Nakata, T. Kimura, Y. Yustiwati, M. Kawasaki, and H. Kuramitz, "Electrochemical decomposition of bisphenol A using Pt/Ti and SnO₂/Ti anodes," *Journal of Applied Electrochemistry*, vol. 32, no. 2, pp. 197–201, 2002.
- [55] J.-F. Zhi, H.-B. Wang, T. Nakashima, T. N. Rao, and A. Fujishima, "Electrochemical incineration of organic pollutants on boron-doped diamond electrode. Evidence for direct electrochemical oxidation pathway," *Journal of Physical Chemistry B*, vol. 107, no. 48, pp. 13389–13395, 2003.
- [56] P. Cañizares, C. Sáez, J. Lobato, and M. A. Rodrigo, "Electrochemical oxidation of polyhydroxybenzenes on boron-doped diamond anodes," *Industrial and Engineering Chemistry Research*, vol. 43, no. 21, pp. 6629–6637, 2004.
- [57] C. A. Martínez-Huitle, M. A. Quiroz, C. Comninellis, S. Ferro, and A. De Battisti, "Electrochemical incineration of chloranilic acid using Ti/IrO₂, Pb/PbO₂ and Si/BDD electrodes," *Electrochimica Acta*, vol. 50, no. 4, pp. 949–956, 2004.
- [58] X. Zhu, S. Shi, J. Wei et al., "Electrochemical oxidation characteristics of p-substituted phenols using a boron-doped diamond electrode," *Environmental Science and Technology*, vol. 41, no. 18, pp. 6541–6546, 2007.
- [59] J. Jiang, M. Chang, and P. Pan, "Simultaneous hydrogen production and electrochemical oxidation of organics using boron-doped diamond electrodes," *Environmental Science and Technology*, vol. 42, no. 8, pp. 3059–3063, 2008.
- [60] M. Murugananthan, S. Yoshihara, T. Rakuma, and T. Shirakashi, "Mineralization of bisphenol A (BPA) by anodic oxidation with boron-doped diamond (BDD) electrode," *Journal of Hazardous Materials*, vol. 154, no. 1–3, pp. 213–220, 2008.
- [61] N. Borràs, R. Oliver, C. Arias, and E. Brillas, "Degradation of atrazine by electrochemical advanced oxidation processes using a boron-doped diamond anode," *Journal of Physical Chemistry A*, vol. 114, no. 24, pp. 6613–6621, 2010.
- [62] M. Govindaraj, M. Muthukumar, and G. Bhaskar Raju, "Electrochemical oxidation of tannic acid contaminated wastewater by RuO₂/IrO₂/TaO₂-coated titanium and graphite anodes," *Environmental Technology*, vol. 31, no. 14, pp. 1613–1622, 2010.
- [63] M. Murugananthan, S. S. Latha, G. Bhaskar Raju, and S. Yoshihara, "Anodic oxidation of ketoprofen-An anti-inflammatory drug using boron doped diamond and platinum electrodes," *Journal of Hazardous Materials*, vol. 180, no. 1–3, pp. 753–758, 2010.
- [64] S. Song, L. Zhan, Z. He et al., "Mechanism of the anodic oxidation of 4-chloro-3-methyl phenol in aqueous solution using Ti/SnO₂-Sb/PbO₂ electrodes," *Journal of Hazardous Materials*, vol. 175, no. 1–3, pp. 614–621, 2010.
- [65] N. Bensalah, B. Louhichi, and A. Abdel-Wahab, "Electrochemical oxidation of succinic acid in aqueous solutions using boron doped diamond anodes," *International Journal of Environmental Science and Technology*, vol. 9, no. 1, pp. 135–143, 2012.
- [66] C. I. Brinzila, M. J. Pacheco, L. Ciriaco, R. C. Ciobanu, and A. Lopes, "Electrodegradation of tetracycline on BDD anode," *Chemical Engineering Journal*, vol. 209, pp. 54–61, 2012.
- [67] J. M. Peralta-Hernandez, M. Mendez-Tovar, R. Guerra-Sanchez, C. A. Martínez-Huitle, and J. L. Nava, "A brief review on environmental application of boron doped diamond electrodes as a new way for electrochemical incineration of synthetic dyes," *International Journal of Electrochemistry*, vol. 2012, Article ID 154316, 18 pages, 2012.
- [68] N. Rabaaoui and M. S. Allagui, "Anodic oxidation of salicylic acid on BDD electrode: variable effects and mechanisms of degradation," *Journal of Hazardous Materials*, vol. 243, pp. 187–192, 2012.
- [69] M. G. Tavares, L. V. A. da Silva, A. M. Sales Solano, J. Tonholo, C. A. Martínez-Huitle, and C. L. P. S. Zanta, "Electrochemical oxidation of methyl red using Ti/Ru_{0.3}Ti_{0.7}O₂ and Ti/Pt anodes," *Chemical Engineering Journal*, vol. 204–206, pp. 141–150, 2012.
- [70] R. B. Alencar de Souza and L. A. Martins Ruotolo, "Phenol electrooxidation in different supporting electrolytes using boron-doped diamond anodes," *International Journal of Electrochemical Science*, vol. 8, no. 1, pp. 643–657, 2013.
- [71] M. Gaber, N. Abu Ghalwa, A. M. Khedr, and M. F. Salem, "Electrochemical degradation of reactive yellow 160 Dye in real wastewater using C/PbO₂, Pb⁺Sn/PbO₂⁺SnO₂, and Pb/PbO₂

- modified electrodes," *Journal of Chemistry*, Article ID 691763, 9 pages, 2013.
- [72] N. Rabaaoui, Y. Moussaoui, M. S. Allagui, B. Ahmed, and E. Elaloui, "Anodic oxidation of nitrobenzene on BDD electrode: variable effects and mechanisms of degradation," *Separation and Purification Technology*, vol. 107, pp. 318–323, 2013.
- [73] N. Rabaaoui, M. E. K. Saad, Y. Moussaoui, M. S. Allagui, A. Bedoui, and E. Elaloui, "Anodic oxidation of o-nitrophenol on BDD electrode: variable effects and mechanisms of degradation," *Journal of Hazardous Materials*, vol. 250–251, pp. 447–453, 2013.
- [74] W. K. Lafi and Z. Al-Qodah, "Combined advanced oxidation and biological treatment processes for the removal of pesticides from aqueous solutions," *Journal of Hazardous Materials*, vol. 137, no. 1, pp. 489–497, 2006.
- [75] J.-M. Herrmann, "Heterogeneous photocatalysis: fundamentals and applications to the removal of various types of aqueous pollutants," *Catalysis Today*, vol. 53, no. 1, pp. 115–129, 1999.
- [76] Z. Wang, F. Zhang, Y. Yang, B. Xue, J. Cui, and N. Guan, "Facile postsynthesis of visible-light-sensitive titanium dioxide/mesoporous SBA-15," *Chemistry of Materials*, vol. 19, no. 13, pp. 3286–3293, 2007.
- [77] Y. J. Acosta-Silva, R. Nava, V. Hernández-Morales, S. A. Macías-Sánchez, M. L. Gómez-Herrera, and B. Pawelec, "Methylene blue photodegradation over titania-decorated SBA-15," *Applied Catalysis B: Environmental*, vol. 110, pp. 108–117, 2011.
- [78] S. Artkla, "Photodecomposition of polyphenols in E. camaldulensis leaves in the presence of hybrid catalyst of titania and MCM-41 synthesized from rice husk silica," *Korean Journal of Chemical Engineering*, vol. 29, no. 5, pp. 555–562, 2012.
- [79] S. Zhu, D. Zhang, X. Zhang et al., "Sonochemical incorporation of nanosized TiO₂ inside mesoporous silica with high photocatalytic performance," *Microporous and Mesoporous Materials*, vol. 126, no. 1–2, pp. 20–25, 2009.
- [80] Y.-J. Do, J.-H. Kim, J.-H. Park et al., "Photocatalytic decomposition of 4-nitrophenol on Ti-containing MCM-41," *Catalysis Today*, vol. 101, no. 3–4, pp. 299–305, 2005.
- [81] K. Gude, V. M. Gun'ko, and J. P. Blitz, "Adsorption and photocatalytic decomposition of methylene blue on surface modified silica and silica-titania," *Colloids and Surfaces A: Physicochemical and Engineering Aspects*, vol. 325, no. 1–2, pp. 17–20, 2008.
- [82] E. A. El-Sharkawy, A. Y. Soliman, and K. M. Al-Amer, "Comparative study for the removal of methylene blue via adsorption and photocatalytic degradation," *Journal of Colloid and Interface Science*, vol. 310, no. 2, pp. 498–508, 2007.
- [83] Y. Li, N. Li, J. Tu et al., "TiO₂ supported on rod-like mesoporous silica SBA-15: preparation, characterization and photocatalytic behaviour," *Materials Research Bulletin*, vol. 46, no. 12, pp. 2317–2322, 2011.
- [84] H. S. Kibombo, D. Zhao, A. Gonshorowski, S. Budhi, M. D. Koppang, and R. T. Koodali, "Cosolvent-induced gelation and the hydrothermal enhancement of the crystallinity of titania-silica mixed oxides for the photocatalytic remediation of organic pollutants," *Journal of Physical Chemistry C*, vol. 115, no. 13, pp. 6126–6135, 2011.
- [85] A. A. Belhekar, S. V. Awate, and R. Anand, "Photocatalytic activity of titania modified mesoporous silica for pollution control," *Catalysis Communications*, vol. 3, no. 10, pp. 453–458, 2002.
- [86] S. Rasalingam, R. Peng, and R. T. Koodali, "An investigation into the effect of porosities on the adsorption of rhodamine B using titania-silica mixed oxide xerogels," *Journal of Environmental Management*, vol. 128, pp. 530–539, 2013.
- [87] J. Aguado, R. van Grieken, M.-J. López-Muñoz, and J. Marugán, "A comprehensive study of the synthesis, characterization and activity of TiO₂ and mixed TiO₂/SiO₂ photocatalysts," *Applied Catalysis A: General*, vol. 312, no. 1–2, pp. 202–212, 2006.
- [88] P. Wilhelm and D. Stephan, "Photodegradation of rhodamine B in aqueous solution via SiO₂@TiO₂ nano-spheres," *Journal of Photochemistry and Photobiology A: Chemistry*, vol. 185, no. 1, pp. 19–25, 2007.
- [89] E. Y. Kim, C. M. Whang, W. I. Lee, and Y. H. Kim, "Photocatalytic property of SiO₂/TiO₂ nanoparticles prepared by sol-hydrothermal process," *Journal of Electroceramics*, vol. 17, no. 2–4, pp. 899–902, 2006.
- [90] D. Sun, Y. Huang, B. Han, and G. Yang, "Ti-Si mixed oxides prepared by polymer in situ sol-gel chemistry with the aid of CO₂," *Langmuir*, vol. 22, no. 10, pp. 4793–4798, 2006.
- [91] H. Yamashita, S. Kawasaki, Y. Ichihashi et al., "Characterization of titanium-silicon binary oxide catalysts prepared by the sol-gel method and their photocatalytic reactivity for the liquid-phase oxidation of 1-octanol," *Journal of Physical Chemistry B*, vol. 102, no. 30, pp. 5870–5875, 1998.
- [92] C. Anderson and A. J. Bard, "Improved photocatalytic activity and characterization of mixed TiO₂/SiO₂ and TiO₂/Al₂O₃ materials," *Journal of Physical Chemistry B*, vol. 101, no. 14, pp. 2611–2616, 1997.
- [93] H. Eccles, "Treatment of metal-contaminated wastes: why select a biological process?" *Trends in Biotechnology*, vol. 17, no. 12, pp. 462–465, 1999.
- [94] N. Lu, J. Pei, Y. Zhao, R. Qi, and J. Liu, "Performance of a biological degradation method for indoor formaldehyde removal," *Building and Environment*, vol. 57, pp. 253–258, 2012.
- [95] W. Chen, S. Z. Jianshun, and Z. Zhang, "Performance of air cleaners for removing multiple volatile organic compounds in indoor air," *SHRAE Transactions*, vol. 111, no. 1, p. 1101, 2005.
- [96] T. N. Obee, "Photooxidation of sub-parts-per-million toluene and formaldehyde levels on titania using a glass-plate reactor," *Environmental Science and Technology*, vol. 30, no. 12, pp. 3578–3584, 1996.
- [97] Z. Wang and J. S. Zhang, "Characterization and performance evaluation of a full-scale activated carbon-based dynamic botanical air filtration system for improving indoor air quality," *Building and Environment*, vol. 46, no. 3, pp. 758–768, 2011.
- [98] C. Di Iaconi, R. Ramadori, and A. Lopez, "Combined biological and chemical degradation for treating a mature municipal landfill leachate," *Biochemical Engineering Journal*, vol. 31, no. 2, pp. 118–124, 2006.
- [99] G. Sudarjanto, B. Keller-Lehmann, and J. Keller, "Optimization of integrated chemical-biological degradation of a reactive azo dye using response surface methodology," *Journal of Hazardous Materials*, vol. 138, no. 1, pp. 160–168, 2006.
- [100] C. Y. Chen, J. T. Kuo, H. A. Yang, and Y. C. Chung, "A coupled biological and photocatalysis pretreatment system for the removal of crystal violet from wastewater," *Chemosphere*, vol. 92, no. 6, pp. 695–701, 2013.
- [101] Y. Lester, H. Mamane, I. Zucker, and D. Avisar, "Treating wastewater from a pharmaceutical formulation facility by biological process and ozone," *Water Research*, vol. 47, no. 13, pp. 4349–4356, 2013.
- [102] R. Rosal, A. Rodríguez, J. A. Perdigón-Melón et al., "Occurrence of emerging pollutants in urban wastewater and their removal

- through biological treatment followed by ozonation,” *Water Research*, vol. 44, no. 2, pp. 578–588, 2010.
- [103] S. Malato, J. Blanco, A. R. Fernández-Alba, and A. Agüera, “Solar photocatalytic mineralization of commercial pesticides: acrinathrin,” *Chemosphere*, vol. 40, no. 4, pp. 403–409, 2000.
- [104] F. Javier Benitez, J. L. Acero, and F. J. Real, “Degradation of carbofuran by using ozone, UV radiation and advanced oxidation processes,” *Journal of Hazardous Materials*, vol. 89, no. 1, pp. 51–65, 2002.
- [105] E. Tamer, Z. Hamid, A. M. Aly, E. T. Ossama, M. Bo, and G. Benoit, “Sequential UV-biological degradation of chlorophenols,” *Chemosphere*, vol. 63, no. 2, pp. 277–284, 2006.
- [106] J. Benner, D. E. Helbling, H. P. E. Kohler et al., “Is biological treatment a viable alternative for micropollutant removal in drinking water treatment processes?” *Water Research*, vol. 47, no. 16, pp. 5955–5976, 2013.
- [107] M. Kröger, M. E. Schumacher, H. Risse, and G. Fels, “Biological reduction of TNT as part of a combined biological-chemical procedure for mineralization,” *Biodegradation*, vol. 15, no. 4, pp. 241–248, 2004.
- [108] S. Le Borgne, D. Paniagua, and R. Vazquez-Duhalt, “Biodegradation of organic pollutants by halophilic bacteria and archaea,” *Journal of Molecular Microbiology and Biotechnology*, vol. 15, no. 2-3, pp. 74–92, 2008.
- [109] G. Lofrano, S. Meriç, G. E. Zengin, and D. Orhon, “Chemical and biological treatment technologies for leather tannery chemicals and wastewaters: a review,” *Science of the Total Environment*, vol. 461–462, pp. 265–281, 2013.
- [110] M. Desai, A. Dogra, S. Vora, P. Bahadur, and R. N. Ram, “Adsorption of some acid dyes from aqueous solutions onto neutral alumina,” *Indian Journal of Chemistry A*, vol. 36, no. 11, pp. 938–944, 1997.
- [111] T. A. Khan, V. V. Singh, and D. Kumar, “Removal of some basic dyes from artificial textile wastewater by adsorption on Akash Kinari coal,” *Journal of Scientific and Industrial Research*, vol. 63, no. 4, pp. 355–364, 2004.
- [112] J. X. Lin, S. L. Zhan, M. H. Fang, X. Q. Qian, and H. Yang, “Adsorption of basic dye from aqueous solution onto fly ash,” *Journal of Environmental Management*, vol. 87, no. 1, pp. 193–200, 2008.
- [113] K. Haarstad, H. J. Bavor, and T. Mæhlum, “Organic and metallic pollutants in water treatment and natural wetlands: a review,” *Water Science and Technology*, vol. 65, no. 1, pp. 76–99, 2012.
- [114] Ş. Kubilay, R. Gürkan, A. Savran, and T. Şahan, “Removal of Cu(II), Zn(II) and Co(II) ions from aqueous solutions by adsorption onto natural bentonite,” *Adsorption*, vol. 13, no. 1, pp. 41–51, 2007.
- [115] M. Rafatullah, O. Sulaiman, R. Hashim, and A. Ahmad, “Adsorption of copper (II), chromium (III), nickel (II) and lead (II) ions from aqueous solutions by meranti sawdust,” *Journal of Hazardous Materials*, vol. 170, no. 2-3, pp. 969–977, 2009.
- [116] J. K. Thomas, “Physical aspects of radiation-induced processes on SiO₂, γ-Al₂O₃, zeolites, and clays,” *Chemical Reviews*, vol. 105, no. 5, pp. 1683–1734, 2005.
- [117] G. Annadurai, R.-S. Juang, and D.-J. Lee, “Adsorption of rhodamine 6G from aqueous solutions on activated carbon,” *Journal of Environmental Science and Health A: Toxic/Hazardous Substances and Environmental Engineering*, vol. 36, no. 5, pp. 715–725, 2001.
- [118] D. Mohan, K. P. Singh, G. Singh, and K. Kumar, “Removal of dyes from wastewater using flyash, a low-cost adsorbent,” *Industrial and Engineering Chemistry Research*, vol. 41, no. 15, pp. 3688–3695, 2002.
- [119] M. Ahmaruzzaman, “Role of fly ash in the removal of organic pollutants from wastewater,” *Energy and Fuels*, vol. 23, no. 3, pp. 1494–1511, 2009.
- [120] G. Dursun, H. Çiçek, and A. Y. Dursun, “Adsorption of phenol from aqueous solution by using carbonised beet pulp,” *Journal of Hazardous Materials*, vol. 125, no. 1–3, pp. 175–182, 2005.
- [121] A. H. El-Sheikh, A. P. Newman, A. J. Said, A. M. Alzawahreh, and M. M. Abu-Helal, “Improving the adsorption efficiency of phenolic compounds into olive wood biosorbents by pre-washing with organic solvents: equilibrium, kinetic and thermodynamic aspects,” *Journal of Environmental Management*, vol. 118, pp. 1–10, 2013.
- [122] L. N. Nguyen, F. I. Hai, S. Yang et al., “Removal of trace organic contaminants by an MBR comprising a mixed culture of bacteria and white-rot fungi,” *Bioresource Technology*, vol. 148, pp. 234–241, 2013.
- [123] H. Tada, M. Akazawa, Y. Kubo, and S. Ito, “Enhancing effect of SiO_x monolayer coverage of TiO₂ on the photoinduced oxidation of rhodamine 6G in aqueous media,” *Journal of Physical Chemistry B*, vol. 102, pp. 6360–6366, 1998.
- [124] R. M. Burton, *Oxidant concentration effects in the hydroxylation of phenol over titanium-based zeolites Al-free Ti-Beta and TS-1 [M.S. thesis]*, Stellenbosch University Chemical Engineering, 2006.
- [125] M. Brigante and P. C. Schulz, “Adsorption of paraquat on mesoporous silica modified with titania: effects of pH, ionic strength and temperature,” *Journal of Colloid and Interface Science*, vol. 363, no. 1, pp. 355–361, 2011.
- [126] K. Cendrowski, X. Chen, B. Zielinska et al., “Synthesis, characterization, and photocatalytic properties of core/shell mesoporous silica nanospheres supporting nanocrystalline titania,” *Journal of Nanoparticle Research*, vol. 13, no. 11, pp. 5899–5908, 2011.
- [127] Y. Xu and C. H. Langford, “UV- or visible-light-induced degradation of X3B on TiO₂ nanoparticles: the influence of adsorption,” *Langmuir*, vol. 17, no. 3, pp. 897–902, 2001.
- [128] Y. S. Ho, C. T. Huang, and H. W. Huang, “Equilibrium sorption isotherm for metal ions on tree fern,” *Process Biochemistry*, vol. 37, no. 12, pp. 1421–1430, 2002.
- [129] Y. S. Ho, J. F. Porter, and G. McKay, “Equilibrium isotherm studies for the sorption of divalent metal ions onto peat: copper, nickel and lead single component systems,” *Water, Air, and Soil Pollution*, vol. 141, no. 1–4, pp. 1–33, 2002.
- [130] Y.-S. Ho, “Isotherms for the sorption of lead onto peat: comparison of linear and non-linear methods,” *Polish Journal of Environmental Studies*, vol. 15, no. 1, pp. 81–86, 2006.
- [131] S. Guiza, M. Bagane, A. H. Al-Soudani, and H. B. Amore, “Adsorption of basic dyes onto natural clay,” *Adsorption Science and Technology*, vol. 22, no. 3, pp. 245–256, 2004.
- [132] M. Bagane and S. Guiza, “Removal of a dye from textile effluents by adsorption,” *Annales de Chimie: Science des Matériaux*, vol. 25, no. 8, pp. 615–626, 2000.
- [133] A. Gürses, S. Karaca, Ç. Doğar, R. Bayrak, M. Açıkıldız, and M. Yalçın, “Determination of adsorptive properties of clay/water system: methylene blue sorption,” *Journal of Colloid and Interface Science*, vol. 269, no. 2, pp. 310–314, 2004.
- [134] D. Ghosh and K. G. Bhattacharyya, “Adsorption of methylene blue on kaolinite,” *Applied Clay Science*, vol. 20, no. 6, pp. 295–300, 2002.

- [135] C. A. P. Almeida, N. A. Debacher, A. J. Downs, L. Cottet, and C. A. D. Mello, "Removal of methylene blue from colored effluents by adsorption on montmorillonite clay," *Journal of Colloid and Interface Science*, vol. 332, no. 1, pp. 46–53, 2009.
- [136] G. Atun, G. Hisarli, W. S. Sheldrick, and M. Muhler, "Adsorptive removal of methylene blue from colored effluents on fuller's earth," *Journal of Colloid and Interface Science*, vol. 261, no. 1, pp. 32–39, 2003.
- [137] S. Hong, C. Wen, J. He, F. Gan, and Y.-S. Ho, "Adsorption thermodynamics of Methylene Blue onto bentonite," *Journal of Hazardous Materials*, vol. 167, no. 1–3, pp. 630–633, 2009.
- [138] R. A. Shawabkeh and M. F. Tutunji, "Experimental study and modeling of basic dye sorption by diatomaceous clay," *Applied Clay Science*, vol. 24, no. 1–2, pp. 111–120, 2003.
- [139] S. Wang, Y. Boyjoo, A. Choueib, and Z. H. Zhu, "Removal of dyes from aqueous solution using fly ash and red mud," *Water Research*, vol. 39, no. 1, pp. 129–138, 2005.
- [140] X. Querol, N. Moreno, J. C. Umaa et al., "Synthesis of zeolites from coal fly ash: an overview," *International Journal of Coal Geology*, vol. 50, no. 1–4, pp. 413–423, 2002.
- [141] K. S. Hui and C. Y. H. Chao, "Synthesis of MCM-41 from coal fly ash by a green approach: influence of synthesis pH," *Journal of Hazardous Materials*, vol. 137, no. 2, pp. 1135–1148, 2006.
- [142] P. Pavasant, R. Apiratikul, V. Sungkhum, P. Suthiparinyanont, S. Wattanachira, and T. F. Marhaba, "Biosorption of Cu^{2+} , Cd^{2+} , Pb^{2+} , and Zn^{2+} using dried marine green macroalga *Caulerpa lentillifera*," *Bioresource Technology*, vol. 97, no. 18, pp. 2321–2329, 2006.
- [143] R. Apiratikul and P. Pavasant, "Batch and column studies of biosorption of heavy metals by *Caulerpa lentillifera*," *Bioresource Technology*, vol. 99, no. 8, pp. 2766–2777, 2008.
- [144] K. Marungrueng and P. Pavasant, "High performance biosorbent (*Caulerpa lentillifera*) for basic dye removal," *Bioresource Technology*, vol. 98, no. 8, pp. 1567–1572, 2007.
- [145] K. S. Low, C. K. Lee, and L. L. Heng, "Sorption of basic dyes by *Hydrilla verticillata*," *Environmental Technology*, vol. 15, no. 2, pp. 115–124, 1994.
- [146] K. S. Low, C. K. Lee, and K. K. Tan, "Biosorption of basic dyes by water hyacinth roots," *Bioresource Technology*, vol. 52, no. 1, pp. 79–83, 1995.
- [147] L. W. Low, T. T. Teng, M. Rafatullah, N. Morad, and B. Azahari, "Adsorption studies of methylene blue and malachite green from aqueous solutions by pretreated lignocellulosic materials," *Separation Science and Technology*, vol. 48, no. 11, pp. 1688–1698, 2013.
- [148] N. F. Cardoso, E. C. Lima, I. S. Pinto et al., "Application of cupuassu shell as biosorbent for the removal of textile dyes from aqueous solution," *Journal of Environmental Management*, vol. 92, no. 4, pp. 1237–1247, 2011.
- [149] T. Al-Khalid and M. H. El-Naas, "Aerobic biodegradation of phenols: a comprehensive review," *Critical Reviews in Environmental Science and Technology*, vol. 42, no. 16, pp. 1631–1690, 2012.
- [150] B. F. Nabavi, M. Nikaeen, M. M. Amin, and H. Farrokhzadeh, "Biological treatment of polychlorinated biphenyls (PCBs) contaminated transformer oil by anaerobic-aerobic sequencing batch biofilm reactors," *International Biodeterioration and Biodegradation*, vol. 85, pp. 451–457, 2013.
- [151] O. B. Yang, J. C. Kim, J. S. Lee, and Y. G. Kim, "Use of activated carbon fiber for direct removal of iodine from acetic acid solution," *Industrial and Engineering Chemistry Research*, vol. 32, no. 8, pp. 1692–1697, 1993.
- [152] R. S. Juang and S. L. Swei, "Effect of dye nature on its adsorption from aqueous solutions onto activated carbon," *Separation Science and Technology*, vol. 31, no. 15, pp. 2143–2158, 1996.
- [153] M. Streat, J. W. Patrick, and M. J. Camporro Perez, "Sorption of phenol and para-chlorophenol from water using conventional and novel activated carbons," *Water Research*, vol. 29, no. 2, pp. 467–472, 1995.
- [154] G. M. Walker and L. R. Weatherley, "Adsorption of dyes from aqueous solution: the effect of adsorbent pore size distribution and dye aggregation," *Chemical Engineering Journal*, vol. 83, no. 3, pp. 201–206, 2001.
- [155] L. D. T. Prola, F. M. Machado, C. P. Bergmann et al., "Adsorption of Direct Blue 53 dye from aqueous solutions by multi-walled carbon nanotubes and activated carbon," *Journal of Environmental Management*, vol. 130, pp. 166–175, 2013.
- [156] D. D. Milenkovic, M. M. Milosavljevic, A. D. Marinkovic, V. R. Dokic, J. Z. Mitrovic, and A. L. Bojic, "Removal of copper(II) ion from aqueous solution by high-porosity activated carbon," *Water SA*, vol. 39, no. 4, pp. 515–522, 2013.
- [157] X. X. Hou, Q. F. Deng, T. Z. Ren, and Z. Y. Yuan, "Adsorption of Cu^{2+} and methyl orange from aqueous solutions by activated carbons of corncob-derived char wastes," *Environmental Science and Pollution Research*, vol. 20, no. 12, pp. 8521–8534, 2013.
- [158] V. K. Gupta, I. Ali, T. A. Saleh, M. N. Siddiqui, and S. Agarwal, "Chromium removal from water by activated carbon developed from waste rubber tires," *Environmental Science and Pollution Research*, vol. 20, no. 3, pp. 1261–1268, 2013.
- [159] K. Ota, Y. Amano, M. Aikawa, and M. Machida, "Removal of nitrate ions from water by activated carbons (ACs)-Influence of surface chemistry of ACs and coexisting chloride and sulfate ions," *Applied Surface Science*, vol. 276, pp. 838–842, 2013.
- [160] M. G. Krivova, D. D. Grinshpan, and N. Hedin, "Adsorption of C(n)TABr surfactants on activated carbons," *Colloids and Surfaces A: Physicochemical and Engineering Aspects*, vol. 436, pp. 62–70, 2013.
- [161] C. Y. Yin, M. K. Aroua, and W. M. A. W. Daud, "Review of modifications of activated carbon for enhancing contaminant uptakes from aqueous solutions," *Separation and Purification Technology*, vol. 52, no. 3, pp. 403–415, 2007.
- [162] A. Bhatnagar, W. Hogland, M. Marques, and M. Sillanpaa, "An overview of the modification methods of activated carbon for its water treatment applications," *Chemical Engineering Journal*, vol. 219, pp. 499–511, 2013.
- [163] Y. Xu and C. H. Langford, "Photoactivity of titanium dioxide supported on MCM-41, zeolite X and zeolite Y," *Journal of Physical Chemistry B*, vol. 101, pp. 3115–3121, 1997.
- [164] L. J. Alemany, M. A. Banares, E. Pardo, F. Martin, M. Galán-Fereres, and J. M. Blasco, "Photodegradation of phenol in water using silica-supported titania catalysts," *Applied Catalysis B*, vol. 13, no. 3–4, pp. 289–297, 1997.
- [165] P. Cheng, M. Zheng, Y. Jin, Q. Huang, and M. Gu, "Preparation and characterization of silica-doped titania photocatalyst through sol-gel method," *Materials Letters*, vol. 57, no. 20, pp. 2989–2994, 2003.
- [166] M. L. Fetterolf, H. V. Patel, and J. M. Jennings, "Adsorption of methylene blue and acid blue 40 on titania from aqueous solution," *Journal of Chemical and Engineering Data*, vol. 48, no. 4, pp. 831–835, 2003.
- [167] K. Bourikas, M. Styliidi, D. I. Kondarides, and X. E. Verykios, "Adsorption of Acid Orange 7 on the surface of titanium dioxide," *Langmuir*, vol. 21, no. 20, pp. 9222–9230, 2005.

- [168] V. Belessi, G. Romanos, N. Boukos, D. Lambropoulou, and C. Trapalis, "Removal of Reactive Red 195 from aqueous solutions by adsorption on the surface of TiO₂ nanoparticles," *Journal of Hazardous Materials*, vol. 170, no. 2-3, pp. 836–844, 2009.
- [169] S. Jafari, S. Azizian, and B. Jaleh, "Adsorption kinetics of methyl violet onto TiO₂ nanoparticles with different phases," *Colloids and Surfaces A: Physicochemical and Engineering Aspects*, vol. 384, no. 1–3, pp. 618–623, 2011.
- [170] C. R. Lee, H. S. Kim, I. H. Jang, J. H. Im, and N. G. Park, "Pseudo first-order adsorption kinetics of N719 dye on TiO₂ surface," *ACS Applied Materials and Interfaces*, vol. 3, no. 6, pp. 1953–1957, 2011.
- [171] H. Ghobarkar, O. Schäf, and U. Guth, "Zeolites: from kitchen to space," *Progress in Solid State Chemistry*, vol. 27, no. 2, pp. 29–73, 1999.
- [172] M. N. Ahmed, J. John, and R. N. Ram, "Kinetics of removal of Basic Violet 1 from aqueous solution using silica as an adsorbent," *Journal of Environmental Science and Health A: Environmental Science and Engineering*, vol. 28, no. 7, pp. 1581–1597, 1993.
- [173] M. N. Ahmed and R. N. Ram, "Removal of basic dye from wastewater using silica as adsorbent," *Environmental Pollution*, vol. 77, no. 1, pp. 79–86, 1992.
- [174] R. G. Avendaño, J. A. de los Reyes, J. A. Montoya, and T. Viveros, "Preparation and characterization of mesoporous titanium-silica and zirconia-silica mixed oxides," *Superficies Y Vacío*, vol. 19, no. 2, pp. 1–6, 2006.
- [175] V. W. Atul, G. S. Gaikwad, M. G. Dhonde, N. T. Khaty, and S. R. Thakare, "Removal of organic pollutant from water by heterogenous photocatalysis: a review," *Research Journal of Chemistry and Environment*, vol. 17, no. 1, pp. 84–94, 2013.
- [176] J. Wu, K. Rudy, and J. Spark, "Oxidation of aqueous phenol by ozone and peroxidase," *Advances in Environmental Research*, vol. 4, no. 4, pp. 339–346, 2000.
- [177] P. Yogeswary, Y. Mohd, R. Mohd, A. Saidina, and A. Nor, "Degradation of phenol by catalytic ozonation," *Journal of Chemical and Natural Resources Engineering*, vol. 2, pp. 34–46, 2007.
- [178] Y. Yamamoto, E. Niki, H. Shiokawa, and Y. Kamiya, "Ozonation of organic compounds. 2. Ozonation of phenol in water," *Journal of Organic Chemistry*, vol. 44, no. 13, pp. 2137–2142, 1979.
- [179] K. Turhan and S. Uzman, "Removal of phenol from water using ozone," *Desalination*, vol. 229, no. 1–3, pp. 257–263, 2008.
- [180] J. Staehelin, R. E. Bühler, and J. Hoigné, "Ozone decomposition in water studied by pulse radiolysis. 2. OH and HO₄ as chain intermediates," *Journal of Physical Chemistry*, vol. 88, no. 24, pp. 5999–6004, 1984.
- [181] H. Einaga and S. Futamura, "Catalytic oxidation of benzene with ozone over Mn ion-exchanged zeolites," *Catalysis Communications*, vol. 8, no. 3, pp. 557–560, 2007.
- [182] H. Einaga, Y. Teraoka, and A. Ogat, "Benzene oxidation with ozone over manganese oxide supported on zeolite catalysts," *Catalysis Today*, vol. 164, no. 1, pp. 571–574, 2011.
- [183] H. Einaga, N. Maeda, and Y. Teraoka, "Effect of catalyst composition and preparation conditions on catalytic properties of unsupported manganese oxides for benzene oxidation with ozone," *Applied Catalysis B: Environmental*, vol. 142, pp. 406–413, 2013.
- [184] J. Kanagaraj and A. B. Mandal, "Combined biodegradation and ozonation for removal of tannins and dyes for the reduction of pollution loads," *Environmental Science and Pollution Research*, vol. 19, no. 1, pp. 42–52, 2012.
- [185] M. M. Huber, S. Canonica, G.-Y. Park, and U. Von Gunten, "Oxidation of pharmaceuticals during ozonation and advanced oxidation processes," *Environmental Science and Technology*, vol. 37, no. 5, pp. 1016–1024, 2003.
- [186] O. Legrini, E. Oliveros, and A. M. Braun, "Photochemical processes for water treatment," *Chemical Reviews*, vol. 93, no. 2, pp. 671–698, 1993.
- [187] S. R. Cater, M. I. Stefan, J. R. Bolton, and A. Safarzadeh-Amiri, "UV/H₂O₂ treatment of methyl tert-butyl ether in contaminated waters," *Environmental Science and Technology*, vol. 34, no. 4, pp. 659–662, 2000.
- [188] J. M. Poyatos, M. M. Muñio, M. C. Almecija, J. C. Torres, E. Hontoria, and F. Osorio, "Advanced oxidation processes for wastewater treatment: state of the art," *Water, Air, and Soil Pollution*, vol. 205, no. 1–4, pp. 187–204, 2010.
- [189] E. Felis, D. Marciocha, J. Surmacz-Gorska, and K. Miksch, "Photochemical degradation of naproxen in the aquatic environment," *Water Science and Technology*, vol. 55, no. 12, pp. 281–286, 2007.
- [190] J. J. Wu, M. Muruganandham, and S. H. Chen, "Degradation of DMSO by ozone-based advanced oxidation processes," *Journal of Hazardous Materials*, vol. 149, no. 1, pp. 218–225, 2007.
- [191] H.-Y. Shu, "Degradation of dyehouse effluent containing C.I. Direct Blue 199 by processes of ozonation, UV/H₂O₂ and in sequence of ozonation with UV/H₂O₂," *Journal of Hazardous Materials*, vol. 133, no. 1–3, pp. 92–98, 2006.
- [192] H.-Y. Shu and M.-C. Chang, "Pre-ozonation coupled with UV/H₂O₂ process for the decolorization and mineralization of cotton dyeing effluent and synthesized C.I. Direct Black 22 wastewater," *Journal of Hazardous Materials*, vol. 121, no. 1–3, pp. 127–133, 2005.
- [193] T. Yonar, G. K. Yonar, K. Kestioglu, and N. Azbar, "Decolorisation of textile effluent using homogeneous photochemical oxidation processes," *Coloration Technology*, vol. 121, no. 5, pp. 258–264, 2005.
- [194] A. Gutowska, J. Kałużna-Czaplińska, and W. K. Józwiak, "Degradation mechanism of Reactive Orange 113 dye by H₂O₂/Fe²⁺ and ozone in aqueous solution," *Dyes and Pigments*, vol. 74, no. 1, pp. 41–46, 2007.
- [195] E. S. Elmolla and M. Chaudhuri, "Degradation of the antibiotics amoxicillin, ampicillin and cloxacillin in aqueous solution by the photo-Fenton process," *Journal of Hazardous Materials*, vol. 172, no. 2-3, pp. 1476–1481, 2009.
- [196] U. I. Gaya and A. H. Abdullah, "Heterogeneous photocatalytic degradation of organic contaminants over titanium dioxide: a review of fundamentals, progress and problems," *Journal of Photochemistry and Photobiology C: Photochemistry Reviews*, vol. 9, no. 1, pp. 1–12, 2008.
- [197] Y. Chen, S. Yang, K. Wang, and L. Lou, "Role of primary active species and TiO₂ surface characteristic in UV-illuminated photodegradation of Acid Orange 7," *Journal of Photochemistry and Photobiology A: Chemistry*, vol. 172, no. 1, pp. 47–54, 2005.
- [198] A. O. Ibhaden and P. Fitzpatrick, "Heterogeneous photocatalysis: recent advances and applications," *Catalysis*, vol. 3, pp. 189–218, 2013.
- [199] D. Sud and P. Kaur, "Heterogeneous photocatalytic degradation of selected organophosphate pesticides: a review," *Critical Reviews in Environmental Science and Technology*, vol. 42, no. 22, pp. 2365–2407, 2011.
- [200] T. Daimon, T. Hirakawa, M. Kitazawa, J. Suetake, and Y. Nosaka, "Formation of singlet molecular oxygen associated with the

- formation of superoxide radicals in aqueous suspensions of TiO₂ photocatalysts," *Applied Catalysis A: General*, vol. 340, no. 2, pp. 169–175, 2008.
- [201] A. Fujishima, X. Zhang, and D. A. Tryk, "TiO₂ photocatalysis and related surface phenomena," *Surface Science Reports*, vol. 63, no. 12, pp. 515–582, 2008.
- [202] M. Styliadi, D. I. Kondarides, and X. E. Verykios, "Visible light-induced photocatalytic degradation of Acid Orange 7 in aqueous TiO₂ suspensions," *Applied Catalysis B: Environmental*, vol. 47, no. 3, pp. 189–201, 2004.
- [203] M. Bizarro, "High photocatalytic activity of ZnO and ZnO:Al nanostructured films deposited by spray pyrolysis," *Applied Catalysis B: Environmental*, vol. 97, no. 1-2, pp. 198–203, 2010.
- [204] S. N. Frank and A. J. Bard, "Heterogeneous photocatalytic oxidation of cyanide and sulfite in aqueous solutions at semiconductor powders," *Journal of Physical Chemistry*, vol. 81, no. 15, pp. 1484–1488, 1977.
- [205] Y. K. Kho, A. Iwase, W. Y. Teoh, L. Mädler, A. Kudo, and R. Amal, "Photocatalytic H₂ evolution over TiO₂ nanoparticles. The synergistic effect of anatase and rutile," *Journal of Physical Chemistry C*, vol. 114, no. 6, pp. 2821–2829, 2010.
- [206] D. Y. C. Leung, X. Fu, C. Wang et al., "Hydrogen production over titania-based photocatalysts," *ChemSusChem*, vol. 3, no. 6, pp. 681–694, 2010.
- [207] T. P. Chou, Q. Zhang, B. Russo, G. E. Fryxell, and G. Cao, "Titania particle size effect on the overall performance of dye-sensitized solar cells," *Journal of Physical Chemistry C*, vol. 111, no. 17, pp. 6296–6302, 2007.
- [208] C. H. Pollema, J. L. Hendrix, E. B. Milosavljević, L. Solujić, and J. H. Nelson, "Photocatalytic oxidation of cyanide to nitrate at TiO₂ particles," *Journal of Photochemistry and Photobiology A: Chemistry*, vol. 66, no. 2, pp. 235–244, 1992.
- [209] H. Hidaka, T. Nakamura, A. Ishizaka, M. Tsuchiya, and J. Zhao, "Heterogeneous photocatalytic degradation of cyanide on TiO₂ surfaces," *Journal of Photochemistry and Photobiology A: Chemistry*, vol. 66, no. 3, pp. 367–374, 1992.
- [210] S. N. Frank and A. J. Bard, "Heterogeneous photocatalytic oxidation of cyanide ion in aqueous solutions at TiO₂ powder," *Journal of the American Chemical Society*, vol. 99, no. 1, pp. 303–304, 1977.
- [211] A. Zafra, J. Garcia, A. Milis, and X. Domènech, "Kinetics of the catalytic oxidation of nitrite over illuminated aqueous suspensions of TiO₂," *Journal of Molecular Catalysis*, vol. 70, no. 3, pp. 343–349, 1991.
- [212] F. Zhang, J. Zhao, T. Shen, H. Hidaka, E. Pelizzetti, and N. Serpone, "TiO₂-assisted photodegradation of dye pollutants II. Adsorption and degradation kinetics of eosin in TiO₂ dispersions under visible light irradiation," *Applied Catalysis B: Environmental*, vol. 15, no. 1-2, pp. 147–156, 1998.
- [213] K. Vinodgopal, D. E. Wynkoop, and P. V. Kamat, "Environmental photochemistry on semiconductor surfaces: photosensitized degradation of a textile azo dye, acid orange 7, on TiO₂ particles using visible light," *Environmental Science and Technology*, vol. 30, no. 5, pp. 1660–1666, 1996.
- [214] H. Lachheb, E. Puzenat, A. Houas et al., "Photocatalytic degradation of various types of dyes (Alizarin S, Crocein Orange G, Methyl Red, Congo Red, Methylene Blue) in water by UV-irradiated titania," *Applied Catalysis B: Environmental*, vol. 39, no. 1, pp. 75–90, 2002.
- [215] J. Li, W. Ma, C. Chen, J. Zhao, H. Zhu, and X. Gao, "Photodegradation of dye pollutants on one-dimensional TiO₂ nanoparticles under UV and visible irradiation," *Journal of Molecular Catalysis A: Chemical*, vol. 261, no. 1, pp. 131–138, 2007.
- [216] H. U. Lee, S. C. Lee, J. H. Seo et al., "Room temperature synthesis of nanoporous anatase and anatase/brookite TiO₂ photocatalysts with high photocatalytic performance," *Chemical Engineering Journal*, vol. 223, pp. 209–215, 2013.
- [217] A. G. Agrios and P. Pichat, "Recombination rate of photogenerated charges versus surface area: opposing effects of TiO₂ sintering temperature on photocatalytic removal of phenol, anisole, and pyridine in water," *Journal of Photochemistry and Photobiology A: Chemistry*, vol. 180, no. 1-2, pp. 130–135, 2006.
- [218] R. Vinu and G. Madras, "Kinetics of simultaneous photocatalytic degradation of phenolic compounds and reduction of metal ions with Nano-TiO₂," *Environmental Science and Technology*, vol. 42, no. 3, pp. 913–919, 2008.
- [219] C. Su, B.-Y. Hong, and C.-M. Tseng, "Sol-gel preparation and photocatalysis of titanium dioxide," *Catalysis Today*, vol. 96, no. 3, pp. 119–126, 2004.
- [220] W. Guo, X. Liu, P. Huo et al., "Hydrothermal synthesis spherical TiO₂ and its photo-degradation property on salicylic acid," *Applied Surface Science*, vol. 258, no. 18, pp. 6891–6896, 2012.
- [221] R. J. Davis and Z. Liu, "Titania–Silica: a model binary oxide catalyst system," *Chemistry of Materials*, vol. 9, no. 11, pp. 2311–2324, 1997.
- [222] K. Brodzik, J. Walendziewski, M. Stolarski, L. Van Ginneken, K. Elst, and V. Meynen, "The influence of preparation method on the physicochemical properties of titania-silica aerogels. Part II," *Journal of Porous Materials*, vol. 15, no. 5, pp. 541–549, 2008.
- [223] A. Wold, "Photocatalytic properties of TiO₂," *Chemistry of Materials*, vol. 5, no. 3, pp. 280–283, 1993.
- [224] I. K. Konstantinou and T. A. Albanis, "TiO₂-assisted photocatalytic degradation of azo dyes in aqueous solution: kinetic and mechanistic investigations: a review," *Applied Catalysis B: Environmental*, vol. 49, no. 1, pp. 1–14, 2004.
- [225] D. Bahnemann, "Photocatalytic water treatment: solar energy applications," *Solar Energy*, vol. 77, no. 5, pp. 445–459, 2004.
- [226] D. R. Sahu, L. Y. Hong, S.-C. Wang, and J.-L. Huang, "Synthesis, analysis and characterization of ordered mesoporous TiO₂/SBA-15 matrix: effect of calcination temperature," *Microporous and Mesoporous Materials*, vol. 117, no. 3, pp. 640–649, 2009.
- [227] T. Kasahara, K. Inumaru, and S. Yamanaka, "Enhanced photocatalytic decomposition of nonylphenol polyethoxylate by alkyl-grafted TiO₂-MCM-41 organic-inorganic nanostructure," *Microporous and Mesoporous Materials*, vol. 76, no. 1–3, pp. 123–130, 2004.
- [228] L. H. Tian, H. T. Liu, and Y. Gao, "Degradation and adsorption of rhodamine B and phenol on TiO₂/MCM-41," *Kinetics and Catalysis*, vol. 53, no. 5, pp. 554–559, 2012.
- [229] J. Yang, J. Zhang, L. Zhu et al., "Synthesis of nano titania particles embedded in mesoporous SBA-15: characterization and photocatalytic activity," *Journal of Hazardous Materials*, vol. 137, no. 2, pp. 952–958, 2006.
- [230] T.-H. Liou and B.-C. Lai, "Utilization of e-waste as a silica source for the synthesis of the catalyst support MCM-48 and highly enhanced photocatalytic activity of supported titania nanoparticles," *Applied Catalysis B: Environmental*, vol. 115–116, pp. 138–148, 2012.
- [231] K. De Witte, V. Meynen, M. Mertens et al., "Multi-step loading of titania on mesoporous silica: influence of the morphology and the porosity on the catalytic degradation of aqueous

- pollutants and VOCs," *Applied Catalysis B: Environmental*, vol. 84, no. 1-2, pp. 125-132, 2008.
- [232] E. Beyers, E. Biermans, S. Ribbens et al., "Combined TiO₂/SiO₂ mesoporous photocatalysts with location and phase controllable TiO₂ nanoparticles," *Applied Catalysis B: Environmental*, vol. 88, no. 3-4, pp. 515-524, 2009.
- [233] S. Anandan, "Photocatalytic effects of titania supported nanoporous MCM-41 on degradation of methyl orange in the presence of electron acceptors," *Dyes and Pigments*, vol. 76, no. 2, pp. 535-541, 2008.
- [234] H. Ding, H. Sun, and Y. Shan, "Preparation and characterization of mesoporous SBA-15 supported dye-sensitized TiO₂ photocatalyst," *Journal of Photochemistry and Photobiology A: Chemistry*, vol. 169, no. 1, pp. 101-107, 2005.
- [235] D. Jyothi, P. A. Deshpande, B. R. Venugopal, S. Chandrasekaran, and G. Madras, "Transition metal oxide loaded MCM catalysts for photocatalytic degradation of dyes," *Journal of Chemical Sciences*, vol. 124, no. 2, pp. 385-393, 2012.
- [236] A. Bhattacharyya, S. Kawi, and M. B. Ray, "Photocatalytic degradation of orange II by TiO₂ catalysts supported on adsorbents," *Catalysis Today*, vol. 98, no. 3, pp. 431-439, 2004.
- [237] H. H. Tseng, W. W. Lee, M. C. Wei, B. S. Huang, M. C. Hsieh, and P. Y. Cheng, "Synthesis of TiO₂/SBA-15 photocatalyst for the azo dye decolorization through the polyol method," *Chemical Engineering Journal*, vol. 210, pp. 529-538, 2012.
- [238] M. Alvaro, C. Aprile, M. Benitez, E. Carbonell, and H. García, "Photocatalytic activity of structured mesoporous TiO₂ materials," *Journal of Physical Chemistry B*, vol. 110, no. 13, pp. 6661-6665, 2006.
- [239] W. A. Adams, M. G. Bakker, T. MacIas, and I. A. Jefcoat, "Synthesis and characterization of mesoporous silica films encapsulating titanium dioxide particles: photodegradation of 2,4-dichlorophenol," *Journal of Hazardous Materials*, vol. 112, no. 3, pp. 253-259, 2004.
- [240] A. Orlov, Q.-Z. Zhai, and J. Klinowski, "Photocatalytic properties of the SBA-15 mesoporous silica molecular sieve modified with titanium," *Journal of Materials Science*, vol. 41, no. 8, pp. 2187-2193, 2006.
- [241] J. Aguado, R. Van Grieken, M. J. López-Muñoz, and J. Marugán, "Removal of cyanides in wastewater by supported TiO₂-based photocatalysts," *Catalysis Today*, vol. 75, no. 1-4, pp. 95-102, 2002.
- [242] M.-J. López-Muñoz, R. V. Grieken, J. Aguado, and J. Marugán, "Role of the support on the activity of silica-supported TiO₂ photocatalysts: structure of the TiO₂/SBA-15 photocatalysts," *Catalysis Today*, vol. 101, no. 3-4, pp. 307-314, 2005.
- [243] S. Artkla, W. Kim, W. Choi, and J. Wittayakun, "Highly enhanced photocatalytic degradation of tetramethylammonium on the hybrid catalyst of titania and MCM-41 obtained from rice husk silica," *Applied Catalysis B: Environmental*, vol. 91, no. 1-2, pp. 157-164, 2009.
- [244] Y. M. Xu and C. H. Langford, "Photoactivity of titanium dioxide supported on MCM41, zeolite X, and zeolite Y," *Journal of Physical Chemistry B*, vol. 101, no. 16, pp. 3115-3121, 1997.
- [245] H. S. Kibombo, R. Peng, S. Sasalingam, and R. T. Koodali, "Versatility of heterogeneous photocatalysis: synthetic methodologies epitomizing the role of silica support in TiO₂ based mixed oxides," *Catalysis Science and Technology*, vol. 2, no. 9, pp. 1737-1766, 2012.
- [246] B. E. Yoldas, "Formation of titania-silica glasses by low temperature chemical polymerization," *Journal of Non-Crystalline Solids*, vol. 38-39, no. 1, pp. 81-86, 1980.
- [247] F. Garbassi and L. Balducci, "Preparation and characterization of spherical TiO₂-SiO₂ particles," *Microporous and Mesoporous Materials*, vol. 47, no. 1, pp. 51-59, 2001.
- [248] C. Murata, H. Yoshida, J. Kumagai, and T. Hattori, "Active sites and active oxygen species for photocatalytic epoxidation of propene by molecular oxygen over TiO₂-SiO₂ binary oxides," *Journal of Physical Chemistry B*, vol. 107, no. 18, pp. 4364-4373, 2003.
- [249] A. S. Soult, D. F. Carter, H. D. Schreiber, L. J. van de Burgt, and A. E. Stieglman, "Spectroscopy of amorphous and crystalline titania-silica materials," *Journal of Physical Chemistry B*, vol. 106, no. 36, pp. 9266-9273, 2002.
- [250] Y. K. Kim, E. Y. Kim, C. M. Whang, Y. H. Kim, and W. I. Lee, "Microstructure and photocatalytic property of SiO₂-TiO₂ under various process condition," *Journal of Sol-Gel Science and Technology*, vol. 33, no. 1, pp. 87-91, 2005.
- [251] S. Lisinski, J. Krause, D. Schaniel, L. Ratke, and T. Woike, "Variable refractive indices in mixed oxide xerogels," *Scripta Materialia*, vol. 58, no. 7, pp. 553-555, 2008.
- [252] S. Imamura, T. Shiomi, S. Ishida, K. Utani, and H. Jindai, "Decomposition of dichlorodifluoromethane on TiO₂/SiO₂," *Industrial and Engineering Chemistry Research*, vol. 29, no. 9, pp. 1758-1761, 1990.
- [253] T.-V. Nguyen and O.-B. Yang, "Photoresponse and AC impedance characterization of TiO₂-SiO₂ mixed oxide for photocatalytic water decomposition," *Catalysis Today*, vol. 87, no. 1-4, pp. 69-75, 2003.
- [254] S. Vives and C. Meunier, "Influence of the synthesis route on sol-gel SiO₂-TiO₂ (1:1) xerogels and powders," *Ceramics International*, vol. 34, no. 1, pp. 37-44, 2008.
- [255] J. Ren, Z. Li, S. Liu, Y. Xing, and K. Xie, "Silica-titania mixed oxides: Si-O-Ti connectivity, coordination of titanium, and surface acidic properties," *Catalysis Letters*, vol. 124, no. 3-4, pp. 185-194, 2008.
- [256] J. M. Miller and L. J. Lakshmi, "Spectroscopic characterization of sol-gel-derived mixed oxides," *Journal of Physical Chemistry B*, vol. 102, no. 34, pp. 6465-6470, 1998.
- [257] M. P. Coles, C. G. Lugmair, K. W. Terry, and T. D. Tilley, "Titania-silica materials from the molecular precursor Ti[OSi(O(t)Bu)₃]₄: selective epoxidation catalysts," *Chemistry of Materials*, vol. 12, no. 1, pp. 122-131, 2000.
- [258] R. Hutter, T. Mallat, A. Peterhans, and A. Baiker, "Control of acidity and selectivity of titania-silica aerogel for the epoxidation of β -isophorone," *Journal of Molecular Catalysis A: Chemical*, vol. 138, no. 2-3, pp. 241-247, 1999.
- [259] G. Mountjoy, D. M. Pickup, G. W. Wallidge, J. M. Cole, R. J. Newport, and M. E. Smith, "In-situ high-temperature XANES observations of rapid and reversible changes in Ti coordination in titania-silica xerogels," *Chemical Physics Letters*, vol. 304, no. 3-4, pp. 150-154, 1999.
- [260] D. M. Pickup, G. Mountjoy, G. W. Wallidge et al., "A structural study of (TiO₂)_x(SiO₂)_(1-x) (x = 0.18, 0.30 and 0.41) xerogels prepared using acetylacetone," *Journal of Materials Chemistry*, vol. 9, no. 6, pp. 1299-1305, 1999.
- [261] A. Pirson, A. Mohsine, P. Marchot et al., "Synthesis of SiO₂-TiO₂ xerogels by sol-gel process," *Journal of Sol-Gel Science and Technology*, vol. 4, no. 3, pp. 179-185, 1995.
- [262] T. Fernandez, G. Jose, S. Mathew, R. Pr, and U. Nv, "An ultra-low hydrolysis sol-gel route for titanosilicate xerogels and their characterization," *Journal of Sol-Gel Science and Technology*, vol. 41, no. 2, pp. 163-168, 2007.

- [263] Z. Deng, J. Wang, Y. Zhang et al., "Preparation and photocatalytic activity of TiO_2 - SiO_2 binary aerogels," *Nanostructured Materials*, vol. 11, no. 8, pp. 1313–1318, 1999.
- [264] A. C. Pierre and G. M. Pajonk, "Chemistry of aerogels and their applications," *Chemical Reviews*, vol. 102, no. 11, pp. 4243–4265, 2002.
- [265] B. E. Handy, M. Maciejewski, A. Baiker, and A. Wokaun, "Genesis and structural properties of alkoxide-prepared titania-silica xerogels," *Journal of Materials Chemistry*, vol. 2, no. 8, pp. 833–840, 1992.
- [266] S. Klein, S. Thorimbert, and W. F. Maier, "Amorphous microporous titania-silica mixed oxides: preparation, characterization, and catalytic redox properties," *Journal of Catalysis*, vol. 163, no. 2, pp. 476–488, 1996.
- [267] X. Gao and I. E. Wachs, "Titania-silica as catalysts: molecular structural characteristics and physico-chemical properties," *Catalysis Today*, vol. 51, no. 2, pp. 233–254, 1999.
- [268] S. Budhi, H. S. Kibombo, D. Zhao, A. Gonshorowski, and R. T. Koodali, "Synthesis of titania-silica xerogels by co-solvent induced gelation at ambient temperature," *Materials Letters*, vol. 65, no. 14, pp. 2136–2138, 2011.
- [269] G. Larsen, H. S. Silva, and R. Venturini De Silva, "Structure of hybrid (organic/inorganic) TiO_2 - SiO_2 xerogels as studied by neopentane adsorption at 273 K and Ti K-edge X-ray absorption spectroscopy," *Journal of Non-Crystalline Solids*, vol. 271, no. 1, pp. 1–11, 2000.
- [270] G. Larsen, M. Buechler-Skoda, C. Nguyen, D. Vu, and E. Lotero, "Structure of hybrid (organic/inorganic) TiO_2 - SiO_2 xerogels II: thermal behavior as monitored by temperature-programmed techniques and spectroscopy," *Journal of Non-Crystalline Solids*, vol. 279, no. 2–3, pp. 161–168, 2001.
- [271] R. Mariscal, M. López-Granados, J. L. G. Fierro, J. L. Sotelo, C. Martos, and R. van Grieken, "Morphology and surface properties of titania-silica hydrophobic xerogels," *Langmuir*, vol. 16, no. 24, pp. 9460–9467, 2000.
- [272] G. Dagan, S. Sampath, and O. Lev, "Preparation and utilization of organically modified silica-titania photocatalysts for decontamination of aquatic environments," *Chemistry of Materials*, vol. 7, no. 3, pp. 446–453, 1995.
- [273] M. Hirano, K. Ota, M. Inagaki, and H. Iwata, "Hydrothermal synthesis of TiO_2 / SiO_2 composite nanoparticles and their photocatalytic performances," *Journal of the Ceramic Society of Japan*, vol. 112, no. 1303, pp. 143–148, 2004.
- [274] Z. Li, B. Hou, Y. Xu et al., "Comparative study of sol-gel-hydrothermal and sol-gel synthesis of titania-silica composite nanoparticles," *Journal of Solid State Chemistry*, vol. 178, no. 5, pp. 1395–1405, 2005.
- [275] Z. Li, B. Hou, Y. Xu, D. Wu, and Y. Sun, "Hydrothermal synthesis, characterization, and photocatalytic performance of silica-modified titanium dioxide nanoparticles," *Journal of Colloid and Interface Science*, vol. 288, no. 1, pp. 149–154, 2005.
- [276] D. C. M. Dutoit, M. Schneider, and A. Baiker, "Titania-silica mixed oxides. I. Influence of sol-gel and drying conditions on structural properties," *Journal of Catalysis*, vol. 153, no. 1, pp. 165–176, 1995.
- [277] D. C. M. Dutoit, M. Schneider, and A. Baiker, "Titania-silica mixed oxides. I. Influence of sol-gel and drying conditions on structural properties," *Journal of Catalysis*, vol. 153, no. 1, pp. 165–176, 1995.
- [278] R. Hutter, T. Mallat, and A. Baiker, "Titania silica mixed oxides. II. Catalytic behavior in olefin epoxidation," *Journal of Catalysis*, vol. 153, no. 1, pp. 177–189, 1995.
- [279] B. E. Handy, M. Maciejewski, A. Baiker, and A. Wokaun, "Genesis and structural properties of alkoxide-prepared titania-silica xerogels," *Journal of Materials Chemistry*, vol. 2, no. 8, pp. 833–840, 1992.
- [280] S. Cao, K. L. Yeung, and P.-L. Yue, "Preparation of freestanding and crack-free titania-silica aerogels and their performance for gas phase, photocatalytic oxidation of VOCs," *Applied Catalysis B: Environmental*, vol. 68, no. 3–4, pp. 99–108, 2006.
- [281] W.-I. Kim, D. J. Suh, T.-J. Park, and I.-K. Hong, "Photocatalytic degradation of methanol on titania and titania-silica aerogels prepared by non-alkoxide sol-gel route," *Topics in Catalysis*, vol. 44, no. 4, pp. 499–505, 2007.
- [282] Z. Y. Wu, Y. F. Tao, Z. Lin, L. Liu, X. X. Fan, and Y. Wang, "Hydrothermal synthesis and morphological evolution of mesoporous titania-silica," *Journal of Physical Chemistry C*, vol. 113, no. 47, pp. 20335–20348, 2009.
- [283] M. Kruk and M. Jaroniec, "Gas adsorption characterization of ordered organic-inorganic nanocomposite materials," *Chemistry of Materials*, vol. 13, no. 10, pp. 3169–3183, 2001.
- [284] W. Dong, C. W. Lee, X. Lu et al., "Synchronous role of coupled adsorption and photocatalytic oxidation on ordered mesoporous anatase TiO_2 - SiO_2 nanocomposites generating excellent degradation activity of RhB dye," *Applied Catalysis B: Environmental*, vol. 95, no. 3–4, pp. 197–207, 2010.
- [285] O. T. Alaoui, Q. T. Nguyen, and T. Rhlalou, "Preparation and characterization of a new TiO_2 / SiO_2 composite catalyst for photocatalytic degradation of indigo carmin," *Environmental Chemistry Letters*, vol. 7, no. 2, pp. 175–181, 2009.
- [286] T. Cetinkaya, L. Neuwirthová, K. M. Kutlákova, V. Tomášek, and H. Akbulut, "Synthesis of nanostructured TiO_2 / SiO_2 as an effective photocatalyst for degradation of acid orange," *Applied Surface Science*, vol. 279, pp. 384–390, 2013.
- [287] Q. Yang, C. Xie, Z. Xu et al., "Effects of synthesis parameters on the physico-chemical and photoactivity properties of titania-silica mixed oxide prepared via basic hydrolyzation," *Journal of Molecular Catalysis A: Chemical*, vol. 239, no. 1–2, pp. 144–150, 2005.
- [288] I. A. Ibrahim, A. A. Ismail, M. S. Ahmed, and A. K. Ismail, "Comparative study of titania silica aerogel and xerogel as photocatalysts for cyanide degradation from wastewaters," *Egyptian Journal of Chemistry*, vol. 45, no. 1, pp. 193–203, 2002.
- [289] A. A. Ismail, I. A. Ibrahim, M. S. Ahmed, R. M. Mohamed, and H. El-Shall, "Sol-gel synthesis of titania-silica photocatalyst for cyanide photodegradation," *Journal of Photochemistry and Photobiology A: Chemistry*, vol. 163, no. 3, pp. 445–451, 2004.
- [290] M. Anpo, H. Nakaya, S. Kodama, Y. Kubokawa, K. Domen, and T. Onishi, "Photocatalysis over binary metal oxides. Enhancement of the photocatalytic activity of TiO_2 in titanium-silicon oxides," *Journal of Physical Chemistry*, vol. 90, no. 8, pp. 1633–1636, 1986.
- [291] S. Imamura, H. Tarumoto, and S. Ishida, "Decomposition of 1,2-dichloroethane on TiO_2 / SiO_2 ," *Industrials and Engineering Chemistry Research*, vol. 28, no. 10, pp. 1449–1452, 1989.
- [292] A. Hanprasopwattana, S. Srinivasan, A. G. Sault, and A. K. Datye, "Titania coatings on monodisperse silica spheres (characterization using 2-propanol dehydration and TEM)," *Langmuir*, vol. 12, no. 13, pp. 3173–3179, 1996.
- [293] M. S. Vohra, J. Lee, and W. Choi, "Enhanced photocatalytic degradation of tetramethylammonium on silica-loaded titania," *Journal of Applied Electrochemistry*, vol. 35, no. 7–8, pp. 757–763, 2005.

- [294] T. Torimoto, S. Ito, S. Kuwabata, and H. Yoneyama, "Effects of adsorbents used as supports for titanium dioxide loading on photocatalytic degradation of propylamide," *Environmental Science and Technology*, vol. 30, no. 4, pp. 1275–1281, 1996.
- [295] Y. Arai, K. Tanaka, and A. L. Khlaifat, "Photocatalysis of SiO₂-loaded TiO₂," *Journal of Molecular Catalysis A: Chemical*, vol. 243, no. 1, pp. 85–88, 2006.
- [296] M. S. Vohra and K. Tanaka, "Photocatalytic degradation of aqueous pollutants using silica-modified TiO₂," *Water Research*, vol. 37, no. 16, pp. 3992–3996, 2003.
- [297] L. J. Alemany, M. A. Banares, E. Pardo, F. Martin, M. Galán-Fereres, and J. Blasco, "Photodegradation of phenol in water using silica-supported titania catalysts," *Applied Catalysis B: Environmental*, vol. 13, no. 3–4, pp. 289–297, 1997.
- [298] B. Malinowska, J. Walendziewski, D. Robert, J. V. Weber, and M. Stolarski, "The study of photocatalytic activities of titania and titania-silica aerogels," *Applied Catalysis B: Environmental*, vol. 46, no. 3, pp. 441–451, 2003.
- [299] S. Rasalingam, H. S. Kibombo, C. M. Wu, R. Peng, J. Baltrusaitis, and R. T. Koodali, "Competitive role of structural properties of titania-silica mixed oxides and a mechanistic study of the photocatalytic degradation of phenol," *Applied Catalysis B: Environmental*, vol. 148–149, pp. 394–405, 2014.
- [300] S. Yang, Y. Guo, X. Zhou, C. Lin, Y. Wang, and W. Zhang, "Enhanced photocatalytic activity for degradation of methyl orange over silica-titania," *Journal of Nanomaterials*, vol. 2011, Article ID 296953, 2011.
- [301] A. Mahyar, M. A. Behnajady, and N. Modirshahla, "Enhanced photocatalytic degradation of C.I. Basic violet 2 using TiO₂-SiO₂ composite nanoparticles," *Photochemistry and Photobiology*, vol. 87, no. 4, pp. 795–801, 2011.
- [302] H. Chun, W. Yizhong, and T. Hongxiao, "Preparation and characterization of surface bond-conjugated TiO₂/SiO₂ and photocatalysis for azo dyes," *Applied Catalysis B: Environmental*, vol. 30, no. 3–4, pp. 277–285, 2001.
- [303] F. Chen, J. Zhao, and H. Hidaka, "Highly selective deethylation of Rhodamine B: adsorption and photooxidation pathways of the dye on the TiO₂/SiO₂ composite photocatalyst," *International Journal of Photoenergy*, vol. 5, no. 4, pp. 209–217, 2003.
- [304] H. S. Kibombo, S. Rasalingam, and R. T. Koodali, "Facile template free method for textural property modulation that enhances adsorption and photocatalytic activity of aperiodic titania supported silica materials," *Applied Catalysis B: Environmental*, vol. 142, pp. 119–128, 2013.
- [305] S. Rasalingam, H. S. Kibombo, C. M. Wu et al., "Influence of Ti–O–Si hetero-linkages in the photocatalytic degradation of Rhodamine B," *Catalysis Communications*, vol. 31, pp. 66–70, 2013.
- [306] C. Shifu and C. Gengyu, "Photocatalytic degradation of organophosphorus pesticides using floating photocatalyst TiO₂-SiO₂/beads by sunlight," *Solar Energy*, vol. 79, no. 1, pp. 1–9, 2005.
- [307] M. V. Phanikrishna Sharma, G. Sadanandam, A. Ratnamala, V. Durga Kumari, and M. Subrahmanyam, "An efficient and novel porous nanosilica supported TiO₂ photocatalyst for pesticide degradation using solar light," *Journal of Hazardous Materials*, vol. 171, no. 1–3, pp. 626–633, 2009.
- [308] M. V. Phanikrishna Sharma, V. Durga Kumari, and M. Subrahmanyam, "TiO₂ supported over SBA-15: an efficient photocatalyst for the pesticide degradation using solar light," *Chemosphere*, vol. 73, no. 9, pp. 1562–1569, 2008.
- [309] W. Jiang, J. A. Joens, D. D. Dionysiou, and K. E. O'Shea, "Optimization of photocatalytic performance of TiO₂ coated glass microspheres using response surface methodology and the application for degradation of dimethyl phthalate," *Journal of Photochemistry and Photobiology A: Chemistry*, vol. 262, pp. 7–13, 2013.
- [310] S. Ahmed, M. G. Rasul, R. Brown, and M. A. Hashib, "Influence of parameters on the heterogeneous photocatalytic degradation of pesticides and phenolic contaminants in wastewater: a short review," *Journal of Environmental Management*, vol. 92, no. 3, pp. 311–330, 2011.

Research Article

Phenol Removal by a Novel Non-Photo-Dependent Semiconductor Catalyst in a Pilot-Scaled Study: Effects of Initial Phenol Concentration, Light, and Catalyst Loading

Xiao Chen,¹ Yan Liang,^{2,3} Xuefei Zhou,¹ and Yanling Zhang³

¹ College of Environmental Science & Engineering, Tongji University, Shanghai, China

² Xinjiang Institute of Ecology and Geography, Chinese Academy of Sciences, 818 South Beijing Road, Urumqi 830011, China

³ Laboratory for Food Safety and Environmental Technology, Shenzhen Institutes of Advanced Technology, Chinese Academy of Sciences, Shenzhen 518055, China

Correspondence should be addressed to Yan Liang; yan.liang@siat.ac.cn and Xuefei Zhou; zhouxuefei@tongji.edu.cn

Received 27 November 2013; Revised 20 April 2014; Accepted 20 April 2014; Published 22 May 2014

Academic Editor: Ranjit T. Koodali

Copyright © 2014 Xiao Chen et al. This is an open access article distributed under the Creative Commons Attribution License, which permits unrestricted use, distribution, and reproduction in any medium, provided the original work is properly cited.

A novel non-photo-dependent semiconductor catalyst (CT) was employed to degrade phenol in the present pilot-scaled study. Effect of operational parameters such as phenol initial concentration, light area, and catalyst loading on phenol degradation, was compared between CT catalyst and the conventional photocatalyst titanium dioxide. CT catalyst excelled titanium dioxide in treating and mineralizing low-level phenol, under both mild UV radiation and thunder conditions of nonphoton. The result suggested that CT catalyst could be applied in circumstances when light is not easily accessible in pollutant-carrying media (e.g., particles, cloudy water, and colored water).

1. Introduction

Heterogeneous photocatalytic oxidation (HPO) can degrade refractory organics through combination of semiconductor photocatalyst (TiO₂ and ZnO), in the presence of energy-provided light source (UV) and oxidant (oxygen or air). This process largely depends on in situ generation of hydroxyl radicals under ambient conditions [1]. Among different semiconducting materials, titanium dioxide, a widely used photocatalyst for oxidizing degradation of organics in the wastewater [2–5], is always preferred for its strong oxidizing ability, bulk nontoxicity, ready availability, and long-term stability [6–8]. Anatase is the crystalline phase of TiO₂ with the highest photocatalytic activity [9]. Generally speaking in heterogeneous photocatalysis, oxidation reaction takes place on the surface of catalyst, and the degradation rates of organics relate mainly to some important parameters including substrate concentration, light intensity, catalyst loading, and the solution pH [10, 11]. Also, photocatalytic oxidation of phenol was usually investigated in a slurry reactor because of the easy handling, less limitation on mass transfer, and more efficiency than a reactor using immobilized catalysts [12].

A novel catalyst, charge transfer autooxidation-reduction-type semiconductor catalyst (CT catalyst), was developed by two Japanese scientists [13]. Our previous bench-scaled research revealed that the CT catalyst could be used for removal of low concentration phenolics under mild UV radiation and total mineralization can be realized, better than the conventional photocatalyst TiO₂ [14]. In general, CT catalyst has two significant advantages: (1) low energy consumption; (2) nonchemical consumption [14].

In the present pilot-scaled study, we aimed to investigate influencing factors, including pollutant initial concentration, lighting area, and catalyst loading, on phenol degradation using CT catalyst. Upon data analysis, optimal operational parameters for application of CT catalyst in wastewater treatment were determined.

2. Materials and Methods

Phenol (analytic grade), chosen as the target pollutant, and TiO₂ (mixture of rutile and anatase nanopowder, <100 nm, 99.5% trace metals basis) as the photocatalyst were purchased

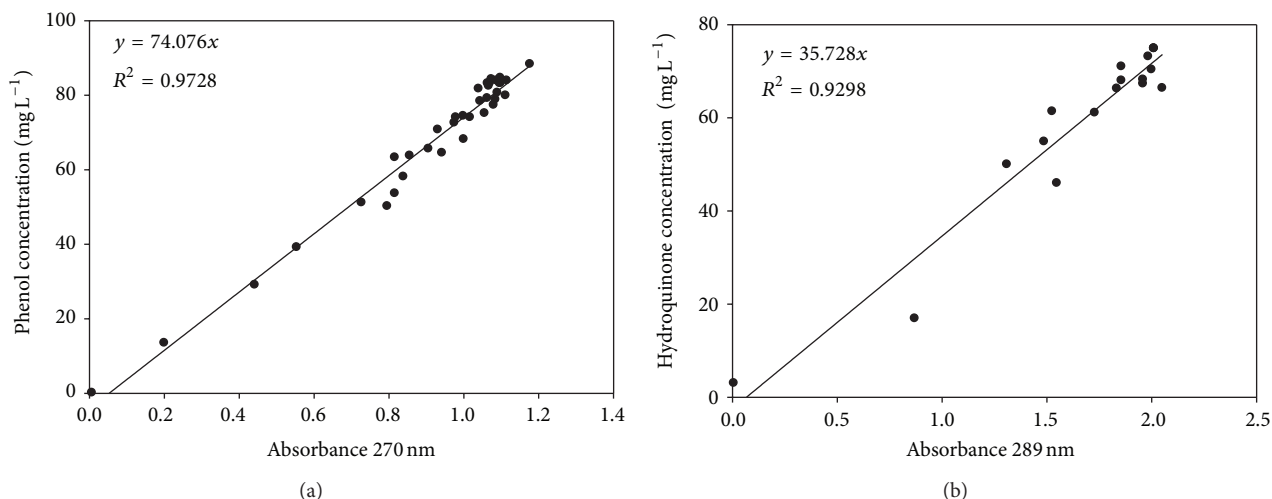


FIGURE 1: (a) Regression of phenol concentration on phenol absorbance at 270 nm and (b) regression of hydroquinone concentration on hydroquinone absorbance at 289 nm.

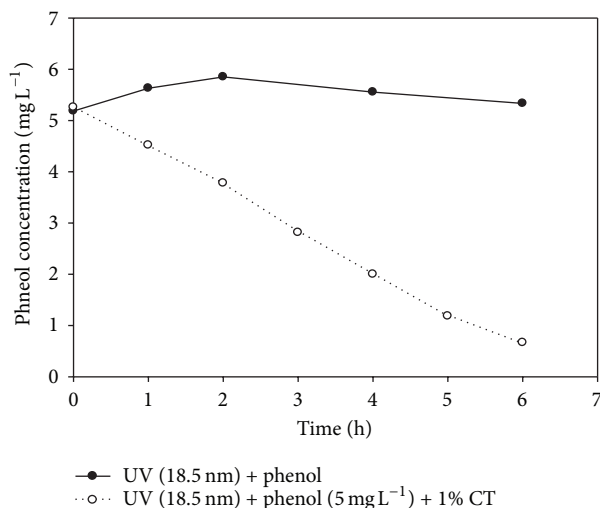


FIGURE 2: Time-dependent phenol concentration under UV radiation with and without the presence of CT catalyst.

from Sigma-Aldrich Chemical Co. CT catalyst was purchased from BOIS Ltd. The phenol solutions were adjusted to pH 3 using hydrochloric acid and sodium hydroxide solutions, simulating the pH level in phenol-containing industrial wastewaters.

The experiments were carried out in a 5 L glass immersion photochemical reactor. The main body of reactor was cylindrical with the radius of 10.5 cm bearing the structure of double jackets. The outer layer of the reactor with running water was for cooling and the inner layer was the reaction space containing 3 L phenol solution. The axis position of reactor was equipped with a stirrer, controlled at 180 rpm to realize a complete mixing of the solution. A low-pressure UV mercury lamp was set in a quartz tube immersed in the solution. The main emission wavelength of the UV lamp was 254 nm UV-C. Levels of the light intensity were approximately $3400 \mu\text{W}/\text{cm}^2$ outside of the quartz tube

and $335 \mu\text{W}/\text{cm}^2$ near the inner wall of the inner reaction cylinder, respectively. Initial concentrations of phenol were 5.0, 20.0, 50.0, and 100.0 mg L^{-1} , respectively. Lengths of the UV lamp were used in the study, including 3.0, 6.0, 8.0, 8.8, and 18.5 cm, respectively. To study the effect of catalyst loading, the phenol solution was first exposed to UV irradiation for 2 h and then the rest of the reactions took place in the dark. The catalyst loading was set at 0.03%, 0.1%, 0.2%, 0.5%, 1%, 2%, and 3%, respectively. In the experiment with thunder condition of nonphoton, 0.1% of the catalyst loading level for both CT and TiO₂ was adopted.

Samples were collected from the reactor during the treatments and filtered through $0.45 \mu\text{m}$ mixed cellulose ester (MCE) membrane before chemical analyses. Concentrations of phenol and hydroquinone were analyzed using a spectrophotometer at 270 nm and 289 nm, respectively [15]. The relationships between absorbance readings

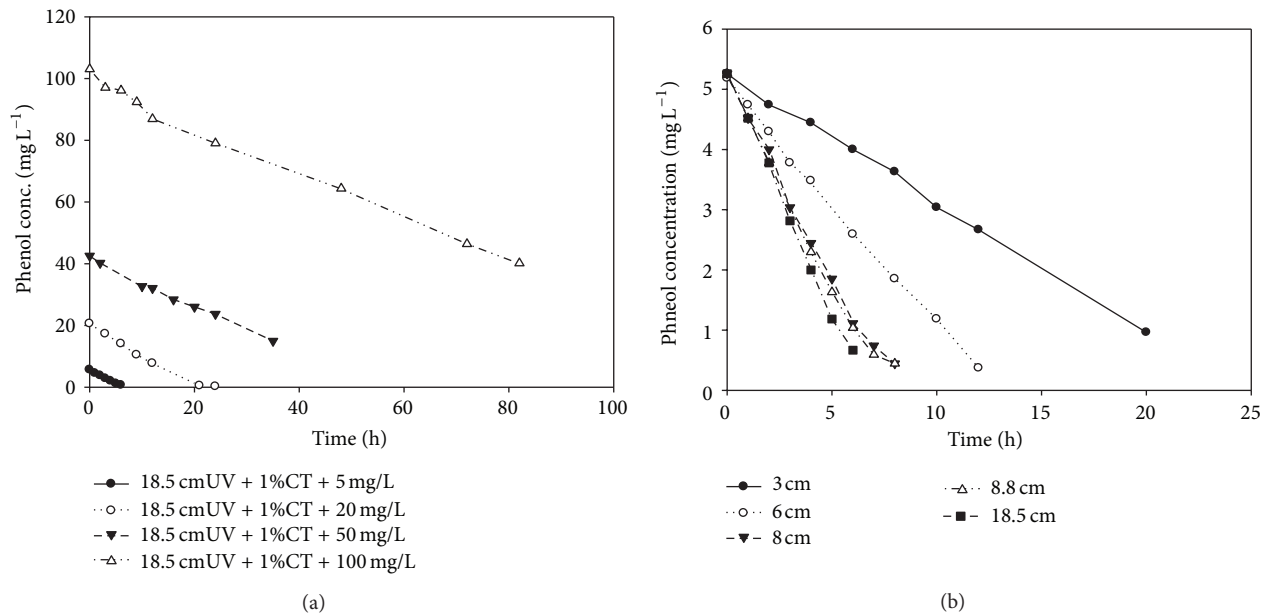


FIGURE 3: (a) Effect of phenol initial load on photocatalytic degradation with the presence of CT. (b) Time dependence of phenol concentration upon exposure to UV radiation with different UV lamp lengths.

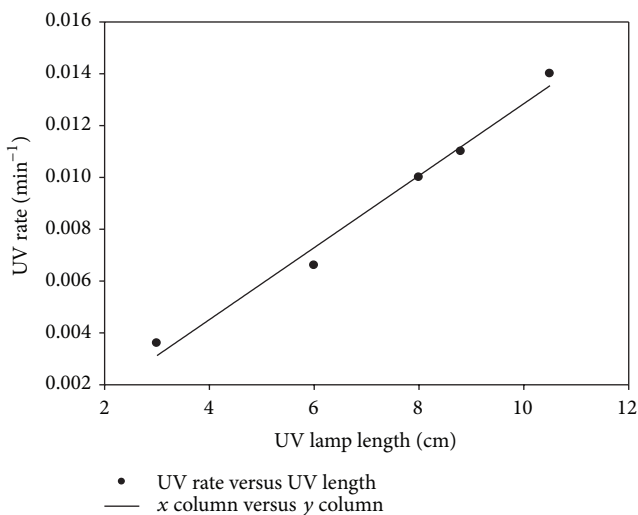


FIGURE 4: Linear relationship between UV lamp length and phenol photocatalytic degradation rate.

and concentrations of phenol or hydroquinone were shown in Figure 1.

3. Results and Discussions

3.1. Effect of Phenol Initial Concentration on Phenol Degradation by CT Catalyst and TiO₂. Phenol degradation upon UV radiation (18.5 cm UV lamp) with and without the presence of 1% CT was compared (Figure 2). It shows that UV radiation alone (without the presence of CT) had ignorable effect on phenol removal, while 1% CT achieved an 87% removal in 6 h.

Contribution of phenol initial concentration in phenol degradation was shown in Figure 3. It seems that, under the condition of UV radiation with the lamp length of 18.5 cm, degradation rate by CT catalyst was maintained at a constant level of 0.017 min⁻¹, regardless of different phenol initial concentrations (5–100 mg L⁻¹). The result demonstrated that phenol photocatalytic degradation by CT was independent of the phenol initial concentration. This is consistent with the pseudo-zero-order kinetics of phenol photocatalytic degradation by CT derived in our previous bench-scaled study [14]. In comparison, the UV light intensity employed in this pilot-scaled experiment (approximately 3400 μW/cm² near

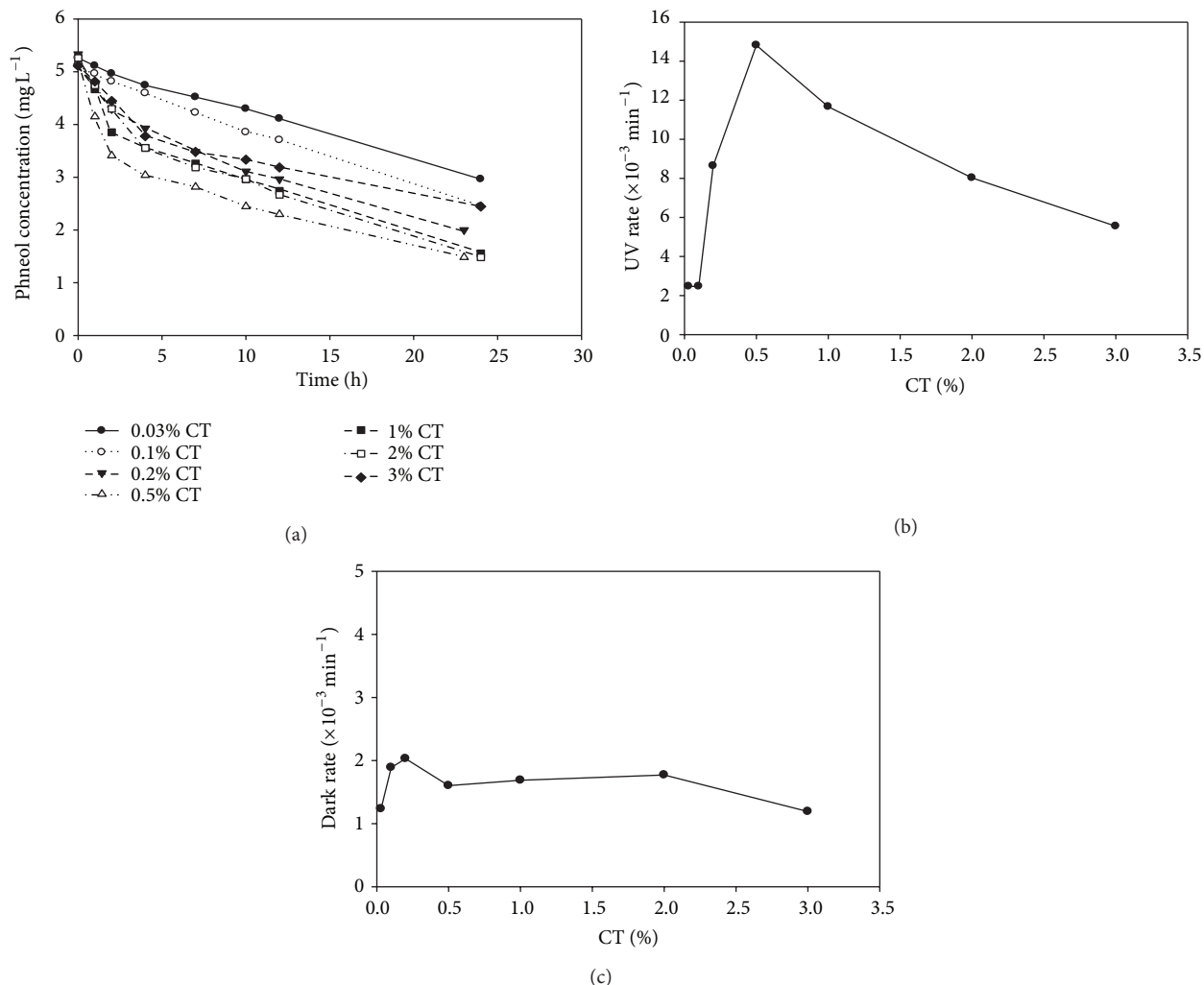


FIGURE 5: (a) Effect of CT loading on phenol degradation upon exposure to UV radiation for 2 h followed by a dark condition. (b) Effect of CT concentration on phenol photocatalytic degradation rate (with UV radiation for 2 h, followed by a dark condition). (c) Effect of CT loading on phenol degradation rate in the dark (treated in the thunder condition of nonphoton after UV radiation for 2 h).

the light tube) was much higher than that in the previous bench-scaled experiment ($<26 \mu\text{W}/\text{cm}^2$) [14]. This probably led to a higher rate constant K (0.017 min^{-1}) obtained in this study than the previous value ($K_{\text{bench-scale}}: 5.28 \times 10^{-3} \text{ min}^{-1}$) [14]. The result suggested that, within the range of initial phenol concentration we set in the present study, reaction sites on the surface of the CT catalyst were not fully occupied by the phenol molecules/activated molecules. A possible process is that the UV radiation activated the aromatic structure of the phenol molecules and subsequently these activated molecules lost their stability due to an electron change on the surface of CT and eventually were decomposed due to nonaromatic substances. The process is different from that of TiO_2 mediated phenol degradations; phenol initial concentration played important role in the reactions, most likely due to light availability and therefore hydroxyl radical generation for the oxidation of the phenol molecules [16]. In addition, the produced intermediates may lead to deactivation of active sites on the surface of TiO_2 [17, 18]. For example, Silva and Faria

reported that photocatalytic oxidation followed pseudo-first-order kinetic model ($[\text{PhOH}] = [\text{PhOH}]_0 e^{-K_{\text{app}} t}$; K_{app} was the apparent first-order kinetic constant) [12]. Hong et al. also reported that phenol photocatalytic degradation rate by TiO_2 decreased as phenol initial concentration increased from 50 to 400 mg L^{-1} [19].

3.2. Effect of UV Light on Phenol Degradation by CT Catalyst and TiO_2 . Figure 4 showed that phenol photocatalytic degradation rate increased with the increase of UV tube length under the condition of phenol initial concentration of 5 mg L^{-1} with 1% CT, and the pseudo-zero-order kinetic rate constants were 0.0036, 0.0066, 0.0104, 0.0114, and 0.0139 min^{-1} , respectively. This phenomenon was expected because the increase of UV tube length results in increase of lighting area and then of UV energy. Figure 5 demonstrated that there was a good linear relationship between UV tube length and phenol photocatalytic degradation rate by

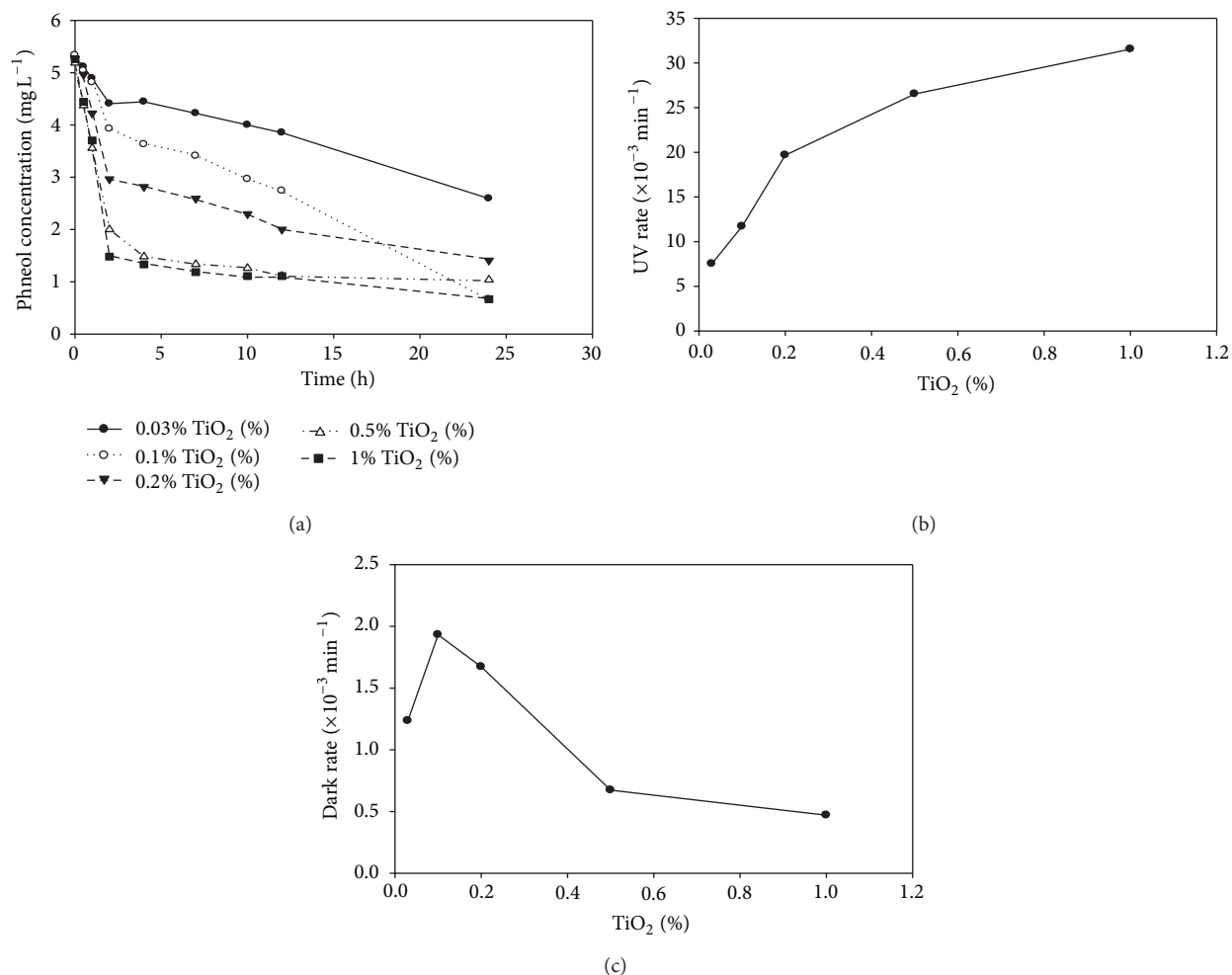


FIGURE 6: (a) Effect of TiO₂ loading on phenol degradation upon exposure to UV radiation for 2 h followed by a dark condition. (b) Effect of TiO₂ concentration on phenol photocatalytic degradation rate (with UV radiation for 2 h, followed by a dark condition). (c) Effect of TiO₂ loading on phenol degradation rate in the dark (treated in the thunder condition of nonphoton after UV radiation for 2 h).

CT ($y = 0.0014x - 0.001$, $R^2 = 0.9853$), which verified the photo-induced nature of the aromatic compounds [12].

For TiO₂, Jafarzadeh et al. reported that photodegradation rate of phenol increased with the increasing medium-pressure mercury UV lamps power from 125 w to 250 w [20]. Chiou et al. reported that the rate constants of different UV power (20, 100, and 400 w) were different (8.3×10^{-3} , 0.012, and 0.031 min^{-1} , resp.) [21]. There was a good linear relationship between the apparent rate constant and light intensity, because of the increasing amount of hydroxyl radicals.

3.3. Effect of Catalyst Loading on Phenol Degradation. After 2 h of UV irradiation, different CT loading degraded phenol and the photocatalytic rates were higher than the corresponding phenol reduction rates in the thunder condition of nonphoton (Figure 6). Phenol photocatalytic degradation rates increased as CT loading increased from 0.03% to 0.5%, resulting from an increment of the active sites available for phenol absorption and degradation. However, the rates

reduced as CT loading further increased from 0.5% to 3%. This may be because of a screen effect due to the redundant dispersion of UV radiation and aggregation of the catalyst particles with consequent decrease in the active sites available to catalytic reaction [1]. Therefore, there was photocatalytic degradation rate peak ($14.815 \times 10^{-3} \text{ min}^{-1}$) at 0.5% CT, whereas different CT catalyst loadings had the similar phenol removal rates without the presence of photon ($1.612 \times 10^{-3} \text{ min}^{-1}$).

The optimal TiO₂ loadings in degrading phenol were reported by the other researchers. TiO₂ concentrations in the suspension varied from 0.1 to 1.5 g L^{-1} . K_{app} increased with the mass of catalyst up to amount of 1.0 g L^{-1} but decreased at 1.5 g L^{-1} [12]. The present study obtained a similar TiO₂ loading level; 1% was the optimum with a maximum K_{app} ($31.54 \times 10^{-3} \text{ min}^{-1}$) (Figure 7). However, different from CT, phenol degradation by titanium in the thunder condition peak ($1.932 \times 10^{-3} \text{ min}^{-1}$) occurred upon 0.1% loading of TiO₂.

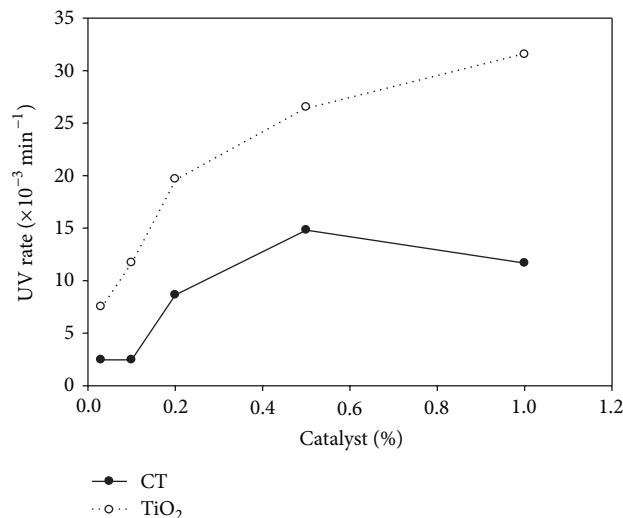


FIGURE 7: Comparison of photocatalytic degradation rates (UV exposure for 2 h) between CT and TiO_2 with variable loadings of the catalysts.

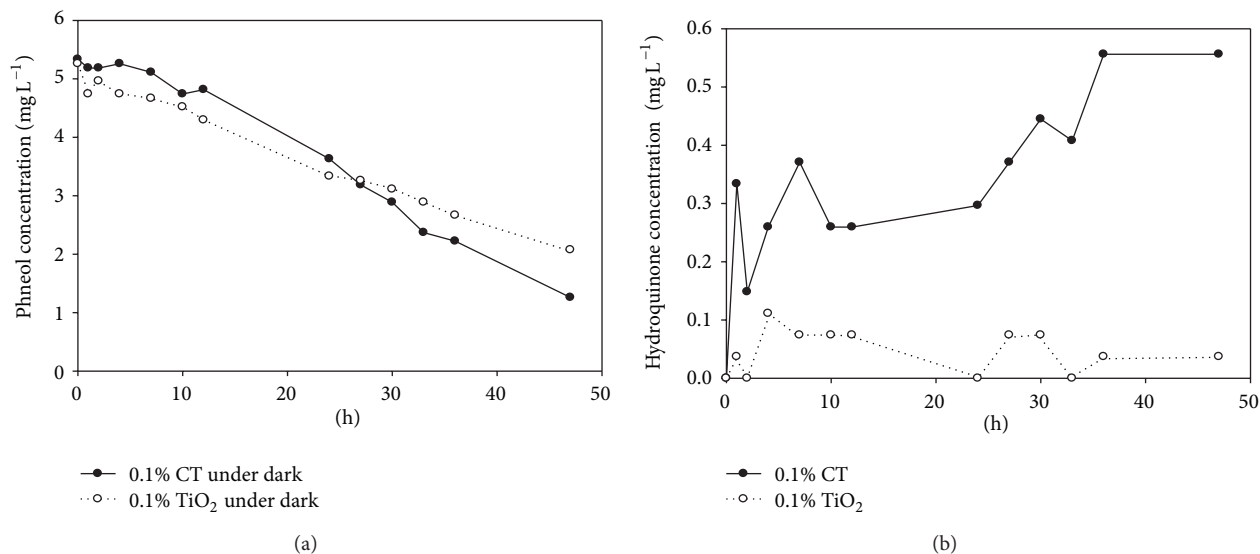


FIGURE 8: Comparison of (a) phenol reduction by CT catalyst and TiO_2 in the thunder condition of nonphoton and (b) generation of the intermediate hydroquinone between CT catalyst and TiO_2 under the thunder condition of nonphoton.

Phenol photocatalytic degradation rate by TiO_2 was faster than that by CT (Figure 8), probably due to the fact that UV intensity (approximately $3400 \mu\text{W}/\text{cm}^2$ near the light tube) was sufficient to excite the valence electrons of TiO_2 . In contrast, CT should have higher potential in phenol removal under conditions when light is not easily accessible in pollutant-carrying media (e.g., particles, cloudy water, and colored water).

3.4. Phenol Degradation by CT and TiO_2 in the Thunder Condition of Nonphoton. In the dark after a brief UV exposure, both CT and TiO_2 removed phenol, and the efficiencies at 47 h were 77% and 60%, respectively (Figure 8(a)). Production of the intermediate hydroquinone was observed in the treatments (Figure 8(b)). For CT catalyst, concentration

of hydroquinone increased with the decrease in phenol. In contrast, hydroquinone was not detected in the treatments by TiO_2 . This verified that CT catalyst could function in the dark via charge transfer to destabilize phenol, a similar result to that observed in the bench-scaled experiments [14]. For TiO_2 , it is possible that phenol molecules were simply adsorbed on the surface, blocking further degradation. This phenomenon was observed previously when using TiO_2 for degrading methylene blue, and, with the increasing initial concentration of methylene blue, the removal efficiency decreased [22]. Liu et al. also reported that nano- TiO_2 had good absorption ability and the absorption rate was above 97% [23]. After all, it is not unexpected that, at TiO_2 , positively charged, adsorbed phenol molecules at pH 3.0 and 0.1% TiO_2 showed the best absorption ability.

4. Conclusions

(1) Phenol photocatalytic degradation by CT catalyst was independent of phenol initial concentration, following a pseudo-zero-order kinetic model. In contrast, phenol photodegradation by TiO₂ followed a pseudo-first-order kinetic model, and the removal rate decreased with the increase in phenol initial concentration.

(2) The increase in the length of the UV lamp led to an increase in radiation area and energy and therefore enhanced phenol degradation in both treatments by CT catalyst and TiO₂.

(3) For photocatalysis, the optimal loadings for CT catalyst and TiO₂ treatments were 0.5% and 1%, respectively.

(4) For phenol removal under thunder condition of nonphoton, CT catalyst mediated the degradation, leading to the formation of hydroquinone, whereas the main function of TiO₂ in the process seemed to be absorption.

Overall, CT catalyst excelled the conventional photocatalyst TiO₂ in polishing low concentration of phenol under either mild UV radiation or thunder condition of nonphoton and eventually realized mineralization. CT catalyst should have enormous potential in phenol removal in wastewater, especially in circumstances when light is not easily accessible in pollutant-carrying media (e.g., particles, cloudy water, and colored water).

Conflict of Interests

The authors declare that there is no conflict of interests regarding the publication of this paper.

Acknowledgments

This study was financially supported by the National Natural Science Foundation of China (no. 41373141) and “One Hundred Talents Program” of the Chinese Academy of Sciences.

References

- [1] S. Ahmed, M. G. Rasul, W. N. Martens, R. Brown, and M. A. Hashib, “Heterogeneous photocatalytic degradation of phenols in wastewater: a review on current status and developments,” *Desalination*, vol. 261, no. 1-2, pp. 3–18, 2010.
- [2] C. Gomes da Silva and J. L. Faria, “Photochemical and photocatalytic degradation of an azo dye in aqueous solution by UV irradiation,” *Journal of Photochemistry and Photobiology A: Chemistry*, vol. 155, no. 1–3, pp. 133–143, 2003.
- [3] O. K. Dalrymple, D. H. Yeh, and M. A. Trotz, “Removing pharmaceuticals and endocrine-disrupting compounds from wastewater by photocatalysis,” *Journal of Chemical Technology and Biotechnology*, vol. 82, no. 2, pp. 121–134, 2007.
- [4] R. Comparelli, E. Fanizza, M. L. Curri et al., “Photocatalytic degradation of azo dyes by organic-capped anatase TiO₂ nanocrystals immobilized onto substrates,” *Applied Catalysis B: Environmental*, vol. 55, no. 2, pp. 81–91, 2005.
- [5] C. G. Silva, W. Wang, and J. L. Faria, “Photocatalytic and photochemical degradation of mono-, di- and tri-azo dyes in aqueous solution under UV irradiation,” *Journal of Photochemistry and Photobiology A: Chemistry*, vol. 181, no. 2-3, pp. 314–324, 2006.
- [6] M. R. Hoffmann, S. T. Martin, W. Choi, and D. W. Bahnemann, “Environmental applications of semiconductor photocatalysis,” *Chemical Reviews*, vol. 95, no. 1, pp. 69–96, 1995.
- [7] M. A. Fox and M. T. Dulay, “Heterogeneous photocatalysis,” *Chemical Reviews*, vol. 93, no. 1, pp. 341–357, 1993.
- [8] A. G. Agrios and P. Pichat, “State of the art and perspectives on materials and applications of photocatalysis over TiO₂,” *Journal of Applied Electrochemistry*, vol. 35, no. 7-8, pp. 655–663, 2005.
- [9] A. Sclafani and J. M. Herrmann, “Comparison of the photoelectronic and photocatalytic activities of various anatase and rutile forms of titania in pure liquid organic phases and in aqueous solutions,” *The Journal of Physical Chemistry*, vol. 100, pp. 13655–13661, 1996.
- [10] Y. V. Kolen’ko, B. R. Cheragulov, and M. Kunst, “Photocatalytic properties of titania powders prepared by hydrothermal methods,” *Applied Catalysis B*, vol. 54, pp. 51–58, 2004.
- [11] J.-M. Herrmann, “Heterogeneous photocatalysis: state of the art and present applications,” *Topics in Catalysis*, vol. 34, no. 1–4, pp. 49–65, 2005.
- [12] C. G. Silva and J. L. Faria, “Effect of key operational parameters on the photocatalytic oxidation of phenol by nanocrystalline sol-gel TiO₂ under UV irradiation,” *Journal of Molecular Catalysis A: Chemical*, vol. 305, no. 1-2, pp. 147–154, 2009.
- [13] S. Ichimura and K. Ichimura, “Charge transfer auto-oxidation-reduction semiconductor catalyst: application to MINOYAKI tiles and its effects,” *Transactions of the Materials Research Society of Japan*, vol. 26, pp. 1045–1048, 2001.
- [14] X. Chen, Y. L. Zhang, X. F. Zhou et al., “Application of a novel semiconductor catalyst, CT, in degradation of aromatic pollutants in wastewater: phenol and catechol,” *Journal of Nanomaterials*, vol. 2014, Article ID 524141, 10 pages, 2014.
- [15] B. Tryba, A. W. Morawski, M. Inagaki, and M. Toyoda, “The kinetics of phenol decomposition under UV irradiation with and without H₂O₂ on TiO₂, Fe-TiO₂ and Fe-C-TiO₂ photocatalysts,” *Applied Catalysis B: Environmental*, vol. 63, no. 3-4, pp. 215–221, 2006.
- [16] W. Bahnemann, M. Muneer, and M. M. Haque, “Titanium dioxide-mediated photocatalysed degradation of few selected organic pollutants in aqueous suspensions,” *Catalysis Today*, vol. 124, no. 3-4, pp. 133–148, 2007.
- [17] D. F. Ollis, E. Pelizzetti, and N. Serpone, “Photocatalyzed destruction of water contaminants,” *Environmental Science and Technology*, vol. 25, no. 9, pp. 1522–1529, 1991.
- [18] J.-M. Herrmann, “Heterogeneous photocatalysis: fundamentals and applications to the removal of various types of aqueous pollutants,” *Catalysis Today*, vol. 53, no. 1, pp. 115–129, 1999.
- [19] S.-S. Hong, C.-S. Ju, C.-G. Lim, B.-H. Ahn, K.-T. Lim, and G.-D. Lee, “A photocatalytic degradation of phenol over TiO₂ prepared by sol-gel method,” *Journal of Industrial and Engineering Chemistry*, vol. 7, no. 2, pp. 99–104, 2001.
- [20] N. K. Jafarzadeh, S. Sharifnia, S. N. Hosseini, and F. Rahimpour, “Statistical optimization of process conditions for photocatalytic degradation of phenol with immobilization of nano TiO₂ on perlite granules,” *Korean Journal of Chemical Engineering*, vol. 28, no. 2, pp. 531–538, 2011.
- [21] C.-H. Chiou, C.-Y. Wu, and R.-S. Juang, “Influence of operating parameters on photocatalytic degradation of phenol in UV/TiO₂ process,” *Chemical Engineering Journal*, vol. 139, no. 2, pp. 322–329, 2008.

- [22] F. F. Du and Q. Y. Chen, "The study of absorption of methylene blue by titanium/ activated carbon composite nanofiber membrane," *Environmental Pollution and Control*, vol. 33, no. 8, pp. 75–80, 2011.
- [23] X. Y. Liu, L. J. Yang, Y. L. Jin, L. Zhang, T. Xu, and N. Li, "Adsorption properties of nano-titanium for cadmium (II)," *The Chinese Journal of Nonferrous Metals*, vol. 21, no. 11, pp. 2972–2977, 2011.

Review Article

Study of Modern Nano Enhanced Techniques for Removal of Dyes and Metals

**Samavia Batool,¹ Shatirah Akib,² Mushtaq Ahmad,³
Khaled S. Balkhair,⁴ and Muhammad Aqeel Ashraf⁵**

¹ *Geology Department, University of Malaya, 50603 Kuala Lumpur, Malaysia*

² *Department of Civil Engineering, University of Malaya, 50603 Kuala Lumpur, Malaysia*

³ *Department of Plant Sciences, Quaid-i-Azam University, Islamabad 45320, Pakistan*

⁴ *Department of Hydrology and Water Resources Management, Faculty of Meteorology, Environment and Arid Land Agriculture, King Abdulaziz University, Jeddah 21589, Saudi Arabia*

⁵ *Department of Geology, Centre for Research in Biotechnology for Agriculture, University of Malaya, 50603 Kuala Lumpur, Malaysia*

Correspondence should be addressed to Muhammad Aqeel Ashraf; aqeelashraf@um.edu.my

Received 16 February 2014; Revised 25 March 2014; Accepted 26 March 2014; Published 20 May 2014

Academic Editor: Fan Dong

Copyright © 2014 Samavia Batool et al. This is an open access article distributed under the Creative Commons Attribution License, which permits unrestricted use, distribution, and reproduction in any medium, provided the original work is properly cited.

Industrial effluent often contains the significant amount of hexavalent chromium and synthetic dyes. The discharge of wastewater without proper treatment into water streams consequently enters the soil and disturbs the aquatic and terrestrial life. A range of wastewater treatment technologies have been proposed which can efficiently reduce both Cr(VI) and azo dyes simultaneously to less toxic form such as biodegradation, biosorption, adsorption, bioaccumulation, and nanotechnology. Rate of simultaneous reduction of Cr(VI) and azo dyes can be enhanced by combining different treatment techniques. Utilization of synergistic treatment is receiving much attention due to its enhanced efficiency to remove Cr(VI) and azo dye simultaneously. This review evaluates the removal methods for simultaneous removal of Cr(VI) and azo dyes by nanomicrobiology, surface engineered nanoparticles, and nanophotocatalyst. Sorption mechanism of biochar for heavy metals and organic contaminants is also discussed. Potential microbial strains capable of simultaneous removal of Cr(VI) and azo dyes have been summarized in some details as well.

1. Introduction

Azo dyes are widely used to dye various materials such as leather, plastics, textiles, food, paper, and cosmetics. Overall production of azo dyes in the world is estimated to be one million tons annually. The use of azo dyes in modern world represents a serious problem worldwide [1, 2]. Azo dyes are synthetic compounds [1]. These azo dyes can be differentiated by the presence of one or more azo groups ($-N=N-$) as a chromophore which linked different aromatic amines or phenols by a double bond [1, 3]. More than 10–15% of applied dyes are released into wastewater during dying process [4]. As fixation of dyestuff on the substrate is not an efficient process, it varies depending upon the method of fixation or level of affinity resulting in production of color water [5], which reduces water quality [6]. As these azo dyes are water-soluble, dyes such as sulfonated azo dyes finally enter into

the environment when released through wastewater and have many carcinogenic and mutagenic effects on various forms of life [7]. It affects photosynthetic activity of plants by limiting penetration of sunlight [6]. Moreover, toxic effects of dyes result in formation of tumor, cancer, and allergies in human and also inhibit growth of bacteria, protozoans, algae, plants, and different animals [8].

Various technologies have been applied for removal of azo dyes including physical, chemical, and biological methods but microbial degradation of dye is an efficient tool for removing pollution from environment [5]. Other microorganisms like fungi and algae decolorize dye in waste water by adsorption instead of degradation; as a result, dyes remain in the environment. However, bacteria completely degrade dyes under certain conditions [9]. Even bacteria can degrade intermediate byproduct such as aromatic amines by the hydroxylase and oxygenase enzyme [2].

Textile industry effluents with organic pollution often contain heavy metals as well as free ionic metals or in complex form [10]. In biodegradation process, both microbial biomass and its activity are of prime importance. High concentration of heavy metals like Pb, Cr, Cu, Zn, As, and Cd may have adverse effect on microbial growth and activity [11]. Microbial community composition is sensitive to long term exposure of heavy metals and may affect the decomposition property of microbes [12]. However, toxicity of these metals depends upon their availability or presence in wastewater [13].

Chromium (CrVI) is highly toxic metal that a slight increase in its level results in various environmental and health problems. The United States Environmental Protection Agency (US EPA) has added the Cr⁺⁶ in the list of 17 poisoning elements that are major threat to humans, plants, and microorganisms [14]. Industrial effluents are frequently cocontaminated with chromium ions and azo dyes [2]. Toxicity of chromium depends upon its oxidation state chromium 6 which is carcinogenic and highly toxic to all forms of life and it is more mobile and soluble in water while its reduced form chromium 3 is comparatively less toxic as it is insoluble in water [15]. Microorganisms have ability to protect themselves against toxicity of heavy metals by adopting certain mechanisms such as adsorption, uptake methylation, oxidation, and reduction [16]. But excessive concentrations of these metals may negatively influence the microbial activity and its resistant potential to heavy metals. Bacterial resistance to chromate is associated with plasmid or arises from mutation in chromosomes [17].

Chromium constitutes an integral part of many complex azo dyes which are used for dye fixation in wood leather, silk, and paper dyeing industries [18]. The structure of chromium complexes formed through chemical reaction between Cr₂O₃ and a variety of azo organic compounds that are very stable and difficult to destroy [19]. Therefore, combining existence of other azo dyes along with chromium is not only adding more contamination in wastewater but also rendering bacterial population.

Shi et al. investigated that Cr and Pb have negative impact on soil microbial activity [20]. The effects of Cr and Pb were determined in terms of ratio of microbial biomass C to soil organic C, basal respiration per unit microbial biomass ($q\text{CO}_2$), and the ratio of substrate-response respiration to microbial biomass C (substrate responsive $q\text{CO}_2$). The ratio of microbial biomass in Cr contaminated soil was 0.42% and in Pb contaminated soil was 0.36%, while $q\text{CO}_2$ and substrate-responsive values were high in Pb as compared to Cr contaminated soil ($P < 0.01$) which indicates like other heavy metals that Cr also has stress on bacterial biomass.

It was studied that sulphate reducing bacteria (SRB) removed 25–30% of initial dye (reactive black B, Ramzol blue, and reactive red RB) from medium in 72 h in the presence of 50 mg L⁻¹ chromium and approximately 95% of chromium VI removal was achieved at the end of 24 h incubation period. Results showed that decolorized dye amount was increased at increasing dye concentration by SRB but decolorization yield remained constant [21]. Such lower yield of dye decolorization shows that chromium has inhibitory effect on bacterial

efficacy of removing dye. Similarly, Khalid et al. has reported that at 250 mg L⁻¹ of chromium only 8% decolorization was obtained after 24 h using Cr₂(SO₄)₃ whereas in case of CrCl₃ in the same time period at higher concentrations (150–250 mg L⁻¹) the decolorization was in the range of 31 to 49% only [22].

Recently, several microorganisms have been found which have enzymatic system for individual or simultaneous removal of azo dyes and hexavalent chromium (Cr VI) [2, 14, 22, 23]. Bacterial strains KI (*Pseudomonas putida*) and SL14 (*Serratia proteamaculans*) have great potential to reduce simultaneously 93% CrVI and 100% decolorization of reactive black-5 azo dye in 24 h at pH 7.2 and 35°C in a batch culture. Individually, 100% removal of CrVI and reactive black-5 dye was obtained in 12 h by strains KI and SL14 [23].

Biodegradation is an effective cleanup technology used for the removal of organic and inorganic contaminants from soil [24]. Only few aerobic bacterial strains that can utilize azo dyes and heavy metals simultaneously as growth substrates have been isolated. Microbial population proliferates when soil is amended with substances capable of sorption and inactivation of growth inhibiting substances [25].

Biochar has adsorption property which can be produced by thermal degradation of organic materials in the absence of air (pyrolysis). As the pyrolysis temperature increases, the surface area and pH of the char increase. Large surface area and high cation exchange capacity increase the effectiveness of the char to adsorb organic and inorganic contaminants [26]. Biochar increases not only the sorption of toxic organic and inorganic contaminants in soil but also the other processes related to sorption such as leaching, dissipation, and toxicity for plants [27]. Degradation of azo dye and heavy metals can be obtained by adsorption, enzymatic degradation, or combining both treatment processes [28]. Efficiency of simultaneous degradation treatment for azo dyes and hexavalent chromium can be enhanced by combining different treatment technologies.

Microbial nanotechnology that is a newly emerged method to produce a nanoparticulate catalyst involves the precipitation of transition metals such as palladium, gold, and iron on bacterial cell wall, resulting in the formation of bionano-Met, where Met = transition metal catalyst [29]. On the base of catalytic nature, metal nanoparticles have been applied in environmental remediation [30]. For example, several studies have investigated the application of Fe(0) nanoparticles to reduce organic and inorganic pollutants [31].

Precipitation of these nanoparticles on bacterial surface increases their degradation potential for pollutants. On availability of electron donor, these nanoparticles tend to catalyze the reduction of contaminants, so rendering them insoluble [32]. A variety of inorganic pollutants such as carcinogenic hexavalent chromium and hexavalent uranium are soluble in their highly oxidized form and become sparingly soluble on reduction (to trivalent chromium and tetravalent uranium in the above case, resp.). On the other hand, several organic compounds such as organic dyes, fertilizers, pharmaceutical

compounds, and intermediates undergo reductive degradation. In all these cases, the contamination levels in the subsurface environment and their downstream flow can be considerably controlled and managed. In this way, study of various useful cleanup technologies is of major concern.

2. Azo Dyes

2.1. Classification of Azo Dyes. Dyes exhibit considerable structural diversity and can be classified by their chemical structure or their application to the fiber type. Dyes must carry one or more functionalities giving the dye color, called chromophores, as well as an electron withdrawing or donating substituents that cause or intensify the color of the chromophores, called auxochrome. The chromophore group can be a base for dye classification. The most important chromophores are azo ($-N=N-$), carbonyl ($-C=O$), methine ($-CH=$), nitro ($-NO_2$), and quinoid groups. The most important auxochromes are amine ($-NH_3$), carboxyl ($-COOH$), sulfonate ($-SO_3H$), and hydroxyl ($-OH$) groups [33]. Based on the origin and complex molecular structure, dyes can be classified into three categories: (1) anionic: acid, direct and reactive dyes; (2) cationic: basic dyes; and (3) nonionic: disperse dyes [34]. Among the various classes of dyes, reactive dyes are one of the prominent and most widely used types of azo dyes and are too difficult to eliminate. They are extensively used in different industries, including rubber, textiles, cosmetics, paper, leather, pharmaceuticals, and food [35–37]. The most common group reactive dyes are azo, anthraquinone, phthalocyanine [38], and reactive group dyes [39, 40]. Most of these dyes are toxic and carcinogenic [41]. Dyes may also be classified according to their solubility into soluble dyes like acid, basic, metal complex, direct, mordant, and reactive dyes or insoluble dyes including sulfur, azoic, vat, and disperse dyes.

Almost 109 kg of dyes is produced annually in the world, of which azo dyes represent about 70% by weight [42]. Because such large quantities of azo dyes are being produced and used daily by leather tanning, textile, paper production, food industry, and so forth, and they are known to transform to carcinogenic aromatic amines in the environment, their incorrect disposal is a major environmental concern and can affect human and animal health [43].

2.2. Reduction of Azo Dyes. The detailed brief method for the reduction of azo dyes is shown in Figure 1.

3. Simultaneous Removal Methods

Physicochemical processes were usually inefficient costly and not feasible to a wide range of dye wastewater [44]. However, biological processes, such as biodegradation, bioaccumulation, and biosorption are more favorable due to cost effectiveness, ability to produce less sludge, and environmental benignity [44–46]. Biosorption and bioaccumulation are the two main technologies in biological process for of dye bearing industrial effluents. They possess good potential to replace conventional methods for the treatment of dyes industry

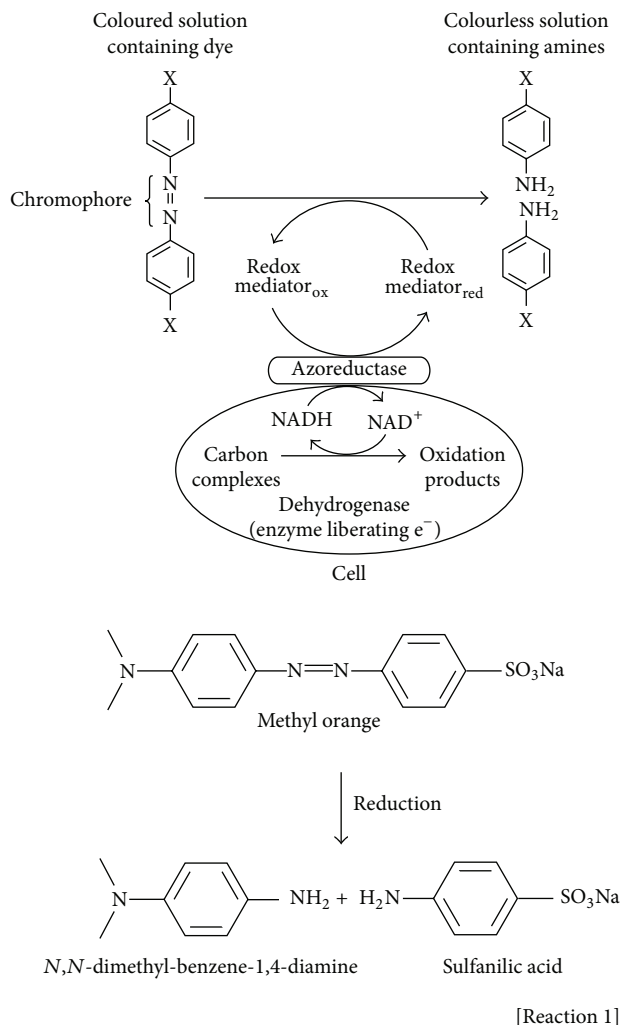


FIGURE 1: Flow sheet diagram for reduction process of azo dyes.

effluents [47]. Biological process can be carried out in situ at the contaminated site; these are usually environmentally benign, that is, no secondary pollution, and they were cost effective. These are the principle advantages of biological technologies for the treatment of dye industry effluents. Hence, in recent years, research attention has been focused greatly on biological methods for the treatment of effluents [36, 48]. The disadvantage of this degradation process is that it suffers from low degradation efficiency or even no degradation for some dyes [1, 5] and practical difficulty in continuous process [36]. Biosorption can be defined as the passive uptake of toxicants by dead or inactive biological materials. The important advantage of biosorption over bioaccumulation process is that the use of living organisms is not advisable for the continuous treatment of highly toxic effluents. This problem can be overcome by the use of dead biomass, which is flexible to environmental conditions and toxicant concentrations.

3.1. Simultaneous Removal by Biochar. Biochar is increasingly receiving attention as a promising functional material in

environmental and agricultural application. It refers to the C-rich residues of incomplete combustion of biomass under oxygen-limited conditions and at relatively low temperatures (<700°C). Various plant tissues and organic-rich wastes including wood chips, animal manure, and crop residues have been used for biochar production. Biochar is produced as a soil amendment for agricultural and environmental gain, which distinguishes it from other carbonaceous products such as activated C (AC) and charcoal [49]. For example, AC is produced from biomass at high temperatures followed by an activation process to increase its surface area for use in industrial processes such as filtration [50].

Extensive work has been done on biochar to slow global warming by sequestering C from atmosphere into soil [33, 49, 51]. Plants absorb atmospheric CO₂ through photosynthesis and store it in their biomass. By heating under oxygen limited condition and at relatively low temperatures, 30–50% C in the biomass is converted to stable biochar, which is primarily composed of condensed aromatic C [49]. Incorporation of biochar into soil has the potential to lock atmospheric C in the solid phase for hundreds to thousands of years [46, 49]. Application of biochar to soil can also help improve soil properties and enhance soil quality by retaining higher moisture and nutrients and microbial activity and therefore increasing crop production [52–54]. Application of biochar to contaminated soils can also reduce the bioavailability of organic contaminants to plants, microbes, and earthworms in contaminated soils [55–57]. The large surface area and high microporosity of biochar are responsible for its high affinity for organic contaminants and large P content is responsible for removal of heavy metals as well (Table 1) [58].

Recently, several studies have been conducted which shows that biochar affects the transport and fate of organic contaminants in soils [55–60]. Hilton and Yuen were the scientists who determined the sorption of pesticide by ashes obtained from burning crop residue even after washing out organic matter with H₂O₂ in 1960s [61]. Addition of wheat straw derived biochar to soil effectively sorbed diuron [56]. Yu et al. indicated that the biochar produced from wood chips was effective in immobilizing chlorpyrifos and carbofuran insecticides in a soil [55].

A study conducted by Cao et al. represents that after 210 days of incubation, biochar (P-rich dairy manure) addition reduced atrazine concentration in CaCl₂ extract by 66–81% in both types of soil (Figures 2(a) and 2(b)) [58]. Similarly, atrazine concentrations in the TCLP extract was reduced by 53–77% (Figures 2(c) and 2(d)).

A similar experiment was also performed by application of Pb and biochar in both types of soil. After 120 days of incubation biochar reduced Pb in CaCl₂ extracts by 65–75% in the SR soil and by 57–68% in the BR soil (Figures 3(a) and 3(b)). Similarly, Pb in the TCLP extract was reduced by 72–89% in the SR soil and by 70–79% in the BR soil (Figures 3(c) and 3(d)). Rate of reduction of atrazine and Pb was amplified with increasing biochar level and duration of incubation (Figures 2 and 3).

Mechanism for stabilization of Pb in soil involves the conversion of less stable PbCO₃ into more stable Pb₅(PO₄)₃OH

by P present in biochar, while adsorption of atrazine on organic C in biochar may be responsible for immobilization of atrazine in soil [56].

Phosphorus originally contained in the biochar induced conversion of less stable PbCO₃ to more stable Pb₅(PO₄)₃OH and is responsible for soil Pb immobilization, whereas atrazine stabilization may result from its adsorption on organic C in biochar (Figure 4) [60].

It was investigated by Han et al. that rice straw biochar has great potential to adsorb cadmium (Cd) and sulfamethoxazole (SMX) from cocontaminated water [62]. The calculated maximum adsorption parameter (Q) of Cd was similar in single and binary systems (34129.69 and 35919.54 mg kg⁻¹, resp.). However, the Q of SMX in a binary system (9182.74 mg kg⁻¹) was much higher than that in a single system (1827.82 mg kg⁻¹).

3.1.1. Sorption Mechanism. The good fit of the Langmuir adsorption isotherm was based on monolayer coverage of the adsorbate on the surface of the adsorbent, indicating that the sorption of Cd on rice straw biochar is monolayer sorption on a fixed number of surface sites on the biochar [63]. It was investigated by several experiments that large surface area (SA) is responsible for improving sorption capacity of biochar for heavy metals such as As, Pb, Cu, Zn, and Cd, which provides more surface sites for their adsorption. For example, corn straw char produced at 600°C has a larger SA than hardwood char produced at 450°C, leading to greater adsorption capacities of corn straw char for Cu and Zn [64]. However, in a study conducted by Han et al., different diameters showed no significant effect on the sorption of Cd on biochar, regardless of the presence of SMX (Figure 5) [62]. Xu et al. stated that, in case of adsorbent having low SA (5.61 m² g⁻¹), sorption may not be influenced by SA of biochar [65]. Therefore, the maximum adsorption capacity of rice straw biochar for Cd calculated by the Langmuir model was similar to the result of the study by Xu et al., which shows that formation of metal-phosphate and carbonate precipitates on the surface of biochar may be attributed to the large adsorption capacity of dairy manure-derived biochar for Cd (32036.85 mg kg⁻¹) [66]. It was also described by Echeverría et al. that precipitation plays a vital role in the sorption of Cd by adsorbents. In our study, the amount of adsorption was also extraordinarily large [67], and the SEM images (Figure 5) of rice straw biochar after Cd adsorption reveal the precipitates on the surface of the biochar, which confirms that precipitation was responsible for adsorption process.

It was suggested by Harvey et al. that Cd sorption takes place through cation-exchange on biochars produced at <350°C, but primarily by two distinctive cation- π bonding mechanisms on biochars produced at $\geq 350^\circ\text{C}$ [68]. Han et al. produced the rice straw biochar at 400°C, which indicates that Cd²⁺- π bonding may contribute to sorption [62]. Sorption of Cd may also be attributed to hydrogen-bonding because of the presence of hydroxyl (-OH) in biochar, indicated by the band at 3374 cm⁻¹ [64]. Besides electrostatic interaction, ion exchange could also contribute to Cd sorption on rice straw biochar.

TABLE I: Adsorption of heavy metals and organic contaminants by biochar.

Type of biochar	Organic compounds	Heavy metals	Maximum adsorption capacity		Time for maximum adsorption		References
			(%)/mg kg ⁻¹		(days)		
			O.C.	Heavy metals	O.C.	Heavy metals	
Rice straw	Sulfamethoxazole (SMX)	Cd(III)	9182.74 mg kg ⁻¹	35919.54 mg kg ⁻¹	—	—	[62]
Wheat straw	Diuron	—	—	—	—	—	[56]
P-rich dairy manure	Atrazine	Pb(II)	66–81%	72–89%	210 days	120 days	[58]
Wood chip	Chlorpyrifos and carbofuran insecticides	—	—	—	—	—	[55]
Corn straw	—	Cu(II), Zn(II)	—	—	—	—	[74]

However, in case of organic contaminant SMX, a positive correlation was found between SA of biochar and the concentration of SMX adsorbed on biochar and the biochar having large diameter (150–250 μm) was found to attain maximum adsorption capacity for SMX. Scanning electron microscopy (SEM) and the Fourier transform infrared spectroscopy (FTIR) showed that the removal of Cd and SMX by rice straw biochar may be attributed to precipitation and the formation of surface complexes between Cd or SMX and carboxyl or hydroxyl groups.

Because of amino functional groups and *N*-heteroaromatic rings, SMX is a strong π -acceptor compound [69]. The mechanism of π - π electron donor-acceptor (EDA) [70] facilitates the strong interaction between nitro aromatics and black carbon (char) [71]. In the FTIR spectrum, the π - π EDA interaction between SMX and biochar is because of the COO⁻ groups (1587 cm^{-1}) in rice straw biochar.

3.1.2. Effect of pH on Sorption of Heavy Metals. Heavy metal sorption on biochar is positively correlated with pH of medium [62]. Negative charge on the surface of the biochar increases with the increase in solution pH from 3 to 5. Thus, the enhanced electrostatic attraction could promote adsorption of cationic heavy metals on the negatively charged surface of the biochar. There is also competition between protons and metal cations for sorption sites on the surface of the biochar [72].

It was pointed out, in a study conducted by [62], that the amount of Cd adsorption increased with increasing pH and became stable after pH 5 in both single and binary systems. As the pH_{zpc} (zero point of charge) of biochar lies between 2.0 and 3.5 [73], the surface charge of biochar in the solution was mainly negative in the pH range (3, 4, 5, 6, and 7.5) in this experiment. When the pH was above 5, adsorption capacity started decreasing because of the formation of hydroxide complexes [64]. Chen et al. and Liu and Zhang have revealed similar outcomes, regardless of the original material of the biochar [74, 75].

3.1.3. Effect of pH on Sorption of Organic Contaminants. A negative correlation exists between sorption of organic compounds and pH of solution. Increase in pH results in

the reduction of neutral species, whereas anionic species increases, and it creates a strong electrostatic repulsion between the negatively charged biochar surface and organic anionic species. The cationic, neutral, and anionic species of SMX dominate at pH values of <1.7, around 3.7, and >5.7, respectively [76]. This is the most possible reason that the amount of SMX sorption on biochar increased as pH value of solution decreased and it was negatively correlated with the pH values [62].

Moreover, there is strong negative correlation between amount of organic pollutant on biochar and solubility of that contaminant in solution. When pH rises, it may cause less solubility of organic complex and results in reduction of hydrophobic partitioning between organic complex and biochar, supporting that mechanism of hydrophobic partitioning plays a vital role for sorption of organic compounds on biochar. Therefore, sorption of SMX on rice straw biochar decreased on rising pH value (3–7.5) [62]. In addition, by increasing pH value, the π -acceptor ability would increase with protonation, resulting in weaker interaction of π - π EDA between SMX and biochar. This is the one possible reason that sorption level was maximum at pH 3 [62].

3.1.4. Effect of Heavy Metals on Sorption Capacity of Biochar for Organic Contaminants. Earlier studies revealed that either antagonistic [77] or synergistic [78] interaction exists between heavy metals and organic compounds. In the cocontaminated solution, positively charged heavy metals would influence the sorption of organic compounds by altering the biochar surface. Cations could first be adsorbed on the surface of the biochar, and the negative charge on the surface of the biochar would be diminished [79]. Then, the electrostatic repulsion between the biochar surface and anionic organic compounds could be mitigated and therefore significant promotion of adsorption of organic compound. Adsorption of cations (Cd⁺², Ca⁺², Mg⁺², and Cr⁺⁶) could lead to the formation of a bridge on the surface of the biochar [80], assisting the adsorption of organic compound. Deposition of cations on biochar surface could reduce the competition between organic compounds and water for sorption sites by declining the hydrophobicity of the local region [81]. This process not only altered the biochar surface but also formed a

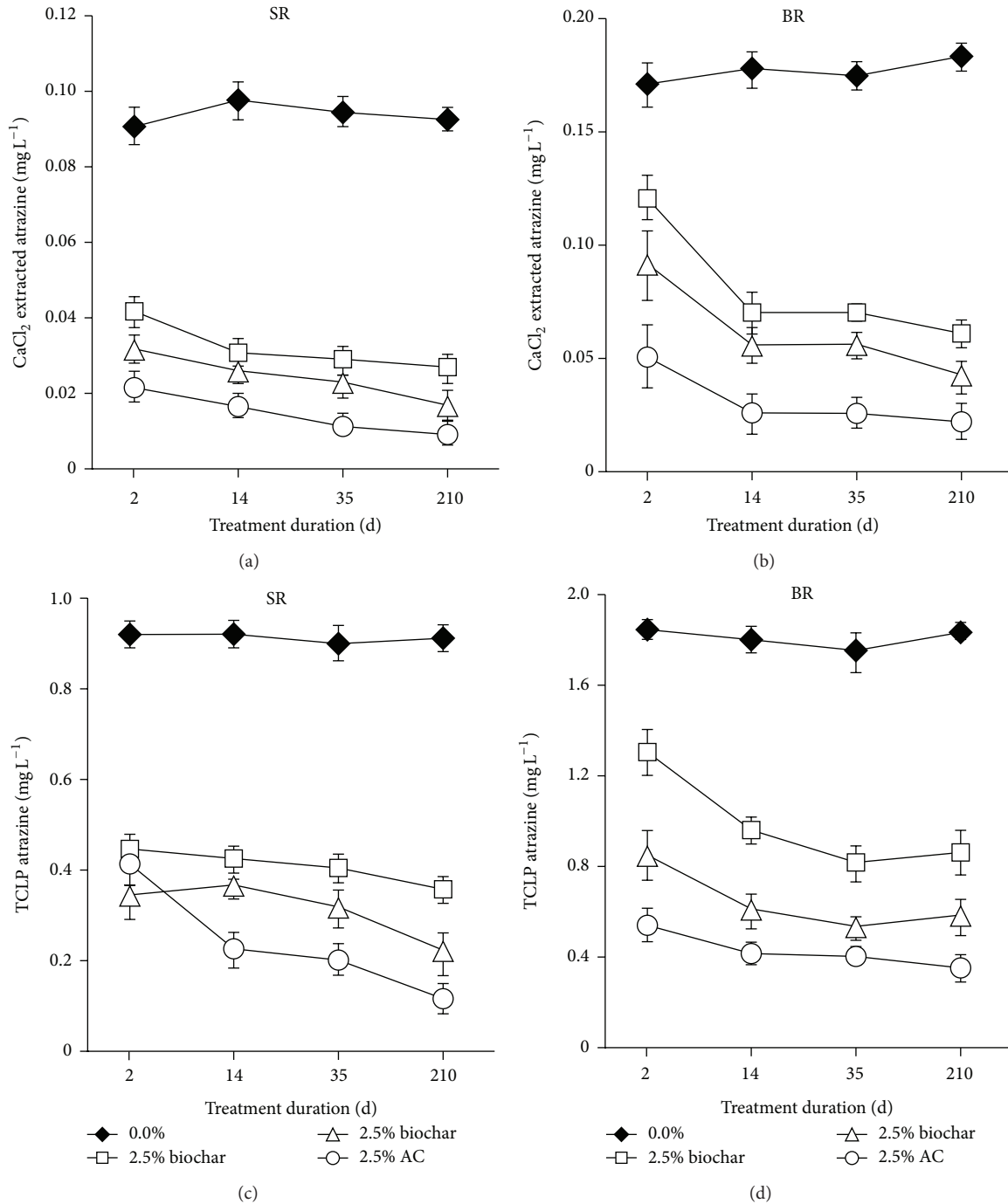


FIGURE 2: Atrazine concentration in the CaCl_2 and TCLP extract obtained from soils treated with different doses of biochar.

heavy metal-organic compound complex [82] with a higher sorption affinity on biochar than SMX, based on the metal complexes [83]. A significant increase of SMX sorption on rice straw biochar by Cd was reported by Han et al. (Figure 5) [62].

3.2. *Simultaneous Removal by Nanotechnology.* In order to solve the problem of water and soil pollution, quick and major

improvements in wastewater treatment have been conducted, comprising photocatalytic oxidation, adsorption/separation processing, and bioremediation; see Table 4 [83]. However, these treatments have been constrained because of many issues such as processing efficiency, operational method, energy requirements, and economic benefit. Currently, nano-materials (NMs) have been recommended as efficient, cost-effective, and environmental friendly substitute to existing

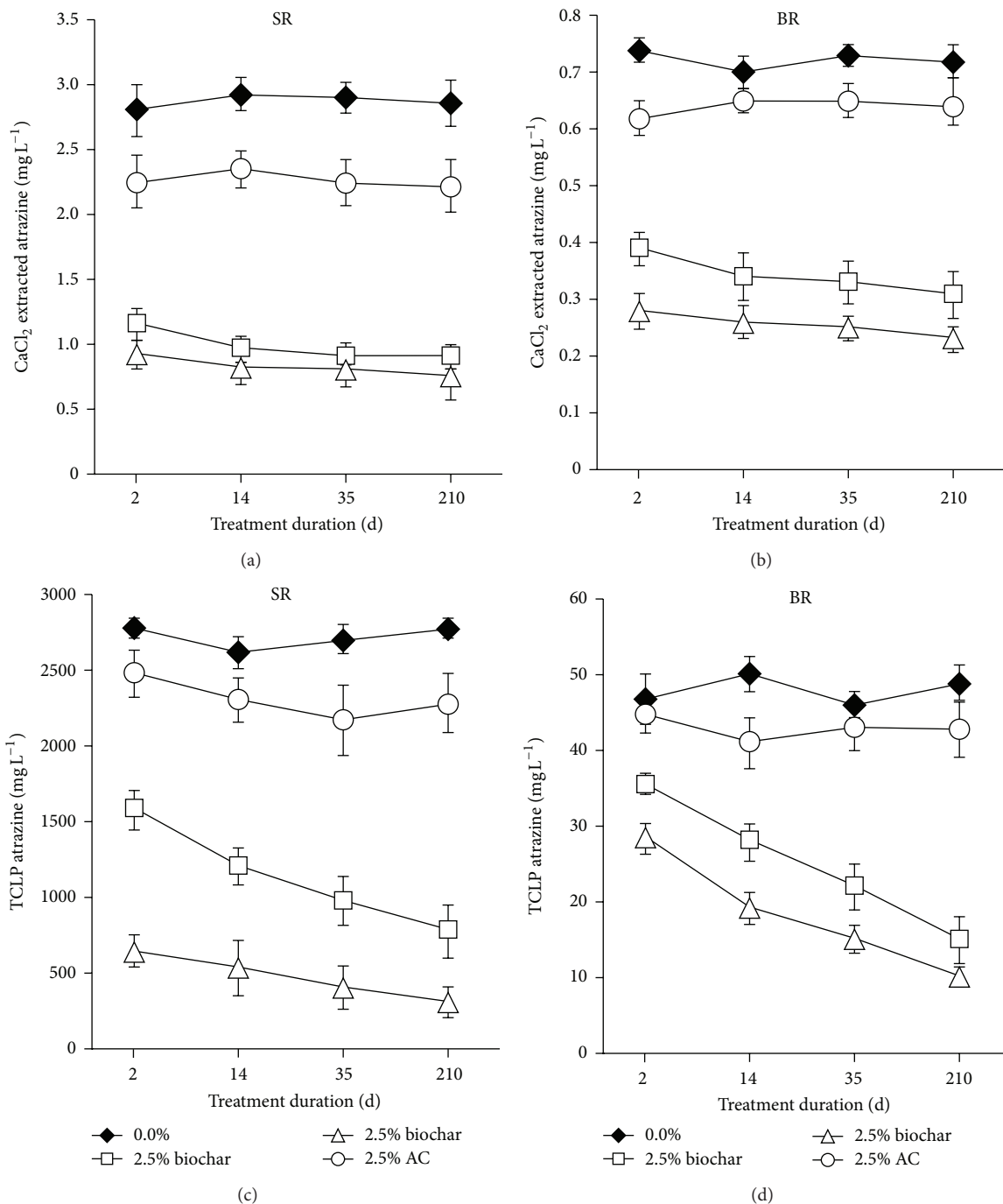


FIGURE 3: Pb concentration in the CaCl₂ and TCLP extract obtained from soils treated with different doses of biochar.

treatment resources from the perspectives of both resource conservation and environmental remediation [84].

Nanotechnology is a field of applied science, focused on the design, synthesis, characterization, and application of materials and devices on the nanoscale. Nanotechnology holds out the promise of massive progresses in manufacturing technologies, electronics, telecommunications, health, and even environmental remediation [24]. It involves the

manufacture and application of a miscellaneous variety of NMs, which include structures and devices that range in size from 1 to 100 nm and exhibit distinctive characteristics not contained by bulk-sized materials [37]. Various types of nanomaterials exist, such as carbon-based NMs [85], TiO₂NMs [86], and iron oxide NMs [66].

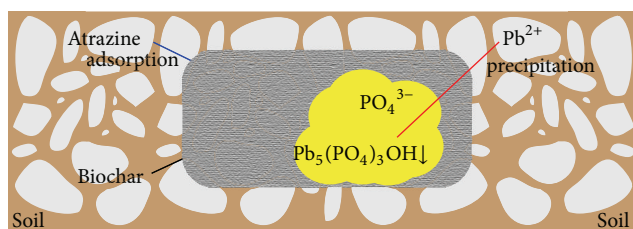


FIGURE 4: Mechanism for Pb(II) precipitation and atrazine adsorption on biochar.

Iron oxides are present in different forms in the universe. Magnetite (Fe_3O_4), maghemite ($\gamma\text{-Fe}_2\text{O}_3$), and hematite ($\alpha\text{-Fe}_2\text{O}_3$) are well known. In recent years, the production and utilization of iron oxide NMs with innovative properties and functions have been extensively studied, because of their size in nanorange, high surface area to volume ratios, and superparamagnetism [87]. Predominantly, the easy manufacturing, coating, or amendment and the ability to control or manipulate matter on anatomic scale could offer incomparable flexibility for utilization [88]. Furthermore, iron oxide NMs with low harmfulness, chemical inertness, and biocompatibility represent a remarkable potential coupling with biotechnology because it has great potential to reduce immobilization of microorganisms and in turn provide greater bioavailability of contaminants. In addition, stabilization of nanoparticles on cell surface can improve its stability, reusability, mechanical strength, and the ease of treatment [89].

3.2.1. Simultaneous Removal by Bionanocatalysis. A new biologically inspired method to produce a nanoparticulate catalyst involves the precipitation of transition metals such as palladium, gold, and iron on bacterial surface, resulting in the formation of bionano-Met [29] which have high potential to remove organic and inorganic contaminants from soil and water [90]. Two gram negative model organisms sulfate-reducing bacterium *Desulfovibrio desulfuricans* [91] and metal-respiring bacterium *Shewanella oneidensis* [92] have been primarily used to reduce Pd(II) and subsequently induce precipitation of Pd(0) nanoparticles on bacteria and formed the bio-Pd(0) nanoparticles. Ashraf et al. produced a bio-Pd(0) nanocatalyst which successfully reduced the hexavalent chromium (VI) [93].

Recently, Johnson et al. has prepared the bio-Pd(0) nanomaterial by precipitating reduced Pd(0) on *C. pasteurianum* (Figure 6) [29]. Bio-Pd(0) NMs efficiently reduced two azo dyes methyl orange (MO) and Evan's blue (EB). Ten ppm of nano-Pd degraded MO almost 100% in 7 minutes (Figure 7) whereas 5 ppm of bio-Pd(0) decolorized EB almost 100% in 7 minutes (Figure 8).

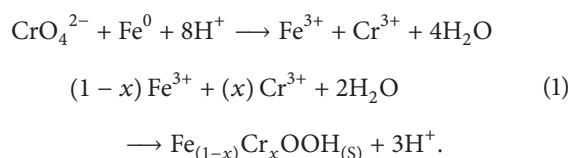
In another study, it was found that only 50 mg L^{-1} of bio-Pd(0) reduced seven highly toxic PCBs up to 27% of their initial level. Whereas, 500 mg L^{-1} of commercial Pd(0) powder

reduced the same concentration of PCBs [92]. Isolated bacterial strains *Pseudomonas aeruginosa* and zerovalent iron (Fe^0) accelerated heavy metal reduction capacity for Cr(VI) and cadmium, 72.97% and 87.63%, respectively [94].

Pang et al. developed a synergistic system by immobilizing the *Saccharomyces cerevisiae* on the surface of chitosan-coated magnetic nanoparticles (SICCM) for adsorption of Cu(II) from aqueous solution (Figures 9(a), 9(b), and 9(c)) [95]. After immobilization, magnetic adsorbent was pure Fe_3O_4 and it was without conglomeration. Initial pH level of Cu(II) solution, concentration of Cu(II) solution, and application time were factors which influenced the final % removal of Cu(II). Highest adsorption potential was obtained at pH 4.5 (Figure 10). When initial dose of Cu(II) was 60 mg L^{-1} , then highest adsorption capacity obtained was 96.8% and this % removal efficiency increased as initial dose of Cu(II) increased (Figure 11). Equilibrium was obtained in 1 hour. The highest adsorption capacity for Cu(II) was assessed to be 144.9 mg g^{-1} . The tremendous feature of CCM for adsorption of heavy metals can be attributed to (1) high hydrophilicity due to large number of hydroxyl groups of glucose units, (2) presence of a large number of functional groups (acetamido, primary amino, so that it can absorb heavy metal ions in wastewater treatment and/or hydroxyl groups), (3) high tendency of these functional groups to react, and (4) flexible structure of the polymer chain.

Polyvinyl alcohol (PVA), sodium alginate, and multiwalled carbon nanotubes (MCNTs) were used by Pang et al. to immobilize a bacterial strain *Pseudomonas aeruginosa*. Prepared beads were kept at freezing temperature to improve its mechanical strength [96]. At 80 mg L^{-1} Cr(VI) concentration, 50% Cr(VI) of its initial concentration was reduced in 84 hours. However, bacterial cells which were not immobilized became deactivate at this concentration. The beads were applied nine times for removal at 50 mg L^{-1} Cr(VI) concentration. On first application, 90% removal was achieved, while in the end 65% removal efficiency was achieved (Table 2).

3.2.2. Reduction of Heavy Metals by Engineered Nanoparticles. Among natural reductant of Cr(VI), zerovalent iron is an alternative in the remediation of polluted sites, converting Cr(VI) to essentially nontoxic Cr(III). At 0.4 g L^{-1} concentration of zerovalent iron, 100% of Cr(VI) (20 mg L^{-1}) was reduced. Reduction potential of Cr(VI) suppressed markedly as initial pH increased. It was concluded that in each case $\text{Cr}(\text{OH})_3$ should be the final product of Cr(VI) (1). In this way, iron nanoparticles are best option for the remediation of heavy metals in groundwater and soil [97]. Consider



High removal efficiency of heavy metals and organic contaminants can be achieved by making amendments to

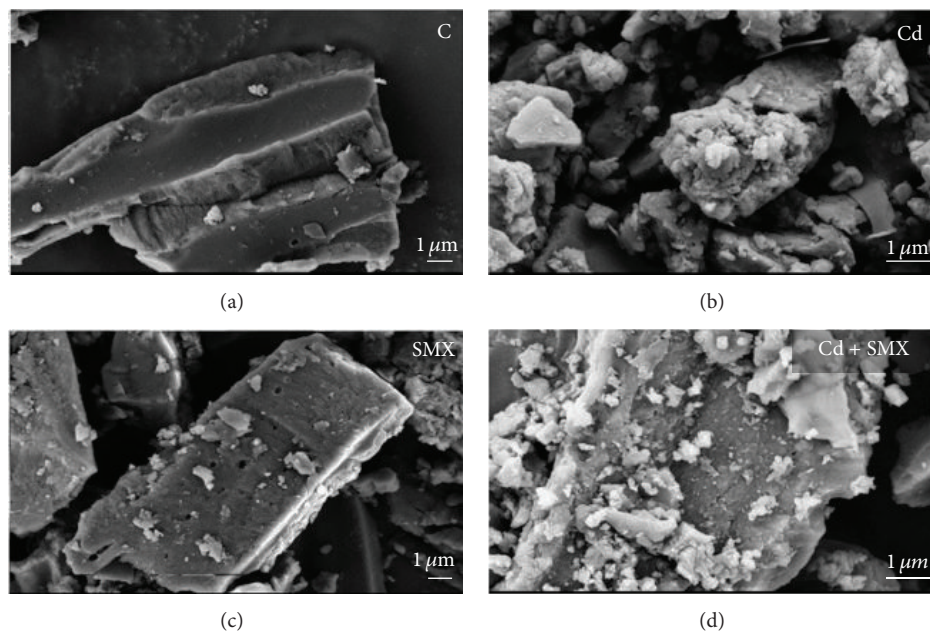


FIGURE 5: ESEM images of rice straw biochar before and after treatment with solutions of Cd and SMX.

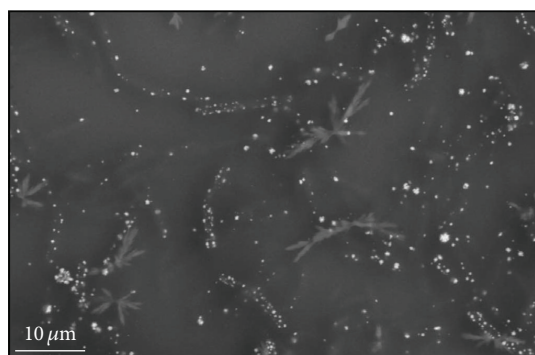


FIGURE 6: SEM image of bio-Pd(0) nanoparticles.

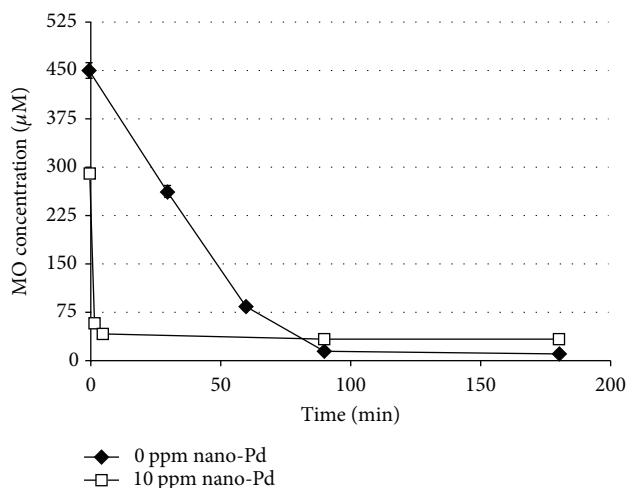


FIGURE 7: Concentration of methyl orange at different levels of bio-Pd(0) nanoparticles.

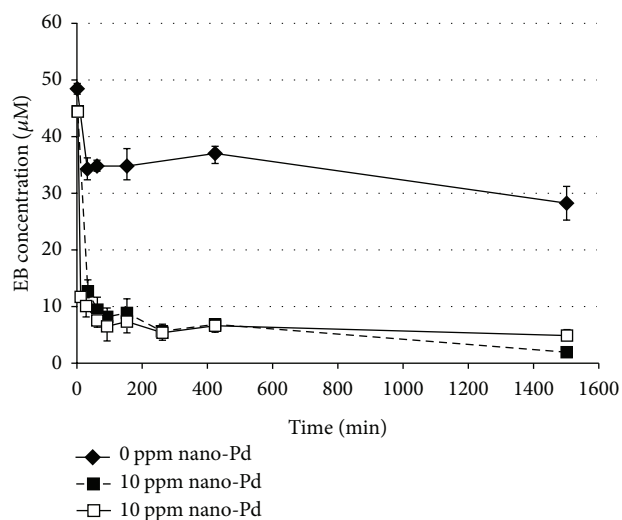


FIGURE 8: Concentration of Evan's blue at different levels of bio-Pd(0) nanoparticles.

NMs. For example, a novel magnetic nanosorbent (MNP-NH₂) has been produced by the covalent binding of 1,6-hexadiazine on the surface of Fe₃O₄ nanoparticles for the removal of Cu²⁺ ions from aqueous solution [98]. The chemisorptions occurred between Cu²⁺ and NH₂ groups on the surface of MNP-NH₂, as shown in



In addition, the prepared nanosorbents had good reusability and stability, and the adsorption capacity of MNP-NH₂ was kept constant (about 25 mg g⁻¹).

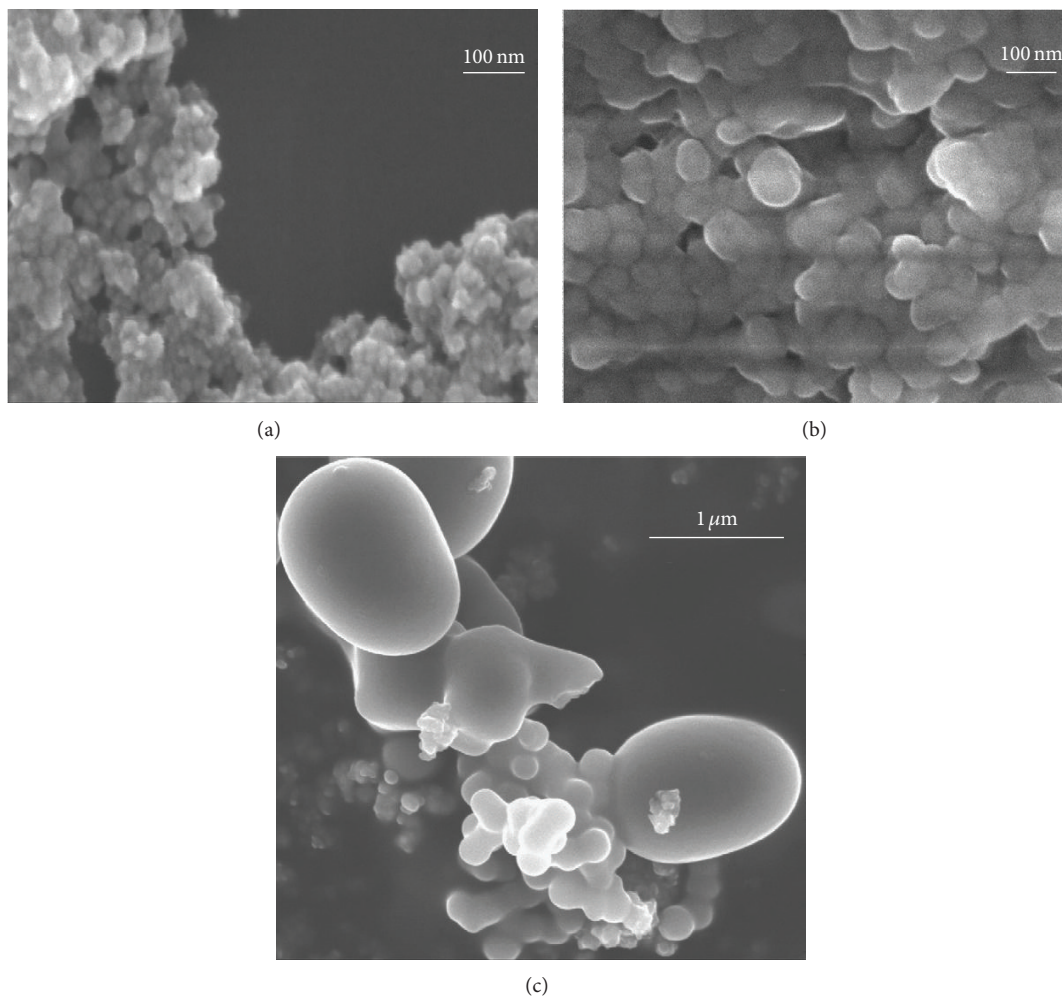


FIGURE 9: (a) Transmission electron micrograph of Fe_3O_4 magnetic nanoparticles and (b) chitosan-coated magnetic nanoparticles. (c) Immobilized *S. cerevisiae* on the surface of chitosan-coated magnetic nanoparticles.

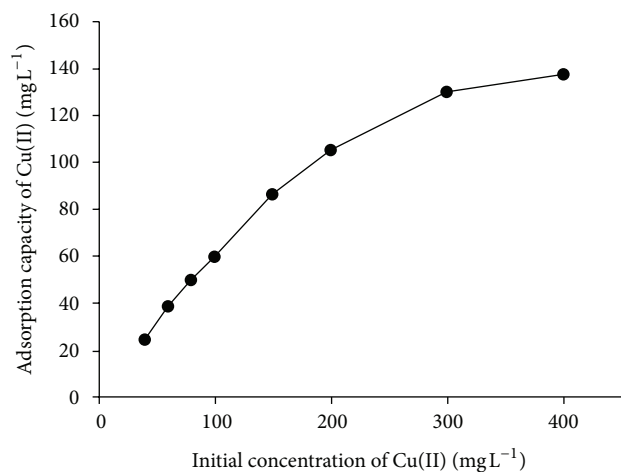


FIGURE 10: Adsorption capacities of Cu(II) mg L^{-1} by *S. cerevisiae* immobilized on chitosan-coated magnetic nanoparticles at different initial concentrations of Cu(II) mg L^{-1} .

Various forms of Fe^0 were compared in the same conditions. The potential to degrade Cr(VI) was in the following order: starch-stabilized Fe^0 nanoparticles > Fe^0 nanoparticles > Fe^0 powder > Fe^0 filings (Figure 12). Figure 13 shows the ESEM images of the alone Fe^0 nanoparticles (a) and starch stabilizer Fe^0 nanoparticles (b). Much larger dendritic flocs have been formed without starch whereas discrete Fe^0 nanoscale particles have been formed in the presence of starch (splinter-shaped crystalloid). The presence of starch effectively prevents accumulation of the iron particles and thus keeps high surface area and great reactivity [97].

Mesoporous $\gamma\text{-Fe}_2\text{O}_3$ nanoparticles possess superparamagnetic properties. It has comparatively great potential to remove Cr(VI) ions from the aqueous solution to that of pristine CMK-3 carbon. It was found that mesoporous $\gamma\text{-Fe}_2\text{O}_3$ nanoparticles (10 nm) had large adsorption capacity as compared to nonporous $\gamma\text{-Fe}_2\text{O}_3$ nanoparticles under same experimental conditions and degradation

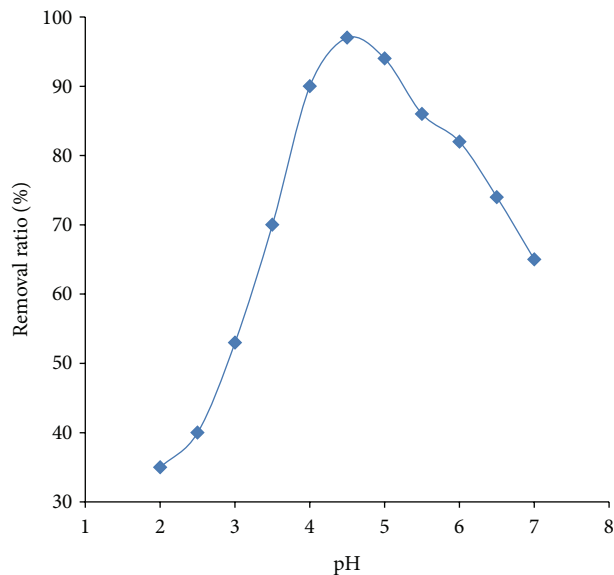


FIGURE 11: Removal ratio (%) of Cu(II) by *S. cerevisiae* immobilized on chitosan-coated magnetic nanoparticles at different pH levels.

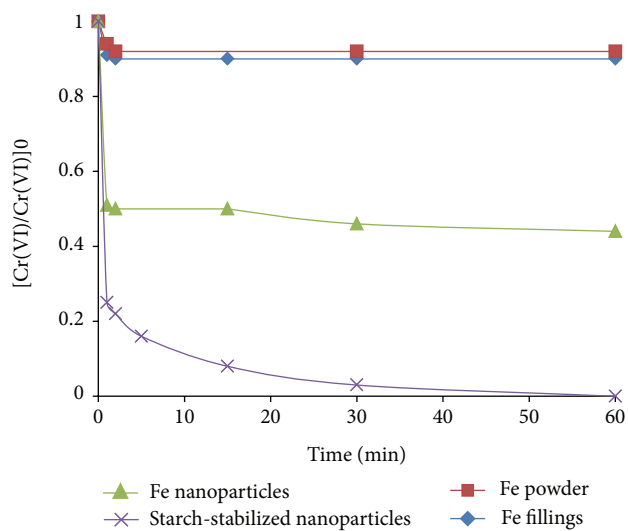


FIGURE 12: Concentration of Cr(VI) treated with different forms of Fe⁰ nanoparticles.

strength of mesoporous gamma-Fe₂O₃ nanoparticles for Cr(VI) increased as pH level of solution decreased [99].

Montmorillonite-supported magnetite nanoparticles were developed by coprecipitation and hydrosol method. The average sizes of the magnetite nanoparticles without and with montmorillonite support are around 25 and 15 nm, respectively. Adsorption potential of montmorillonite-supported magnetite nanoparticles was significantly higher per unit mass of magnetite (15.3 mg g⁻¹) than that of unsupported magnetite (10.6 mg g⁻¹) for heavy metal [100]. Similarly, bentonite-supported nanoscale zerovalent iron (B-nZVI) was prepared using liquid-phase reduction. Electroplating wastewater was treated with B-nZVI which exhibited higher potential to remove Cr, Pb, and Cu > 90% [20].

Nanoscale zerovalent iron- (nZVI-) multiwalled carbon nanotube (MWCNT) nanocomposites were applied to reduce Cr(VI) from wastewater. These were synthesized by embedding nZVI particles onto MWCNTs by in situ reduction of ferrous sulfate. The nZVI-MWCNT nanocomposites revealed around 36% higher reduction potential for Cr(VI) removal than that of bare nZVI or nZVI-activated carbon composites. Rate of removal of Cr(VI) increased at low pH and initial Cr(VI) concentration. Anions, such as (SO₄)²⁻, NO₃⁻, and HCO₃⁻, exerted negative impacts on the removal of Cr(VI), while the influence of PO₄³⁻ and SiO₃²⁻ was not significant [101].

Li et al. developed silica fume-supported Fe(0) nanoparticles (SF-Fe(0)) that were prepared using commercial silica fume as a support [102]. The feasibility of using this SF-Fe(0) immobilized the Cr(VI) by adsorption on its surface following the reduction of Cr(VI) to Cr(III). The rate of reduction of Cr(VI) could be explained by pseudofirst-order reaction kinetics.

Surface engineered magnetic nanoparticles Fe₃O₄ were produced by facile soft-chemical approaches. Nanoadsorbents were functionalized with carboxyl (succinic acid), amine (ethylenediamine), and thiol (2,3-dimercaptosuccinic acid). It has been suggested that nanoparticles formed in carboxyl, thiol, and amine functionalized Fe₃O₄ have average sizes of about 10, 6, and ~40 nm, respectively. Rate of removal for heavy metals (Cr³⁺, Co²⁺, Ni²⁺, Cu²⁺, Cd²⁺, Pb²⁺, and As³⁺) and bacterial pathogens (*Escherichia coli*) from water was highly efficient. Mechanism of removal of heavy metals involves the formation of chelate complexes or ion exchange process or electrostatic interaction depending upon the surface functionality (COOH, NH₂, or SH) of magnetic nanoadsorbents [94].

It was explored by Wei et al. that magnetically iron-nickel oxide has great power for selective adsorption of Cr(VI) from the wastewater having Cr(VI)-Ni (II) [103]. The maximum adsorption capacity of Cr(VI) is about 30 mg g⁻¹ at pH 5.00 ± 0.02, and it was negatively correlated with total dissolved substance (TDS). Magnetic iron oxide nanoparticles were synthesized by a coprecipitation method followed by modification with 3-aminopropyl triethoxysilane (APTES) and acryloyl chloride (AC) subsequently. Then, the surface of modified nanoparticles was amended by graft polymerization with acrylic acid. The grafted magnetite nanoparticles exhibited great potential to capture heavy metal cations such as Cd²⁺, Pb²⁺, Ni²⁺, and Cu²⁺. Their size was in range of 10 to 23 nm. Adsorption capacity was reported to be 57.1 emu g⁻¹ [104]. Nanoscale δ-MnO₂ particles were embedded on the surfaces of GNS. It was found that GNS/MnO₂ have efficient capturing potential for Ni (II) from solution and it is 46.6 mg g⁻¹ at room temperature, which is 1.5 and 15 times higher than those of pure δ-MnO₂ and GNS, respectively [105].

Wastewaters often contain organics and heavy metals. Several experiments have been conducted to remove organic contaminants and heavy metals simultaneously using iron-based NMs stabilized on a surface. Currently, Long et al.

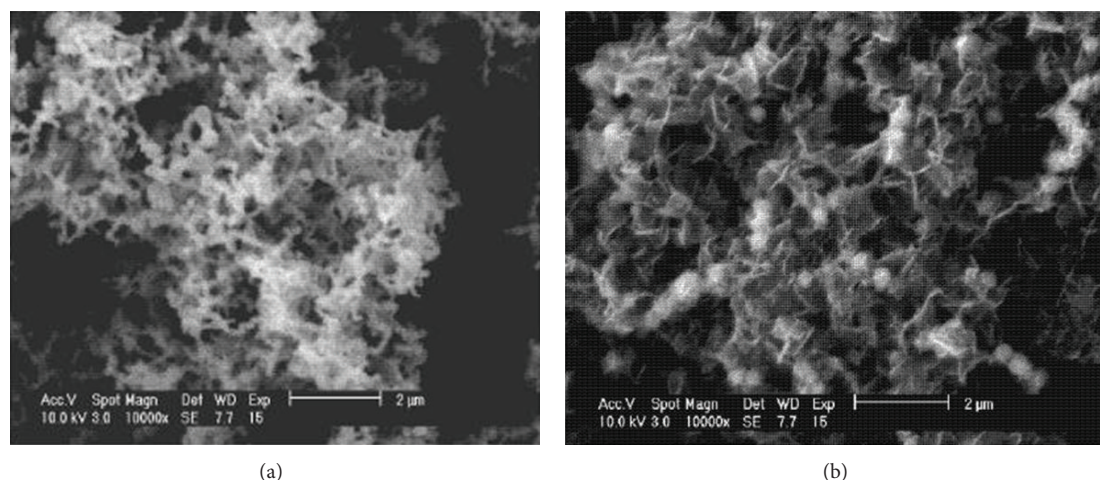


FIGURE 13: ESEM images of (a) alone Fe^0 nanoparticles and (b) starch stabilizer Fe^0 nanoparticles.

TABLE 2: Bio-nanocatalysts to remove heavy metals and organic contaminants.

Bionanocatalysts	Organic compounds	Heavy metals	Initial concentration of bionanocatalysts (ppm/mg L ⁻¹)	Initial concentration of heavy metals (mg L ⁻¹)	Maximum reduction (%)		Time for maximum reduction (min/h)		References
					O.C.	Heavy metals	O.C.	Heavy metals	
[Bio-Pd(0) NMs] Pd(0) precipitated on <i>C. pasteurianum</i>	Methyl orange (MO)	—	10 ppm	—	100%	—	7 min	—	[29]
Pd(0) precipitated on <i>C. pasteurianum</i>	Evan's blue (EB)	—	5 ppm	—	100%	—	7 min	—	[29]
Bio-Pd(0) NMs	PCBs	—	50 mg L ⁻¹	—	27%	—	—	—	[92]
<i>P. aeruginosa</i> immobilized (Fe^0)	—	Cr(VI)	—	—	—	72.97%	—	—	[95]
<i>P. aeruginosa</i> immobilized (Fe^0)	—	Cd(II)	—	—	—	87.63%	—	—	[92]
<i>S. cerevisiae</i> immobilized on chitosan-coated magnetic nanoparticles	—	Cu(II)	—	60 mg L ⁻¹	—	96.8%	—	1 h	[95]
<i>P. aeruginosa</i> immobilized on multiwalled carbon nanotubes	—	Cr(VI)	—	80 mg L ⁻¹	—	50%	—	84 h	[95]

synthesized chitosan-stabilized bimetallic Fe/Ni nanoparticles (CS-Fe/Ni) which efficiently reduced the amoxicillin by 68.9% and adsorbed Cd(II) by 81.3% from a cocontaminated water [83], whereas separate reduction and adsorption rate for amoxicillin and Cd(II) were 93.0% and 90.9%, respectively, within 60 minutes. In this way, this remediation technique involves the reduction chemically and adsorption (Table 3).

3.2.3. Simultaneous Removal by Nanophotocatalysis. In this synergistic system, N-F-codoped TiO_2 was used as a photocatalyst under visible light with enhanced photo efficiency to reduce Cr(VI) and benzoic acid (BA). Ratio of Cr/BA

and concentration of N-F-codoped TiO_2 and pH were the selected variables, which effected significantly the removal of Cr(VI) and BA. Maximum degradation of Cr(VI) and BA was achieved at pH = 4, ratio Cr/BA = 5, and N-F-codoped TiO_2 = 600 mg L⁻¹. Reduction of Cr(VI) was suppressed as pH level increased, because of the anionic-type adsorption on TiO_2 and its acid-catalyzed photocatalytic reduction and the same trend was followed by BA. Figures 14 and 15 represent that, in binary system, no degradation was observed in the presence of only N-F-codoped TiO_2 after incubation for 240 min, whereas, in case of direct photolysis only, reduction of Cr(VI) and BA occurred at very slow rate. On the other hand, in single system, photocatalytic treatment completely reduced

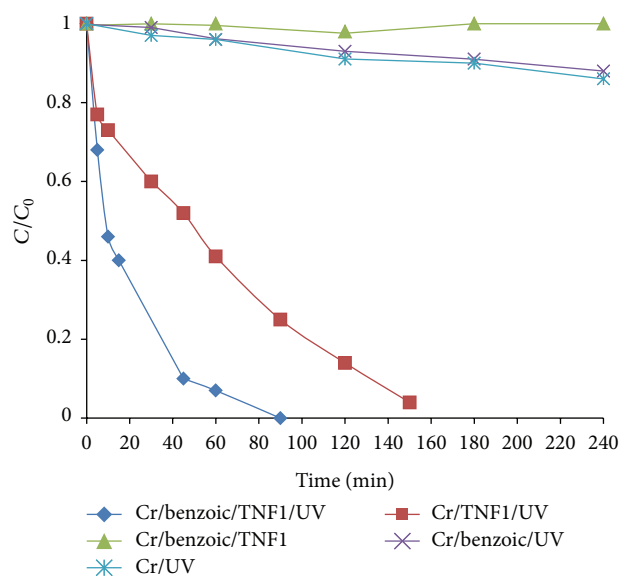


FIGURE 14: Photocatalytic reduction of Cr(VI) in single and binary system.

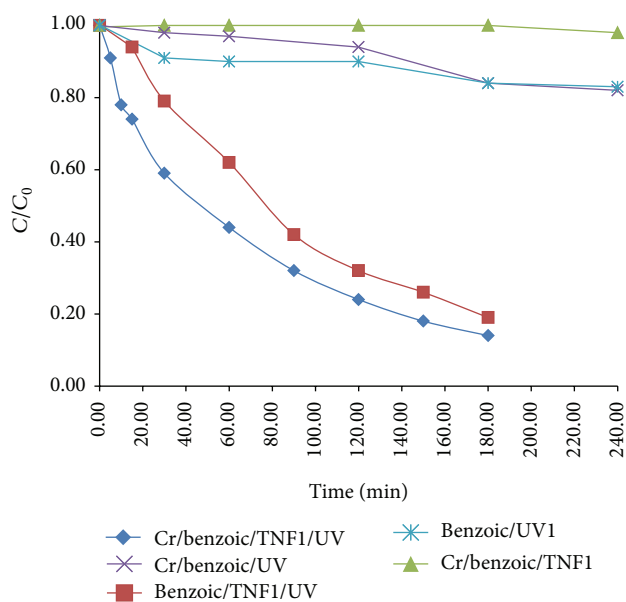


FIGURE 15: Photocatalytic reduction of benzoic acid (BA) in single and binary system.

Cr(VI) and BA after 150 and 240 min, respectively, while in binary system photocatalytic reduction of Cr(VI) and BA significantly boosted the oxidation/reduction of substrate and complete reduction of Cr(VI) maximum reduction of BA was achieved after incubation for 90 and 180 min, respectively. Mechanism for enhanced degradation includes the coupled oxidation of the BA that consumes photogenerated holes and/or $\cdot\text{OH}$ radicals efficiently, blocking the electron-hole recombination and, thus, increasing the total efficiency [38].

Moreover, the efficiency of (EDAS/TiO₂-Au) (nps) nanocomposite materials for photocatalytic oxidation and

reduction was assessed by applying them on Cr(VI) and methylene blue (MB) dye under irradiation. Deposition of Au nanoparticles on TiO₂ nanoparticles and then its spreading over silicate sol-gel film (EDAS/(TiO₂-Au)) (nps) enhanced the photocatalytic reduction for Cr(VI) and oxidation of MB. Mechanism involves the most active interfacial electron transfer from the conduction band of the TiO₂ to Au (nps) by minimizing the charge recombination process when compared to the TiO₂ and (TiO₂-Au) (nps) in the absence of EDAS [106].

Similarly, Doong et al. prepared metal-deposited Degussa P25 TiO₂ nanoparticles. Copper and silver ions were embedded on TiO₂ to accelerate photocatalytic degradation of methylene blue (MB) [107]. It was found that presence of formate stimulated the photocatalytic reduction of heavy metal ions by dropping its oxidation number and resulting in fast rate of photoreduction. In case of Degussa P25 TiO₂ nanoparticles, rate constant (k (obs)) for MB photodegradation was found to be $3.94 \times 10^{-2} \text{ min}^{-1}$, whereas rate constant (k (obs)) increased by 1.4–1.7 times when metal-deposited Degussa P25 TiO₂ nanoparticles were applied. Concentration of heavy metal ions was also a factor which prompted the photodegradation of MB. Therefore, the rate constant reached up to $4.64\text{--}7.28 \times 10^{-2} \text{ min}^{-1}$ for Ag/TiO₂ and to $5.14\text{--}7.61 \times 10^{-2} \text{ min}^{-1}$ for Cu/TiO₂. Furthermore, the electrons released from TiO₂ may contribute to reducing heavy metal ions and MB simultaneously.

Simultaneous degradation of Cr(VI) and di-n-butyl phthalate (DBP) by UV/TiO₂ treatment was carried out by Xu et al. [65]. Concentration of Cr(VI) and DBP was significantly reduced and Cr(VI) exerted positive effect on DBP degradation and vice versa.

Similarly, simultaneous photocatalytic reduction/oxidation of Cr/salicylic acid was reported by Wang and Lo [108]. Both Cr(VI) and salicylic acid were successively reduced. It was investigated that when photocatalytic reduction of Cr(VI) was carried out for long time, it resulted in deposition of Cr(III) on the surface of TiO₂ particles, which in turn deactivated the photocatalyst. However, this problem was overcome by oxidation of salicylic acid at the same time.

Peng et al. synthesized the polymer-sensitized TiO₂ for efficient reduction of Cr(VI) and oxidation of phenol simultaneously [109]. Poly(fluorene-co-thiophene) (PFT) showed the ability to reduce Cr(VI). When PFT was joined with TiO₂, not only it increased electron donor efficiency of PFT, but also it started to act as a sensitizer. This catalytic reduction of Cr(VI) was enhanced by the phenol existence. It was investigated by Tabassum et al. that the ultraviolet- (UVA-) induced photocatalytic application reduced the azo dye acid orange 20 (AO20) and Cr(VI) simultaneously [110]. The complete reduction was obtained after 120 min or 240 min at 500 or 250 mg l⁻¹ concentration of catalyst UV-induced TiO₂ at neutral pH. The synergistic effect of TiO₂ under visible light ($\lambda > 420 \text{ nm}$) to reduce the azo dye acid orange 7 (AO7) and Cr(VI), simultaneously, was extraordinary. Presence of metal ions enhanced the degradation rate of AO7. Similarly AO7 participated in increasing reduction rate of Cr(VI) [111].

A novel metal-semiconductor heterojunction with a tube-in-tube structure was synthesized by Luo et al. [112].

TABLE 3: Removal of heavy metals by surface stabilized nanomaterials (NMs).

Stabilized nanomaterials (NMs)	Heavy metals	Maximum removal %/mg L ⁻¹ /emu g ⁻¹	References
Starch stabilizer Fe ⁰ nanoparticles	Cr(VI)	—	[97]
Mesoporous gamma-Fe ₂ O ₃ nanoparticles	Cr(VI)	—	[99]
Montmorillonite-supported magnetite nanoparticles	—	—	[100]
Bentonite-supported nanoscale zerovalent iron (B-nZVI)	Cr(VI), Pb(II), and Cu(II)	>90%	[28]
Nanoscale zerovalent iron (nZVI)-multiwalled carbon nanotube (MWCNT)	Cr(VI)	—	[101]
Silica fume supported-Fe(0) nanoparticles (SF-Fe(0))	Cr(VI)	—	[102]
Surface engineered Fe ₃ O ₄	Cr(III), Co(II), and Ni(II)	—	[115]
Magnetically iron-nickel oxide	Cr(VI)	30 mg L ⁻¹	[103]
Iron oxide nanoparticles modified with 3-aminopropyltriethoxysilane (APTES) and acryloyl chloride (AC)	Ni(II), Cr(VI), Pb(II), and Cu(II)	57.1 emu g ⁻¹	[104]
Nanoscale δ-MnO ₂ embedded on graphene nanosheet	Ni(II)	46.6 mg L ⁻¹	[105]
Chitosan stabilized bimetallic Fe/Ni nanoparticles (CS-Fe/Ni)	Cd(II)	90.9%	[83]

TABLE 4: Simultaneous removal of heavy metals and organic contaminants by nanophotocatalysts.

Synergistic system	Organic contaminants	Heavy metals	Maximum removal (%)		Removal method		Time for maximum removal (min)		References
			O.C.	Heavy metals	O.C.	Heavy metals	O.C.	Heavy metals	
N-F-codoped TiO ₂ + visible light	Benzoic acid (BA)	Cr(VI)	Around 98%	100%	Oxidation	Reduction	90 min	180 min	[38]
EDAS/(TiO ₂ -Au) nps + radiations	Methylene blue (MB)	Cr(VI)	—	—	Oxidation	Reduction	—	—	[106]
Metal-deposited Degussa (P25 TiO ₂) nps + radiations	Methylene blue (MB)	Cr(VI)	—	—	Reduction	Reduction	—	—	[107]
UV/TiO ₂	Di-n-butyl phthalate (DBP)	Cr(VI)	—	—	—	Reduction	—	—	[65]
UV/TiO ₂	Salicylic acid	Cr(VI)	—	—	Oxidation	Reduction	—	—	[108]
Polymer-sensitized TiO ₂ + irradiations	Phenol	Cr(VI)	—	—	Oxidation	Reduction	—	—	[20]
UV-induced TiO ₂	Acid orange 20 (AO20)	Cr(VI)	100%	100%	Reduction	Reduction	120 min	120 min	[110]
UV/TiO ₂	Acid orange 7 (AO7)	Cr(VI)	100%	100%	Reduction	Reduction	—	—	[111]
Gold nanotubes embedded in pores of TiO ₂ nanotubes + radiations	Acid orange 7 (AO7)	Cr(VI)	—	—	Oxidation	Reduction	—	—	[112]

Gold nanotubes comprised of compressed and minute Au particles were deposited in the pores of anodic TiO₂ nanotube arrays by a simple pulse electrodeposition technique. An electric potential difference created at the interface of Au/TiO₂ heterojunction assisted the availability of photodegraded hole-electron, which in turn enhanced the photocatalytic activity. In binary system, Cr(VI) and AO7 reduced very rapidly because of synergistic effect of Cr(VI)-AO7 as well.

3.3. Simultaneous Biodegradation. Biological treatment is usually considered as an effective method and can significantly reduce the quantity of heavy metals in aqueous solutions. Few microbial strains have been isolated to reduce the organic contaminants and adsorption of heavy metals at the same time when cocultured. The most effective fungal strain *Phanerochaete chrysosporium* has been isolated by Chen et al. which can degrade the 2,4-dichlorophenol and adsorb the cadmium simultaneously in a cocontaminated wastewater [74]. Highest removal (%) was obtained at pH 6.5 of initial Cd(II) and 2,4-dichlorophenol doses

TABLE 5: Simultaneous biodegradation of organic contaminants and heavy metals.

Microbial strains	Organic contaminants	Heavy metals	Initial level (mg l ⁻¹) O.C.	Heavy metals	% removal O.C.	Heavy metals	Time for maximum removal	pH	Temperature °C	Removal method (O.C./heavy metals)	References
<i>P. chrysosporium</i>	2,4-dichlorophenol	Cd(II)	20 mg l ⁻¹	5 mg l ⁻¹	83.90%	63.62%		6.5		Sorption/reduction	[64]
<i>P. putida</i> DMP-1 and <i>E. coli</i> ATCC 33456	Phenol	Cr(VI)								Reduction/reduction	[113]
<i>P. putida</i> DMP-1 and <i>E. coli</i> ATCC 33456 (Fixed film bio-reactor)	Phenol	Cr(VI)	840–3350 mg l ⁻¹	5–21 mg l ⁻¹	Almost 100%	Almost 100%				Reduction/reduction	[114]
<i>P. aeruginosa</i> CCTCC AB91095	Phenol	Cr(VI)	100 mg l ⁻¹	20 mg l ⁻¹	100%	100%	24/12 h (inocula 5% v/v)			Reduction/reduction	[27]
<i>B. casei</i>	Acid orange 7 (AO7)	Cr(VI)			40.7%	83.4%		7	35 °C	Reduction/reduction	[16]
<i>P. putida</i> KI and <i>S. proteamaculans</i> SL14	Reactive black-5 (RB5)	Cr(VI)			100%	93%	24/12 h (individually)	7.2	35 °C	Reduction/reduction	[23]

(5 and 20 mg L⁻¹), respectively. The reduction and sorption limit for 2,4-dichlorophenol and Cd(II) were 83.90% and 63.62%, respectively. Furthermore, degradation of 2,4-dichlorophenol was indicated by production of lignin peroxidase and manganese peroxidase in surplus amount (i.e., 7.35 U mL⁻¹ and 8.30 U mL⁻¹, resp.). However, production of protein was suppressed as the Cd(II) level increased.

In another experiment, cocontaminated wastewater was treated by combining two bacterial strains *Pseudomonas putida* DMP-1 and *Escherichia coli* ATCC 33456. These two bacterial strains rapidly reduced the Cr(VI) and phenol simultaneously. Reduction of Cr(VI) occurred by metabolism of *E. coli*. At small population size of *E. coli*, phenol degradation negatively affected the Cr(VI) degradation. Phenol degradation by *P. putida* was highly sensitive to Cr(VI) even at its low concentration, whereas phenol exerted inhibitory effect on Cr(VI) reduction only when phenol concentration was >9 Mm [113]. Similarly, Nkhalambayausi-Chirwa and Wang explored in an experiment that Cr(VI) and phenol can be reduced simultaneously by two bacterial strains *Escherichia coli* ATCC 33456 and *Pseudomonas putida* DMP-1, respectively, in a fixed-film bioreactor [114]. Almost 100% reduction of Cr(VI) and phenol degradation were achieved at initial concentrations (5–21 mg L⁻¹) of Cr(VI) and (840–3350 mg L⁻¹) phenol. Metabolites of phenol detected were 1, 2-hydroxymuconic semialdehyde (2HMSA), succinate, and acetate which contributed to increasing TOC by 13–23% in the treated wastewater.

By the development in biodegradation technology, remediation of Cr(VI) and organic contaminant simultaneously from wastewater and soil can be achieved by application of single microbial strain. Recently, simultaneous reduction of Cr(VI) and phenol has been carried out by application of only single strain for both contaminants. Song et al. isolated a fungal strain *Pseudomonas aeruginosa* CCTCC AB91095 [27]. Phenol served as a source of carbon and in turn energy produced was utilized for Cr(VI) reduction. Reduction of Cr(VI) and degradation of phenol was negatively influenced when Cr(VI) concentration was >20 mg L⁻¹ or phenol concentration was <100 mg L⁻¹. Nearly 100% reduction of Cr(VI) and phenol occurred after 24 hrs. The most effective concentration of inocula was 5% (v/v), at which Cr(VI) and phenol were abruptly suppressed from 20 and 100 to 3.36 and 29.51 mg L⁻¹ after 12 h.

Chromate Cr(VI) and azo dyes are common pollutants which may coexist in some industrial effluents. Therefore, few bacterial strains have been isolated which can reduce Cr(VI) and decolorize the azo dye simultaneously. A bacterial strain *Brevibacterium casei* was isolated from sewage sludge of a dyeing factory. Reduction of Cr(VI) and decolorization of azo dye acid orange 7 (AO7) simultaneously by application of *B. casei* were under nutrient-limiting condition, at pH 7 and 35°C. Chromate Cr(VI) and AO7 reduced by 83.4 ± 0.6 and 40.7 ± 1.7%, respectively. The mechanism of reduction involves that AO7 reduced by reduction enzyme(s) released from *B. casei* and AO7 served as an electron donor to reduce

Cr(VI) to Cr(III). In turn, Cr(III) formed a complex with oxidized AO7 and purple color appeared [16].

Currently, two potential bacterial strains *Pseudomonas putida* KI and *Serratia proteamaculans* SL14 were isolated from wastewater and sludge of tannery industry, capable of simultaneous reduction of Cr(VI) and decolorization of azo dye reactive black-5 (RB5). Maximum reduction of Cr(VI) and RB5 obtained was 93% and 100% after incubation for 24 h at pH 7.2 and 35°C. Individually, removal of Cr(VI) and RB5 was 100% after 12 h incubation (Table 5) [23].

4. Conclusions

Azo dyes and Cr(VI) most often coexist in industrial wastewater. These contaminants enter the environment when released through wastewater and exert many carcinogenic and mutagenic effects on plants, animals, and human health. Therefore, treatment of wastewater and its reuse is a practice related not only to a number of benefits with regard to eater balance and management but also to a number of question marks. Immediate research must be launched towards the direction so as to protect human health and environmental ecosystem. Microorganism (bacteria, fungi) are the potential source to remove these contaminants from soil and wastewater because they are cost effective and environmental friendly and remediate contaminants at faster rate. However, their immobilization can accelerate this treatment more efficiently. In this regard, surface modified nanomaterial and biochar have achieved much attention to remove heavy metals and azo dyes simultaneously. As illustrated in this review, a range of nanomicrobiological techniques have been proposed or are under active development for treatment of polluted soil and wastewater, but many techniques are still at experimental or pilot stage. In conclusion, there is much recent interest in the use of engineered nanomaterial combined with biotechnology as in in situ. In general, the attention in this field is not enough and additional studies should be conducted to increase the knowledge in this field. In addition, health impacts and environmental fate of these nanomaterials need to be addressed before their widespread application.

Conflict of Interests

The authors declare that there is no conflict of interests regarding the publication of this paper.

Acknowledgment

This research is supported by High Impact Research MoE Grant UM.C/625/1/HIR/MoE/SC/04 from the Ministry of Education Malaysia. Thanks also for the support by UMRG (RG257-13AFR) and FRGS (FP038-2013B).

References

- [1] A. Stolz, "Basic and applied aspects in the microbial degradation of azo dyes," *Applied Microbiology and Biotechnology*, vol. 56, no. 1-2, pp. 69–80, 2001.

- [2] A. Pandey, P. Singh, and L. Iyengar, "Bacterial decolorization and degradation of azo dyes," *International Biodeterioration and Biodegradation*, vol. 59, no. 2, pp. 73–84, 2007.
- [3] H. Leub, *Industrial Dyes, Chemistry, Properties and Applications*, Wiley VCH, Weinheim, Germany, 2003.
- [4] A. A. Pourbabae, F. Malekzadeh, M. N. Sarbolouki, and F. Najafi, "Aerobic decolorization and detoxification of a disperse dye in textile effluent by a new isolate of *Bacillus* sp.," *Biotechnology and Bioengineering*, vol. 93, no. 4, pp. 631–635, 2006.
- [5] C. I. Pearce, J. R. Lloyd, and J. T. Guthrie, "The removal of colour from textile wastewater using whole bacterial cells: a review," *Dyes and Pigments*, vol. 58, no. 3, pp. 179–196, 2003.
- [6] G. Bayramoğlu, G. Çelik, and M. Y. Arica, "Biosorption of reactive blue 4 dye by native and treated fungus batch and continuous flow system studies," *Journal of Hazardous Materials*, vol. 137, no. 3, pp. 1689–1697, 2006.
- [7] F. O. Topaç, E. Dindar, S. Uçaroglu, and H. S. Başkaya, "Effect of a sulfonated azo dye and sulfanilic acid on nitrogen transformation processes in soil," *Journal of Hazardous Materials*, vol. 170, no. 2–3, pp. 1006–1013, 2009.
- [8] D. T. Sponza, "Necessity of toxicity assessment in Turkish industrial discharges," *Environmental Monitoring and Assessment*, vol. 73, no. 1, pp. 41–66, 2002.
- [9] S. Asad, M. A. Amoozegar, A. A. Pourbabae, M. N. Sarbolouki, and S. M. M. Dastgheib, "Decolorization of textile azo dyes by newly isolated halophilic and halotolerant bacteria," *Bioresource Technology*, vol. 98, no. 11, pp. 2082–2088, 2007.
- [10] H. Moawad, W. M. Abd El-Rahim, and M. Khalafallah, "Evaluation of biotoxicity of textile dyes using two bioassays," *Journal of Basic Microbiology*, vol. 43, no. 3, pp. 218–229, 2003.
- [11] E. Bååth, "Thymidine incorporation into macromolecules of bacteria extracted from soil by homogenization-centrifugation," *Soil Biology and Biochemistry*, vol. 24, no. 11, pp. 1157–1165, 1992.
- [12] J. L. Bader, G. Gonzalez, P. C. Goodell, A. S. Ali, and S. D. Pillai, "Chromium-resistant bacterial populations from a site heavily contaminated with hexavalent chromium," *Water, Air, and Soil Pollution*, vol. 109, no. 1–4, pp. 263–276, 1999.
- [13] E. Bååth, "Growth rates of bacterial communities in soils at varying pH: a comparison of the thymidine and leucine incorporation techniques," *Microbial Ecology*, vol. 36, no. 3, pp. 316–327, 1998.
- [14] C. Desai, R. Y. Parikh, T. Vaishnav, Y. S. Shouche, and D. Madamwar, "Tracking the influence of long-term chromium pollution on soil bacterial community structures by comparative analyses of 16S rRNA gene phylogenies," *Research in Microbiology*, vol. 160, no. 1, pp. 1–9, 2009.
- [15] G. Dönmez and N. Koçberber, "Isolation of hexavalent chromium resistant bacteria from industrial saline effluents and their ability of bioaccumulation," *Enzyme and Microbial Technology*, vol. 36, no. 5–6, pp. 700–705, 2005.
- [16] E. K. Nyer, *Treatment Methods for Inorganic Compounds, Ground Water Treatment Technology*, Van Nostrand Reinhold, New York, NY, USA, 3rd edition, 1992.
- [17] C. Cervantes and S. Silver, "Plasmid chromate resistance and chromate reduction," *Plasmid*, vol. 27, no. 1, pp. 65–71, 1992.
- [18] X. Weng, S. Lin, Y. Zhong, and Z. Chen, "Chitosan stabilized bimetallic Fe/Ni nanoparticles used to remove mixed contaminants-amoxicillin and Cd (II) from aqueous solutions," *Bioresource Technology*, vol. 102, no. 22, pp. 10733–10736, 2011.
- [19] W. Delee, C. O. Neili, and F. R. Hawks, "Anaerobic treatment of textile effluents a review," *Journal of Chemical Technology and Biotechnology*, vol. 73, no. 4, pp. 323–335, 1998.
- [20] L.-N. Shi, X. Zhang, and Z.-L. Chen, "Removal of Chromium (VI) from wastewater using bentonite-supported nanoscale zero-valent iron," *Water Research*, vol. 45, no. 2, pp. 886–892, 2011.
- [21] D. Çetin, S. Dönmez, and G. Dönmez, "The treatment of textile wastewater including chromium(VI) and reactive dye by sulfate-reducing bacterial enrichment," *Journal of Environmental Management*, vol. 88, no. 1, pp. 76–82, 2008.
- [22] A. Khalid, M. Arshad, and D. E. Crowley, "Biodegradation potential of pure and mixed bacterial cultures for removal of 4-nitroaniline from textile dye wastewater," *Water Research*, vol. 43, no. 4, pp. 1110–1116, 2009.
- [23] S. Mahmood, A. Khalid, T. Mahmood, M. Arshad, and R. Ahmad, "Potential of newly isolated bacterial strains for simultaneous removal of hexavalent chromium and reactive black-5 azo dye from tannery," *Journal of Chemical Technology and Biotechnology*, vol. 88, no. 8, pp. 1506–1513, 2013.
- [24] M. N. Moore, "Do nanoparticles present ecotoxicological risks for the health of the aquatic environment?" *Environment International*, vol. 32, no. 8, pp. 967–976, 2006.
- [25] J. Lehmann and S. Joseph, *Biochar for Environmental Management: Science and Technology*, Earthscan, London, UK, 2009.
- [26] J. Lehmann, "A handful of carbon," *Nature*, vol. 447, no. 7141, pp. 143–144, 2007.
- [27] H. Song, Y. Liu, W. Xu et al., "Simultaneous Cr(VI) reduction and phenol degradation in pure cultures of *Pseudomonas aeruginosa* CCTCC AB91095," *Bioresource Technology*, vol. 100, no. 21, pp. 5079–5084, 2009.
- [28] W. Shi, M. Bischoff, R. Turco, and A. Konopka, "Long-term effects of chromium and lead upon the activity of soil microbial communities," *Applied Soil Ecology*, vol. 21, no. 2, pp. 169–177, 2002.
- [29] A. Johnson, G. Merilis, J. Hastings, M. E. Palmer, J. P. Fitts, and D. Chidambaram, "Reductive degradation of organic compounds using microbial nanotechnology," *Journal of the Electrochemical Society*, vol. 160, no. 1, pp. 0013–4651, 2013.
- [30] D. Chidambaram, T. Hennebel, S. Taghavi et al., "Concomitant microbial generation of palladium nanoparticles and hydrogen to immobilize chromate," *Environmental Science and Technology*, vol. 44, no. 19, pp. 7635–7640, 2010.
- [31] J. Fan, Y. Guo, J. Wang, and M. Fan, "Rapid decolorization of azo dye methyl orange in aqueous solution by nanoscale zerovalent iron particles," *Journal of Hazardous Materials*, vol. 166, no. 2–3, pp. 904–910, 2009.
- [32] M. Otto, M. Floyd, and S. Bajpai, "Nanotechnology for site remediation," *Journal of Remediation*, vol. 19, no. 1, pp. 99–108, 2008.
- [33] K. Z. Elwakeel, "Removal of Reactive Black 5 from aqueous solutions using magnetic chitosan resins," *Journal of Hazardous Materials*, vol. 167, no. 1–3, pp. 383–392, 2009.
- [34] M. Greluk and Z. Hubicki, "Kinetics, isotherm and thermodynamic studies of reactive black 5 removal by acid acrylic resins," *Chemical Engineering Journal*, vol. 162, no. 3, pp. 919–926, 2010.
- [35] Z. Aksu and G. Dönmez, "Combined effects of molasses sucrose and reactive dye on the growth and dye bioaccumulation properties of *Candida tropicalis*," *Process Biochemistry*, vol. 40, no. 7, pp. 2443–2454, 2005.

- [36] K. Vijayaraghavan and Y.-S. Yun, "Biosorption of C.I. Reactive Black 5 from aqueous solution using acid-treated biomass of brown seaweed *Laminaria* sp.," *Dyes and Pigments*, vol. 76, no. 3, pp. 726–732, 2008.
- [37] F. Y. Wang, H. Wang, and J. W. Ma, "Adsorption of cadmium (II) ions from aqueous solution by a new low-cost adsorbent-Bamboo charcoal," *Journal of Hazardous Materials*, vol. 177, no. 1–3, pp. 300–306, 2010.
- [38] M. Antonopoulou, A. Giannakas, and I. Konstantinou, "Simultaneous photocatalytic reduction of Cr(VI) and oxidation of benzoic acid in aqueous N-F-Codoped TiO₂ suspension: optimization and modeling using the response surface methodology," *International Journal of Photoenergy*, vol. 2012, Article ID 520123, 10 pages, 2012.
- [39] R. Sanghi, A. Dixit, and S. Guha, "Sequential batch culture studies for the decolorisation of reactive dye by *Coriolus versicolor*," *Bioresource Technology*, vol. 97, no. 3, pp. 396–400, 2006.
- [40] N. Daneshvar, M. Ayazloo, A. R. Khataee, and M. Pourhassan, "Biological decolorization of dye solution containing Malachite Green by microalgae *Cosmarium* sp.," *Bioresource Technology*, vol. 98, no. 6, pp. 1176–1182, 2007.
- [41] E. Acuner and F. B. Dilek, "Treatment of tectilon yellow 2G by *Chlorella vulgaris*," *Process Biochemistry*, vol. 39, no. 5, pp. 623–631, 2004.
- [42] L. Ai, C. Zhang, and Z. Chen, "Removal of methylene blue from aqueous solution by a solvothermal-synthesized graphene/magnetite composite," *Journal of Hazardous Materials*, vol. 192, no. 3, pp. 1515–1524, 2011.
- [43] E. Forgacs, T. Cserháti, and G. Oros, "Removal of synthetic dyes from wastewaters: a review," *Environment International*, vol. 30, no. 7, pp. 953–971, 2004.
- [44] S. Erdal and M. Taskin, "Uptake of textile dye reactive black-5 by *Penicillium chrysogenum* MT-6 isolated from cement-contaminated soil," *African Journal of Microbiology Research*, vol. 4, no. 8, pp. 618–625, 2010.
- [45] H. Wang, X.-W. Zheng, J.-Q. Su, Y. Tian, X.-J. Xiong, and T.-L. Zheng, "Biological decolorization of the reactive dyes Reactive Black 5 by a novel isolated bacterial strain *Enterobacter* sp. EC3," *Journal of Hazardous Materials*, vol. 171, no. 1–3, pp. 654–659, 2009.
- [46] Z. Aksu, "Application of biosorption for the removal of organic pollutants: a review," *Process Biochemistry*, vol. 40, no. 3–4, pp. 997–1026, 2005.
- [47] P. K. Malik, "Dye removal from wastewater using activated carbon developed from sawdust: adsorption equilibrium and kinetics," *Journal of Hazardous Materials*, vol. 113, no. 1–3, pp. 81–88, 2004.
- [48] M. N. V. Prasad and H. M. De Oliveira Freitas, "Metal hyperaccumulation in plants—biodiversity prospecting for phytoremediation technology," *Electronic Journal of Biotechnology*, vol. 6, no. 3, pp. 110–146, 2003.
- [49] M. A. Ashraf, M. J. Maah, and I. Yusoff, "Heavy metals accumulation in plants growing in ex tin mining catchment," *International Journal of Environmental Science and Technology*, vol. 8, no. 2, pp. 401–416, 2011.
- [50] J. E. Tomaszewski, D. Werner, and R. G. Luthy, "Activated carbon amendment as a treatment for residual DDT in sediment from a superfund site in San Francisco Bay, Richmond, California, USA," *Environmental Toxicology and Chemistry*, vol. 26, no. 10, pp. 2143–2150, 2007.
- [51] D. Woolf, J. E. Amonette, F. A. Street-Perrott, J. Lehmann, and S. Joseph, "Sustainable biochar to mitigate global climate change," *Nature Communications*, vol. 1, no. 5, 2010.
- [52] D. D. Warnock, J. Lehmann, T. W. Kuyper, and M. C. Rillig, "Mycorrhizal responses to biochar in soil—concepts and mechanisms," *Plant and Soil*, vol. 300, no. 1–2, pp. 9–20, 2007.
- [53] J. Major, C. Steiner, and A. Downie, "Biochar effects on nutrient leaching," in *Biochar for Environmental Management: Science and Technology*, Earthscan, London, UK, 3rd edition, 2009.
- [54] J. M. Novak, W. J. Busscher, D. L. Laird, M. Ahmedna, D. W. Watts, and M. A. S. Niandou, "Impact of biochar amendment on fertility of a southeastern coastal plain soil," *Soil Science*, vol. 174, no. 2, pp. 105–112, 2009.
- [55] X.-Y. Yu, G.-G. Ying, and R. S. Kookana, "Reduced plant uptake of pesticides with biochar additions to soil," *Chemosphere*, vol. 76, no. 5, pp. 665–671, 2009.
- [56] Y. Yang and G. Sheng, "Enhanced pesticide sorption by soils containing particulate matter from crop residue burns," *Environmental Science and Technology*, vol. 37, no. 16, pp. 3635–3639, 2003.
- [57] B. Wen, R.-J. Li, S. Zhang et al., "Immobilization of pentachlorophenol in soil using carbonaceous material amendments," *Environmental Pollution*, vol. 157, no. 3, pp. 968–974, 2009.
- [58] X. Cao, L. Ma, Y. Liang, B. Gao, and W. Harris, "Simultaneous immobilization of lead and atrazine in contaminated soils using dairy-manure biochar," *Environmental science & technology*, vol. 45, no. 11, pp. 4884–4889, 2011.
- [59] R. J. Smernik, "Biochar and sorption of organic compounds," in *Biochar for Environmental Management: Science and Technology*, Earthscan, London, UK, 3rd edition, 2009.
- [60] Y. Yang, G. Sheng, and M. Huang, "Bioavailability of diuron in soil containing wheat-straw-derived char," *Science of the Total Environment*, vol. 354, no. 2–3, pp. 170–178, 2006.
- [61] G. Cornelissen, Ö. Gustafsson, T. D. Bucheli, M. T. O. Jonker, A. A. Koelmans, and P. C. M. Van Noort, "Extensive sorption of organic compounds to black carbon, coal, and kerogen in sediments and soils: mechanisms and consequences for distribution, bioaccumulation, and biodegradation," *Environmental Science and Technology*, vol. 39, no. 18, pp. 6881–6895, 2005.
- [62] X. Han, L. Cheng-feng Liang, T. Li, K. Wang, and H. Huang X Yang, "Simultaneous removal of cadmium and sulfamethoxazole from aqueous solution by rice straw biochar," *Journal of Zhejiang University Science B*, vol. 102, no. 19, pp. 8877–8884, 2013.
- [63] C.-T. Wang, "Photocatalytic activity of nanoparticle gold/iron oxide aerogels for azo dye degradation," *Journal of Non-Crystalline Solids*, vol. 353, no. 11–12, pp. 1126–1133, 2007.
- [64] A. Chen, G. Zeng, G. Chen et al., "Simultaneous cadmium removal and 2,4-dichlorophenol degradation from aqueous solutions by *Phanerochaete chrysosporium*," *Applied Microbiology and Biotechnology*, vol. 91, no. 3, pp. 811–821, 2011.
- [65] X. Xu, X. Cao, L. Zhao, H. Wang, H. Yu, and B. Gao, "Removal of Cu, Zn, and Cd from aqueous solutions by the dairy manure-derived biochar," *Environmental Science and Pollution Research*, pp. 1–11, 2012.
- [66] X.-R. Xu, H.-B. Li, and J.-D. Gu, "Photocatalytic reduction of hexavalent chromium and degradation of Di-N-Butyl phthalate in aqueous TiO₂ suspensions under ultraviolet light irradiation," *Environmental Technology*, vol. 28, no. 9, pp. 1055–1061, 2007.

- [67] J. C. Echeverría, M. T. Morera, C. Mazkiarán, and J. J. Garrido, "Competitive sorption of heavy metal by soils. Isotherms and fractional factorial experiments," *Environmental Pollution*, vol. 101, no. 2, pp. 275–284, 1998.
- [68] O. R. Harvey, B. E. Herbert, R. D. Rhue, and L.-J. Kuo, "Metal interactions at the biochar-water interface: energetics and structure-sorption relationships elucidated by flow adsorption microcalorimetry," *Environmental Science and Technology*, vol. 45, no. 13, pp. 5550–5556, 2011.
- [69] D. Zhang, B. Pan, H. Zhang, P. Ning, and B. Xing, "Contribution of different sulfamethoxazole species to their overall adsorption on functionalized carbon nanotubes," *Environmental Science and Technology*, vol. 44, no. 10, pp. 3806–3811, 2010.
- [70] D. Zhu and J. J. Pignatello, "Characterization of aromatic compound sorptive interactions with black carbon (charcoal) assisted by graphite as a model," *Environmental Science and Technology*, vol. 39, no. 7, pp. 2033–2041, 2005.
- [71] D. Zhu, S. Hyun, J. J. Pignatello, and L. S. Lee, "Evidence for π - π electron donor-acceptor interactions between π -donor aromatic compounds and π -acceptor sites in soil organic matter through pH effects on sorption," *Environmental Science and Technology*, vol. 38, no. 16, pp. 4361–4368, 2004.
- [72] R. J. E. Martins, R. Pardo, and R. A. R. Boaventura, "Cadmium(II) and zinc(II) adsorption by the aquatic moss *Fontinalis antipyretica*: effect of temperature, pH and water hardness," *Water Research*, vol. 38, no. 3, pp. 693–699, 2004.
- [73] A. Mukherjee, A. R. Zimmerman, and W. Harris, "Surface chemistry variations among a series of laboratory-produced biochars," *Geoderma*, vol. 163, no. 3–4, pp. 247–255, 2011.
- [74] X. Chen, G. Chen, L. Chen et al., "Adsorption of copper and zinc by biochars produced from pyrolysis of hardwood and corn straw in aqueous solution," *Bioresource Technology*, vol. 102, no. 19, pp. 8877–8884, 2011.
- [75] Z. Liu and E.-S. Zhang, "Removal of lead from water using biochars prepared from hydrothermal liquefaction of biomass," *Journal of Hazardous Materials*, vol. 167, no. 1–3, pp. 933–939, 2009.
- [76] R. Qiu, D. Zhang, Z. Diao et al., "Visible light induced photocatalytic reduction of Cr(VI) over polymer-sensitized TiO₂ and its synergism with phenol oxidation," *Water Research*, vol. 46, no. 7, pp. 2299–2306, 2012.
- [77] N. Wang, Y. Xu, L. Zhu, X. Shen, and H. Tang, "Reconsideration to the deactivation of TiO₂ catalyst during simultaneous photocatalytic reduction of Cr(VI) and oxidation of salicylic acid," *Journal of Photochemistry and Photobiology A: Chemistry*, vol. 201, no. 2–3, pp. 121–127, 2009.
- [78] W. Feng, D. Nansheng, and H. Helin, "Degradation mechanism of azo dye C. I. reactive red 2 by iron powder reduction and photooxidation in aqueous solutions," *Chemosphere*, vol. 41, no. 8, pp. 1233–1238, 2000.
- [79] D. Wu, B. Pan, M. Wu, H. Peng, D. Zhang, and B. Xing, "Coadsorption of Cu and sulfamethoxazole on hydroxylized and graphitized carbon nanotubes," *Science of the Total Environment*, 2012.
- [80] Y. Wan, Y. Bao, and Q. Zhou, "Simultaneous adsorption and desorption of cadmium and tetracycline on cinnamon soil," *Chemosphere*, vol. 80, no. 7, pp. 807–812, 2010.
- [81] J. Chen, D. Zhu, and C. Sun, "Effect of heavy metals on the sorption of hydrophobic organic compounds to wood charcoal," *Environmental Science and Technology*, vol. 41, no. 7, pp. 2536–2541, 2007.
- [82] W. WU, H. WANG, J. XU, and Z. XIE, "Adsorption characteristic of bensulfuron-methyl at variable added Pb²⁺ concentrations on paddy soils," *Journal of Environmental Sciences*, vol. 21, no. 8, pp. 1129–1134, 2009.
- [83] F. Long, J.-L. Gong, G.-M. Zeng et al., "Removal of phosphate from aqueous solution by magnetic Fe-Zr binary oxide," *Chemical Engineering Journal*, vol. 171, no. 2, pp. 448–455, 2011.
- [84] R. Dastjerdi and M. Montazer, "A review on the application of inorganic nano-structured materials in the modification of textiles: focus on anti-microbial properties," *Colloids and Surfaces B: Biointerfaces*, vol. 79, no. 1, pp. 5–18, 2010.
- [85] V. K. K. Upadhyayula, S. Deng, M. C. Mitchell, and G. B. Smith, "Application of carbon nanotube technology for removal of contaminants in drinking water: a review," *Science of the Total Environment*, vol. 408, no. 1, pp. 1–13, 2009.
- [86] K. Shankar, J. I. Basham, N. K. Allam et al., "Recent advances in the use of TiO₂ nanotube and nanowire arrays for oxidative photoelectrochemistry," *Journal of Physical Chemistry C*, vol. 113, no. 16, pp. 6327–6359, 2009.
- [87] B. Pan, H. Qiu, B. Pan et al., "Highly efficient removal of heavy metals by polymer-supported nanosized hydrated Fe(III) oxides: behavior and XPS study," *Water Research*, vol. 44, no. 3, pp. 815–824, 2010.
- [88] A. M. G. C. Dias, A. Hussain, A. S. Marcos, and A. C. A. Roque, "A biotechnological perspective on the application of iron oxide magnetic colloids modified with polysaccharides," *Biotechnology Advances*, vol. 29, no. 1, pp. 142–155, 2011.
- [89] A. K. Gupta and M. Gupta, "Synthesis and surface engineering of iron oxide nanoparticles for biomedical applications," *Biomaterials*, vol. 26, no. 18, pp. 3995–4021, 2005.
- [90] M. A. Ashraf, K. Mahmood, A. Wajid, A. K. Qureshi, and M. Gharibreza, "Chemical constituents of *Haloxylon salicornicum* plant from Cholistan Desert, Bahawalpur, Pakistan," *Journal of Food, Agriculture and Environment*, vol. 11, no. 3–4, pp. 1176–1182, 2013.
- [91] A. F. Abu Bakar, I. Yusoff, N. T. Fatt, F. Othman, and M. A. Ashraf, "Arsenic, zinc and aluminum removal from gold mine wastewater effluents and accumulation by submerged aquatic plants (*Cabomba piauhyensis*, *Egeria densa*, and *Hydrilla verticillata*)," *BioMed Research International*, vol. 2013, Article ID 890803, 7 pages, 2013.
- [92] B. R. White, B. T. Stackhouse, and J. A. Holcombe, "Magnetic γ -Fe₂O₃ nanoparticles coated with poly-L-cysteine for chelation of As(III), Cu(II), Cd(II), Ni(II), Pb(II) and Zn(II)," *Journal of Hazardous Materials*, vol. 161, no. 2–3, pp. 848–853, 2009.
- [93] M. A. Ashraf, I. Yusoff, I. Yusof, and Y. Alias, "Removal of Cd (II) onto *Raphanus sativus* peels biomass: equilibrium, kinetics, and thermodynamics," *Desalination and Water Treatment*, vol. 51, no. 22–24, pp. 4402–4412, 2013.
- [94] S. Singh, K. C. Barick, and D. Bahadur, "Surface engineered magnetic nanoparticles for removal of toxic metal ions and bacterial pathogens," *Journal of Hazardous Materials*, vol. 192, no. 3, pp. 1539–1547, 2011.
- [95] Y. Pang, G.-M. Zeng, L. Tang et al., "Cr(VI) reduction by *Pseudomonas aeruginosa* immobilized in a polyvinyl alcohol/sodium alginate matrix containing multi-walled carbon nanotubes," *Bioresource Technology*, vol. 102, no. 22, pp. 10733–10736, 2011.
- [96] M. A. Ashraf, M. J. Maah, A. K. Qureshi, M. Gharibreza, and I. Yusoff, "Synthetic polymer composite membrane for the desalination of saline water," *Desalination and Water Treatment*, vol. 51, no. 16–18, pp. 3650–3661, 2013.

- [97] S.-F. Niu, Y. Liu, X.-H. Xu, and Z.-H. Lou, "Removal of hexavalent chromium from aqueous solution by iron nanoparticles," *Journal of Zhejiang University: Science*, vol. 6, no. 10, pp. 1022–1027, 2005.
- [98] Y.-M. Hao, C. Man, and Z.-B. Hu, "Effective removal of Cu (II) ions from aqueous solution by amino-functionalized magnetic nanoparticles," *Journal of Hazardous Materials*, vol. 184, no. 1–3, pp. 392–399, 2010.
- [99] M. Baikousi, A. B. Bourlinos, A. Douvalis et al., "Synthesis and characterization of γ -Fe₂O₃/carbon hybrids and their application in removal of hexavalent chromium ions from aqueous solutions," *Langmuir*, vol. 28, no. 8, pp. 3918–3930, 2012.
- [100] P. Yuan, M. Fan, D. Yang et al., "Montmorillonite-supported magnetite nanoparticles for the removal of hexavalent chromium [Cr(VI)] from aqueous solutions," *Journal of Hazardous Materials*, vol. 166, no. 2–3, pp. 821–829, 2009.
- [101] X. Lv, J. Xu, G. Jiang, and X. Xu, "Removal of chromium(VI) from wastewater by nanoscale zero-valent iron particles supported on multiwalled carbon nanotubes," *Chemosphere*, vol. 85, no. 7, pp. 1204–1209, 2011.
- [102] Y. Li, Z. Jin, T. Li, and S. Li, "Removal of hexavalent chromium in soil and groundwater by supported nano zero-valent iron on silica fume," *Water Science and Technology*, vol. 63, no. 12, pp. 2781–2787, 2011.
- [103] L. Wei, G. Yang, R. Wang, and W. Ma, "Selective adsorption and separation of chromium (VI) on the magnetic iron-nickel oxide from waste nickel liquid," *Journal of Hazardous Materials*, vol. 164, no. 2–3, pp. 1159–1163, 2009.
- [104] A. R. Mahdavian and M. A.-S. Mirrahimi, "Efficient separation of heavy metal cations by anchoring polyacrylic acid on superparamagnetic magnetite nanoparticles through surface modification," *Chemical Engineering Journal*, vol. 159, no. 1–3, pp. 264–271, 2010.
- [105] I. Yusoff, Y. Alias, M. Yusof, and M. A. Ashraf, "Assessment of pollutants migration at Ampar Tenang landfill site, Selangor, Malaysia," *ScienceAsia*, vol. 39, pp. 392–409, 2013.
- [106] A. Pandikumar and R. Ramaraj, "Titanium dioxide-gold nanocomposite materials embedded in silicate sol-gel film catalyst for simultaneous photodegradation of hexavalent chromium and methylene blue," *Journal of Hazardous Materials*, vol. 203–204, pp. 244–250, 2012.
- [107] R.-A. Doong, T.-C. Hsieh, and C.-P. Huang, "Photoassisted reduction of metal ions and organic dye by titanium dioxide nanoparticles in aqueous solution under anoxic conditions," *Science of the Total Environment*, vol. 408, no. 16, pp. 3334–3341, 2010.
- [108] P. Wang and I. M. C. Lo, "Synthesis of mesoporous magnetic γ -Fe₂O₃ and its application to Cr(VI) removal from contaminated water," *Water Research*, vol. 43, no. 15, pp. 3727–3734, 2009.
- [109] Q. Peng, Y. Liu, G. Zeng, W. Xu, C. Yang, and J. Zhang, "Biosorption of copper(II) by immobilizing *Saccharomyces cerevisiae* on the surface of chitosan-coated magnetic nanoparticles from aqueous solution," *Journal of Hazardous Materials*, vol. 177, no. 1–3, pp. 676–682, 2010.
- [110] N. Tabassum, U. Rafique, K. S. Balkhair, and M. A. Ashraf, "Chemodynamics of methyl parathion and ethyl parathion: adsorption models for sustainable agriculture," *Biomedical Research International*, vol. 2014, Article ID 831989, 8 pages, 2014.
- [111] H. Kyung, J. Lee, and W. Choi, "Simultaneous and synergistic conversion of dyes and heavy metal ions in aqueous TiO₂ suspensions under visible-light illumination," *Environmental Science and Technology*, vol. 39, no. 7, pp. 2376–2382, 2005.
- [112] S. Luo, Y. Xiao, L. Yang et al., "Simultaneous detoxification of hexavalent chromium and acid orange 7 by a novel Au/TiO₂ heterojunction composite nanotube arrays," *Separation and Purification Technology*, 2011.
- [113] H. Shen and Y.-T. Wang, "Simultaneous chromium reduction and phenol degradation in a coculture of *Escherichia coli* ATCC 33456 and *Pseudomonas putida* DMP-1," *Applied and Environmental Microbiology*, vol. 61, no. 7, pp. 2754–2758, 1995.
- [114] E. M. Nkhalambayausi-Chirwa and Y.-T. Wang, "Simultaneous chromium(VI) reduction and phenol degradation in a fixed-film coculture bioreactor: reactor performance," *Water Research*, vol. 35, no. 8, pp. 1921–1932, 2001.
- [115] R. Singh, N. R. Bishnoi, A. Kirrolia, and R. Kumar, "Synergism of *Pseudomonas aeruginosa* and Fe⁰ for treatment of heavy metal contaminated effluents using small scale laboratory reactor," *Bioresource Technology*, vol. 127, pp. 49–58, 2013.

Research Article

The Use of Biofloculant and Biofloculant-Producing *Bacillus mojavensis* Strain 32A to Synthesize Silver Nanoparticles

Sahar Zaki,¹ Marwa Etarahony,¹ Marwa Elkady,² and Desouky Abd-El-Haleem¹

¹ Environmental Biotechnology Department, Genetic Engineering and Biotechnology Research Institute (GEBRI), City of Scientific Research and Technological Applications (SRTA-City), Alexandria, Egypt

² Fabrication Technology Department, Advanced Technology and New Materials Research Institute (ATNMRI), City of Scientific Research and Technological Applications (SRTA-City), Alexandria, Egypt

Correspondence should be addressed to Sahar Zaki; saharzaki@yahoo.com

Received 21 November 2013; Accepted 20 April 2014; Published 13 May 2014

Academic Editor: Haiqiang Wang

Copyright © 2014 Sahar Zaki et al. This is an open access article distributed under the Creative Commons Attribution License, which permits unrestricted use, distribution, and reproduction in any medium, provided the original work is properly cited.

It is preferable to use an organism to produce more than one product at the same time. So, the aim of this study was to investigate the ability of biofloculant-producing *Bacillus mojavensis* strain 32A as a nanosilver synthesizer beside biofloculant production. To achieve this target, three media, nutrient broth, biofloculant-producing medium, and pure biofloculant, were tested. Produced nanosilver was characterized by UV-vis, XRD, and TEM. In all cases, the results demonstrated that UV-vis showed a peak at ~420 nm corresponding to the plasmon absorbance of nanosilver. XRD spectrum exhibited 2θ values corresponding to the silver nanocrystal that is produced in hexagonal and cubic crystal configurations. TEM confirmed formation, size, shape, and morphologies of nanosilver particles. The results emphasized that purified biofloculant has the ability to produce anisotropy clusters of nanosilver ranging in size from 6 to 72 nm proving that the biofloculant functioned as reducing and stabilizing agent in nanosilver synthesis.

1. Introduction

Nanotechnology, appearing abruptly in the 20th century, is an area of science devoted to the manipulation of atoms and molecules in the nanometer size range 1–100 nm [1]. Like many future areas of scientific exploration, nanoscience and nanotechnology exist on the borders between disciplines including but not restricted to catalysis, electronic, medicine, biotechnology, and environmental remediation and agricultural research. Nanomaterials often show unique and considerably changed physical, chemical, thermodynamic, magnetic, and biological properties compared to their macroscaled ones [2, 3]. Out of all kinds of nanoparticles, silver nanoparticles (AgNPs) seem to have attracted the most interests in terms of their potential application. Indeed, the widespread use of this precious metal in nanosize form from household paints to artificial prosthetic devices has imparted significant effects on our daily lives [2, 4].

AgNPs can be prepared by two methods; the first one is a physical approach that utilizes several methods such as

evaporation/condensation and laser ablation. The second one is a chemical approach in which the metal ions in solution are reduced in conditions favoring the subsequent formation of small metal clusters or aggregates. Most of these techniques are extremely expensive and capital intensive; they also involve the use of toxic, hazardous chemicals which may pose potential environmental and biological risks as well as inefficiency in materials and energy use [5]. However, development of simple and ecofriendly synthetic method would help promoting further interest in the synthesis and applications of metallic nanoparticles [6, 7]. Recently, biosynthetic methods employing naturally occurring reducing agents such as polysaccharides, biological microorganisms such as bacteria and fungus, or plants extract, that is, green chemistry, have emerged as a simple and viable alternative to more complex chemical synthetic procedures to obtain AgNPs. It provides advancement over chemical and physical methods as it is of slower kinetics, offers better manipulation, is cost effective, is environmentally safe, and is easily scaled up for large scale synthesis; in addition, there is no need to use high pressure,

energy, temperature, and toxic chemicals to control crystal growth and its stabilization [2].

Many microorganisms including bacteria [8], fungi [9–11], actinomycetes [12, 13], and algae [14] can aggregate inorganic materials and form nanoparticles (NPs) intracellularly or extracellularly. Natural compounds such as microbial biopolymers are also one of the resources which could be used for green synthesis of AgNPs. Recently, Sathiyarayanan et al. [15] reported that polysaccharides from microbial origin such as bioflocculants are a promising alternative for the synthesis and stabilization of nanoparticles. Indeed, this is an interesting area of research where both biosynthetic nanosilvers and bioflocculants are economically important. Bioflocculants are biodegradable, safe, and ecofriendly biopolymers secreted by microorganisms [16, 17]. They are used in the field of wastewater treatment for removing suspended solids and metal ions, at which colloids come out of suspension in the form of floc or flakes [18]. In this regard, recently in our lab *Bacillus mojavensis* strain 32A was isolated as an efficient bioflocculant producer [19]. In the present study, synthesis of nanosilver particles using bioflocculant-producing strain 32A and its extracted and purified bioflocculant was investigated. Produced nanoparticles were characterized using transmission electron microscope (TEM) and X-ray diffraction (XRD) techniques.

2. Material and Methods

2.1. Chemicals, Strain, and Cultural Conditions. Silver nitrate (AgNO_3) required for synthesis of AgNPs was obtained from Sigma-Aldrich. Other required chemicals were purchased from Merck. *Bacillus mojavensis* strain 32A used in this study was previously identified as an efficient bioflocculant producer by Elkady et al. [19]. Culturing, media, and production of bioflocculant and/or synthesis of silver nanoparticles were performed as described elsewhere [5, 19]. The initial pH of all media was adjusted to 7.2 to 7.5 with NaOH (1M) and HCl (0.5 M). All media were prepared with distilled water and sterilized at 121°C for 20 min.

2.2. Synthesis of AgNPs. The following three media were examined to synthesize AgNPs using the bioflocculant and bioflocculant-producing bacterial strain 32A.

2.2.1. In Nutrient Broth Medium. AgNPs were synthesized as described by Zaki et al. [20]. Strain 32A was precultured for overnight in LB medium at 30°C in a rotary shaker with 200 rpm. Subsequently, 10% of precultured LB were transferred into 100 mL nutrient broth medium (NB) containing (w/v) 1% peptone, 0.5% yeast extract, and 0.5% beef extract supplemented with 3.5 mM of AgNO_3 in 500 mL flask. The mixture was incubated in darkness for 7 days at 30°C with 200 rpm shaking. The extracellular synthesis of AgNPs was monitored by visual inspection of the change in medium color from a clear light yellow to brown. The control was maintained without addition of AgNO_3 with the experimental flask containing NB medium.

2.2.2. In Bioflocculant-Producing Medium. About 10% of the precultured LB medium was used as a seeding medium of the bioflocculant-producing medium (BP) as described by Elkady et al. [19]. The BP medium contained (per liter) L-glutamic acid 20 g, NH_4Cl 7 g, K_2HPO_4 0.5 g, MgSO_4 0.5 g, FeCl_3 40 mg, CaCl_2 150 mg, and MnSO_4 140 mg supplemented with 3.5 mM of AgNO_3 , and 80 mL sterile glycerol was added just before the cultivation. Synthesis and monitoring of AgNPs occurred as described above. The control was maintained without addition of AgNO_3 with the experimental flask containing BP medium.

2.2.3. In Purified Bioflocculant Solution. Purified bioflocculant (PB) from strain 32A was obtained as described by Elkady et al. [19]. The cell-free supernatant was concentrated to 0.2 volumes with a rotary evaporator and dialyzed overnight at 4°C in deionized water. Three volumes of cold anhydrous ethanol (4°C) were added to the dialyzed broth. The precipitate obtained was redissolved in deionized water followed by the addition of 10% cetylpyridinium chloride (CPC) with stirring. After several hours, the resultant precipitate was collected by centrifugation (5000 rpm, 15 min) and dissolved in 0.5 M NaCl. Three volumes of cold anhydrous ethanol (4°C) were then added to obtain the precipitate, which was then washed with 75% ethanol three times and lyophilized to obtain purified biopolymer. The final concentration of 3 mM AgNO_3 was added into 200 mL of 10% bioflocculant solution in 500 mL flask. The flasks were incubated in darkness for 2 days. The monitoring of AgNPs synthesis was performed as described above. The control was maintained without addition of AgNO_3 with the experimental flask containing purified bioflocculant.

2.3. Characterization of AgNPs. The synthesized AgNPs were first characterized by UV-visible spectrophotometer (Labomed model UV-vis double beam spectrophotometer) in the range of 200–600 nm. Quartz cuvettes with optical path length of 10 mm were used in the measurements. One milliliter from each AgNPs production way was withdrawn and the absorbance after centrifugation was measured. The produced AgNPs were collected by centrifugation at 10,000 rpm for 10 min. The finely powdered samples were dried in vacuum oven at 60°C overnight. Subsequently, the finely powdered samples were analyzed using X-ray diffractometer (Schimadzu-7000, USA). Through packing the dried samples into a flat aluminum sample holder, where the X-ray source was a rotating anode operating at 30 kV and 30 mA with a copper target, data were collected between 10° and 80° in 2θ . Transmission electron microscope (JEOL JEM-1230, Japan) was utilized to confirm and detect morphology of AgNPs under an accelerating voltage of 120 kV; samples were prepared by placing a drop of hydrophobic nanosilver colloid or its aqueous coordinate on carbon-coated copper grids and drying at room temperature.

3. Results and Discussion

3.1. Visual Examination. In all cases, appearance of a stable brown color indicates AgNPs formation in aqueous solution,

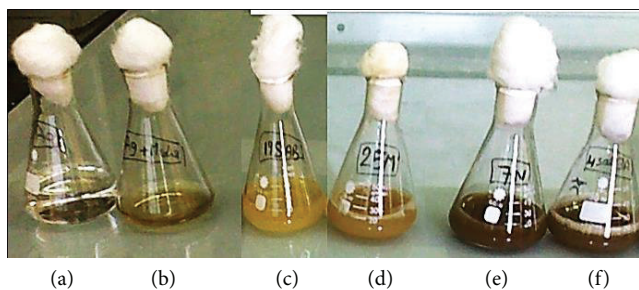


FIGURE 1: The optical photograph of three studied ways to produce AgNPs: (a) 3.5 mM AgNO_3 solution control without cells; (b) broth with 3.5 mM AgNO_3 solution and without culture; (c) culture broth without AgNO_3 as a negative control; (d), (e), and (f) are the results of AgNPs production in NB medium, BP bioflocculant-producing medium, and PB purified bioflocculant, respectively, after 7 days of incubation.

while there was no color change that could be observed in the negative controls (Figure 1). However, the light yellow color appearing with the control broth was due to the components of NB medium which include yeast and beef extracts. It is established that color change of solutions is due to excitation of surface plasmon resonances (SPR) in metal nanoparticles [21, 22].

3.2. UV-Vis Spectrophotometer Analysis. Previously, it has been proved that UV-vis analysis is a very useful and quite sensitive technique for the analysis of nanoparticles [23]. In the present study, AgNPs were characterized by UV-vis after 7 days of incubation as described by Zaki et al. [20]. As shown in Figure 2, it is clear that when we used NB and BP media to produce AgNPs, a typical, sharp, strong, and single plasmon peak at 400 nm was obtained. Shrivastava et al. [24] reported that the AgNO_3 solution showed at about 300 nm; however, in the present study gradually underwent red shift with appearance of a hump at 400 nm was observed (Figures 2(a) and 2(b)). These results were consistent with formation of small and narrow size distribution of the spherical nanoparticles as described by Kumar et al. [25]. However, observation of such ideal bell, sharp plasmon band which appeared to exhibit semisymmetric shape and the absence of tailing at higher wavelength confirm that the solution exhibits monodispersity and does not contain many aggregated particles.

As shown in Figure 2(c), the UV-vis analysis of the AgNPs produced in PB demonstrated that the optical absorption spectrums of metal nanoparticles are dominated by surface response plasmon (SRP) shifts to longer wavelengths with increasing particle size [21]. In addition, about 2 SRP bands were detected at 465 and 510 nm indicating the presence of anisotropic large particles. Also, absorbance intensity provided indication on the reduction, productivity, and amount of Ag^+ ion [21]. This may be due to the availability of more reducing biomolecules and concentrations of AgNPs. The absence of symmetric SPR bands and presence of tailing at high wavelength may be attributed to the agglomeration of AgNPs with different size distribution [26].

3.3. TEM. TEM has been employed to characterize the size, shape, and morphologies of the formed AgNPs and their producing biofactory. As an electron beam passes through the particles at a slower rate than through the carbon grid due to the difference in atomic electron density, having an increased chance of scattering, the electron sensor is able to identify the high-density area from the overall background by collecting the number of electrons. Particles with high density will appear darker in the TEM [27]. In the NB medium used to produce AgNPs, cells appeared to have normal characteristics, their cell walls and cytoplasmic membranes were intact, and the internal structure showed unanimous homogeneous electron density cytoplasm. This suggested that cells are in normal conditions without environmental disturbance and DNA molecules distribute randomly (Figure 3(a)). In addition, tiny biogenic nanoparticles less than 6 nm in size were deposited as seeds like on the cytoplasmic membrane which appeared as electron opaque. As illustrated in Figure 3(b), cell-free supernatant of NB medium indicates that biosynthesized AgNPs were spherical, small, and monodispersed.

However, in the bioflocculant-producing medium (BP) it seems that bacteria differ from the previous one due to the difference in incubation media, where the glutamic acid and ammonium chloride were usually used as carbon and nitrogen sources, respectively, which are considered being the precursor substrate for biopolymer production [17, 28], while glycerol enhanced the polymer synthesis as reported by [29]. So it exhibits enhancement for two types of biopolymers that were defined by their cellular location, as indicated in Figures 4(a) and 4(b). Firstly, intracellular inclusion bodies that can be distinguished in TEM as electron light granules reach more than 60% of cell volume and about 30 to 500 nm in diameter; such nanobiopolymers like lipid, polyhydroxyalkanoates (PHAs), triacylglycerols, wax esters, polyphosphates, and glycogen have been reported in many bacteria [8]. Secondly, extracellular polysaccharides (EPSs) which were secreted in the growth medium exhibiting flocculating properties cannot be distinguished easily with TEM due to processing rupture. Contrary to AgNPs produced in NB medium, small spherical silver nanoparticles were not detected on the cytoplasmic membrane of the cell but detected outside the cell in little agglomeration on ruptured extracellular bioflocculant.

To explain biosynthesis of AgNPs in NB and BP media, encoded proteins such as nitrate reductase appear to be the choice of *Bacillus mojavensis* 32A strain to detoxify silver ions by its reduction to less toxic oxidative state. It is known that nitrate reductase enzyme shuttles the electron to the silver ions in an aqueous solution and in the presence of NAD and H^+ ions that act as a reducing agent. Some of other peptides/proteins may be responsible for the subsequent stabilization of silver nanoparticles as well [30, 31].

The TEM observations of AgNPs produced in the purified bioflocculant solution (PB) show several shapes of AgNPs in varying sizes including nanospheres, hexagonal, polygonal, nanoprisms, and uneven shapes (Figure 5). These nanoparticles are polydisperse and aggregated, and their particle sizes were ranging from 6 to 72 nm; such variation in shape and size

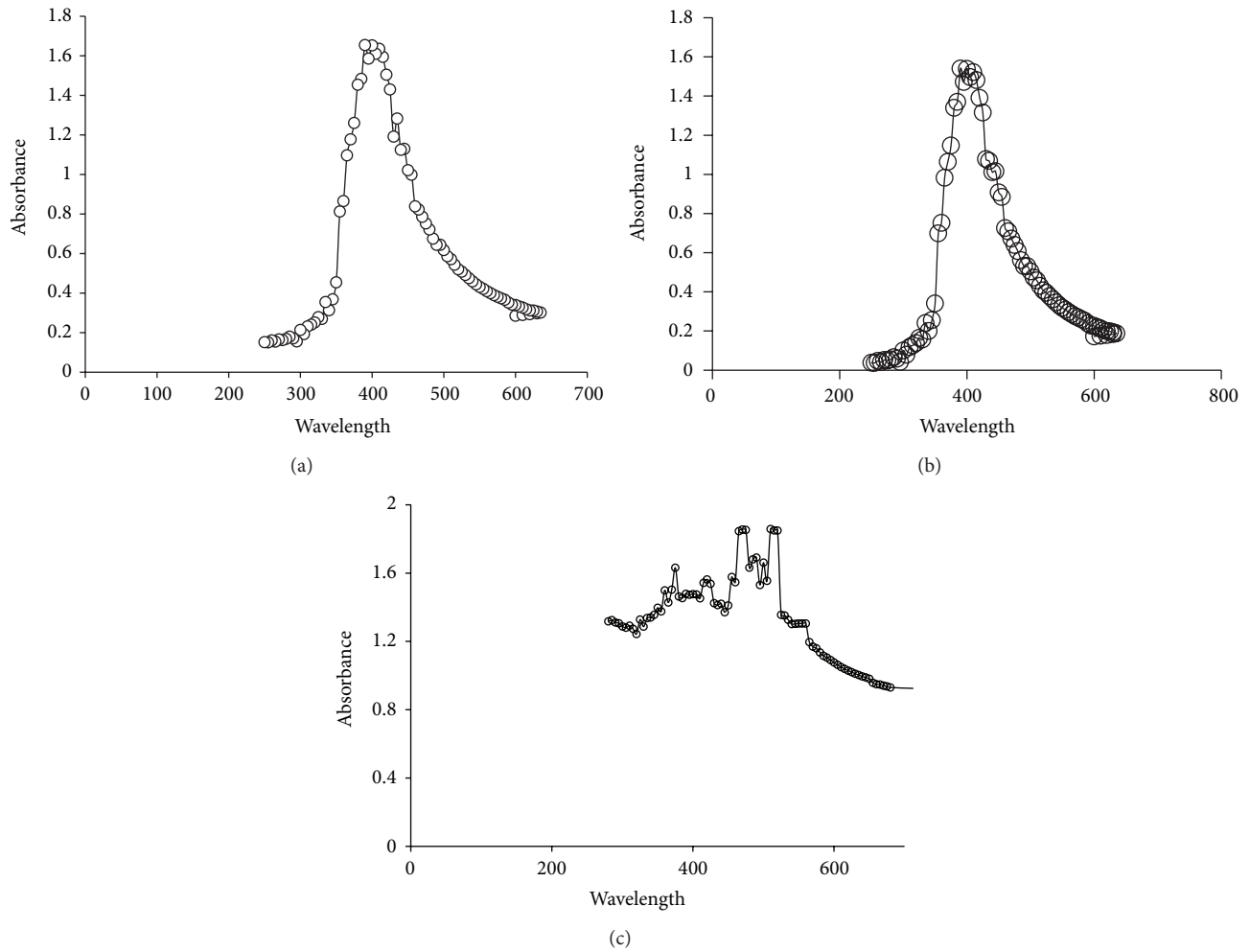


FIGURE 2: ((a)–(c)) The UV-vis spectra of the silver nanoparticles obtained from all examined ways: (a) NB medium, (b) BP medium, and (c) PB solution, respectively.

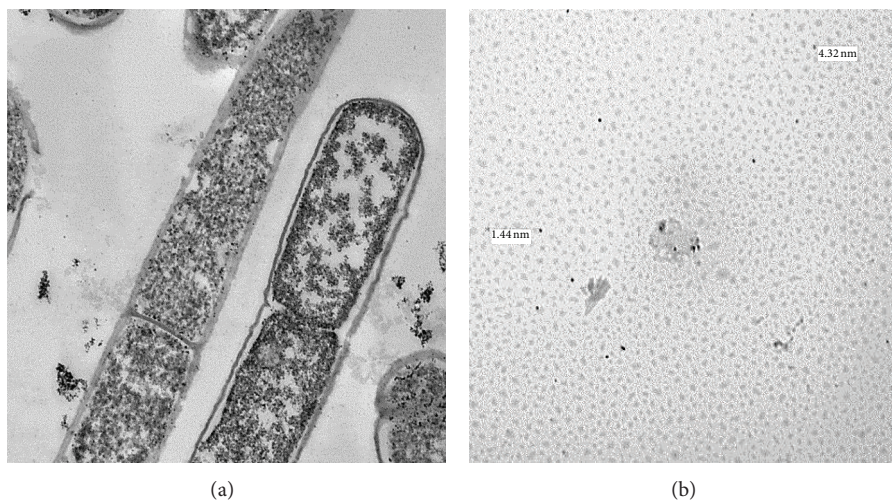


FIGURE 3: TEM images recorded from the drop-coated film of the AgNPs synthesized by strain 32A cells cultured in NB medium (a) and cell-free supernatant of the same medium (b).

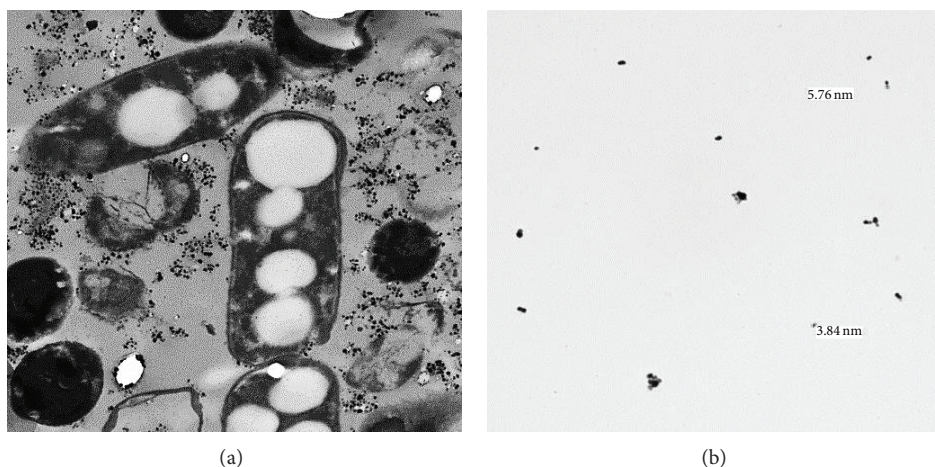


FIGURE 4: TEM images recorded from the drop-coated film of the AgNPs synthesized by strain 32A cells cultured in BP medium (a) and cell-free supernatant of the same medium (b).

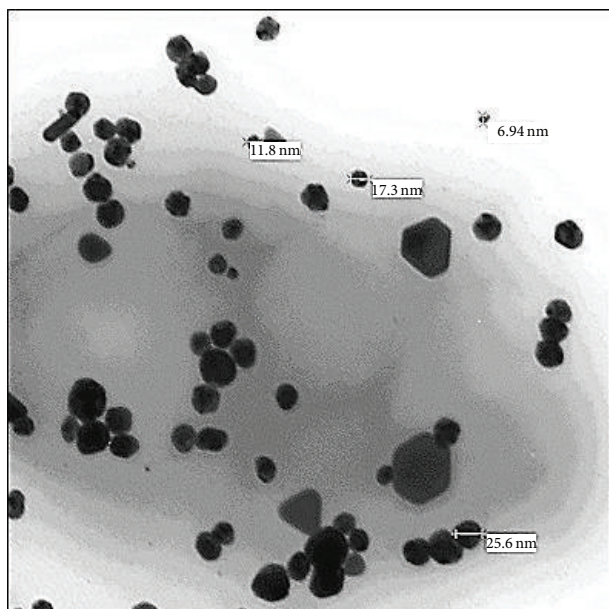


FIGURE 5: TEM image recorded from the drop-coated film of the silver nanoparticles synthesized by the silver nitrate solution with purified bioflocculant (PB).

of nanoparticles synthesized by biological systems is common [32].

To date, most of the preparation methods published are based on using organic materials due to the hydrophobicity of the stabilizing agents used, such as natural polymers [33]. The purified bioflocculant was used as bioreductant for silver ion. As reported by Elkady et al. [19], the chemical analysis of the purified biopolymer demonstrates that it contains 1.6% (w/w) protein and 98.4% polysaccharide. However, its amino acid analysis indicates the presence of glutamic acid (38%), aspartic acid, and glycine, respectively. In addition, FTIR spectrum

was used to reveal the functional groups of the biopolymer which were hydroxyl, amino groups, aliphatic C–H, C=O, and CH₃ CH₂. Generally, the carboxyl groups in aspartic and/or glutamine residues and the hydroxyl group in tyrosine residues of the proteins were suggested to be responsible for the Ag⁺ ion reduction and stabilization [3]. Firstly, these silver ions oxidize the hydroxyl groups to carbonyl groups, during which the silver ions are reduced to elemental silver. Subsequently, the reducing end of polysaccharides can be used to introduce an amino functionality that is capable of complexion and stabilizing metallic nanoparticles carbohydrates with such amino groups binding tightly to the surface of the AgNPs giving them a hydrophilic surface [34].

Finally, both hydroxyl and carbonyl groups of bioflocculant are involved in the synthesis of AgNPs and both amino and carboxylate groups of it are involved in the capping and stabilizing of AgNPs and that is in agreement with [15]. These results are in concurrence with an earlier biosynthesis of AgNPs carried out with fungus *Trichoderma asperellum* and gum kondagogu. It is known that proteins can bind to nanoparticles either through free amino groups or by electrostatic interaction of negatively charged carboxylate groups. The gum tragacanth is known to contain protein, and the protein content was reported to be in the range of 1.0–3.6% [35], so *Bacillus mojavensis* 32A strain bioflocculant acts as reducing and stabilizing agent in AgNPs synthesis.

3.4. XRD. The X-ray diffraction (XRD) technique was used to establish the metallic nature of particles. X-rays are electromagnetic radiation with typical photon energies that can penetrate deep into the materials and provide information about the bulk structure. In all studied cases, XRD pattern showed intense Bragg's reflections that can be indexed on the basis of the fcc structure of silver (Figure 6). The 2θ values of the XRD pattern were ranging from 30° to 80° and three strong peaks were observed at 38.1°, 46.3°, and 77.5° and corresponded to the planes 111, 200, and 311 and exhibited that

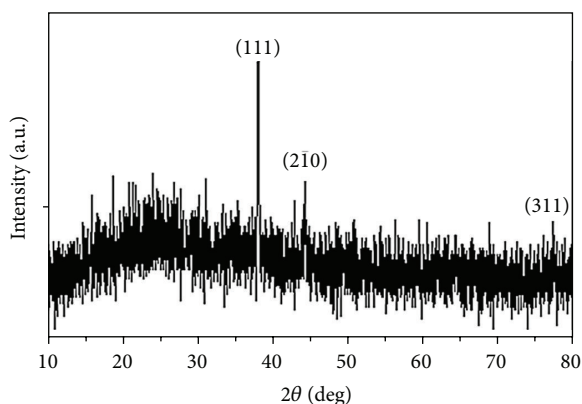


FIGURE 6: XRD patterns for the AgNPs produced by strain 32A.

the synthesized AgNPs were crystalline in nature. The values agree well with those which are indexed to the face centered cubic structures of silver nanoparticles [20].

4. Conclusion

In this study, the biofloculant-producing *Bacillus mojavensis* strain 32A and its pure biofloculant were examined as nanosilver producers; such a technique is important from both the economic and the scientific points of view where that the knowledge of the way in which biofloculant contributes to convert silver nitrate to AgNPs still needs several successive researches. This understanding will help in the use of biopolymers in general and biofloculants, in particular in the synthesis of AgNPs. The results showed that both bacteria and their biofloculant were able to synthesize AgNPs. However, TEM studies show that there are differences in the shape and size of nanoparticles manufactured by bacteria from those manufactured by biopolymer. These results were confirmed by the analysis of synthesized AgNPs spectrum as well as XRD. In addition, it is speculated that *Bacillus mojavensis* strain 32A has the ability to produce extracellular biofloculant and intracellular nanobiopolymer and activate nitrate reductase to produce AgNPs, as well. The study emphasized that in addition to its ability in aggregation and precipitation of suspended particles, the biofloculant is acting as reducing and stabilizing agent in AgNPs biosynthesis.

Conflict of Interests

The authors declare that there is no conflict of interests regarding the publication of this paper.

Acknowledgment

This work was supported by grants from the Egyptian Science and Technology Development Fund (STDF) (Grants no. 743 and 2148).

References

- [1] S. Lu, W. Gao, and H. Y. Gu, "Construction, application and biosafety of silver nanocrystalline chitosan wound dressing," *Burns*, vol. 34, no. 5, pp. 623–628, 2008.
- [2] K. Sahayaraj and S. Rajesh, "Bionanoparticles: synthesis and antimicrobial applications, science against microbial pathogens communicating," in *Current Research and Technological Advances*, pp. 228–244, 2011.
- [3] V. K. Sharma, R. A. Yngard, and Y. Lin, "Silver nanoparticles: green synthesis and their antimicrobial activities," *Advances in Colloid and Interface Science*, vol. 145, no. 1-2, pp. 83–96, 2009.
- [4] E. Binaeian, A. M. Rashidi, and H. Attar, "Toxicity study of two different synthesized silver nanoparticles on bacteria *Vibrio fischeri*," *World Academy of Science, Engineering and Technology*, vol. 67, pp. 1219–1225, 2009.
- [5] S. Zaki, M. F. Elkady, S. Farag, and D. Abd-El-Haleem, "Determination of the effective origin source for nanosilver particles produced by *Escherichia coli* strain S78 and its application as antimicrobial agent," *Materials Research Bulletin*, vol. 47, pp. 4286–4290, 2012.
- [6] R. Vaidyanathan, K. Kalishwaralal, S. Gopalram, and S. Guranathan, "Nanosilver—the burgeoning therapeutic molecule and its green synthesis," *Biotechnology Advances*, vol. 27, no. 6, pp. 924–937, 2009.
- [7] S. Behera, A. Ojha, J. Rout, and P. L. Nayak, "Plant mediated synthesis of silver nanoparticles: opportunity and challenge," *International Journal of Biology Pharmacy and Allied Sciences*, vol. 1, pp. 1637–1658, 2012.
- [8] A. Cauerhff and G. R. Castro, "Bionanoparticles, a green nanotechnology approach," *Electronic Journal of Biotechnology*, vol. 16, pp. 1–10, 2013.
- [9] A. Ahmad, P. Mukherjee, S. Senapati et al., "Extracellular biosynthesis of silver nanoparticles using the fungus *Fusarium oxysporum*," *Colloids and Surfaces B: Biointerfaces*, vol. 28, no. 4, pp. 313–318, 2003.
- [10] A. K. Gade, P. Bonde, A. P. Ingle, P. D. Marcato, N. Durán, and M. K. Rai, "Exploitation of *Aspergillus niger* for synthesis of silver nanoparticles," *Journal of Biobased Materials and Bioenergy*, vol. 2, no. 3, pp. 243–247, 2008.
- [11] A. R. Shahverdi, S. Minaeian, H. R. Shahverdi, H. Jamalifar, and A.-A. Nohi, "Rapid synthesis of silver nanoparticles using culture supernatants of Enterobacteria: a novel biological approach," *Process Biochemistry*, vol. 42, no. 5, pp. 919–923, 2007.
- [12] R. S. Prakasham, B. S. Kumar, Y. S. Kumar, and G. G. Shankar, "Characterization of silver nanoparticles synthesized by using marine isolate *Streptomyces albidoflavus*," *Journal of Microbiology and Biotechnology*, vol. 22, pp. 614–621, 2012.
- [13] S. Silambarasan and J. Abraham, "Biosynthesis of silver nanoparticles," *African Journal of Biotechnology*, vol. 12, pp. 3088–3098, 2013.
- [14] S. M. Landage and A. I. Wasif, "Nanosilver—an effective antimicrobial agent for finishing textile," *International Journal of Engineering Sciences & Emerging Technologies*, vol. 4, pp. 66–78, 2012.
- [15] G. Sathiyarayanan, G. S. Kiran, and J. Selvin, "Synthesis of silver nanoparticles by polysaccharide biofloculant produced from marine *Bacillus subtilis* MSBN17," *Colloids and Surfaces B: Biointerfaces*, vol. 102, pp. 13–20, 2013.
- [16] S. B. Deng, R. B. Bai, X. M. Hu, and Q. Luo, "Characteristics of a biofloculant produced by *Bacillus mucilaginosus* and its

- use in starch wastewater treatment," *Applied Microbiology and Biotechnology*, vol. 60, no. 5, pp. 588–593, 2003.
- [17] B. Bhunia, D. Mukhopadhy, S. Goswami, T. Mandal, and A. Dey, "Improved production, characterization and flocculation properties of poly (γ)-glutamic acid produced from *Bacillus subtilis*," *Journal of Biochemical Technology*, vol. 3, pp. 389–394, 2012.
- [18] Y. Li, N. He, H. Guan, G. Du, and J. Chen, "A novel polygalacturonic acid bioflocculant REA-II produced by *Corynebacterium glutamicum*: a proposed biosynthetic pathway and experimental confirmation," *Applied Microbiology and Biotechnology*, vol. 63, no. 2, pp. 200–206, 2003.
- [19] M. F. Elkady, S. Farag, S. Zaki, G. Abu-Elreesh, and D. Abd-El-Haleem, "*Bacillus mojavensis* strain 32A, a bioflocculant-producing bacterium isolated from an Egyptian salt production pond," *Bioresource Technology*, vol. 102, no. 17, pp. 8143–8151, 2011.
- [20] S. Zaki, M. F. El Kady, and D. Abd-El-Haleem, "Biosynthesis and structural characterization of silver nanoparticles from bacterial isolates," *Materials Research Bulletin*, vol. 46, no. 10, pp. 1571–1576, 2011.
- [21] S. Hamed, S. M. Ghaseminezhad, S. A. Shojaosadati, and S. Shokrollahzadeh, "Comparative study on silver nanoparticles properties produced by green methods," *Iranian Journal of Biotechnology*, vol. 10, pp. 191–197, 2012.
- [22] A. K. Mondal, S. Mondal, S. Samanta, and S. Mallick, "Synthesis of ecofriendly silver nanoparticle from plant latex used as an important taxonomic tool for phylogenetic interrelationship," *Advances in Bioresearch*, vol. 2, pp. 122–133, 2011.
- [23] A. J. i. Kora, S. R. Beedu, and A. Jayaraman, "Size-controlled green synthesis of silver nanoparticles mediated by gum ghatti (*Anogeissus latifolia*) and its biological activity," *Organic and Medicinal Chemistry Letters*, vol. 2, pp. 1–10, 2012.
- [24] S. Shrivastava, T. Bera, A. Roy, G. Singh, P. Ramachandrarao, and D. Dash, "Characterization of enhanced antibacterial effects of novel silver nanoparticles," *Nanotechnology*, vol. 18, no. 22, pp. 1–9, 2007.
- [25] P. Kumar, S. S. Senthamil, P. A. Lakshmi, K. Prem, R. S. Ganeshkumar, and M. Govindaraju, "Synthesis of silver nanoparticles from *Sargassum tenerrimum* and screening phytochemicals for its anti-bacterial activity," *Nano Biomedical Engineering*, vol. 4, pp. 12–16, 2012.
- [26] S. Pal, Y. K. Tak, and J. M. Song, "Does the antibacterial activity of silver nanoparticles depend on the shape of the nanoparticle? A study of the gram-negative bacterium *Escherichia coli*," *Applied and Environmental Microbiology*, vol. 73, no. 6, pp. 1712–1720, 2007.
- [27] G. Lei, *Synthesis of nano-silver colloids and their anti-microbial effects [M.S. thesis]*, Faculty of the Virginia Polytechnic Institute and State University, 2007.
- [28] I. B. Bajaj and R. S. Singhal, "Sequential optimization approach for enhanced production of poly(γ -glutamic acid) from newly isolated *Bacillus subtilis*," *Food Technology and Biotechnology*, vol. 47, no. 3, pp. 313–322, 2009.
- [29] G. Du, G. Yang, Y. Qu, J. Chen, and S. Lun, "Effects of glycerol on the production of poly(γ -glutamic acid) by *Bacillus licheniformis*," *Process Biochemistry*, vol. 40, no. 6, pp. 2143–2147, 2005.
- [30] D. H. Nies and S. Silver, "Ion efflux systems involved in bacterial metal resistances," *Journal of Industrial Microbiology*, vol. 14, no. 2, pp. 186–199, 1995.
- [31] A. Prakash, S. Sharma, N. Ahmad, A. Ghosh, and P. Sinha, "Bacteria mediated extracellular synthesis of metallic nanoparticles," *International Research Journal of Biotechnology*, vol. 1, pp. 071–079, 2010.
- [32] M. Bubey, S. Bhaduria, and B. S. Kushwaha, "Green synthesis of nanosilver particles from extract of *Eucalyptus hybrida* (safeda) leaf, dig," *Journal of Nanomaterial Biostructure*, vol. 4, pp. 537–543, 2009.
- [33] M. Darroudi, M. B. Ahmad, A. H. Abdullah, and N. A. Ibrahim, "Green synthesis and characterization of gelatin-based and sugar-reduced silver nanoparticles," *International Journal of Nanomedicine*, vol. 6, no. 1, pp. 569–574, 2011.
- [34] Y. Park, Y. N. Hong, A. Weyers, Y. S. Kim, and R. J. Linhardt, "Polysaccharides and phytochemicals: a natural reservoir for the green synthesis of gold and silver nanoparticles," *IET Nanobiotechnology*, vol. 5, no. 3, pp. 69–78, 2011.
- [35] A. J. Kora and J. Arunachalam, "Green fabrication of silver nanoparticles by gum tragacanth (*Astragalus gummifer*): a dual functional reductant and stabilizer," *Journal of Nanomaterials*, vol. 2012, Article ID 869765, 8 pages, 2012.

Research Article

Preparation and Characterization of Lecithin-Nano Ni/Fe for Effective Removal of PCB77

Shu Ding, Lin Zhao, Yun Qi, and Qian-qian Lv

School of Environmental Science and Engineering, Tianjin University, Tianjin 300072, China

Correspondence should be addressed to Lin Zhao; zhaolin@tju.edu.cn

Received 5 February 2014; Revised 14 April 2014; Accepted 14 April 2014; Published 30 April 2014

Academic Editor: Fan Dong

Copyright © 2014 Shu Ding et al. This is an open access article distributed under the Creative Commons Attribution License, which permits unrestricted use, distribution, and reproduction in any medium, provided the original work is properly cited.

A kind of combined material (named lecithin-nano Ni/Fe) that is composed of lecithin and nanoscale Ni/Fe bimetal was synthesized via microemulsion method. The efficacy of such an original material was tested using 3,3',4,4'-tetrachlorobiphenyl (PCB77) as target pollutant. A microemulsion system was optimized as template to prepare Ni/Fe nanoparticles, which was followed by an in-site loading process with the deposition of lecithin carrier. It was proved by the characterization that subtle Ni/Fe nanoparticles can be uniformly dispersed and closely combined with lecithin carrier. Lecithin was an environmentally compatible biosurfactant that acted as both the component of the microemulsion and the functional material to accumulate organic contaminants. It was expected that the combined material can integrate the functions of lecithin and bimetal. The effectiveness was exhibited through the more rapid and sufficient removal of PCB77 by lecithin-nano Ni/Fe than that by blank carrier. Although requiring further improvement, the constitution of lecithin-nano Ni/Fe was a beneficial attempt to acquire the synergistic effect for intensified removal of environmental contaminants. It was promising that the original system and convenient method described in this work will facilitate the development of the organic-inorganic combined materials.

1. Introduction

Polychlorinated biphenyls (PCBs) are a family comprised of 209 structurally related congeners which are listed as priority chemicals for eventual elimination by 2025 [1]. Their long-term heavy usage together with their high toxicity, chemical stability, long distance transfer, biologic accumulation, and persistence has resulted in their widespread distribution and large environmental risk [2, 3]. Since the natural degradation of PCBs is very difficult with a conspicuous low speed, PCBs are able to affect the environment and the health of various organisms in a long term. Both the damage of PCBs in the environment and inability of natural degradation at a significant rate highlight the requirement for effective treatment of PCBs. Thus, 3,3',4,4'-tetrachlorobiphenyl (PCB77), as a coplanar congener (see Figure 1) with high level of toxicity [4], is chosen to be the target compound for the research of contaminant removal.

Recently iron-based bimetallic nanoparticles, as a successful modified material of traditional zerovalent iron, got

general attention and further research owing to the obvious advantages including small particle diameter, large specific surface area, and optimal reactive activity [5, 6]. It had been proved that the iron-based bimetallic nanoparticles were effective in removing chlorinated organic compounds such as PCBs [7, 8]. While Fe acted as the reductant, Ni could be a proper catalytic metal with good corrosion stability and low cost [9]. But the insufficient activity of Ni/Fe nanoparticles required the usage of the expensive catalytic Pd to remove PCBs, which affected the application potential of the bimetallic material. To reinforce the removal efficacy of Ni/Fe nanoparticles, a possible method was to combine them with another material. In this paper, the lecithin carriers were synthesized to load Ni/Fe nanoparticles. It was expected that lecithin could contribute to the accumulation of PCB77 around Ni/Fe nanoparticles. The great regional concentration of PCB77 will facilitate its interaction with bimetal, which correlated with a good removal efficacy.

The attempts of utilizing lecithin as accumulation material were based on the existing studies about the usage of

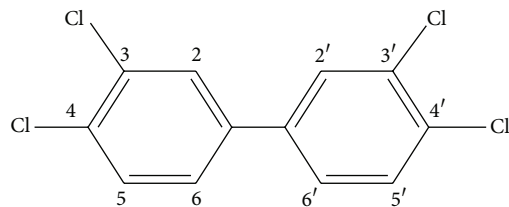


FIGURE 1: Structural formula of 3,3',4,4'-tetrachlorobiphenyl (PCB77).

surfactant to intensify the treatability of the organic contaminants. Such applications involving the washing process [10–12] and the aids for biodegradation [13, 14] took advantage of the effects including the solubilization and the emulsification which were offered by surfactant to influence the distribution of the contaminant molecules. The hydrophobic end of the surfactant molecules clustered together inside with the hydrophilic end exposed to the exterior in aqueous solution. This structure can be called the micelle or emulsified droplet. The interior of the micelles or droplets constitutes the dispersed phase wherein the hydrophobic organic contaminant was compatible and accumulated. Therefore the mechanism behind the great apparent solubility and good mobilization of the contaminant was its accumulation in the micelles or droplets.

Surfactants produced from chemically based materials were known as synthetic surfactants and those from biologically based materials were biosurfactants. In general synthetic chemical surfactants were found to persist and exert toxic effects [15–17]. In comparison with synthetic surfactants, biosurfactants had the advantages including being easily produced on renewable resources, possible reuse by regeneration, high specificity, less toxicity, and good biodegradability [18–20]. They were better suited to environmental applications than synthetic ones due to better environmental compatibility and higher activity [21, 22].

Therefore lecithin, as a type of biosurfactant which was low-cost by-product of oil seed industry [23], was a promising accumulation material and expected to be effective in assisting the contaminant removal by Ni/Fe bimetal. It was oil soluble and thereby beneficial for the binding of the organic contaminants such as PCBs. Indeed, it had been found that lecithin was effective in interacting with PCBs and assisted the removal process [24, 25]. However, the combined utilization of lecithin and Ni/Fe bimetal had never been tested and may be attractive. Additionally, it was reported that lecithin has been used to generate w/o microemulsion with the addition of coemulsifiers such as short-chained alcohols [26, 27]. The subtle water droplets that dispersed into the microemulsion were able to dissolve metallic salt and accordingly become the templates for the preparation of Ni/Fe nanoparticles. If such a hypothesis was ensured, the synthesis and loading of Ni/Fe nanoparticles can be accomplished in one step before the insite generation of lecithin carrier. It was promising to prepare the combined material with convenient technology and to synthesize Ni/Fe nanoparticles

with advanced character including small particle size, good dispersion, and high activity.

The present work was undertaken to synthesize lecithin carriers loading Ni/Fe bimetal to remove PCB77. The material efficacy was investigated through the removal of PCB77 in 50/50 (v/v) ethanol/water solution. Lecithin acted not only to accumulate PCB77 but also to constitute a microemulsion system which was the template for the insite generation of Ni/Fe nanoparticles with advanced character. The combined material was expected to integrate the function of lecithin and bimetal. To the best of our knowledge, this was the first work in which (a) the microemulsion containing lecithin was produced to be the template for the generation of Ni/Fe nanoparticles, (b) lecithin carriers loading Ni/Fe bimetal were synthesized, and (c) such a type of combined material was tested to remove PCBs. It was offered by this research that an innovative method to design and prepare functional material for the environmental decontamination. Although requiring further improvement, the method was valuable because the combined material can be prepared conveniently utilizing the stuff including the metallic salt and lecithin which were abundant, low cost, and environmentally compatible.

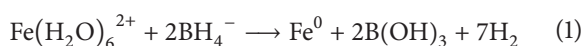
2. Materials and Methods

2.1. Materials. Soybean lecithin powder was purchased from Tianjin Boshuai Industrial & Trading Co., Ltd. Tween 80 was purchased from Tianjin Guang Fu Chemical Reagents Factory. Analytical grade $\text{FeSO}_4 \cdot 7\text{H}_2\text{O}$, analytical grade $\text{NiCl}_2 \cdot 6\text{H}_2\text{O}$, and superior grade NaBH_4 were all purchased from Kemiou Chemical Reagent Co., Ltd. The water used to prepare the solution in the experiment was distilled water. The standard substance of 3,3',4,4'-tetrachlorobiphenyl (PCB77) was provided by AccuStandard Inc. with a purity of >99.5%. Unless otherwise stated, all other chemicals were of analytical grade and used without further purification prior to use.

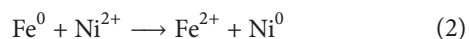
2.2. Formulation Studies for the Microemulsion. Five-component system consisting of oil/surfactant (comprised of lecithin and Tween 80)/cosurfactant and water can be described with pseudo ternary phase diagram. The mass ratio of lecithin to Tween 80 was determined to be 0.8 : 1 for the stabilization of the system and the solubilization of more contents of water. According to the preliminary experiments, isopropanol was chosen as the cosurfactant while cyclohexane was chosen to be the oil phase with the advantages that they were abundant, low cost, and relatively low toxic. A mixture of emulsifiers containing equal quantities of the surfactant and the cosurfactant was blended with oil phase at determined mass ratios. The resulting mixture was titrated with distilled water. The volume of water added was recorded while the turbid system turned clear and vice versa. The procedure based on visual inspection was repeated several times at different mass ratios of cyclohexane to emulsifiers. The pseudo ternary phase diagram was constructed by plotting the amounts of oil, surfactant/cosurfactant, and water to identify

the microemulsion region and thereby define the template formulation for the preparation of Ni/Fe nanoparticles.

2.3. Preparation of Lecithin Carriers Loading Ni/Fe Nanoparticles. After the content of each constituent was determined, the premixed solution of lecithin, Tween 80, isopropanol, and cyclohexane was stirred while a freshly prepared solution of NaBH_4 was dropped in the mixture to form the microemulsion template. The microemulsion system was treated using the ultrasound and then transferred into four-necked bottle. Under a nitrogen gas, required amount of the solution of FeSO_4 was slowly added into the aforementioned system with high speed stirring at room temperature. Solution color was observed to change to black, which indicated that the ferrous iron was reduced. The generation of Fe^0 can be interpreted through the following reaction:



Subsequently, after a session for the accomplishment of the reduction, an aqueous solution of $\text{NiCl}_2 \cdot 6\text{H}_2\text{O}$ was dropped in the system with stirring to react with the wet Fe^0 nanoparticles according to the following equation:



When the Ni/Fe nanoparticles were synthesized in the microemulsion, the demulsifier of tetrahydro furan was slowly added to acquire the uniform deposition of the lecithin carriers with the Ni/Fe nanoparticles loading on them. As-prepared combined material was collected by the high speed centrifugation and rinsed with acetone and ethanol that were both precooled at 4°C . The products were dried under vacuum before further experiments. Blank lecithin carriers were prepared according to the procedure above except that there was no addition of NaBH_4 and metallic salts.

2.4. Characterization of Lecithin Carriers Loading Ni/Fe Nanoparticles. The morphology of lecithin carriers loading Ni/Fe nanoparticles (in short lecithin-nano Ni/Fe) was investigated using the transmission electron microscopy (TEM, Tecnai G² F20, Holland) with EDS mapping to study the distribution and the loading ensemble of bimetal component on the carrier. For TEM analysis operated at an acceleration voltage of 200 kV, the samples were dispersed by an ultrasonicator in acetone and dropped to a copper grid with a lacy carbon layer. The scanning electron microscopy (SEM, SUPRA 55VP, Germany) was employed to precisely reflect the size, structure, and surface morphology of lecithin-nano Ni/Fe for which the samples were dried under vacuum at 50°C and then affixed onto adhesive tapes.

The character analyses involving the nitrogen Brunauer-Emmett-Teller (BET) surface areas, the X-ray diffraction (XRD), and the Fourier transform infrared spectrophotometer (FT-IR) were performed for lecithin-nano Ni/Fe with that for soybean lecithin powder and blank lecithin carriers (nanolecithin) as comparisons. BET surface areas were obtained by nitrogen adsorption using Quadrasorb SI analyzer (Quantachrome, USA). XRD analysis was carried

out using XRD diffractometer (Rigaku, Japan) at 40 kV and 100 mA over the scanning range of 10° – 90° 2θ . Samples for FT-IR (NICOLET6700, USA) measurement were prepared by mixing specimens with KBr powder and then pressing the mixtures into a sheer slice for analysis in the range of 400 – 4000 cm^{-1} . An average of 9 scans was collected for each measurement with a resolution of 2 cm^{-1} .

2.5. Removal of PCB77 in Solution. The abilities to remove PCB77, respectively, by lecithin-nano Ni/Fe and nanolecithin were determined. The working solution of 50/50 (v/v) ethanol/water containing about 5 $\mu\text{g}\cdot\text{mL}^{-1}$ PCB77 was prepared from the stock solutions. For each sample, about 0.5 g of the target material was measured and added into a 50 mL conical flask. Each system was then filled with 40 mL working solution that had been sufficiently deoxygenated and admixed. The blank system only containing the working solution was simultaneously prepared. The flasks were sealed after their headspace was filled with nitrogen gas and then placed on an orbital shaker. Constant temperature of 30°C and rotation speed of 200 rpm were selected as the identical condition for all experiments. At specific reaction time intervals, small amounts of solution were withdrawn to acquire the supernatant phase following centrifugation. For each sample, 600 μL of the supernatant phase was transferred into a 2 mL screw cap bottle and extracted with n-hexane. PCB77 was quantitatively analyzed by GC-ECD (Agilent 7890A GC coupled with a μ -ECD detector) using a DB-1701 column. The injection port was set at 250°C and detector temperature was set at 280°C . A split-splitless injector in the splitless mode was used with 2 μL of injection volume for each sample and nitrogen as the carrier gas. The column temperature was programmed as follows: initial temperature at 120°C and temperature program rate at $20^\circ\text{C}\cdot\text{min}^{-1}$ to 210°C and then $25^\circ\text{C}\cdot\text{min}^{-1}$ to 260°C .

3. Result and Discussion

3.1. Formulation Studies for the Microemulsion. A phase diagram was required to determine the extent of the monophasic area that corresponds to w/o microemulsion. Before the description, the optimized mass ratio of lecithin to Tween 80 (0.8 : 1) and that of surfactant to cosurfactant (Km, 1 : 1) were determined to profit the water incorporation with the fixed composition of the other factors. The w/o area for the five-component systems that consisted of cyclohexane, lecithin, Tween 80, isopropanol, and water was visualized in the pseudo ternary phase diagram (Figure 2). With the narrow feasible region, it was essential to select the appropriate point for preparing the formulation which was consistent with the maximum water incorporation. The existence of sufficient water in w/o microemulsion was beneficial for the good template efficacy through the high loading efficiency and effective dispersion of the metallic components. The optimized mass ratio of cyclohexane/lecithin/Tween 80/isopropanol/water was 73.5 : 7 : 8.75 : 15.75 : 27. The addition of required concentration of NaBH_4 was tested and did not obviously affect the stabilization of the w/o microemulsion.

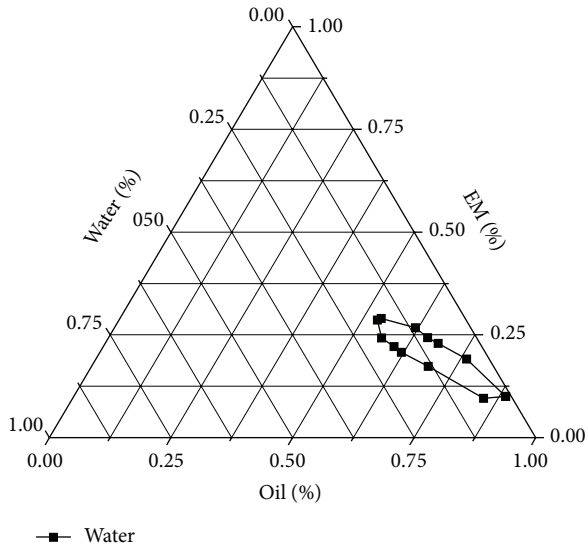


FIGURE 2: Pseudo ternary phase diagram of the w/o microemulsion.

Therefore such a composition of microemulsion was determined to be the template condition for the further synthesis of target materials.

3.2. Morphological Analysis of Lecithin-Nano Ni/Fe. The morphology and state of lecithin-nano Ni/Fe were observed by TEM. It was revealed that lots of small spherical nanoparticles were uniformly dispersed on the substrate (Figure 3(a)). The dispersion state of the nanoparticles was consistent with the distribution of the elements of nickel and iron according to the mapping of energy dispersive spectroscopy (EDS) (see Figure 3(b)). Under close inspection of a portion of the carrier, it can be found that the subtle dark-colored nanoparticles had identical size in the range of several nanometers (Figure 3(c)). Based on these results, it was signified that the Ni/Fe nanoparticles were reliably synthesized and had a widespread loading state on the carriers. The accurate surface morphology can be obtained from the SEM photogram which presented the dispersion state more clearly (Figure 4). While the lecithin carrier was roughly spherical in overall shape with the size range of 600–700 nm, its surface with abundant interstices was sufficiently covered by the small Ni/Fe nanoparticles which were about 10 nm. The structure feature corresponded with the larger surface area and more active sites which will facilitate the effectiveness of lecithin-nano Ni/Fe in removing PCB77.

3.3. Analysis of BET Surface Area. The data from the analysis of BET surface area were summarized and displayed in Table 1. It was obvious that the values of the surface area, the pore volume, and the pore diameter for both the lecithin-nano Ni/Fe and nanolecithin were significantly larger than that for raw material powder, which was attributed to the influence of nanoscale. The slightly larger values for lecithin-nano Ni/Fe than that for nanolecithin were possibly dedicated

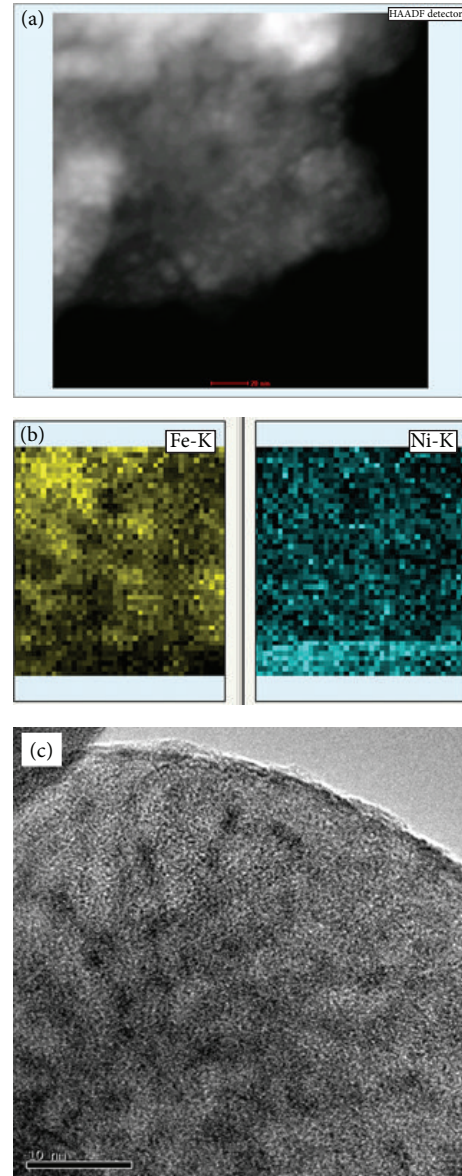


FIGURE 3: TEM micrograph (a) and correlated EDS mapping (b) of lecithin-nano Ni/Fe, and (c) closely TEM inspection of a portion of the carrier.

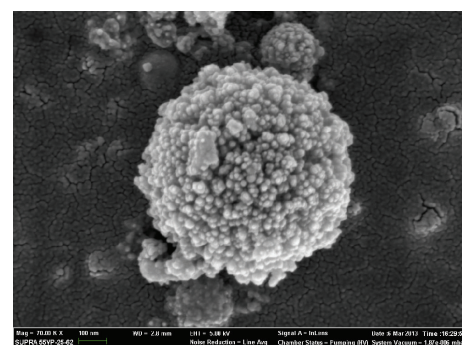


FIGURE 4: SEM micrograph of lecithin-nano Ni/Fe.

TABLE 1: Data arose from the analysis of BET surface area.

Sample	S_{BET} (m^2/g)	Pore volume (cm^3/g)	Pore diameter (nm)
Lecithin-nano Ni/Fe	16.24	0.0694	17.10
Nanolecithin	15.38	0.0542	14.10
Lecithin powder	1.725	0.00201	4.66

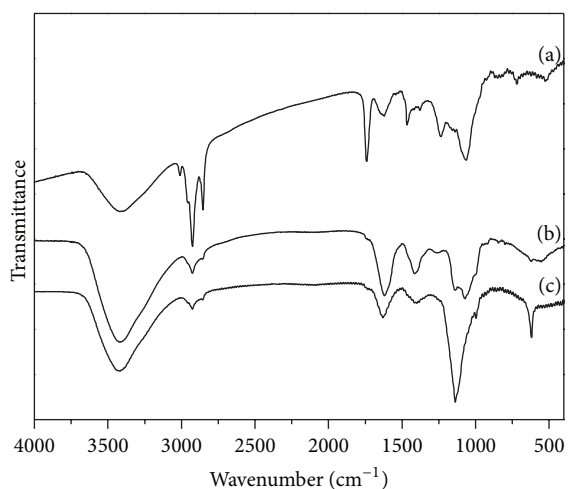


FIGURE 5: FT-IR spectra of (a) lecithin powder, (b) nanolecithin, and (c) lecithin-nano Ni/Fe.

by the interstices from the loading of bimetallic nanoparticles, which will profit the interaction between lecithin-nano Ni/Fe and PCB77 during removal process. However, the inconspicuous difference represented the insufficiently loading amount of bimetallic nanoparticles which resulted in only a thin loading layer on the surface. This problem was possibly caused by the limited content of water for the microemulsion which was difficult to solve and probably affected the efficacy of the designed material in removing PCB77.

3.4. FT-IR Spectroscopy. The typical adsorption bands of various functional groups, respectively, for lecithin-nano Ni/Fe, nanolecithin, and lecithin powder were shown in Figure 5. From the spectrum of nanolecithin, it was observed that the notable absorbance peaks at 1620 cm^{-1} and 1418 cm^{-1} correspond to the asymmetrical and symmetrical stretching vibrations of C=O groups [28]. The absorbance peaks at 2926 cm^{-1} and 2854 cm^{-1} were assigned to the asymmetrical and symmetrical stretching vibrations of CH_2 groups. The broad band at 3419 cm^{-1} was attributed to the presence of water. The characteristic peaks at 1138 cm^{-1} and 1072 cm^{-1} were typical of PO_2^- group which was attributed to the P=O and P-O stretches. Considering the neat composition of nanolecithin, all of the peaks above represented the character of lecithin. Although the spectrum of raw powder presented relative absorbance as aforementioned involving the peaks at

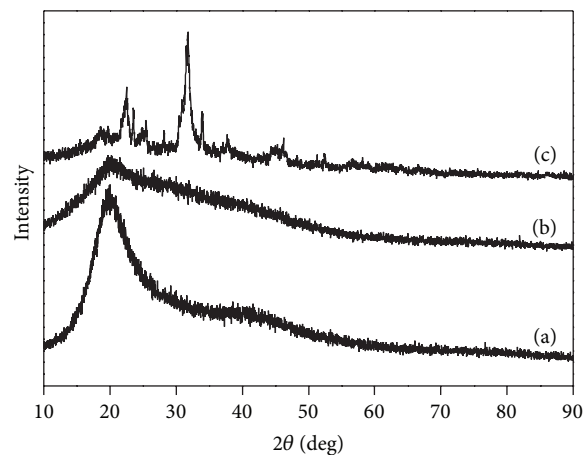


FIGURE 6: XRD patterns of (a) lecithin powder, (b) nanolecithin, and (c) lecithin-nano Ni/Fe.

3406 cm^{-1} , 1236 cm^{-1} , and 1065 cm^{-1} , it had some differences in the regions in carbonyl stretching and methylene stretching. The asymmetrical and symmetrical stretches of C=O groups had shifted to 1622 cm^{-1} and 1426 cm^{-1} with a split peak at 1739 cm^{-1} , while those of CH_2 groups intensified with split peaks at 2956 cm^{-1} and 3010 cm^{-1} [29]. It was predicted that the complex composition of the raw powder was purified through the deposition procedure, which correlated with the unitary adsorption bands of the nanocarrier with neat lecithin composition. The significant differences of spectra between lecithin-nano Ni/Fe and nanolecithin revealed the notable influence of the loading of Ni/Fe bimetal. Although the carbonyl stretches in lecithin-nano Ni/Fe were similar to those in nanolecithin, the characteristic peaks of PO_2^- group in nanolecithin had been obscured in lecithin-nano Ni/Fe due to the entity of a broad and intense band of the C-O ester at 1138 cm^{-1} . The presence of this new band was indicative of a change in the dielectric constant of the environment of the ester groups which was likely ascribed to the association of the lecithin carrier with the Ni/Fe nanoparticle. It was signified by the FT-IR spectra that there was notable interaction of bimetal with lecithin which promoted the stable combination and effective loading of nanoparticles on the carrier.

3.5. XRD Patterns. The XRD patterns of all samples were displayed in Figure 6. The patterns of both nanolecithin and raw powder showed the same main diffraction peak appearing at 2θ value near 22° . While such a sole peak certainly corresponded to lecithin, it was more broad in the pattern of nanolecithin probably due to the broadening effect of the nanoscale. The loading of Ni/Fe nanoparticles afforded abundant diffraction peaks in the pattern of lecithin-nano Ni/Fe. Apart from the characteristic peak of lecithin, the main peaks at 2θ values of 28° , 32° , 38° , 44° , 52° , and 56° were related to the metallic component. It was suggested that lecithin-nano Ni/Fe had significantly distinguishing structure from

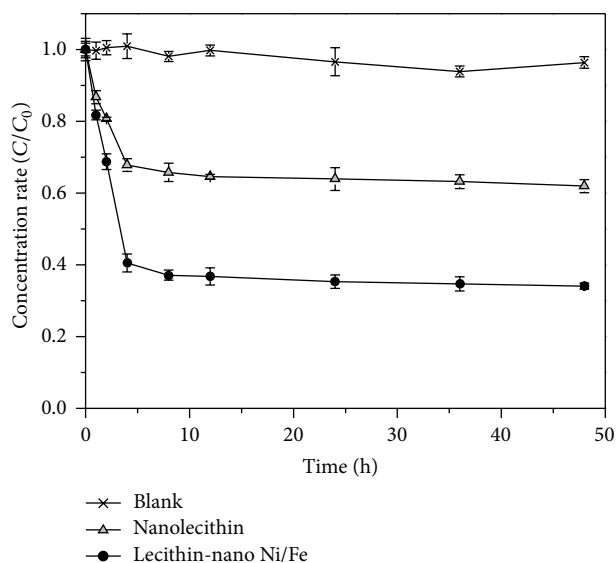


FIGURE 7: Removal of PCB77 in 50/50 (v/v) ethanol/water solution by lecithin-nano Ni/Fe and nanolecithin.

the other samples through the effective loading of metallic particles. However, the characteristic peaks of metallic oxide, especially the intensity peak at 32° , exhibited the apparent oxidation extent of iron. The oxidation was possibly ascribed to the exposure of the active nanoparticles and will affect their reductive ability.

3.6. Removal of PCB77. The efficacy of different materials in removing PCB77 in 50/50 (v/v) ethanol/water solution was depicted in Figure 7. Approximately 67% of PCB77 was removed from the solution in 48 h by lecithin-nano Ni/Fe, while 39% of PCB77 was removed by nanolecithin. Since parallel experiment of laboratory blank indicated insignificant leakage, it was confirmed that nanolecithin had a certain activity to remove PCB77 as the blank carrier. The removal efficacy will further be improved by the Ni/Fe nanoparticles loading on the carriers. Compared to nanolecithin, lecithin-nano Ni/Fe was able to decrease the concentration of PCB77 to a lower level in the same short period, which finally resulted in the lower residuary ratio. The synergistic effect of bi-metal and lecithin apparently contributed to the rapid removal of PCB77 at the beginning. However, the favorable trend for the removal was slowed down after 4 h of experiment to achieve an almost constant concentration of PCB77. The limited loading content and difficultly escapable oxidation of the small bimetallic particles that had been revealed by part of the characterization presumably caused the rapid exhaustion of the activity. Although the function of the lecithin-nano Ni/Fe still required to be improved, the rapid removal process at the beginning indicated the potentiality for the research of such an original combined material. Considering that the preliminary effectiveness of the combined material was proved in this work, the constitution should be optimized in the future for the better stabilization and loading

efficiency of Ni/Fe nanoparticles on the carrier, which will make the further researches about lecithin-nano Ni/Fe more attractive.

4. Conclusion

In this literature, lecithin carriers were loading Ni/Fe nanoparticles through microemulsion method to generate a kind of combined material named lecithin-nano Ni/Fe. Lecithin participated in the composition of the microemulsion template that directed the synthesis of subtle Ni/Fe nanoparticles and then formed the carrier through the deposition with the insite loading of bimetal. Besides the above role, lecithin, as an environmentally compatible biosurfactant, had a certain ability to accumulate organic contaminants, which was beneficial for the removal of the contaminants by Ni/Fe nanoparticles. It was proved by the characterization that Ni/Fe nanoparticles can be uniformly dispersed and closely combined with lecithin carrier which indicated the successful generation of lecithin-nano Ni/Fe. The synergistic effect of lecithin and Ni/Fe nanoparticles was examined through the removal experiment of PCB77, while parallel test for the blank carrier of nanolecithin was operated as comparison. The preliminary functionality of lecithin-nano Ni/Fe was supported by the more rapid removal of PCB77 at the beginning. Although it still required improvement owing to the exhaustion of activity in a relatively short period, lecithin-nano Ni/Fe represented a beneficial attempt to acquire the combined material with the advantages of both the biosurfactant and the bimetal. The original synthetic method described in this paper was convenient with the stuff that was abundant, inexpensive, and relatively low toxic. It was prospective that this work can be the evocation for the development of innovative decontaminant and similar organic-inorganic combined material.

Conflict of Interests

The authors declare that there is no conflict of interests.

Acknowledgment

This work was supported by National Natural Science Foundation of China (21076140).

References

- [1] J. H. Li, N. N. Zhao, X. Liu, and X. Y. Wu, "Achieving target of Stockholm Convention on PCBs elimination: Asia-Pacific case," in *Proceedings of the International Conference on Management Science and Engineering (ICMSE '13)*, pp. 2147–2154, 2013.
- [2] D. Megson, G. O'Sullivan, S. Comber et al., "Elucidating the structural properties that influence the persistence of PCBs in humans using the National Health and Nutrition Examination Survey (NHANES) dataset," *Science of the Total Environment*, vol. 461-462, pp. 99–107, 2013.

- [3] A. Ruus, I. A. Daae, and K. Hylland, "Accumulation of polychlorinated biphenyls from contaminated sediment by Atlantic cod (*Gadus morhua*): direct accumulation from resuspended sediment and dietary accumulation via the polychaete *Nereis virens*," *Environmental Toxicology and Chemistry*, vol. 31, no. 11, pp. 2472–2481, 2012.
- [4] M. Olufsen and A. Arukwe, "Developmental effects related to angiogenesis and osteogenic differentiation in Salmon larvae continuously exposed to dioxin-like 3, 3', 4, 4'-tetrachlorobiphenyl (congener 77)," *Aquatic Toxicology*, vol. 105, no. 3–4, pp. 669–680, 2011.
- [5] X. Liu, Z. Chen, Z. Chen, M. Megharaj, and R. Naidu, "Remediation of Direct Black G in wastewater using kaolin-supported bimetallic Fe/Ni nanoparticles," *Chemical Engineering Journal*, vol. 223, pp. 764–771, 2013.
- [6] S. Mossa Hosseini, B. Ataie-Ashtiani, and M. Kholghi, "Nitrate reduction by nano-Fe/Cu particles in packed column," *Desalination*, vol. 276, no. 1–3, pp. 214–221, 2011.
- [7] X. Wang, M. Zhu, H. Liu, J. Ma, and F. Li, "Modification of Pd-Fe nanoparticles for catalytic dechlorination of 2, 4-dichlorophenol," *Science of the Total Environment*, vol. 449, pp. 157–167, 2013.
- [8] E. M. Zahran, D. Bhattacharyya, and L. G. Bachas, "Reactivity of Pd/Fe bimetallic nanotubes in dechlorination of coplanar polychlorinated biphenyls," *Chemosphere*, vol. 91, no. 2, pp. 165–171, 2013.
- [9] S. K. Singh, A. K. Singh, K. Aranishi, and Q. Xu, "Noble-metal-free bimetallic nanoparticle-catalyzed selective hydrogen generation from hydrous hydrazine for chemical hydrogen storage," *Journal of the American Chemical Society*, vol. 133, no. 49, pp. 19638–19641, 2011.
- [10] Y. Gao, H. Yang, X. Zhan, and L. Zhou, "Scavenging of BHCs and DDTs from soil by thermal desorption and solvent washing," *Environmental Science and Pollution Research*, vol. 20, no. 3, pp. 1482–1492, 2013.
- [11] A. Singh and S. Cameotra, "Efficiency of lipopeptide biosurfactants in removal of petroleum hydrocarbons and heavy metals from contaminated soil," *Environmental Science and Pollution Research*, vol. 20, no. 10, pp. 7367–7376, 2013.
- [12] E. Ceschia, J. R. Harjani, C. Liang et al., "Switchable anionic surfactants for the remediation of oil-contaminated sand by soil washing," *RSC Advances*, vol. 4, no. 9, pp. 4638–4645, 2014.
- [13] N. Manickam, A. Bajaj, H. S. Saini, and R. Shanker, "Surfactant mediated enhanced biodegradation of hexachlorocyclohexane (HCH) isomers by *Sphingomonas* sp. NM05," *Biodegradation*, vol. 23, no. 5, pp. 673–682, 2012.
- [14] S. Mohanty and S. Mukherji, "Surfactant aided biodegradation of NAPLs by *Burkholderia multivorans*: comparison between Triton X-100 and rhamnolipid JBR-515," *Colloids and Surfaces B: Biointerfaces*, vol. 102, pp. 644–652, 2013.
- [15] X. Y. Qv and J. G. Jiang, "Toxicity evaluation of two typical surfactants to *Dunaliella bardawil*, an environmentally tolerant alga," *Environmental Toxicology and Chemistry*, vol. 32, no. 2, pp. 426–433, 2013.
- [16] A. Azizullah, P. Richter, M. Jamil, and D. P. Häder, "Chronic toxicity of a laundry detergent to the freshwater flagellate *Euglena gracilis*," *Ecotoxicology*, vol. 21, no. 7, pp. 1957–1964, 2012.
- [17] M. Song and A. R. Bielefeldt, "Toxicity and inhibition of bacterial growth by series of alkylphenol polyethoxylate nonionic surfactants," *Journal of Hazardous Materials*, vol. 219–220, pp. 127–132, 2012.
- [18] P. Foley, A. Kermanshahi Pour, E. S. Beach, and J. B. Zimmerman, "Derivation and synthesis of renewable surfactants," *Chemical Society Reviews*, vol. 41, no. 4, pp. 1499–1518, 2012.
- [19] E. Kaczorek, "Effect of external addition of rhamnolipids biosurfactant on the modification of gram positive and gram negative bacteria cell surfaces during biodegradation of hydrocarbon fuel contamination," *Polish Journal of Environmental Studies*, vol. 21, no. 4, pp. 901–909, 2012.
- [20] X. Zhang, D. Xu, C. Zhu, T. Lundaa, and K. E. Scherr, "Isolation and identification of biosurfactant producing and crude oil degrading *Pseudomonas aeruginosa* strains," *Chemical Engineering Journal*, vol. 209, pp. 138–146, 2012.
- [21] R. M. Jain, K. Mody, A. Mishra, and B. Jha, "Physicochemical characterization of biosurfactant and its potential to remove oil from soil and cotton cloth," *Carbohydrate Polymers*, vol. 89, no. 4, pp. 1110–1116, 2012.
- [22] C. Zheng, M. Wang, Y. Wang, and Z. Huang, "Optimization of biosurfactant-mediated oil extraction from oil sludge," *Biore-source Technology*, vol. 110, pp. 338–342, 2012.
- [23] D. M. Cabezas, R. Madoery, B. W. K. Diehl, and M. C. Tomás, "Emulsifying properties of different modified sunflower lecithins," *Journal of the American Oil Chemists' Society*, vol. 89, no. 2, pp. 355–361, 2012.
- [24] A. Diab and M. Sandouka, "Effect of a phyto-genic biosurfactant on the microbial community and on the bioremediation of highly oil-polluted desert soil," *Journal of American Science*, vol. 8, no. 1, pp. 544–550, 2012.
- [25] F. Occulti, G. C. Roda, S. Berselli, and F. Fava, "Sustainable decontamination of an actual-site aged PCB-polluted soil through a biosurfactant-based washing followed by a photocatalytic treatment," *Biotechnology and Bioengineering*, vol. 99, no. 6, pp. 1525–1534, 2008.
- [26] F. Sahle, H. Metz, J. Wohlrab, and R. H. Neubert, "Lecithin-based microemulsions for targeted delivery of ceramide AP into the stratum corneum: formulation, characterizations, and in vitro release and penetration studies," *Pharmaceutical Research*, vol. 30, no. 2, pp. 538–551, 2013.
- [27] P. Fadda, M. Monduzzi, F. Caboi, S. Piras, and P. Lazzari, "Solid lipid nanoparticle preparation by a warm microemulsion based process: influence of microemulsion microstructure," *International Journal of Pharmaceutics*, vol. 446, no. 1–2, pp. 166–175, 2013.
- [28] C. Rosca, M. I. Popa, G. Lisa, and G. C. Chitanu, "Interaction of chitosan with natural or synthetic anionic polyelectrolytes. 1. The chitosan-carboxymethylcellulose complex," *Carbohydrate Polymers*, vol. 62, no. 1, pp. 35–41, 2005.
- [29] W. Jiang, J. A. Joens, D. D. Dionysiou, and K. E. O'Shea, "Optimization of photocatalytic performance of TiO₂ coated glass microspheres using response surface methodology and the application for degradation of dimethyl phthalate," *Journal of Photochemistry and Photobiology A: Chemistry*, vol. 262, pp. 7–13, 2013.

Research Article

Quantitative Fractal Evaluation of Herbicide Effects on the Water-Absorbing Capacity of Superabsorbent Polymers

Renkuan Liao, Shumei Ren, and Peiling Yang

College of Water Conservancy & Civil Engineering, China Agricultural University, Beijing, China

Correspondence should be addressed to Peiling Yang; yangpeiling@126.com

Received 15 January 2014; Revised 23 March 2014; Accepted 24 March 2014; Published 22 April 2014

Academic Editor: Haiqiang Wang

Copyright © 2014 Renkuan Liao et al. This is an open access article distributed under the Creative Commons Attribution License, which permits unrestricted use, distribution, and reproduction in any medium, provided the original work is properly cited.

The water absorption capacity of superabsorbent polymers (SAPs) is important for agricultural drought resistance. However, herbicides may leach into the soil and affect water absorption by damaging the SAP three-dimensional membrane structures. We used 100-mesh sieves, electron microscopy, and fractal theory to study swelling and water absorption in SAPs in the presence of three common herbicides (atrazine, alachlor, and tribenuron-methyl) at concentrations of 0.5, 1.0, and 2.0 mg/L. In the sieve experiments it was found that 2.0 mg/L atrazine reduces the capacity by 9.64–23.3% at different swelling points; no significant diminution was observed for the other herbicides or for lower atrazine concentrations. We found that the hydrogel membrane pore distributions have fractal characteristics in both deionized water and atrazine solution. The 2.0 mg/L atrazine destroyed the water-retaining polymer membrane pores and reduced the water-absorbing mass by modifying its three-dimensional membrane structure. A linear correlation was observed between the fractal analysis and the water-absorbing mass. Multifractal analysis characterized the membrane pore distribution by using the range of singularity indexes $\Delta\alpha$ (relative distinguishing range of 16.54–23.44%), which is superior to single-fractal analysis that uses the fractal dimension D (relative distinguishing range of 2.5–4.0%).

1. Introduction

Superabsorbent polymer (SAP) hydrogels are three-dimensional, crosslinked, linear, or branched polymers with a considerable number of hydrophilic groups that can absorb water, saline solutions, or physiological fluids in amounts as high as 10–1000 times their own weight [1, 2]. SAPs are ideal for use in water absorption applications in agriculture, forestry, construction, sanitation, biology, and medicine [3–6]. Their rapid and reversible water absorbency and biocompatibility enable usage in arid and semiarid environments for holding rain and irrigation water for plants in sandy or loamy soils that perform poorly in drought conditions [7, 8]. They also improve plant growth [9]. Agricultural polymers are usually applied at the root zone, and the retained water is not released from the network structure under normal physical pressure. However, when the soil is dry, the water is slowly released by root pressure, ensuring normal growth.

Large quantities of herbicides are introduced into farmland ecosystems every year; the global herbicide market accounted for half of the total pesticide market in 2010 [10].

Herbicides that migrate deep into the soil because of irrigation water and rainfall [11] may affect the water-absorbing capacity of SAPs by damaging their hydrogel membrane structure and micromorphology. Previous studies indicate that nutrient ions may reduce the absorbency of SAPs, and highly charged ions may modify SAP structures to the point of losing water-retaining capacity [12, 13]. Despite the concerns, there have been few reports concerning herbicide effects on the water-absorbing capacity, and the mechanisms are not clear.

After water absorption and swelling of the SAP, the three-dimensional hydrogel network is wrapped in a membrane structure to hold the water. The water is retained because of osmotic pressure and molecular forces. During swelling, the three-dimensional network unfolds continuously until it reaches equilibrium and stops absorbing water [14]. When the membrane structure is destroyed, the water stored in the internal network will be released, the SAP absorbency will be reduced, and the hydrogel will have a complex distribution of membrane pores. Therefore, to reveal the water-absorbing mechanism, studies on the hydrogel membrane pore

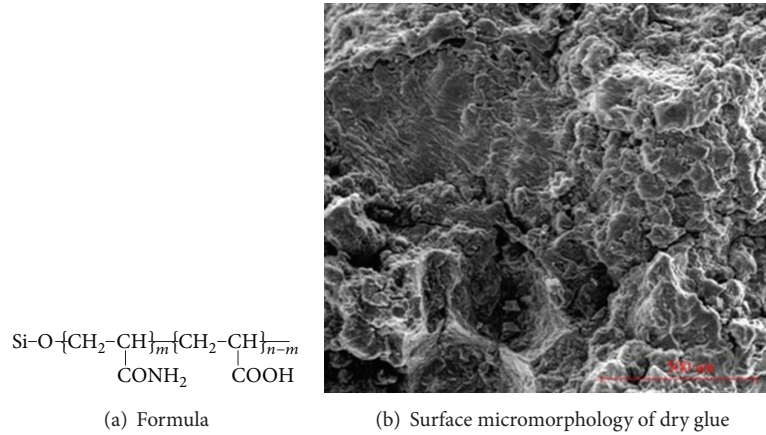


FIGURE 1: The formula and surface micromorphology of SAPs.

distributions of SAPs after absorption and swelling are very important [15]. However, the membrane pores are distributed randomly and have complicated shapes, making it difficult to correctly reveal the geometrical characteristics.

Fractal theory describes complex, natural, and nonlinear phenomena [16] and is used for shape structure characterization in non-Euclidean geometrical systems with complex structures and chaotic phenomena. Previous studies [15, 17, 18] show that, after water absorption and swelling in SAPs, the distribution of hydrogel membrane pores has fractal characteristics that can be described quantitatively. Here, fractal theory is used to characterize the micromorphology characteristics of the hydrogel and the mechanism of herbicide-induced deterioration of the SAP water-absorbing capacity. An agricultural SAP and three common herbicides are studied in 100-mesh sieve experiments, and images of the hydrogel membrane pore distribution are obtained with an environmental scanning electronic microscope (ESEM). The results provide a better understanding of the water absorption mechanisms of SAPs and enable future enhancements.

2. Materials and Methods

2.1. Experimental Materials. SAPs produced by HuaYe New Material Co., Ltd. (Shandong Province, China) were organic-inorganic composites of attapulgite clay in polyacrylamide-acrylic crosslinked polymers. They were faint yellow, 1.0–2.0 mm solid particles, with a moisture content $\leq 8\%$, a deionized water uptake of 100–700 g/g, and a 0.9% NaCl uptake ≥ 32 g/g. Its constitutional formula is shown in Figure 1(a) and the surface micromorphology of dry glue is shown in Figure 1(b).

Herbicides produced by American Standard Co., Ltd. (New Haven, CT, USA) were *atrazine* ($\text{C}_8\text{H}_{14}\text{ClN}_5$, 100% purity), *alachlor* ($\text{C}_{14}\text{H}_{20}\text{ClNO}_2$, 99.4% purity), and *tribenuron-methyl* ($\text{C}_{15}\text{H}_{17}\text{N}_5\text{O}_6\text{S}$, 99.5% purity).

2.2. Experimental Methods

2.2.1. Swelling Curves and Water Absorption Characteristics. The water absorption characteristics of SAPs were tested

by 100-mesh filtering. Solutions (0.5, 1, and 2 mg/L) of atrazine, alachlor, and tribenuron-methyl were prepared, and deionized water (0 mg/L) was used as a control. There were three replicas for each treatment. SAP (0.30 g) was added into 0.5 L solutions for swelling and filtering at time intervals of 2, 4, 6, 8, 10, 15, 20, 25, 30, and 40 min (every 10 min afterward) until equilibrium was established as determined by pretests. The mass of the SAP hydrogels was determined at the elapsed times to obtain the amount of water absorption.

2.2.2. Scanning Internal Micromorphology. A FEI Quanta 200 ESEM was used to characterize the SAP structures. A cutting blade was used to obtain the middle portion of the SAP hydrogels after the water absorption tests were performed. They were imaged in low-vacuum conditions (130 Pa) and with an acceleration voltage of 20 kV. Each 1024×678 -pixel image was stored as eight-bit grayscale files.

2.3. Analysis Methods

2.3.1. Fractal Dimension of Surface Topography. The fractal dimension D is a characteristic parameter that quantitatively describes the complex degree [12]. Slit island analysis [16] was used to calculate the fractal dimensions of the cross-sectional internal pore structure of SAP hydrogels, which can be formulated as

$$\alpha_D(\varepsilon) = \frac{L^{1/D}(\varepsilon)}{A^{1/2}(\varepsilon)}, \quad (1)$$

where L denotes the pore perimeter (μm); A denotes the pore area (μm^2); and D denotes the fractal dimension $\varepsilon = \eta/L_0$, where η is the absolute measurement scale, L_0 is the initial perimeter of the image with constant scale of η , and $\alpha_D(\varepsilon)$ is a constant and is only a function of the selected scale and not the image size. The logarithm for both sides of (1) is

$$\log L(\varepsilon) = D \log \alpha_D(\varepsilon) + \frac{D}{2} \log A(\varepsilon). \quad (2)$$

Image-Pro Software was used to analyze each ESEM image after digitizing and then used to measure the area and

perimeter of each pore. D is twice as large as the slope of the double-log curve between the area and the perimeter.

2.3.2. Multifractals and Singularity Spectra. Multifractal analysis takes a certain area or volume and decomposes it into a series of subdomains according to the singularity, and every subdomain forms a fractal. Multifractals not only have fractal dimensions but also have a singularity for each measurement. A multifractal singularity spectrum is the main parameter to quantitatively describe the nonuniformity, which can be expressed by $\alpha \sim f(\alpha)$ and $q \sim D(q)$. The relationship between $\alpha \sim f(\alpha)$ and $q \sim D(q)$ is obtained by the Legendre transform. The probability for the i th grid can be calculated from

$$\mu_i(\varepsilon) = \frac{N_i(\varepsilon)}{N_t}, \quad (3)$$

where ε is a set of different grids with square cells that is superimposed on the whole field studied, $N_i(\varepsilon)$ is the measurement of i , and N_t is the total measurement of the fractal set.

For multifractal distributed measurements, the partition function $\chi_q(\varepsilon) = \sum_{i=1}^{N(\varepsilon)} \mu_i(\varepsilon)^q$ scales with the cell size as

$$\chi_q(\varepsilon) \propto \varepsilon^{\tau(q)}, \quad (4)$$

where $\tau(q)$ is the mass exponent of the order q and can be estimated from the slope of best-fit line. The generalized fractal dimension $D(q)$ of uniformly distributed soil pores can be defined as

$$D(q) = \frac{\tau(q)}{(q-1)} = \lim_{\varepsilon \rightarrow 0} \frac{1}{q-1} \frac{\log \left[\sum_{i=1}^{N(\varepsilon)} \mu_i(\varepsilon)^q \right]}{\log \varepsilon} \quad (q \neq 1),$$

$$D_1 = \lim_{\varepsilon \rightarrow 0} \frac{\sum_{i=1}^{N(\varepsilon)} \mu_i(\varepsilon) \log \mu_i(\varepsilon)}{\log \varepsilon} \quad (q = 1). \quad (5)$$

From the Legendre transform, we obtain

$$\alpha(q) = \frac{\partial}{\partial q} \tau(q), \quad (6)$$

$$f(\alpha(q)) = q\alpha(q) - \tau(q),$$

where $q = 0, 1, 2$ and $D(q)$ corresponds to the fractal capacity dimension, the information dimension, and the correlation dimension, respectively [18]. The range of $D(q)$ increases with the slope $q \sim D(q)$ and indicates that the distribution ranges of different singularity strengths of fractal structures are wider, and the nonuniformity and complexity of the measured physical quantity are increased. From the above, it can be found that $q \sim D(q)$ and $\alpha \sim f(\alpha)$ are equivalent for describing multiple fractals, and the subset of different exponents can be discerned by changing the iterative order q . The span of singularity indexes $\Delta\alpha = \alpha_{\max} - \alpha_{\min}$ of multiple fractal singularity spectra can be used to characterize the degree of nonuniformity of SAP hydrogel pores distributions [19].

The calculations have the following steps. (1) Select a grid size ε and then measure and calculate the probability for each grid. (2) Choose a different q and calculate the partition function $\chi_q(\varepsilon)$. (3) Change the grid size ε and repeat the above process to calculate a series of $\chi_q(\varepsilon)$. (4) Trace the graph of $\ln(\chi_q(\varepsilon)) \sim \ln(\varepsilon)$. (5) For each q , calculate $\tau(q)$ by straight line fitting of $\chi_q(\varepsilon) \sim \varepsilon$. (6) Trace the graph of $\tau(q) \sim q$ and calculate D_q . (7) Calculate $\alpha(q)$ and $f(\alpha)$ with Legendre transforms and obtain the final multifractal spectrum $\alpha \sim f(\alpha)$.

2.3.3. Data Analysis. SPSS software (15.0, one-way analysis of variance) was used for correlation and significant structure analysis.

3. Results and Analysis

3.1. Swelling and Absorbency of Superabsorbent Polymers. Figure 2 plots the dynamic change of hydrogel weight after water absorption by SAPs in deionized water and in three different herbicide solutions. The “parabolic” shapes of the plots indicate that the absorbency is constantly changing and that the rate gradually reduces to a swelling equilibrium point (150 min) where absorption stops. From the significance tests in Table 1, there is no appreciable reduction of the water-absorbing mass for the SAPs ($P > 0.05$) for the three solutions of alachlor and tribenuron-methyl and for two of the atrazine solutions (0.5, 1 mg/L) at the equilibrium point. Only for the 2 mg/L atrazine solution is the water-absorbing mass of the SAP significantly reduced ($P < 0.05$).

Therefore, we examined the effect of the 2 mg/L atrazine on the SAP. In Figure 2, we can see that, for the 2 mg/L atrazine solution at 10, 40, 70, 100, and 150 min, the water-absorbing mass is reduced by 17.8%, 23.3%, 15.5%, 10.4%, and 9.64%, respectively. Thus the effect of atrazine is greater during the initial phase of absorption, that is, during the first 10–40 min. The effect is reduced with continued absorption and swelling (Table 2).

3.2. Micromorphology Characteristics of Hydrogel after Water and Atrazine Absorption. Figures 3(a)–3(e) are images of the SAP hydrogel surface micromorphology after 10, 40, 70, 100, and 150 min of swelling in deionized water, respectively. We can see that, with the SAP water absorption and swelling, the overlapping surface is a hydrogel with water stored in its three-dimensional, crosslinked membrane structure. At longer absorption times, the membrane structure is more pronounced. When the swelling membrane pore structure increases uniformly, the SAP can hold more water. In Figures 4(a)–4(e), the same development of hydrogel micromorphology is observed in 2 mg/L atrazine. However, in the atrazine, the SAP membrane pores are not uniformly enlarged with the swelling. Large pores develop after 40 min and increase steadily with swelling. Compared with the hierarchical, three-dimensional, crosslinked membrane structure (Figure 3(e)) in deionized water at the swelling equilibrium, there are damaging large pores in the hydrogel (Figure 4(e)) in the 2 mg/L atrazine solution.

TABLE 1: Water-absorbing mass (WAM) of SAP (0.3 g) at swelling equilibrium.

Mass concentration/(mg·L ⁻¹)	Water-absorbing mass/g		
	Atrazine	Alachlor	Tribenuron-methyl
0	67.27 ^a	67.27 ^a	67.27 ^a
0.5	63.55 ^{ab}	65.23 ^a	65.76 ^a
1.0	63.49 ^{ab}	66.19 ^a	66.04 ^a
2.0	60.79 ^b	65.66 ^a	65.55 ^a

Within the columns, values followed by the same letter are not significantly different at the 0.05 probability level.

TABLE 2: Water-absorbing mass (WAM) of SAP (0.3 g) in deionized water and atrazine solution at different swelling times.

Swelling time/min	Atrazine mass concentration/mg·L ⁻¹			
	0	SD	2.0	SD
	WAM/g		WAM/g	
10	18.45	±0.46	15.16	±0.30
40	48.21	±2.46	37.00	±1.82
70	57.80	±1.41	48.83	±1.45
100	62.11	±1.99	55.63	±0.45
150	67.27	±1.43	60.79	±1.11

SD means the standard deviation.

3.3. Single Fractal Feature of Surface Micromorphology of Superabsorbent Polymers. Table 3 lists the single fractal characteristic parameters (or single fractal dimension) D and the correlation coefficients R^2 from the correlative analysis of $\log L(\epsilon) \sim \log A(\epsilon)$ on the SAP hydrogel membrane pore distributions in deionized water and in the 2 mg/L atrazine solution at different swelling points. A significant correlation ($P < 0.01$) is observed, which indicates that it is valid to use fractal theory in the analysis of hydrogel micromorphology. In addition, we can see that, for both the deionized water and atrazine solutions, D increases gradually with SAP absorption and swelling. At various swelling points, the atrazine solution reduces D relative to that in deionized water. In Figure 5, there is a linear correlation ($P < 0.05$) between D and the SAP water-absorbing mass, which indicates that D can reflect the change in water-absorbing mass.

The water held by SAPs is mainly stored in the crosslinked membrane pore structure. The membrane structure and its pore have a direct effect on the water-absorbing capacity. Small values of the D index indicate less complexity in the membrane pore distribution and less water-absorbing mass. However, we find that the use of D to quantitatively characterize the micromorphology and the SAP water-absorbing capacity is limited. Comparing the different atrazine concentrations at the same state of swelling, we see that the relative discrimination is only 2.5–4.0%, while for the same atrazine concentrations at different swelling times, the accumulated relative discrimination is 7.0–8.5%. All of them indicate that the membrane pore distribution characteristics of the hydrogels, as analyzed by single fractal theory, are close and need a more sensitive characteristic index.

3.4. Multifractal Characteristics of Surface Micromorphology of Superabsorbent Polymer. Table 4 lists the general multifractal dimensions Dq and the correlation coefficients R^2 for

the correlative analysis of $\ln(\chi_q(\epsilon)) \sim \ln(\epsilon)$ for hydrogel membrane pore distributions in deionized water and the 2 mg/L atrazine solutions at different swelling points. A significant correlation ($P < 0.05$) is observed and indicates that multifractal theory is also valid in the analysis on hydrogel micromorphology. Table 5 lists the multifractal characteristic parameters (the singularity index span) Δa for the hydrogel membrane pore distributions in deionized water and atrazine solutions at different swelling points. The linear correlation ($P < 0.05$) indicates that Δa more clearly reflects (relative to D) the change in SAP water-absorbing mass (Figure 6). For different atrazine concentrations at the same swellings, the relative discrimination is 16.54–23.44%, while for the same atrazine concentrations at different swellings, the accumulated relative discrimination is 25.02–33.04%. Both are higher than those obtained from the D index (above).

4. Discussion

The key factors for the absorbency and swelling characteristics of SAPs are the additive compounds. Liang et al. [20] examined the effect of wheat straw in SAPs and found that the highest water absorbency was obtained with 20% wheat straw in the feed. Wang et al. [21, 22] reported that the SAPs containing 15 wt% sodium humate had the highest water absorbency with natural guar gum, partially neutralized acrylic acid, and sodium humate as the raw materials; moreover, the absorbency was improved further by adding cation-exchanged vermiculite. Here, the SAP was produced by adding attapulgite clay to the polyacrylamide-acrylic crosslinked polymer. The absorbency in deionized water is 224 g/g, which is less than that of SAPs using attapulgite clay as reported by Liu et al. [23]. That is because the SAP here is an agricultural water absorbent that requires a stable crosslinked structure to enhance reversible absorbency,

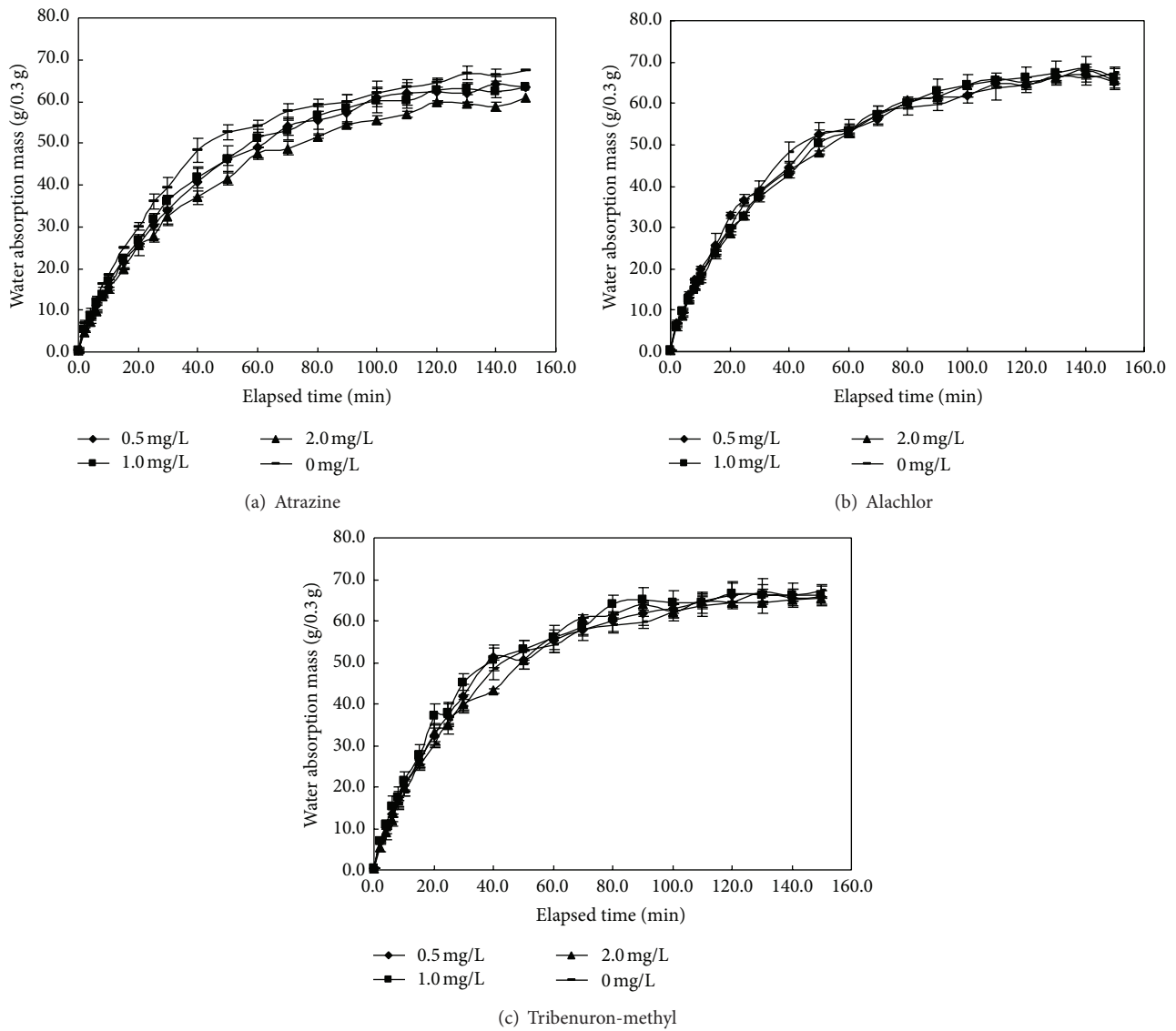


FIGURE 2: Swelling curves of SAP in three herbicide solutions.

TABLE 3: Single fractal dimension D of SAP hydrogel microtopography at different swelling times.

Swelling time/min	Atrazine mass concentration/ $\text{mg}\cdot\text{L}^{-1}$				Relative discrimination/%
	0		2		
	D	R^2	D	R^2	
10	1.072	0.962**	1.029	0.951**	4.0
40	1.091	0.947**	1.047	0.957**	4.0
70	1.115	0.952**	1.081	0.924**	3.0
100	1.139	0.954**	1.109	0.950**	2.6
150	1.151	0.939**	1.122	0.956**	2.5
Accumulated relative discrimination/%	7.0		8.5		

Correlation is significant at the 0.01 level “**” (two-tailed).

Relative discrimination = $(x_2 - x_0)/x_0$; accumulated relative discrimination = $\sum(x_{i+1} - x_i)/x_i$.

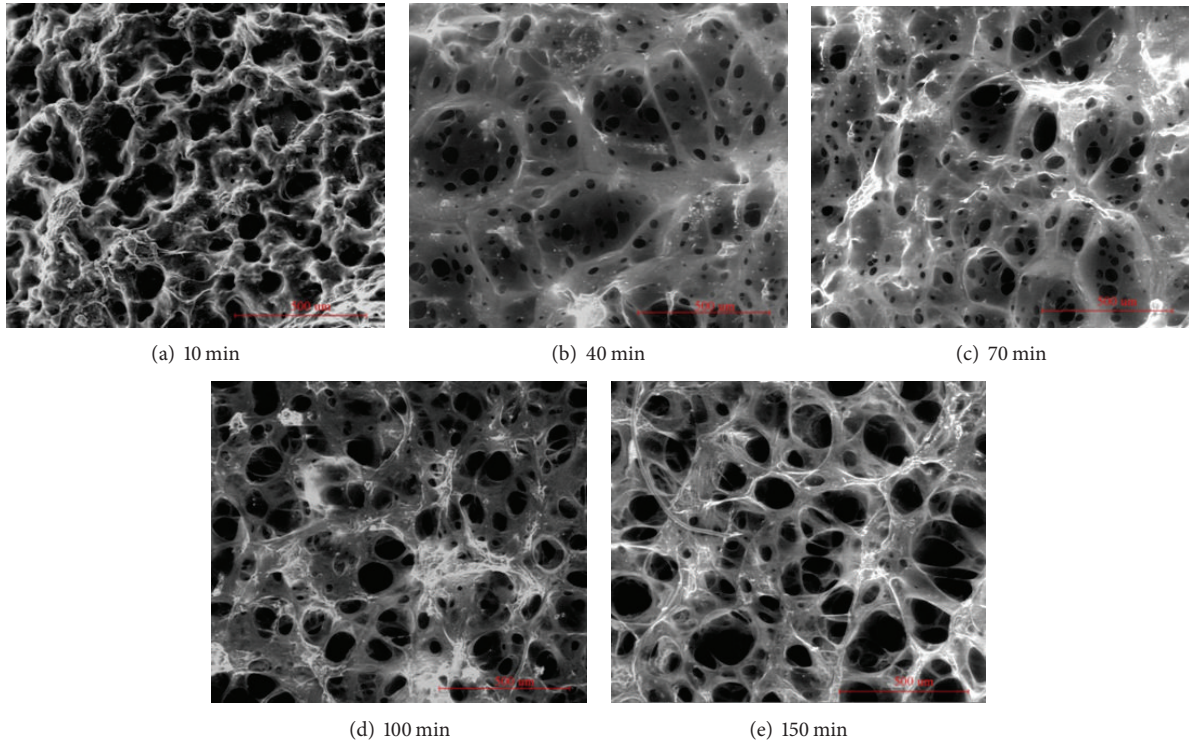


FIGURE 3: Hydrogel microtopography of SAP in deionized water.

TABLE 4: Generalized multifractal dimension Dq for SAP hydrogel microtopography at different swelling times.

Atrazine/ $\text{mg}\cdot\text{L}^{-1}$	Swelling/min	q											
		1	3	5	7	9	0	-1	-3	-5	-7	-9	
0	10	Dq	1.919	1.902	1.898	1.897	1.898	1.953	2.047	2.223	2.311	2.356	2.383
		R^2	0.99**	0.99**	0.99**	0.99**	0.99**	0.99**	0.98**	0.90**	0.87**	0.85**	0.84**
	40	Dq	1.987	1.981	1.981	1.981	1.982	2.008	2.103	2.314	2.413	2.463	2.494
		R^2	0.99**	0.99**	0.99**	0.99**	0.99**	0.99**	0.98**	0.93**	0.91**	0.90**	0.89**
	70	Dq	1.993	1.984	1.983	1.983	1.983	2.013	2.104	2.337	2.446	2.503	2.536
		R^2	0.99**	0.99**	0.99**	0.99**	0.99**	0.99**	0.99**	0.94**	0.92**	0.91**	0.90**
	100	Dq	2.059	2.055	2.053	2.052	2.052	2.068	2.116	2.366	2.500	2.569	2.609
		R^2	0.99**	0.99**	0.99**	0.99**	0.99**	0.99**	0.99**	0.97**	0.95**	0.94**	0.94**
	150	Dq	2.078	2.071	2.068	2.067	2.067	2.089	2.137	2.399	2.541	2.614	2.657
		R^2	0.99**	0.99**	0.99**	0.99**	0.99**	0.99**	0.99**	0.95**	0.92**	0.91**	0.91**
2	10	Dq	1.806	1.800	1.803	1.805	1.808	1.838	1.927	2.063	2.125	2.157	2.176
		R^2	0.99**	0.99**	0.99**	0.99**	0.99**	0.99**	0.95**	0.83*	0.79*	0.77*	0.76*
	40	Dq	1.821	1.814	1.816	1.819	1.821	1.853	1.949	2.102	2.170	2.203	2.223
		R^2	0.99**	0.99**	0.99**	0.99**	0.99**	0.99**	0.96**	0.86**	0.83*	0.82*	0.81*
	70	Dq	1.941	1.934	1.933	1.932	1.932	1.962	2.040	2.219	2.301	2.343	2.369
		R^2	0.99**	0.99**	0.99**	0.99**	0.99**	0.99**	0.97**	0.90**	0.88**	0.87**	0.86**
	100	Dq	2.006	2.001	2.002	2.003	2.004	2.023	2.096	2.282	2.380	2.430	2.460
		R^2	0.99**	0.99**	0.99**	0.99**	0.99**	0.99**	0.98**	0.90**	0.87**	0.85**	0.84**
	150	Dq	2.008	2.005	2.004	2.005	2.005	2.023	2.106	2.329	2.433	2.486	2.518
		R^2	0.99**	0.99**	0.99**	0.99**	0.99**	0.99**	0.99**	0.93**	0.92**	0.91**	0.90**

Correlation is significant at the 0.01 level “***” and 0.05 level “**” (two-tailed).

TABLE 5: Multifractal characteristic parameter Δa of SAP hydrogel microtopography at different swelling times.

Swelling time/min	Atrazine mass concentration/mg·L ⁻¹						Relative discrimination/%
	0			2			
	$a(q)_{\max}$	$a(q)_{\min}$	Δa	$a(q)_{\max}$	$a(q)_{\min}$	Δa	
10	2.491	1.898	0.593	2.254	1.800	0.454	23.44
40	2.616	1.980	0.636	2.306	1.814	0.492	22.64
70	2.671	1.982	0.689	2.470	1.932	0.538	21.92
100	2.775	2.052	0.723	2.582	2.001	0.581	19.64
150	2.834	2.066	0.768	2.646	2.004	0.642	16.54
Accumulated relative discrimination/%			25.02			33.04	

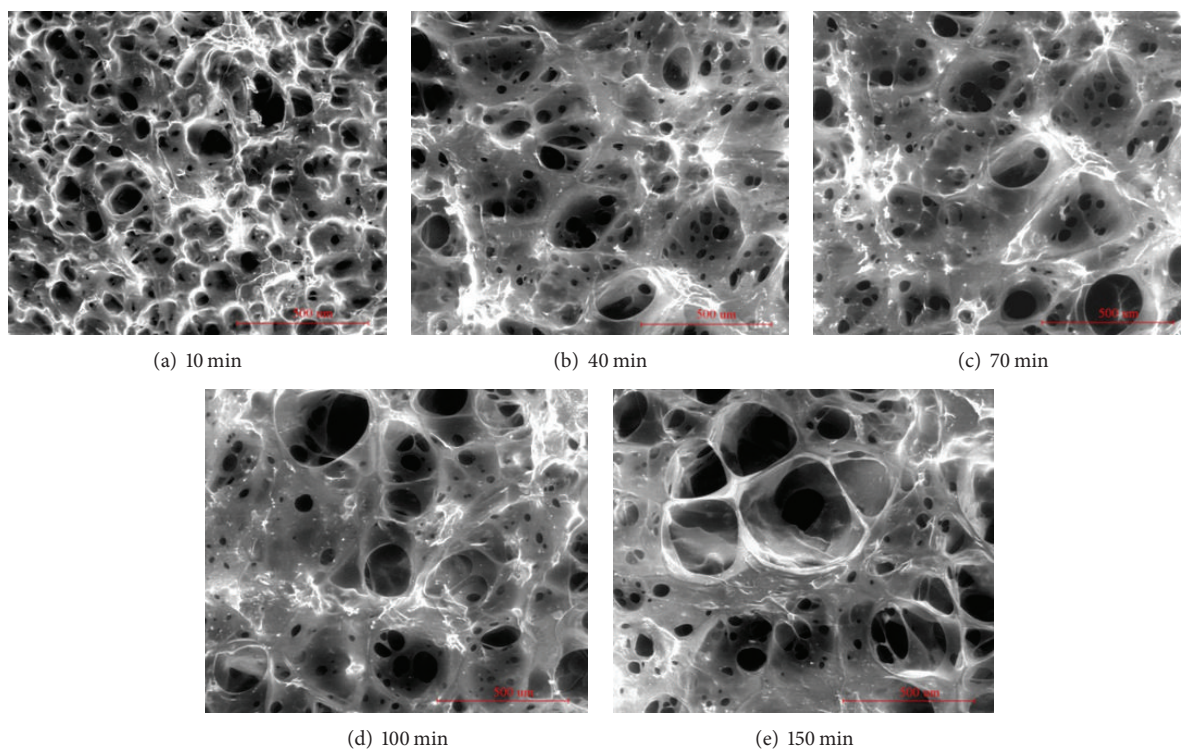


FIGURE 4: Hydrogel microtopography of SAP in 2 mg/L atrazine solutions.

rather than attapulgite clay. The absorbency of SAPs is influenced by many other factors, such as particle size, temperature, soil texture [24, 25], and other soil conditions. Electrolytes in soils can have appreciable impact on SAP absorbency, depending on ion type and concentration [26, 27]. Because SAPs have hydrophilic groups, they may have a stronger interaction with polar molecules and thus make the absorbency more sensitive. Here, the 2 mg/L atrazine solution significantly reduces the water-absorbing mass of the SAP. ESEM imaging reveals that, relative to those structures in deionized water, damaged membrane structures are observed in 2 mg/L atrazine solution. These are caused by hydrogen bonding and Van der Waals interactions among the atrazine and the hydroxyl and carboxyl groups of the SAP [28]. These interactions induce large-scale damage to the membrane, resulting in reduced water-absorbing mass.

In the fractal analysis, Δa becomes larger with SAP water absorption and swelling. At various swelling points in 2 mg/L atrazine, all Δa indices for the hydrogel microtopography are smaller relative to deionized water. This correlates with the D index observations and with the change in water-absorbing mass. In contrast to the 2.5–4.0% relative discrimination for the D index, that of Δa is 16.54%–23.44%. Thus fractal analysis over multiple scales is more sensitive than that in a single scale. In addition, multifractal analysis can reveal specific structures and characteristics induced by different local conditions or levels. It will reveal overall features from part of the system, which is more accurate than a single fractal describing complex morphology [19, 29, 30]. Moreover, no other quantification methods are effective in evaluating the hydrogel membrane pore distribution. The fractal analysis supports the notion that the membrane pore

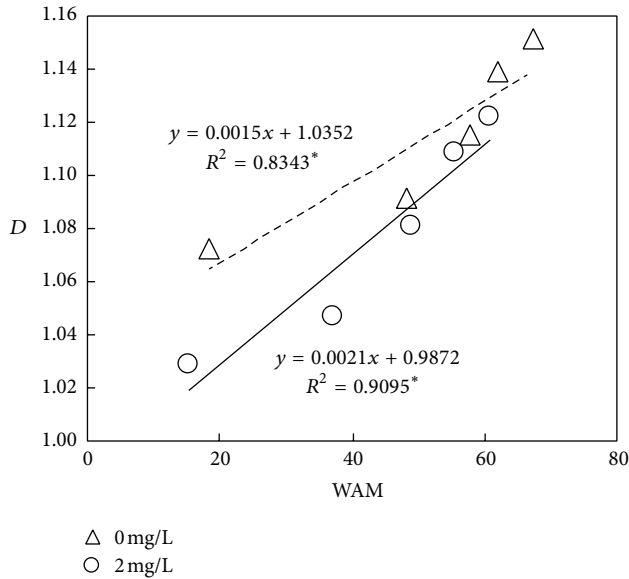


FIGURE 5: Correlation analysis between D and WAM.

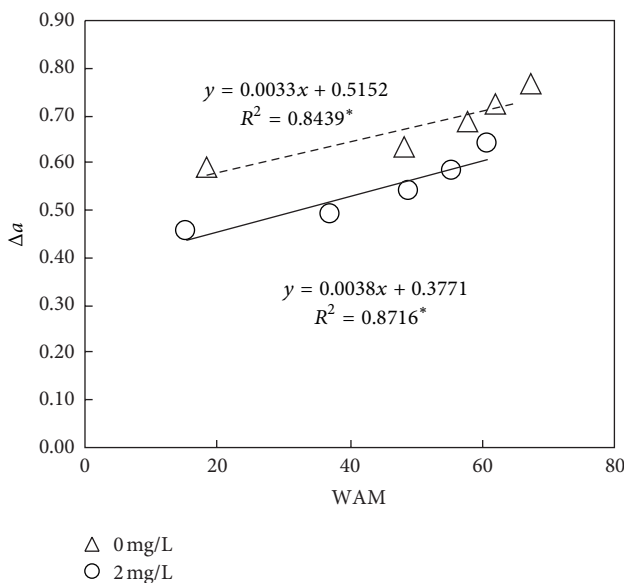


FIGURE 6: Correlation analysis between Δa and WAM.

three-dimensional structure unfolds continuously during water absorption and swelling [14]. Both the D and Δa indices in the 2 mg/L atrazine solution are less than those in deionized water, which confirms the notion that the forces between the atrazine and the hydroxyls and carboxyls in the SAP reduce the complexity of the membrane structure [28]. All of these conclusions are strongly supported by the SAP water-absorbing mass data. We can conclude that the combination of image analysis and fractal theory can be used to quantitatively evaluate the water-absorbing capacity of SAPs and could be applied to other areas in environmental and materials science. Fractal theory could also be used for evaluating nonlinear processes, such as soil pore distributions

for soil permeability and complex crystal structures. Finally, it could be used to design structures for materials fabrication that would have unique features.

5. Conclusions

- (1) Alachlor and tribenuron-methyl herbicides at concentrations of 0.5, 1, and 2 mg/L have no observable effects on the water-absorbing capacity of SAPs. Similarly, 0.5 and 1.0 mg/L solutions of atrazine have no effect. Only at 2 mg/L atrazine concentration will the SAP water-absorbing mass be significantly reduced. The effect gradually weakens with swelling of the SAP, and the relative reduction is 9.64%–23.3%.
- (2) The micromorphology of the hydrogel is changed to a hierarchical, three-dimensional, crosslinked membrane structure following SAP swelling in deionized water. The membrane pores grow uniformly with water absorption and swelling. However, in the 2.0 mg/L atrazine solution, larger pores are observed during swelling tales and the membrane structure is destroyed at the swelling equilibrium point.
- (3) Fractal analysis reveals clear differences in the hydrogel membrane pore distributions formed during water absorption and swelling in deionized water versus 2.0 mg/L atrazine. The single fractal dimension D index gradually increases less with swelling in atrazine solution relative to that in deionized water. Along with the micromorphology characteristics of the hydrogel, the 2.0 mg/L atrazine solution may destroy the membrane structure that retains the water. This reduces both the complexity of the three-dimensional membrane structure and the water-absorbing mass of the SAP.
- (4) Compared with single fractal analysis, multifractal analysis enables a more detailed characterization of the hydrogel membrane pore distribution and improves the ability to distinguish effects of the atrazine on the SAP water-absorbing mass from 2.5–4.0% to 16.54–23.44%. Furthermore, both the D and Δa indices exhibit a significant linear correlation with the water-absorbing mass.

Conflict of Interests

The authors declare that there is no conflict of interests regarding the publication of this paper.

Acknowledgment

This work was financially supported by the National Natural Science Foundation of China (51379210).

References

- [1] M. J. Ramazani-Harandi, M. J. Zohuriaan-Mehr, A. A. Yousefi, A. Ershad-Langroudi, and K. Kabiri, "Rheological determination of the swollen gel strength of superabsorbent polymer hydrogels," *Polymer Testing*, vol. 25, no. 4, pp. 470–474, 2006.

- [2] A. Pourjavadi, M. Ayyari, and M. S. Amini-Fazl, "Taguchi optimized synthesis of collagen-g-poly(acrylic acid)/kaolin composite superabsorbent hydrogel," *European Polymer Journal*, vol. 44, no. 4, pp. 1209–1216, 2008.
- [3] F. L. Zhang, M. Z. Liu, M. Y. Guo, and L. Wu, "Preparation of superabsorbent polymer with slow-release phosphate fertilizer," *Journal of Applied Polymer Science*, vol. 92, no. 5, pp. 3417–3421, 2004.
- [4] A. Hüttermann, L. J. B. Orikiriza, and H. Agaba, "Application of superabsorbent polymers for improving the ecological chemistry of degraded or polluted lands," *Clean—Soil, Air, Water*, vol. 37, no. 7, pp. 517–526, 2009.
- [5] M. A. Molina, C. R. Rivarola, and C. A. Barbero, "Study on partition and release of molecules in superabsorbent thermosensitive nanocomposites," *Polymer*, vol. 53, no. 2, pp. 445–453, 2012.
- [6] A. Hebeish, M. Hashem, M. M. El-Hady et al., "Development of CMC hydrogels loaded with silver nano-particles for medical applications," *Carbohydrate Polymers*, vol. 92, no. 1, pp. 407–413, 2013.
- [7] J. Akhter, K. Mahmood, K. A. Malik, A. Mardan, M. Ahmad, and M. M. Iqbal, "Effects of hydrogel amendment on water storage of sandy loam and loam soils and seedling growth of barley, wheat and chickpea," *Plant, Soil and Environment*, vol. 50, no. 10, pp. 463–469, 2004.
- [8] V. Arbona, D. J. Iglesias, J. Jacas, E. Primo-Millo, M. Talon, and A. Gómez-Cadenas, "Hydrogel substrate amendment alleviates drought effects on young citrus plants," *Plant and Soil*, vol. 270, no. 1, pp. 73–82, 2005.
- [9] S. S. Dorraji, A. Golchin, and S. Ahmadi, "The effects of hydrophilic polymer and soil salinity on corn growth in sandy and loamy soils," *Clean—Soil, Air, Water*, vol. 38, no. 7, pp. 584–591, 2010.
- [10] L. Zhao, S. M. Luo, H. S. Li et al., "Eco-toxicological effects of four herbicides on typical aquatic snail *Pomacea canaliculata* and Crown conchs," *Acta Ecologica Sinica*, vol. 31, no. 19, pp. 5720–5727, 2011.
- [11] V. C. Albright III, I. J. Murphy, J. A. Anderson et al., "Fate of atrazine in switchgrass-soil column system," *Chemosphere*, vol. 90, no. 6, pp. 1847–1853, 2013.
- [12] B. Zhou, R. K. Liao, Y. K. Li et al., "Water-absorption characteristics of organic-inorganic composite superabsorbent polymers and its effect on summer maize root growth," *Journal of Applied Polymer Science*, vol. 126, pp. 423–435, 2012.
- [13] W. B. Wang and A. Q. Wang, "Nanocomposite of carboxymethyl cellulose and attapulgite as a novel pH-sensitive superabsorbent: synthesis, characterization and properties," *Carbohydrate Polymers*, vol. 82, no. 1, pp. 83–91, 2010.
- [14] T. K. Mudiyansele and D. C. Neckers, "Highly absorbing superabsorbent polymer," *Journal of Polymer Science A: Polymer Chemistry*, vol. 46, no. 4, pp. 1357–1364, 2008.
- [15] Y. K. Li, T. W. Xu, Z. Y. Ouyang et al., "Micromorphology of macromolecular superabsorbent polymer and its fractal characteristics," *Journal of Applied Polymer Science*, vol. 113, no. 6, pp. 3510–3519, 2009.
- [16] B. B. Mandelbrot, D. E. Passoja, and A. J. Paullay, "Fractal character of fracture surfaces of metals," *Nature*, vol. 308, no. 5961, pp. 721–722, 1984.
- [17] A. Jurjua, T. Koslowski, C. von Ferbera et al., "Dynamics and scaling of polymer networks: vicsek fractals and hydrodynamic interactions," *Chemical Physics*, vol. 294, no. 2, pp. 187–199, 2003.
- [18] A. N. D. Posadas, D. Giménez, R. Quiroz, and R. Protz, "Multifractal characterization of soil pore systems," *Soil Science Society of America Journal*, vol. 67, no. 5, pp. 1361–1369, 2003.
- [19] Y. K. Li, Y. Z. Liu, G. B. Li et al., "Surface topographic characteristics of suspended particulates in reclaimed wastewater and effects on clogging in labyrinth drip irrigation emitters," *Irrigation Science*, vol. 30, no. 1, pp. 43–56, 2012.
- [20] R. Liang, H. B. Yuan, G. X. Xi et al., "Synthesis of wheat straw-g-poly(acrylic acid) superabsorbent composites and release of urea from it," *Carbohydrate Polymers*, vol. 77, no. 2, pp. 181–187, 2009.
- [21] W. B. Wang and A. Q. Wang, "Synthesis, swelling behaviors, and slow-release characteristics of a guar gum-g-poly(sodium acrylate)/sodium humate superabsorbent," *Journal of Applied Polymer Science*, vol. 112, no. 4, pp. 2102–2111, 2009.
- [22] W. B. Wang, N. H. Zhai, and A. Q. Wang, "Preparation and swelling characteristics of a superabsorbent nanocomposite based on natural guar gum and cation-modified vermiculite," *Journal of Applied Polymer Science*, vol. 119, no. 6, pp. 3675–3686, 2011.
- [23] R. F. Liu, J. P. Zhang, A. Q. Wang et al., "Water absorbency and its influence factor of PAM-atta superabsorbent composite," *Transactions of the Chinese Society of Agricultural Engineering*, vol. 21, no. 9, pp. 47–50, 2005.
- [24] K. Kabiri, S. Hesarian, M. J. Zohuriaan-Mehr et al., "Superabsorbent polymer composites: does clay always improve properties?" *Journal of Materials Science*, vol. 46, no. 20, pp. 6718–6725, 2011.
- [25] J. Yu, I. Shainberg, Y. L. Yan, J. G. Shi, G. J. Levy, and A. I. Mamedov, "Superabsorbents and semiarid soil properties affecting water absorption," *Soil Science Society of America Journal*, vol. 75, no. 6, pp. 2305–2313, 2011.
- [26] Y. Zhao, J. Kang, and T. W. Tan, "Salt-, pH- and temperature-responsive semi-interpenetrating polymer network hydrogel based on poly(aspartic acid) and poly(acrylic acid)," *Polymer*, vol. 47, no. 22, pp. 7702–7710, 2006.
- [27] H. A. Abd El-Rehim, E.-S. A. Hegazy, and H. L. Abd El-Mohdy, "Radiation synthesis of hydrogels to enhance sandy soils water retention and increase plant performance," *Journal of Applied Polymer Science*, vol. 93, no. 3, pp. 1360–1371, 2004.
- [28] W. C. Yang, Q. Q. Wang, and W. P. Liu, "Adsorption of herbicide atrazine on soils," *Chinese Journal of Environmental Science*, vol. 21, no. 4, pp. 94–97, 2000.
- [29] J. J. Francisco, G. RavéE, J. V. Giráldez et al., "The influence of the geometry of idealised porous media on the simulated flow velocity: a multifractal description," *Geoderma*, vol. 150, no. 1–2, pp. 196–204, 2009.
- [30] N. Bird, M. C. Diaz, A. Saa, and A. M. Tarquis, "Fractal and multifractal analysis of pore-scale images of soil," *Journal of Hydrology*, vol. 322, no. 1–4, pp. 211–219, 2006.

Research Article

Application of a Novel Semiconductor Catalyst, CT, in Degradation of Aromatic Pollutants in Wastewater: Phenol and Catechol

Xiao Chen,^{1,2} Yanling Zhang,³ Xuefei Zhou,² Shoji Ichimura,⁴ Guoxiu Tong,¹ Qiming Zhou,^{1,3} Xi Chen,⁵ Wenzhao Wang,³ and Yan Liang^{1,3,5,6}

¹ Department of Biology, Hong Kong Baptist University, Kowloon, Hong Kong

² College of Environmental Science & Engineering, Tongji University, Shanghai, China

³ Shenzhen Institutes of Advanced Technology, Chinese Academy of Sciences, Shenzhen 518055, China

⁴ FIRAC International Co., Ltd., 455-1 Fukude, Fukude-Cho Iwata-Gun, Shizuoka 437-1203, Japan

⁵ Xinjiang Institute of Ecology and Geography, Chinese Academy of Sciences, P.O. Box 9825, Beijing 100029, China

⁶ Laboratory for Food Safety and Environmental Technology, Institute of Biomedicine and Biotechnology, Shenzhen Institutes of Advanced Technology, Chinese Academy of Sciences, Shenzhen 518055, China

Correspondence should be addressed to Xuefei Zhou; zhouxuefei@tongji.edu.cn and Yan Liang; yan.liang@siat.ac.cn

Received 15 November 2013; Revised 10 February 2014; Accepted 10 February 2014; Published 14 April 2014

Academic Editor: Fan Dong

Copyright © 2014 Xiao Chen et al. This is an open access article distributed under the Creative Commons Attribution License, which permits unrestricted use, distribution, and reproduction in any medium, provided the original work is properly cited.

Water-soluble phenol and phenolic compounds were generally removed via advanced oxidation processes. A novel semiconductor catalyst, CT, was the first-time employed in the present study to degrade phenol and catechol. The phenolic compounds (initial concentration of 88 mg L⁻¹) were completely mineralized by the CT catalytic nanoparticles (1%) within 15 days, under acidic condition and with the presence of mild UV radiation (15 w, the emitted wavelength is 254 nm and the light intensity <26 μw/cm²). Under the same reaction condition, 1% TiO₂ (mixture of rutile and anatase, nanopowder, <100 nm) and H₂O₂ had lower removal efficiency (phenol: <42%; catechol: <60%), whereas the control (without addition of catalysts/H₂O₂) only showed <12% removal. The processes of phenol/catechol removal by CT followed pseudo-zero-order kinetics. The aromatic structures absorbed the UV energy and passed to an excited state, which the CT worked on. The pollutants were adsorbed on the CT's surface and oxidized via charge-transfer and hydroxyl radical generation by CT. Given low initial concentrations, a circumstance encountered in wastewater polishing, the current set-up should be an efficient and less energy- and chemical-consumptive treatment method.

1. Introduction

Phenol and phenolic substances, such as catechol and hydroquinone, are widely used as raw materials in petrochemical, chemical, and pharmaceutical industries [1]. They also occur in various common phenolated industrial effluents, with concentrations ranging between 35 and 8000 mg L⁻¹ [2]. These highly water-soluble and stable compounds are toxic, carcinogenic, mutagenic, and teratogenic [3] and potentially may lead to adverse effects in human and aquatic organisms [4]. Therefore, their concentrations in the industrial effluents are usually regulated. For example, in China, phenol at concentrations above 0.3 mg L⁻¹, respectively, is not allowed

to be discharged to the natural water bodies, according to the Integrated Wastewater Discharge Standard [5].

Treatment processes for phenolic wastewater include physical, biological, and chemical methods. High concentration phenolic wastewaters refer to those with phenol more than 1000 mg L⁻¹, which are recycled via methods such as adsorption or solvent extraction [6–8]. Intermediate concentration phenolic wastewaters are those with phenol levels between 5 and 500 mg L⁻¹, which are treated by biological methods [9] or chemical oxidation [10]. Generally speaking, it is practically impossible to remove phenol and phenolic substances simply by using conventional biologic treatment [11]. Advanced oxidation processes (AOPs) have been widely

used for the treatments over the last few decades. Particularly, AOPs combining oxidants (e.g., ozone and H_2O_2), UV radiation, catalysts (e.g., TiO_2 and V_2O_5), and ultrasound have received most of the attention [12]. For example, Gurol and Vatistas [13] treated mixtures of phenol, p-cresol, 2, 3-xyleneol, and catechol by ozone, UV light, and a combination of ozone and UV light (photolytic ozonation). They observed that the photolytic ozonation removed more than 95% of the total organic carbon (much higher than the <30% of the removal by ozonation and UV radiation alone). Li et al. [14] observed that phenol was oxidized rapidly by a $\text{Ti}/\text{SnO}_2\text{-Sb}$ anode, and its concentration decreased from around 490 mg/L to 0 after the electrolysis for 5 hr. Ügurlu and Karaoğlu [15] reported that more than 90% phenol was degraded within 24 hr using UV/ H_2O_2 and UV/ $\text{H}_2\text{O}_2/\text{TiO}_2/\text{Sepiolite}$, much greater than by simply using UV or H_2O_2 alone.

Despite the progress in AOPs research, it seems that practical applications of these AOPs have some limitations such as consumption of large amounts of chemicals (e.g., ozone and H_2O_2) and energy (UV and electrochemical oxidation) [16]. In this regard, we attempted to employ a novel catalyst, charge transfer auto oxidation-reduction type semiconductor catalyst (CT catalyst), for the degradation of phenol and phenolic substances. This nanosized (around 70 nm) material/crystal was developed by one of the authors, Dr. Shoji Ichimura, via sintering of a mixture of MnO , CoO , and TiO_2 in Pt and Pd complex powder at 1350°C [17]. CT is a crystal with an 8-phased perovskite form inside a 6-phased spinel structure. The core of the crystal has the base composition form with arranged electron donor and acceptor pair and electron carrier chain and oxidation/reduction center, which allows electron chain reactions to take place and be mediated. It simply relies on thermal energy to vibrate the crystal and cause electron transfer [17], which is different from photocatalysts, function with the presence of UV radiation [18]. With enough thermal energy, electron donor in CT produces electron (e^-) and positive hole (h^+). h^+ moves to oxidation centre in CT to oxidize the pollutant in solution motivated by oxidation activator. The electron moves to the electron acceptor in CT by electron carrier and then reaches the reduction centre in CT to reduce substances like oxygen in water motivated by reduction activator. This catalyst has been widely used in tiles in Japan (>8000 buildings as an environmentally friendly material for odor removal), but not in any other applications such as water/wastewater treatment. Yet, according to CT's remarkable characteristic that it can function in the dark, CT should have enormous potential in pollutant removal/degradation, especially in circumstances when light is not easily accessible in pollutant-carrying media (e.g., particles, cloudy water, and colored water). However, such chemical- and energy-saving applications have not been attempted previously.

In this study, we conducted experiments to degrade phenol and catechol in water using CT catalytic nanoparticles. A mild UV radiation (15 w, the emitted wavelength is 254 nm and the light intensity $<26 \mu\text{w}/\text{cm}^2$), not sufficient to induce effective photocatalysis in pure TiO_2 catalyst [1], was provided. The hypothesis was that, following exposure to UV

radiation, aromatic compounds would absorb the UV energy and reach excited state [19], upon which the CT catalysts could react (causing electron transfers). This eventually might lead to decomposition of these compounds. Compared with TiO_2 , we expected that CT might need low energy (mild UV radiation). Compared with H_2O_2 , CT catalyst might be more efficient, because hydroxyl radicals released by H_2O_2 should be depleted with a short period of time, not be sufficient to support the mineralization of these phenolic compounds.

Overall, the objectives of this study were as follows: (1) to identify whether CT catalyst can be applied in treating/removing phenolic compound in water; (2) to determine kinetics of the catalysis process; and (3) to understand catalytic mechanisms of the CT catalysts. We hope that the data would provide fundamental information for a future design of reactors in phenolic wastewater treatment using CT catalyst.

2. Materials and Methods

The CT catalyst is invented by one of the authors, Dr. Shoji Ichimura, and is commercially available. CT in this study was provided by FIRAC International Co., Ltd. (Dr. Shoji Ichimura owned company) for free. Phenol, catechol, hydrogen peroxide (30% w/w), and TiO_2 (mixture of rutile and anatase, nanopowder, <100 nm) were of analytic grade (Sigma-Aldrich Chemical Co.). Phenol and catechol were chosen as the target pollutants, and the initial concentrations were chosen at 88 mg L^{-1} (chemical oxygen demand (COD): 179 mg L^{-1} ; total organic carbon (TOC): 54 mg L^{-1}) and 91.8 mg L^{-1} (COD: 164 mg L^{-1} ; TOC: 57 mg L^{-1}), respectively. The pH level of 3, simulating phenol-containing industrial wastewater, was adjusted using hydrochloride acid and sodium hydroxide solutions.

Four treatments, namely, pollutant + UV, pollutant + UV + 1% CT, pollutant + UV + 1% TiO_2 , and pollutant + UV + H_2O_2 ($60 \mu\text{L H}_2\text{O}_2$ added into 200 mL phenolic solution), were applied to the solutions containing phenol and catechol. Each treatment has 2 replicates. The choice of the level of CT (1%) was based on our preliminary tests. H_2O_2 amount, as hydroxyl radical generator and scavenger, was chosen according to previous reports [20]. Flasks (250 mL) with the phenolic solutions were placed in a shaker, which located between two mercury UV lamps (15 w, the emitted wavelength is 254 nm and the light intensity $<26 \mu\text{w}/\text{cm}^2$). Positions of the flasks were rotated in order to prevent an uneven exposure of the UV radiation. The experiments were conducted at room temperature (20°C) and had lasted for 10–15 days until complete elimination of TOC in the flasks occurred in any treatment.

To further investigate mechanism of CT catalyst in degrading phenolic compounds, the role of CT and UV radiation in reacting with the phenol was compared. One treatment involved that a phenol solution (initial concentration of 76 mg L^{-1}) was exposed to UV radiation for 4 days followed by 1% CT treatment in the dark. The other treatment involved a reversed sequence of the treatments in which a solution (initial concentration of 76 mg L^{-1}) was subjected

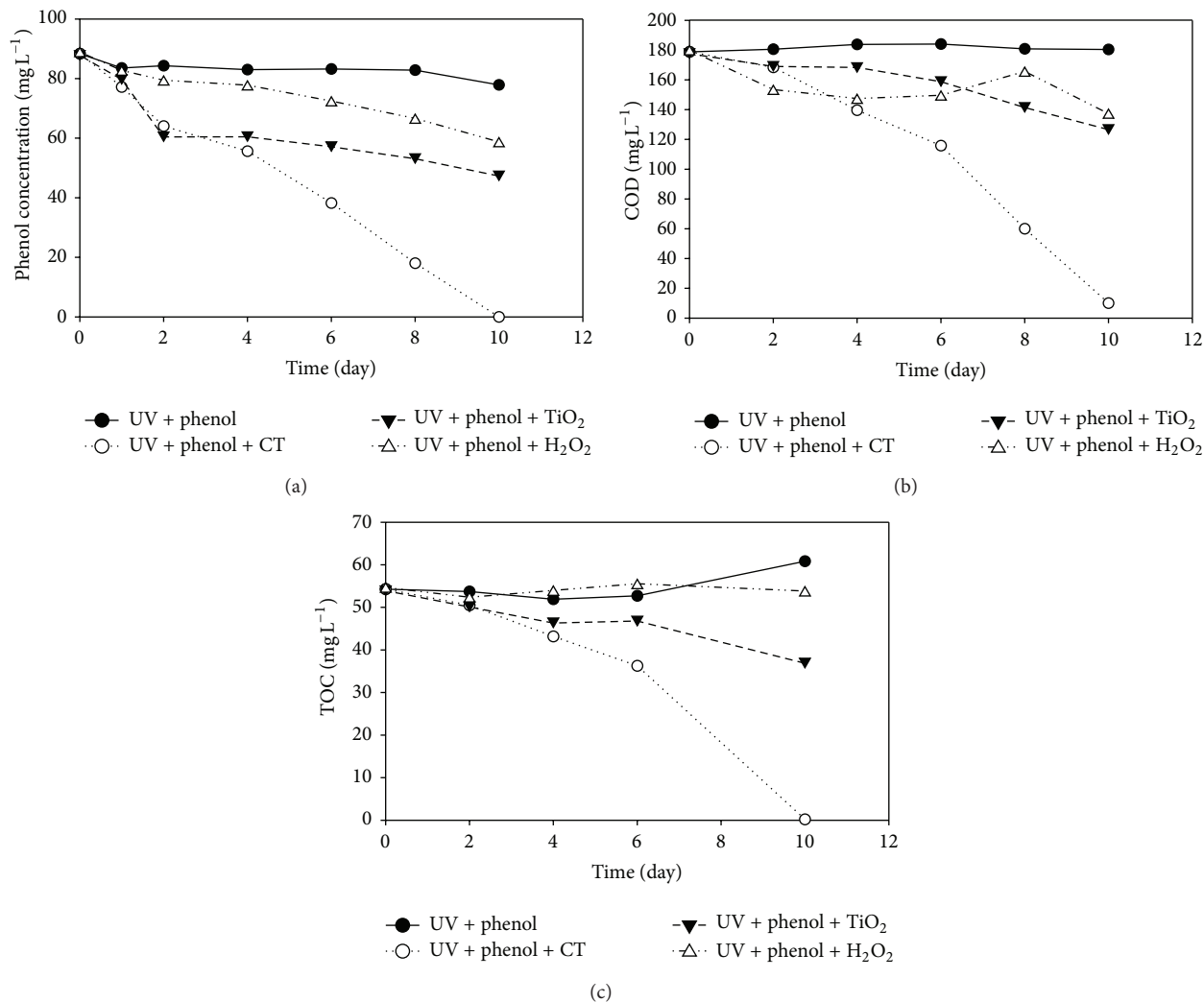


FIGURE 1: Time-dependent degradation of phenol by CT catalyst compared with TiO₂, H₂O₂ ((a) phenol concentration; (b) COD; (c) TOC).

to 1% CT treatment and then followed by the UV radiation. The comparison of the outcome allowed for an identification of difference between functions of UV radiation and CT catalyst.

During the experiments, the flasks were withdrawn from the shaker at predetermined time and the solutions were centrifuged at 3000 r/min for 30 min using a centrifuge (Allegra 6R). Concentrations of phenol, catechol, total organic carbon (TOC), chemical oxygen demand (COD), and pH were analyzed. Briefly, the phenol concentration was measured using the 4-aminoantipyrine method as described in Standards Methods [21], while that of catechol was measured according to Liu et al. [22]. Level of TOC was analyzed using a TOC analyzer (TOC-VCPH) based on the combustion-infrared method [23]. Level of COD was measured using open reflux method [21]. Level of pH was determined using a pH meter.

High performance liquid chromatography (HPLC, Agilent 1200), equipped with a ZORBAX column (Eclipse XDB-C18 ID = 4.6 mm, length = 150 mm) and a UV detector (used at working wavelength of 215 nm), was used to analyze

the intermediate compounds of catechol, hydroquinone, and benzoquinone from the treatments of UV + CT + phenol and UV + TiO₂ + phenol, respectively. A ratio of 1/3 (V/V) of methanol/5% orthophosphoric acid was used as the mobile phase at a flow rate of 1.0 mL min⁻¹. The injection volume was 10 μL, while the column temperature was set at 25°C. Before HPLC analysis, each sample was filtered through a 0.22 μm membrane filter (water phase filter, polyethersulfone).

3. Results and Discussion

3.1. Removal of Phenolic Compounds by CT Catalyst. Heterogeneous photocatalytic oxidation process generally is not suitable for high concentration phenolic wastewater. Instead, it is used as the pretreatment or the posttreatment combined with the biological treatment to achieve acceptable concentration efficiently and economically feasible [16, 24] (Table 1).

Time-dependent degradation of phenol and catechol was shown in Figures 1 and 2, respectively. Phenol was completely removed in the treatment of phenol + UV + 1% CT

TABLE 1: Summary of phenol treatment processes.

Processes	Phenol level in wastewater	Capacity	Stage of development	Capital cost	Operating cost	Performance	Complete destruction of phenol	Residue generation	Reference
Physical	High (>500 mg L ⁻¹)	High		High	High	For phenol recovery, >99%	No		
Liquid-liquid extraction, carbon adsorption, resin adsorption, and so forth			Well developed					Recovered/condensed phenol for further treatment; adsorbate must be processed for regeneration; spent adsorbates needs treatment/disposal	[25]
Liquid membrane			Developed					Recovered/condensed phenol for further treatment	[25]
Biological	Intermediate (<500 mg L ⁻¹)	High	Developed	High	Low	For final treatment, >99%	No	Sludge needs further treatment/disposal	[25]
Chemical									
Wet air oxidation	High	High	Well developed	High	High	Pretreatment for bio-treatment, high temperature/pressure technology	No	Some	[25]
Supercritical water oxidation	High	High	Developed	High	High	Up to 100%, high temperature/pressure technology	Yes	Not likely	[25, 26]
Ozonation	Low-intermediate	High	Developed	High	High	>99%	No	Off gasses needs further treatment	[25]
Oxidation by chlorine dioxide, hydrogen peroxide and potassium permanganate		Low	Developed	Low	High	Up to 100%, generally require facilities for oxidants generation on site,	Yes	Likely	[26, 27]
Electrolysis	Intermediate	High	Not fully developed	Low	High	Up to 100%, requires high energy input	No	Possible	[26]
Ultrasound	Intermediate	Low	Not fully developed	Low	High	Up to 100%, requires high energy input	Yes	Not likely	[26]
Homogeneous photocatalysis	Low (<5 mg L ⁻¹)	Low	Not fully developed	Low	High	Up to 100%, requires input of UV energy, H ₂ O ₂ , Fe ²⁺ , O ₃ , and so forth	Yes	Not likely	[26]
Heterogeneous photocatalysis	Low (<5 mg L ⁻¹)	Low	Not fully developed	Low	High	Up to 100%, requires high UV radiation intensity (>100 W)	Yes	Not likely	[26]
Catalysis by CT	Low (<5 mg L ⁻¹)	Low	Laboratory feasible	Low	Low	Up to 100%, requires LOW UV radiation intensity (<30 W)	Yes	No	This study

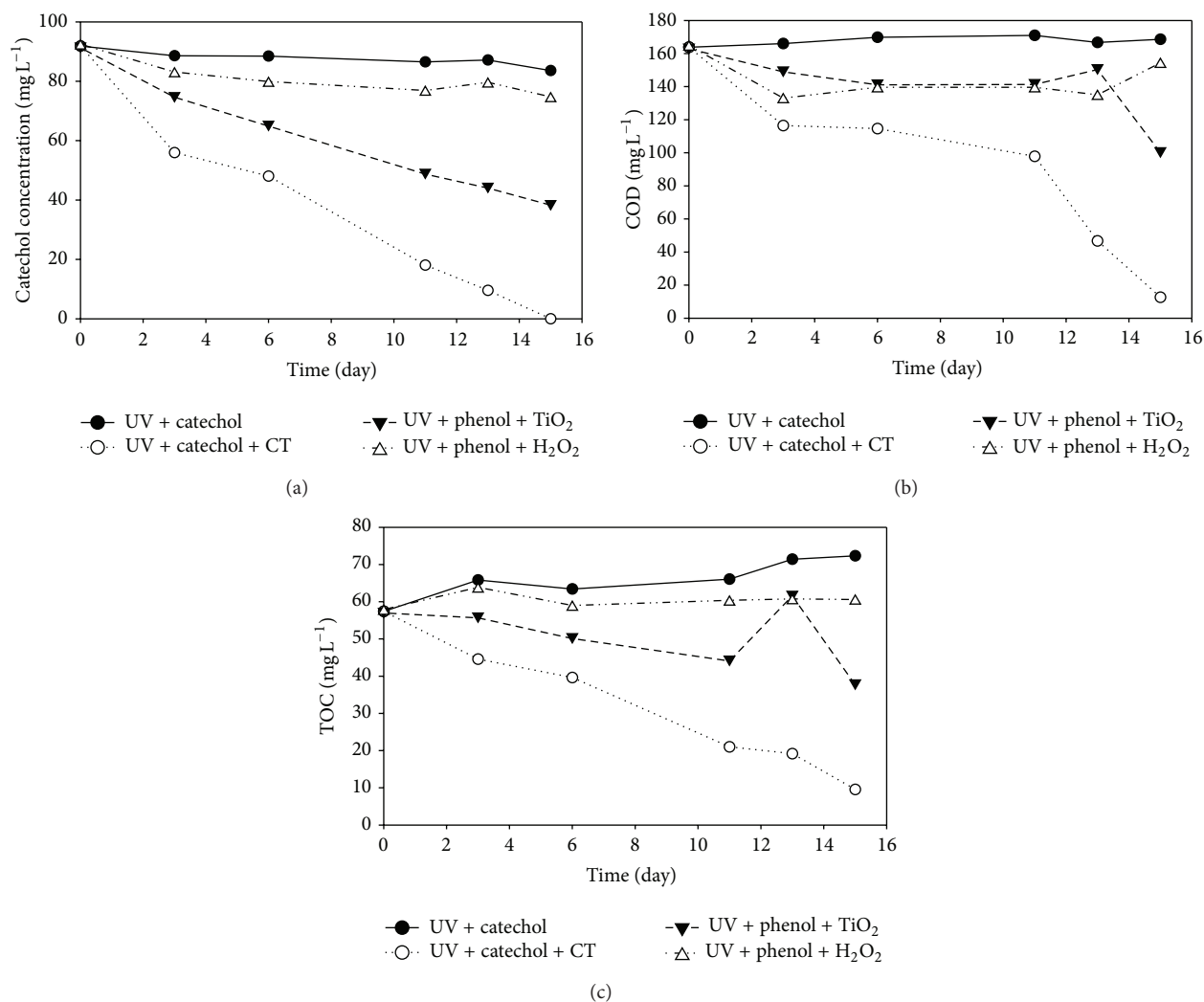


FIGURE 2: Time-dependent degradation of catechol by CT catalyst compared with TiO₂, H₂O₂ ((a) catechol concentration; (b) COD; (c) TOC).

after 10 days (Figure 1(a)), with residues of COD (10.0 mg L⁻¹) and TOC (0.206 mg L⁻¹) (Figures 1(b) and 1(c)). In contrast, the control (phenol + UV) only had a slight degradation (<12% phenol reduction), while TiO₂ and H₂O₂ showed similar phenol removal efficiencies (34–41% phenol reduction) (Figure 1). Pattern of the removal of catechol was similar to that of phenol (Figure 2), but a longer reaction time was required for a complete removal by CT (15 d). Additionally, TiO₂ was more potent than H₂O₂ in treating catechol (Figure 2(a)) that up to 57.8% of the catechol removal occurred in the treatment by TiO₂, much higher than the treatment by H₂O₂ (19.3%) and the control (8.9%).

The processes of phenol/catechol removal followed pseudo-zero-order kinetics (Figure 3), whereas correlation coefficients for the pseudo-first-order kinetic model were generally low. This suggested that mass transfer was not a rate controlling process in the experiments [23]. However, the result was different from previous studies that phenol removal mostly followed pseudo-first-order kinetics [16, 28–30]. Further investigation is needed in order to understand

more of the mechanisms. UV+TiO₂ for phenol and catechol and UV + H₂O₂ for phenol and catechol follow pseudo-first-order kinetics, and the calculated rate constant k values were $0.03 \times 10^{-3}/\text{min}$, $0.04 \times 10^{-3}/\text{min}$, $0.03 \times 10^{-3}/\text{min}$, and $0.01 \times 10^{-3}/\text{min}$, respectively. But UV + CT follows pseudo-zero-order kinetic calculated rate constant k values (for phenol and catechol) were $5.28 \times 10^{-3} \text{ mol L}^{-1} \text{ min}^{-1}$ and $4.59 \times 10^{-3} \text{ mol L}^{-1} \text{ min}^{-1}$, according to slopes of the regression models (Figure 3) (slope = $k/\text{initial concentration of phenol/catechol}$).

The result demonstrated that CT catalyst could be used for a complete removal of phenolic compounds in wastewater, with the presence of mild UV radiation (15 w, the emitted wavelength is 254 nm and the light intensity $<26 \mu\text{w}/\text{cm}^2$). Compared with previous reports on phenol degradation, such as employing sono-/photo-Fenton reactions [11], immobilized TiO₂ photodegradation [31], or electrochemical oxidation [28], the present treatment using CT catalyst had notably advantage of (1) less energy consumption and (2) no chemical consumption. Further comparison of the UV

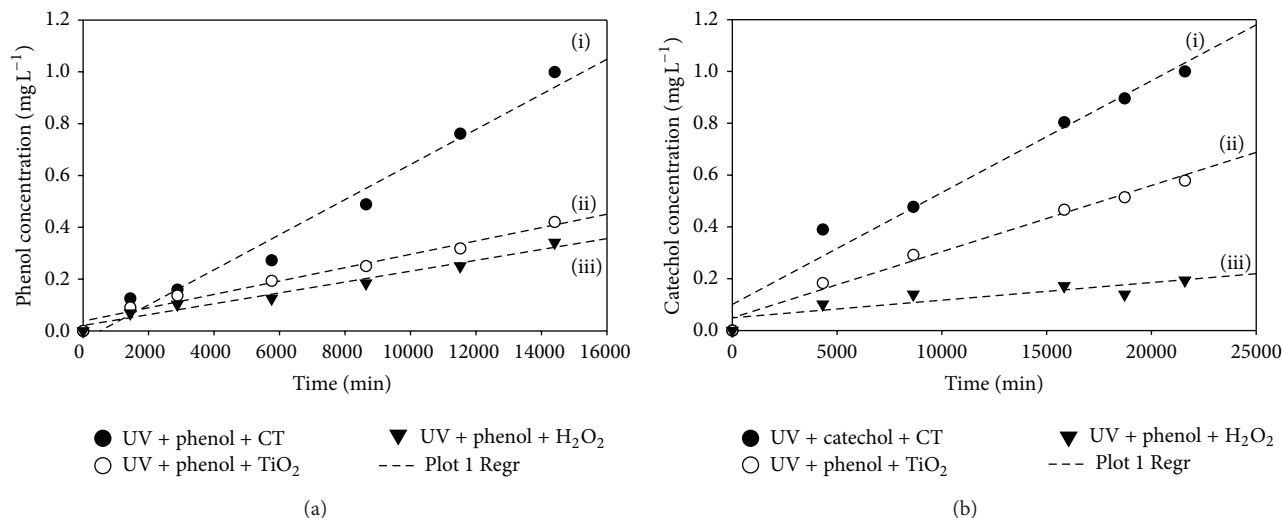


FIGURE 3: Degradation kinetics of (a) phenol: (i) $y = 7 * 10^{-5}x - 0.0288$, $r^2 = 0.9761$; (ii) $y = 3 * 10^{-5}x + 0.0349$, $r^2 = 0.9767$; (iii) $y = 2 * 10^{-5}x + 0.0628$, $r^2 = 0.9902$; and (b) catechol: (i) $y = 4 * 10^{-5}x + 0.0951$, $r^2 = 0.9686$; (ii) $y = 3 * 10^{-5}x + 0.0426$, $r^2 = 0.9831$; (iii) $y = 7 * 10^{-6}x + 0.0432$, $r^2 = 0.7685$.

TABLE 2: Comparison of UV intensity adopted by varied studies in photodegradation of phenol.

Treatment	Reaction condition	Performance	Study
UV + H ₂ O ₂ + TiO ₂ supported on sepiolite	UV intensity 17 w; pH 5.5; solid/liquid 0.5 g L ⁻¹ ; H ₂ O ₂ : 30 mL L ⁻¹	$k = 0.87 \times 10^{-3}/\text{min}$, within 24-25 h, conversion >90%	Üğurlu and Karaoğlu 2011 [15]
UV + TiO ₂ /perlite	UV intensity 250 w, pH 10.7; initial phenol concentration 0.5 mmol L ⁻¹ ; TiO ₂ /perlite dosage, 6 g L ⁻¹ ; reaction temperature 27°C	Experimental conversion (%): 97.3	Jafarzadeh et al. 2011 [1]
Sono-photo-Fenton	UV intensity 250 w, emitting radiation between 300–420 nm; pH 3; Fe ²⁺ 20 mg L ⁻¹ , H ₂ O ₂ 700 mg L ⁻¹ , room temperature	93% phenol reduction, 84.6% COD reduction within 60 min, $k = 0.1186/\text{min}$	Babuponnusami and Muthukumar 2011 [11]
UV/H ₂ O ₂	UV intensity 5000 w output; H ₂ O ₂ concentration: 7.08 mmol L ⁻¹	Within 50 min, 50 mg L ⁻¹ phenol degraded into 10 mg L ⁻¹	Huang and Shu [33]
UV/TiO ₂ supported on fiberglass cloth	a UV/Vis mercury lamp: 6 Kw, 330 Wm ⁻² initial phenol Concentration: 25 mg L ⁻¹	80% phenol reduction within 15 h	Mozaia et al. 2012 [32]
UV/CT	UV intensity 15 w, the emitted wavelength is 254 nm and the light intensity <26 $\mu\text{w}/\text{cm}^2$; pH 3, initial phenol concentration 88 mg L ⁻¹ (0.936 mmol L ⁻¹), 1% CT nanoparticles; room temperature	Within 10 day, 100% degradation, $k = 5.28 \times 10^{-3} \text{ mol L}^{-1} \text{ min}^{-1}$	This study

intensity among varied photodegradation of phenol (Table 2) demonstrated that CT catalyst required low UV radiation (15 w, the emitted wavelength is 254 nm and the light intensity <26 $\mu\text{w}/\text{cm}^2$). This suggested that the present set-up using CT catalysis could be applied in removing wastewater containing low levels of phenol. Although it took CT 10 and 15 days to mineralize phenol and catechol (both with the initial concentration of 88 mg L⁻¹), respectively, CT/UV followed zero-order kinetics, suggesting the reaction rate constant was not

a function of phenol concentration. If CT/UV is applied for posttreatment, with much lower concentrations (<5 mg L⁻¹) of phenol or catechol, less removal time is expected. Nevertheless, our follow-up experiments verified our hypothesis (unpublished). The band gap energy of TiO₂ is up to 3.2 eV. Usually TiO₂ absorbs light with the wavelength less than 385 nm. Previous reports by other researchers showed that the UV intensity is a critical parameter in order to allow TiO₂ to function efficiently [16, 32]. Compared with TiO₂/UV,

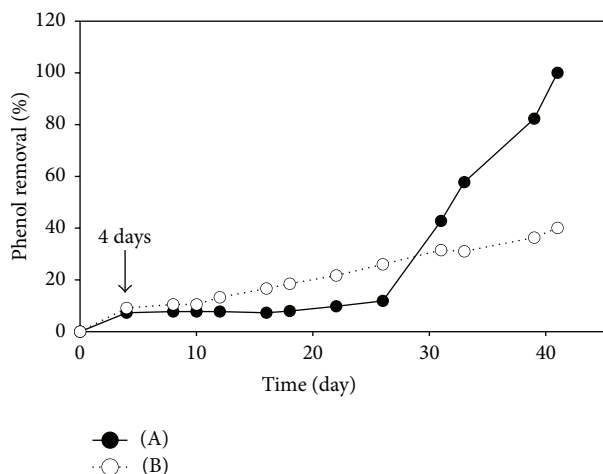


FIGURE 4: Sequential degradation of phenol: (A) four days of UV radiation followed by 1% CT treatment in the dark; (B) four days of 1% CT in the dark followed by UV radiation.

CT has the advantage that it works better under mild UV intensity. Further investigation will be needed for treating water with higher phenol level; the pollutants treatment efficiency also needs to be improved and optimized.

The result of the treatments of UV + H₂O₂ and UV + TiO₂ was expected. For the former treatment, the one-time spiking of H₂O₂ limited a continuous supply of hydroxyl radicals, leading to an incomplete mineralization of the phenolic compounds. For example, we observed that the solution in the treatment of phenol + UV + H₂O₂ turned from colorless at the start of the experiment to dark brown at the end (10 days). For the latter, due to the low UV intensity provided, TiO₂ did not absorb enough photon energy to form sufficient holes (h⁺) and hydroxyl radicals [34], which are the most important species for oxidation organic compounds [31]. As a result, low levels of phenolic compounds were decomposed.

3.2. Mechanism of CT Catalyst in Degrading Phenolic Compounds. Although complete removal of phenol was achieved with the copresence of CT and UV (Figure 1), sequential degradations of phenol (treatment by UV followed by CT (A) and treatment by CT followed by UV (B)) showed much lower efficiency (Figure 4). For example, both treatments (A and B) at 4 days showed <10% phenol removal (Figure 4), whereas the treatment with the copresence of CT and UV at 4 days removed 26.8% phenol (Figure 1(a)). It took 40 days for a complete removal of phenol in treatment A (Figure 4), but 10 days in the copresence of CT and UV (Figure 1(a)). This indicated that the copresence of CT and UV had a synergistic effect in degrading phenol.

Moreover, remarkable difference was observed between treatments A and B (Figure 4). At 26 days, treatment A started to show a remarkable increasing removal percentage (>6%/day), and eventually at 40 days phenol was completely removed (100%). In contrast, the increase in the removal percentage of treatment B was not significant (<40%) during the whole treatment period (40 days). This proved that CT and UV did not play an equal role in phenol degradation. For

treatment B, the slight decrease in phenol in the treatment B (by CT and then UV) most likely was due to residue CT catalyst in the filtrate after filtration. However, for treatment A, it is more probable that the phenolic compounds absorbed the UV energy and passed to the higher state of energy (excited state) first, and then in the dark the unstable excited-state phenolic compounds underwent charge transfer processes mediated by the CT catalyst. In particular, under acidic condition, electron donor of CT generated holes, which moved towards the oxidation center, and pulled electrons out from the phenolic compounds, and therefore the phenolic compounds were oxidized. The reduction center of the CT accepted those electrons and sent them to electron acceptors, such as oxygen in the water. In this regard, whether the pseudo-zero-order kinetic model derived from the present kinetic study reflected a rate limiting influence by the charge transfer process remained to be investigated. Another explanation can be that hydroxyl radicals were generated from CT in the solution [35] that the phenolic compounds adsorbed on the surface of CT were oxidized and mineralized. However, concentration of the hydroxyl radicals was not measured in the present study, but should be examined in the future. The contrast of the result of treatments A and B partially supported our hypothesis on the functions of UV and CT and the associated mechanism, which indicates that CT has the potential for degrading organics in the dark condition, although uncertainties remained to be clarified in our future work.

Probable pathway of phenol degradation in water was established according to previous studies, that is, phenol-catechol or hydroquinone/benzoquinone-maleic acid-acrylic acid/succinic-malonic acid-acetic acid-CO₂ + H₂O [14, 36–38], and the identified and quantified intermediates in the present phenol degradations (UV + CT and UV + TiO₂) were shown in Figure 5. Furthermore, levels of TOC calculated based on the carbon concentrations in the intermediates (Figure 5) were also compared with the corresponding measured TOC concentrations using a TOC analyzer (Figures 1(c) and 2(c)) (Table 3). For the treatment of UV + CT, it seems that the three measured compounds (catechol, hydroquinone, and benzoquinone) were the predominant intermediates, accounting for more than 95% of the measured TOC (Figure 5(a)). Concentrations of catechol and hydroquinone reached the maxima (catechol: 0.826 mg L⁻¹; hydroquinone: 4.43 mg L⁻¹) at 2 d, while that of benzoquinone only peaked at 6 days (1.02 mg L⁻¹). At 10 days, a complete mineralization occurred, in which all intermediates were transformed into the end products (CO₂ and H₂O). However, varied acids as intermediates between benzoquinone and the end products were not detectable. Based on mass balance, these compounds accounted for <5% of the TOC (Table 3). Similarly, acids were not detected in the treatment of UV + TiO₂, accounting for <10% of the TOC (Table 3), whereas only catechol and hydroquinone were identified and quantifiable (Figure 5(b)). The difference between these two treatments was expected as the UV intensity was low and TiO₂ could not generate adequate energy and radicals for the degradation.

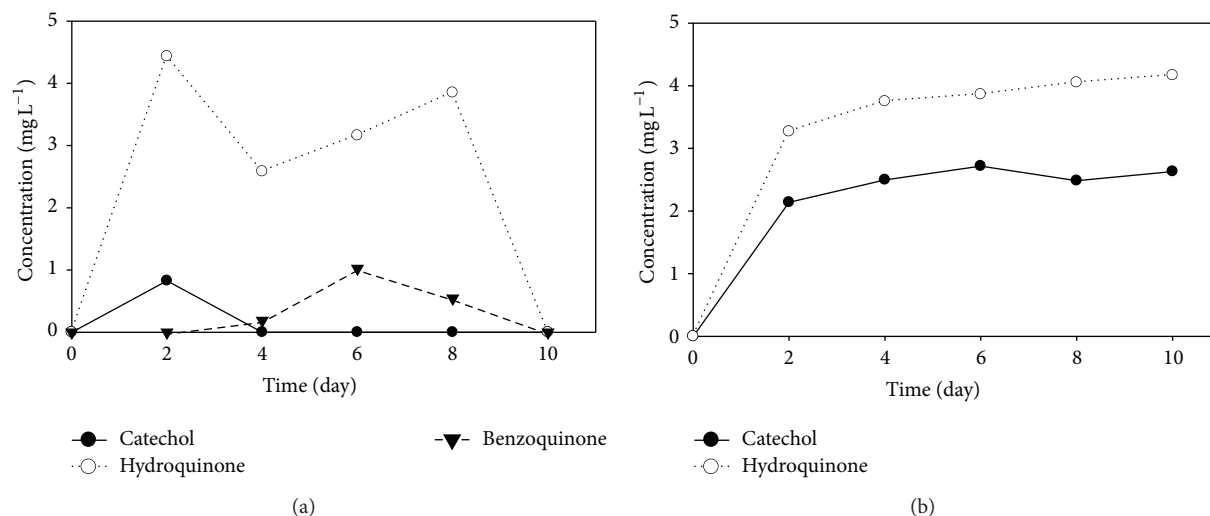


FIGURE 5: Degradation intermediates of phenol from the treatment of (a) UV + CT and (b) UV + TiO₂.

TABLE 3: Levels of TOC calculated from carbon contents in phenol and its intermediates compared with TOC concentrations measured by a TOC analyzer.

TOC (mg L ⁻¹)	Time (day)				
	0	2	4	6	10
UV + CT					
Phenol	67.4	49.0	42.6	29.3	ND
Catechol	ND	0.541	ND	ND	ND
Hydroquinone	ND	2.90	1.69	2.07	ND
Benzoquinone	ND	ND	0.125	0.683	ND
Total calculated value	67.4	52.4	44.4	32.0	ND
Measured value	54.3	50.5	43.2	36.3	0.206
UV + TiO ₂					
Phenol	67.4	46.7	46.7	44.2	36.7
Catechol	ND	1.40	1.63	1.78	1.72
Hydroquinone	ND	2.14	2.45	2.53	2.73
Total calculated value	67.4	50.3	50.8	48.5	41.1
Measured value	54.3	50.5	46.7	47.1	37.3

ND: undetectable; method detection limits (MDLs) of phenol, catechol, hydroquinone and benzoquinone were 0.0158, 0.0240, 0.0124 and 0.0190 mg C L⁻¹, respectively.

4. Conclusions

This is the first report on employing CT catalyst, a novel charge transfer auto oxidation-reduction type of semiconductor, in degrading aromatic compounds in water. Phenolic compounds (initial concentrations, phenol: 88 mg L⁻¹ and catechol: 91.8 mg L⁻¹) were completely mineralized by the CT catalytic nanoparticles (1%) within 15 days, under acidic condition and with the presence of mild UV radiation (15 w, the emitted wavelength is 254 nm and the light intensity <math><26 \mu\text{W}/\text{cm}^2</math>). The reaction condition allowed CT to be applied in pollutant removal in wastewater that light transfer was quite often a challenge if photocatalysis was attempted. Phenol elimination followed pseudo-zero-order kinetics with a rate constant of $5.28 \times 10^{-3} \text{ mol L}^{-1} \text{ min}^{-1}$ under the present treatment condition. It seems that, given low initial phenol

concentration, a circumstance encountered in wastewater polishing, the current set-up should be more efficient and less energy-/chemical-consumptive.

A probable mechanism of the CT's functions related to a synergistic performing between UV radiation and the CT. In particular, the aromatic structures in phenol absorbed the UV energy and passed to an excited state. The CT worked on these excited compounds by absorbing pollutants on the surface, oxidizing the pollutants via charge transfer, and producing hydroxyl radicals and eventually completely transformed all the pollutants to CO₂ and H₂O. Analysis of the degradation intermediates of phenol showed that the reaction in the CT's treatment followed general pathway observed by other researchers. In the practical application, CT can be separated from the effluent through nanofiltration.

Conflict of Interests

The authors declare that there is no conflict of interests regarding the publication of this paper.

Acknowledgments

This study was supported by “100 Talents Program” of Chinese Academy of Sciences and the Faculty Research Grant (FRG2/09-10/027, Faculty of Science of Hong Kong Baptist University) awarded to Yan Liang.

References

- [1] N. K. Jafarzadeh, S. Sharifnia, S. N. Hosseini, and F. Rahimpour, “Statistical optimization of process conditions for photocatalytic degradation of phenol with immobilization of nano TiO₂ on perlite granules,” *Korean Journal of Chemical Engineering*, vol. 28, no. 2, pp. 531–538, 2011.
- [2] S. P. Mahajan, *Pollution Control in Processes Industries*, Tata McGraw-Hill, New Delhi, India, 1994.
- [3] Y. M. Dong, G. L. Wang, P. P. Jiang, A. M. Zhang, L. Yue, and X. M. Zhang, “Catalytic ozonation of phenol in aqueous solution by Co₃O₄ nanoparticles,” *Bulletin of the Korean Chemical Society*, vol. 31, no. 10, pp. 2830–2834, 2010.
- [4] U.S. Environmental Protection Agency, “Toxicological review of phenol,” Support of Summary Information on the Integrated Risk Information System EPA /635/r-02/006, Environmental Protection Agency, Washington, DC, USA, 2002.
- [5] Ministry of Environmental Protection of the P.R. China (SEPA), *Integrated Wastewater Discharge Standard (GB 8978-1996)*, Environmental Protection National Standard of the People’s Republic of China, 1996.
- [6] M. Ahmaruzzaman and D. K. Sharma, “Adsorption of phenols from wastewater,” *Journal of Colloid and Interface Science*, vol. 287, no. 1, pp. 14–24, 2005.
- [7] M. J. Gonzalez-Munoz, S. Luque, J. R. Alvarez, and J. Coca, “Recovery of phenol from aqueous solutions using hollow fibre contactors,” *Journal of Membrane Science*, vol. 213, no. 1-2, pp. 181–193, 2003.
- [8] J.-Q. Xu, W.-H. Duan, X.-Z. Zhou, and J.-Z. Zhou, “Extraction of phenol in wastewater with annular centrifugal contactors,” *Journal of Hazardous Materials*, vol. 131, no. 1–3, pp. 98–102, 2006.
- [9] S. Li, R. Kong, L. Sun, S. F. Li, and S. C. Yang, “study on treatment methods of phenol in industrial wastewater,” *International Journal of Scientific & Engineering Research*, vol. 4, no. 5, pp. 230–232, 2013.
- [10] X. Han, *The Study of Photocatalytic Oxidation of the Wastewater with High Concentration of Phenol and Formaldehyde*, Si Chuan University, Chengdu, China, 2004.
- [11] A. Babuponnusami and K. Muthukumar, “Degradation of phenol in aqueous solution by fenton, sono-fenton and sono-photo-fenton methods,” *Clean—Soil, Air, Water*, vol. 39, no. 2, pp. 142–147, 2011.
- [12] P. J. Ranjit, K. Palanivelu, and C. S. Lee, “Degradation of 2,4-dichlorophenol in aqueous solution by sono-fenton method,” *Korean Journal of Chemical Engineering*, vol. 25, no. 1, pp. 112–117, 2008.
- [13] M. D. Gurol and R. Vatistas, “Oxidation of phenolic compounds by ozone and ozone+UV radiation: a comparative study,” *Water Research*, vol. 21, no. 8, pp. 895–900, 1987.
- [14] X.-Y. Li, Y.-H. Cui, Y.-J. Feng, Z.-M. Xie, and J.-D. Gu, “Reaction pathways and mechanisms of the electrochemical degradation of phenol on different electrodes,” *Water Research*, vol. 39, no. 10, pp. 1972–1981, 2005.
- [15] M. Ügurlu and M. H. Karaoğlu, “TiO₂ supported on sepiolite: preparation, structural and thermal characterization and catalytic behaviour in photocatalytic treatment of phenol and lignin from olive mill wastewater,” *Chemical Engineering Journal*, vol. 166, no. 3, pp. 859–867, 2011.
- [16] J. C. Costa and M. Madalena, “posttreatment of Olive mill wastewater by immobilized TiO₂ photocatalysis,” *Photochemistry and Photobiology*, vol. 89, pp. 545–551, 2013.
- [17] S. Ichimura and K. Ichimura, “Charge transfer auto-oxidation-reduction semiconductor catalyst: application to MINOYAKI tiles and its effects,” *Transactions of the Materials Research Society of Japan*, vol. 26, no. 3, pp. 1045–1048, 2001.
- [18] M. R. Hoffmann, S. T. Martin, W. Choi, and D. W. Bahnemann, “Environmental applications of semiconductor photocatalysis,” *Chemical Reviews*, vol. 95, no. 1, pp. 69–96, 1995.
- [19] F. J. Beltrbn, G. Ovejero, J. F. Garcla-Araya, and J. Rivas, “Oxidation of polynuclear aromatic hydrocarbons in water. 2. UV radiation and ozonation in the presence of UV radiation,” *Industrial and Engineering Chemistry Research*, vol. 34, no. 5, pp. 1607–1615, 1995.
- [20] M. L. Zhou, L. Li, and Y. Li, “Study on effect of catalytic oxidation of phenol by H₂O₂,” *Environmental Science Survey*, vol. 28, no. 2, pp. 8–10, 2009.
- [21] The American Public Health Association, *Standard Methods for the Examination of Water and Waste Water*, American Public Health Association, Washington DC, USA, 20th edition, 1998.
- [22] W. Liu, J. D. Liu, Z. L. Wang et al., “Determination of catechol content of the willow by Colorimetry,” *Chinese Traditional and Herbal Drugs*, vol. 33, p. 134, 2002.
- [23] P. S. Kumar, K. Ramakrishnan, S. D. Kirupha, and S. Sivanesan, “Thermodynamic, kinetic, and equilibrium studies on phenol removal by use of cashew nut shell,” *Canadian Journal of Chemical Engineering*, vol. 89, no. 2, pp. 284–291, 2011.
- [24] H. Liu and P. Liu, “The study of heterogeneous photocatalytic oxidation of coking wastewater,” *Environmental Science and Technology*, vol. 29, no. 2, pp. 103–105, 2006.
- [25] USEPA, “Technical resources document: treatment technologies for solvent containing wastes,” Hazardous Waste Engineering Research Laboratory EPA/600/2-86/O095, Cincinnati, Ohio, USA, 1986.
- [26] X. Deng, D. S. Li, Y. F. Li, F. J. Liang, and C. Y. Zhang, “Advanced oxidation technologies of the removal of phenol wastewater,” *Water Science and Engineering Technology*, vol. 1, pp. 26–30, 2008.
- [27] Siemens Water Technologies, “Application Note: Phenol Destruction with Chlorine Dioxide,” WT. 085. 272. 013.IE.AN. 0409, Siemens, 2009, <http://www.industry.siemens.com/industry-solutions/de/en/water-treatment/Pages/Default.aspx>.
- [28] Y. H. Cui, Y. J. Feng, and X. Y. Li, “Kinetics and efficiency analysis of electrochemical oxidation of phenol: influence of anode materials and operational conditions,” *Chemical Engineering and Technology*, vol. 34, no. 2, pp. 265–272, 2011.
- [29] R. Kar, O. Gupta, K. Mandol, and S. Bhattacharjee, “Performance study on photocatalysis of phenol solution in a UV

- irradiated reactor,” *Journal of Chemical Engineering & Process Technology*, vol. 4, article 143, 2013.
- [30] M. Delnavaz, B. Ayati, H. Ganjidoust, and S. Sanjabi, “kinetics study of photocatalytic process for treatment of phenolic wastewater by TiO_2 nano powder immobilized on concrete surfaces,” *Toxicological and Environmental Chemistry*, vol. 94, no. 6, pp. 1086–1098, 2012.
- [31] H.-J. Wang and X.-Y. Chen, “Kinetic analysis and energy efficiency of phenol degradation in a plasma-photocatalysis system,” *Journal of Hazardous Materials*, vol. 186, no. 2-3, pp. 1888–1892, 2011.
- [32] S. Mozia, P. Brozek, J. Przepiorski, B. Tryba, and A. W. Morawski, “Immobilized TiO_2 for phenol degradation in a pilot-scale photocatalytic reactor,” *Journal of Nanomaterials*, vol. 2012, Article ID 949764, 10 pages, 2012.
- [33] C. R. Huang and H. Y. Shu, “The reaction kinetics, decomposition pathways and intermediate formations of phenol in ozonation, UV/O_3 , and $\text{UV}/\text{H}_2\text{O}_2$ processes,” *Journal of Hazardous Materials*, vol. 41, pp. 47–64, 1995.
- [34] J.-C. Lee, M.-S. Kim, C. K. Kim et al., “Removal of paraquat in aqueous suspension of TiO_2 in an immersed UV photoreactor,” *Korean Journal of Chemical Engineering*, vol. 20, no. 5, pp. 862–868, 2003.
- [35] K. L. Chow, N. A. Mak, M. H. Wong, X. F. Zhou, and Y. Liang, “Generation of reactive oxygen species and oxidative stress in *Escherichia coli* and *Staphylococcus aureus* by a novel semiconductor catalyst,” *Journal of Nanoparticle Research*, vol. 13, no. 3, pp. 1007–1017, 2011.
- [36] N. Al-Hayek and M. Dore, “Oxidation of phenols in water by hydrogen peroxide on alumine supported iron,” *Water Research*, vol. 24, no. 8, pp. 973–982, 1990.
- [37] L. F. Liotta, M. Gruttadauria, G. DiCarlo, G. Perrini, and V. Librando, “Heterogeneous catalytic degradation of phenolic substrates: catalysts activity,” *Journal of Hazardous Materials*, vol. 162, no. 2-3, pp. 588–606, 2009.
- [38] A. Mokrini, D. Ousse, and S. Esplugas, “Oxidation of aromatic compounds with UV radiation/ozone/hydrogen peroxide,” *Water Science and Technology*, vol. 35, no. 4, pp. 95–102, 1997.

Review Article

Chitosan and Its Derivatives Applied in Harvesting Microalgae for Biodiesel Production: An Outlook

Guanyi Chen,¹ Liu Zhao,¹ Yun Qi,¹ and Yuan-Lu Cui²

¹ School of Environment Science and Engineering, State Key Laboratory of Engines, Tianjin University, No. 92 Weijin Road, Nankai District, Tianjin 300072, China

² Tianjin State Key Laboratory of Modern Chinese Medicine, Tianjin University of Traditional Chinese Medicine, Tianjin 300193, China

Correspondence should be addressed to Yun Qi; qiyun@tju.edu.cn

Received 6 February 2014; Accepted 10 March 2014; Published 9 April 2014

Academic Editor: Ranjit T. Koodali

Copyright © 2014 Guanyi Chen et al. This is an open access article distributed under the Creative Commons Attribution License, which permits unrestricted use, distribution, and reproduction in any medium, provided the original work is properly cited.

Although oil-accumulating microalgae are a promising feedstock for biodiesel production, large-scale biodiesel production is not yet economically feasible. As harvesting accounts for an important part of total production cost, mass production of microalgae biodiesel requires an efficient low-energy harvesting strategy so as to make biodiesel production economically attractive. Chitosan has emerged as a favorable flocculating agent in harvesting of microalgae. The aim of this paper is to review current research on the application of chitosan and chitosan-derived materials for harvesting microalgae. This offers a starting point for future studies able to invalidate, confirm, or complete the actual findings and to improve knowledge in this field.

1. Introduction

Fossil fuels currently account for about 80% of global energy production. As demand for energy continues to increase, oil prices will rise and fossil fuels will be exhausted at some point in the future. Meanwhile, extensive utilization of fossil fuels has led to adverse effects including global climate change, environmental pollution, and public health problems [1].

Therefore, many countries have started to take series of measures to resolve this problem [2]. Identifying alternative renewable sources of fuel that are carbon neutral is important for many countries. Among the potential sources of renewable energy, biodiesel is of particular interest. Major advantages of biodiesel include mitigation of carbon dioxide emissions and potential use as a substitute for petroleum [3]. Biodiesel also has a higher energy density than competing biofuels measured in kilojoules per unit of mass. Furthermore, widespread adoption of biodiesel could improve urban air quality as emissions of carbon monoxide and volatile organic compounds are significantly lower than petroleum-derived diesel. Biodiesel may become a primary energy source for sustainable development and could play a crucial role in the global energy infrastructure in the future. Energy

security may drive biodiesel production as nations attempt to reduce their reliance on petroleum imports.

More than 95% of biodiesel sources are first generation agricultural edible crop oils [4] such as palm oil, oilseed rape, and soybean. However, these vegetable oils are also used for human consumption, which may lead to an increase in price of food-grade oils. Meanwhile, any transition to biodiesel production based upon these crops would require arable land, with a corresponding drop in other forms of agricultural productivity. In theory, it should be possible to produce low-cost biodiesel using nonedible oils (second generation biofuels), such as frying oils, animal fats, soap stocks, and grease. However, these nonedible oils are rarely available in quantities suitable for industrial-scale biodiesel production [5]. As a consequence, there is renewed interest in methods of producing biodiesel from microalgae.

As a promising feedstock for biodiesel production, microalgae offers compelling advantages compared to other oil crops: (1) the cultivation of microalgae does not need much land as terraneous plants [6]; indeed, biomass growth might not require any arable land at all if offshore farming proves feasible [7]; (2) microalgae have much higher biomass productivities than land plants; (3) some microalgae species

are rich in oils; they can accumulate up to 20–50% (w/w DW) triacylglycerols [8] and certain strains may have content as high as 85% lipid under limited condition [9]; (4) microalgae utilize CO₂ from the atmosphere via photosynthesis, offsetting greenhouse gas emissions; (5) microalgae require less freshwater for cultivation than terrestrial crops. Microalgae growth effectively removes nutrients, such as nitrogen and phosphorus, and heavy metals from wastewater; (6) biodiesel produced from microalgal oil has advantageous properties compared to standard biodiesel. These advances suggest that industrial production of biodiesel from microalgal oils may be feasible in the near future.

2. Microalgae Harvest Strategy

Although oil-accumulating microalgae are a promising feedstock for biodiesel production, large-scale biodiesel production is not yet economically feasible. This is mainly due to the high-energy inputs required for harvesting [10]. However, as microalgae' diameters are often as small as 3–30 μm, harvesting the microalgae is a significant problem. In some commercial production systems, the culture broths are below 0.5 kg/m³ dry biomass, which means that huge volumes need to be handled before algae oil can be extracted. Molina et al. estimated that harvesting can account for 20–30% of the total production cost [11]. Chisti even reported that the cost of the recovery process in his study contributed about 50% to the final cost of oil production [6].

Consequently, mass production of microalgae biodiesel acquires efficient low-energy harvesting strategy so as to make biodiesel production economically feasible. Microalgae can be harvested by centrifugation, filtration, flotation, sedimentation, and electrophoresis techniques [12].

Centrifugation can recover most microalgae from the liquid broth and is used in many commercial systems. Although centrifugation is effective, this process is energy intensive [13], which reduces the net energy return on investment (EROI) from the biodiesel produced from the microalgae, making this option less attractive both in financial and environmental terms. Norsker et al. calculated centrifugation required as much as 50% of the available energy in the recovered biomass [14]. From an energetic point of view, harvesting a large amount of microalgae using centrifugation is time consuming and costly [15]. Filtration is another option for harvesting cells, but this technology is only useful for the harvest of large species such as *Spirulina* but fails to recover small microalgae such as *Chlorella* or *Scenedesmus* [10].

Coagulation/flocculation processes offer high microalgae biomass recovery at reasonable costs [16]. These harvesting techniques have been successfully used in aquaculture, wastewater treatment, and removal of microalgae [10] and also reduce the net energy input required to produce biodiesel from microalgae feedstock.

Several flocculants have been developed to induce flocculation of microalgae cells that can be applied to the treatment of large amount of microalgae. According to their chemical compositions, there are two classifications of flocculants: inorganic flocculants and organic flocculants/polyelectrolyte flocculants [1].

The commonly used inorganic flocculants include ferric chloride (FeCl₃), aluminum sulfate (Al₂(SO₄)₃), and ferric sulfate (Fe₂(SO₄)₃) [17]. These multivalent metal salts are effective flocculants or coagulants and have been widely used to flocculate algal biomass. prepolymerized metal salts (such as polyaluminium chloride and polyferric sulfate) have proved to be efficient over a wider pH range [18]. However, flocculation by metal salts is not an appropriate method for cheap and sustainable harvesting of microalgae in large-scale microalgae culture. This is because these flocculants are expensive and may produce large amounts of sludge, which can kill or prevent the growth of the microalgae and leave a residue in the water, and the excess cationic flocculant needs to be removed before it can be reused [19]. Another disadvantage of metal salts as flocculants is the concern about the human health, such as involvement in Alzheimer's disease and carcinogenesis [20–22].

The organic flocculants, such as synthetic polymeric flocculants and modified natural polymers, have also been applied to the microalgae harvesting process. In the last few decades, chitosan has emerged as a favorable flocculating agent in harvesting microalgae. Chitosan is becoming increasingly important as a natural biopolymer due to its unique combination of properties like biodegradability, biocompatibility, renewability, bioactivity, and ecological acceptability, in addition to attractive physical and mechanical properties [23]. It also has variety of current and potential applications in wastewater treatment [24], biomedical engineering [25], food processing [26], and so forth. In particular, chitosan has also been examined to formulate nanoparticles to facilitate targeting drug to specified organ [27].

3. General Aspects of Chitosan

Chitosan, poly-β(1-4)-2-amino-2-deoxy-d-glucopyranose, is a cationic polyelectrolyte obtained by deacetylation of chitin. Chitin and chitosan are both aminoglucopyrans composed of N-acetylglucosamine (GlcNAc) and glucosamine (GlcN) residues. The chemical structures of chitin and chitosan are shown in Figure 1 [28]. Acetamide group of chitin can be converted into amino group to give chitosan, when the degree of deacetylation of chitin reaches about 50% (depending on the origin of the polymer). Chitosan is also polyelectrolyte which has several million Daltons. The average molecular weight of commercially available chitosan ranges between 3800 and 20,000 Daltons and is 66% to 95% deacetylated. The chitosan toxicity tests showed that the toxicity was negligible [29]. Because chitosan can be produced in various forms such as powder, paste, film, and fiber, it is more widely applied in industry than chitin [30].

Due to the presence of three different polar functional groups (–OH, –NH₂, and C–O–C), chitosan has high water capacity [28]. Chitosan has the special quality of gelling upon contact with anions, forming beads under very mild conditions [31]. And the presence of amino groups makes chitosan a cationic polyelectrolyte (pKa = 6.5), one of the few found in nature [32]. Ordinary chitosan is insoluble in water at near neutral pH and most common organic

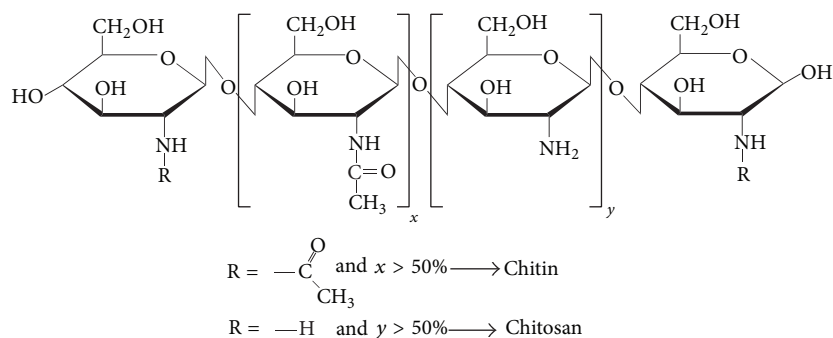
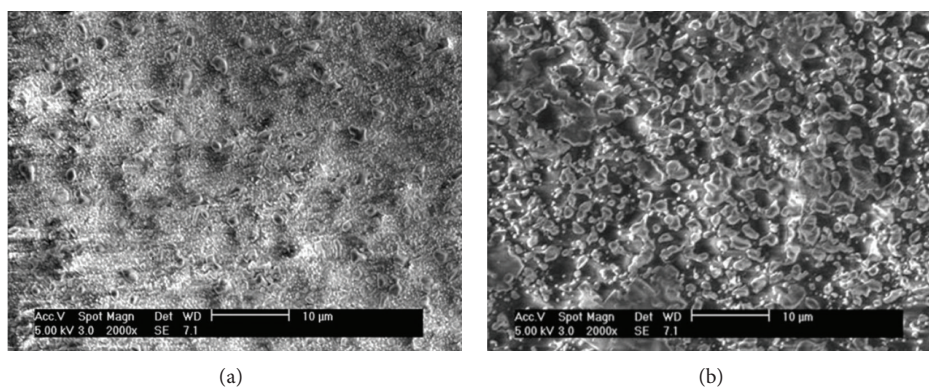


FIGURE 1: Structures of chitin and chitosan [28].

FIGURE 2: (a) SEM of *C. vulgaris* before harvesting. (b) SEM of *C. vulgaris* after harvesting [38].

solvents (e.g., DMSO, DMF, NMP, organic alcohols, and pyridine), which is attributed to extensive intramolecular and intermolecular hydrogen bonding between the chains and sheets, respectively [33]. Chitosan can be soluble in some diluted organic acids (such as acetic, formic, and lactic acids) and some inorganic acid. Although the distribution of acetyl groups along the chain may modify solubility [34], the solubilization is mainly due to the protonation of NH_2 groups on the C_2 position of the β -glucosamine unit.

4. Chitosan Applied in Harvesting Microalgae

Chitosan not only has been proved highly effective for water treatment and environmental protection, but also shows interesting properties in removing both freshwater algae and marine algae.

The most likely mechanisms involved in this coagulation are adsorption and charge neutralization. Chitosan has a net positive charge because of the high charge density of the chitosan. As the overall charge of microalgae cells is negative, the positively charged chitosan is strongly adsorbed on microalgae cells, which results in most of the charged groups being close to the surface of the cells [35] and effectively destabilize the microalgae [36]. Chitosan first neutralizes charges on the microalgae cells, weakens the electrostatic repulsion between the microalgae cells, and then reduces the interparticle repulsion. Such effect is called charge neutralization [37].

Some authors report chitosan as an effective algal flocculant. Figure 2 shows the scan electron microscope (SEM) of *Chlorella vulgaris* before and after flocculation by chitosan. After flocculation, *C. vulgaris* algae were surrounded by chitosan, and the surface became fibrillar. This change of surface was observably caused by chitosan, which possesses heterogeneous surface structure [38].

Using life cycle assessment (LCA), Beach compared the chitosan method to centrifugation and filtration/chamber press methods [39]. Figure 3 showed the system used as a basis for the comparison, where the cultivation and downstream were assumed to be equivalent among all methods. LCA showed that flocculation by chitosan for harvesting *N. oleoabundans* is the least energy intensive and had the best profile across all other categories of environmental impacts.

4.1. Effect of Chitosan Dosage on Flocculation Efficiency. In general, chitosan can effectively flocculate algal species at 5 mg/L to 200 mg/L. Divakaran and Sivasankara Pillai [40] reported that chitosan successfully removed 90% of turbidity with chitosan concentration of 5 mg/L. Ahmad et al. [41] reported a $99.0 \pm 0.4\%$ of *Chlorella* sp. removal at 10 ppm of chitosan. In order to obtain 95–100% flocculation efficiency, chitosan concentration was about 20 mg/L for *Chlorella* and 2 mg/L for *S. Costatum* [16]. Chitosan is required in low dosage in freshwater but its flocculating power is reduced in salt water.

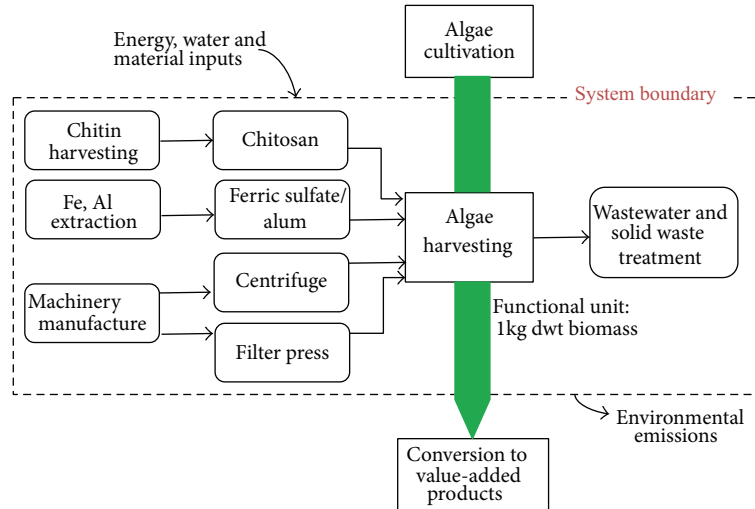


FIGURE 3: Overview of the system used as a basis for the comparison [39].

Chitosan's ability to remove microalgae effectively at low dosage is partly caused by its' properties. Chitosan not only acts as an adsorbent, but also spontaneously coagulates to agglomerate the microalgae cells. However, when using overdose of chitosan, the percentage of microalgae cells removed declined sharply, which may be caused by charge neutralization and bridging phenomena. During the flocculation, cationic charge of chitosan attracts the negatively charged microalgae, reducing the electrostatic repulsion among microalgal cells and then forming the flocs. Excess amino group led to restabilization of the microalgae and decreasing of separation efficiency [38].

4.2. Effect of pH on Flocculation Efficiency. The importance of pH on flocculation of microalgae was investigated by many researchers [41–44]. The influence of pH on chitosan's molecular structure can be due to differences in the protonation of the biopolymer amine groups and variations in the conformation of the macromolecule chain and in the structure of the flocs [37]. In alkaline solutions, the positive charge gradually disappeared and chitosan is able to produce large and dense flocs. When the pH increases to neutralization point, the algal cells have the highest negative charge, and the flocculation efficiency is enhanced as the electrostatic interaction between the algal cells and chitosan, whereas, in acidic solutions, chitosan becomes a more extended chain and therefore produces smaller looser flocs [20]. In the study of Divakaran and Sivasankara Pillai [40], maximum clarification was obtained at pH 7 for the freshwater species. Cheng et al. reported that a higher pH at 8.5 was optimal for *Chlorella sorokiniana* [42]. In the study of an even higher pH at 9.9, 90% of *Phaeodactylum tricornerutum* was harvested with 20 ppm chitosan [18].

Morales suggested that chitosan activity and flocculation efficiency were increased as the viscosity and the mean surface charge of algal cells were decreased when pH was below 7 [16]. While Xu et al. reported that when the working

pH was at 6 or 5, half the amount of chitosan was needed to induce effective flocculation compared to pH 7 [43].

These differences in response to pH can be explained by difference in culture media, growth conditions, and unique strain properties, such as cell morphology, extracellular organic matter, and cell surface charge [44].

4.3. Effect of Algae Species on Flocculation Efficiency. The flocculation efficiency of algal suspension is different from one algal species to another. *Chlorella vulgaris* reached 99.7% removal rate at 200 mg/L chitosan [45]. While 150 mg/L of chitosan was required for optimal flocculation of *Chaetoceros muelleri* [46]. For *Skeletonema costatum* 2 mg/L of chitosan was needed when 95% flocculation efficiency was obtained. Optimal flocculation of some species was list in Table 1.

5. Chitosan Modified Flocculants and Their Flocculation Efficiency

Chitosan exhibits limitations in its reactivity and process ability. For a breakthrough in utilization of chitosan in flocculation of microalgae, chitosan modification to introduce a variety of functional groups will be a key point. Chitosan can be modified by chemical or physical processes to improve the mechanical and chemical properties. The efficiency of adsorption depends on physicochemical properties, mainly surface area, porosity, and particle size of adsorbents. As such procedure would not change the fundamental skeleton of polymers, chitosan would keep its original physicochemical and biochemical properties and finally would bring new or improved properties [47]. A great number of chitosan derivatives have been obtained by grafting new functional groups on the chitosan backbone to increase adsorption capacity. The new functional groups are incorporated to increase the density of sorption sites, to change the pH range for sorption, and to change the sorption sites in order to increase sorption. The chemical modification affords a wide range of derivatives

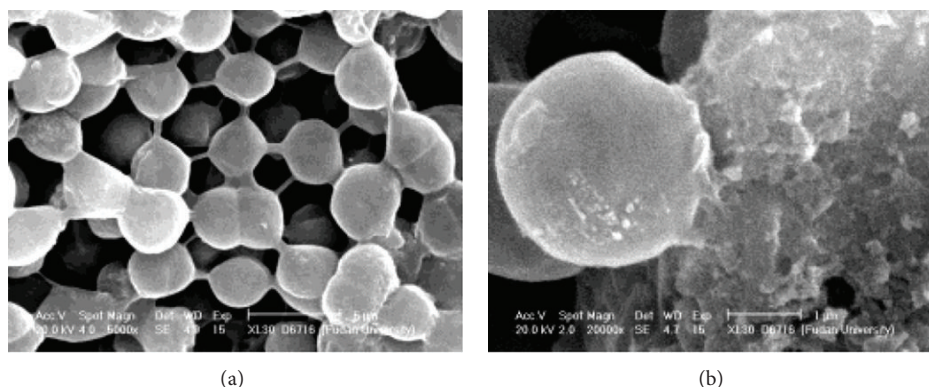


FIGURE 4: SEM images of algae treated with chitosan modified adsorbent [53].

TABLE 1: Optimal flocculation of some microalgae.

Species	Chitosan dosage	Parameters	Flocculation efficiency	References
<i>Chaetoceros calcitrans</i>	80 mg/L	pH 8.0	80%	[46]
<i>Chaetoceros muelleri</i>	150 mg/L	pH 8.0	95%	[46]
<i>Chlorella</i>	5.0 mg/L	pH 7.0,	90%	[63]
<i>Chlorella consortium</i>	25 mg/L	Stirring for 1 min, settling for 10 min	58 ± 8	[10]
<i>Chlorella sorokiniana</i>	10 mg/gram algal dry weight	pH 6	99%	[43]
<i>Chlorella sorokiniana</i>	25 mg/L	Stirring for 1 min, settling for 10 min	30 ± 11	[10]
<i>Chlorella</i> sp.	10 ppm	Mixing for 20 min, mixing at 150 ppm, and sedimenting for 20 min	99.0 ± 0.4%	[41]
<i>Chlorella vulgaris</i>	200 mg/L	In a logarithmic growth phase	99.7%	[45]
<i>Chlorella vulgaris</i>	30 mg/L	pH 8.7, 300 rpm, and settling for 10 min.	92%	[38]
<i>Chlorella vulgaris</i> and <i>Microcystis</i> sp.	214 mg/L	Fish-processing wastewater, agitation speed of 131 rpm	91.9%	[64]
<i>Chlorococcum</i> sp.	25 mg/L	Stirring for 1 min, settling for 10 min	38 ± 1	[10]
<i>Nannochloropsis</i> sp.	100 mg/L	pH 9.0	92%	[62]
<i>Neochloris oleoabundans</i>	100 mg/L	Mixing time for 10 min, mixing rate of 350 rpm	95%	[39]
<i>Pavlova lutheri</i>	80 mg/L	pH 8.0	80%	[46]
<i>Phaeodactylum tricornerutum</i>	20 mg/L	pH 9.9 Settling time of 10 min	92%	[18]
<i>Scenedesmus costatum</i>	2 mg/L	pH 7	95–100%	[16]
<i>Scenedesmus obliquus</i>	25 mg/L	Stirring for 1 min, settling for 10 min	20 ± 15	[10]
<i>Scenedesmus quadricauda</i>	10 mg/L	pH 8.0; SDS was used as the collector	90%	[65]
<i>Skeletonema costatum</i>	80 mg/L	pH 8.0	70%	[46]
<i>Synechocystis</i>	15 mg/L	pH 7.0	>90%	[63]
<i>Tahitian Isochrysis</i>	40 mg/L	pH 8.0	90%	[46]
<i>Tetraselmis chui</i>	40 mg/L	pH 8.0	80%	[46]
<i>Thalassiosira pseudonana</i>	40 mg/L	pH 8.0	90%	[46]



FIGURE 5: Flocculation character of CMK and *M. aeruginosa* NIES-843 at different CMK loading levels [54].

with modified properties for specific use and applications in diversified areas mainly of pharmaceutical, biomedical, and biotechnological fields [32]. Such modification can also be applied to harvesting microalgae.

5.1. Chitosan Modified Soils. Chitosan modified by soil particles (including the silica sand and local soil) showed highly effective in flocculating algae cells [48–52]. Pan and coworkers found that local soil particles including sand were critical for speeding up the kinetic processes of flocculation and sedimentation of algal flocs. The polymeric netting and bridging function of chitosan were the key mechanisms that allowed local soil particles to quickly flocculate algal biomass. Chitosan modified adsorbent has the functions of both flocculation and adsorption. Figure 4(a) shows the function of bridging, while Figure 4(b) illustrates the function of adsorption [53]. The chitosan made a “net” that captured the algae cells and other particles, and the soils provided the ballast or mass to carry the aggregates to the bottom. Chitosan was also important in inhibiting the escape of cells from the flocs. Chitosan and polyaluminium chloride used together as modifiers make it possible to use local beach sand for harvesting microalgae in seawater [50].

Shao et al. studied the physiological responses of *Microcystis aeruginosa* under the stress of chitosan modified kaolinite (CMK). When flocculated with CMK, Chl a, carotenoids, phycocyanin, and allophycocyanin were much lower than the control. The results indicated that high level of CMK could cause cellular membranes damage and then the intracellular substances leakage and finally could cause the death of *M. aeruginosa* NIES-843 cell. Figure 5 showed that the strain can be effectively flocculated by CMK at 80 and 160 mg/L. However, the *Microcystis* cultures turned to be bluish at that time, which indicated the leakage of phycobilins [54].

5.2. Aluminum Chloride and Aluminium Sulphate Modified Chitosan Used as Flocculants

5.2.1. Aluminum Chloride Modified Chitosan. Chitosan could enhance the flocculation performance of polyaluminium chloride (PAC), when the high algae-laden water was treated by coagulation/flocculation/dissolved air flotation (C/F/DAF) [55]. The removal rate of algae cells was increased apparently compared with adding PAC alone. The structure and strength of flocs were improved when less than 1.0 mg/L chitosan was added, which significantly reduced the residual aluminum concentration.

Zhang et al. reported a composite coagulant (PACI-CTS), which was made of polyaluminium chloride and chitosan. When 21.0 mg/L of the coagulant is added, 98.15% turbidity, 67.78% COD, and 84.05% TP can be removed. This coagulant can be applied in the pretreatment of blue algae biogas slurry [56]. Figure 6 showed the SEM of PACI-CTS. PACI with certain crystal structure was embedded in chitosan, which enabled the composite coagulant to possess much more positive charge. When the PACI-CTS was added to the algal water, it can decrease the negative charge on the surface of microalgae and enhance the flocculation by polymer bridging.

5.2.2. Aluminium Sulphate Modified Chitosan. Wang et al. used aluminium sulphate and chitosan as coagulants to treat the high algae-laden water. The compound action of aluminium sulphate and chitosan can reduce dosage of aluminium salt coagulant for meeting the treatment requirements, which in turn reduces the residual aluminium in treated water. Moreover, with the coagulation aid of chitosan, the algae flocs were larger and more compact and had a faster settling velocity [57].

5.3. Fly Ash Modified Chitosan. The performance of activated fly ash modified chitosan (FA-MC) as a flocculant to remove *Microcystis aeruginosa* was reported by Qiao et al. [58]. 90% of algae can be removed at the dosage of 0.25 mg/L chitosan within 1 h or at the dosage of 0.35 mg/L chitosan within 40 min. The authors found that the algal extracellular organic matter had a priority to consumption of flocculant in initial period of flocculation. In the late stage of flocculation, extracellular organic matter can decrease the adsorption bridging and entrapping-weeping functions of fly ash modified chitosan.

5.4. Magnetic Chitosan. Ferroferric oxide modified with chitosan was used to remove algal in freshwater [59]. This magnetic polymer could remove over 99% algal cells, which is much more effective when comparing with chitosan or Fe_3O_4 alone. The author found that the high algal removal efficiency of magnetic polymer is due to the cooperation between chitosan and Fe_3O_4 particles. Chitosan can enhance the function of netting and bridging in flocculating algal cells, while the Fe_3O_4 could separate the flocculated algal cells from water by its high magnetic response in the presence of magnetic field. Figure 7 showed the SEM of algal cells that was captured by magnetic polymer. The network bridge of chitosan and the magnetic Fe_3O_4 agglomerated the cells. After flocculation, the algae cells were still kept in original shape, which indicated that the flocculant did not destroy the cells.

This technique has been successfully applied to pilot experiments in Chaohu Lake, China.

5.5. Nanochitosan. Nanoscaled chitosan particles are prepared by some researchers. Such chitosan-coated nanoparticles have overcome the limitation of microscaled particles

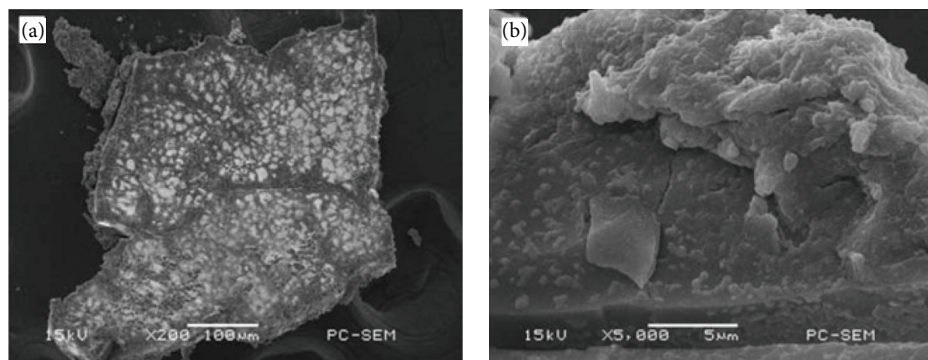


FIGURE 6: SEM of PACl-CTS [56].

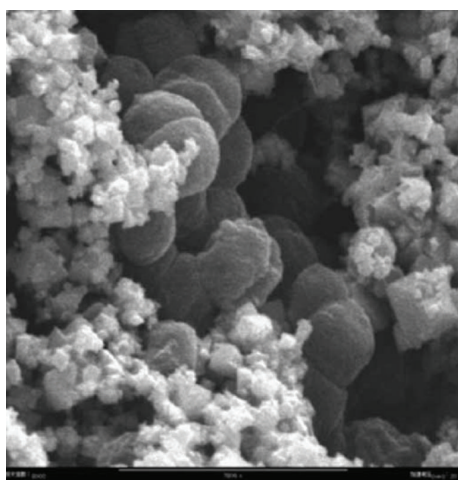


FIGURE 7: SEM images of the floccules of magnetic polymer algal cells ($\times 8,000$) [59].

by providing larger surface area. Owing to high adsorption capacity and stability, these particles can be used as adsorbents for food dyes adsorption [60], protein [61], and microalgae.

Farid et al. prepared chitosan nanopolymer using ionic gelation method, which added sodium tripolyphosphate to chitosan solution [62]. The average of particle size was 13.7 nm.

When nanochitosan was used as flocculant agent, the dosage of flocculant consumption decreased to 60 mg/L, while the optimum chitosan dosage was 100 mg/L for harvesting. The removal efficiency was about 98%, which increased by 9% when nanochitosan instead of chitosan was used. The author figured out that the nanochitosan had high harvesting rate because its particle had ions cross-linked with sodium tripolyphosphate. When chitosan is dissolved in water at acidic pH, it gives both hydrated amino group and $-\text{NH}_3^+$ ions. The sodium tripolyphosphate (STPP, $\text{Na}_5\text{P}_3\text{O}_{10}$) presents both hydroxyl and phosphoric ions in water. These phosphoric ions of STPP can interact with $-\text{NH}_3^+$ ions of chitosan, lead to crosslinking between chitosan and STPP, and result in big network of polymers, which adsorb microalgae and create a greater degree of bridging. In addition, the

nanosize particles increase the adsorption ability and contact surfaces.

The author also analyzed the cost of harvesting process. For production of 1 kg of dry biomass, harvesting process would cost about \$0.0246, which showed the feasibility of using nanochitosan as flocculation agent.

6. Conclusions

Flocculation using chitosan is becoming a promising alternative to replace conventional flocculants in removing/harvesting microalgae. Although chitosan itself can flocculate algae, the use of some modification process may improve the properties of chitosan. Arguments on which flocculant is better in harvesting microalgae are still going on as each of the flocculants has its own advantages and disadvantages. Due to the different experimental conditions, such as pH, microalgae species, and ionic strength, it is different to compare the low-cost flocculants. Meanwhile, more studies should transfer to industrial scale.

Conflict of Interests

The authors declare that there is no conflict of interests.

Acknowledgments

Financial support from the National Natural Science Foundation of China (Grant nos. 51108310 and 51036006) and support from the Project for Developing Marine Economy by Science and Technology in Tianjin (KX2010-0005) are highly appreciated.

References

- [1] C.-Y. Chen, K.-L. Yeh, R. Aisyah, D.-J. Lee, and J.-S. Chang, "Cultivation, photobioreactor design and harvesting of microalgae for biodiesel production: a critical review," *Bioresource Technology*, vol. 102, no. 1, pp. 71–81, 2011.
- [2] G. Huang, F. Chen, D. Wei, X. Zhang, and G. Chen, "Biodiesel production by microalgal biotechnology," *Applied Energy*, vol. 87, no. 1, pp. 38–46, 2010.

- [3] Y. Chisti, "Biodiesel from microalgae beats bioethanol," *Trends in Biotechnology*, vol. 26, no. 3, pp. 126–131, 2008.
- [4] I. Rawat, R. R. Kumar, T. Mutanda et al., "Biodiesel from microalgae: a critical evaluation from laboratory to large scale production," *Applied Energy*, vol. 103, pp. 444–467, 2013.
- [5] T. M. Mata, A. A. Martins, and N. S. Caetano, "Microalgae for biodiesel production and other applications: a review," *Renewable and Sustainable Energy Reviews*, vol. 14, no. 1, pp. 217–232, 2010.
- [6] Y. Chisti, "Biodiesel from microalgae," *Biotechnology Advances*, vol. 25, no. 3, pp. 294–306, 2007.
- [7] S. A. Scott, M. P. Davey, J. S. Dennis et al., "Biodiesel from algae: challenges and prospects," *Current Opinion in Biotechnology*, vol. 21, no. 3, pp. 277–286, 2010.
- [8] H. M. Amaro, A. C. Guedes, and F. X. Malcata, "Advances and perspectives in using microalgae to produce biodiesel," *Applied Energy*, vol. 88, no. 10, pp. 3402–3410, 2011.
- [9] I. Rawat, R. R. Kumar, T. Mutanda et al., "Biodiesel from microalgae: a critical evaluation from laboratory to large scale production," *Applied Energy*, vol. 103, pp. 444–467, 2013.
- [10] I. de Godos, H. O. Guzman, R. Soto et al., "Coagulation/flocculation-based removal of algal-bacterial biomass from piggery wastewater treatment," *Bioresource Technology*, vol. 102, no. 2, pp. 923–927, 2011.
- [11] G. E. Molina, E.-H. Belarbi, F. G. Acien Fernández, A. Robles Medina, and Y. Chisti, "Recovery of microalgal biomass and metabolites: process options and economics," *Biotechnology Advances*, vol. 20, no. 7–8, pp. 491–515, 2003.
- [12] N. Uduman, Y. Qi, M. K. Danquah, G. M. Forde, and A. Hoadley, "Dewatering of microalgal cultures: a major bottleneck to algae-based fuels," *Journal of Renewable and Sustainable Energy*, vol. 2, no. 1, Article ID 012701, 2010.
- [13] D. Vandamme, I. Foubert, B. Meesschaert, and K. Muylaert, "Flocculation of microalgae using cationic starch," *Journal of Applied Phycology*, vol. 22, no. 4, pp. 525–530, 2010.
- [14] N.-H. Norsker, M. J. Barbosa, M. H. Vermuë, and R. H. Wijffels, "Microalgal production—a close look at the economics," *Biotechnology Advances*, vol. 29, no. 1, pp. 24–27, 2011.
- [15] E. M. Grima, E. H. Belarbia, F. G. A. Fernández et al., "Recovery of microalgal biomass and metabolites: process options and economics," *Biotechnology Advances*, vol. 20, no. 7–8, pp. 491–515, 2003.
- [16] J. Morales, J. de la Nouë, and G. Picard, "Harvesting marine microalgae species by chitosan flocculation," *Aquacultural Engineering*, vol. 4, no. 4, pp. 257–270, 1985.
- [17] L. Brennan and P. Owende, "Biofuels from microalgae—a review of technologies for production, processing, and extractions of biofuels and co-products," *Renewable and Sustainable Energy Reviews*, vol. 14, no. 2, pp. 557–577, 2010.
- [18] S. Şirin, R. Trobajo, C. Ibanez, and J. Salvadó, "Harvesting the microalgae *Phaeodactylum tricornutum* with polyaluminum chloride, aluminium sulphate, chitosan and alkalinity-induced flocculation," *Journal of Applied Phycology*, vol. 24, no. 5, pp. 1067–1080, 2011.
- [19] P. M. Schenk, S. R. Thomas-Hall, E. Stephens et al., "Second generation biofuels: high-efficiency microalgae for biodiesel production," *BioEnergy Research*, vol. 1, pp. 20–43, 2008.
- [20] C. Huang, S. Chen, and J. Ruhsing Pan, "Optimal condition for modification of chitosan: a biopolymer for coagulation of colloidal particles," *Water Research*, vol. 34, no. 3, pp. 1057–1062, 2000.
- [21] T. Okuda, A. U. Baes, W. Nishijima, and M. Okada, "Improvement of extraction method of coagulation active components from *Moringa oleifera* seed," *Water Research*, vol. 33, no. 15, pp. 3373–3378, 1999.
- [22] M. Özacar and I. A. Şengil, "Evaluation of tannin biopolymer as a coagulant aid for coagulation of colloidal particles," *Colloids and Surfaces A*, vol. 229, no. 1–3, pp. 85–96, 2003.
- [23] A. J. Varma, S. V. Deshpande, and J. F. Kennedy, "Metal complexation by chitosan and its derivatives: a review," *Carbohydrate Polymers*, vol. 55, no. 1, pp. 77–93, 2004.
- [24] C. Y. Hu, S. L. Lo, Chang, C. L. et al., "Treatment of highly turbid water using chitosan and aluminum salts," *Separation and Purification Technology*, vol. 104, pp. 322–326, 2013.
- [25] J. M. Silva, N. Georgi, R. Costa et al., "Nanostructured 3D constructs based on chitosan and Chondroitin Sulphate multilayers for cartilage tissue engineering," *Plos ONE*, vol. 8, no. 2, Article ID e55451, 2013.
- [26] F. Shahidi, J. K. V. Arachchi, and Y.-J. Jeon, "Food applications of chitin and chitosans," *Trends in Food Science and Technology*, vol. 10, no. 2, pp. 37–51, 1999.
- [27] K. Ganguly, T. M. Aminabhavi, and A. R. Kulkarni, "Colon targeting of 5-fluorouracil using polyethylene glycol cross-linked chitosan microspheres enteric coated with cellulose acetate phthalate," *Industrial and Engineering Chemistry Research*, vol. 50, no. 21, pp. 11797–11807, 2011.
- [28] J. Ma and Y. Sahai, "Chitosan biopolymer for fuel cell applications," *Carbohydrate Polymers*, vol. 92, no. 2, pp. 955–975, 2013.
- [29] L. Illum, "Chitosan and its use as a pharmaceutical excipient," *Pharmaceutical Research*, vol. 15, no. 9, pp. 1326–1331, 1998.
- [30] S. A. Agnihotri, N. N. Mallikarjuna, and T. M. Aminabhavi, "Recent advances on chitosan-based micro- and nanoparticles in drug delivery," *Journal of Controlled Release*, vol. 100, no. 1, pp. 5–28, 2004.
- [31] S. C. Angadi, L. S. Manjeshwar, and T. M. Aminabhavi, "Stearic acid-coated chitosan-based interpenetrating polymer network microspheres: controlled release characteristics," *Industrial and Engineering Chemistry Research*, vol. 50, no. 8, pp. 4504–4514, 2011.
- [32] P. Miretzky and A. F. Cirelli, "Fluoride removal from water by chitosan derivatives and composites: a review," *Journal of Fluorine Chemistry*, vol. 132, no. 4, pp. 231–240, 2011.
- [33] T. Yui, K. Imada, K. Okuyama, Y. Obata, K. Suzuki, and K. Ogawa, "Molecular and crystal structure of the anhydrous form of chitosan," *Macromolecules*, vol. 27, no. 26, pp. 7601–7605, 1994.
- [34] M. Rinaudo, "Characterization and properties of some polysaccharides used as biomaterials," *Macromolecular Symposia*, vol. 245–246, no. 1, pp. 549–557, 2006.
- [35] D. M. Ruthven, *Encyclopedia of Separation Technology*, vol. 1 of *A Kirk-Othmer Encyclopedia*, John Wiley & Sons, New York, NY, USA, 1997.
- [36] X. Wu, X. Ge, D. Wang, and H. Tang, "Distinct coagulation mechanism and model between alum and high Al13-PACl," *Colloids and Surfaces A*, vol. 305, no. 1–3, pp. 89–96, 2007.
- [37] F. Renault, B. Sancey, P.-M. Badot, and G. Crini, "Chitosan for coagulation/flocculation processes—an eco-friendly approach," *European Polymer Journal*, vol. 45, no. 5, pp. 1337–1348, 2009.
- [38] N. Rashid, M. S. Rehman, and J. I. Han, "Use of chitosan acid solutions to improve separation efficiency for harvesting of the microalga *Chlorella vulgaris*," *Chemical Engineering Journal*, vol. 226, pp. 238–242, 2013.

- [39] E. S. Beach, M. J. Eckelman, Z. Cui et al., "Preferential technological and life cycle environmental performance of chitosan flocculation for harvesting of the green algae *Neochloris oleoabundans*," *Bioresource Technology*, vol. 121, pp. 445–449, 2012.
- [40] R. Divakaran and V. N. Sivasankara Pillai, "Flocculation of river silt using chitosan," *Water Research*, vol. 36, no. 9, pp. 2414–2418, 2002.
- [41] A. L. Ahmad, N. H. Mat Yasin, C. J. C. Derek, and J. K. Lim, "Optimization of microalgae coagulation process using chitosan," *Chemical Engineering Journal*, vol. 173, no. 3, pp. 879–882, 2011.
- [42] Y.-S. Cheng, Y. Zheng, J. M. Labavitch, and J. S. Vanderghenst, "The impact of cell wall carbohydrate composition on the chitosan flocculation of *Chlorella*," *Process Biochemistry*, vol. 46, no. 10, pp. 1927–1933, 2011.
- [43] Y. N. Xu, S. Purton, and F. Baganz, "Chitosan flocculation to aid the harvesting of the microalga *Chlorella sorokiniana*," *Bioresource Technology*, vol. 129, pp. 296–301, 2013.
- [44] R. Henderson, S. A. Parsons, and B. Jefferson, "The impact of algal properties and pre-oxidation on solid-liquid separation of algae," *Water Research*, vol. 42, no. 8–9, pp. 1827–1845, 2008.
- [45] Y. R. Chang and D. J. Lee, "Coagulation-membrane filtration of *Chlorella vulgaris* at different growth phases," *Drying Technology*, vol. 30, no. 11–12, pp. 1317–1322, 2012.
- [46] M. Heasman, J. Diemar, W. O'Connor, T. Sushames, and L. Foulkes, "Development of extended shelf-life microalgae concentrate diets harvested by centrifugation for bivalve molluscs—a summary," *Aquaculture Research*, vol. 31, no. 8–9, pp. 637–659, 2000.
- [47] G. G. D'Ayala, M. Malinconico, and P. Laurienzo, "Marine derived polysaccharides for biomedical applications: chemical modification approaches," *Molecules*, vol. 13, no. 9, pp. 2069–2106, 2008.
- [48] G. Pan, M.-M. Zhang, H. Chen, H. Zou, and H. Yan, "Removal of cyanobacterial blooms in Taihu Lake using local soils. I. Equilibrium and kinetic screening on the flocculation of *Microcystis aeruginosa* using commercially available clays and minerals," *Environmental Pollution*, vol. 141, no. 2, pp. 195–200, 2006.
- [49] G. Pan, H. Zou, H. Chen, and X. Yuan, "Removal of harmful cyanobacterial blooms in Taihu Lake using local soils. III. Factors affecting the removal efficiency and an in situ field experiment using chitosan-modified local soils," *Environmental Pollution*, vol. 141, no. 2, pp. 206–212, 2006.
- [50] G. Pan, J. Chen, and D. M. Anderson, "Modified local sands for the mitigation of harmful algal blooms," *Harmful Algae*, vol. 10, no. 4, pp. 381–387, 2011.
- [51] G. Pan, L. Dai, L. Li et al., "Reducing the recruitment of sedimented algae and nutrient release into the overlying water using modified soil/sand flocculation-capping in eutrophic lakes," *Environmental Science and Technology*, vol. 46, no. 9, pp. 5077–5084, 2012.
- [52] H. Zou, G. Pan, H. Chen, and X. Yuan, "Removal of cyanobacterial blooms in Taihu Lake using local soils. II. Effective removal of *Microcystis aeruginosa* using local soils and sediments modified by chitosan," *Environmental Pollution*, vol. 141, no. 2, pp. 201–205, 2006.
- [53] X. Yang, C. Wu, Y. He, B. Zhang, and F. Li, "Removal effects and mechanisms of *Microcystis aeruginosa* by Chitosan-modified adsorbent," in *Proceedings of the 2nd International Symposium on Aqua Science, Water Resource and Low Carbon Energy*, vol. 1251 of *AIP Conference Proceedings*, pp. 125–128, December 2009.
- [54] J. Shao, Z. Wang, Y. Liu et al., "Physiological responses of *Microcystis aeruginosa* NIES-843 (cyanobacterium) under the stress of chitosan modified kaolinite (CMK) loading," *Ecotoxicology*, vol. 21, no. 3, pp. 698–704, 2011.
- [55] Y. H. Wang, S. G. Zhou, and Y. X. Yang, "Application of chitosan in removing algae by dissolved air flotation," in *Advanced Materials Research*, G. Li, Y. Huang, and C. Chen, Eds., vol. 347–353, pp. 1911–1916, 2011.
- [56] W. Zhang, P. Fan, Q. Li et al., "Synthesis of PACl-CTS composite coagulant and application in the pre-treatment of the blue algae biogas slurry," *Environmental Chemistry*, vol. 31, no. 7, pp. 1057–1062, 2012.
- [57] Y. H. Wang, S. G. Zhuo, X. Y. Zhou et al., "Improvement of high algae-laden water treatment by coagulation aid of chitosan," in *Advanced Materials Research*, G. Li, Y. Huang, and C. Chen, Eds., vol. 250–253, pp. 3454–3459, 2011.
- [58] J. Qiao, L. Dong, and Y. Hu, "Removal of harmful algal blooms using activated fly ash-modified chitosan," *Fresenius Environmental Bulletin A*, vol. 20, no. 3, pp. 764–772, 2011.
- [59] D. Liu, F. Li, and B. Zhang, "Removal of algal blooms in freshwater using magnetic polymer," *Water Science and Technology*, vol. 59, no. 6, pp. 1085–1091, 2009.
- [60] Z. K. Zhou, S. Q. Lin, T. L. Yue et al., "Adsorption of food dyes from aqueous solution by glutaraldehyde cross-linked magnetic chitosan nanoparticles," *Journal of Food Engineering*, vol. 126, pp. 133–141, 2014.
- [61] J. S. Gonzalez, P. Nicolás, M. L. Ferreira et al., "Fabrication of ferrogels using different magnetic nanoparticles and their performance on protein adsorption," *Polymer International*, vol. 63, no. 2, pp. 258–265, 2014.
- [62] M. S. Farid, A. Shariati, A. Badakhshan et al., "Using nanochitosan for harvesting microalga *Nannochloropsis* sp.," *Bioresource Technology*, vol. 131, pp. 555–559, 2013.
- [63] R. Divakaran and V. N. S. Pillai, "Flocculation of algae using chitosan," *Journal of Applied Phycology*, vol. 14, no. 5, pp. 419–422, 2002.
- [64] B. Riaño, B. Molinuevo, and M. C. García-González, "Optimization of chitosan flocculation for microalgal-bacteria biomass harvesting via response surface methodology," *Ecological Engineering*, vol. 38, no. 1, pp. 110–113, 2012.
- [65] Y. M. Chen, J. C. Liu, and Y.-H. Ju, "Flotation removal of algae from water," *Colloids and Surfaces B: Biointerfaces*, vol. 12, no. 1, pp. 49–55, 1998.

Research Article

Photodegradation of Methyl Orange Using Magnetically Recoverable AgBr@Ag₃PO₄/Fe₃O₄ Photocatalyst under Visible Light

Zhen Wang, Lu Yin, Ziwen Chen, Guowang Zhou, and Huixiang Shi

Department of Environmental Engineering, Zhejiang University, Yu Hang Tang Road, Hangzhou, Zhejiang 310058, China

Correspondence should be addressed to Huixiang Shi; lanyueheyu@163.com

Received 7 February 2014; Accepted 26 February 2014; Published 1 April 2014

Academic Editor: Haiqiang Wang

Copyright © 2014 Zhen Wang et al. This is an open access article distributed under the Creative Commons Attribution License, which permits unrestricted use, distribution, and reproduction in any medium, provided the original work is properly cited.

A novel magnetically recoverable AgBr@Ag₃PO₄/Fe₃O₄ hybrid was prepared by a simple deposition-precipitation approach and characterized by X-ray diffraction (XRD), transmission electron microscopy (TEM), and UV-Vis diffuse reflectance spectroscopy (DRS). The results revealed that the photocatalytic activity and stability of AgBr@Ag₃PO₄/Fe₃O₄ composite toward decomposition of methyl orange (MO) dye were superior to those of pure Ag₃PO₄ under visible light irradiation. The photocatalytic activity enhancement of AgBr@Ag₃PO₄/Fe₃O₄ is closely related to the efficient separation of electron-hole pairs derived from the matching band potentials between Ag₃PO₄ and AgBr, as well as the good conductivity of Fe₃O₄. Moreover, the photocatalyst could be easily separated by applying an external magnetic field due to its magnetic property. The quenching effects of different scavengers proved that active h⁺ and [•]O₂⁻ played the major role for the MO degradation. This work would provide new insight for the construction of visible light responsible photocatalysts with high performance, good stability, and recoverability.

1. Introduction

As a promising way to meet the challenges of environmental pollution, photocatalysis has attracted considerable interest over the past few decades [1–4]. With the shortage of energy sources becoming severe, significant efforts have now been directed toward the exploitation of highly efficient visible light responsible photocatalysts which can potentially utilize solar energy [5–8]. Very recently, Ag₃PO₄ has been put forward as a novel photocatalyst with excellent oxidative capability for the purification of water under visible light irradiation, which thus inspired great enthusiasm [9–13]. It seems to be a promising material for efficient photodecomposition of organic contaminants. Nevertheless, it should be noted that, in the present Ag₃PO₄ photocatalytic system, Ag₃PO₄ is prone to be photochemically decomposed to Ag if no sacrificial reagent is involved [14], which inevitably becomes a main obstacle for Ag₃PO₄ in practical application.

Recent reports indicated that epitaxial growth of an AgX (X = Br, I) nanoshell on the surface of Ag₃PO₄ could greatly

enhance the chemical stability and activity of Ag₃PO₄ [15–17]. For instance, Bi et al. introduced AgX (X = Cl, Br, I) for the modification of Ag₃PO₄ by a simple in situ ion-exchange method and revealed the enhanced photocatalytic properties and stability [16]. Cao et al. successfully synthesized AgBr/Ag₃PO₄ as highly efficient and stable photocatalyst [17]. This is mainly because AgX and Ag₃PO₄ have matching band potentials, which could promote the transfer and separation of photoexcited carriers through their heterojunctions. Other researchers also confirmed the enhancement in AgBr-based composites [16]. Thus, combining Ag₃PO₄ with AgX is a more promising and fascinating visible light response photocatalyst than pure Ag₃PO₄.

For nano- or micro-sized photocatalysts, another problem that restrains their application is how to effectively separate the used photocatalysts from the mixed system in a simple way [18, 19]. Immobilizing catalysts on magnetic substrates by feasible methods is proven to be an effective approach for removing and recycling particles [20–23]. Moreover, Fe₃O₄ has excellent conductivity. Thus, Fe₃O₄ could act as an

electron-transfer channel and acceptor, which would suppress the photogenerated carrier recombination [24]. Therefore, given the magnetic separation ability and conducting properties of Fe_3O_4 , it can be foreseen that fabrication of $\text{AgBr}@Ag_3PO_4/\text{Fe}_3O_4$ heterostructures could combine the advantages of activity of $\text{AgBr}@Ag_3PO_4$ with the merit of easy separation due to the incorporation of Fe_3O_4 .

Nowadays, toxic organic dyes and their effluents are among the largest groups of water pollutants. The removal of these nonbiodegradable dye molecules from the environment is a crucial ecological problem, for their toxicity and potential carcinogenicity. To solve such pollution, the methyl orange (MO), which is a typical azo dye for textile industry, is chosen as the targeted pollutant in this paper. Herein, we prepared a novel magnetically separable $\text{AgBr}@Ag_3PO_4/\text{Fe}_3O_4$ composite via a simple deposition-precipitation approach. The catalysts can be easily recovered by applying an external magnetic field. Furthermore, we demonstrate that this composite favors the separation of electron-hole pairs and exhibits the enhancement of stability and activity in the photocatalytic decomposition of MO under visible light.

2. Experimental

2.1. Materials. All chemicals were of analytical grade and used as received without purification. Nano Fe_3O_4 (particle size <50 nm) was purchased from Sigma-Aldrich.

2.2. Sample Preparation. Firstly, the Fe_3O_4 nanoparticles were dispersed in distilled water (20 mL, 7.5 mM) and then added to the AgNO_3 solution (10 mL, 0.1 M). The solution was sonicated for 10 min. Subsequently, Na_2HPO_4 aqueous solution (5 mL, 0.5 mM) was added dropwise to the above suspension. After sonicating for 10 min, a definite concentration of NaBr solution was added slowly into the above mixture. The theoretical molar percentage of added Br/original P was controlled to be 80%. The reaction was allowed to proceed for 10 min under sonication. Finally, the obtained precipitate was separated by an external magnetic field, washed with deionized water for several times, and then dried in a vacuum oven at 60°C for 12 h. The final sample was labeled as $\text{AgBr}@Ag_3PO_4/\text{Fe}_3O_4$.

For comparison, pure Ag_3PO_4 particles were prepared by a simple precipitation method according to the previous study [14]. $\text{Ag}_3\text{PO}_4/\text{Fe}_3O_4$ and $\text{AgBr}@Ag_3PO_4$ were also prepared by the same conditions by replacing the NaBr or Fe_3O_4 solution with water.

2.3. Characterization. For XRD studies, the samples were recorded on X'Pert Pro PANalytical automatic diffractometer, using $\text{Cu-K}\alpha$ radiation ($\lambda = 0.154\text{ nm}$) in the 2θ range of 10° – 80° . TEM images were taken on a JEM-1200 (JEOL) microscope with an acceleration voltage of 80 kV. The UV-Vis diffuse reflectance spectra in the range of 230–700 nm were recorded on a Pgeneral TU-1901 PC spectrometer, using BaSO_4 as a standard.

2.4. Photocatalytic Tests. The photocatalytic activity of the sample was evaluated by photodegradation of MO at room temperature. Briefly, 60 mg of photocatalyst was added to an

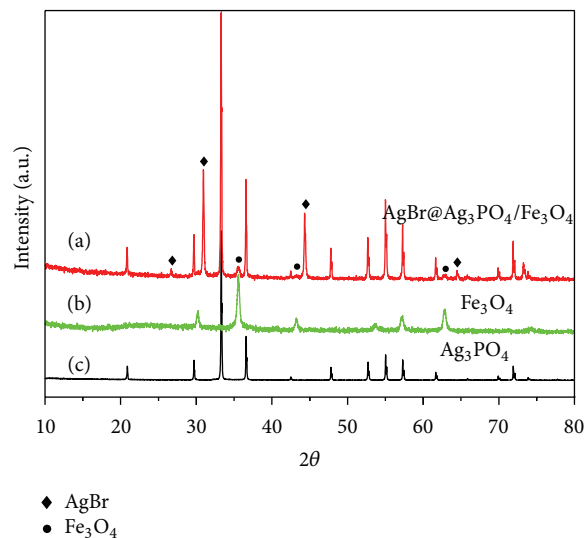


FIGURE 1: XRD patterns of (a) Ag_3PO_4 , (b) Fe_3O_4 , and (c) $\text{AgBr}@Ag_3PO_4/\text{Fe}_3O_4$.

aqueous solution of MO (100 mL, 20 mg/L). The suspension was mechanically stirred for 45 min in dark conditions to reach complete adsorption-desorption equilibrium. Then, it was irradiated with a 150 W Xe lamp with a 400 nm light filter. During the illumination, at given time intervals, about 3 mL aliquots were sampled, magnetically separated, and centrifuged at 10,000 rpm for 5 min to remove the remaining particles. The concentrations of MO were analyzed on a UV-Vis spectrophotometer at 461 nm.

Additionally, the recycling experiments were performed for three consecutive cycles to test the stability and reusability of the as-prepared $\text{AgBr}@Ag_3PO_4/\text{Fe}_3O_4$ composite. After each cycle, the photocatalyst was separated by an external magnetic field, washed thoroughly with deionized water, and then dried at 60°C for the next test.

3. Results and Discussion

3.1. Structural Characterization. XRD was used to investigate the different crystalline structures of the as-prepared photocatalysts. As shown in Figure 1(a), all the characteristic diffraction peaks can be readily indexed as the different crystalline planes of Ag_3PO_4 (JCPDS, card number 06-0505). From Figure 1(b), the diffraction peaks can be well indexed to magnetite Fe_3O_4 (JCPDS, card number 19-0629). For the pattern of $\text{AgBr}@Ag_3PO_4/\text{Fe}_3O_4$ (Figure 1(c)), besides the peaks of Ag_3PO_4 and Fe_3O_4 , the diffraction peaks of AgBr at 26.6° , 30.9° , 44.3° , and 64.4° corresponding to the (111), (200), (220), and (400) have also been detected, confirming that AgBr have been formed on the Ag_3PO_4 surface after reaction with NaBr. The diffraction peaks of Fe_3O_4 at 35.5° , 43.2° , and 62.8° correspond to the (311), (400), and (440). However, as shown in Figures 1(b) and 1(c), the diffraction peaks from Fe_3O_4 turn weaker in the as-prepared $\text{AgBr}@Ag_3PO_4/\text{Fe}_3O_4$ composite due to the low content of Fe_3O_4 . These observations indicate the successful synthesis of $\text{AgBr}@Ag_3PO_4/\text{Fe}_3O_4$ heterostructure.

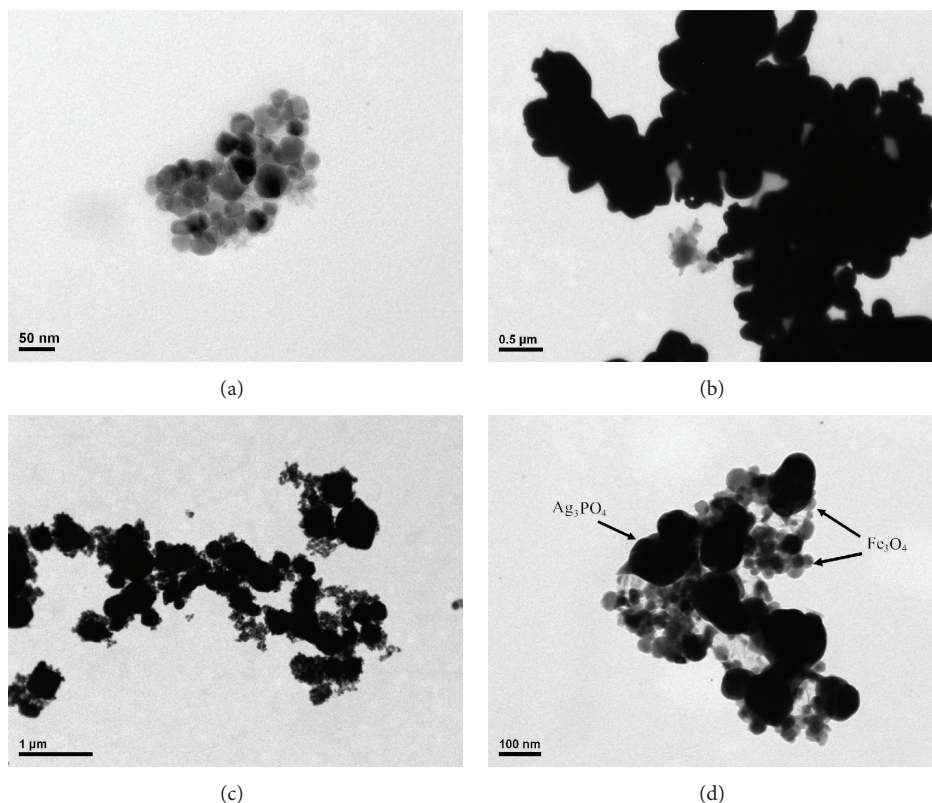


FIGURE 2: TEM images of (a) Fe_3O_4 , (b) Ag_3PO_4 , and (c, d) $\text{AgBr}@Ag_3\text{PO}_4/\text{Fe}_3\text{O}_4$ at different magnification.

The morphological and microstructural details of the $\text{AgBr}@Ag_3\text{PO}_4/\text{Fe}_3\text{O}_4$ composite were then examined by TEM measurement. As shown in Figure 2(a), the Fe_3O_4 exhibits regular spherical shape with diameter of about 20–40 nm. Figure 2(b) reveals that the Ag_3PO_4 possess an irregularly spherical morphology with diameter of 100–500 nm. Some big particles can be attributed to the agglomeration of small particles. In the case of $\text{AgBr}@Ag_3\text{PO}_4/\text{Fe}_3\text{O}_4$ hybrid, as can be seen from Figures 2(c) and 2(d) in different magnification, it is evident that, alongside the Ag_3PO_4 , the Fe_3O_4 nanoparticles are firmly anchored. This suggests a good combination between Ag_3PO_4 and Fe_3O_4 particles. Unfortunately, we failed to obtain TEM images of the $\text{AgBr}@Ag_3\text{PO}_4/\text{Fe}_3\text{O}_4$ samples, because AgBr nanoshells were easily destroyed by the high-energy electron beam during the measurements, as Wang et al. reported [25].

Figure 3 shows the UV-Vis diffuse reflectance spectra of Ag_3PO_4 , Fe_3O_4 , and the related complex photocatalysts. Pure Ag_3PO_4 shows a sharp fundamental absorption edge at about 520 nm, in accordance with the previous observation [26]. In contrast to pure Ag_3PO_4 , the absorption of $\text{AgBr}@Ag_3\text{PO}_4/\text{Fe}_3\text{O}_4$ sample toward the visible light region is remarkably enhanced. It could be mainly attributed to the introduction of Fe_3O_4 nanoparticles, which is a well-performing light harvesting material as we can see in Figure 3.

3.2. Photocatalytic Performance. The photocatalytic activity of the as-prepared $\text{AgBr}@Ag_3\text{PO}_4/\text{Fe}_3\text{O}_4$ was evaluated

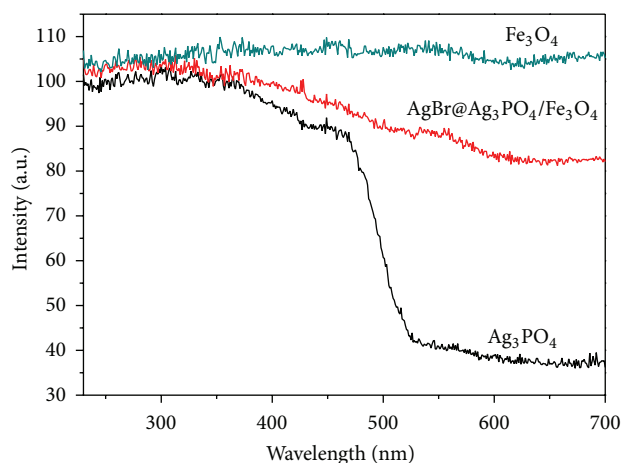


FIGURE 3: UV-Vis diffuse reflectance spectra of Ag_3PO_4 , Fe_3O_4 , and $\text{AgBr}@Ag_3\text{PO}_4/\text{Fe}_3\text{O}_4$.

by the degradation of MO under visible light irradiation. Figure 4 gives the absorption spectra of an aqueous solution of MO exposed to visible irradiation for various time periods. In the reaction process, the color of the MO solution gradually diminished (as the inset shows), and the typical absorption peak at 461 nm disappeared after 15 min, indicating that the chromophoric structure of the dye was completely destroyed assisted by $\text{AgBr}@Ag_3\text{PO}_4/\text{Fe}_3\text{O}_4$.

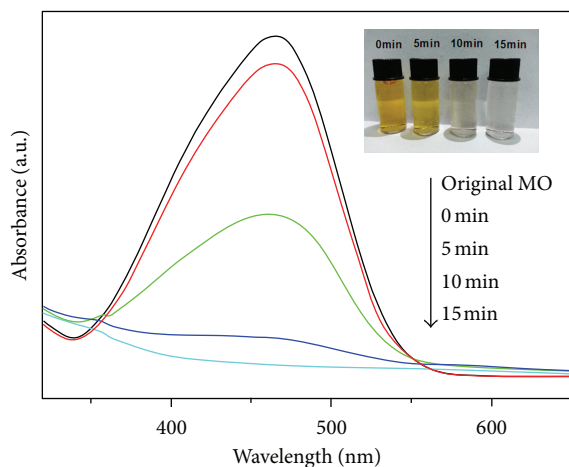


FIGURE 4: Absorption spectral changes of MO over $\text{AgBr}@Ag_3PO_4/\text{Fe}_3O_4$ composite as a function of irradiation time. The inset shows the color changes of the MO solutions corresponding to the degradation times.

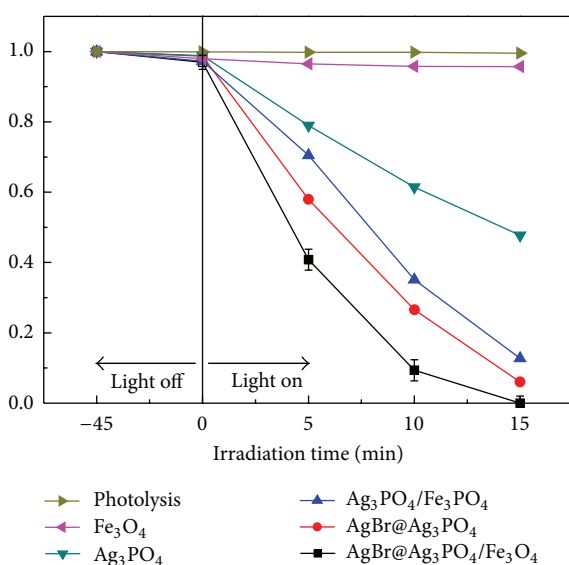


FIGURE 5: Photocatalytic degradation curves of MO over different photocatalysts under visible light irradiation.

For comparison, the photodegradation of MO was also performed with photolysis, pure Ag_3PO_4 , Fe_3O_4 , $\text{Ag}_3\text{PO}_4/\text{Fe}_3\text{O}_4$, and $\text{AgBr}@Ag_3\text{PO}_4$.

As can be seen from Figure 5, negligible degradation was detected under photolysis or using Fe_3O_4 as photocatalyst. Similar to the previous reports, the pure Ag_3PO_4 sample reveals a nice photodegradation performance under visible light (47.7% in 15 min). For comparison, after epitaxial growth of AgBr nanoshell on the surface of Ag_3PO_4 , the $\text{AgBr}@Ag_3\text{PO}_4$ show much higher photocatalytic activity for the degradation of MO dye (94% in 15 min). This is mainly due to the effective coupling where the conduction band and valence band potentials of AgBr semiconductor are more negative than that of Ag_3PO_4 , which could promote the

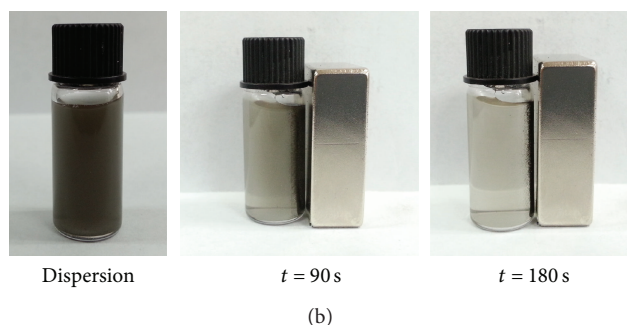
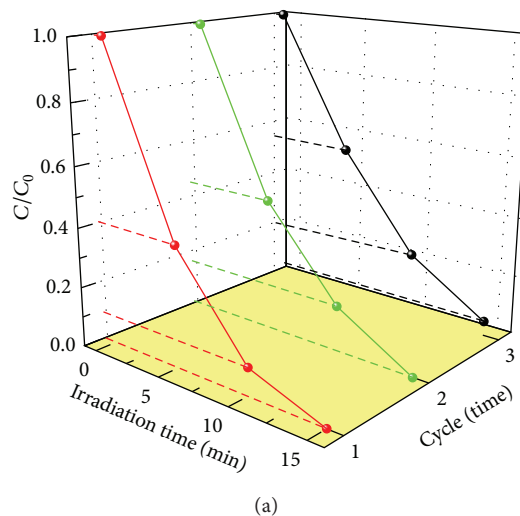


FIGURE 6: (a) Cycling runs in the photocatalytic degradation of MO over $\text{AgBr}@Ag_3PO_4/\text{Fe}_3O_4$ under visible light irradiation. (b) Magnetic separation tests for $\text{AgBr}@Ag_3PO_4/\text{Fe}_3O_4$ via a cubic Nd-Fe-B magnet (3 mm*20 mm*10 mm), revealing that the photocatalyst can be recycled with an external magnetic field within 3 min.

transfer and separation of photoexcited electron-hole pairs [16]. In addition, the combination of Fe_3O_4 with Ag_3PO_4 also achieved good degradation efficiency (87.3% in 15 min). As Xi et al. explained, because of the excellent conductivity, the charge transport is improved after introduction of Fe_3O_4 into the composite, which would enhance the separation of electron-hole pairs [24]. Furthermore, just as the experimental results confirmed, once integrating the conductivity of Fe_3O_4 and the structural match of AgBr with Ag_3PO_4 particles, the $\text{AgBr}@Ag_3PO_4/\text{Fe}_3O_4$ exhibits the highest photocatalytic efficiency.

3.3. Stability and Recyclability of $\text{AgBr}@Ag_3PO_4/\text{Fe}_3O_4$. The stability of a photocatalyst is one of the most important parameters for its application. As our previous study demonstrated [27], Ag_3PO_4 is quite unstable at repeated use. However, as Figure 6(a) presents, the MO solution is quickly bleached after every MO decomposition experiment, and photocatalyst ternary $\text{AgBr}@Ag_3PO_4/\text{Fe}_3O_4$ is stable enough during the three repeated experiments without exhibiting any obvious loss of photocatalytic activity. Besides, the magnetic separation ability of the photocatalyst is impressive. As shown in Figure 6(b), the as-prepared $\text{AgBr}@Ag_3PO_4/\text{Fe}_3O_4$ can be

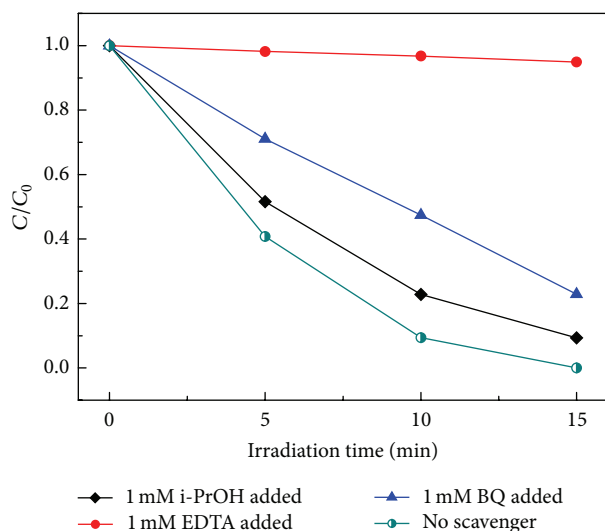


FIGURE 7: Effects of different scavengers on the degradation of MO over AgBr@Ag₃PO₄/Fe₃O₄ photocatalyst.

conveniently collected from the solution by applying an external magnetic field within 3 min. This desirable property is what other conventional powder photocatalysts lack. Therefore, the as-prepared AgBr@Ag₃PO₄/Fe₃O₄ composite can work as an effective photocatalyst for pollutant degradation with good stability and recoverability.

3.4. Involved Active Species in the Photocatalysis. In order to investigate the photocatalytic degradation mechanism of AgBr@Ag₃PO₄/Fe₃O₄, it is necessary to verify the active species involved in the photocatalysis. Generally, photoinduced active species including h⁺, •OH radicals, and •O₂⁻ are expected to be involved in the photocatalytic process. Herein, i-PrOH was added to the reaction system as an •OH scavenger, EDTA-Na₂ was introduced as a scavenger of h⁺, and BQ was adopted to quench •O₂⁻ [28].

Figure 7 shows that, in the presence of EDTA, the photodegradation of MO was drastically inhibited with the degradation efficiency less than 5%. However, the employment of i-PrOH in the same photocatalytic system made a minor change caused in the photocatalytic degradation of MO. Furthermore, when the •O₂⁻ radical scavenger (BQ) was introduced, an evident decreasing photocatalytic activity of the AgBr@Ag₃PO₄/Fe₃O₄ composite was observed. These results indicate that active species h⁺ and •O₂⁻ contribute most to the photocatalytic system, and the presence of •OH radicals is considered to be of less importance to the reaction. Thus, we can anticipate the possible mechanism for the photocatalytic degradation of MO by AgBr@Ag₃PO₄/Fe₃O₄ composites. Under visible light irradiation, Ag₃PO₄ and AgBr can be simultaneously excited to form electron-hole (h⁺) pairs. As is known, AgBr and Ag₃PO₄ have matching band potentials; the photoinduced electrons can transfer from the CB bottom of AgBr to that of Ag₃PO₄, further migrate to Fe₃O₄ particles, and react with the adsorbed oxygen molecule

to yield •O₂⁻. At the same time, the holes also move in the opposite direction from the VB top of Ag₃PO₄ to that of AgBr. The separated h⁺ then mainly participate in the degradation of MO by direct oxidation, which would be together with •O₂⁻. However, a small number of h⁺ can still react with water to produce •OH radicals to degrade MO.

4. Conclusions

In summary, we reported an investigation on the preparation and photocatalytic activity of a novel magnetically recoverable AgBr@Ag₃PO₄/Fe₃O₄ hybrid. Because of the magnetism of Fe₃O₄ and the matching band between AgBr and Ag₃PO₄, the as-synthesized AgBr@Ag₃PO₄/Fe₃O₄ nanoparticles exhibited efficient photocatalytic activity, good stability, and recyclability toward decomposition of MO under visible light irradiation. In addition, the quenching effects of different scavengers proved that reactive h⁺ and •O₂⁻ played the major role for the MO degradation. We expected that this kind of magnetically separable AgBr@Ag₃PO₄/Fe₃O₄ composite would provide new insight for the design and fabrication of high performance photocatalysts toward environmental protection.

Conflict of Interests

The authors declare that there is no conflict of interests regarding the publication of this paper.

Acknowledgment

The authors genuinely appreciate the financial support of this work from Major Science and Technology Projects Focus on Social Development Projects of Zhejiang Province (2010C03003 and 2012C03004-1).

References

- [1] S. Malato, P. Fernández-Ibáñez, M. I. Maldonado, J. Blanco, and W. Gernjak, "Decontamination and disinfection of water by solar photocatalysis: recent overview and trends," *Catalysis Today*, vol. 147, no. 1, pp. 1–59, 2009.
- [2] M. N. Chong, B. Jin, C. W. K. Chow, and C. Saint, "Recent developments in photocatalytic water treatment technology: a review," *Water Research*, vol. 44, no. 10, pp. 2997–3027, 2010.
- [3] Y. Qu and X. Duan, "Progress, challenge and perspective of heterogeneous photocatalysts," *Chemical Society Reviews*, vol. 42, pp. 2568–2580, 2013.
- [4] H. Tong, S. Ouyang, Y. Bi, N. Umezawa, M. Oshikiri, and J. Ye, "Nano-photocatalytic materials: possibilities and challenges," *Advanced Materials*, vol. 24, no. 2, pp. 229–251, 2012.
- [5] W. Ren, Z. Ai, F. Jia, L. Zhang, X. Fan, and Z. Zou, "Low temperature preparation and visible light photocatalytic activity of mesoporous carbon-doped crystalline TiO₂," *Applied Catalysis B: Environmental*, vol. 69, no. 3–4, pp. 138–144, 2007.
- [6] H. Lin, J. Cao, B. Luo, B. Xu, and S. Chen, "Synthesis of novel Z-scheme AgI/Ag/AgBr composite with enhanced visible light photocatalytic activity," *Catalysis Communications*, vol. 21, pp. 91–95, 2012.

- [7] J. Ren, W. Wang, S. Sun, L. Zhang, and J. Chang, "Enhanced photocatalytic activity of Bi_2WO_6 loaded with Ag nanoparticles under visible light irradiation," *Applied Catalysis B: Environmental*, vol. 92, no. 1-2, pp. 50–55, 2009.
- [8] X. Zhang, G. Zhou, H. Zhang, C. Wu, and H. Song, "Characterization and activity of visible light-driven TiO_2 photocatalysts co-doped with nitrogen and lanthanum," *Transition Metal Chemistry*, vol. 36, no. 2, pp. 217–222, 2011.
- [9] Y. Bi, S. Ouyang, N. Umezawa, J. Cao, and J. Ye, "Facet effect of single-crystalline Ag_3PO_4 sub-microcrystals on photocatalytic properties," *Journal of the American Chemical Society*, vol. 133, no. 17, pp. 6490–6492, 2011.
- [10] Y. Bi, H. Hu, S. Ouyang, Z. Jiao, G. Lu, and J. Ye, "Selective growth of Ag_3PO_4 submicro-cubes on Ag nanowires to fabricate necklace-like heterostructures for photocatalytic applications," *Journal of Materials Chemistry*, vol. 22, pp. 14847–14850, 2012.
- [11] H. Wang, Y. Bai, J. Yang, X. Lang, J. Li, and L. Guo, "A facile way to rejuvenate Ag_3PO_4 as a recyclable highly efficient photocatalyst," *Chemistry—A European Journal*, vol. 18, no. 18, pp. 5524–5529, 2012.
- [12] Y. S. Xu and W. D. Zhang, "Monodispersed Ag_3PO_4 nanocrystals loaded on the surface of spherical Bi_2MoO_6 with enhanced photocatalytic performance," *Dalton Transactions*, vol. 42, pp. 1094–1101, 2013.
- [13] P. Dong, Y. Wang, B. Cao et al., " Ag_3PO_4 /reduced graphite oxide sheets nanocomposites with highly enhanced visible light photocatalytic activity and stability," *Applied Catalysis B: Environmental*, vol. 132–133, pp. 45–53, 2013.
- [14] W. Wang, B. Cheng, J. Yu, G. Liu, and W. Fan, "Visible-light photocatalytic activity and deactivation mechanism of Ag_3PO_4 spherical particles," *Chemistry—An Asian Journal*, vol. 7, pp. 1902–1908, 2012.
- [15] B. Wang, X. Gu, Y. Zhao, and Y. Qiang, "A comparable study on the photocatalytic activities of Ag_3PO_4 , AgBr and AgBr/ Ag_3PO_4 hybrid microstructures," *Applied Surface Science*, vol. 283, pp. 396–401, 2013.
- [16] Y. Bi, S. Ouyang, J. Cao, and J. Ye, "Facile synthesis of rhombic dodecahedral AgX/ Ag_3PO_4 (X = Cl, Br, I) heterocrystals with enhanced photocatalytic properties and stabilities," *Physical Chemistry Chemical Physics*, vol. 13, no. 21, pp. 10071–10075, 2011.
- [17] J. Cao, B. Luo, H. Lin, B. Xu, and S. Chen, "Visible light photocatalytic activity enhancement and mechanism of AgBr/ Ag_3PO_4 hybrids for degradation of methyl orange," *Journal of Hazardous Materials*, vol. 217–218, pp. 107–115, 2012.
- [18] S. Linley, T. Leshuk, and F. X. Gu, "Magnetically separable water treatment technologies and their role in future advanced water treatment: a patent review," *Clean-Soil Air Water*, vol. 41, pp. 1152–1156, 2013.
- [19] V. Polshettiwar, R. Luque, A. Fihri, H. Zhu, M. Bouhrara, and J.-M. Basset, "Magnetically recoverable nanocatalysts," *Chemical Reviews*, vol. 111, no. 5, pp. 3036–3075, 2011.
- [20] X. Xu, X. Shen, G. Zhu, L. Jing, X. Liu, and K. Chen, "Magnetically recoverable Bi_2WO_6 - Fe_3O_4 composite photocatalysts: fabrication and photocatalytic activity," *Chemical Engineering Journal*, vol. 200–202, pp. 521–531, 2012.
- [21] L. Zhang, W. Wang, S. Sun, Y. Sun, E. Gao, and Z. Zhang, "Elimination of BPA endocrine disruptor by magnetic $\text{BiOBr@SiO}_2/\text{Fe}_3\text{O}_4$ photocatalyst," *Applied Catalysis B: Environmental*, vol. 148–149, pp. 164–169, 2014.
- [22] L. Zhang, W. Wang, L. Zhou, M. Shang, and S. Sun, " Fe_3O_4 coupled BiOCl : a highly efficient magnetic photocatalyst," *Applied Catalysis B: Environmental*, vol. 90, no. 3–4, pp. 458–462, 2009.
- [23] H. Liu, Z. Jia, S. Ji, Y. Zheng, M. Li, and H. Yang, "Synthesis of $\text{TiO}_2/\text{SiO}_2/\text{Fe}_3\text{O}_4$ magnetic microspheres and their properties of photocatalytic degradation of dyestuff," *Catalysis Today*, vol. 175, no. 1, pp. 293–298, 2011.
- [24] G. Xi, B. Yue, J. Cao, and J. Ye, " $\text{Fe}_3\text{O}_4/\text{WO}_3$ hierarchical core-shell structure: high-performance and recyclable visible-light photocatalysis," *Chemistry—A European Journal*, vol. 17, no. 18, pp. 5145–5154, 2011.
- [25] W. S. Wang, H. Du, R. X. Wang, T. Wen, and A. W. Xu, "Heterostructured $\text{Ag}_3\text{PO}_4/\text{AgBr}/\text{Ag}$ plasmonic photocatalyst with enhanced photocatalytic activity and stability under visible light," *Nanoscale*, vol. 5, pp. 3315–3321, 2013.
- [26] G. Chen, M. Sun, Q. Wei, Y. Zhang, B. Zhu, and B. Du, " Ag_3PO_4 /graphene-oxide composite with remarkably enhanced visible-light-driven photocatalytic activity toward dyes in water," *Journal of Hazardous Materials*, vol. 244–245, pp. 86–93, 2013.
- [27] Z. Wang, L. Yin, M. Zhang et al., "Synthesis and characterization of Ag_3PO_4 /multiwalled carbon nanotube composite photocatalyst with enhanced photocatalytic activity and stability under visible light," *Journal of Materials Science*, vol. 49, pp. 1585–1593, 2013.
- [28] M. Ge, N. Zhu, Y. Zhao, J. Li, and L. Liu, "Sunlight-assisted degradation of dye pollutants in Ag_3PO_4 suspension," *Industrial and Engineering Chemistry Research*, vol. 51, no. 14, pp. 5167–5173, 2012.

Research Article

A Novel Nanomodified Cellulose Insulation Paper for Power Transformer

Yuan Yuan^{1,2} and Ruijin Liao¹

¹ State Key Laboratory of Power Transmission Equipment & System Security and New Technology, Chongqing University, Shapingba District, Chongqing 400044, China

² School of Materials Science and Engineering, Chongqing University, Shapingba District, Chongqing 400044, China

Correspondence should be addressed to Yuan Yuan; yuanyc@cq.edu.cn

Received 6 February 2014; Accepted 10 March 2014; Published 31 March 2014

Academic Editor: Fan Dong

Copyright © 2014 Y. Yuan and R. Liao. This is an open access article distributed under the Creative Commons Attribution License, which permits unrestricted use, distribution, and reproduction in any medium, provided the original work is properly cited.

A novel cellulose insulation paper handsheet has successfully been modified with various contents of montmorillonite (MMT). Relative permittivity and breakdown strength were investigated. The microstructure of MMT in Kraft paper was observed with scanning electron microscopy (SEM) and X-ray diffraction. The relative permittivity of the immersed oil Kraft-MMT handsheets (K-MMT) initially decreased with the increasing amount of MMT. For MMT concentration of 9 wt%, K-9% MMT possessed the lowest relative permittivity of approximately 2.3 at 50 Hz. The breakdown voltage of the paper-oil-paper composite insulation system increased from 50.3 kV to 56.9 kV. The tensile strength of the paper handsheet was also measured.

1. Introduction

Kraft paper is widely used as a form of cellulose insulation in oil-filled transformer equipment [1–5]. For very long time, it has been made from wood fiber. However, Kraft paper is the preferred insulation for all oil-filled transformers for its low price and reasonably good performance. The relative permittivity of immersed oil Kraft is about 4.4 or more than twice that of oil (about 2.1 at 50 Hz). Thus, the oil gap shares higher electric field strength [6]. The electric field strength of the oil gap would become lower, when the relative permittivity of Kraft paper was reduced. Uniform electric field distributions can be achieved in paper-oil-paper composite insulation systems. Therefore, the insulating distance in transformers can also be decreased, which means the miniaturization of transformer and the reduced amount of cellulose insulation paper.

In my previous work of our group, low relative permittivity polyimide (PI)-SiO₂ films and Kraft-SiO₂ paper handsheet were successfully prepared using SiO₂ hollow spheres with different weight percentages [7–9]. The relative permittivity of all the composites has been decreased, and electric field strength has been improved at the same time.

In the present work, Kraft-montmorillonite insulation paper handsheets (K-MMT) were obtained successfully with different contents of MMT. The distribution of the MMT in the handsheet was observed by scanning electron microscopy (SEM). The effect of the content of the MMT on the relative permittivity of the oil-immersed handsheet was investigated by broadband dielectric spectroscopy. Breakdown tests of the paper-oil-paper composite insulation system with different relative permittivity papers were performed. The tensile strength of the paper handsheet was also measured.

2. Material and Methods

The pulp was coniferous wood pulp from Russia, purchased by Qingdao Xinhaifeng Co., Ltd. (Qingdao, China). A natural montmorillonite (Nanomer I.31PS, Nanacor) clay surface modified with octadecylamine and silane coupling agent was used as the reinforcement filler. The nanocomposite was prepared by physical blending.

The dielectric property was measured by a Novo Control Broadband Dielectric Spectrometer with the films dipped in oil over the frequency varying from 1 Hz to 10 MHz at room

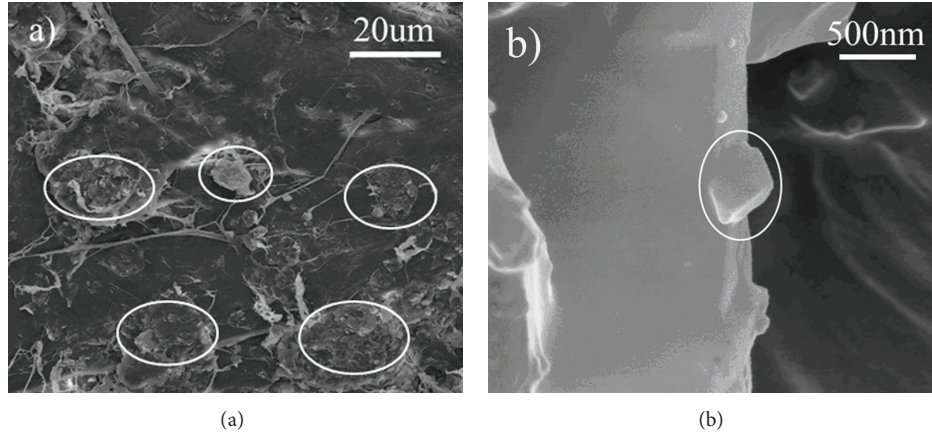


FIGURE 1: SEM images of the cross-sectional surface of K-MMT composites (a) the dispersed condition of MMT and (b) MMT nanoparticle.

temperature. The morphology of the cross-sectional surface of K-MMT paper handsheet was observed on an NOVA400 field emission scanning electron microscope (SEM) (FEI, USA) with a working voltage of 10 KV. The composites were fractured first in liquid nitrogen and mounted on conductive glass by means of a double-sided adhesive tape; then, a thin layer of gold is sputtered onto the cross-sectional surface before SEM observation. The condensed structure is analyzed from the figure on a Empyrean X-ray Diffraction Equipment (PANalytical Corporation, Almelo, Netherland), with 2θ changes from 2° to 30° , a scan speed of $2^\circ/\text{min}$, and $\text{CuK}\alpha$ radiation ($\lambda = 0.154 \text{ nm}$) as the X-ray source. The thermal property was measured by Q50 thermogravimetry analysis instrument with heating rate $10^\circ\text{C}/\text{min}$. Meanwhile, the tensile strength was characterized by AT-L-1 tensile machine (ANMT Corporation, Jinan, China) using ISO 1924-2:1994 method.

3. Results and Discussion

3.1. Preparation of Kraft-Montmorillonite (K-MMT) Paper Handsheet. The MMT were dissolved in deionized water (1:100 wt%) and the slurry was homogenized by vigorous agitation with a magnetic stir bar for 10 min. MMT powder with different weight percentages were added to Kraft pulps. The mixtures were stirred for 3 min at 3000 r/min in a fiber disintegrating device and were used to prepare the handsheet. Each wet handsheet was pressed at 15 MPa for 5 min at 80°C and dried at 105°C for 7 min under a vacuum. Handsheet with a target basis weight of $120 \text{ g}/\text{m}^2$ was produced. MMT with a low content were uniformly dispersed with increased concentration (Figure 1(a)). The MMT locally aggregated as almost individual particles in the matrix (Figure 1(b)).

The structures of the Kraft, K-MMT, and MMT were characterized by X-ray diffraction. Figure 2 presented the X-ray diffraction spectrum of Kraft, K-MMT, and MMT. From the figure, both K-MMT and MMT have obviously peaks at about 4° , and Kraft did not have any sharp peak but a broad peak. This clearly proved the successful modification of the K-MMT composite.

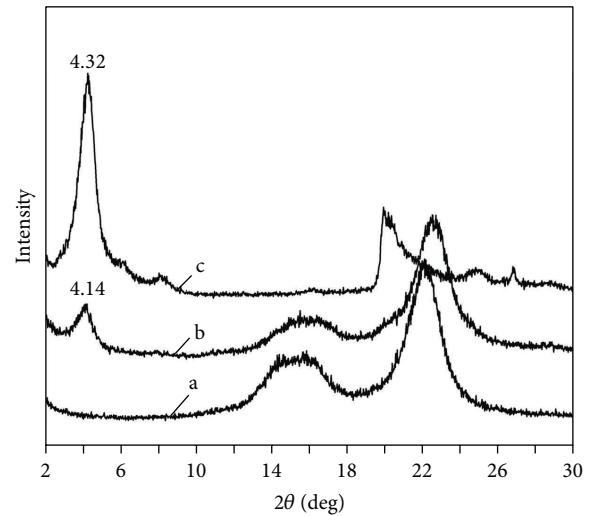


FIGURE 2: X-ray diffraction spectrum for (a) Kraft; (b) K-MMT; (c) MMT.

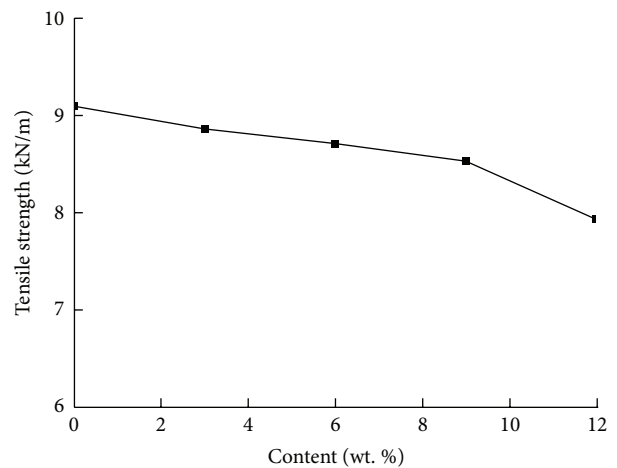


FIGURE 3: Effect of MMT content on the tensile strength of oil immersed K-MMT handsheet.

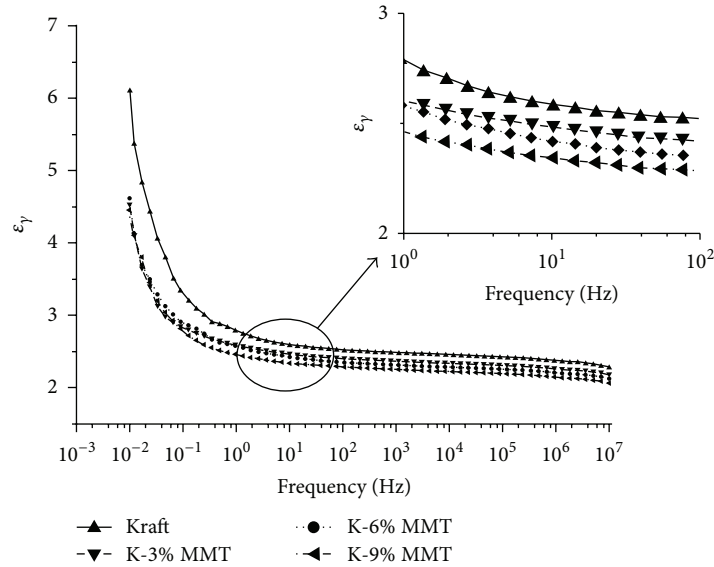


FIGURE 4: The relation of relative permittivity with different frequency and content of MMT in the oil immersed K-MMT handsheet.

The contents of MMT nanoparticles in the handsheets were 0%, 3%, 6%, 9%, and 12%; they were thus designated as Kraft, K-3% MMT, K-6% MMT, K-9% MMT, and K-12% MMT, respectively.

3.2. The Tensile Strength of Kraft-Montmorillonite (K-MMT) Paper Handsheet. The tensile strength of Kraft (immersed oil) modified of MMT nanosheet was measured following the ISO 1924-2:1994 method. Figure 3 contained the mechanical property of the series of modified K-MMT. From the figure, the tensile strength had a tiny decrease with the increase of the MMT content from 0 to 9%. However, the tensile strength exhibited a dramatic reduction when the MMT content exceeded the 9%. So K-12% MMT would not be discussed for its poor mechanical property.

3.3. The Relative Permittivity of Kraft-Montmorillonite (K-MMT) Paper Handsheet. The relative permittivities of Kraft (immersed oil) modified of MMT nanosheet was tested at different frequencies ranging from 10^{-2} Hz to 10^7 Hz at 25°C . Figure 4 possessed the relative permittivity spectrum of the K-MMT. It showed that the variation trends of the four samples were similar. The changes in the relative permittivities decreased moderately in the range from 1 Hz to 10^7 Hz and dramatically from 0.01 Hz to 1 Hz.

The relative permittivity of the K-MMT (K-3% MMT, K-6% MMT, and K-9% MMT) composite was lower than that of Kraft at different frequencies. The relative permittivity of air is 1.0. Thus, air voids stored in MMT nanosheet were a cause of reduced relative permittivity [10]. The existence of MMT nanosheet improves the distance of fiber chains. The oil content of handsheet increased due to air voids in the composite [11]. Therefore, the relative permittivity decreased [12–15]. Noticeably, the relative permittivity (at 50 Hz) of the handsheet decreased from 2.55 (Kraft) to 2.30 (K-9% MMT). K-9% MMT exhibited the lowest relative permittivity.

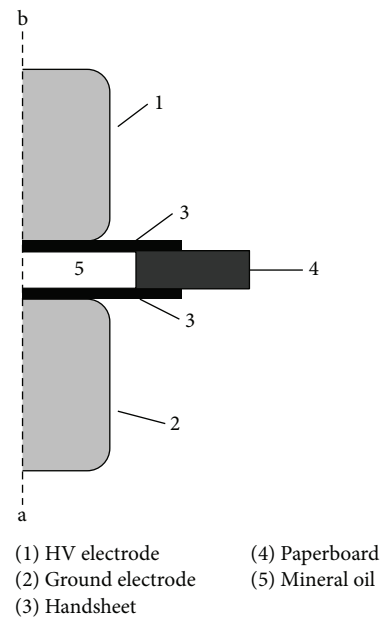


FIGURE 5: Computational domain.

A low content of MMT nanosheet (<9%) improved the distance of fiber chains. The order of permittivity was Kraft > K-3% MMT > K-6% MMT > K-9% MMT.

3.4. Breakdown Electrical Strength of a Paper-Oil-Paper Composite Insulation System. A uniformly distributed electric field between two test electrodes was proven by simulation analysis. Figure 5 depicts the computational domain for the dielectric test electrode. Line ab is the symmetry axis of electrode. The developed model was built under two-dimensional axial symmetry configurations and implemented using

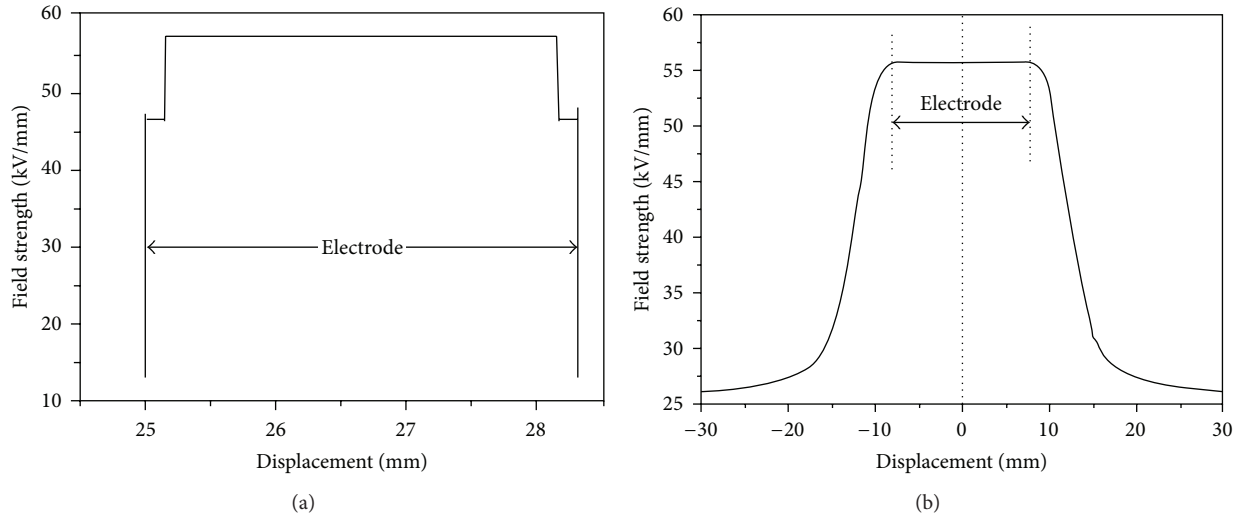


FIGURE 6: Electric field distribution of oil gap (a) symmetry is x -axis, the bottom center of ground electrode is origin; (b) vertical symmetry axis is x -axis, the center of oil gap is origin.

a COMSOL Multiphysics package based on the finite element method. A sinusoidal voltage of 50 Hz with a peak value of 100 kV was applied to the dielectric test setup.

The electric field distribution between the two test electrodes was shown in Figure 6. The two test electrodes (Figure 5) had a range from 25 mm to 28.3 mm (Figure 6(a)) and -9.5 mm to 9.5 mm (Figure 6(b)). The electric field of paper or oil was uniform along the direction of line ab between the two test electrodes (Figure 6(a)). The curve (Figure 6(b)) shows the electric field distribution of oil along the vertical direction of line ab . The electric field distribution of paper along the vertical direction of line ab was in accordance with that in Figure 6(b). Thus, the electric field of paper or oil was also uniform in the vertical direction of line ab between the two test electrodes. Therefore, the electric field distribution between the two test electrodes was uniform.

The diagram of the electrodes for measuring the breakdown voltage of the handsheet was shown in Figure 7. The diameter and height of the high-voltage (HV) and ground electrodes were both 25 mm. A copper bar was used to connect the HV electrode with the HV AC current power. In this test, mineral oil was used for the dielectric in the stainless steel box.

The focus of the experiment was the effect of the relative permittivity on the breakdown voltage of the composite insulation system. Therefore, the thickness of the oil gap was only 3 mm. The oil gap was formed in the 3 cm diameter hole of the 3 mm thick paperboard. The external diameter of the paperboard was 6 cm. The thickness of the four kinds of experimental handsheet papers (Kraft, K-3% MMT, K-6% MMT, and K-9% MMT) were 0.15 mm in this experiment. Their relative permittivity at 50 Hz was 2.55, 2.51, 2.48, and 2.30, respectively. The handsheet paper was cut into 4 cm diameter circles. All samples were put into the vacuum chamber and were dried at 90°C for 48 h, and then the mineral oil at 40°C was infused into the glass bottles in the vacuum chamber to immerse samples for 24 h. The moisture

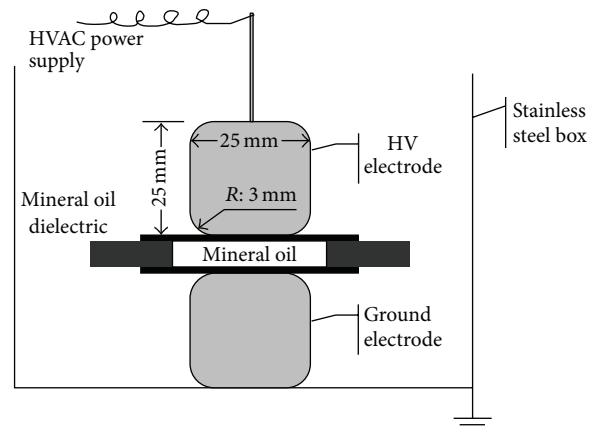


FIGURE 7: Diagram of electrodes.

content of oil impregnated paper was 0.4% through such processing. MMT was a kind of phyllosilicate with wide specific surface area. As a very good barrier, MMT nanosheet could certainly resist the current going through the insulating paper. Figure 8 presented the mechanism of MMT resisting the current. It seemed to increase the growth path for the electrical tree; thereby the breakdown electrical field strength has been improved.

The effect of the relative permittivity of the handsheet on the breakdown voltage of the composite insulation system is shown in Figure 9. The breakdown voltage of the paper-oil-paper composite insulation system increased from 50.3 kV to 56.9 kV with decreased relative permittivity of the paper from 2.55 to 2.30.

4. Conclusions

Kraft-montmorillonite insulation paper handsheets (K-MMT) are obtained successfully with different contents of

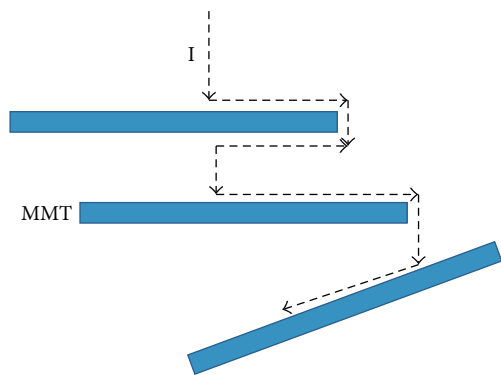


FIGURE 8: Schematic of MMT blocking the current.

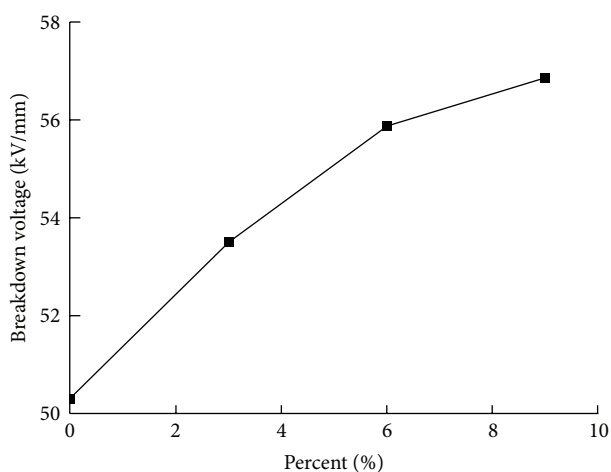


FIGURE 9: Effect of MMT content on the breakdown voltage of oil immersed K-MMT handsheet.

MMT. The MMT was uniformly dispersed in the handsheet. The effect of the content of the MMT on the relative permittivity of the oil-immersed handsheet was investigated by broadband dielectric spectroscopy. In the paper-oil-paper composite insulation system, the electric field strength of the oil gap decreased with decreased relative permittivity of the paper. Simulation analysis indicated that the electric field distribution between the two test electrodes was uniform. The breakdown voltage of the paper-oil-paper composite insulation system increased as well as the MMT content in the handsheet. The breakdown voltage of the composite insulation system increased from 50.3 to 56.9 kV when the relative permittivity of the paper decreased from 2.55 to 2.30. The experimental results were also consistent with the theoretically calculated data. The study has great significance for transformer miniaturization and reducing consumption of the cellulose insulation paper.

Conflict of Interests

The authors declare that there is no conflict of interests regarding the publication of this paper.

Acknowledgments

The work is supported by the Fundamental Research Funds for the Central Universities (Project no. CDJZR12130046), the Natural Science Foundation Project of CQ CSTC (Project no. cstcjjA50007), and the Special Financial Grant from the Chongqing Postdoctoral Science Foundation (Project no. XM20120037).

References

- [1] T. A. Prevost and T. V. Oommen, "Cellulose insulation in oil-filled power transformers: part I—history and development," *IEEE Electrical Insulation Magazine*, vol. 22, no. 1, pp. 28–35, 2006.
- [2] Z. Deng, M. Chen, S. Zhou, B. You, and L. Wu, "A novel method for the fabrication of monodisperse hollow silica spheres," *Langmuir*, vol. 22, no. 14, pp. 6403–6407, 2006.
- [3] A. M. Emsley, X. Xiao, R. J. Heywood, and M. Ali, "Degradation of cellulosic insulation in power transformers. Part 2: formation of furan products in insulating oil," *IEE Proceedings: Science, Measurement and Technology*, vol. 147, no. 3, pp. 110–114, 2000.
- [4] L. E. Lundgaard, W. Hansen, D. Linhjell, and T. J. Painter, "Aging of oil-impregnated paper in power transformers," *IEEE Transactions on Power Delivery*, vol. 19, no. 1, pp. 230–239, 2004.
- [5] T. V. Oommen and T. A. Prevost, "Cellulose insulation in oil-filled power transformers: part II—maintaining insulation integrity and life," *IEEE Electrical Insulation Magazine*, vol. 22, no. 2, pp. 5–14, 2006.
- [6] Y. Kamata, E. Ohe, K. Endoh et al., "Development of low-permittivity pressboard and its evaluation for insulation of oil-immersed EHV power transformers," *IEEE Transactions on Electrical Insulation*, vol. 26, no. 4, pp. 819–825, 1991.
- [7] Y. Yuan, Y. Wang, and B. Xie, "Preparation and properties of polyimide/SiO₂ hollow spheres composite films with good dielectric property and amazing XRD spectra," *Materials Science Forum*, vol. 663–665, pp. 584–587, 2011.
- [8] Y. Yuan, B.-P. Lin, and Y.-M. Sun, "Novel low-dielectric-constant copolyimide thin films composed with SiO₂ hollow spheres," *Journal of Applied Polymer Science*, vol. 120, no. 2, pp. 1133–1137, 2011.
- [9] T. Liu, R. J. Liao, F. Z. Zhang, and L. J. Yang, "Preparation and performance of a low relative permittivity insulation paper," in *Proceedings of the International Conference on High Voltage Engineering and Application*, pp. 211–214, 2012.
- [10] M. A. Wahab, I. Kim, and C.-S. Ha, "Microstructure and properties of polyimide/poly(vinylsilsesquioxane) hybrid composite films," *Polymer*, vol. 44, no. 16, pp. 4705–4713, 2003.
- [11] Y. B. Kim and K.-S. Yoon, "A physical method of fabricating hollow polymer spheres directly from oil/water emulsions of solutions of polymers," *Macromolecular Rapid Communications*, vol. 25, no. 18, pp. 1643–1649, 2004.
- [12] J. Lin and X. Wang, "Preparation, microstructure, and properties of novel low- κ brominated epoxy/mesoporous silica composites," *European Polymer Journal*, vol. 44, no. 5, pp. 1414–1427, 2008.
- [13] C.-L. Chung and S.-H. Hsiao, "Novel organosoluble fluorinated polyimides derived from 1,6-bis(4-amino-2-trifluoromethylphenoxy)naphthalene and aromatic dianhydrides," *Polymer*, vol. 49, no. 10, pp. 2476–2485, 2008.

- [14] Y.-J. Lee, J.-M. Huang, S.-W. Kuo, and F.-C. Chang, "Low-dielectric, nanoporous polyimide films prepared from PEO-POSS nanoparticles," *Polymer*, vol. 46, no. 23, pp. 10056–10065, 2005.
- [15] S.-H. Hsiao, C.-P. Yang, and C.-L. Chung, "Synthesis and characterization of novel fluorinated polyimides based on 2,7-bis(4-amino-2-trifluoromethylphenoxy)naphthalene," *Journal of Polymer Science A: Polymer Chemistry*, vol. 41, no. 13, pp. 2001–2018, 2003.

Research Article

SO₂ Poisoning Behaviors of Ca-Mn/TiO₂ Catalysts for Selective Catalytic Reduction of NO with NH₃ at Low Temperature

Qingqing Tian,^{1,2} Hongfeng Liu,^{1,2} Weiyuan Yao,^{1,2} Yan Wang,^{1,2} Yue Liu,^{1,2}
Zhongbiao Wu,^{1,2} Haiqiang Wang,^{1,2} and Xiaole Weng^{1,2}

¹ Department of Environmental Engineering, Zhejiang University, Hangzhou 310058, China

² Zhejiang Provincial Engineering Research Center of Industrial Boiler & Furnace Flue-Gas Pollution Control, Hangzhou 310058, China

Correspondence should be addressed to Yue Liu; yueliu@zju.edu.cn

Received 15 January 2014; Accepted 22 February 2014; Published 31 March 2014

Academic Editor: Fan Dong

Copyright © 2014 Qingqing Tian et al. This is an open access article distributed under the Creative Commons Attribution License, which permits unrestricted use, distribution, and reproduction in any medium, provided the original work is properly cited.

The sulfur tolerance of Ca modified MnO_x/TiO₂ catalysts in low-temperature SCR process was investigated. Experimental results revealed that the durability of developed catalysts in the presence of SO₂ could be improved by Ca modification. After being subjected to a range of analytical techniques, it was found that the surface Ca species could act as a SO₂ trap by preferentially reacting with SO₂ to form bulk-like CaSO₄, inhibiting the sulfation of active phase. Furthermore, the introduction of SO₂ had also preserved part of Lewis sites over the MnO_x. Both of these are conducive to NH₃ adsorption and activation at low temperature, hence improving the sulfur tolerance of Ca doped catalysts.

1. Introduction

Selective Catalytic Reduction (SCR) of NO_x with NH₃ in excess O₂ is one of the most effective ways to eliminate NO_x emissions from stationary sources [1]. However, by using commercialized V₂O₅/TiO₂-based catalysts, the SCR reactors have to be located upstream of the particulate control device due to their high operation temperature. This brings inherent problems like SO₂ oxidation, installation difficulty, and high deactivation risk. Therefore, the development of low-temperature SCR catalysts has attracted great research interests in recent years [2].

Up to now, lots of transitional metal modified low-temperature catalysts have been reported, among which, manganese oxides have been studied extensively due to their superior low-temperature SCR activity [3–9]. However, the Mn-based catalysts still suffer from SO₂ poisoning due to the presence of residual SO₂ (even after desulfurization), whose deactivation mechanism has been reported due to the sulfation of active phase or/and the blockage of catalysts' micropores by the deposition of (NH₄)₂SO₄ and NH₄HSO₄ [10]. As such, improvement of sulfur tolerance of the low-temperature SCR catalysts was also needed to widely concern.

One of the effective ways is the modifications by adding some metal oxides into the catalysts. Chang et al. [6] had reported that the addition of Sn into MnO_x-CeO₂ catalysts could greatly enhance the SO₂ resistance owing to the enhanced Lewis acid sites. Shen et al. [11] concluded that the iron doping would improve SO₂ tolerance of Mn-Ce/TiO₂ due to the inhibition of surface sulfate formation. Our previous work had demonstrated that adding Ce to Mn/TiO₂ could inhibit the active phase sulfation, contributing to the promotion in SO₂ resistance [12].

In our previous study [13], we reported that the Ca doping could greatly improve the low-temperature SCR activity of Mn/TiO₂ catalysts due to its positive effects on MnO_x dispersion and adsorptive capacity of NO_x, but the work did not look insightfully into the reaction behaviors of these catalysts in the presence of SO₂. As an alkali earth metal, Ca might have stronger chemical affinity to SO_x, which could lessen the sulfation of MnO_x, thereby enhancing the sulfur tolerance of catalysts. Similar finding was also observed by Du et al. [14] for Cu-Ce/TiO₂ system. Therefore, in this paper, the effects of Ca doping on SO₂ tolerance of Mn/TiO₂ catalysts were performed and the detailed mechanisms were analyzed by using XRD, BET, XPS, and DRIFT.

2. Experimental

2.1. Catalyst Preparation. The Ca-modified Mn/TiO₂ catalysts were prepared via a sol-gel method using butyl tetratitanate (0.1 mol), ethanol (0.8 mol), water (0.6 mol), acetic acid (0.3 mol), manganese nitrate (0.04 mol), and certain amount of calcium nitrate as we reported in the previous work [13]. The catalysts were hereafter denoted by Ca(*x*)Mn(0.4)/Ti, where *x*, 0.4 represented the molar ratio of CaO to TiO₂ and MnO_x to TiO₂, respectively.

2.2. Catalytic Activity Measurements. SCR activity measurements were carried out in a fixed-bed, quartz tubular flow reactor within the 60–200°C range of temperature. The typical reactant gas composition was NO of 600 ppm, NH₃ of 600 ppm, SO₂ of 50 ppm, O₂ of 3%, and balanced N₂, and the GHSV (gas hourly space velocity) was 40,000 h⁻¹. The concentrations of NO, NO₂, and N₂O were monitored by nondispersive infrared- (NDIR-) based gas analyzer (Photon-PGD-100 Madur Electronics).

2.3. Characterization. X-ray diffraction patterns (XRD) were recorded on a Rigaku D/Max-RA powder diffractometer using Cu Kα radiation (40 kV and 150 mV). X-ray photoelectron spectroscopy (XPS) was recorded with Al Kα X-rays (Thermal, ESCALAB 250). FT-IR spectra were acquired using an *in situ* DRIFT cell equipped with a gas flow system (Nicolet 6700 FTIR spectrometers). Samples were pretreated at 400°C in a He environment for 2 h and then cooled to 160°C. The background spectrum was recorded with flowing He and was subtracted from the catalyst spectrum.

3. Results and Discussion

3.1. Catalytic Activity in the Presence of SO₂. The effects of SO₂ on the SCR activities of Mn/TiO₂ and Ca doped Mn/TiO₂ catalysts were illustrated in Figure 1, which showed that SO₂ had obvious poisoning effect on SCR activity over all the catalysts. The Mn(0.4)/TiO₂ catalyst was much more susceptible to SO₂ than the Ca doped ones, where the NO conversion of Mn(0.4)/TiO₂ catalyst declined from 100% to 30% after introducing 50 ppm SO₂ over 4 h, but about 80% NO conversion was preserved over the Ca(0.1)-Mn(0.4)/TiO₂ catalyst. This indicated that the Ca doping could enhance the SO₂ tolerance of Mn/TiO₂ catalyst to some extent. However, the deactivation of catalysts could not be avoided in long-term running.

3.2. XRD and XPS Results

3.2.1. XRD Analysis. Figure 2 showed the XRD spectra of Mn(0.4)/TiO₂ and Ca(0.1)-Mn(0.4)/TiO₂ catalysts before and after SO₂ poisoning (fresh catalysts and used catalysts after SCR reaction in the presence of SO₂). After SO₂ poisoning, no obvious differences were observed on Mn(0.4)/TiO₂ catalyst, but peaks for CaSO₄ (PDF-no. 30-0279) were detected on Ca(0.1)-Mn(0.4)/TiO₂ catalysts, indicating the formation of bulk-like CaSO₄ during the SCR reaction. There

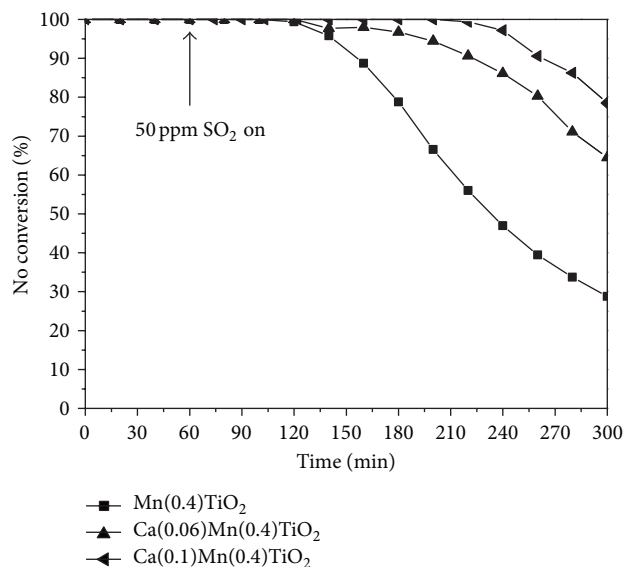


FIGURE 1: SCR activities of Mn/TiO₂ and Ca-Mn/TiO₂ prepared by a sol-gel method in the presence of SO₂ at 160°C ([NH₃]=[NO] = 600 ppm, [O₂] = 3%, [SO₂] = 50 ppm, N₂ balance, GHSV = 40,000 h⁻¹).

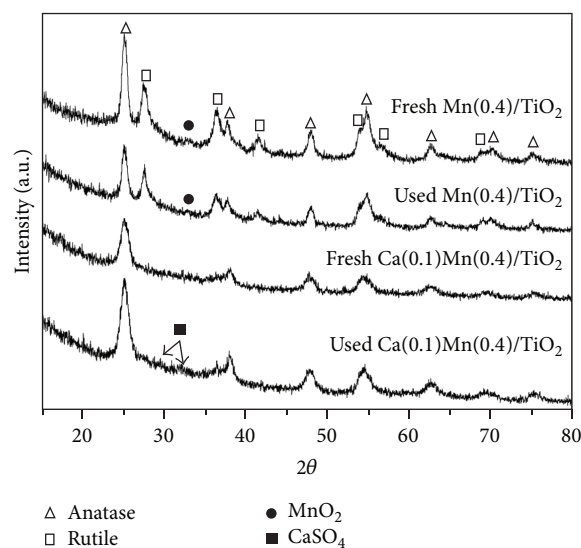


FIGURE 2: XRD patterns of Mn/TiO₂ and Ca(0.1)-Mn/TiO₂ before and after SCR reaction in the presence of SO₂: Δ, anatase; □, rutile; ●, MnO₂; ■, CaSO₄.

were no peaks for (NH₄)₂SO₄ and NH₄HSO₄ that existed for both catalysts, suggesting that the deactivation under SO₂ atmosphere could be due to the sulfation of active phase. The BET results (see Table S1) also confirmed this assumption as only minor changes of pore volume and surface area were detected.

3.2.2. XPS Analysis. The photoelectron spectra of Mn 2p for different catalysts before and after SO₂ poisoning were displayed in Figures 3(a) and 3(b), respectively. After being

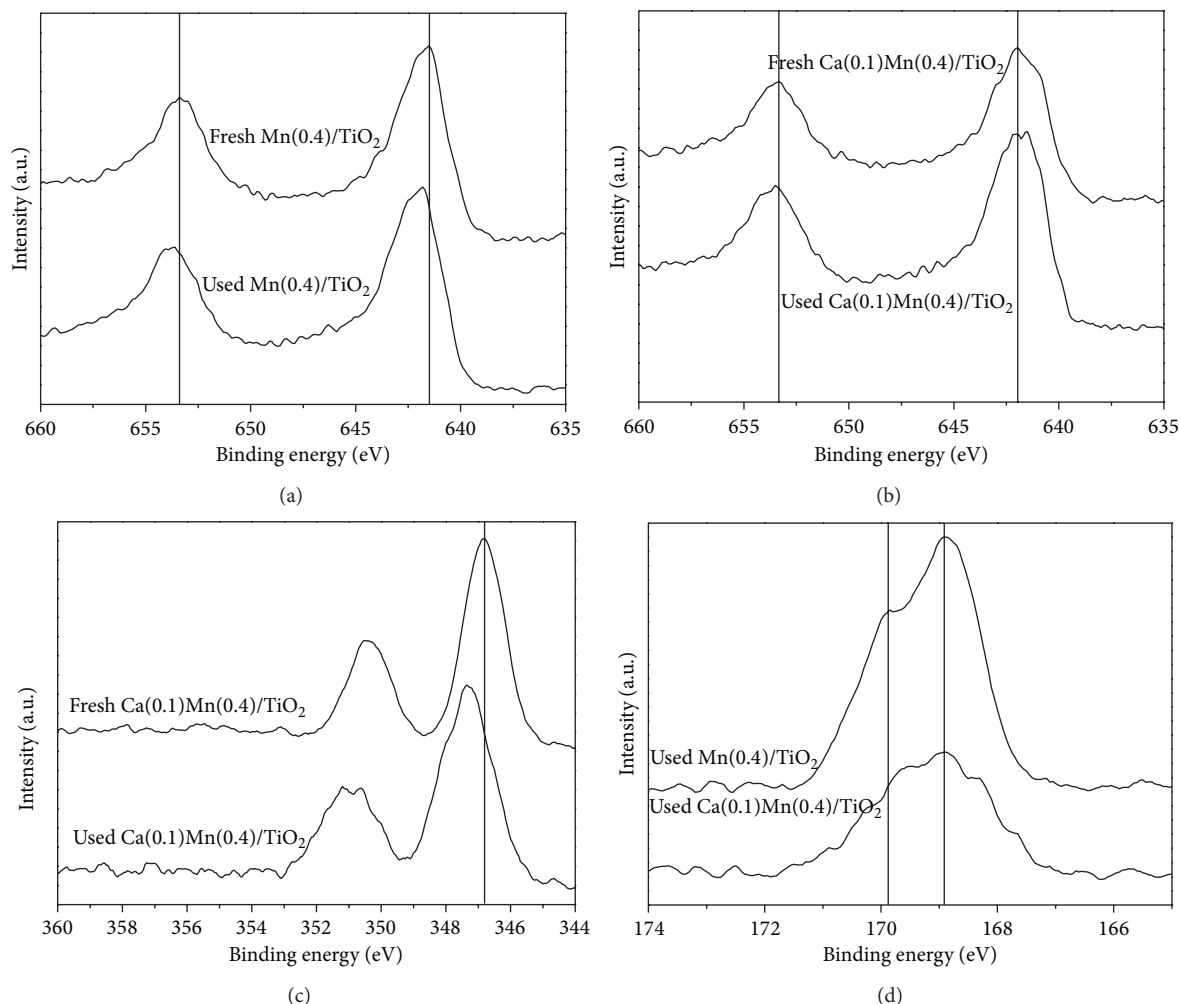


FIGURE 3: XPS spectra of Mn/TiO₂ and Ca(0.1)-Mn/TiO₂ before and after SCR reaction in the presence of SO₂ ((a) Mn 2p Mn/TiO₂, (b) Mn 2p Ca(0.1)-Mn/TiO₂, (c) Ca 2p, and (d) S 2p).

pretreated by SO₂, Mn 2p_{3/2} peak of Mn(0.4)/TiO₂ obviously shifted to about 0.5 eV higher binding energy, which indicated that some new surface species were formed. Similar phenomena were reported that the XPS peaks of metal-oxides catalysts could migrate to higher binding energy due to the active phase sulfation [15, 16]. Therefore, we could conclude that the MnO_x was sulfated during the SCR in the presence of 50 ppm SO₂. In contrast, for Ca doped Mn(0.4)/TiO₂ catalyst, there were no noticeable changes in the binding energy of Mn 2p_{3/2} being observed after SO₂ introduction, which illustrated that the Ca addition could efficiently restrain the sulfation of MnO_x on catalysts surface, shielding the active phases. Figure 3(c) revealed the binding energies of Ca 2p photoelectron peaks. For fresh Ca(0.1)-Mn(0.4)/TiO₂, the binding energy of Ca 2p_{3/2} was 346.8 eV, which was close to the value of CaO (347.2 eV) reported in the literature [17]. After SO₂ treated, the XPS peaks of Ca 2p_{3/2} shifted to higher binding energy range. Combined with the XRD results, the shift in binding energy was mainly ascribed to the formation of sulfated calcium (Ca 2p peaks for CaSO₄ at about 348.1 eV) [18]. Figure 4(d) also represented

the photoelectron spectra of S 2p for Mn/TiO₂ and Ca(0.01)-Mn/TiO₂ after SO₂ poisoning. The peaks at 168.9 and 169.8 eV all could be attributed to the S(VI), indicating the formation of sulfate species after SO₂ poisoning [19, 20].

Additionally, it can be also observed that the surface sulfur content of Ca(0.1)-Mn(0.4)/TiO₂ was lower than that of Mn(0.4)/TiO₂ after SCR reaction (see Table S2), which suggested that the deposition of sulfate species on catalyst surface was inhibited after Ca doping. The possible reason is that Ca dopants would preferentially react with SO₂ to form CaSO₄ and thereby weaken the sulfation of MnO_x. However, it should be noted that the sulfate species could also migrate into the bulk phase as CaSO₄ (see XRD results) would also lead to the decline of surface sulfur content.

3.3. In Situ DRIFT Study

3.3.1. SO₂ Adsorption on Mn/TiO₂ and Ca-Mn/TiO₂. Figure 4 showed the DRIFT spectra of adsorbed species over Mn(0.4)/TiO₂ and Ca(0.1)-Mn(0.4)/TiO₂ catalysts in

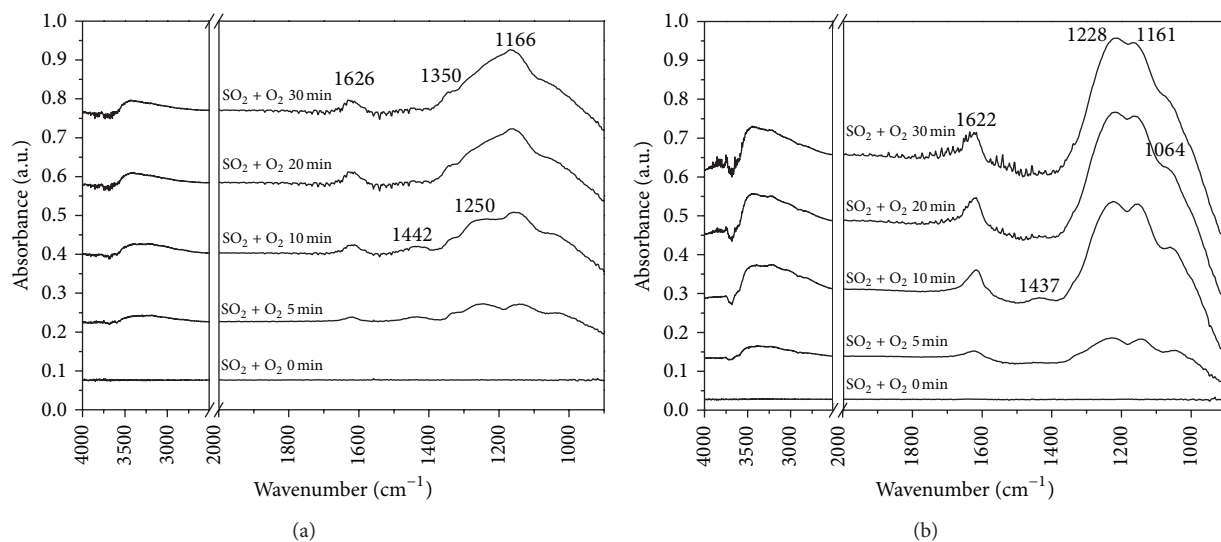


FIGURE 4: DRIFT spectra of Mn/TiO₂ and Ca(0.1)-Mn/TiO₂ exposed to SO₂ at 160°C.

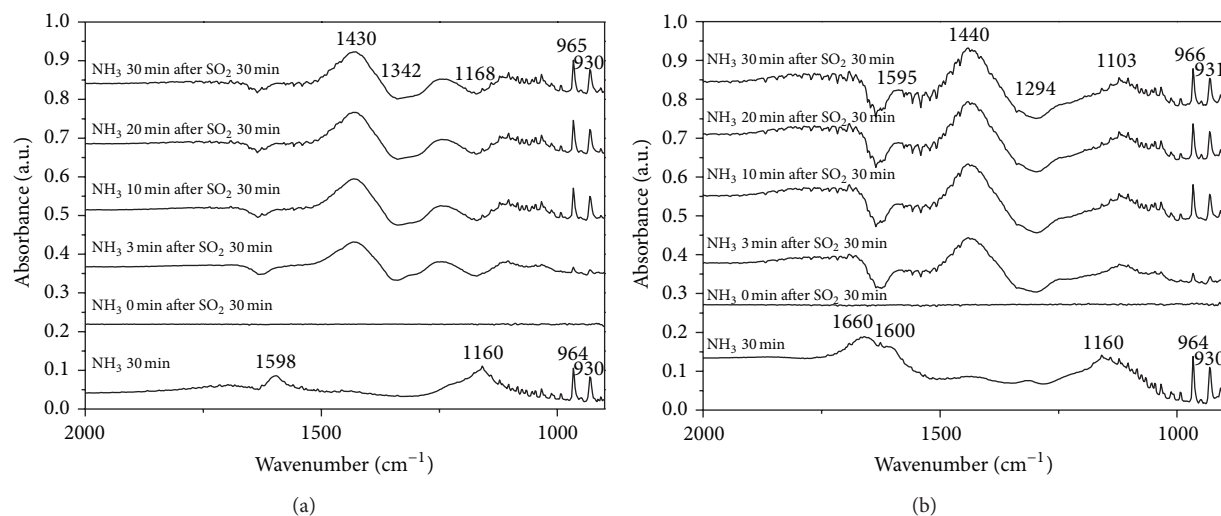


FIGURE 5: DRIFT spectra of Mn/TiO₂ and Ca(0.1)-Mn/TiO₂ exposed to NH₃ after SO₂ pretreated at 160°C.

flowing SO₂ + O₂/He at 160°C as a function of time. As shown in Figure 4(a), several bands at 1166, 1250, 1350, 1442, and 1626 cm⁻¹ were attributed to adsorbed sulfate species. The bands at around 1200 cm⁻¹ (1166 and 1250 cm⁻¹) were caused by bulk-like sulfated species and assigned to the vibrations of S-O and S=O [21–23], and the bands at 1442 and 1350 cm⁻¹ were caused by the bonds vibrations of surface sulfate [22]. Moreover, the bands around 1626 cm⁻¹ were assigned to the adsorbed H₂O due to the reaction between SO₂ and surface hydroxyl groups [24]. In contrast, the IR spectra of Ca(0.1)-Mn(0.4)/TiO₂ were somewhat different from that of Mn(0.4)/TiO₂ as shown in Figure 4(b), which is the characterized peaks of bulk sulfate [22]. According to the XRD and XPS results, these bulk sulfate species should be attributed to bulk-like CaSO₄. This indicated that after Ca

addition, the sulfate species tended to form in bulk rather than on surface, protecting the active phases of the catalysts.

3.3.2. NH₃ Adsorption after SO₂ Pretreatment on Catalysts' Surface. DRIFT spectra of NH₃ adsorption on Mn(0.4)/TiO₂ and Ca(0.1)-Mn(0.4)/TiO₂ catalysts at 160°C after SO₂ pretreatment for 30 min were presented in Figures 5(a) and 5(b), respectively. And as a comparison, the spectra of the fresh catalysts treated with NH₃ for 30 min were also shown in Figure 5 as the first curve. As shown in Figure 5(a), the spectrum taken after 30 min of NH₃ adsorption on Mn(0.4)/TiO₂ was characterized by bands at 930, 964, 1160, and 1598 cm⁻¹ [3]. The bands located in 930 and 964 cm⁻¹ were attributed to the weakly adsorbed NH₃ or gas phase NH₃. In the

NH stretching region, the bands at 1160, 1598 cm^{-1} were indicative of coordinative adsorbed NH_3 on Lewis sites [25–27]. As for SO_2 treated catalyst, new bands at 1430, 1342, and 1105 cm^{-1} emerged. According to the reports [8, 28], the band at 1430 cm^{-1} could be attributed to the bending vibrations of NH_4^+ ions formed on Brønsted acid sites and the band at 1105 cm^{-1} could be assigned to the hydrogen bonds of adsorbed NH_3 [21]. Compared with the fresh sample, SO_2 pretreatment would significantly promote the formation of Brønsted acid sites, where the Lewis acid sites almost disappeared after introducing SO_2 . Moreover, the negative peak at 1342 cm^{-1} was ascribed to S=O band, which tended to bond with NH_3 on catalyst surface according to the previous study [10].

As for Ca(0.1)-Mn(0.4)/ TiO_2 catalysts (Figure 5(b)), similar bands were observed for NH_3 adsorption after SO_2 pretreatment. The band at 1103 cm^{-1} was assigned to hydrogen-bonded NH_3 adspecies. The band at 1440 cm^{-1} was due to the NH_4^+ ions formed on Brønsted acid sites. The negative peaks at 1294 cm^{-1} could be attributed to (S=O) bond due to the interaction between sulfate species and NH_3 . However, the IR spectra also showed some differences with that for Ca-free catalyst. It was found that the band at 1598 cm^{-1} due to NH_3 adsorption on Lewis acid sites was preserved although the intensity was reduced, and the peak at 1160 cm^{-1} (NH_3 adsorption on Lewis acid sites) still can be detected, which was probably overlapped by the bands at 1103 cm^{-1} . Thus, since the NH_3 adsorption and activation on Lewis acid sites played a critical role in the low-temperature SCR process [25, 29], we can conclude that the lessen in MnO_x sulfation and the preservation of part of Lewis acid sites could be the key reason for the great enhancement in SO_2 tolerance of the catalysts after Ca addition.

4. Conclusion

Ca modifications of $\text{MnO}_x/\text{TiO}_2$ catalysts using a sol-gel method would bring an obvious enhancement in SO_2 tolerance for low-temperature SCR of NO with NH_3 . Experimental results showed that around 80% NO conversion could be remained for Ca(0.1)-Mn(0.4)/ TiO_2 catalyst in the presence of 50 ppm SO_2 for 4 h, while that was less than 30% for Ca-free catalyst. Based on the characterizations by XRD, XPS, and IR, it was concluded that the sulfation of MnO_x was greatly inhibited by Ca doping, which was assumed to be due to the fact that the Ca dopants would preferentially react with SO_2 to form bulk-like sulfate species. Furthermore, DRIFT results also indicated that part of Lewis acid sites could be preserved on Ca doped catalysts that was pretreated with SO_2 , which was beneficial to the fulfillment of the low-temperature SCR cycle.

Conflict of Interests

The authors declare that there is no conflict of interests regarding the publication of this paper.

Acknowledgments

This work is financially supported by Key Project of Zhejiang Provincial Science and Technology Program (no. 2012C03003-4), National High-Tech Research and Development Program (863) of China (2011AA060801), and Zhejiang Provincial Natural Science Foundation of China (no. LQ12E08011).

References

- [1] L. Casagrande, L. Lietti, I. Nova, P. Forzatti, and A. Baiker, "SCR of NO by NH_3 over TiO_2 -supported V_2O_5 - MoO_3 catalysts: reactivity and redox behavior," *Applied Catalysis B: Environmental*, vol. 22, no. 1, pp. 63–77, 1999.
- [2] P. G. Smirniotis, D. A. Peña, and B. Uphade, "Low-temperature selective catalytic reduction (SCR) of NO with NH_3 by using Mn, Cr, and Cu oxides supported on TiO_2 ," *Angewandte Chemie International Edition*, vol. 40, pp. 2479–2482, 2001.
- [3] G. Qi, R. T. Yang, and R. Chang, " MnO_x - CeO_2 mixed oxides prepared by co-precipitation for selective catalytic reduction of NO with NH_3 at low temperatures," *Applied Catalysis B: Environmental*, vol. 51, no. 2, pp. 93–106, 2004.
- [4] F. D. Liu, H. He, Y. Ding, and C. B. Zhang, "Effect of manganese substitution on the structure and activity of iron titanate catalyst for the selective catalytic reduction of NO with NH_3 ," *Applied Catalysis B: Environmental*, vol. 93, no. 1-2, pp. 194–204, 2009.
- [5] M. Casapu, O. Kröcher, and M. Elsener, "Screening of doped MnO_x - CeO_2 catalysts for low-temperature NO-SCR," *Applied Catalysis B: Environmental*, vol. 88, no. 3-4, pp. 413–419, 2009.
- [6] H. Chang, J. Li, X. Chen et al., "Effect of Sn on MnO_x - CeO_2 catalyst for SCR of NO_x by ammonia: enhancement of activity and remarkable resistance to SO_2 ," *Catalyst Communication*, vol. 27, pp. 54–57, 2012.
- [7] B. Thirupathi and P. G. Smirniotis, "Nickel-doped Mn/ TiO_2 as an efficient catalyst for the low-temperature SCR of NO with NH_3 : catalytic evaluation and characterizations," *Journal of Catalysis*, vol. 288, pp. 74–83, 2012.
- [8] B. Shen, X. Zhang, H. Ma, Y. Yao, and T. Liu, "A comparative study of Mn/ CeO_2 , Mn/ ZrO_2 and Mn/Ce- ZrO_2 for low temperature selective catalytic reduction of NO with NH_3 in the presence of SO_2 and H_2O ," *Journal of Environmental Science*, vol. 25, no. 4, pp. 791–800, 2013.
- [9] Z. Wu, B. Jiang, Y. Liu, H. Wang, and R. Jin, "DRIFT study of manganese/titania-based catalysts for low-temperature selective catalytic reduction of NO with NH_3 ," *Environmental Science and Technology*, vol. 41, no. 16, pp. 5812–5817, 2007.
- [10] F. Liu, K. Asakura, H. He, W. Shan, X. Shi, and C. Zhang, "Influence of sulfation on iron titanate catalyst for the selective catalytic reduction of NOx with NH_3 ," *Applied Catalysis B: Environmental*, vol. 103, no. 3-4, pp. 369–377, 2011.
- [11] B. Shen, T. Liu, N. Zhao, X. Yang, and L. Deng, "Iron-doped Mn-Ce/ TiO_2 catalyst for low temperature selective catalytic reduction of NO with NH_3 ," *Journal of Environmental Sciences*, vol. 22, no. 9, pp. 1447–1454, 2010.
- [12] Z. Wu, R. Jin, H. Wang, and Y. Liu, "Effect of ceria doping on SO_2 resistance of Mn/ TiO_2 for selective catalytic reduction of NO with NH_3 at low temperature," *Catalysis Communications*, vol. 10, no. 6, pp. 935–939, 2009.

- [13] T. Gu, R. Jin, Y. Liu, H. Liu, and X. Weng, "Promoting effect of calcium doping on the performances of $\text{MnO}_x/\text{TiO}_2$ catalysts for NO reduction with NH_3 at low temperature," *Applied Catalysis B: Environmental*, vol. 129, pp. 30–38, 2013.
- [14] X.-S. Du, X. Gao, L.-W. Cui, Y.-C. Fu, Z.-Y. Luo, and K.-F. Cen, "Investigation of the effect of Cu addition on the SO_2 -resistance of a CeTi oxide catalyst for selective catalytic reduction of NO with NH_3 ," *Fuel*, vol. 92, no. 1, pp. 49–55, 2012.
- [15] B. M. Reddy, P. M. Sreekanth, Y. Yamada, Q. Xu, and T. Kobayashi, "Surface characterization of sulfate, molybdate, and tungstate promoted TiO_2 - ZrO_2 solid acid catalysts by XPS and other techniques," *Applied Catalysis A: General*, vol. 228, no. 1-2, pp. 269–278, 2002.
- [16] H. C. Luo, B. C. Huang, M. L. Fu, J. L. Liang, and D. Q. Dai, " SO_2 deactivation mechanism of $\text{MnO}_x/\text{MWCNTs}$ catalyst for low-temperature selective catalytic reduction of NO_x by ammonia," *Acta Physico-Chimica Sinica*, vol. 28, no. 9, pp. 2175–2182, 2012.
- [17] N. Ohtsu, K. Sato, K. Saito, K. Asami, and T. Hanawa, "Calcium phosphates formation on CaTiO_3 coated titanium," *Journal of Materials Science: Materials in Medicine*, vol. 18, no. 6, pp. 1009–1016, 2007.
- [18] E. J. Romano and K. H. Schulz, "A XPS investigation of SO_2 adsorption on ceria-zirconia mixed-metal oxides," *Applied Surface Science*, vol. 246, no. 1-3, pp. 262–270, 2005.
- [19] Z. Sheng, Y. Hu, J. Xue, X. Wang, and W. Liao, " SO_2 poisoning and regeneration of Mn-Ce/ TiO_2 catalyst for low temperature NO_x reduction with NH_3 ," *Journal of Rare Earths*, vol. 30, no. 7, pp. 676–682, 2012.
- [20] H. Lu and P. G. Smirniotis, "Calcium oxide doped sorbents for CO_2 uptake in the presence of SO_2 at high temperatures," *Industrial and Engineering Chemistry Research*, vol. 48, no. 11, pp. 5454–5459, 2009.
- [21] H. Abdulhamid, E. Fridell, J. Dawody, and M. Skoglundh, "In situ FTIR study of SO_2 interaction with Pt/ $\text{BaCO}_3/\text{Al}_2\text{O}_3$ NO_x storage catalysts under lean and rich conditions," *Journal of Catalysis*, vol. 241, no. 1, pp. 200–210, 2006.
- [22] M. Waqif, P. Bazin, O. Saur, J. C. Lavalley, G. Blanchard, and O. Touret, "Study of ceria sulfation," *Applied Catalysis B: Environmental*, vol. 11, no. 2, pp. 193–205, 1997.
- [23] C. Sedlmair, K. Seshan, A. Jentys, and J. A. Lercher, "Studies on the deactivation of NO_x storage-reduction catalysts by sulfur dioxide," *Catalysis Today*, vol. 75, no. 1-4, pp. 413–419, 2002.
- [24] W. Xu, H. He, and Y. Yu, "Deactivation of a Ce/ TiO_2 catalyst by SO_2 in the selective catalytic reduction of NO by NH_3 ," *Journal of Physical Chemistry C*, vol. 113, no. 11, pp. 4426–4432, 2009.
- [25] D. A. Peña, B. S. Uphade, E. P. Reddy, and P. G. Smirniotis, "Identification of surface species on titania-supported manganese, chromium, and copper oxide low-temperature SCR catalysts," *Journal of Physical Chemistry B*, vol. 108, no. 28, pp. 9927–9936, 2004.
- [26] P. R. Ettireddy, N. Ettireddy, T. Boningari, and R. Pardemann, "Investigation of the selective catalytic reduction of nitric oxide with ammonia over Mn/ TiO_2 catalysts through transient isotopic labeling and in situ FT-IR studies," *Journal of Catalysis*, vol. 292, pp. 53–63, 2012.
- [27] F. Liu and H. He, "Selective catalytic reduction of NO with NH_3 over manganese substituted iron titanate catalyst: reaction mechanism and $\text{H}_2\text{O}/\text{SO}_2$ inhibition mechanism study," *Catalysis Today*, vol. 153, no. 3-4, pp. 70–76, 2010.
- [28] L. Chen, J. Li, and M. Ge, "DRIFT study on cerium—tungsten/titania catalyst for selective catalytic reduction of NO_x with NH_3 ," *Environmental Science and Technology*, vol. 44, no. 24, pp. 9590–9596, 2010.
- [29] G. Qi and R. T. Yang, "Characterization and FTIR studies of MnO_x - CeO_2 catalyst for low-temperature selective catalytic reduction of NO with NH_3 ," *Journal of Physical Chemistry B*, vol. 108, no. 40, pp. 15738–15747, 2004.

Research Article

The Poisoning Effect of Na Doping over Mn-Ce/TiO₂ Catalyst for Low-Temperature Selective Catalytic Reduction of NO by NH₃

Liu Yang, Yue Tan, Zhongyi Sheng, and Aiyi Zhou

Department of Environmental Science and Engineering, Nanjing Normal University, Nanjing 210023, China

Correspondence should be addressed to Zhongyi Sheng; 09377@njnu.edu.cn

Received 13 January 2014; Revised 16 February 2014; Accepted 17 February 2014; Published 30 March 2014

Academic Editor: Fan Dong

Copyright © 2014 Liu Yang et al. This is an open access article distributed under the Creative Commons Attribution License, which permits unrestricted use, distribution, and reproduction in any medium, provided the original work is properly cited.

Sodium carbonate (Na₂CO₃), sodium nitrate (NaNO₃), and sodium chloride (NaCl) were chosen as the precursors to prepare the Na salts deposited Mn-Ce/TiO₂ catalysts through an impregnation method. The influence of Na on the performance of the Mn-Ce/TiO₂ catalyst for low-temperature selective catalytic reduction of NO_x by NH₃ was investigated. Experimental results showed that Na salts had negative effects on the activity of Mn-Ce/TiO₂ and the precursors of Na salts also affected the catalytic activity. The precursor Na₂CO₃ had a greater impact on the catalytic activity, while NaNO₃ had minimal effect. The characterization results indicated that the significant changes in physical and chemical properties of Mn-Ce/TiO₂ were observed after Na was doped on the catalysts. The significant decreases in surface areas and NH₃ adsorption amounts were observed after Na was doped on the catalysts, which could be considered as the main reasons for the deactivation of Na deposited Mn-Ce/TiO₂.

1. Introduction

The selective catalytic reduction (SCR) of nitrogen oxides (NO_x) with NH₃ is an effective process for cleaning NO_x from stationary sources [1]. Low-temperature SCR technology is a promising method to remove NO_x in flue gas because the unit can be placed downstream of the particle control device and desulfurization system, and the temperature at this point is below 160°C [2, 3]. Some researchers have recently reported that manganese-cerium (Mn-Ce) mixed oxides supported on TiO₂ catalysts showed high SCR activity and good SO₂ resistance at low temperature [4–7]. It has been found that the manganese oxides (MnO_x) contain various kinds of labile oxygen and the ceria (CeO₂) owns high oxygen storage and redox capacity, which are proved to be very active in catalyzing the NO reduction by NH₃ [8, 9]. And the TiO₂ as the supporter also can provide large surface area, high thermal stability, strong mechanical strength, and high sulfur resistance [10].

Although the low-temperature SCR unit is commonly arranged after particulate control device, there is still a small amount of dust which contains many physical and chemical

deactivating species such as alkali/alkaline earth metals in flue gas. It could reduce catalytic activity when the catalyst is exposed in this complex flue gas for long time [11, 12]. In addition, when the low-temperature SCR technology is used to remove the NO_x emission from some industrial furnace, such as cement kiln and glass kiln, the Mn-Ce/TiO₂ catalyst could be subjected to greater influence by deposition of alkali/alkaline earth metals [13, 14]. Therefore, it is valuable to investigate the effects of alkali/alkaline earth metals on Mn-Ce/TiO₂ for low-temperature SCR, which few researchers have concerned about. In this study, we try to investigate the impact of deposited sodium (Na) on the physical and chemical properties of Mn-Ce/TiO₂ catalysts. Sodium carbonate (Na₂CO₃), sodium nitrate (NaNO₃), and sodium chloride (NaCl) were chosen as the sodium-containing precursors to prepare the Na deposited Mn-Ce/TiO₂ catalysts.

2. Experimental

2.1. Catalyst Preparation. All chemicals used in this study were of analytical grade and were used without further purification. In this experiment, the molar ratio of Ce : Mn : Ti

was 0.07:0.4:1, which has been reported by Wu et al. [15] with high SCR activity. The Na deposited Mn-Ce/TiO₂ catalysts were prepared by impregnation of TiO₂ (Degussa P25) with Mn(NO₃)₂, Ce(NO₃)₃, and three kinds of sodium salts (Na₂CO₃, NaNO₃, and NaCl). 4.0 g TiO₂ powder was dispersed into 100 mL aqueous solution. Then 0.02 mol of Mn(NO₃)₂, 0.0035 mol of Ce(NO₃)₃, and a certain amount of Na salts were added into the solution. The loading amounts of sodium were 0.05, 0.1, 0.2, 0.5, 1, and 2 wt.%. The slurry was then stirred for 48 h. After that, it was heated at 105 °C for 12 h. The solid samples were crushed and sieved to 60–100 mesh and then calcined at 400 °C for 2 h in air. The Na₂CO₃, NaCl, and NaNO₃ deposited Mn-Ce/TiO₂ catalyst were denoted by Mn-Ce/TiO₂ (C), Mn-Ce/TiO₂ (Cl), and Mn-Ce/TiO₂ (N), respectively.

2.2. Catalyst Characterization. The structures of the samples were determined by X-ray diffraction patterns (XRD) obtained on a Bruker D8 Advance diffractometer. The surface areas of catalysts were calculated by using the Brunauer-Emmett-Teller (BET) method, with Micromeritics ASSP 2020 equipment by N₂ physisorption at 77 K. The surface atomic states of the catalysts were analyzed by X-ray photoelectron spectroscopy (XPS) with Thermo Escalab 250Xi. Transmission electron microscopy (TEM) images were examined by JEM 2010. Temperature programmed desorption (TPD) was carried out on a custom-made TCD setup in a conventional flow system at atmospheric pressure using 100 mg catalysts (40–60 mesh). After being pretreated in He at 400 °C for 1 h, the samples were saturated with a stream of 4% NH₃ and He balance at a flow rate of 30 mL/min for 30 min. The NH₃ desorption was carried out by heating NH₃-adsorbed samples from 100 to 900 °C at the rate of 5 °C/min in He (30 mL/min).

2.3. Activity Tests. The SCR activity measurements were carried out in a fixed-bed reactor at 60–160 °C containing 4 g catalyst with a gas hourly space velocity (GHSV) of 24,000 h⁻¹. The typical reactant gas consisted of 500 ppm NO, 500 ppm NH₃, 5 vol.% O₂, and balance N₂. NO, NO₂, and O₂ were measured by a flue gas analyzer (MRU Vario Plus, Germany). NH₃ was analyzed with a portable NH₃ analyzer (Nantong Water Environmental Protection Technology Co. Ltd., Model MOT 400).

3. Results and Discussion

3.1. Catalytic Activity. The activity of the prepared catalysts with the variation of temperature is presented in Figure 1. It can be seen from Figure 1(a) that the NO conversion of all samples increased with the increasing temperature. The Mn-Ce/TiO₂ catalyst showed high catalytic activity for the low-temperature SCR of NO with NH₃. Over 99% of NO conversion was obtained when the temperature reached 100 °C. The SCR activities of 1% Mn-Ce/TiO₂ (C), Mn-Ce/TiO₂ (Cl), and Mn-Ce/TiO₂ (N) all declined when Na salts were deposited on the catalysts. Figure 1(a) also shows that the SCR activity decreased in the following sequence: Mn-Ce/TiO₂ > Mn-Ce/TiO₂ (N) > Mn-Ce/TiO₂ (Cl) > Mn-Ce/TiO₂ (C).

It is indicated that Na salts had a negative effect on the activity of Mn-Ce/TiO₂ and the precursors of Na also affected the catalytic activity. The precursor Na₂CO₃ had a greater impact on the catalytic activity, while NaNO₃ had minimal effect. The deposited NaNO₃ could decompose to NaNO₂ and O₂ after calcination at 400 °C for 12 h, while Na₂CO₃ and NaCl could not decompose at 400 °C. Therefore, the massive agglomeration of Na₂CO₃ and NaCl could block the micropores and covered the active sites, which is considered as the reason for the deactivation of Na doped Mn-Ce/TiO₂ catalyst [11]. The NO_x conversions of Mn-Ce/TiO₂ (C) and Mn-Ce/TiO₂ (N) were shown in the Figures 1(b) and 1(c). The catalytic activity of samples declined with the increasing amounts of Na doped from 0 to 2%. 2% Mn-Ce/TiO₂ (C) showed the lowest activity and only 17.8% of NO conversion was obtained at 160 °C. The results demonstrated that the Mn-Ce/TiO₂ catalyst could be gradually deactivated as the loading amounts of Na salts increased.

3.2. Catalyst Microstructure. The XRD patterns of Na doped Mn-Ce/TiO₂ catalysts with different Na precursors were shown in Figure 2. For the undoped Mn-Ce/TiO₂ catalyst, the XRD pattern only existed as a mixing form of anatase and rutile [14]. And the peaks of manganese or cerium oxides were not detected, which indicated that manganese or cerium oxides were well dispersed on the TiO₂ carrier. After different Na salts were deposited, two extra peaks around 28.72° and 33.02° were detected. It has been reported that the two peaks were identified as Mn₃O₄ and Mn₂O₃ [14, 15]. The results implied that Na salts doping could induce the crystallization of MnO_x phases, which had adverse effect on catalytic activity due to the transformation of the amorphous manganese oxides to crystal phase [16]. On the other hand, the Mn-Ce/TiO₂ (N) catalyst had peaks of weak intensity for Mn₃O₄ and Mn₂O₃, which could be considered as one of the reasons that NaNO₃ had weaker impact on the deactivation of Mn-Ce/TiO₂ catalyst. In particular, for all Mn-Ce/TiO₂ samples, characteristic peaks of anatase and rutile with similar position, intensities, and widths were detected, which implied that the phase structure and the crystallite size of TiO₂ particles in as-prepared samples had no obvious changes after Na doping.

The morphology of 2% Mn-Ce/TiO₂ (C) catalyst was further investigated by TEM and HR-TEM images as shown in Figure 3. From the insert image of Figure 3, it can be seen that primary particles have the diameters predominantly ranged from 10 to 20 nm. From the HR-TEM image illustrated in Figure 3, four kinds of clear lattice fringes could be observed for 2% Mn-Ce/TiO₂ (C) catalyst. The spacing distances between the lattice planes of 0.352 nm and 0.32 nm matched with the anatase (101) phase and rutile (110) phase [17]. And the lattice fringes with lattice plane distances observed about 0.384 nm and 0.492 nm corresponded to Mn₂O₃ (211) and Mn₃O₄ (101) planes [14], which were in agreement with the information obtained from the XRD results.

The specific surface areas, pore volumes, and pore sizes of the Mn-Ce/TiO₂ catalysts prepared with different Na precursors are summarized in Table 1. Significant decreases

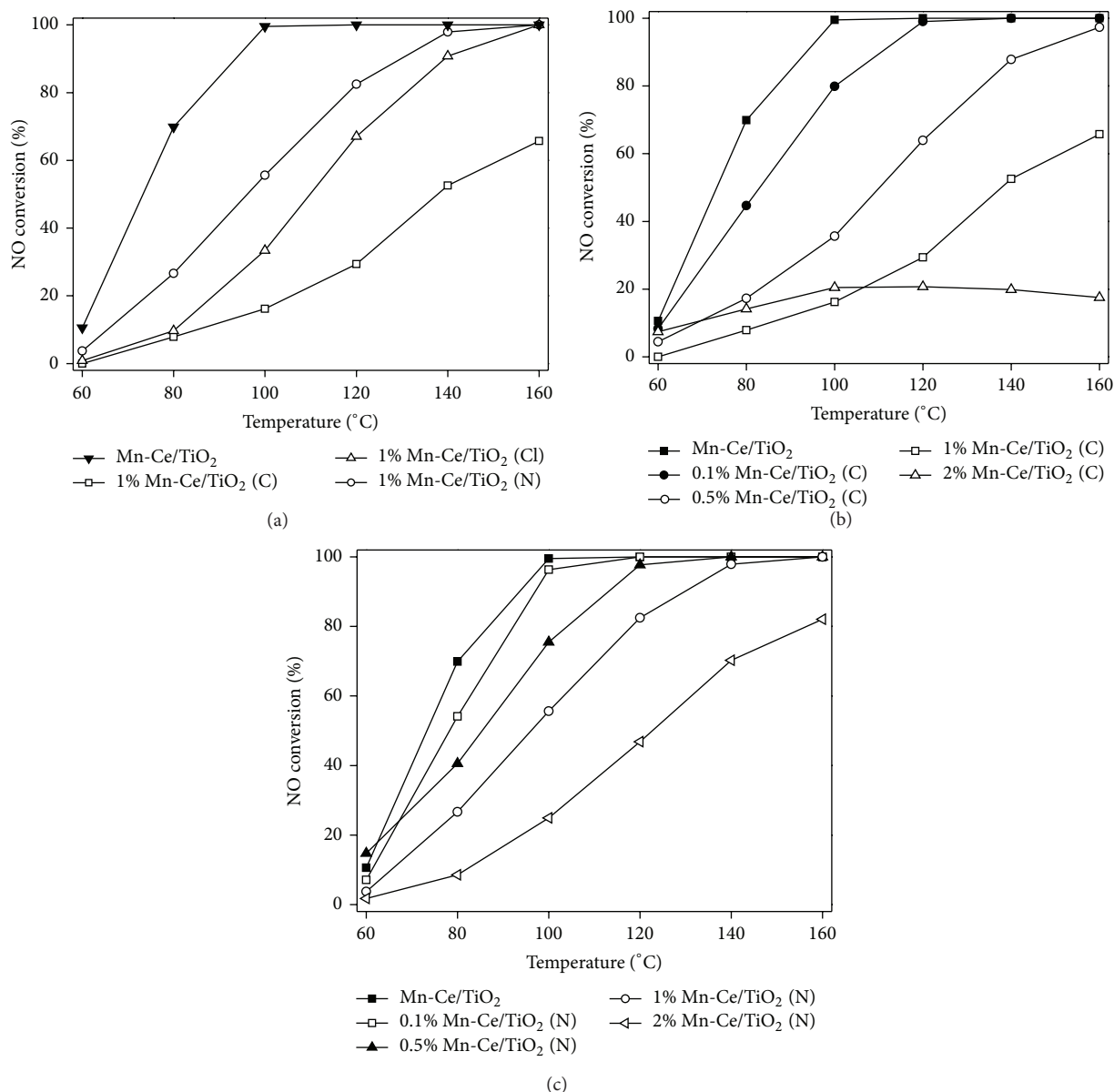


FIGURE 1: Variations of NO conversion efficiency with temperature for prepared Mn/Ce-TiO₂ catalysts. (a) Comparison of catalytic activity over the Na doped Mn-Ce/TiO₂ prepared by different Na precursors. (b) Comparison of catalytic activity over Mn-Ce/TiO₂ (C) with different Na doping amounts. (c) Comparison of catalytic activity over Mn-Ce/TiO₂ (N) with different Na doping amounts. Operating conditions: 500 ppm NO, 500 ppm NH₃, 5% O₂, and balance N₂, GHSV = 24,000 h⁻¹.

in surface areas and pore volumes were observed after Na deposited on the catalysts. This could be caused by the massive agglomeration of Mn-Ce/TiO₂ due to the Na salts deposited, which blocked the micropores in Mn-Ce/TiO₂ lattice and increased average pore size. It was also observed that the surface area and pore volume of Mn-Ce/TiO₂ (N) were larger than those of Mn-Ce/TiO₂ (Cl) and Mn-Ce/TiO₂ (C). It is indicated that the precursor NaNO₃ has little effect on pore structure of the catalyst. The variations in specific surface areas of catalysts were in good agreement with the catalytic activities. Mn-Ce/TiO₂ (N) with the larger specific surface area showed better SCR activity.

3.3. Catalyst Composition Analysis. In order to identify the states of surface species on the prepared catalysts, the samples were examined by XPS high-resolution scans over Ti 2p, Mn 2p, Ce 3d, O 1s, and Na 1s spectra regions. And the atomic compositions of Ti, Mn, Ce, and O on the surface are shown in Table 2.

The Ce 3d XPS spectra are presented in Figure 4(a). The XPS spectra revealed that Ce 3d orbit was composed of two multiplets (v and u). The peaks labeled u and v were due to 3d_{3/2} and 3d_{5/2} spin-orbit states, respectively. The u, u'', and u''' and v, v'', and v''' peaks were attributed to Ce⁴⁺ species,

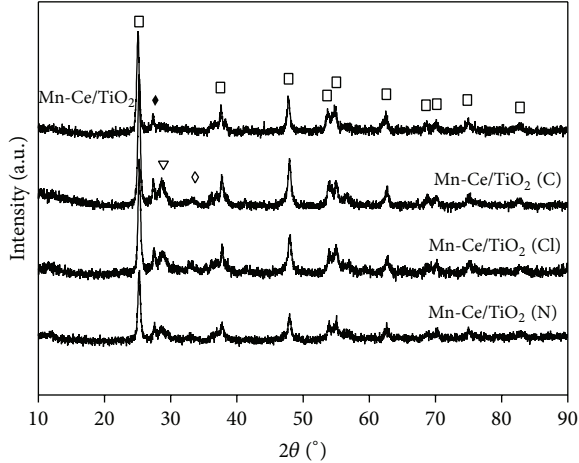


FIGURE 2: XRD patterns of Na doped Mn-Ce/TiO₂ catalysts prepared by different Na precursors (□ TiO₂-anatase, ◆ TiO₂-rutile, ∇ Mn₃O₄, and ◇ Mn₂O₃).

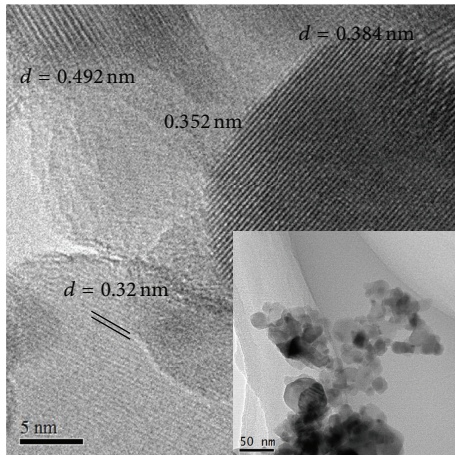


FIGURE 3: TEM and HR-TEM images of 2% Mn-Ce/TiO₂ (C) sample.

TABLE 1: Physical properties of the catalysts prepared with different Na precursors.

Catalysts	BET surface area (m ² /g)	Pore volume (×10 ⁻² cm ³ /g)	Average pore diameter (nm)
Mn-Ce/TiO ₂	44.52	28.39	25.51
2% Mn-Ce/TiO ₂ (C)	31.48	22.04	30.85
2% Mn-Ce/TiO ₂ (Cl)	32.42	25.65	31.64
2% Mn-Ce/TiO ₂ (N)	36.58	27.58	28.61

while u' and v' were assigned to Ce³⁺ species [15]. No obvious difference was observed from the Ce 3d XPS spectra for Mn-Ce/TiO₂ and Na doped Mn-Ce/TiO₂ samples.

As shown in Figure 4(b), the Mn 2p region consists of a spin-orbit doublet with Mn 2p_{1/2} having binding energy of about 653 eV and Mn 2p_{3/2} with binding energy of 642 eV,

TABLE 2: Surface atomic concentrations of Mn-Ce/TiO₂ catalysts with different sodium oxides.

Catalysts	Surface atomic concentrations (%)			
	Mn	Ti	Ce	O
Mn-Ce/TiO ₂	8.32	26.5	3.23	61.95
2% Mn-Ce/TiO ₂ (C)	3.57	24.77	1.56	42.14
2% Mn-Ce/TiO ₂ (Cl)	4.59	15.43	1.44	66.82
2% Mn-Ce/TiO ₂ (N)	7.17	25.7	2.97	58.9

which are characteristic of a mixed-valence manganese system [18, 19]. The Mn 2p_{3/2} spectra could be split into three peaks at binding energy of 642.8, 641.2, and 646.5 eV, which were ascribed to Mn⁴⁺, Mn³⁺, and Mn-nitrate, respectively [20, 21]. For undoped Mn-Ce/TiO₂, the Mn-nitrate could be originated from Mn(NO₃)₂, as one of the precursors for the preparation of Mn-Ce/TiO₂. It can be clearly seen from Figure 4(a) that the atomic concentration of Mn-nitrate on Mn-Ce/TiO₂ (N) is much higher than that on undoped Mn-Ce/TiO₂, which may be attributed to the decomposition of Mn(NO₃)₂ restrained with the Na salts doping. The decrease of Mn³⁺ and Mn⁴⁺ on Na salts deposited Mn-Ce/TiO₂ could be considered as one of the reasons for the decrease of catalyst activity [22].

3.4. NH₃-TPD Analysis. The surface acidity properties of the catalysts were analyzed by NH₃-TPD. The NH₃-TPD curves of Mn-Ce/TiO₂ and 2% Mn-Ce/TiO₂ (N) are shown in Figure 5. As shown in Figure 5, one broad peak spanned in the temperature range of 100–300°C was observed for both samples, attributed to NH₃ desorbed by weak and medium acid sites. For undoped Mn-Ce/TiO₂, the desorption peaks centered at 552 and 663°C could be ascribed to the nature of Brønsted acid and Lewis acid, respectively [23]. At the temperature around 743°C, the strong peak observed was probably due to the N₂ desorption [24]. The shape of the NH₃-TPD curve obtained from 2% Mn-Ce/TiO₂ (N) was very different. The peak at 670°C disappeared, while the peak of N₂ desorption increased greatly. It is indicated that the Lewis acid sites of Mn-Ce/TiO₂ were reduced after Na salts were deposited. It is known that the strong acidity on catalyst could play an important role in the adsorption capacity of NH₃ for the sample [25]. The decrease of Lewis acid sites could be considered as the main factor for decrease of NH₃ adsorption amount on Na deposited Mn-Ce/TiO₂.

4. Conclusions

The catalytic activity experiments showed that Na salts had strong poisoning influence on Mn-Ce/TiO₂ catalyst, which seriously reduced the low-temperature SCR activity. The precursor Na₂CO₃ had more negative impact on the catalytic activity, while NaNO₃ had minimal effect. XPS results indicated that the atomic content of Mn³⁺ and Mn⁴⁺ on catalyst surface could decrease with the addition of Na. BET and NH₃-TPD results showed that the significant decreases in surface areas and NH₃ adsorption amounts were observed

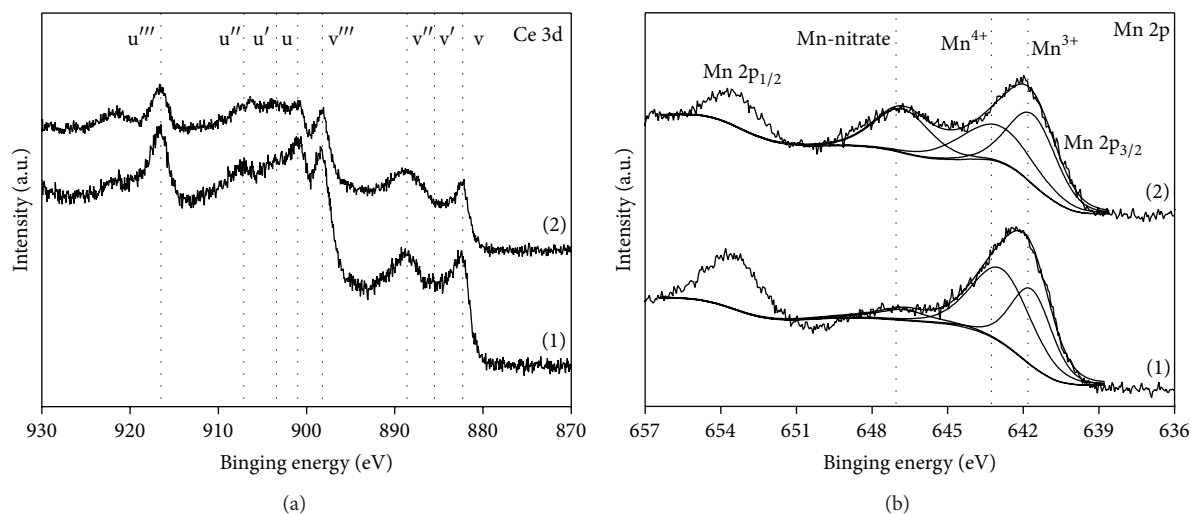


FIGURE 4: XPS high-resolution scans over (a) Ce 3d and (b) Mn 2p peaks on (1) Mn-Ce/TiO₂ and (2) 2% Mn-Ce/TiO₂ (N) catalyst.

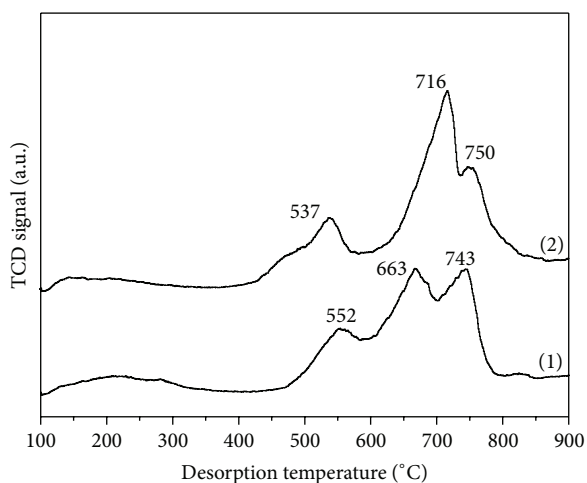


FIGURE 5: NH₃-TPD profiles for Mn-Ce/TiO₂ catalysts prepared with different Na precursors, (1) Mn-Ce/TiO₂ and (2) 2% Mn-Ce/TiO₂ (N).

after Na salts were deposited on the catalysts, which could be considered as the main reasons for the deactivation of Na doped Mn-Ce/TiO₂.

Conflict of Interests

The authors declare that there is no conflict of interests regarding the publication of this paper.

Acknowledgments

The project is financially supported by the Natural Science Foundation of Jiangsu Province (no. BK20130907), Program of Natural Science Research of Jiangsu Higher Education Institutions of China (no. 13KJB610012), the Research Start-up Funds Program for High Level Talent of Nanjing Normal

University (no. 2013105XGQ0056), and Zhejiang Provincial Engineering Research Center of Industrial Boiler & Furnace Flue Gas Pollution Control.

References

- [1] Z. G. Huang, Z. P. Zhu, Z. Y. Liu, and Q. Y. Liu, "Formation and reaction of ammonium sulfate salts on V₂O₅/AC catalyst during selective catalytic reduction of nitric oxide by ammonia at low temperatures," *Journal of Catalysis*, vol. 214, no. 2, pp. 213–219, 2003.
- [2] R. P. Jin, Y. Liu, Z. B. Wu, H. Q. Wang, and T. T. Gu, "Low-temperature selective catalytic reduction of NO with NH₃ over Mn single bond Ce oxides supported on TiO₂ and Al₂O₃: a comparative study," *Chemosphere*, vol. 78, no. 9, pp. 1160–1166, 2010.
- [3] G. Qi and R. T. Yang, "Performance and kinetics study for low-temperature SCR of NO with NH₃ over MnOx-CeO₂ catalyst," *Journal of Catalysis*, vol. 217, no. 2, pp. 434–441, 2003.
- [4] W. S. Kijlstra, D. S. Brands, E. K. Poels, and A. Blik, "Kinetics of the selective catalytic reduction of NO with NH₃ over MnOx/Al₂O₃ catalysts at low temperature," *Catalysis Today*, vol. 50, no. 1, pp. 133–140, 1999.
- [5] G. Carja, Y. Kameshima, K. Okada, and C. D. Madhusoodana, "Mn-Ce/ZSM5 as a new superior catalyst for NO reduction with NH₃," *Applied Catalysis B: Environmental*, vol. 73, no. 1-2, pp. 60–64, 2007.
- [6] X. Wang, Y. Y. Zheng, and J. X. Lin, "Highly dispersed Mn-Ce mixed oxides supported on carbon nanotubes for low-temperature NO reduction with NH₃," *Catalysis Communications*, vol. 37, pp. 96–99, 2013.
- [7] B. X. Shen, T. Liu, N. Zhao, X. Y. Yang, and L. D. Deng, "Iron-doped Mn-Ce/TiO₂ catalyst for low temperature selective catalytic reduction of NO with NH₃," *Journal of Environmental Sciences*, vol. 22, no. 9, pp. 1447–1454, 2010.
- [8] M. Wallin, S. Forser, P. Thormählen, and M. Skoglundh, "Screening of TiO₂-supported catalysts for selective NOx reduction with ammonia," *Industrial and Engineering Chemistry Research*, vol. 43, no. 24, pp. 7723–7731, 2004.

- [9] M. Casapu, O. Kröcher, and M. Elsener, "Screening of doped MnOx-CeO₂ catalysts for low-temperature NO-SCR," *Applied Catalysis B: Environmental*, vol. 88, no. 3-4, pp. 413-419, 2009.
- [10] P. R. Ettireddy, N. Ettireddy, S. Mamedov, P. Boolchand, and P. G. Smirniotis, "Surface characterization studies of TiO₂ supported manganese oxide catalysts for low temperature SCR of NO with NH₃," *Applied Catalysis B: Environmental*, vol. 76, no. 1-2, pp. 123-134, 2007.
- [11] S. S. Kim, Y. S. Kang, H. D. Lee, J. K. Kim, and S. C. Hong, "Release of potassium and sodium species during combustion of various rank coals, biomass, sludge and peats," *Journal of Industrial and Engineering Chemistry*, vol. 18, no. 6, pp. 2199-2203, 2012.
- [12] J. P. Chen, M. A. Buzanowski, R. T. Yang, and J. E. Cichanowicz, "Deactivation of the vanadia catalyst in the selective catalytic reduction process," *Journal of the Air and Waste Management Association*, vol. 40, no. 10, pp. 1403-1409, 1990.
- [13] Y. Liu, T. T. Gu, Y. Wang, X. L. Weng, and Z. B. Wu, "Influence of Ca doping on MnOx/TiO₂ catalysts for low-temperature selective catalytic reduction of NOx by NH₃," *Catalysis Communications*, vol. 18, pp. 106-109, 2012.
- [14] T. T. Gu, R. B. Jin, Y. Liu, H. F. Liu, X. L. Weng, and Z. B. Wu, "Promoting effect of calcium doping on the performances of MnOx/TiO₂ catalysts for NO reduction with NH₃ at low temperature," *Applied Catalysis B: Environmental*, vol. 129, pp. 30-38, 2013.
- [15] Z. B. Wu, R. B. Jin, Y. Liu, and H. Q. Wang, "Ceria modified MnOx/TiO₂ as a superior catalyst for NO reduction with NH₃ at low-temperature," *Catalysis Communications*, vol. 9, no. 13, pp. 2217-2220, 2008.
- [16] Z. B. Wu, B. Q. Jiang, and Y. Liu, "Effect of transition metals addition on the catalyst of manganese/titania for low-temperature selective catalytic reduction of nitric oxide with ammonia," *Applied Catalysis B: Environmental*, vol. 79, no. 4, pp. 347-355, 2008.
- [17] Z. B. Wu, Z. Y. Sheng, Y. Liu, H. Q. Wang, N. Tang, and J. Wang, "Characterization and activity of Pd-modified TiO₂ catalysts for photocatalytic oxidation of NO in gas phase," *Journal of Hazardous Materials*, vol. 164, no. 2-3, pp. 542-548, 2009.
- [18] X. Zhang, L. Y. Ji, S. C. Zhang, and W. S. Yang, "Synthesis of a novel polyaniline-intercalated layered manganese oxide nanocomposite as electrode material for electrochemical capacitor," *Journal of Power Sources*, vol. 173, no. 2, pp. 1017-1023, 2007.
- [19] D. A. Peña, B. S. Uphade, and P. G. Smirniotis, "TiO₂-supported metal oxide catalysts for low-temperature selective catalytic reduction of NO with NH₃: I. Evaluation and characterization of first row transition metals," *Journal of Catalysis*, vol. 221, no. 2, pp. 421-431, 2004.
- [20] K. Zhuang, J. Qiu, F. S. Tang, B. L. Xu, and Y. N. Fan, "The structure and catalytic activity of anatase and rutile titania supported manganese oxide catalysts for selective catalytic reduction of NO by NH₃," *Physical Chemistry Chemical Physics*, vol. 13, no. 10, pp. 4463-4469, 2011.
- [21] S. M. Lee, K. H. Park, and S. C. Hong, "MnOx/CeO₂-TiO₂ mixed oxide catalysts for the selective catalytic reduction of NO with NH₃ at low temperature," *Chemical Engineering Journal*, vol. 195, pp. 323-331, 2012.
- [22] F. Kapteijn, L. Singoredjo, A. Andreini, and J. A. Moulijn, "Activity and selectivity of pure manganese oxides in the selective catalytic reduction of nitric oxide with ammonia," *Applied Catalysis B, Environmental*, vol. 3, no. 2-3, pp. 173-189, 1994.
- [23] F. Lónyi, J. Vályon, J. Engelhardt, and F. Mizukami, "Characterization and catalytic properties of sulfated ZrO₂-TiO₂ mixed oxides," *Journal of Catalysis*, vol. 160, no. 2, pp. 279-289, 1996.
- [24] Y. Wang, "Adsorption action of NO gas on the TiO₂ surface," *Acta Chimica Sinica*, vol. 64, no. 15, pp. 1611-1614, 2006.
- [25] L. Lietti, I. Nova, G. Ramis et al., "Characterization and reactivity of V₂O₅-MoO₃/TiO₂ De-NOx SCR catalysts," *Journal of Catalysis*, vol. 187, no. 2, pp. 419-435, 1999.

Research Article

The Research of Nanoparticle and Microparticle Hydroxyapatite Amendment in Multiple Heavy Metals Contaminated Soil Remediation

Zhangwei Li, Man-man Zhou, and Weidian Lin

Department of Chemistry, Hanshan Normal University, Chaozhou 521041, China

Correspondence should be addressed to Zhangwei Li; 99094001@163.com

Received 30 December 2013; Accepted 20 February 2014; Published 20 March 2014

Academic Editor: Wing-Kei Ho

Copyright © 2014 Zhangwei Li et al. This is an open access article distributed under the Creative Commons Attribution License, which permits unrestricted use, distribution, and reproduction in any medium, provided the original work is properly cited.

It was believed that when hydroxyapatite (HAP) was used to remediate heavy metal-contaminated soils, its effectiveness seemed likely to be affected by its particle size. In this study, a pot trial was conducted to evaluate the efficiency of two particle sizes of HAP: nanometer particle size of HAP (nHAP) and micrometer particle size of HAP (mHAP) induced metal immobilization in soils. Both mHAP and nHAP were assessed for their ability to reduce lead (Pb), zinc (Zn), copper (Cu), and chromium (Cr) bioavailability in an artificially metal-contaminated soil. The pakchoi (*Brassica chinensis* L.) uptake and soil sequential extraction method were used to determine the immobilization and bioavailability of Pb, Zn, Cu, and Cr. The results indicated that both mHAP and nHAP had significant effect on reducing the uptake of Pb, Zn, Cu, and Cr by pakchoi. Furthermore, both mHAP and nHAP were efficient in covering Pb, Zn, Cu, and Cr from nonresidual into residual forms. However, mHAP was superior to nHAP in immobilization of Pb, Zn, Cu, and Cr in metal-contaminated soil and reducing the Pb, Zn, Cu, and Cr utilized by pakchoi. The results suggested that mHAP had the better effect on remediation multiple metal-contaminated soils than nHAP and was more suitable for applying in *in situ* remediation technology.

1. Introduction

Heavy metal pollution in the soil has become a serious environmental problem in China, particularly following the rapid industrialization of the nation. Heavy metal in soil readily accumulates in plants and is then transported through the food chain, thus becoming a major threat to human health [1]. A number of remediation methods have been developed in an attempt to control heavy metal pollution, including the use of organic manure, soil amendment addition, cultivation of heavy metal hyperaccumulator plants, and the application of agroecological engineering techniques [2, 3].

Supplementation of phosphate-based materials has been found to have a great effect on immobilizing Pb in contaminated soil and has recently become a commonly used technique due to its cost-effectiveness and decreased disruptive nature [4, 5]. Hydroxyapatite (HAP) is considered to be the most effective supplement among P-based materials and is

commonly used in Pb-contaminated soil. It has been reported that HAP not only facilitates the remediation of Pb, but it is also quite effective in immobilizing other heavy metals, such as Zn, Cd, and Cu [6, 7]. However, the overall effectiveness of using phosphate to immobilize metals and its mechanisms of action remain unknown.

With the rapid development of nanotechnology there has been an increased usage of HAP nanoparticles put into use in wastewater and for soil remediation. Nanometer size particle HAP (nHAP) has a larger specific surface area than micrometer sized particle HAP (mHAP). Moreover, theoretically nHAP has larger reactivity and sorption capacities than that of common size of HAP [8, 9]. However, few studies have focused on the remediation differences between mHAP and nHAP. Furthermore, little work has been done identifying the effectiveness of the effect of nHAP on a number of different heavy metals. Therefore, the aim of this study was to compare the effectiveness/differences between mHAP and nHAP to

reduce the uptake of multiple heavy metals (Pb and Zn, Cu and Cr) by plants and to immobilize these heavy metals in contaminated soil.

2. Material and Methods

2.1. Soil Sample Properties. The soil samples were derived from vegetable gardens. After being air-dried, the soil samples were grounded to pass through a 10 mm sieve for the pot trial. Soil pH was measured in 1:2.5 soil water suspensions with a combination pH electrode. Soil organic matter was determined by wet digestion with $K_2Cr_2O_7$ and H_2SO_4 ; available N, P, and K were determined according to standard methods recommended by Lu [10]. Some basic physiochemical properties of the soil and the concentrations of Pb, Zn, Cu, and Cr in this soil were listed in Table 1.

2.2. Pot Experiments. Two soil amendments were used in this study: mHAP (micrometer hydroxyapatite, bought from Nanjing Emperor Nano Material Co., Ltd., China, average particle diameter = 12 μm) and nHAP (nanometer particle hydroxyapatite, bought from Nanjing Emperor Nano Material Co., Ltd., China, average particle diameter = 60 nm). No Pb, Zn, Cu, and Cr were detected in these two materials. Both soil amendments were applied at two levels, 15 $\text{g}\cdot\text{kg}^{-1}$ and 30 $\text{g}\cdot\text{kg}^{-1}$. The Pb, Zn, Cu, and Cr were supplied to soil as solutions of $PbSO_4$, $CuSO_4\cdot 5H_2O$, $ZnSO_4\cdot 7H_2O$, and $KCrO_4$. The four soil treatments were T0 (without metals added), T1 (250/100 $\text{mg}\cdot\text{kg}^{-1}$ Pb/Zn added, resp.), T2 (500/200 $\text{mg}\cdot\text{kg}^{-1}$ Pb/Zn added, resp.), T3 (100/25 $\text{mg}\cdot\text{kg}^{-1}$ Cu/Cr added, resp.), and T4 (200/50 $\text{mg}\cdot\text{kg}^{-1}$ Cu/Cr added, resp.). Altogether, each metal level has mHAP and nHAP treatments. There were four replications in each treatment. The concentration of Pb, Zn, and Cu supplied to the soil exceeded those of the soil environmental quality standards in China, so the metal amended soil can be regarded as slightly metal contaminated (T1 and T3 treatment level) and heavy metal contaminated (T2 and T4 treatment level), respectively. Soil amendments were thoroughly mixed with soil prior to potting nitrogen (6 $\text{g}\cdot\text{pot}^{-1}$ soil as NH_4NO_3) and potassium (6 $\text{g}\cdot\text{pot}^{-1}$ soil as KCl). Pots containing 3.0 kg of soil were used in this experiment. Deionized water was supplied to keep the soil water content to about 60% of maximum water holding capacity.

The soil was left to equilibrate for 20 days before planting pakchoi (*Brassica chinensis* L.). Ten pregerminated seeds were sown in each pot. At seven days after emergence, seedlings were thinned to six per pot. The pakchoi was grown in a greenhouse with temperatures between 25 and 30°C. Pakchois were harvested 60 days after emergence.

2.3. Metal Analysis. After harvest, the pakchois were removed from the pots and cut into two parts: shoots and roots. The shoots and roots were washed three times by deionized water, then put into the oven to dry at 70°C, and passed through 2 mm sieve for further experiment. The soil samples were taken from the pots after harvesting

the vegetables and were air-dried at room temperature, followed by passing through 0.149 mm sieve.

Pb, Zn, Cu, and Cr in pakchoi were extracted by using acid digestion mixture (HNO_3 and $HClO_4$). The pakchoi samples were heated with HNO_3 and $HClO_4$ mixture until the color became clear, filtered, reconstituted to the desired volume, and measured by the inductively coupled plasma optical emission spectrometry (ICP-OES) for Pb, Zn, Cu, and Cr content. For the analysis of Pb, Zn, Cu, and Cr in soil, 0.3 g of homogenized soil samples was digested with HNO_3 , $HClO_4$, and HF. The samples were heated until the color became clear, dissolved with several drops of 1% HNO_3 , filtered, diluted to a volume of 50 mL with distilled water, and analyzed for the content of Pb, Zn, Cu, and Cr [6].

2.4. Sequential Extraction of Soil Samples. The method of sequential extraction developed by BCR sequential extraction procedure [11] was employed in this study. Each of the chemical fractions was operationally defined as follows: acid soluble fraction: 1 g soil (dry wt) was extracted with 40 mL 0.1 $\text{mol}\cdot\text{L}^{-1}$ HOAc, shaking for 16 h; reducible fraction: residue from the acid soluble fraction was extracted with 40 mL 0.5 $\text{mol}\cdot\text{L}^{-1}$ $NH_2OH\cdot HCl$ (pH 1.5) shaking for 16 h; oxidizable fraction: residue from the reducible fraction was extracted with 10 mL H_2O_2 for 1 h at 85°C and an additional 10 mL H_2O_2 for 1 h at 85°C, and then 50 mL 1 $\text{mol}\cdot\text{L}^{-1}$ NH_4Ac was added, shaking for 16 h; residual fraction: residue from the oxidizable fraction was digested with $HNO_3\text{--}HClO_4\text{--}HF$. After each extraction, separation was performed by centrifugation at 10,000 rpm for 20 min. Metal concentration in the soil solutions was determined by ICP-OES.

2.5. Statistical Analysis. The means and standard deviations (SD) were calculated by Excel 2003. Statistical analysis including the analysis of variance was conducted using SPSS version 17.0 software (SPSS Inc., USA) and differences ($P < 0.05$) between means were determined using the Duncan test. The figures were plotted by origin 7.5.

3. Results and Discussions

3.1. Effect of mHAP and nHAP on the Biomass of the Pakchoi. The biomass of the pakchoi shoots and roots was significantly decreased by metal application at T2 and T4 treatment levels but increased at T1 and T3 treatment levels compared to the control treatment (Table 2). This result corresponds with Chen and Cui [12], who reported that, at low metal contaminated treatment level, the growth of plant can be promoted while, at high metal contaminated treatment level, the growth of plant can be stunted down. Excessive heavy metals, such as Pb, Zn, Cu, and Cr contents in soil, have been reported to inhibit the development of root system of plant, block down the photosynthesis, and led to the decrease of plant yield [13]. The application of mHAP and nHAP both increased the shoots and roots biomass of the pakchoi at all the treatment levels. The result showed that, by supplement of 30 $\text{g}\cdot\text{kg}^{-1}$ mHAP, the increment of shoots biomass was 21.98% in T2 treatment level and 25.62% in T4 treatment

TABLE 1: Basic properties of the soil.

pH	Organic matter (g·kg ⁻¹)	Available (mg·kg ⁻¹)			Total (mg·kg ⁻¹)			
		N	P	K	Pb	Zn	Cu	Cr
4.95	14.5	88.9	11.2	95.0	42.0	60.7	23.8	55.2

TABLE 2: Biomass of pakchoi (*Brassica chinensis* L.) grown in the uncontaminated soil and contaminated soil with mHAP and nHAP (dry weigh).

Treatment	Shoot (g·pot ⁻¹ DW)	Root (g·pot ⁻¹ DW)
T0 (CK)	3.61 ± 0.26 ^{efg}	0.62 ± 0.04 ^{bc}
T0 + 1.5% mHAP	3.96 ± 0.28 ^{ij}	0.63 ± 0.08 ^{cd}
T0 + 3% mHAP	3.64 ± 0.17 ^{fgh}	0.62 ± 0.18 ^{cd}
T0 + 1.5% nHAP	3.83 ± 0.22 ^{hi}	0.64 ± 0.09 ^{cde}
T0 + 3% nHAP	3.60 ± 0.31 ^{efg}	0.62 ± 0.11 ^{bc}
T1 (250/100 mg·kg ⁻¹ Pb/Zn)	3.96 ± 0.25 ^{ij}	0.62 ± 0.06 ^{bc}
T1 + 1.5% mHAP	4.20 ± 0.10 ^{kl}	0.69 ± 0.18 ^{efgh}
T1 + 3% mHAP	4.31 ± 0.53 ^l	0.82 ± 0.09 ^k
T1 + 1.5% nHAP	4.04 ± 0.16 ^{ij}	0.65 ± 0.13 ^{cdef}
T1 + 3% nHAP	4.15 ± 0.14 ^{jkl}	0.66 ± 0.10 ^{cdef}
T2 (500/200 mg·kg ⁻¹ Pb/Zn)	3.23 ± 0.12 ^{bc}	0.56 ± 0.11 ^{ab}
T2 + 1.5% mHAP	3.39 ± 0.18 ^{cde}	0.65 ± 0.07 ^{cdef}
T2 + 3% mHAP	3.94 ± 0.27 ^{ij}	0.76 ± 0.21 ^{ij}
T2 + 1.5% nHAP	3.40 ± 0.43 ^{cde}	0.61 ± 0.11 ^{bc}
T2 + 3% nHAP	3.59 ± 0.15 ^{efg}	0.69 ± 0.15 ^{dgh}
T3 (100/25 mg·kg ⁻¹ Cu/Cr)	3.81 ± 0.34 ^{hi}	0.66 ± 0.17 ^{cdef}
T3 + 1.5% mHAP	4.01 ± 0.18 ^{ijk}	0.80 ± 0.09 ^{jk}
T3 + 3% mHAP	4.06 ± 0.16 ^{jk}	0.82 ± 0.11 ^k
T3 + 1.5% nHAP	3.97 ± 0.49 ^{ijk}	0.74 ± 0.15 ^{hij}
T3 + 3% nHAP	4.04 ± 0.59 ^{ijk}	0.78 ± 0.08 ^{ijk}
T4 (200/50 mg·kg ⁻¹ Cu/Cr)	2.81 ± 0.10 ^a	0.51 ± 0.12 ^a
T4 + 1.5% mHAP	3.27 ± 0.25 ^{bc}	0.64 ± 0.11 ^{cdef}
T4 + 3% mHAP	3.53 ± 0.24 ^{ef}	0.71 ± 0.18 ^{gh}
T4 + 1.5% nHAP	3.08 ± 0.11 ^b	0.64 ± 0.06 ^{cdef}
T4 + 3% nHAP	3.31 ± 0.19 ^{cd}	0.67 ± 0.13 ^{cdef}

Mean values denoted by the same letter in a column do not differ significantly according to the Duncan test.

level as compared to control. As to the nHAP, it was showed that when treated with 30 g·kg⁻¹ nHAP, the increment of shoots biomass was 11.14% in T2 treatment level and 17.79% in T4 treatment level when compared to that of control. It can be found that the application of mHAP and nHAP both increased the shoots and roots biomass of the pakchoi in all treatment levels. This result may be due to the fact that the mHAP and nHAP can release the toxic effect on pakchoi caused by heavy metal treatment, resulting in the increment of the biomass of pakchoi. Another reason may lie in the fact that more phosphate nutrition supplement after phosphate amendments addition can promote the growth of the pakchoi [6]. Furthermore, in this study, mHAP appeared to be more efficient in increasing the biomass of pakchoi in T2 and T4 treatment levels.

3.2. Effect of mHAP and nHAP on the Uptake of Pb, Zn, Cu, and Cr by Pakchoi. The application of mHAP and nHAP

significantly reduced the concentration of Pb, Zn, Cu, and Cr in the shoots and roots of the pakchoi grown in the contaminated soil (Tables 3 and 4). However, the addition of mHAP has better effect than nHAP in heavy metal treatment levels (T2 and T4). The result showed that, by the addition of the 30 g·kg⁻¹ mHAP, the concentrations of Pb, Zn, Cu, and Cr in shoots decreased by 58.1%, 47.3%, 49.4%, and 38.9% in T2 and T4 treatment level, respectively, while the roots reduction was 53.0%, 45.5%, 47.5%, and 44.6% compared to the control. As to the 30 g·kg⁻¹ nHAP application, the reduction in concentration of Pb, Zn, Cu, and Cr in the shoots was 53.4% for Pb, 32.1% for Zn, 32.2% for Cu, and 30.9% for Cr in T2 and T4 treatment levels, respectively, whereas roots Pb, Zn, Cu, and Cr decreased by 42.2% for Pb, 39.3% for Zn, 39.6% for Cu, and 37.5% for Cr when compared with that of control. The result showed that both the mHAP and nHAP can significantly influence Pb, Zn, Cu, and Cr concentrations in the pakchoi vegetable shoots and roots.

TABLE 3: Concentration of Pb and Zn in pakchoi (*Brassica chinensis* L.) grown in Pb-Zn multiple metal-contaminated soil in pot culture receiving mHAP and nHAP amendments (dry weigh).

	Pb		Zn	
	Shoot (mg·kg ⁻¹)	Root (mg·kg ⁻¹)	Shoot (mg·kg ⁻¹)	Root (mg·kg ⁻¹)
T0 (CK)	0.40 ± 0.02 ^a	2.93 ± 0.15 ^a	28.05 ± 1.66 ^{bcd}	38.29 ± 1.94 ^f
T0 + 1.5% mHAP	0.34 ± 0.02 ^a	2.62 ± 0.12 ^a	24.54 ± 0.99 ^b	31.88 ± 1.87 ^d
T0 + 3% mHAP	0.32 ± 0.03 ^a	2.25 ± 0.10 ^a	18.45 ± 1.24 ^a	24.90 ± 1.99 ^a
T0 + 1.5% nHAP	0.34 ± 0.01 ^a	2.43 ± 0.09 ^a	24.90 ± 1.02 ^{bc}	31.22 ± 2.93 ^{cd}
T0 + 3% nHAP	0.30 ± 0.02 ^a	2.22 ± 0.07 ^a	20.35 ± 1.73 ^a	27.23 ± 2.17 ^b
T1	4.45 ± 0.23 ^d	26.92 ± 0.76 ^{de}	40.91 ± 2.36 ^f	48.53 ± 2.05 ^g
T1 + 1.5% mHAP	3.48 ± 0.11 ^c	20.20 ± 1.54 ^c	30.47 ± 1.41 ^{de}	32.91 ± 1.07 ^d
T1 + 3% mHAP	1.80 ± 0.08 ^b	15.08 ± 0.88 ^b	22.52 ± 0.23 ^a	29.31 ± 2.44 ^{bc}
T1 + 1.5% nHAP	3.42 ± 0.21 ^c	22.14 ± 1.32 ^c	32.24 ± 2.00 ^c	35.53 ± 2.82 ^e
T1 + 3% nHAP	2.16 ± 0.08 ^b	16.39 ± 1.00 ^b	25.80 ± 1.25 ^{bc}	31.39 ± 1.63 ^{cd}
T2	12.15 ± 0.77 ^h	53.94 ± 2.69 ^h	51.02 ± 3.58 ^g	86.84 ± 5.85 ^k
T2 + 1.5% mHAP	7.21 ± 0.62 ^g	28.25 ± 1.36 ^e	31.63 ± 1.97 ^e	59.50 ± 2.55 ⁱ
T2 + 3% mHAP	5.09 ± 0.39 ^e	25.35 ± 1.82 ^d	26.89 ± 1.55 ^{bc}	47.37 ± 3.43 ^g
T2 + 1.5% nHAP	7.59 ± 0.56 ^g	37.67 ± 2.04 ^g	38.44 ± 1.61 ^f	63.83 ± 5.01 ^j
T2 + 3% nHAP	5.66 ± 0.50 ^f	31.20 ± 1.91 ^f	31.59 ± 1.26 ^e	52.70 ± 3.38 ^h

Mean values denoted by the same letter in a column do not differ significantly according to the Duncan test.

TABLE 4: Concentration of Cu and Cr in pakchoi (*Brassica chinensis* L.) grown in Cu-Cr multiple metal-contaminated soil in pot culture receiving mHAP and nHAP amendments.

	Cu		Cr	
	Shoot (mg·kg ⁻¹)	Root (mg·kg ⁻¹)	Shoot (mg·kg ⁻¹)	Root (mg·kg ⁻¹)
T0 (CK)	6.32 ± 0.36 ^a	9.72 ± 0.54 ^a	1.94 ± 0.08 ^b	3.54 ± 0.14 ^a
T0 + 1.5% mHAP	5.90 ± 0.20 ^a	9.51 ± 0.77 ^a	1.58 ± 0.06 ^{ab}	2.89 ± 0.09 ^a
T0 + 3% mHAP	4.78 ± 0.29 ^a	7.68 ± 0.64 ^a	1.45 ± 0.06 ^a	2.53 ± 0.07 ^a
T0 + 1.5% nHAP	5.84 ± 0.41 ^a	8.60 ± 0.26 ^a	1.75 ± 0.05 ^{ab}	2.96 ± 0.20 ^a
T0 + 3% nHAP	5.32 ± 0.35 ^a	7.94 ± 0.81 ^a	1.51 ± 0.11 ^{ab}	2.67 ± 0.18 ^a
T3	17.16 ± 0.76 ^f	33.75 ± 1.53 ^d	4.25 ± 0.20 ^e	15.25 ± 0.78 ^e
T3 + 1.5% mHAP	13.20 ± 0.79 ^{cd}	23.89 ± 1.44 ^c	3.07 ± 0.26 ^d	10.34 ± 0.65 ^c
T3 + 3% mHAP	10.06 ± 0.42 ^b	19.61 ± 0.86 ^b	2.65 ± 0.15 ^c	9.44 ± 0.53 ^b
T3 + 1.5% nHAP	14.04 ± 1.38 ^{de}	24.19 ± 0.99 ^c	3.28 ± 0.23 ^d	13.17 ± 0.10 ^d
T3 + 3% nHAP	12.14 ± 0.74 ^c	20.98 ± 1.30 ^b	2.99 ± 0.17 ^{cd}	9.49 ± 0.04 ^b
T4	30.39 ± 1.90 ⁱ	76.00 ± 4.11 ^h	6.76 ± 0.48 ^h	34.54 ± 1.87 ^j
T4 + 1.5% mHAP	20.64 ± 1.36 ^h	53.22 ± 2.76 ^g	5.02 ± 0.17 ^{fg}	22.66 ± 2.33 ^h
T4 + 3% mHAP	15.37 ± 0.85 ^e	39.92 ± 2.53 ^e	4.13 ± 0.26 ^e	19.14 ± 0.86 ^f
T4 + 1.5% nHAP	22.06 ± 1.03 ^h	54.90 ± 3.53 ^g	5.30 ± 0.32 ^g	25.35 ± 1.92 ⁱ
T4 + 3% nHAP	18.77 ± 1.12 ^g	45.88 ± 1.92 ^f	4.67 ± 0.35 ^f	21.60 ± 2.90 ^g

Mean values denoted by the same letter in a column do not differ significantly according to the Duncan test.

Similar to the result of pakchoi biomass, the mHAP has better effect on reducing the Pb, Zn content in T2 treatment and Cu, Cr content in T4 treatment in pakchoi shoots and roots. However, it can be observed that the application of 30 g·kg⁻¹ mHAP can significantly reduce the T1 and T3 concentration level of metals in pakchois and therefore produce vegetable with Pb, Zn, Cu, and Cr concentrations under the Chinese national food safety standard (GB2762-2005, in China) level.

3.3. Effect of mHAP and nHAP on the pH of the Soil. Some researchers [14] suggested that the pH was one of the most

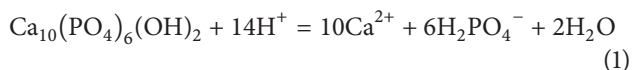
important parameters affected metal bioavailability to plants. In the low pH (pH < 5) condition, the metal in soil has higher solubility. As a result, more metal ion released to the soil solution. The metal therefore was more bioavailable to the plants. The application of HAP amendment can increase the soil pH and reduce the metal bioavailability, especially in the low pH soil conditions. This study indicated that the supplement of mHAP and nHAP both significantly increased the soil pH compared to the unamended metals contaminated soil (Table 5). However, it can be observed that the mHAP had better effect than nHAP in increasing the pH of each

TABLE 5: pH value in the tested soil as affected by mHAP and nHAP amendments.

Treatment	pH
T0 (CK)	4.95
T0 + 1.5% mHAP	5.46
T0 + 3% mHAP	5.99
T0 + 1.5% nHAP	5.20
T0 + 3% nHAP	5.76
T1	5.08
T1 + 1.5% mHAP	5.76
T1 + 3% mHAP	6.07
T1 + 1.5% nHAP	5.42
T1 + 3% nHAP	5.83
T3	5.11
T3 + 1.5% mHAP	5.60
T3 + 3% mHAP	5.99
T3 + 1.5% nHAP	5.18
T3 + 3% nHAP	5.74
T2	5.16
T2 + 1.5% mHAP	5.72
T2 + 3% mHAP	6.24
T2 + 1.5% nHAP	5.45
T2 + 3% nHAP	5.74
T4	4.97
T4 + 1.5% mHAP	5.68
T4 + 3% mHAP	6.19
T4 + 1.5% nHAP	5.39
T4 + 3% nHAP	5.87

treatment level, especially in 30 g·kg⁻¹ application rate. The result showed that when compared with the contaminated soil without adding amendment, after applying for 30 g·kg⁻¹ mHAP, the pH value was raised by 0.99 in T1 treatment level, 1.08 in T2 treatment level, 0.88 in T3 treatment level, and 1.22 in T4 treatment level. As to the nHAP, the enhancement of pH value was 0.75 in T1 treatment level, 0.58 in T2 treatment level, 0.63 in T3 treatment level, and 0.90 in T4 treatment level when compared with the contaminated soil without adding amendment.

pH was an important parameter which affected metal immobilization and dissolution in soil [15]. The metal solubility and mobility increased with the decrease of pH. In contrast, when the soil pH increased, the solubility and mobility of metal in soil went down. Bolisson et al. [16] reported that the application of HAP can increase the soil pH value. This was attributed to the fact that the dissolution of HAP in soil solution can consume H⁺, resulting in the increase of soil pH:



It was reported that when HAP was dissolved in deionized water and 0.1 mol/L KNO₃ solution, the dissolution rate of HAP mainly depended on pH [17, 18]. Soil solution was more complicated when compared with deionized water or

single electrolyte solution. Generally speaking, in low pH soil condition, the dissolution rate of HAP was more faster than in neutral and alkali soil. As in the acidic soil condition, the PO₄³⁻ in hydroxyapatite had higher efficiency to dissolve and release to the soil solution. In this study, the application of mHAP had better effect in increasing the soil pH than nHAP, suggesting that mHAP has a larger dissolution rate than nHAP.

3.4. Speciation of Soil Pb, Zn, Cu, and Cr. The distribution of Pb, Zn, Cu, and Cr in the uncontaminated soil and metal-contaminated soil as analyzed by the BCR sequential extraction method was shown in Figure 1. The metal (Pb, Zn, Cu, and Cr) in the treatments without mHAP and nHAP was mainly associated with the nonresidual fraction. The percentage of Pb, Zn, and Cu bound with the nonresidual fraction (including acid soluble fraction, reducible fraction, and oxidizable fraction) accounted for over 74.1% for Pb and 76.3% for Zn in T1 treatment level and 79.72% for Pb and 62.96% for Zn in T2 treatment level, 88.1% for Cu and 60.73% for Cr in T3 treatment level, and 88.12% for Cu and 56.47% for Cr in T4 treatment level, respectively. This indicated that a substantial fraction of Pb, Zn, Cu, and Cr in the contaminated soil without amendment may be available for pakchoi to uptake. As to the HAP amended soil, both mHAP and nHAP translocated nonresidual fractions of Pb, Zn, Cu, and Cr to the residual fraction. For instance, by addition of 30 g·kg⁻¹ mHAP, the reduction in the nonresidual fraction was 36.0% for Pb and 34.9% for Zn in T1 treatment level, 36.1% for Pb and 27.5% for Zn in T2 treatment level, 32.5% for Cu and 26.8% for Cr in T3 treatment level, and 26.6% for Cu and 20.0% for Cr in T4 treatment level. The reduction in the nonresidual fraction was 29.8% for Pb and 29.4% for Zn in T1 treatment level, 20.7% for Pb and 27.5% for Zn in T2 treatment level, 23.1% for Cu and 21.9% for Cr in T3 treatment level, and 17.1% for Cu and 14.8% for Cr in T4 treatment level by addition of 30 g·kg⁻¹ nHAP treatment.

The result showed that nonresidual fraction of Pb, Zn, Cu, and Cr decreased with the increase of soil pH, hinting that the pH values play an important role in decreasing the nonresidual fraction. The increase of pH values induced by HAP favored the precipitation of heavy metals. In addition, Gray et al. [19] found that the increase of soil pH values increased the negative charges of variably charged colloids in soil, such as organic matter, clays, Fe and Al oxides, and silicon oxides, resulting in stronger sorption and precipitation of heavy metals and hence lower soluble metal concentrations in soil. In this study, it can be found that mHAP has better effect on transforming metals from the nonresidual to the residual fraction, which was consistent with the result of soil pH changed by mHAP and nHAP, indicating that larger soil pH values with mHAP addition than nHAP were the main reason for the superior ability of immobilization Pb, Zn, Cu, and Cr in soil of mHAP.

In this paper, we identified the effectiveness of mHAP and nHAP to reduce the amounts of heavy metals in contaminated soil. The efficiency of *in situ* remediation of metal-contaminated soils can be evaluated by using fractionation

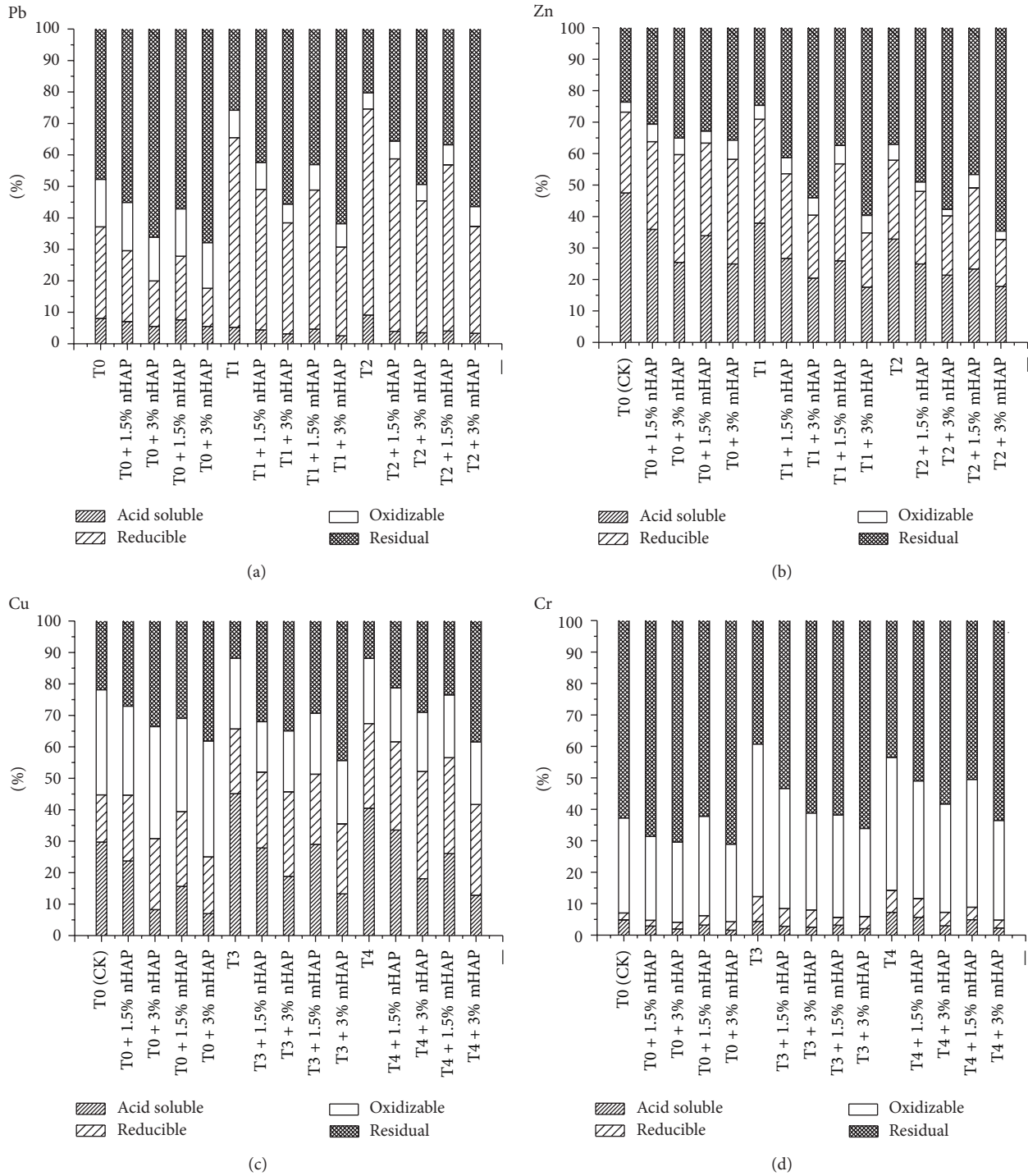


FIGURE 1: Relative percentages of Pb, Zn, Cu, and Cr in each fraction of the soils from the CK, mHAP, and nHAP treated pots.

procedures; the more effective the treatment, the greater the amount of metals transferred from the nonresidual to the residual fraction [20, 21]. BCR sequential extraction procedures were widely used to assess the bioavailability and mobility of heavy metals in soils as well as the efficacy of decontamination amendment. The nonresidual metal fractionation, which includes acid soluble (weakly bound

with organic matter and carbonates fraction), reducible (iron and manganese oxides fraction), and oxidizable (organically bound and sulfide fraction) fractions, is more mobile and is considered to have a higher bioavailability as compared with the residual fraction [22, 23]. In the current study, both mHAP and nHAP were highly capable of modifying Pb, Zn, Cu, and Cr in contaminated soils, with a concurrent

increase in the residual fractionation and a decrease in the nonresidual fractionation, especially the acid soluble fractionation. Moreover, mHAP and nHAP were more effective in transforming the nonresidual fractionation of Pb than the other three heavy metals, as expected. One of the most important effects of HAP modification is the formation of pyromorphite from Pb, thus resulting in the transformation of Pb from nonresidual fractions to the residual fraction [24]. This study confirmed that the supplementation of both mHAP and nHAP significantly enhanced the residual fraction of Pb in soils, corresponding to a reduction of Pb in pakchoi shoots and roots.

We also found that the addition of mHAP and nHAP decreased the nonresidual fraction of Cu, Zn, and Cr in the soil. However, the immobilization efficacy was lower than Pb. We hypothesized two reasons for this phenomenon. Firstly, the solubility products of Cu, Zn, and Cr phosphate are known to be much greater than that of Pb phosphate. However, hopeite $[\text{Zn}_3(\text{PO}_4)_2]$, $\text{Cu}_3(\text{PO}_4)_2$, and $\text{Cr}_2(\text{PO}_4)_7$ are much more soluble than pyromorphite. As such, Cu, Zn, and Cr phosphate may not control the solubility of these heavy metals in this case [6]. And secondly, we believe that the primary mechanism is likely due to the adsorption potential of the surface of HAP. For instance, Cao et al. [25] reported that the application of HAP in Pb, Cu, and Zn contaminated soil and showed that 78% of Pb that reacted with HAP was formed of pyromorphite. Meanwhile, only 25% of Cu and 5% of Zn were formed of $\text{Cu}_2(\text{PO}_4)_3$ and $\text{Zn}_2(\text{PO}_4)_2$ and 75% Cu and 95% Zn were adsorbed upon the surface of HAP. Results from this study confirmed that mHAP and nHAP had great ability for reducing Pb bioavailability and also for inhibiting the uptake of Pb to a greater degree than Zn, Cu, and Cr. However, mHAP was more capable of decreasing the overall amount of metals taken up by the pakchoi plant.

The reduction of Pb content in the pakchoi shoots and roots can be attributed to the formation of pyromorphite in the soil. As to the decrease of Zn, Cu, and Cr in pakchoi shoots and roots, the main reason involved of Zn, Cu and Cr adsorption on the HAP and the higher solubility of $[\text{Zn}_3(\text{PO}_4)_2]$, $\text{Cd}_3(\text{PO}_4)_2$ and $\text{Cr}_2(\text{PO}_4)_7$ than pyromorphite. Moreover, the reduction of Pb, Zn, Cu, and Cr content in the pakchoi shoots and roots was as follows: $\text{Pb} > \text{Zn} \approx \text{Cu} > \text{Cr}$. These results are consistent with the sequence in the reduction of Pb, Zn, Cu, and Cr of the nonresidual fraction found in contaminated soil, suggesting that the nonresidual fraction of heavy metals can readily be taken up by the pakchoi plant and also shows the highest levels of bioavailability for the pakchoi.

Many studies have been conducted in recent years focused on the heavy metal remediation potential of nanomaterials in contaminated soil [26, 27]. Phosphate-based nanoparticles have been found to be one of the most effective nanomaterials for the reclamation of heavy metal contaminated soil. For instance, Liu and Zhao [28] reported that the application of iron phosphate nanoparticles in Pb-contaminated soil can effectively reduce the leachability and bioavailability of Pb^{2+} in soil. Moreover, Liu [29] also reported an effective reclamation of a lead-contaminated soil

using synthesized apatite nanoparticles. Their experimental results clearly showed that the apatite nanoparticles solution could significantly reduce the TCLP-leachable Pb fraction in Pb-contaminated soil by 9.56% to 66.43%. Many studies have suggested that nanomaterials are superior to traditional modifications using commonly particle sizes for soil remediation due to nanomaterials having a higher reactivity and a greater ability for absorption and for its relatively easy delivery methods. Theoretically, in this study a larger amount of Pb, Zn, Cu, and Cr was able to be immobilized by nHAP, likely due to its smaller particle sizes yet larger surface area, as compared to mHAP. However, we found that mHAP was more effective than nHAP in immobilizing Pb, Zn, Cu, and Cr. Furthermore, the pH value of the soil was more greatly enhanced by mHAP. Gilbert et al. [30] and Cui et al. [18] suggested that nanomaterials can easily aggregate, leading to an alteration to their surface sorption and ability to migrate while decreasing their dissolution rates. mHAP has a larger particle size, as compared to nHAP making it much more difficult for mHAP to aggregate. Therefore, we hypothesized that the higher dissolution rate was the primary reason for the increases in the pH value and for its increased immobilization effects. Nevertheless, further studies are needed in order to verify this hypothesis.

4. Conclusions

The effectiveness of two different sizes of HAP particle, nanometer size particle of HAP (nHAP) and micrometer size particle of HAP (mHAP), was assessed for their ability of reducing the bioavailability of Pb, Zn, Cu, and Cr. The results showed that both mHAP and nHAP had significant effect on reducing the uptake of Pb, Zn, Cu, and Cr by pakchoi. Furthermore, both mHAP and nHAP were efficient in covering Pb, Zn, Cu, and Cr from nonresidual into residual forms. However, mHAP was superior to nHAP immobilization of Pb, Zn, Cu, and Cr in metal-contaminated soil and reducing the Pb, Zn, Cu, and Cr by pakchoi. In addition, mHAP and nHAP were both more efficient in transferring bioavailable Pb into less bioavailable form than Zn, Cu, and Cr. This may be due to the fact that more Pb was formed into insoluble pyromorphite like minerals after treated with HAP. However, in this study, it was suggested that HAP with micrometer size was more effective immobilization soil metals than nanometer size HAP, possibly due to its higher dissolution rate.

Conflict of Interests

The authors declare that there is no conflict of interests regarding the publication of this paper.

Acknowledgment

This work was supported by the National Spark Program of China (no. 2012GA780051).

References

- [1] I. Mohamed, B. Ahamadou, M. Li et al., "Fractionation of copper and cadmium and their binding with soil organic matter in a contaminated soil amended with organic materials," *Journal of Soils and Sediments*, vol. 10, no. 6, pp. 973–982, 2010.
- [2] N. Karami, R. Clemente, E. Moreno-Jiménez, N. W. Lepp, and L. Beesley, "Efficiency of green waste compost and biochar soil amendments for reducing lead and copper mobility and uptake to ryegrass," *Journal of Hazardous Materials*, vol. 191, no. 1–3, pp. 41–48, 2011.
- [3] H. M. Chen, C. R. Zheng, C. Tu, and Y. G. Zhu, "Heavy metal pollution in soils in China: status and countermeasures," *Ambio*, vol. 28, no. 2, pp. 130–134, 1999.
- [4] X. D. Cao, L. Q. Ma, M. Chen, S. P. Singh, and W. G. Harris, "Phosphate-induced metal immobilization in a contaminated site," *Environmental Pollution*, vol. 122, no. 1, pp. 19–28, 2003.
- [5] X. D. Cao, A. Wahbi, L. Ma, B. Li, and Y. Yang, "Immobilization of Zn, Cu, and Pb in contaminated soils using phosphate rock and phosphoric acid," *Journal of Hazardous Materials*, vol. 164, no. 2–3, pp. 555–564, 2009.
- [6] S. B. Chen, M. G. Xu, Y. B. Ma, and J. Yang, "Evaluation of different phosphate amendments on availability of metals in contaminated soil," *Ecotoxicology and Environmental Safety*, vol. 67, no. 2, pp. 278–285, 2007.
- [7] V. Misra and P. K. Chaturvedi, "Plant uptake/bioavailability of heavy metals from the contaminated soil after treatment with humus soil and hydroxyapatite," *Environmental Monitoring and Assessment*, vol. 133, no. 1–3, pp. 169–176, 2007.
- [8] J. Chen, Y. Wang, D. Zhou, Y. Cui, S. Wang, and Y. Chen, "Adsorption and desorption of Cu(II), Zn(II), Pb(II), and Cd(II) on the soils amended with nanoscale hydroxyapatite," *Environmental Progress and Sustainable Energy*, vol. 29, no. 2, pp. 233–241, 2010.
- [9] Z. Z. Zhang, M. Y. Li, W. Chen, S. Zhu, N. Liu, and L. Zhu, "Immobilization of lead and cadmium from aqueous solution and contaminated sediment using nano-hydroxyapatite," *Environmental Pollution*, vol. 158, no. 2, pp. 514–519, 2010.
- [10] R. K. Lu, *Analytical Methods for Soils and Agricultural Chemistry*, China Agricultural Science and Technology Press, Beijing, China, 1999.
- [11] G. Rauret, R. Rubio, and J. F. Lopez-sanchez, "Optimization of tesserprocedure for metal solid speciation in river sediments," *Trends in Analytical Chemistry*, vol. 36, pp. 69–83, 1989.
- [12] X. C. Chen and Y. S. Cui, "Effects of dry and fresh states of *Brassica chinensis* on the oral bioaccessibility of lead," *Asian Journal of Ecotoxicology*, vol. 4, no. 6, pp. 793–799, 2009 (Chinese).
- [13] P. Li, X. X. Wang, T. L. Zhang, D. Zhou, and Y. He, "Effects of several amendments on rice growth and uptake of copper and cadmium from a contaminated soil," *Journal of Environmental Sciences*, vol. 20, no. 4, pp. 449–455, 2008.
- [14] P. Zhang and J. A. Ryan, "Formation of chloropyromorphite from Galena (PbS) in the presence of hydroxyapatite," *Environmental Science and Technology*, vol. 33, no. 4, pp. 618–624, 1999.
- [15] X. D. Cao, L. Q. Ma, S. P. Singh, and Q. Zhou, "Phosphate-induced lead immobilization from different lead minerals in soils under varying pH conditions," *Environmental Pollution*, vol. 152, no. 1, pp. 184–192, 2008.
- [16] J. Boisson, A. Ruttens, M. Mench, and J. Vangronsveld, "Evaluation of hydroxyapatite as a metal immobilizing soil additive for the remediation of polluted soils. Part 1. Influence of hydroxyapatite on metal exchangeability in soil, plant growth and plant metal accumulation," *Environmental Pollution*, vol. 104, no. 2, pp. 225–233, 1999.
- [17] H. Eslami, M. Solati-Hashjin, and M. Tahriri, "Effect of fluorine ion addition on structural, thermal, mechanical, solubility and biocompatibility characteristics of hydroxyapatite nanopowders," *Advances in Applied Ceramics*, vol. 109, no. 4, pp. 200–212, 2010.
- [18] H. B. Cui, J. Zhou, and Q. G. Zhao, "Fractions of Cu, Cd and enzyme activities in a contaminated soil as affected by applications of micro- and nanohydroxyapatite," *Journal of Soils and Sediments*, vol. 13, no. 4, pp. 742–752, 2013.
- [19] C. W. Gray, R. G. McLaren, A. H. C. Roberts, and L. M. Condon, "Sorption and desorption of cadmium from some New Zealand soils: effect of pH and contact time," *Australian Journal of Soil Research*, vol. 36, no. 2, pp. 199–216, 1998.
- [20] L. Q. Ma and G. N. Rao, "Effects of phosphate rock on sequential chemical extraction of lead in contaminated soils," *Journal of Environmental Quality*, vol. 26, no. 3, pp. 788–794, 1997.
- [21] N. T. Basta and R. Gradwohl, "Estimation of Cd, Pb, and Zn bioavailability in smelter-contaminated soils by a sequential extraction procedure," *Soil and Sediment Contamination*, vol. 9, no. 2, pp. 149–164, 2000.
- [22] P. J. C. Favas, J. Pratas, M. E. P. Gomes, and V. Cala, "Selective chemical extraction of heavy metals in tailings and soils contaminated by mining activity: environmental implications," *Journal of Geochemical Exploration*, vol. 111, no. 3, pp. 160–171, 2011.
- [23] D. S. Lin and Q. X. Zhou, "Effects of soil amendments on the extractability and speciation of cadmium, lead, and copper in a contaminated soil," *Bulletin of Environmental Contamination and Toxicology*, vol. 83, no. 1, pp. 136–140, 2009.
- [24] S. B. Chen, Y. G. Zhu, Y. B. Ma, and G. McKay, "Effect of bone char application on Pb bioavailability in a Pb-contaminated soil," *Environmental Pollution*, vol. 139, no. 3, pp. 433–439, 2006.
- [25] X. D. Cao, L. Q. Ma, D. R. Rhue, and C. S. Appel, "Mechanisms of lead, copper, and zinc retention by phosphate rock," *Environmental Pollution*, vol. 131, no. 3, pp. 435–444, 2004.
- [26] R. Q. Liu and R. Lai, "Nanoenhanced materials for reclamation of mine lands and other degraded soils: a review," *Journal of Nanotechnology*, vol. 2012, Article ID 461468, 18 pages, 2012.
- [27] M. Wang, L. Chen, S. B. Chen, and Y. Ma, "Alleviation of cadmium-induced root growth inhibition in crop seedlings by nanoparticles," *Ecotoxicology and Environmental Safety*, vol. 79, pp. 48–54, 2012.
- [28] R. Liu and D. Zhao, "Reducing leachability and bioaccessibility of lead in soils using a new class of stabilized iron phosphate nanoparticles," *Water Research*, vol. 41, no. 12, pp. 2491–2502, 2007.
- [29] R. Liu, "In-Situ lead remediation in a shoot-range soil using stabilized apatite Nanoparticles," in *Proceedings of the 85th ACS Colloid and surface Science Symposium*, McGill University, Montreal, Canada, June 2011.
- [30] B. Gilbert, R. K. Ono, K. A. Ching, and C. S. Kim, "The effects of nanoparticle aggregation processes on aggregate structure and metal uptake," *Journal of Colloid and Interface Science*, vol. 339, no. 2, pp. 285–295, 2009.

Research Article

Effects of Surfactants on High Regularity of 3D Porous Nickel for Zn^{2+} Adsorption Application

Xiaogang Guo,¹ Xueming Li,¹ Yonghong Zheng,² Chuan Lai,¹ Wulin Li,¹
Binbin Luo,¹ and Daixiong Zhang¹

¹ College of Chemistry and Chemical Engineering, Chongqing University, No. 174, Shazhengjie, Shapingba District, Chongqing 400044, China

² Chongqing Fiber Inspection Bureau, No. 5, Yunshan North Road, Gaoxin Park, Beibu New District, Chongqing 401121, China

Correspondence should be addressed to Xueming Li; lixuemingcqu@126.com

Received 23 November 2013; Revised 13 January 2014; Accepted 15 January 2014; Published 18 March 2014

Academic Editor: Fan Dong

Copyright © 2014 Xiaogang Guo et al. This is an open access article distributed under the Creative Commons Attribution License, which permits unrestricted use, distribution, and reproduction in any medium, provided the original work is properly cited.

Three-dimensional porous nickel (3D-PN) film with large specific surface area (A_s) and high porosity has been successfully prepared by hydrogen bubble dynamic template (HBDT) method. This work presents the effects of PEG 10000 and 1,4-butyne diol as new additive combination on surface morphology of the PN film. Meanwhile, the application of 3D-PN in Zn^{2+} adsorption was preliminarily investigated in the paper. The surface area is determined as large as $166.7 \text{ cm}^2/\text{mg}$ and the porosity is 0.762 when the concentration of PEG 10000 and 1,4-butyne diol was $0.3 \text{ g}/100 \text{ mL}$ and $0.1 \text{ g}/100 \text{ mL}$, respectively. The adsorption capacity (Q_t and Q (%)) of PN for Zn^{2+} is observed to be 9.145 mg/g and 0.691 for $\text{Zn}(\text{NO}_3)_2 \cdot 6\text{H}_2\text{O}$. The morphology and the microstructure, the product formation, the A_s , the concentration of the metal ions were characterized by scanning electron microscopy (SEM), X-ray powder diffraction (XRD), electrochemical impedance spectroscopy (EIS), and atomic absorption spectrometry (AAS), respectively.

1. Introduction

Three-dimensional (3D) porous metals (Ni, Cu, Sn, etc.) [1–4], with highly porous dendritic walls and numerous nanoparticles, are considered as promising nanomaterials due to their importance to both academic study and technological applications in separation systems [5], sensors [6, 7], fuel batteries [8, 9], electrochemistry [10, 11], electronic materials [12], and high performance supercapacitors [13]. Many researchers have successfully developed the 3D porous metal films electrode materials by template-directed synthesis method. And commonly used templates are considered such as liquid crystal, high internal phase emulsion (HIPE), photonic crystals, porous polycarbonate membranes [14, 15], anodic alumina membranes [16], colloidal crystals [17], and echinoid skeletal structures [18]. Compared with other approaches, hydrogen bubble dynamic template (HBDT) with hydrogen bubbles as the template on the cathode at high current densities is the green and promising one with lots

of advantages: low-cost equipment, controllable structure, facile one-step synthesis process, and easy elimination of the template [11, 19].

Recently, many efforts have been devoted to improving the morphology and developing performance of porous metal films, especially preparation of high surface area of three-dimensional porous nickel (3D-PN) films and application of their alloys in catalysis aspect and electrochemical pseudocapacitors. For example, Šimpraga et al. obtained a very high roughness factor value of the order of 2800 for Ni-Fe composite electrode prepared by simple electrochemical co-deposition process [20]. Rausch and Wendt described the high surface area sintered Ni and Raney Ni for their electrocatalytic properties [1, 21]. This mesoporous material was used as a positive electrode in hybrid supercapacitors/battery systems. Recently, the preparation of a highly porous large surface area nickel has been reported by Brown and Sotiropoulos [22]. Moreover, the nickel foam-supported porous $\text{Ni}(\text{OH})_2/\text{NiOOH}$ composite film application for

advanced pseudocapacitor material was studied by Yuan et al. [23]. However, how to control the bubble size to easily obtain attractive structure is still a great challenge.

The treatment of metal-contaminated wastewater has always been a serious issue in mining, electroplating, and the chemical and electronic industries. The impact of toxic heavy metal ions on health and on the environment has been widely reported. Metal ion treatment by adsorption into porous materials has attracted considerable attention due to their high efficiencies and economic feasibility [24, 25]. For instance, active carbon is often used to adsorb heavy metal ions and other toxic chemicals [25, 26]. Since the adsorption ability of porous materials can to a large extent be attributed to their high porosity, the adsorption ability of PN should be improved if there are suitable additives or additive combination. However, there are few studies on depollution of environment by the 3D-PN.

In electroplate industry, surfactants have been widely used as stabilizers in aqueous media to alter the surface tension of the sol/gas and protect the bubbles from coalescence. Therefore, a highly stable, well-dispersed bubble template can be obtained [27, 28]. However, there has been very little research on the effects of additive on the surface of PN film. Meanwhile, the mechanism of additive is not yet fully understood.

The research objectives of this study include first, fabricating 3D-PN film by HBTD method; second, developing 3D-network structure of PN film with the novel additive combination (PEG 10000 and 1,4-butanediol) and undertaking preliminary exploration of the impacting mechanism of additives on the morphology of PN films. In addition, the application of 3D-PN film for Zn^{2+} adsorption has been investigated in this paper, which is built upon previous respectable attempts.

2. Materials and Methods

2.1. Materials and Reagents. The electrolyte consisted of nickel sulfate, ammonium chloride, concentrated sulfuric acid, and boric acid, with the new additive combination of PEG 10000 and 1,4-butanediol. Zinc nitrate hexahydrate ($Zn(NO_3)_2 \cdot 6H_2O$) was prepared for Zn^{2+} adsorption. All the reagents mentioned were of analytical grade. Copper plate and nickel plate were purchased from Shanghai Jinan Metal Product Co., Ltd. (Shanghai, China), respectively. In the process of deposition, the solution was kept stationary. Deionized water was used throughout the experiment.

2.2. Electrode Preparation. In the study, a thin sheet of copper (99.99%) was selected for the cathode substrate material, which was repeatedly polished to highlight by numbers 400, 600, 800, and 1000 metallographic sandpaper in flowing water, cut into an area of $0.01\text{ m} \times 0.05\text{ m}$, and then sealed by insulating epoxy resin; only a $0.01\text{ m} \times 0.01\text{ m}$ surface exposed to the electrolyte was kept, and a nickel plate (99.99%) with more than 0.03 m^2 acted as anode material. The distance between the two electrodes was 1 cm. Before electrodeposition, the copper substrate was dried in ovens at 150°C for

TABLE 1: Optimal compositions and operating conditions of the basic electrolyte.

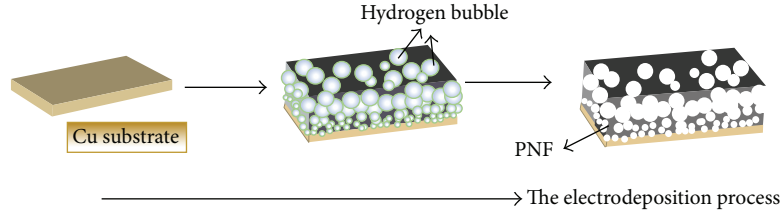
Principal element	Optimum conditions
$NiSO_4$ (mol/L)	0.2
NH_4Cl (mol/L)	1.5
Concentrated H_2SO_4 (mL/100 mL)	0.9
H_3BO_3 (mol/L)	1.2
J_k (A/cm^2)	4.0
t (s)	25

10 min, cooled to room temperature, and weighed; then the thickness of the area to be electroplated by micrometer screw was measured. And both cathode and anode were washed with deionized water in the CNC ultrasound and successively treated in the 45 g/L Na_2CO_3 , 45 g/L NaOH, and 45 g/L Na_2SO_4 to remove oil; then they were immediately etched in hydrochloric acid for rough surface and then washed with deionized water. Deposition was performed in a stationary electrolyte solution (without stirring or N_2 bubbling). And it should be stressed that 3D-PN film was soaked in water for 2 min at 30°C after rinse for 1 min with deionized water. Then it was left to dry to remove residual impurities and water in constant temperature oven at 80°C for 90 min; the film was used for Zn^{2+} adsorption. All the experiments and measurements were carried out at room temperature ($25 \pm 1^\circ\text{C}$).

2.3. Electrolyte and Operating Conditions Preparation. In this paper, the optimal process conditions were determined by previous experience and orthogonal test with six factors of the concentration of nickel sulfate, ammonium chloride, sulfuric acid, boric acid, cathode current density, and deposition time. In order to express easily and intuitively, the six factors above were successively referred to as C_{NiSO_4} , C_{NH_4Cl} , $C_{H_2SO_4}$, $C_{H_3BO_3}$, J_k , and t , which were generally considered to be the most important factors. Optimization of the suitable 3D-network structure can be carried out by a giant amount of research. And optimal compositions and operating conditions of the basic electrolyte were shown in Table 1. However, it was found that 3D structure of PN film was not obvious enough without additives. As shown in Table 2, different concentrations of additives (the PEG 10000 and 1,4-butanediol) were considered to be added to the electrolyte and this modificatory PN film was obtained with high specific surface area and porosity. Meanwhile, the schematic diagram of formation of PNF supported on Cu substrate was shown in Scheme 1.

2.4. Porosity and Surface Area Measurements

2.4.1. Porosity Measurements. The analytical balance was used to weigh the mass of copper substrate before deposition of the PN film and after electrodeposition process. The film was dried in oven and then reweighed. With micrometer



SCHEME 1: A schematic diagram of formation of PNF supported on Cu substrate.

TABLE 2: Optimal combination and variation range of additive agent.

PEG 10000 (a) and 1, 4-butyne diol (b)	Variation range (g/100 mL)	Optimal combination
Level 1	a: 0.01~0.07, b: 0	
Level 2	a: 0, b: 0.01~0.05	
Level 3	a: 0.05, b: 0.01~0.05	
Level 4	a: 0.01~0.05, b: 0.01	a: 0.03 g/100 mL, b: 0.01 g/100 mL

screw, we can determine the thickness of PN film and analyze mass variation of electrodeposition process to calculate porosity of the sample preparation. The formula was

$$\omega = \frac{\Delta m}{\rho \times \Delta h \times s}, \quad (1)$$

where Δm is the mass specimen weight (mg), ρ is the density of nickel (g/cm^3), Δh is PN film thickness (cm), and s is the contact area of the test piece and the bath (cm^2).

2.4.2. Surface Area Measurements. In the study, the A_s (specific surface area of the electrode) was performed by using electrochemical impedance spectrum (EIS) on CHI660B electrochemical workstation. Originally, the working electrode was held at -1.50 V (versus SCE) for 30 min in order to reduce the film on the electrode surface and a reproducible electrode surface could be obtained. A three-electrode test cell was used with the A_s -prepared PN film as working electrode, platinum foil as the counter, and a saturated calomel electrode (SCE) as the reference electrode. The sulfuric acid solution (0.5 mol/L) was used as the test solution. The EIS measurement was carried out in the frequency range from 100 kHz to 0.01 Hz under AC stimulus with 5 mV of amplitude and no applied voltage bias, which was performed on CHI660B electrochemical workstation. Subsequently, using Z-view software to fit initial EIS data, we can calculate the differential capacitance C_d . Therefore, specific surface area of the electrode is [29]:

$$A_s = \frac{C_d}{C_N \Delta m}, \quad (2)$$

where A is the surface area of specimen and $C_N = 20 \mu\text{F}$.

2.4.3. Environmental Applications of 3D-PN Film. Zinc nitrate solution (50 mg/L) was prepared to simulate the heavy metal ions (Zn^{2+}) in sewage. A_s -prepared PN film fabricated under identical optimal conditions was added into 100 mL zinc nitrate solution stirred at 120 r/min by ITCES (intelligent

TABLE 3: Significant factors of adsorption processes of the Zn^{2+} by the PN.

Elements	Control value
$C_0 C_0$ ($\text{Zn}(\text{NO}_3)_2 \cdot 6\text{H}_2\text{O}$) (mg/L)	5
C_0 (Zn^{2+}) (mg/L)	1.099
T (min)	0.5, 2, 5, 10, 30, 40, 70, 120
m (g)	0.0083
V (L)	0.1
Temperature ($^\circ\text{C}$)	25 ± 1

Note: the m is the mass of adsorbent-porous nickel by electrodeposition after 25 s under the optimal condition.

temperature control electromagnetic stirrer) at $25 \pm 1^\circ\text{C}$. After the adsorption process, the flame atomic absorption spectrometry was used to determine the concentration of the metal ions with a standard calibration curve [30]. The mass of adsorbent could be determined by weighing the mass of cathode substrate before and after electrodeposition, respectively. Significant factors of porous nickel on the sewage purification treatment were shown in Table 3. Purification effect can be calculated by the following formulas:

$$Q_e = \frac{V(C_0 - C_e)}{m}$$

$$Q_t = \frac{V(C_0 - C_T)}{m} \quad (3)$$

$$Q(\%) = \frac{(C_0 - C_e)}{C_0} \times 100\%,$$

where Q_t (mg/g), Q_e (mg/g), C_0 (mg/L), C_e (mg/L), C_T (mg/L), m (g), Q (%), and V (L) represent the adsorption capacity after a certain period of time, the equilibrium adsorption capacity, the initial concentration, adsorption equilibrium concentration of ions, concentration of ions after a certain period of time, the sorbent mass, purifying rate, and solution volume separately.

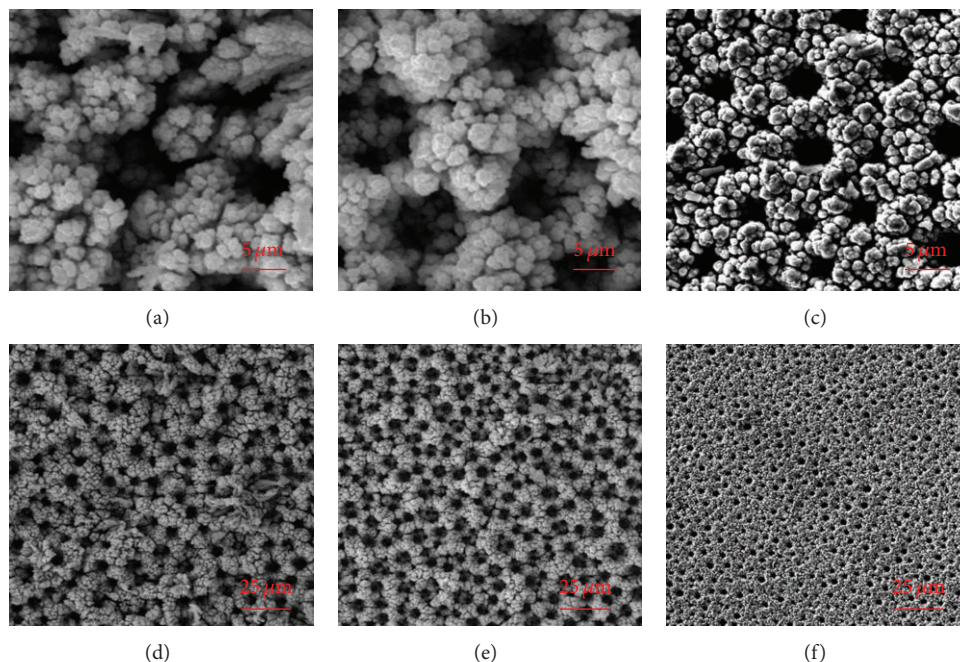


FIGURE 1: SEM morphology of PN film under different concentrations of PEG 10000 (0.01 (a, d), 0.05 (b, e), and 0.07 (c, f) g/100 mL).

2.4.4. SEM, XRD, and AAS Measurements. The surface morphology of as-prepared electrodes was investigated by scanning electron microscopy (SEM) (TESCAN VEGA II LMU). Crystallographic structure was studied by X-ray diffraction (XRD) using an X-ray diffraction using an automatic XRD analyzer (XRD-6000 Lab X SHIMADZU) with monochromatic Cu K_{α} radiation ($\lambda = 0.15405$ nm) from 10° to 80° at a speed of $4^{\circ}/\text{min}$. Additionally, the accelerating voltage and emission current of the XRD were, respectively, 40 kV and 30 mA. And the concentration of the zinc ion after the adsorption process was determined by atomic absorption spectrometry (AAS, 180-80 atomic absorption spectrophotometer, Hitachi, Japan) with detection wavelength of 214 nm and width of slit of 1.3 nm, respectively.

3. Results and Discussion

3.1. Effect of the PEG 10000. Figure 1 showed the surface morphology figures of PN film obtained in the electrode position of 25 s under different concentrations of PEG 10000 and fixed current density ($4 \text{ A}/\text{cm}^2$) at the room temperature ($25 \pm 1^{\circ}\text{C}$). Meanwhile, the constituents of the electrolyte were illustrated in Table 1. And Figure 1 showed the porous structure obviously formed on the surface of the as-prepared nickel film when the concentration of the additive PEG 10000 was 0.01 g/100 mL in the electrolyte. However, the structure of hole wall of the PN film significantly changed when the concentration of that increases gradually to 0.05 g/100 mL. The diameter of main holes increased to about 10 microns and hole wall thickness decreased. Meanwhile, the grains were refined, hole density increased gradually, and surface area calculated by formula (2) also increased according to Figure 2. It should be noted that membrane structure of

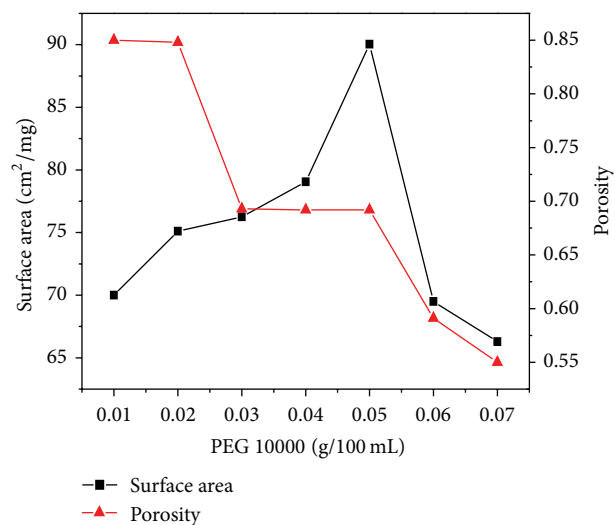


FIGURE 2: Effect of PEG 10000 on surface area and porosity of PN film.

the prepared PN was transformed into a 3D structure one. However, relatively more amount of additive to some extent gradually destroyed 3D structure while the concentration of PEG 10000 exceeded 0.07 g/100 mL; this could be the reason of a certain effect of nickel ions and hydrogen ions reduction reaction. And Figure 2 showed that porosity had a trend of decreasing sharply along with the increase of PEG 1000 concentration. When the amount of additive was 0.05 g/100 mL, PN film with the uniform distribution reached maximum specific surface area with relatively high porosity (Figures 1(b) and 1(e)). Therefore, the required optimization

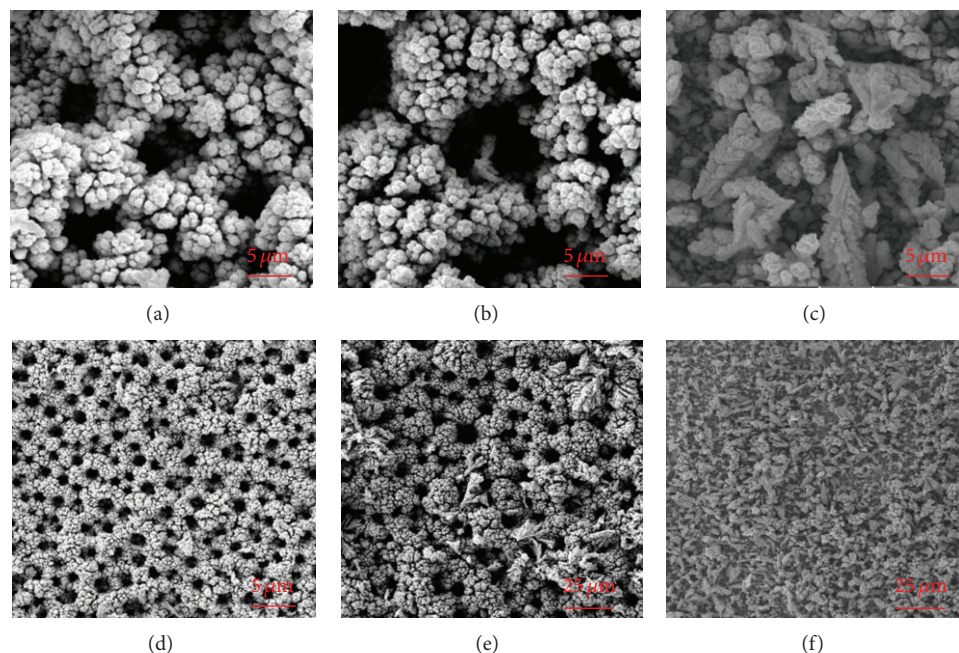


FIGURE 3: SEM morphology of PN film under different concentrations of 1,4-butyne diol (0.01 (a, d), 0.03 (b, e), and 0.05 (c, f) g/100 mL).

characteristics of PN film should be prepared by controlling the amount of additive PEG 10000.

3.2. Effect of the 1,4-Butyne diol. Figure 3 presented the surface morphology outline of PN film in the base plating solution of 0.2 mol/L nickel sulfate, 1.2 mol/L boric acid, 0.9 mL/100 mL concentrated sulfuric acid, and 1.5 mol/L ammonium chloride with different concentrations (0.01~0.05 g/100 mL) of 1,4-butyne diol. The temperature and current density were the same as above. When adding 0.01 g/100 mL of 1,4-butyne diol into electrolyte, 3D porous structure was obviously seen in Figures 3(a) and 3(d). Figure 4 showed that the porosity decreased with the concentration of 1,4-butyne diol increasing (from 0.01 g/100 mL to 0.05 g/100 mL). Meanwhile, the variation tendency of porosity in Figure 4 was similar to that affected by PEG 10000 as well. However, new complex structure similar to the leaves emerged on the PN film surface with increasing concentration. Meanwhile, hole wall became thicker and sedimentary layer of dendrite coarsened. The smaller aperture was associated with the fast release rate of hydrogen bubble, resulting in an acceleration of reduction of Ni^{2+} speed-up, which also explained why dendrite of the coating coarsened. However, network structure of 3D-PN film will disappear (Figures 3(c) and 3(f)) when the concentration of additive 1,4-butyne diol increases to a certain extent. Therefore, 1,4-butyne diol could be also the optional additive to obtain the 3D-PN film with high surface area and appropriate porosity.

3.3. Synergy Effect of PEG 10000 and 1,4-Butyne diol. Top-view SEM images of the synergy effect of 1,4-butyne diol and

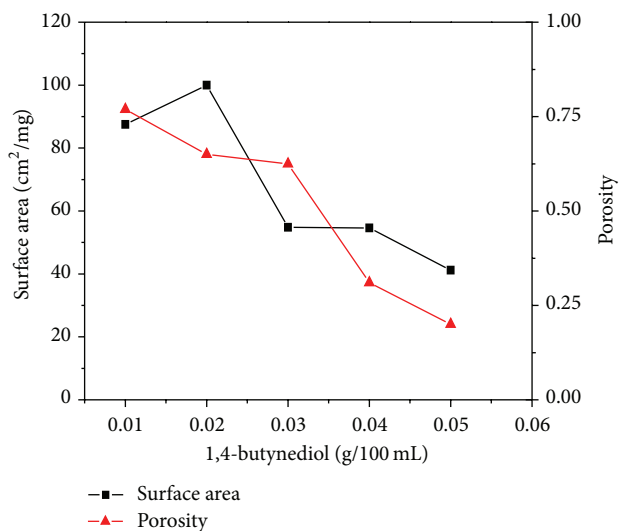


FIGURE 4: Effect of 1,4-butyne diol on surface area and porosity of PN film.

PEG 10000 on PN film were shown in Figure 5. The concentration of 1,4-butyne diol was controlled at 0.01 g/100 mL. With the concentration of PEG 10000 continuing to increase (from 0.01 to 0.05 g/100 mL), the hole wall of as-prepared PN film became thicker and dendrites of deposits coarsened, which was similar to the complex structure of the leaves. If the concentration of PEG 10000 was larger than 0.05 g/100 mL, a mesh and irregular structure came into being in PN film, which was largely because of some inhibitory effect of PEG 10000 on reduction reaction of nickel ions and hydrogen ions. It can be obviously seen from Figures 5(b)–5(f) that

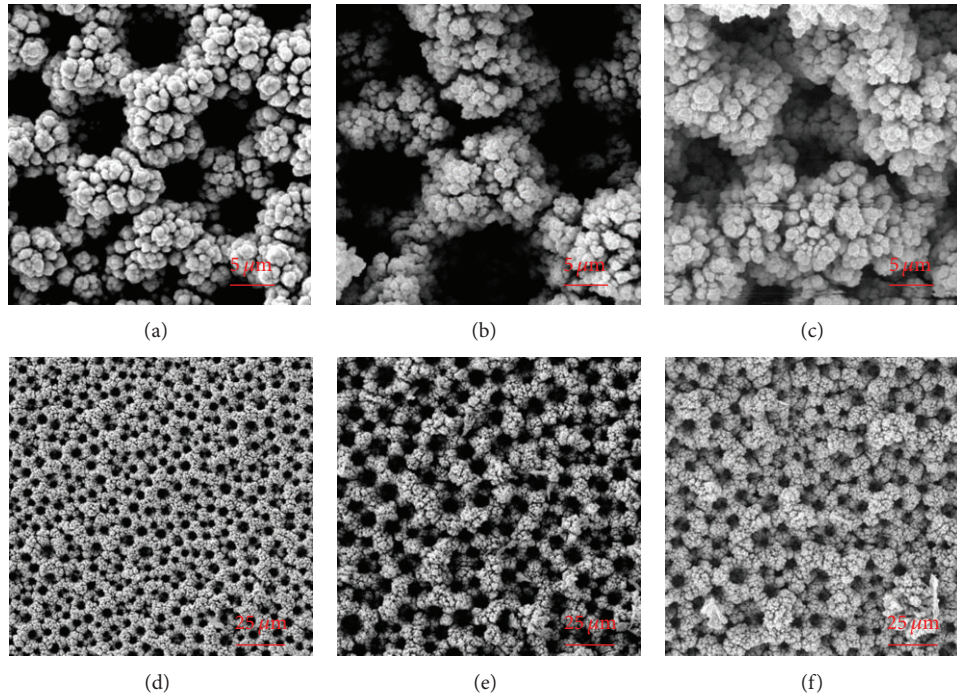


FIGURE 5: Top-view SEM images of the synergy effect of 1,4-butyne diol and PEG 10000 on PN film. The concentration ratio of PEG 10000 to 1,4-butyne diol is 1:1 (a, d), 3:1 (b, e), and 5:1 (c, f), respectively. And the concentration of 1,4-butyne diol is 0.01 g/100 mL (0.01 gram of surfactant is added into 100 mL of electrolyte).

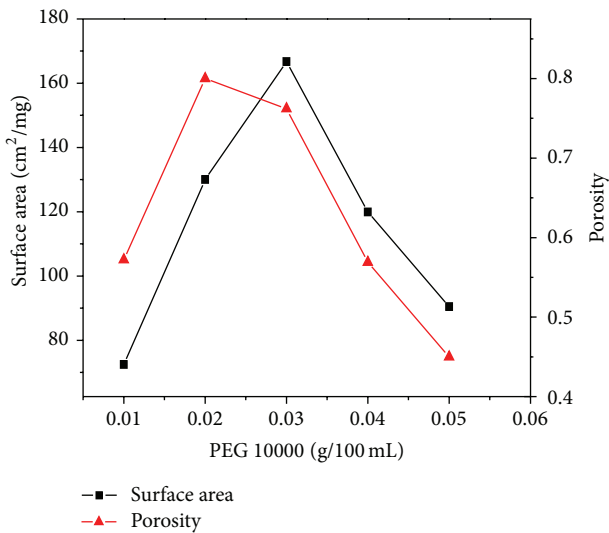
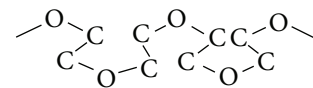


FIGURE 6: Effect of 1,4-butyne diol and PEG 10000 simultaneously on PN film, and the concentration of 1,4-butyne diol is controlled at 0.01 g/100 mL.

the aperture can increase to 12 microns (then decrease) and relatively homogeneous distribution. On the other hand, A_s at level 3 reached a maximum of 140.8 mg/cm^2 with sharp decline and 3D structure will be gone by continuously adding the 1,4-butyne diol. The 3D-PN film with a maximum of A_s ($166.7 \text{ cm}^2/\text{mg} > 140.8 \text{ cm}^2/\text{mg}$) and porosity (0.762) was

obtained when the concentration of PEG 10000 and 1,4-butyne diol was 0.03 g/100 mL and 0.01 g/100 mL (Figure 6). As mentioned, tracing changes of concentration of PEG 10000 or 1,4-butyne diol could adjust and control porous structure of nickel film. And similar study about 3D porous structure with the additive was reported by Huang et al. [31]. Moreover, the more ideal 3D-PN film was fabricated by HBDT with the additive combination of PEG 10000 and 1,4-butyne diol added into electrolyte. In this paper, the additive PEG 10000 with certain adsorption of metal cations [32] and good hydrophilicity because of hydrogen bond can decrease interfacial tension between the hydrogen bubble and the cathode plate (Scheme 1) and directionally align in the form of meandering structure



in the solution. And as a kind of gemini surfactant, the 1,4-butyne diol with ideal solution interface adsorption capacity could depress rapid accumulation of hydrogen bubble (Scheme 1) and bubble size increase and largely promote the migration rate of the hydrogen bubble from cathode plate to the solution interface. Meanwhile, the additives PEG 10000 and 1,4-butyne diol with a certain concentration ratio (PEG 10000: 1,4-butyne diol = 3:1) appeared to have optimal activity to regulate the surface photography of 3D-PN film instead of mixing them together randomly. Bernardes et al. [33] observed that a cosurfactant such as decanol can induce

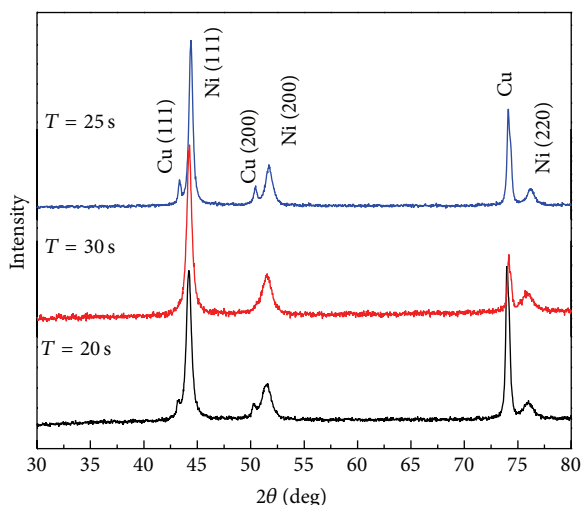
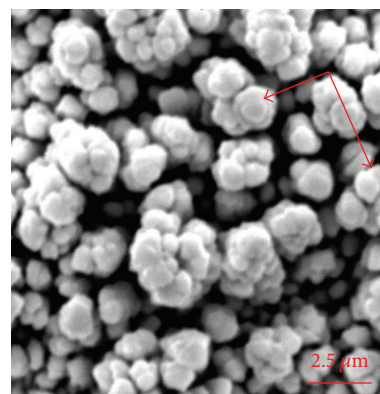


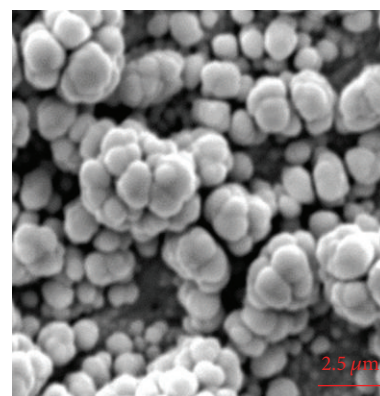
FIGURE 7: Typical XRD spectra of the PN film at different deposition times in optimized plating solution with additives (the concentration of nickel sulfate, ammonium chloride, concentrated sulfuric acid and boric acid, PEG 10000, 1,4-butyne diol, cathode current density, and deposition time are 0.2 mol/L, 1.5 mol/L, 0.9 mL/100 mL, 1.2 mol/L, 0.3 g/100 mL 0.1 g/100 mL, 4.0 A/cm², and 25 s, resp.).

a lamellar structure. Polymer surfactant could effectively block mutual adsorption among particles, mainly relying on the solvation layer of polymer. It was worth mentioning that there was no reaction between PEG 10000 and 1,4-butyne diol. Meanwhile, when the additives (PEG 10000 and 1,4-butyne diol) influenced the structure of PN film simultaneously, the final effect was better than the simple individual effect, which was the key reason why the 3D structure of PN film was optimized by changing their concentrations at different levels. Therefore, the reticular 3D structure of PN film was prepared by HBDT method by controlling the concentration of the novel additive combination (Table 2).

This result was further supported by XRD spectrum. As shown in Figure 7, all of the diffraction peaks were indexed at different temperatures. The characteristics of the face-centered cubic (fcc) nickel crystal structure was evident as indicated by the orientations along the Ni (111), Ni (200), and Ni (220) directions. It was obvious that the feature peak of the copper in the X-ray diffraction pattern was caused by the copper substrate, and both the crystalline and the intensity ratios of nickel can vary with temperature. These results indicated that dendritic nickel is abundant in {111} facets. It has been known that more facets with a slower growth rate would be exposed on the crystal surface and consequently exhibit relatively stronger diffraction intensity in the corresponding XRD pattern [34]. The intensity ratio between the (111) and (200) diffraction peaks was higher than the ratio of other peaks, especially at 25°C. These strong and sharp peaks indicated that the obtained Ni crystals were highly crystalline. No detectable diffraction peaks of impurities such as copper oxide or nickel oxide signified the high purity and stability of the as-obtained products.



(a)



(b)

FIGURE 8: Top-view SEM images of before and after adsorption of heavy metal ions. (a) Adsorption of zinc; (b) porous nickel without zinc.

3.4. Adsorption Behavior of PN Film for Simulated Wastewater (Zn^{2+}). The PN film with high specific surface area prepared under optimal conditions exhibited certain advantages in sewage purification. Figure 8 showed surface morphology of before and after adsorption of heavy metal ions (Zn^{2+}). Compared with Figure 8(b), rough and glistening areas in the direction of arrows in Figure 8(a) were confirmed as the adsorbed Zn^{2+} . At the same time, the reliability of the zinc absorption was further demonstrated by AAS. Time-variation tendencies of Q_t and Q (%) of adsorption process of Zn^{2+} were clearly shown in Figures 9 and 10. Meanwhile, Figure 10 presented the concentration changes of Zn^{2+} during the adsorption process. The purification effect was continuously improved with the increase of time, especially in the first dozens of seconds. As time increased, the concentration of Zn^{2+} had reached equilibrium value. Meanwhile, Q_t gradually increased until maximum value (Q_e) of 9.145 mg/g for $Zn(NO_3)_2 \cdot 6H_2O$ concentrations over 5 mg/L and Q (%) 0.691, concentration of the purified sewage basically to tend stable limited to surface effective adsorption sites when the adsorption time continued to increase. The adsorption rate of PN with large specific surface area and porous structure of overlapping layers was more rapid than that of granular porous adsorbent in adsorbing heavy metal

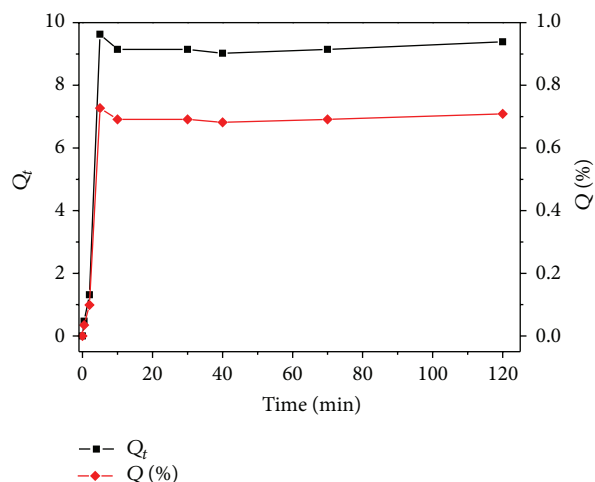


FIGURE 9: Effect of contact time on Q_t and Q (%) of adsorption process of zinc by PN. (conditions: volume 100 mL; temperature $25 \pm 1^\circ\text{C}$; stirring speed 120 r/min).

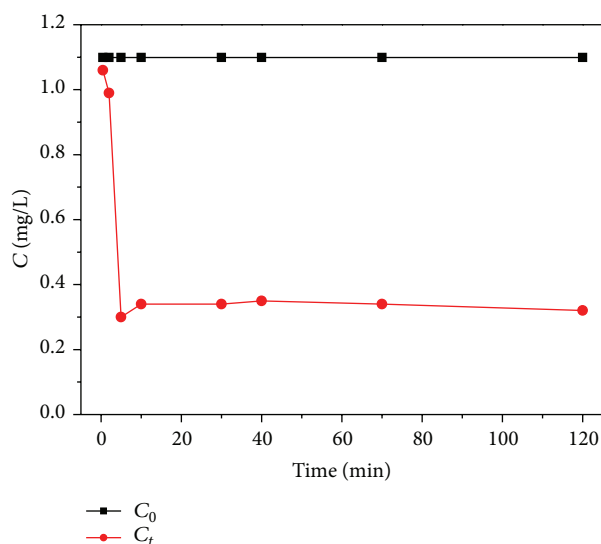


FIGURE 10: Concentration (C_t) changes of adsorption process of Zn^{2+} with time. (conditions: volume 100 mL; temperature $25 \pm 1^\circ\text{C}$; stirring speed 120 r/min).

ions, contributing to reaching adsorption equilibrium within a short time. It is needed to be emphasized that the time elapsed for the Zn^{2+} adsorption to reach its maximum was about 10 min for the PN and there was no nickel ions in the zinc nitrate solution after adsorption equilibrium detected by AAS.

4. Conclusions

The PN film with reticular 3D network structure has been successfully fabricated by HBDT, adding novel additive combination (PEG 10000 and 1,4-butyne diol) into the electrolyte. Meanwhile, the PN film with high specific surface area ($A_s =$

$166.7\text{ cm}^2/\text{mg}$) and high porosity (0.762) had open interconnected macroporous walls. The experiment conditions were optimized such that the concentration of nickel sulfate, ammonium chloride, concentrated sulfuric acid and boric acid, PEG 10000, 1,4-butyne diol, cathode current density, and deposition time were 0.2 mol/L, 1.5 mol/L, 0.9 mL/100 mL, 1.2 mol/L, 0.3 g/100 mL, 0.1 g/100 mL, 4.0 A/cm², and 25 s, respectively, which were determined by SEM microscopic image analysis and extensive explorations. Meanwhile, the sewage (Zn^{2+}) purification of 3D-PN was investigated in this study. Adsorption capacity (Q_e and Q (%)) of PN for Zn^{2+} can reach 9.145 mg/g and 0.691 for $\text{Zn}(\text{NO}_3)_2 \cdot 6\text{H}_2\text{O}$ concentrations over 5 mg/L, which provided the possibility of the novel application of 3D-PN or other porous metals.

Conflict of Interests

The authors declare that there is no conflict of interests regarding the publication of this paper.

Acknowledgments

This work was supported by the National Natural Science Foundation of China (no. 61271059), the Natural Science Foundation Project of Chongqing (no. 2010BB4246), and the Science and Technology Development Project of Chongqing (no. CSTC2012gg-yyjs90007).

References

- [1] P. A. Nelson and J. R. Owen, "A high-performance supercapacitor/battery hybrid incorporating templated mesoporous electrodes," *Journal of the Electrochemical Society*, vol. 150, no. 10, pp. A1313–A1317, 2003.
- [2] H.-C. Shin and M. Liu, "Copper foam structures with highly porous nanostructured walls," *Chemistry of Materials*, vol. 16, no. 25, pp. 5460–5464, 2004.
- [3] H.-C. Shin, J. Dong, and M. Liu, "Porous tin oxides prepared using an anodic oxidation process," *Advanced Materials*, vol. 16, no. 3, pp. 237–240, 2004.
- [4] H.-C. Shin, J. Dong, and M. Liu, "Nanoporous structures prepared by an electrochemical deposition process," *Advanced Materials*, vol. 15, no. 19, pp. 1610–1614, 2003.
- [5] K. Kusakabe, T. Kuroda, A. Murata, and S. Morooka, "Formation of a Y-type zeolite membrane on a porous α -alumina tube for gas separation," *Industrial and Engineering Chemistry Research*, vol. 36, no. 3, pp. 649–655, 1997.
- [6] A. Salehi and D. Jamshidi Kalantari, "Characteristics of highly sensitive Au/porous-GaAs Schottky junctions as selective CO and NO gas sensors," *Sensors and Actuators B: Chemical*, vol. 122, no. 1, pp. 69–74, 2007.
- [7] G. Zhang, C. Li, F. Cheng, and J. Chen, " ZnFe_2O_4 tubes: synthesis and application to gas sensors with high sensitivity and low-energy consumption," *Sensors and Actuators B: Chemical*, vol. 120, no. 2, pp. 403–410, 2007.
- [8] L. Wang, H. W. Xu, P. C. Chen, D. W. Zhang, C. X. Ding, and C. H. Chen, "Electrostatic spray deposition of porous Fe_2O_3 thin films as anode material with improved electrochemical performance for lithium-ion batteries," *Journal of Power Sources*, vol. 193, no. 2, pp. 846–850, 2009.

- [9] L. Yuan, Z. P. Guo, K. Konstantinov, H. K. Liu, and S. X. Dou, "Nano-structured spherical porous SnO₂ anodes for lithium-ion batteries," *Journal of Power Sources*, vol. 159, no. 1, pp. 345–348, 2006.
- [10] J.-Y. Li, S. Xiong, J. Pan, and Y. Qian, "Hydrothermal synthesis and electrochemical properties of urchin-like core-shell copper oxide nanostructures," *Journal of Physical Chemistry C*, vol. 114, no. 21, pp. 9645–9650, 2010.
- [11] N. Kanetake and M. Kobashi, "Innovative processing of porous and cellular materials by chemical reaction," *Scripta Materialia*, vol. 54, no. 4, pp. 521–525, 2006.
- [12] Y.-S. Hu, Y.-G. Guo, W. Sigle, S. Hore, P. Balaya, and J. Maier, "Electrochemical lithiation synthesis of nanoporous materials with superior catalytic and capacitive activity," *Nature Materials*, vol. 5, no. 9, pp. 713–717, 2006.
- [13] G. X. Pan, X. Xia, F. Cao, P. S. Tang, and H. F. Chen, "Porous Co(OH)₂/Ni composite nanoflake array for high performance supercapacitors," *Electrochimica Acta*, vol. 63, pp. 335–340, 2012.
- [14] Y. Guo, H. Yui, H. Minamikawa et al., "Dimension control of glycolipid nanotubes by successive use of vesicle extrusion and porous template," *Chemistry of Materials*, vol. 18, no. 6, pp. 1577–1580, 2006.
- [15] I. Kazeminezhad, A. C. Barnes, J. D. Holbrey, K. R. Seddon, and W. Schwarbacher, "Templated electrodeposition of silver nanowires in a nanoporous polycarbonate membrane from a nonaqueous ionic liquid electrolyte," *Applied Physics A: Materials Science and Processing*, vol. 86, no. 3, pp. 373–375, 2007.
- [16] J. H. Yuan, F. Y. He, D. C. Sun, and X. H. Xia, "A simple method for preparation of through-hole porous anodic alumina membrane," *Chemistry of Materials*, vol. 16, no. 10, pp. 1841–1844, 2004.
- [17] W. Chen, J.-H. Yuan, and X.-H. Xia, "Characterization and manipulation of the electroosmotic flow in porous anodic alumina membranes," *Analytical Chemistry*, vol. 77, no. 24, pp. 8102–8108, 2005.
- [18] F. C. Meldrum and R. Seshadri, "Porous gold structures through templating by echinoid skeletal plates," *Chemical Communications*, no. 1, pp. 29–30, 2000.
- [19] D. D. Krassimir, D. S. Valkovska, and P. A. Kralchevsky, "Hydrodynamic instability and coalescence in trains of emulsion drops or gas bubbles moving through a narrow capillary," *Journal of Colloid and Interface Science*, vol. 267, no. 1, pp. 243–258, 2003.
- [20] R. Šimpraga, G. Tremiliosi-Filho, S. Y. Qian, and B. E. Conway, "In situ determination of the "real area factor" in H₂ evolution electrocatalysis at porous Ni-Fe composite electrodes," *Journal of Electroanalytical Chemistry*, vol. 424, no. 1-2, pp. 141–151, 1997.
- [21] S. Rausch and H. Wendt, "Morphology and utilization of smooth hydrogen-evolving raney nickel cathode coatings and porous sintered-nickel cathodes," *Journal of the Electrochemical Society*, vol. 143, no. 9, pp. 2852–2862, 1996.
- [22] I. J. Brown and S. Sotiropoulos, "Electrodeposition of Ni from a high internal phase emulsion (HIPE) template," *Electrochimica Acta*, vol. 46, no. 17, pp. 2711–2720, 2001.
- [23] Y. F. Yuan, X. H. Xia, J. B. Wu, J. L. Yang, Y. B. Chen, and S. Y. Guo, "Nickel foam-supported porous Ni(OH)₂/NiOOH composite film as advanced pseudocapacitor material," *Electrochimica Acta*, vol. 56, no. 6, pp. 2627–2632, 2011.
- [24] W. S. W. Ngah and M. A. K. M. Hanafiah, "Biosorption of copper ions from dilute aqueous solutions on base treated rubber (*Hevea brasiliensis*) leaves powder: kinetics, isotherm, and biosorption mechanisms," *Journal of Environmental Sciences*, vol. 20, no. 10, pp. 1168–1176, 2008.
- [25] N. Zhang, H. Qiu, Y. Si, W. Wang, and J. Gao, "Fabrication of highly porous biodegradable monoliths strengthened by graphene oxide and their adsorption of metal ions," *Carbon*, vol. 49, no. 3, pp. 827–837, 2011.
- [26] S. Babel and T. A. Kurniawan, "Low-cost adsorbents for heavy metals uptake from contaminated water: a review," *Journal of Hazardous Materials*, vol. 97, no. 1–3, pp. 219–243, 2003.
- [27] L. Wang and R.-H. Yoon, "Role of hydrophobic force in the thinning of foam films containing a nonionic surfactant," *Colloids and Surfaces A: Physicochemical and Engineering Aspects*, vol. 282–283, pp. 84–91, 2006.
- [28] F. Melo and J. S. Laskowski, "Fundamental properties of flotation frothers and their effect on flotation," *Minerals Engineering*, vol. 19, no. 6-8, pp. 766–773, 2006.
- [29] X. S. Dong, J. Q. Jiang, and T. Tian, "Effect of process parameters on specific surface area of porous nickel film obtained by electrodeposition with hydrogen bubbles as template," *Electroplating & Finishing*, vol. 30, no. 2, pp. 1–3, 2011.
- [30] I. S. I. Adam and A. N. Anthemidis, "Flow injection wetting-film extraction system for flame atomic absorption spectrometric determination of cadmium in environmental waters," *Talanta*, vol. 77, no. 3, pp. 1160–1164, 2009.
- [31] L. Huang, H.-B. Wei, F.-S. Ke, X.-Y. Fan, J.-T. Li, and S.-G. Sun, "Electrodeposition and lithium storage performance of three-dimensional porous reticular Sn-Ni alloy electrodes," *Electrochimica Acta*, vol. 54, no. 10, pp. 2693–2698, 2009.
- [32] H. J. Sun, H. B. Jiang, S. H. Li et al., "Effect of alcohols as additives on the performance of a nano-sized Ru-Zn(2.8%) catalyst for selective hydrogenation of benzene to cyclohexene," *Chemical Engineering Journal*, vol. 218, pp. 415–424, 2003.
- [33] J. S. Bernardes, J. Norrman, L. Piculell, and W. Loh, "Complex polyion-surfactant ion salts in equilibrium with water: changing aggregate shape and size by adding oil," *Journal of Physical Chemistry B*, vol. 110, no. 46, pp. 23433–23442, 2006.
- [34] Y. Xiong and Y. Xia, "Shape-controlled synthesis of metal nanostructures: the case of palladium," *Advanced Materials*, vol. 19, no. 20, pp. 3385–3391, 2007.

Research Article

Tuning the Morphological Structure and Photocatalytic Activity of Nitrogen-Doped $(\text{BiO})_2\text{CO}_3$ by the Hydrothermal Temperature

Chongjun Wang,¹ Zaiwang Zhao,¹ Bin Luo,¹ Min Fu,^{1,2} and Fan Dong^{1,2}

¹ Chongqing Key Laboratory of Catalysis and Functional Organic Molecules, College of Environmental and Biological Engineering, Chongqing Technology and Business University, Chongqing 400067, China

² Chongqing Key Laboratory for Urban Atmospheric Environment Integrated Observation & Pollution Prevention and Control, Environmental Monitoring Center of Chongqing, Chongqing 401147, China

Correspondence should be addressed to Min Fu; fumin1022@126.com

Received 21 November 2013; Accepted 2 January 2014; Published 13 February 2014

Academic Editor: Haiqiang Wang

Copyright © 2014 Chongjun Wang et al. This is an open access article distributed under the Creative Commons Attribution License, which permits unrestricted use, distribution, and reproduction in any medium, provided the original work is properly cited.

Various nitrogen-doped hierarchical $(\text{BiO})_2\text{CO}_3$ nanosheets architectures were synthesized by a facile one-step template-free hydrothermal method through controlling the hydrothermal temperature (HT). The as-synthesized samples were characterized by XRD, SEM, FT-IR, XPS, and UV-vis DRS. The photocatalytic activity of the samples was evaluated towards degradation of NO at ppb level in air under visible light (VIL). It was found that HT acted as a crucial factor in determining the morphology of the samples. The rosa chinensis-like, red camellia-like, and lamina-like of nitrogen-doped $(\text{BiO})_2\text{CO}_3$ (N-BOC) micro-/nanostructures can be selectively fabricated under hydrothermal temperatures of 150, 180, and 210°C. The thickness of the nanosheets was in direct proportion to the increasing HT. Nitrogen-doping can extend the light absorption spectra of $(\text{BiO})_2\text{CO}_3$ to visible light region and enhance the VIL photocatalytic activity. Especially, the red camellia-like N-BOC-180 exhibited the highest photocatalytic performance, superior to the well-known VIL-driven photocatalyst C-doped TiO_2 and N-doped TiO_2 . The high photocatalytic performance of N-BOC was attributed to the synergetic effects of enhanced visible light absorption, multiple light-reflections between the nanosheets, and accelerated transfer of reactants and product. This research could provide new insights to the development of excellent photocatalyst with efficient performance for pollution control.

1. Introduction

Over the past decades, photocatalysis technology has attracted tremendous attention due to its great potential in solving energy and environmental problems [1]. Generally, photocatalysts were semiconductor materials, among which, TiO_2 bears tremendous hope in helping ease the energy crisis and environment pollution [2, 3]. However, the shortage of demanding UV light in the solar energy severely impedes the scale-up application of TiO_2 [4–6]. Therefore, it is imperative to explore novel photocatalyst with enhanced visible light (VIL) absorption. Generally, two strategies were applied to develop visible-light-driven photocatalysts. One is chemical modification on the UV-driven photocatalysts, such as TiO_2 , willing to narrow the band gap [7]. The other is to fabricate

new types of semiconductor with narrow band gap working directly under visible light [8].

Bismuth compounds, such as BiVO_4 , Bi_2MoO_6 , Bi_2WO_6 , and BiOX ($X = \text{Cl}, \text{Br}, \text{I}$), have received considerable attention due to their high visible light photocatalytic activity [9–13]. A typical “Sillén” phase was reported by Grice’s group [14]. $(\text{BiO})_2\text{CO}_3$ belongs to the Aurivillius-related oxide family and owns an intergrowth of $\text{Bi}_2\text{O}_2^{2+}$ layers and CO_3^{2-} layers, with the plane of the CO_3^{2-} group orthogonal to the plane of the $\text{Bi}_2\text{O}_2^{2+}$ layer. Although bismuth subcarbonate $(\text{BiO})_2\text{CO}_3$ was first used for medical and healthcare application, it also joined the photocatalyst family because of its semiconductor properties. For example, Zheng et al. reported the photocatalytic activity of the $(\text{BiO})_2\text{CO}_3$, and discovered that samples with {001} plane exposed demonstrate the best

photocatalytic activities [15]. Liu et al. obtained $(\text{BiO})_2\text{CO}_3$ nanoflowers at relatively low temperature of 60°C , exhibiting high photocatalytic efficiency towards the degradation of wastewater dyes under UV-vis light irradiation [16]. Chen et al. synthesized $(\text{BiO})_2\text{CO}_3$ with different morphology which exhibited enhanced antibacterial properties [17]. Zhou et al. prepared nanostructured $\text{Bi}_2\text{O}_2\text{CO}_3$ by an environmentally friendly method and applied the material in humidity sensing [18]. Besides, photocatalysts with microsphere structure demonstrated fascinating photocatalytic activity. For example, Zhao et al. fabricated hierarchical rose-like $(\text{BiO})_2\text{CO}_3$ microspheres with superior photocatalytic property under sunlight [19]. Dong et al. prepared rose-like monodisperse bismuth subcarbonate hollow microspheres through one-pot template-free method, accompanied with high NO degradation under modulated solar light irradiation [20]. Also, Madhusudan et al. fabricated hierarchical $(\text{BiO})_2\text{CO}_3$ microstructures with decent photocatalytic activities in degradation of organic dyes under visible light [21]. Recently, Dong et al. have prepared uniform $(\text{BiO})_2\text{CO}_3$ hierarchical hollow microspheres with outstanding photocatalytic activities under both UV and visible light [22]. The formation of hollow hierarchical inorganic micro- and nanostructures can be ascribed to the synergetic effects of the well-known physical phenomena, such as, Ostwald ripening [23], Kirkendall-effect, and oriented attachment [24, 25]. Furthermore, the enhanced photocatalytic activity of flower-like microsphere nanostructures can be ascribed to the strengthened light absorption due to the multiple reflections between the nanosheets and hierarchical microstructures which is beneficial to improve light-harvesting efficiency [26].

Hierarchical hollow structured materials were usually synthesized based on templating approaches, which contain hard templates and soft templates [27–35]. Template synthesis usually suffers from tedious processes, including template modification, precursor attachment, and core removal [36, 37], which may lead to a cumbersome process and reluctant overexpenditure, limiting the potential applications. Hence, development of facile template-free methods for obtaining inorganic hierarchical architectures is highly desirable. Facile template-free methods could obviously simplify the fabrication process, cut down the production expenditure, and promote large-scale applications of hierarchical materials.

Following a breakthrough that Asahi et al. firstly discovered that nitrogen doping can promote the VIL photocatalytic activity of TiO_2 by reducing the band gap of TiO_2 , various types of nonmetal-doped TiO_2 have been explored [38, 39]. Among them, N-doped TiO_2 is the most representative and has been on the focus of intensive investigation [39]. Although nitrogen doping is still under dispute, the concept of nitrogen doping has been successfully applied to narrow the band gap of various types of photocatalyst, such as Bi_3NbO_7 , SrTiO_3 , and $\text{Sr}_2\text{Ta}_2\text{O}_7$ [40–42]. Inspired by the convenient scale-up N-doping processes to gain favourable VIL activity, it is potentially feasible to apply this strategy to $(\text{BiO})_2\text{CO}_3$ with large band gap, aiming to narrow the band gap of $(\text{BiO})_2\text{CO}_3$. Recently, Dong et al. have synthesized N-doping of $(\text{BiO})_2\text{CO}_3$ (N-BOC) hierarchical microspheres

self-assembled with nanoplates using bismuth citrate and ammonia as precursors [43, 44]. It was found that the content of ammonia and the hydrothermal temperature imparted significant effects on the microstructure and activity of N-BOC [43, 44]. Though some advances have been made on the fabrication of N-BOC nanostructured materials, current knowledge about physical chemical properties and formation mechanisms on N-BOC architectures is still limited. It is necessary to explore and systematically unravel the influence factors that determine the potential growth pattern, physical chemical properties and, photocatalytic activity of the samples.

Herein, we implement a temperature-dependent research to explore the influence of hydrothermal temperature (HT) on morphology and photocatalytic activity of N-BOC micro/nanostructures. We synthesized novel N-BOC materials via a template-free hydrothermal method based on aqueous solution of bismuth citrate and concentrated ammonia with HT changing from 150 , 180 to 210°C , respectively. As a result, diverse morphology of N-BOC microstructures can be selectively fabricated upon different HT. Besides, HT plays a crucial role in determining the photocatalytic activity of N-BOC. Furthermore, it is worthy to note that N-BOC-180 exhibited enhanced photocatalytic activity compared with samples proceeded in 150°C and 210°C , exceeding that of other typical VIL photocatalysts C-doped TiO_2 and N-doped TiO_2 .

2. Experimental

2.1. Fabrication of $(\text{BiO})_2\text{CO}_3$ Nano-/Microstructures. All chemicals were analytical grade (sigma Aldrich) and were used without further purification. In a typical fabrication, appropriate amounts of bismuth citrate (1.6 g) were dissolved in concentrated ammonia solution (28 wt%) of 7.6 mL. The acquired transparent solution was stirred for 5 min. Distilled water was added to the obtained solution to make the total volume of 75 mL. The mixture was transferred to an autoclave Teflon vessel of 100 mL and stirred for 30 min. The aqueous precursor suspension was then hydrothermally treated under different HT for 24 h. After the hydrothermal reaction, the solid product was collected by filtration, washed with distilled water and ethanol four times, and dried at 60°C to get the final N-doping of $(\text{BiO})_2\text{CO}_3$ without further disposal. Depending on the HT (150 , 180 , and 210°C), N-doped $(\text{BiO})_2\text{CO}_3$ with different morphologies can be fabricated and labeled as N-BOC-150, N-BOC-180, and N-BOC-210, respectively. Comparing to the photocatalytic activity, N-doped TiO_2 and C-doped TiO_2 were used as reference samples [45, 46].

2.2. Characterization. The crystal phase was analyzed by X-ray diffraction with $\text{Cu K}\alpha$ radiation (XRD: model D/max RA, Japan). The morphology was characterized by scanning electron microscope (SEM, JEOL model JSM-6490, Japan). The UV-vis diffuse reflection spectra were obtained using a Scan UV-vis spectrophotometer (UV-vis DRS: UV-2450, shimadzu, Japan) equipped with an integrating sphere assembly, using BaSO_4 as reflectance sample. FT-IR spectra were recorded on a Nicolet Nexus spectrometer on samples

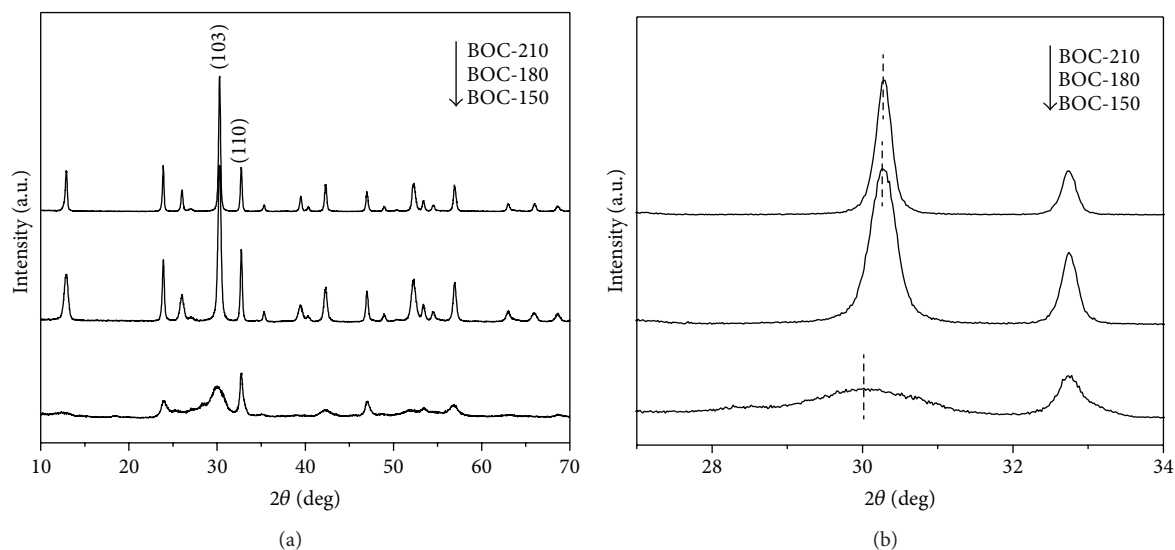


FIGURE 1: XRD patterns of N-BOC-150, N-BOC-180, and N-BOC-210 samples (a) and enlarged view of (103) and (110) diffraction region (b).

embedded in KBr pellets. X-ray photoelectron spectroscopy with Al K α X-rays ($h\nu = 1486.6$ eV) radiation operated at 150 W (XPS: Thermo ESCALAB 250, USA) was used to investigate the surface properties. Nitrogen adsorption-desorption was conducted on a nitrogen adsorption apparatus (ASAP 2020, USA) to determine the specific surface areas. All the samples were degassed at 150°C prior to measurements.

2.3. Evaluation of Photocatalytic Activity. The photocatalytic activity was investigated by removal of NO at ppb levels in a continuous flow reactor at ambient temperature. The volume of the rectangular reactor, which was made of polymethyl methacrylate plastics and covered with Saint-Glass, was 4.5 L (30 cm \times 15 cm \times 10 cm). A 100 W commercial tungsten halogen lamp (General Electric) was vertically placed outside the reactor above the reactor. Four minifans were used to cool the flow system. Adequate distance was also kept from the slamp to the reactor for the same purpose to keep the temperature at a constant level. For the visible light photocatalytic activity test experiment, UV cutoff filter (420 nm) was adopted to remove UV light in the light beam. For each photocatalytic activity test, two sample dishes (with a diameter of 12.0 cm) containing 0.1 g of photocatalyst powder were placed in the center of reactor. The photocatalyst samples were prepared by coating aqueous suspension of the samples onto the glass dishes. The coated dish was pretreated at 70°C to remove water in the suspension and then cooled to room temperature before photocatalytic test. The NO gas was acquired from a compressed gas cylinder at a concentration of 100 ppm of NO (N₂ balance, BOC gas) with traceable National Institute of Standards and Technology (NIST) standard. The initial concentration of NO was diluted to about 630 ppb by the air stream supplied by a zero air generator (Thermo Environmental Inc., model 111). The desired relative humidity (RH) level of the NO flow was controlled at 70% by passing the zero air streams through a humidification chamber.

The gas streams were premixed completely by a gas blender, and the flow rate was controlled at 2.4 L min⁻¹ by a mass flow controller. After the adsorption-desorption equilibrium was achieved, the lamp was turned on. The concentration of NO was continuously measured by a chemiluminescence NO analyzer (Thermo Environmental Instruments Inc., model 42c), which monitors NO, NO₂, and NO_x (NO_x represents NO + NO₂) with a sampling rate of 0.7 L min⁻¹. The removal ratio (η) of NO was calculated as

$$\eta (\%) = \left(1 - \frac{C}{C_0}\right) \times 100\%, \quad (1)$$

where C and C_0 are concentrations of NO in the outlet steam and the feeding stream, respectively.

3. Results and Discussion

3.1. Phase Structure. XRD was used to investigate the phase structure of the obtained powders. Figure 1(a) shows the XRD patterns of all as-prepared samples. All the diffraction peaks can be indexed to the tetragonal phase of (BiO)₂CO₃ compared with standard PDF card (JCPDS-ICDD Card No. 25-1464). The growth tendency of (110) peak always rises up gradually as HT increases from 150, 180 to 210°C, compared with that of (103) peak initially increases as HT increases from 150°C to 180°C but subsequently decreases as HT increases from 180°C to 210°C. The above results also suggest that HT has a significant effect on the crystallinity of all samples and the relative higher temperature benefits the preferred crystal growth along the (110) planes. Further observation in the enlarged view of XRD in Figure 1(b) indicates that the dominant (103) diffraction peak exhibits higher diffraction angles with HT increasing from 150, 180 to 210°C. These results implied that the distance between crystal planes slightly decreased under higher HT, demonstrating that the crystal structure tends to be more stable.

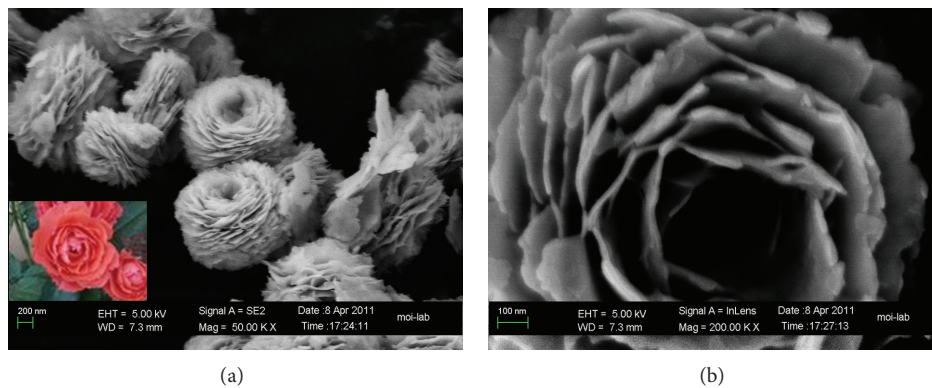


FIGURE 2: SEM images for N-BOC-150 ((a), (b)).

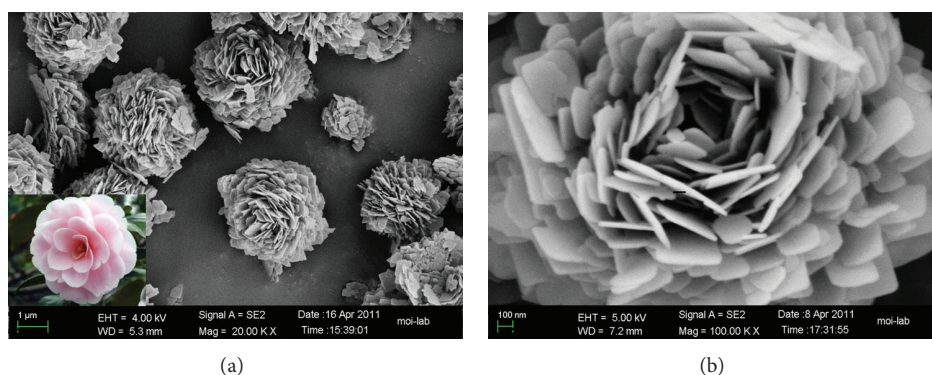


FIGURE 3: SEM images for N-BOC-180 ((a), (b)).

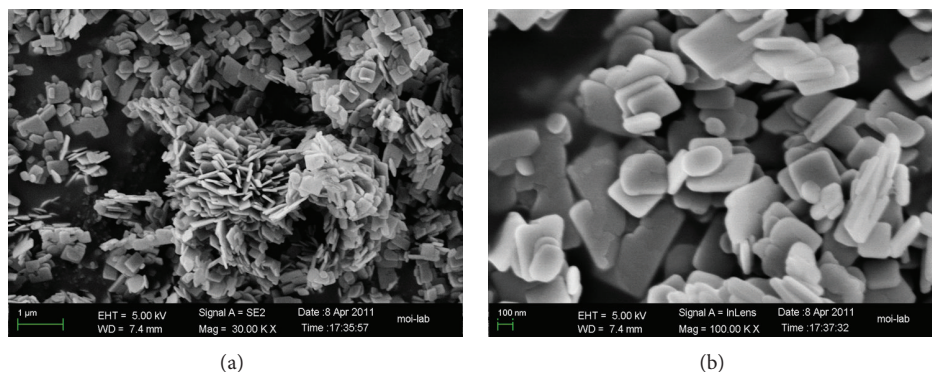


FIGURE 4: SEM images for N-BOC-210 ((a), (b)).

3.2. Morphological Evolution. Figures 2, 3, and 4 show typical SEM images of the as-prepared products, where large quantity of uniform $(\text{BiO})_2\text{CO}_3$ hierarchical microflowers composed of 2D nanosheets can be observed. No other morphologies could be found, which demonstrates the high yield of the hierarchical microstructures. The SEM images with higher magnification (Figures 2(b), 3(b), and 4(b)) give more detailed structural information of the microstructures, which are closely related to the photocatalytic activity.

For N-BOC-150 sample, a large number of *rosa chinensis*-like hierarchical microspheres, with a concavity in the center, were shown in the typical SEM images in Figure 2(a). The higher magnification SEM image (Figure 2(b)) reveals that these monodisperse *rosa chinensis*-like microspheres have average diameter of about $1.2 \mu\text{m}$ with a concavity in the center of about $0.5 \mu\text{m}$. The special nanostructures are self-assembled by many thin nanosheets in a hierarchical form. The nanosheets are arranged at progressively increasing angles to the radial axis and highly directed to form arrays in

TABLE 1: Morphology, average microsphere diameter, average concavity diameter, and nanosheets thickness of N-BOC-150, N-BOC-180, and N-BOC-210 samples.

Samples	Morphology	Average microsphere diameter (μm)	Average concavity diameter (μm)	Nanosheets thickness (nm)
N-BOC-150	Rosa chinensis-like	1.2	0.5	27
N-BOC-180	Red camellia-like	3.0	1.1	36
N-BOC-210	Lamina-like	—	—	47

a hierarchical fashion, which is advantageous for promoting the photocatalytic activity by enhancing the photo-energy harvesting and strengthening reactants transfer to the interior space.

For N-BOC-180 sample, the morphology of nitrogen-doped $(\text{BiO})_2\text{CO}_3$ is transformed into large numbers of red camellia-like hierarchical microspheres (Figure 3(a)). The average diameter of the microspheres is increased to about $3.0 \mu\text{m}$ and the average diameter of the concavity is increased to about $1.1 \mu\text{m}$ (Figure 3(b)). The red camellia-like microspheres are also organized by hierarchically self-assembled nanosheets. When the HT increases from 150 to 180°C , the thickness of the nanosheets is increased from 27 to 36 nm (Table 1). According to above observations, the as-prepared nitrogen-doping of $(\text{BiO})_2\text{CO}_3$ microstructures can be classified as hierarchical microflowers obtained through the oriented self-assembly of nanosheets. Although the nanosheets do not pack densely, the $(\text{BiO})_2\text{CO}_3$ microflowers cannot collapse into dispersed nanosheets, even after long-time ultrasonication.

For N-BOC-210 sample, the microstructure of nitrogen-doped $(\text{BiO})_2\text{CO}_3$ consists of large numbers of irregular aggregated lamina-like nanosheets (Figure 4(a)), which is obviously different from N-BOC-150 and N-BOC-180. The average thickness of the nanosheets is about 47 nm, which is further increased compared with that of others under HT of 150 and 180°C (Figure 4(b)). The SEM image with higher magnification (Figure 4(b)) shows that the obtained compound consists of plentiful different sizes of nanosheets with irregular shape.

The SEM images in Figure 2-4 imply that the HT plays a crucial role in forming various morphology of N-doped $(\text{BiO})_2\text{CO}_3$ nano/microstructures. As HT increases, thickness of the nanoplates augments correspondingly. At low temperatures of 150 and 180°C , the nanosheets could self-assemble to construct hierarchical microspheres. Nevertheless, the nanosheets could not be self-assembled as the HT increases to 210°C , due to the accelerating hydrothermal reaction and the increasing thickness, forming randomly and irregularly arranged lamina-like nanoplates. The S_{BET} values of as-prepared N-BOC obtained at 150, 180, and 210°C were 22, 21, and $13 \text{ m}^2/\text{g}$, respectively, which is consistent with microstructures of the samples (Table 2). Dong has revealed the effect of hydrothermal temperature on the morphological structure of N-BOC from bismuth citrate (1.6 g) and concentrated ammonia solution (1.9 mL). However, the present investigation increased the content of concentrated ammonia

TABLE 2: BET surface areas, reaction constants, and NO removal ratio of N-BOC-150, N-BOC-180, and N-BOC-210.

Samples	S_{BET} (m^2/g)	Reaction constants (k/min^{-1})	Removal ratio (%)
N-BOC-150	22	0.6570	24.7
N-BOC-180	21	1.2698	44.1
N-BOC-210	13	0.6022	23.6

solution to 7.8 mL and found that the hydrothermal temperature has different effects on the morphological structure. Especially when the temperature was increased to 210°C , the microspheres were destroyed (Figure 4(b)), which was different from the previous report [44].

3.3. Chemical Composition by FT-IR and XPS. The samples were further analyzed by FT-IR, as shown in Figure 5(a). The “free” CO_3^{2-} group (point group symmetry D_{3h}) had four internal vibrations, including 1067 cm^{-1} (symmetric stretching mode ν_1), 846 and 820 cm^{-1} (out of plane bending mode ν_2), 1468 and 1391 cm^{-1} (anti-symmetric vibration ν_3), and 670 cm^{-1} (in-plane deformation ν_4). Besides, vibration peaks of 1756 and 1730 cm^{-1} ($\nu_1 + \nu_4$) are observed for both samples [20]. Figure 5(a) also shows that the peak intensity associated with CO_3^{2-} group increases with HT increasing from 150, 180 to 210°C . The broad peak at $1500\text{--}1600 \text{ cm}^{-1}$ can be assigned to the characteristic stretching vibrations of hydroxyl groups, derived from the absorbed water molecule [20]. When the ammonia solution was not added during synthesis, the bismuth citrate would not be decomposed and CO_3^{2-} group would not be produced [47]. Hence, a potential conclusion may be postulated that bismuth citrate was first hydrolyzed by the ammonia, followed by decomposition of citrate ions to produce CO_3^{2-} ions during hydrothermal treatment.

The XPS measurements were applied to determine the chemical state of the doped nitrogen, as shown in Figure 5(b). The N1s peak centers at 400.4 eV , which indicates that nitrogen was in situ doped into the $(\text{BiO})_2\text{CO}_3$ structure during the hydrothermal reaction. The doped nitrogen atomic ratio of N-BOC-180 samples was measured to be 0.55%. The doped nitrogen must be derived from the ammonia solution added in the precursor solution. The ammonia acts as a dual role in the synthesis of N-doped $(\text{BiO})_2\text{CO}_3$. One is to hydrolyze

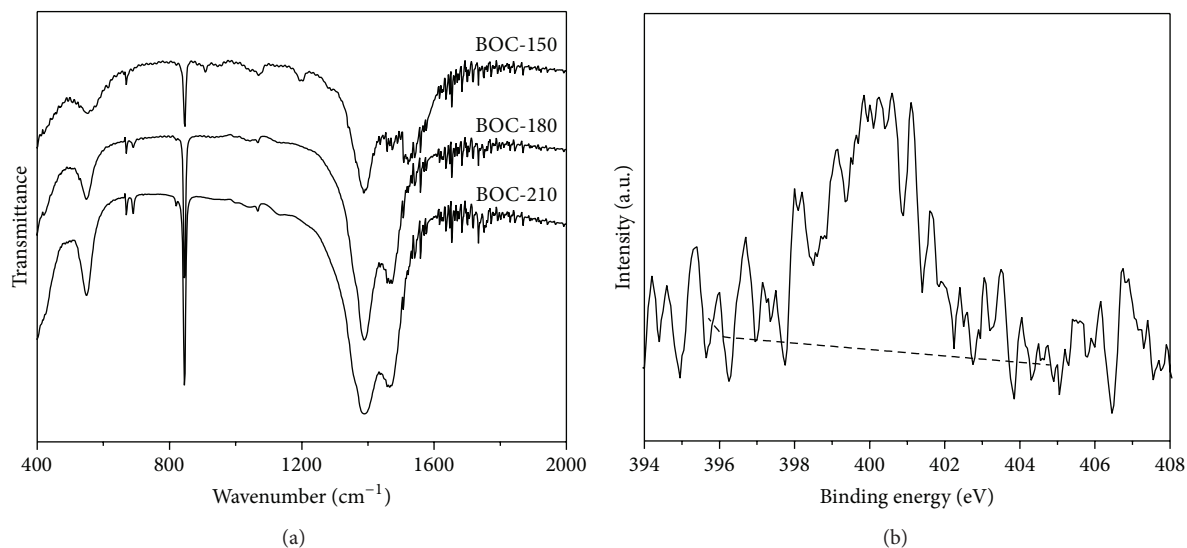


FIGURE 5: FT-IR spectra of N-BOC-150, N-BOC-180, and N-BOC-210 samples (a) and XPS spectra of N-BOC-180 for N1s (b).

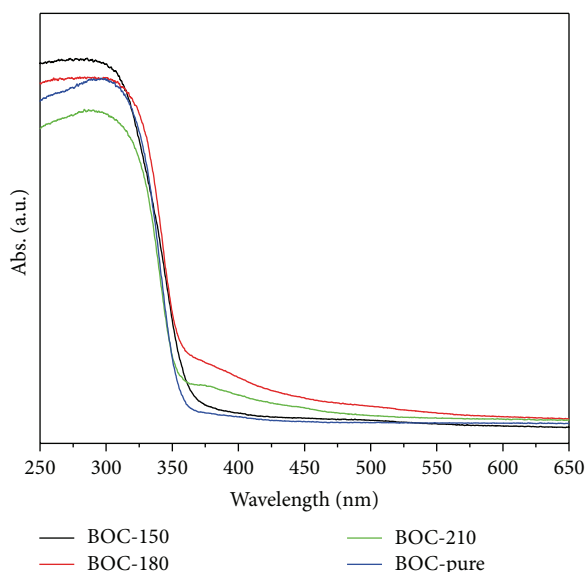


FIGURE 6: UV-vis DRS of BOC, N-BOC-150, N-BOC-180, and N-BOC-210 samples.

bismuth citrate and the other is to engage in nitrogen doping sources [48]. The N1s peaks approximately at 400.4 eV have been observed in the widely used N-doped TiO_2 , where nitrogen substituted for oxygen in TiO_2 and subsequently narrowed the band gap value due to the hybridization of N and O orbital in valence band [48, 49]. Under this mechanism, the doped nitrogen may also substitute for oxygen in $(\text{BiO})_2\text{CO}_3$ molecular, which could subsequently modify the band structure and enhance light absorption proficiency of $(\text{BiO})_2\text{CO}_3$ (Figure 6). Nevertheless, on account of the presence of two different kinds of oxygen atoms in $(\text{BiO})_2\text{CO}_3$ (Bi-O and C-O), current investigations are far from sufficient to reveal which oxygen atom is substituted significantly by

the doped nitrogen. Further theoretical investigation about potential mechanisms on this issue is underway.

3.4. UV-Vis DRS Analysis. The UV-vis DRS spectra of N-BOC-150, N-BOC-180, N-BOC-210, and the undoped $(\text{BiO})_2\text{CO}_3$ are shown in Figure 6. Utilizing VIL to stimulate photocatalytic reactions is a key challenge since lots of oxide photocatalysts mainly absorb UV light. Compared to undoped $(\text{BiO})_2\text{CO}_3$, the three nitrogen-doped $(\text{BiO})_2\text{CO}_3$ samples exhibit enhanced visible light absorption. Besides, the absorption edges shift from 330 nm to 350 nm. Furthermore, the as-prepared N-BOC-180 demonstrates the most intensity of VIL absorption, which could be the crucial factor for VIL photocatalytic activities. Combining with the XPS result, the doped nitrogen has made a vital effect on enhancing the VIL absorption. The changes of the absorption spectra were also suggested by the color variation of samples from white for undoped $(\text{BiO})_2\text{CO}_3$ to yellow for N-doped $(\text{BiO})_2\text{CO}_3$.

Meanwhile, the light absorption in the UV region indicates that the absorption intensity decreases as the HT increases from 150, 180 to 210 °C. Compared with N-BOC-210, the enhanced UV absorption of BOC-150 and BOC-180 can be attributed to the self-assembled hierarchical microstructure (Figures 2(a) and 3(c)). As conceivable illustration, the absorbed UV light can be multiply reflected between the interconnected nanosheets, subsequently enhancing the light absorption and utilization [25].

3.5. Photocatalytic Activity under Visible Light Irradiation. The photocatalytic performance of as-prepared N-doped $(\text{BiO})_2\text{CO}_3$ was further evaluated by removal of NO in a continuous gas phase reactor in order to demonstrate their potential ability for air purification using visible light (Figure 7). There are four reactions related to the photocatalytic reactivity, in which NO reacted with the

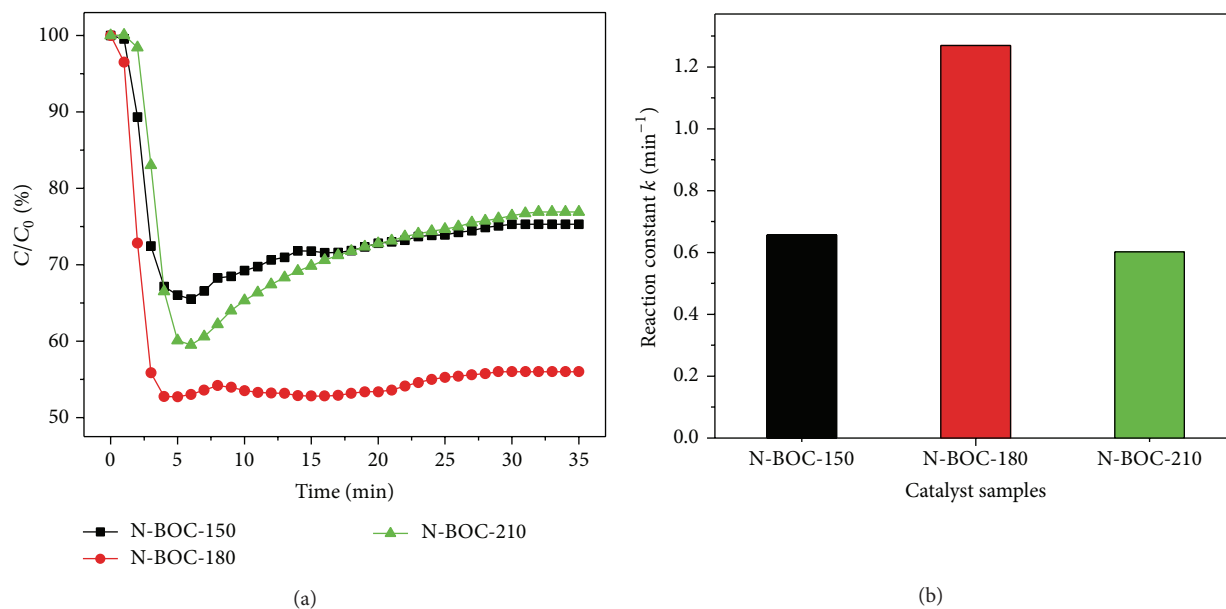


FIGURE 7: Photocatalytic activity of the as-prepared N-BOC-150, N-BOC-180, N-BOC-210 and undoped (BiO)₂CO₃ samples for removal of NO under visible light irradiation ($\lambda > 420$ nm) (a), and reaction rate constant at room temperature (b).

photo-generated reactive radicals and produced HNO₂ and HNO₃ displayed in (2)–(5) [50]:

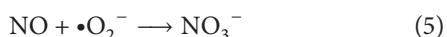
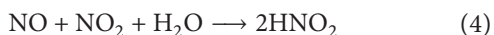
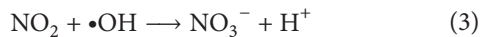
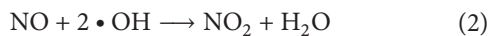


Figure 7(a) shows the variation of NO concentration (C/C_0 %) with irradiation time t over the samples under VIL irradiation ($\lambda > 420$ nm). Here, C_0 presents the initial concentration of NO, and C represents the instant concentration of NO during the photocatalytic reaction. NO could not be degraded without photocatalyst or without light irradiation. Under the irradiation of visible light and presence of photocatalyst, the as-prepared photocatalytic materials, NO reacts with the photo-generated reactive radicals to produce final NO_3^- product [51]. The undoped (BiO)₂CO₃ showed negligible VIL activity due to its UV absorption [44]. As shown in Figure 7(a), NO concentration decreases rapidly for all N-doped (BiO)₂CO₃ in the first 5 min. The initial reaction rate constants of N-BOC-150, N-BOC-180, and N-BOC-210 were 0.6570, 1.2698, and 0.6022 min⁻¹ (Table 2, Figure 7(b)), which were much higher than those of undoped (BiO)₂CO₃ [44]. The improved visible light photocatalytic activity may be ascribed to the nitrogen doping (Figures 2, 3, and 4) and hierarchical structures (Figures 2 and 3) compared with that of pure BOC [43, 44].

However, after about 6 min, the removal ratio of NO decreases slightly, which should be ascribed to the intermediates and final products, occupying the active sites of photocatalyst. After about 35 min irradiation, the removal

rates of N-BOC-180 (44.1%) are higher than those of N-BOC-150 (24.7%) and N-BOC-210 (23.6%) (Table 2). Besides, the NO removal ratio reaches about 20.3% over C-doped TiO₂, which is well known as a good VIL-driven photocatalyst [22]. Also, the N-doped TiO₂ demonstrated good VIL activities, by which the NO removal rates could reach to about 36% from well published articles [52]. Inspiringly, the as-prepared N-BOC-180 hierarchical microspheres exhibit superior photocatalytic activity with NO removal rates highly reaching up to 44.1% under VIL irradiation, much higher than that of C-doped TiO₂ and N-doped TiO₂.

Nevertheless, the S_{BET} of N-BOC-180 is much lower than that of C-doped TiO₂ (122.5 m²/g) (Table 2) [20], from which we can draw a conclusion that S_{BET} could not be the dominant factor for the outstanding photocatalytic activity of N-BOC-180. Furthermore, recent reports have demonstrated that the hierarchical and hollow structures have significant advantages in enhancing the photocatalytic activity. A novel 0020BiVO₄/Bi₂O₂CO₃ hierarchical micro/nanoarchitecture prepared by Madhusudan et al. exhibited wonderful photocatalytic performance due to the inhibition of electron/hole pair recombination [26]. The hollow NiO microspheres fabricated by Song and Gao have showed notably enhanced photocatalytic activity over NiO rods due to the increasing number of surface active sites and enhanced surface charge carrier transfer rate [53]. Thus, the conspicuously outstanding VIL photocatalytic activity of N-BOC-180 could mainly be ascribed to the special hierarchical and hollow structure. With nanoplates self-assembled hierarchical structure, multiple light reflections were extraordinarily strengthened between the interconnected nanosheets, thus enhancing light-harvesting and increasing the quantity of photogenerated electrons and holes available to participate in the photocatalytic redox reaction. Furthermore,

the extremely decent activity of N-BOC-180 samples is much higher than that of N-BOC-150. This result can be ascribed to the following potential factors. The larger surface areas (Table 1) and more smooth nanosheets (Figures 2(b) and 3(b)) can both successfully accelerate immediate transfer for intermediates and final products; in spite of that both of them have the same hierarchical morphology with a hollow in the center. Therefore, the remarkable photocatalytic activity may be dominated mainly by the synergy effects of the two factors mentioned above. The present work not only gains deeper understanding of temperature-dependent morphology-controlling mechanisms for N-BOC fabrication, but also paves the way for further modification of $(\text{BiO})_2\text{CO}_3$ with higher performance for environmental pollution control.

4. Conclusion

In summary, we have developed a one-pot template-free method to synthesize N-doped $(\text{BiO})_2\text{CO}_3$ hierarchical microspheres based on hydrothermal treatment of bismuth citrate and concentrated ammonia solution in water. N-BOC with different morphologies (rosa chinensis-like, red camellia-like and lamina-like nanostructures) was fabricated based on different HT ranging from 150, 180 to 210°C. The rosa chinensis-like N-BOC-150 and red camellia-like, N-BOC-180 was hierarchically self-assembled by nanosheets, while the lamina-like N-BOC-210 was randomly composed of abundant irregular nanosheets. The thickness of nanoplates was augmented with the increasing HT. Moreover, the as-prepared N-BOC-180 exhibited the highest photocatalytic activity, which was ascribed to the special hierarchical morphology and the enhanced visible light absorption. This work not only elucidates the mechanism of temperature-dependent morphology control on $(\text{BiO})_2\text{CO}_3$ fabrication, but also opens new avenue for the design of optimized photocatalysts with enhanced visible-light-driven activity.

Conflict of Interests

The authors declare that they do not have any conflict of interests.

Acknowledgments

This research is financially supported by the Science and Technology Project of CQ CSTC (stc2013yykfb50008, cstc2013jcyjA20018), the Science and Technology Project from Chongqing Education Commission (KJ120713, KJ130725), the Innovative Research Team Development Program in University of Chongqing (KJTD201314), and the key discipline development project of CTBU (1252001).

References

- [1] M. R. Hoffmann, S. T. Martin, W. Choi, and D. W. Bahnemann, "Environmental applications of semiconductor photocatalysis," *Chemical Reviews*, vol. 95, no. 1, pp. 69–96, 1995.
- [2] Y. Li, X. Fang, N. Koshizaki et al., "Periodic TiO_2 nanorod arrays with hexagonal nonclose-packed arrangements: excellent field emitters by parameter optimization," *Advanced Functional Materials*, vol. 19, no. 15, pp. 2467–2473, 2009.
- [3] Y. Li, T. Sasaki, Y. Shimizu, and N. Koshizaki, "A hierarchically ordered TiO_2 hemispherical particle array with hexagonal-non-close-packed tops: synthesis and stable superhydrophilicity without UV irradiation," *Small*, vol. 4, no. 12, pp. 2286–2291, 2008.
- [4] F. Dong, H. Q. Wang, S. Guo, Z. B. Wu, and S. C. Lee, "Enhanced visible light photocatalytic activity of novel Pt/C-doped $\text{TiO}_2/\text{PtCl}_4$ three-component nanojunction system for degradation of toluene in air," *Journal of Hazardous Materials*, vol. 187, no. 1–3, pp. 509–516, 2011.
- [5] F. Dong, Y. J. Sun, and M. Fu, "Enhanced visible light photocatalytic activity of V_2O_5 cluster modified N-doped TiO_2 for degradation of toluene in air," *International Journal of Photoenergy*, vol. 2012, Article ID 569716, 10 pages, 2012.
- [6] F. Dong, S. Guo, H. Q. Wang, X. F. Li, and Z. B. Wu, "Enhancement of the visible light photocatalytic activity of C-doped TiO_2 nanomaterials prepared by a green synthetic approach," *The Journal of Physical Chemistry C*, vol. 115, no. 27, pp. 13285–13292, 2011.
- [7] Z. F. Bian, J. Zhu, S. H. Wang, Y. Cao, X. F. Qian, and H. X. Li, "Self-assembly of active $\text{Bi}_2\text{O}_3/\text{TiO}_2$ visible photocatalyst with ordered mesoporous structure and highly crystallized anatase," *The Journal of Physical Chemistry C*, vol. 112, no. 16, pp. 6258–6262, 2008.
- [8] J. Tang, Z. Zou, and J. H. Ye, "Efficient photocatalytic decomposition of organic contaminants over CaBi_2O_4 under visible-light irradiation," *Angewandte Chemie—International Edition*, vol. 43, no. 34, pp. 4463–4466, 2004.
- [9] Z. Zhu, L. Zhang, J. Li, J. Du, Y. Zhang, and J. Zhou, "Synthesis and photocatalytic behavior of BiVO_4 with decahedral structure," *Ceramics International*, vol. 39, no. 7, pp. 7461–7465, 2013.
- [10] Z. Chen, L. W. Qian, J. Zhu, Y. P. Yuan, and X. F. Qian, "Controlled synthesis of hierarchical Bi_2WO_6 microspheres with improved visible-light-driven photocatalytic activity," *Cryso-EngComm*, vol. 12, no. 7, pp. 2100–2106, 2010.
- [11] Y. Q. Lei, G. H. Wang, S. Y. Song et al., "Room temperature, template-free synthesis of BiOI hierarchical structures: visible-light photocatalytic and electrochemical hydrogen storage properties," *Dalton Transactions*, vol. 39, no. 13, pp. 3273–3278, 2010.
- [12] X. Zhang, Z. H. Ai, F. L. Jia, and L. Z. Zhang, " BiOCl nano/microstructures on substrates: synthesis and photocatalytic properties," *The Journal of Physical Chemistry C*, vol. 112, no. 7, pp. 747–753, 2008.
- [13] T. Wu, X. G. Zhou, H. Zhang, and X. H. Zhong, " Bi_2S_3 nanostructures: a new photocatalyst," *Nano Research*, vol. 3, no. 5, pp. 379–386, 2010.
- [14] J. D. Grice, "A solution to the crystal structures of bismutite and beyerite," *Canadian Mineralogist*, vol. 40, no. 2, pp. 693–698, 2002.
- [15] Y. Zheng, F. Duan, M. Chen, and Y. Xie, "Synthetic $\text{Bi}_2\text{O}_2\text{CO}_3$ nanostructures: novel photocatalyst with controlled special surface exposed," *Journal of Molecular Catalysis A*, vol. 317, no. 1–2, pp. 34–40, 2010.
- [16] Y. Y. Liu, Z. Y. Wang, B. B. Huang et al., "Preparation, electronic structure, and photocatalytic properties of $\text{Bi}_2\text{O}_2\text{CO}_3$ nanosheet," *Applied Surface Science*, vol. 257, no. 1, pp. 172–175, 2010.

- [17] R. Chen, G. Cheng, M. H. So et al., "Bismuth subcarbonate nanoparticles fabricated by water-in-oil microemulsion-assisted hydrothermal process exhibit anti-Helicobacter pylori properties," *Materials Research Bulletin*, vol. 45, no. 5, pp. 654–658, 2010.
- [18] Y. Zhou, H. Wang, M. Sheng et al., "Environmentally friendly room temperature synthesis and humidity sensing applications of nanostructured $\text{Bi}_2\text{O}_2\text{CO}_3$," *Sensors and Actuators B*, vol. 188, no. 2013, pp. 1312–1318, 2013.
- [19] T. Zhao, J. T. Zai, M. Xu et al., "Hierarchical $\text{Bi}_2\text{O}_2\text{CO}_3$ microspheres with improved visible-light-driven photocatalytic activity," *CrystEngComm*, vol. 13, no. 12, pp. 4010–4017, 2011.
- [20] F. Dong, S. C. Lee, Z. Wu et al., "Rose-like monodisperse bismuth subcarbonate hierarchical hollow microspheres: one-pot template-free fabrication and excellent visible light photocatalytic activity and photochemical stability for NO removal in indoor air," *Journal of Hazardous Materials*, vol. 195, pp. 346–354, 2011.
- [21] P. Madhusudan, J. Zhang, B. Cheng, and G. Liu, "Photocatalytic degradation of organic dyes with hierarchical $\text{Bi}_2\text{O}_2\text{CO}_3$ microstructures under visible light," *CrystEngComm*, vol. 15, no. 2, pp. 231–240, 2013.
- [22] F. Dong, W.-K. Ho, S. C. Lee et al., "Template-free fabrication and growth mechanism of uniform $(\text{BiO}_2)_2\text{CO}_3$ hierarchical hollow microspheres with outstanding photocatalytic activities under both UV and visible light irradiation," *Journal of Materials Chemistry*, vol. 21, no. 33, pp. 12428–12436, 2011.
- [23] H. C. Zeng, "Ostwald ripening: a synthetic approach for hollow nanomaterials," *Current Nanoscience*, vol. 3, no. 2, pp. 177–181, 2007.
- [24] H. J. Fan, U. Gösele, and M. Zacharias, "Formation of nanotubes and hollow nanoparticles based on kirkendall and diffusion processes: a review," *Small*, vol. 3, no. 10, pp. 1660–1671, 2007.
- [25] J. Zhang, F. Huang, and Z. Lin, "Progress of nanocrystalline growth kinetics based on oriented attachment," *Nanoscale*, vol. 2, no. 1, pp. 18–34, 2010.
- [26] P. Madhusudan, J. Ran, J. Zhang, J. Yu, and G. Liu, "Novel urea assisted hydrothermal synthesis of hierarchical $\text{BiVO}_4/\text{Bi}_2\text{O}_2\text{CO}_3$ nanocomposites with enhanced visible-light photocatalytic activity," *Applied Catalysis B*, vol. 110, pp. 286–295, 2011.
- [27] M. Yang, J. Ma, C. L. Zhang, Z. Z. Yang, and Y. F. Lu, "General synthetic route toward functional hollow spheres with double-shelled structures," *Angewandte Chemie—International Edition*, vol. 117, no. 41, pp. 6885–6888, 2005.
- [28] J. G. Yu and X. X. Yu, "Hydrothermal synthesis and photocatalytic activity of zinc oxide hollow spheres," *Environmental Science and Technology*, vol. 42, no. 13, pp. 4902–4907, 2008.
- [29] S.-W. Kim, M. Kim, W. Y. Lee, and T. Hyeon, "Fabrication of hollow palladium spheres and their successful application to the recyclable heterogeneous catalyst for Suzuki coupling reactions," *Journal of the American Chemical Society*, vol. 124, no. 26, pp. 7642–7643, 2002.
- [30] J. H. Gao, B. Zhang, X. X. Zhang, and B. Xu, "Magnetic-dipolar-interaction-induced self-assembly affords wires of hollow nanocrystals of cobalt selenide," *Angewandte Chemie—International Edition*, vol. 45, no. 8, pp. 1220–1223, 2006.
- [31] A. D. Dinsmore, M. F. Hsu, M. G. Nikolaidis, M. Marquez, A. R. Bausch, and D. A. Weitz, "Colloidosomes: selectively permeable capsules composed of colloidal particles," *Science*, vol. 298, no. 5595, pp. 1006–1009, 2002.
- [32] Y. S. Li, J. L. Shi, Z. L. Hua, H. R. Chen, M. L. Ruan, and D. S. Yan, "Hollow spheres of mesoporous aluminosilicate with a three-dimensional pore network and extraordinarily high hydrothermal stability," *Nano Letters*, vol. 3, no. 5, pp. 609–612, 2003.
- [33] H. G. Yang and H. C. Zeng, "Creation of intestine-like interior space for metal-oxide nanostructures with a quasi-reverse emulsion," *Angewandte Chemie—International Edition*, vol. 43, no. 39, pp. 5206–5209, 2004.
- [34] D. H. M. Buchold and C. Feldmann, "Nanoscale $\gamma\text{-AlO}(\text{OH})$ hollow spheres: synthesis and container-type functionality," *Nano Letters*, vol. 7, no. 11, pp. 3489–3492, 2007.
- [35] J. Zhou, W. Wu, D. Caruntu et al., "Synthesis of porous magnetic hollow silica nanospheres for nanomedicine application," *The Journal of Physical Chemistry C*, vol. 111, no. 47, pp. 17473–17477, 2007.
- [36] M. R. Jones, K. D. Osberg, R. J. MacFarlane, M. R. Langille, and C. A. Mirkin, "Templated techniques for the synthesis and assembly of plasmonic nanostructures," *Chemical Reviews*, vol. 111, no. 6, pp. 3736–3827, 2011.
- [37] J. G. Yu and X. X. Yu, "Hydrothermal synthesis and photocatalytic activity of zinc oxide hollow spheres," *Environmental Science and Technology*, vol. 42, no. 13, pp. 4902–4907, 2008.
- [38] R. Asahi, T. Morikawa, T. Ohwaki, K. Aoki, and Y. Taga, "Visible-light photocatalysis in nitrogen-doped titanium oxides," *Science*, vol. 293, no. 5528, pp. 269–271, 2001.
- [39] A. Fujishima, X. T. Zhang, and D. A. Tryk, " TiO_2 photocatalysis and related surface phenomena," *Surface Science Reports*, vol. 63, no. 12, pp. 515–582, 2008.
- [40] J. Hou, R. Cao, Z. Wang, S. Jiao, and H. Zhu, "Hierarchical nitrogen doped bismuth niobate architectures: controllable synthesis and excellent photocatalytic activity," *Journal of Hazardous Materials*, vol. 217–218, pp. 177–186, 2012.
- [41] F. Zou, Z. Jiang, X. Qin et al., "Template-free synthesis of mesoporous N-doped SrTiO_3 perovskite with high visible-light-driven photocatalytic activity," *Chemical Communications*, vol. 48, no. 68, pp. 8514–8516, 2012.
- [42] A. Mukherji, B. Seger, G. Q. Lu, and L. Wang, "Nitrogen doped $\text{Sr}_2\text{Ta}_2\text{O}_7$ coupled with graphene sheets as photocatalysts for increased photocatalytic hydrogen production," *ACS Nano*, vol. 5, no. 5, pp. 3483–3492, 2011.
- [43] F. Dong, Y. J. Sun, W. K. Ho, and Z. B. Wu, "Controlled synthesis, growth mechanism and highly efficient solar photocatalysis of nitrogen-doped bismuth subcarbonate hierarchical nanosheets architectures," *Dalton Transactions*, vol. 41, no. 27, pp. 8270–8284, 2012.
- [44] F. Dong, T. Xiong, Z. W. Zhao, Y. J. Sun, and M. Fu, "Ammonia induced formation of N-doped $(\text{BiO}_2)_2\text{CO}_3$ hierarchical microspheres: the effect of hydrothermal temperature on the morphology and photocatalytic activity," *CrystEngComm*, vol. 15, no. 48, pp. 10522–10532, 2013.
- [45] Z. H. Ai, L. L. Zhu, S. C. Lee, and L. Z. Zhang, "NO treated TiO_2 as an efficient visible light photocatalyst for NO removal," *Journal of Hazardous Materials*, vol. 192, no. 1, pp. 361–367, 2011.
- [46] F. Dong, H. Q. Wang, and Z. B. Wu, "One-step "green" synthetic approach for mesoporous C-doped TiO_2 with efficient visible light photocatalytic activity," *The Journal of Physical Chemistry C*, vol. 113, no. 38, pp. 16717–16723, 2009.
- [47] F. Dong, A. M. Zheng, Y. J. Sun et al., "One-pot template-free synthesis, growth mechanism and enhanced photocatalytic activity of monodisperse $(\text{BiO}_2)_2\text{CO}_3$ hierarchical hollow microspheres self-assembled with single-crystalline nanosheets," *CrystEngComm*, vol. 14, no. 10, pp. 3534–3544, 2012.

- [48] X. B. Chen and C. Burda, "Photoelectron spectroscopic investigation of nitrogen-doped titania nanoparticles," *The Journal of Physical Chemistry B*, vol. 108, no. 40, pp. 15446–15449, 2004.
- [49] Q. J. Xiang, J. G. Yu, W. G. Wang, and M. Jaroniec, "Nitrogen self-doped nanosized TiO_2 sheets with exposed 001 facets for enhanced visible-light photocatalytic activity," *Chemical Communications*, vol. 47, no. 24, pp. 6906–6908, 2011.
- [50] H. T. Tian, J. W. Li, M. Ge, Y. P. Zhao, and L. Liu, "Removal of bisphenol A by mesoporous BiOBr under simulated solar light irradiation," *Catalysis Science & Technology*, vol. 2, no. 11, pp. 2351–2355, 2012.
- [51] F. Dong, H. T. Liu, W. K. Ho, M. Fu, and Z. B. Wu, " $(\text{NH}_4)_2\text{CO}_3$ mediated hydrothermal synthesis of N-doped $(\text{BiO}_2)\text{CO}_3$ hollow nanoplates microspheres as high-performance and durable visible light photocatalyst for air cleaning," *Chemical Engineering Journal*, vol. 214, no. 10, pp. 198–207, 2013.
- [52] Z. H. Ai, W. K. Ho, S. C. Lee, and L. Z. Zhang, "Efficient photocatalytic removal of NO in indoor air with hierarchical bismuth oxybromide nanoplate microspheres under visible light," *Environmental Science and Technology*, vol. 43, no. 11, pp. 4143–4150, 2009.
- [53] X. F. Song and L. Gao, "Facile synthesis and hierarchical assembly of hollow nickel oxide architectures bearing enhanced photocatalytic properties," *The Journal of Physical Chemistry C*, vol. 112, no. 39, pp. 15299–15305, 2008.

Research Article

Photocatalytic Degradation of 2-Chlorophenol Using Ag-Doped TiO₂ Nanofibers and a Near-UV Light-Emitting Diode System

Ju-Young Park^{1,2} and In-Hwa Lee¹

¹ Department of Environmental Engineering, Chosun University, Gwangju 501-759, Republic of Korea

² Center for Novel States of Complex Materials Research, Department of Physics and Astronomy, Seoul National University, Seoul 151-747, Republic of Korea

Correspondence should be addressed to In-Hwa Lee; ihlee@chosun.ac.kr

Received 4 October 2013; Accepted 11 December 2013; Published 8 January 2014

Academic Editor: Ranjit T. Koodali

Copyright © 2014 J.-Y. Park and I.-H. Lee. This is an open access article distributed under the Creative Commons Attribution License, which permits unrestricted use, distribution, and reproduction in any medium, provided the original work is properly cited.

This report investigated the photocatalytic degradation of 2-chlorophenol using TiO₂ nanofibers and Ag-doped TiO₂ nanofibers, synthesized using the sol-gel and electrospinning techniques, and an ultraviolet light-emitting diode (UV-LED) system as a UV light source. The crystallite size of the Ag-doped TiO₂ nanofibers was smaller than that of the TiO₂ nanofibers, because silver restrained phase transformation not only controls the phase transformation but also inhibits the growth of anatase crystallites. The activation energies for the grain growth of the TiO₂ nanofibers and the Ag-doped TiO₂ nanofibers were estimated to be 20.84 and 27.01 kJ/mol, respectively. The photocatalytic degradation rate followed a pseudo-first-order equation. The rate constants (*k*) of the TiO₂ nanofibers and the Ag-doped TiO₂ nanofibers were 0.056 and 0.144 min⁻¹, respectively.

1. Introduction

TiO₂ is the most widely used photocatalyst owing to its photostability, nontoxicity, low cost, and insolubility in water under most environmental conditions [1]. Excitation of TiO₂ generates highly reactive electron-hole pairs that subsequently produce highly potent radicals (such as $\cdot\text{OH}$ and $\text{O}_2\cdot^-$) that oxidize organic and inorganic pollutants. However, the optimal design of the reactor and the various operational conditions are major concerns in the development and potential applications of photocatalytic processes. Virtually all previous work on photocatalytic degradation with respect to the removal of pollutants from wastewater has been carried out using broad spectral radiation sources, such as UV lamps, and TiO₂ as the photocatalyst. The traditional UV source is a mercury vapor high-pressure lamp, which is also a source of gas discharge [2, 3]. The mercury used in this UV lamp is specified as a hazardous air pollutant by the U.S. Environmental Protection Agency and can damage the brain and kidneys. Ultraviolet light-emitting diodes (UV-LEDs) are a new, safer, and energy efficient alternative to traditional

gas discharge sources. LEDs are a directional light source, in which the maximum emitted power is in the direction perpendicular to the emitting surface. A typical lifetime of 100,000 h is another advantage of UV-LEDs, whereas the lifetime of gas discharge sources is approximately 1000 h. The electrospinning technique has been recognized as a versatile and effective method for the preparation of nanofibers with small diameters and high surface-to-volume ratios [4–7], and the fabrication of TiO₂ nanofibers by electrospinning was first reported in 2003 [8]. Some researchers have already prepared pure inorganic fibers comprised of TiO₂ [9–11]. Based on these previous reports, TiO₂ fibers were fabricated from a mixture of titanium isopropoxide (TiP) and a polymer using electrospinning techniques. After thermal treatment, TiO₂ (anatase and/or rutile phase) fibers were obtained. Bender et al. [12], Alves et al. [13], and Ding et al. [14] studied the electrospun TiO₂ nanofibers as a photocatalyst to be applied to the degradation of dye pollutants. However, there has been very little research on photocatalytic degradation using metal-doped (Ag, Pd, and Pt) TiO₂ nanofibers. Some metal materials, such as Ag, Pd, and Pt, supported on

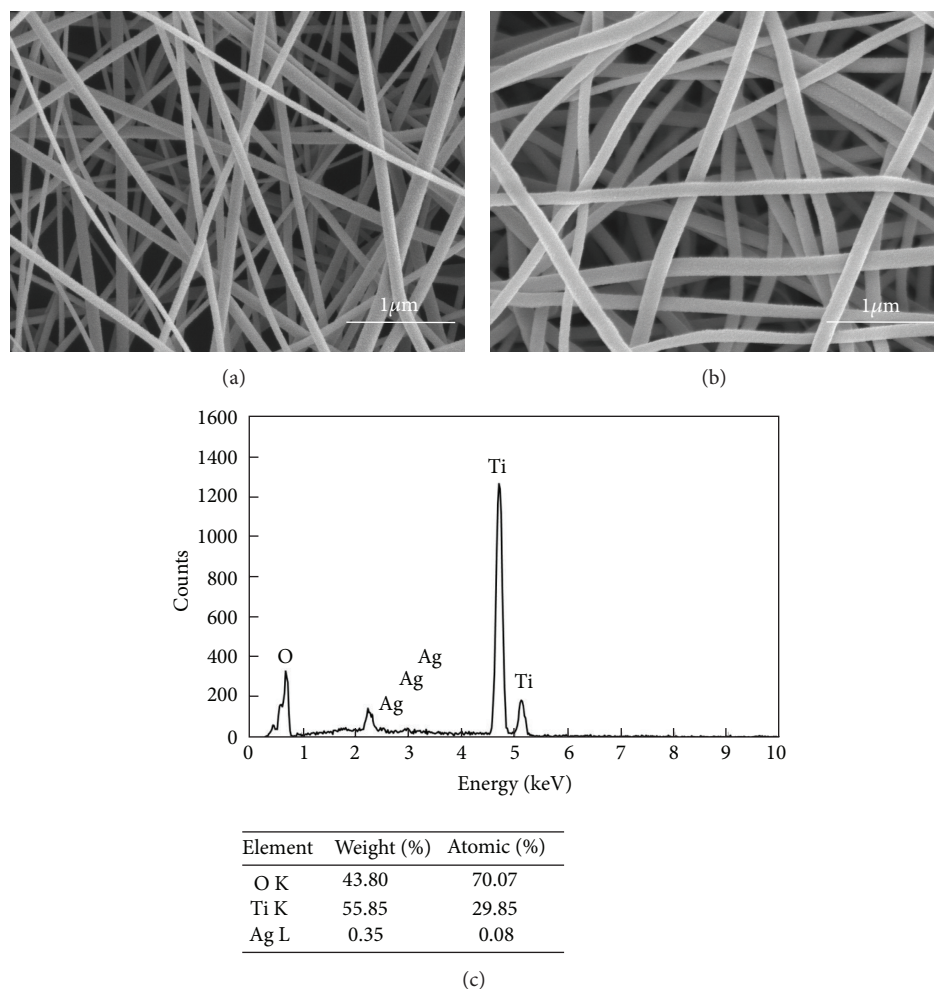


FIGURE 1: FE-SEM images of (a) TiO_2 nanofibers and (b) Ag-doped TiO_2 nanofibers. (c) EDX spectrum of Ag-doped TiO_2 nanofibers.

the TiO_2 surface can greatly accelerate the decomposition rate of organic compound by effectively consuming the photoproduced electrons in the reduction of oxygen, thereby reducing the recombination of electrons (e^-) and holes (h^+) [15–18].

Recently, some researchers have demonstrated the photocatalytic degradation of organic materials using the TiO_2 and UV-LED system [19–21]. The TiO_2 nanofibers photocatalyst is illuminated by the near-UV-LED light source in order to activate its band gap energy and to produce subsequently electron-hole pairs that act as oxidizing and reducing agents.

In this work, Ag-doped TiO_2 nanofibers were prepared using the electrospinning method in order to prevent recombination, which causes the relatively low photocatalytic efficiency. TiO_2 presents the relatively high electron-hole recombination rate which is detrimental to its photoactivity. In this sense, Ag-doped TiO_2 could make a double effect: (1) Firstly, it could reduce the band gap energy, thus shifting the adsorption; (2) secondly, Ag could provoke a decrease in electron-hole recombination rate, acting as electron traps [18]. The photocatalyst samples (TiO_2 nanofibers and Ag-doped TiO_2 nanofibers) were characterized using field-emission scanning electron microscopy (FE-SEM), X-ray

diffraction (XRD), and Brunauer-Emmett-Teller (BET) surface area. The activation energy for the grain growth of the TiO_2 nanofibers was calculated by the Arrhenius equation, based on the XRD results. The photocatalysts were evaluated for the photodecomposition of 2-chlorophenol under the UV-LED system.

2. Experimental

TiO_2 nanofibers and Ag-doped TiO_2 nanofibers were fabricated using the method described by Park et al. [7]. Electrospun nanofibers were prepared using TiP and polyvinylpyrrolidone (PVP) as precursors. 6 mL of TiP was first mixed with 12 mL of acetic acid and 12 mL of ethanol. After 60 min, this solution was added to 30 g of ethanol, which contained 10 wt% PVP and 1.986 mL of 0.5 N AgNO_3 (5% of the molar amount of TiP), followed by magnetic stirring for 24 h. The mixture was immediately loaded into a glass syringe equipped with a 21 G stainless steel needle, and the needle was then connected to a high voltage supply (DC power supply PS/ER 50R06 DM22, Glassman High Voltage Inc., USA). A voltage of 20 kV was applied between the needle

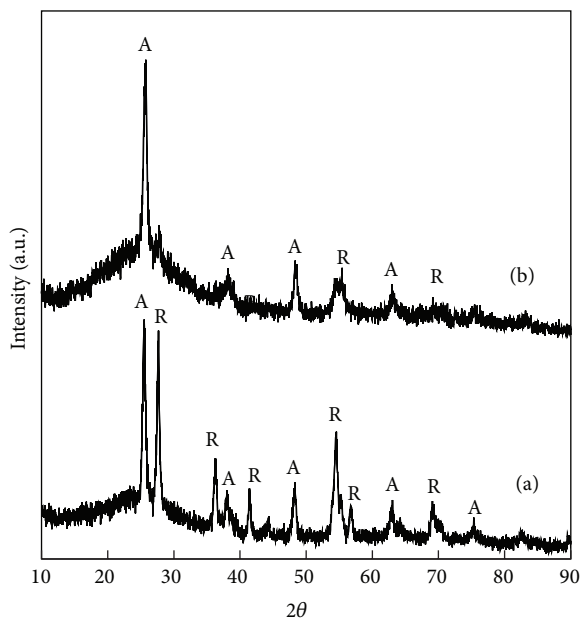


FIGURE 2: XRD patterns of (a) TiO_2 nanofibers and (b) Ag-doped TiO_2 nanofibers.

and the collector, and the distance between the needle and the target was 15 cm. The flow rate was maintained at $50 \mu\text{L}/\text{min}$ using a syringe.

The prepared electrospun TiP/PVP nanofibers were calcined at 500°C . The morphology of the electrospun TiO_2 nanofibers was observed using FE-SEM (Hitachi, S-4800) with the energy dispersive X-ray (EDX). XRD patterns were recorded using a Philips (X'Pert PR O MPO) diffractometer (Cu $K\alpha$ radiation) at a scanning rate of $0.01^\circ/\text{sec}$ in the 2θ range of 10° to 90° .

The photo-reactor consists of a planar cell comprised entirely of SS 316 L glass. The planar reactor contained two hollow fillisters that were 205 mm long and 45 mm wide at the top and bottom fixtures, respectively. The UV-LED system, which was used as the UV light source, consisted of a 3×11 array of UV-LEDs (3.3 V, 8 mW, and 365 nm). The 2-chlorophenol (99.9% trace metal basis, Aldrich) was analytical grade, and deionized water was used in all decomposition experiments. The concentrations of the 2-chlorophenol aqueous solutions were analyzed by HPLC (Sykam S210) with an ODS C18 column (150 mm \times 4.6 mm). The eluent was 65% acetonitrile, the flow rate was $1 \text{ mL}/\text{min}$, and the absorbance was monitored at 280 nm.

3. Results and Discussion

Figures 1 and 2 show FE-SEM images and XRD patterns, respectively, of the TiO_2 nanofibers and the Ag-doped TiO_2 nanofibers, at a calcination temperature of 500°C . After calcination of the TiP/PVP composite nanofibers, the TiO_2 nanofibers were fabricated by removing the PVP during calcination. TiO_2 nanofibers (Figure 1(a)) and Ag-doped TiO_2 nanofibers (Figure 1(b)) with a diameter of 100 to 150 nm were obtained after calcination at 500°C . Figure 1(c) showed

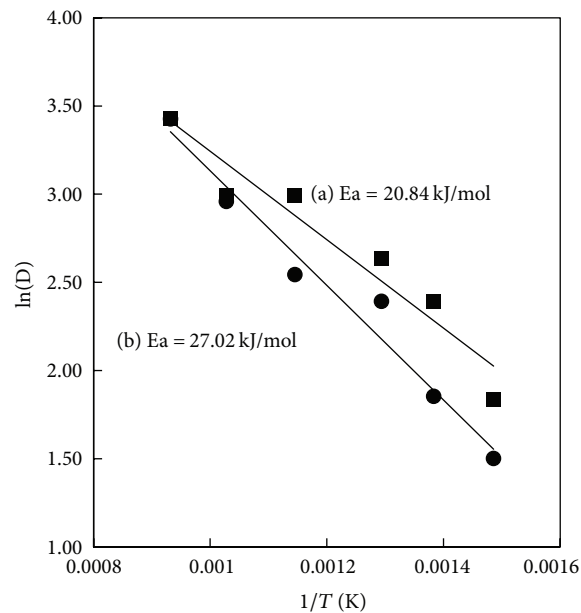


FIGURE 3: Plot of $\ln(D)$ versus $1/T$. The slope provides information about the activation energy for the grain growth of (a) TiO_2 nanofibers and (b) Ag-doped TiO_2 nanofibers.

EDX spectrum at a calcination temperature of 500°C . An Ag doping amount of 0.35 wt.% was estimated from the EDX analysis. According to Park et al. [7], the Ag controlled the phase transformation temperature of the TiO_2 nanofibers. At the Bragg angle (2θ) of 25.2° , the anatase ratio of the corresponding plane (101) (extracted from XRD pattern) was calculated from the Spurr equation against corresponding plane (101) [22]. TiO_2 nanofibers were observed in both the 46% anatase phase and the 54% rutile phase, and the Ag-doped TiO_2 nanofibers were only observed in the anatase phase.

The grain growth is a thermal activation process, satisfying the well-known Arrhenius equation:

$$D = A \exp\left(\frac{-E_a}{RT}\right), \quad (1)$$

where D is the average grain size, A is preexponential factor, E_a is the activation energy for the atomic diffusion near the grain boundary, R is the gas constant, and T is temperature in Kelvin. Figure 3 shows the plot of $\ln(D)$ as a function of $1/T$ in Kelvin. The activation energy for the grain growth of TiO_2 nanofibers was estimated to be 20.84 kJ/mol from the slope of $\ln(D)$ versus $1/T$, which is lower than the 27.02 kJ/mol value of the Ag-doped TiO_2 nanofibers. The lower activation energy for the growth of nanograins is a result of the chemical potential of the atoms in the nanosize grains being much higher, which leads to more active growth.

Figure 4 shows nitrogen-adsorption measurements of the sample. The Brunauer-Emmett-Teller (BET) surface area of TiO_2 nanofibers and Ag-doped TiO_2 nanofibers was 215.2 and $219.9 \text{ m}^2/\text{g}$, respectively. The pore volume and pore size of the sample were determined using the DFT method. For the TiO_2 nanofibers and the Ag-doped TiO_2 nanofibers,

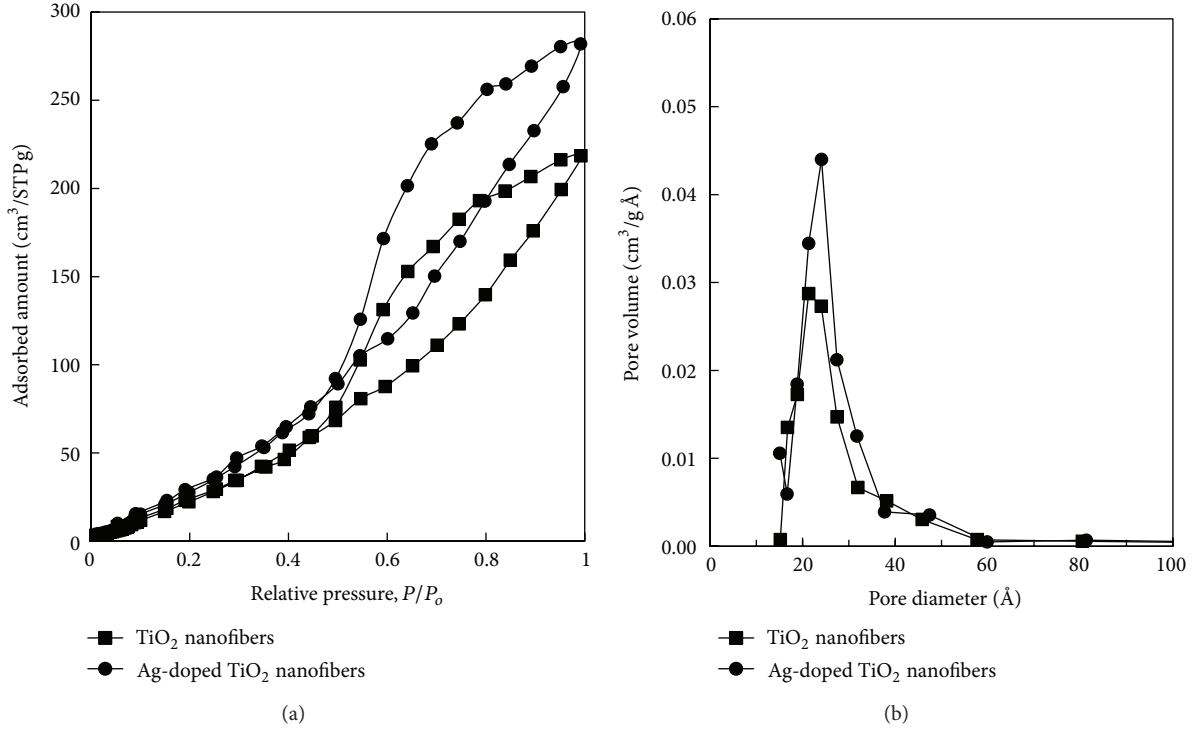


FIGURE 4: Nitrogen adsorption-desorption isotherms and the calculated pore-size distribution.

the pore volumes were 0.136 and 0.410 cm³/g and the pore sizes were 45.40 and 13.85 Å, respectively.

Figure 5 shows the changes in 2-chlorophenol concentration with respect to irradiation time during the UV-LED process. In the case of Ag-doped TiO₂ nanofibers, photodegradation of 2-chlorophenol was increased, which may have been attributed to the following four reasons. (1) Appropriate amount of the doped and deposited Ag species on the surface layer of TiO₂ nanofibers effectively captured the photoinduced electrons and holes. (2) Photoinduced electrons were quickly transferred to the oxygen adsorbed on the surface of TiO₂ nanofibers. (3) The amount of the surface hydroxyl was increased. (4) The response range to light was expanded to the visible region [15]. These advantages of the Ag-doped TiO₂ nanofibers remarkably improved its photocatalytic performance.

We calculated the kinetic constant using a pseudo-first-order equation (2) and a simplified version of the Lagergren equation (3). Based on the adsorption capacity, Lagergren [20] proposed a rate equation for the sorption of a solute from a liquid solution. The Lagergren equation is the most widely used rate equation in liquid-phase sorption processes, and this kinetic model is expressed as

$$\frac{dq_t}{dt} = k_1 (q_e - q_t). \quad (2)$$

Integrating the above equation for the boundary conditions $t = 0$ to $t = t$ and $q_e = q_t$ yields

$$\ln(q_e - q_t) = \ln(q_e - k_1 t). \quad (3)$$

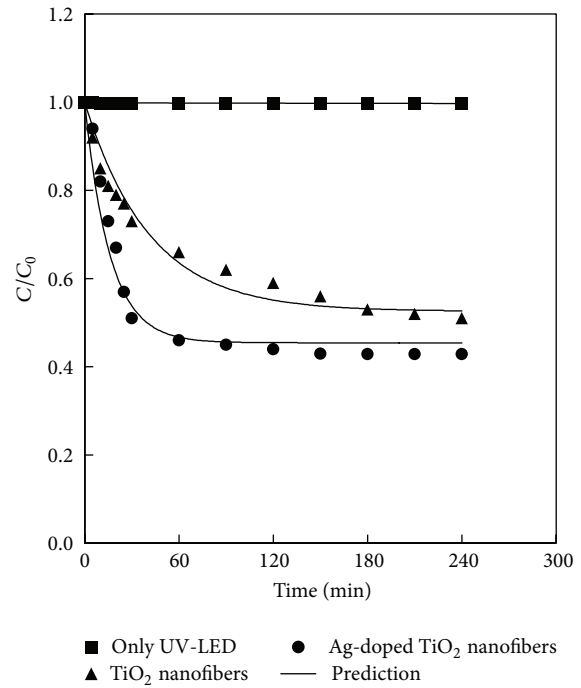


FIGURE 5: Photocatalytic degradation of 2-chlorophenol with the UV-LED system.

The kinetic constant k_1 (min⁻¹) can be determined by plotting $\ln(q_e - q_t)$ against t or $\ln(q_e - q_t)/q_e$ versus t . It is important to note that the correlation coefficients (R^2) of the pseudo-first-order model for the linear plots

TABLE 1: First-order rate constants of the photocatalytic degradation of 2-chlorophenol.

Sample name	Rate constant k (min^{-1})
TiO ₂ nanofibers	0.056
Ag-doped TiO ₂ nanofibers	0.144

of TiO₂ nanofibers are very close to 1. This result implies that the photocatalytic degradation kinetics can be successfully described by this model. The values of the rate constant (k) are listed in Table 1. The rate constants (k) of the TiO₂ nanofibers and the Ag-doped TiO₂ nanofibers were 0.056 and 1.144 min^{-1} , respectively.

4. Conclusions

TiO₂ nanofibers and Ag-doped TiO₂ nanofibers were fabricated by applying the sol-gel and electrospinning techniques. TiO₂ nanofibers and Ag-doped TiO₂ nanofibers were applied as a photocatalyst system with UV-LEDs in order to measure the photocatalytic degradation of 2-chlorophenol. The crystallite size of the Ag-doped TiO₂ nanofibers was smaller than that of the TiO₂ nanofibers, because silver is restrained in this phase transformation. The activation energies for the grain growth of the TiO₂ nanofibers and the Ag-doped TiO₂ nanofibers were 20.48 and 27.02 kJ/mol, respectively. These photocatalysts were evaluated based on the photodecomposition of methylene blue under UV-LEDs. The photocatalytic degradation rate followed a pseudo-first-order equation. The rate constants (k) of the TiO₂ nanofibers and Ag-doped TiO₂ nanofibers were 0.056 and 0.144 min^{-1} , respectively.

Conflict of Interests

The authors declare that there is no conflict of interests regarding the publication of this paper.

Acknowledgments

This work was supported by research fund from Chosun University, 2011. This work was supported by the Human Resources Development Program (no. 20134010200560) of the Korea Institute of Energy Technology Evaluation and Planning (KETEP) grant funded by the Korean Government Ministry of Trade, Industry, and Energy.

References

- [1] D. Li and Y. Xia, "Fabrication of titania nanofibers by electrospinning," *Nano Letters*, vol. 3, no. 4, pp. 555–560, 2003.
- [2] P. Viswanathamurthi, N. Bhattarai, C. K. Kim, H. Y. Kim, and D. R. Lee, "Ruthenium doped TiO₂ fibers by electrospinning," *Inorganic Chemistry Communications*, vol. 7, no. 5, pp. 679–682, 2004.
- [3] Y. Xiaodan, W. Qingyin, J. Shicheng, and G. Yihang, "Nanoscale ZnS/TiO₂ composites: preparation, characterization, and visible-light photocatalytic activity," *Materials Characterization*, vol. 57, no. 4-5, pp. 333–341, 2006.
- [4] X. Zhang, S. Xu, and G. Han, "Fabrication and photocatalytic activity of TiO₂ nanofiber membrane," *Materials Letters*, vol. 63, no. 21, pp. 1761–1763, 2009.
- [5] S. Madhugiri, B. Sun, P. G. Smirniotis, J. P. Ferraris, and K. J. Balkus Jr., "Electrospun mesoporous titanium dioxide fibers," *Microporous and Mesoporous Materials*, vol. 69, no. 1-2, pp. 77–83, 2004.
- [6] B. Xin, L. Jing, Z. Ren, B. Wang, and H. Fu, "Effects of simultaneously doped and deposited Ag on the photocatalytic activity and surface states of TiO₂," *Journal of Physical Chemistry B*, vol. 109, no. 7, pp. 2805–2809, 2005.
- [7] J. Y. Park, I. H. Lee, and G. N. Bea, "Optimization of the electrospinning conditions for preparation of nanofibers from polyvinylacetate (PVAc) in ethanol solvent," *Journal of Industrial and Engineering Chemistry*, vol. 14, no. 6, pp. 707–713, 2008.
- [8] J.-Y. Park and I.-H. Lee, "Characterization and morphology of prepared titanium dioxide nanofibers by electrospinning," *Journal of Nanoscience and Nanotechnology*, vol. 10, no. 5, pp. 3402–3405, 2010.
- [9] S. Ramakrishna, K. Fujihara, W. E. Teo, T. C. Lim, and M. Zuwe M, *An Introduction Electrospinning and Nanofibers*, World Scientific Publishing Company, Singapore, 2005.
- [10] B. Ding, H. Y. Kim, C. K. Kim, M. S. Khil, and S. J. Park, "Morphology and crystalline phase study of electrospun TiO₂-SiO₂ nanofibres," *Nanotechnology*, vol. 14, no. 5, pp. 532–537, 2003.
- [11] C. Pan, L. Dong, and Z.-Z. Gu, "Surface functionalization of electrospun TiO₂ nanofibers by Au sputter coating for photocatalytic applications," *International Journal of Applied Ceramic Technology*, vol. 7, no. 6, pp. 895–901, 2010.
- [12] E. T. Bender, P. Katta, G. G. Chase, and R. D. Ramsier, "Spectroscopic investigation of the composition of electrospun titania nanofibers," *Surface and Interface Analysis*, vol. 38, no. 9, pp. 1252–1256, 2006.
- [13] A. K. Alves, F. A. Berutti, F. J. Clemens, T. Graule, and C. P. Bergmann, "Photocatalytic activity of titania fibers obtained by electrospinning," *Materials Research Bulletin*, vol. 44, no. 2, pp. 312–317, 2009.
- [14] B. Ding, C. K. Kim, H. Y. Kim, M. K. Seo, and S. J. Park, "Titanium dioxide nanofibers prepared by using electrospinning method," *Fibers and Polymers*, vol. 5, no. 2, pp. 105–109, 2004.
- [15] B. Xin, L. Jing, Z. Ren, B. Wang, and H. Fu, "Effects of simultaneously doped and deposited Ag on the photocatalytic activity and surface states of TiO₂," *Journal of Physical Chemistry B*, vol. 109, no. 7, pp. 2805–2809, 2005.
- [16] J. C. Yang, Y. C. Kim, Y. G. Shul, C. H. Shin, and T. K. Lee, "Characterization of photoreduced Pt/TiO₂ and decomposition of dichloroacetic acid over photoreduced Pt/TiO₂ catalysts," *Applied Surface Science*, vol. 121-122, pp. 525–529, 1997.
- [17] C.-C. Chang, J.-Y. Chen, T.-L. Hsu, C.-K. Lin, and C.-C. Chan, "Photocatalytic properties of porous TiO₂/Ag thin films," *Thin Solid Films*, vol. 516, no. 8, pp. 1743–1747, 2008.
- [18] J. C. Colmenares, M. A. Aramendía, A. Marinas, J. M. Marinas, and F. J. Urbano, "Synthesis, characterization and photocatalytic activity of different metal-doped titania systems," *Applied Catalysis A*, vol. 306, pp. 120–127, 2006.
- [19] J. M. G. Amores, V. S. Escibano, and G. Busca, "Anatase crystal growth and phase transformation to rutile in high-area TiO₂,

- MoO₃-TiO₂ and other TiO₂-supported oxide catalytic systems,” *Journal of Materials Chemistry*, vol. 5, no. 8, pp. 1245–1249, 1995.
- [20] J. M. G. Amores, V. S. Escibano, G. Busca, and V. Lorenzelli, “Solid-state and surface chemistry of CuO–TiO₂ (anatase) powders,” *Journal of Materials Chemistry*, vol. 4, no. 6, pp. 965–971, 1994.
- [21] H. E. Chao, Y. U. Yun, H. U. Xingfang, and A. Larbot, “Effect of silver doping on the phase transformation and grain growth of sol-gel titania powder,” *Journal of the European Ceramic Society*, vol. 23, no. 9, pp. 1457–1464, 2003.
- [22] B. D. Cullity and S. R. Stock, *Elements of X-Ray Diffraction*, Prentice Hall, Upper Saddle River, NJ, USA, 3rd edition, 2001.

Research Article

The Key Role of pH Value in the Synthesis of Titanate Nanotubes-Loaded Manganese Oxides as a Superior Catalyst for the Selective Catalytic Reduction of NO with NH₃

Xiongbo Chen, Chaoping Cen, Zhixiong Tang, Wenhao Zeng, Dingsheng Chen, Ping Fang, and Zhihang Chen

South China Institute of Environmental Sciences, The Ministry of Environmental Protection of PRC, No. 7 West Street, Yuancun, Guangzhou 510655, China

Correspondence should be addressed to Chaoping Cen; cenchaoping@scies.org

Received 30 November 2013; Accepted 13 December 2013

Academic Editor: Fan Dong

Copyright © 2013 Xiongbo Chen et al. This is an open access article distributed under the Creative Commons Attribution License, which permits unrestricted use, distribution, and reproduction in any medium, provided the original work is properly cited.

Titanate nanotubes (TNTs) synthesized by hydrothermal method were increasingly used as the catalyst support for the selective catalytic reduction (SCR) of NO with ammonia. This paper reports the critical process of postwashing to prepare satisfactory TNTs for the uses of SCR catalysts. Herein, alkaline TNTs (TNTs-AL), acidic TNTs (TNTs-AC), and neutral TNTs (TNTs-NE) were synthesized by controlling washing pH value. When these TNTs were utilized as the catalyst supports for manganese oxides (Mn/TNTs-AL, Mn/TNTs-AC, and Mn/TNTs-NE), the key role of pH value was found. Titanate nanosheets, titanate nanorods and titanate nanotubes were dominated in Mn/TNTs-AL, Mn/TNTs-AC, and Mn/TNTs-NE, respectively. MnO₂ crystal was observed when using TNTs-AC or TNTs-NE as the support. By contrast, Mn₃O₄ and NaNO₃ were observed when using TNTs-AL as the support. Mn/TNTs-NE showed the best SCR activity, in line with the largest surface area, the best dispersion, and the most active redox property of manganese oxides. Mn/TNTs-AL showed negligible SCR activity, resulting from the minimum surface area, the Mn₃O₄-dominating crystal structure, and the bad dispersion of manganese oxides.

1. Introduction

In recent years, particular interest has been given to the catalytic application of nanotubular materials including carbon nanotubes (CNTs) and titanate nanotubes (TNTs) [1, 2]. The tubular channels of these materials act as confined places for both the growth of active particles and catalytic reaction [3, 4]. In confined circumstances, the redox property of active particles can be tuned and a unique metal-support interaction may occur [5–7]. Furthermore, the interaction between reactants and products within the confined places is enhanced [1, 3, 4]. All these unique properties make nanotubular materials be promising supports for catalysts.

TiO₂, mostly nanoparticles, has been one of the most popular supports for both photocatalysts and thermocatalysts [8]. With respect to DeNO_x catalysts, which are catalysts for the selective catalytic reduction (SCR) of NO_x with ammonia, TiO₂ is preferable to other commonly used supports, for

example, Al₂O₃ and SiO₂ due to the reversible combination with SO₂, which is beneficial to preventing SO₂ deactivation [9]. The catalyst system V₂O₅-WO₃/TiO₂ or V₂O₅-MoO₃/TiO₂ is world widely used for removing NO_x from stationary sources. In the meantime, the existing problems including toxicity of vanadium pentoxide, relatively high operation temperature, and N₂O formation become huge concerns [10–12]. Therefore nonvanadium SCR catalysts have been a hot area of research. Since the successful synthesis by hydrothermal method, titanate nanotubes were promptly used as supports for DeNO_x catalysts [2, 13]. Wang et al. found that ceria confined in TNTs showed a superiority in SCR of NO due to the improved redox potential and special adsorption of NH₃ [14, 15]. Nian et al. synthesized Cu loaded TNTs with high activity for the SCR of NO and believed that the specific feature and layered structure of TNTs facilitated the Cu dispersion and the formation of solid solution Cu_xTi_{1-x}O₂ [16]. Yao et al. investigated the performance

of manganese supported on titanate nanotubes for the low-temperature SCR of NO and confirmed the superiority of TNTs to TiO₂ nanopowder [17]. These TNTs-supported DeNOx catalysts are good attempts to explore non-vanadium SCR catalysts [18].

The hydrothermal synthesis of titanate nanotubes is typically divided into four steps: pretreatment of reagent, hydrothermal reaction, posttreatment washing, and drying [13, 19]. It is worth noting that the posttreatment washing process is one of the key steps affecting the structure and the composition of the final products [20]. It was proved by Tsai and Teng and Yang et al. that Na⁺ → H⁺ substitution occurred during the washing process and the structural transformation of titanate nanosheets → titanate nanotubes → anatase TiO₂ could be observed, together with the change of elementary composition [20–22]. So it is reasonable that the posttreatment washing process will greatly affect the final property of the TNTs-supported DeNOx catalysts, including the structure, the chemical state of active species, and the SCR activity.

Herein, three different types of TNTs named alkaline TNTs (TNTs-AL), acidic TNTs (TNTs-AC), and neutral TNTs (TNTs-NE) are synthesized and used as catalyst supports for manganese. These catalysts are characterized systematically by SCR activity test, X-ray diffraction (XRD), transmission electron microscopy (TEM), X-ray photoelectron spectroscopy (XPS), and so on. Afterwards, the variation of physicochemical property and catalytic performance are discussed systemically.

2. Experimental

2.1. Support Preparation. Commercial available P25 TiO₂ (Degussa, Germany) was chosen as precursor for the synthesis of TNTs by hydrothermal method. P25 was mixed with 10 mol/L NaOH solution and then transferred to a Teflon lined autoclave. Then, hydrothermal treatment was conducted at 140°C for 24 h. Following the hydrothermal reaction, the filtered precipitate was washed according to the special requirements. TNTs-AL were washed with 0.1 mol/L HCl solution to pH value near 12. TNTs-AC were washed with 0.1 mol/L HCl solution to pH value near 2. TNTs-NE were washed firstly with 0.1 mol/L HCl solution to pH value near 2 and secondly with distilled water to pH value near 7. After the postwashing process, the mixture was filtrated and then dried in oven at 80°C for 12 h.

2.2. Catalyst Preparation. Mn/TNTs catalysts with different TNTs supports were prepared by a wetness impregnation technique. Mn(NO₃)₂·4H₂O was selected as the precursor for manganese oxides. 5 mL aqueous solution of 50 wt.% Mn(NO₃)₂·4H₂O was diluted with 100 mL deionized water, in which 4 g of the prepared TNTs was impregnated. The mixture was dried at 80°C for 12 h and then calcined at 400°C in air for 3 h.

2.3. Catalyst Characterization. The specific surface areas of the Mn/TNTs catalysts were measured by using a nitrogen

adsorption apparatus (ASAP 2020, USA). The samples were degassed at 200°C for 6 h under vacuum. Total pore size distributions were measured from the N₂ desorption isotherm using the cylindrical pore model. X-ray photoelectron spectroscopy with Al Kα X-ray (hν = 1486.6 eV) radiation operated at 150 W (XPS: Thermo ESCALAB250, USA) was used to investigate the surface properties of the samples. The shift in the binding energy due to relative surface charging was corrected using the C 1s level at 284.8 eV as an internal standard.

The crystalline phase of the samples was characterized by using an X-ray diffractometer (Rigaku Co., Japan) with Cu Kα radiation (λ = 0.15418 nm). The scattering angle was 2θ = 10°–80° with step size of 0.02°/s. The morphology, structure, and grain size of the samples were examined by TEM (JEM-2010, Japan).

Temperature programmed reduction (TPR) and temperature programmed desorption (TPD) experiments were carried out using a TP-5085 supplied by Tianjin Xianquan Industry and Trade Development Co. Ltd, China. 0.05 g of sample was placed in the middle of quartz tube and held in position with silica wool. Prior to TPR experiments, the sample was heated to 400°C with a dwelling time of 1 h and then cooled to 100°C. The process was operated with purge of flowing N₂ gas at the rate of 28.5 mL/min⁻¹. The TPR runs were then carried out with the linear heating rate 10°C/min in pure N₂ containing 4% H₂ at flow rate of 28.5 mL/min. With respect to TPD experiments, 0.1 g of sample was pre-treated at 400°C for 1 h, cooled to room temperature like TPR, and then saturated with anhydrous NH₃ (4% in N₂) at flow rate of 10 mL/min for about 30 min. Desorption was carried out by heating the sample in N₂ from 70 to 800°C with heating rate at 10°C/min.

2.4. Catalytic Activity Tests. Catalytic experiments were carried out between 150 and 470°C using a fixed-bed quartz reactor with an 8 mm inner diameter under atmospheric pressure. The feed streams were as follows: 700 ppm NO, 700 ppm NH₃, 4% O₂, and balanced with N₂ as the carrier gas with a total flow rate of 1.8 L/min. After crushing and sieving, 500 mg of catalyst in the range of 40–60 mesh was used in each experiment. NO, NO₂, N₂O, and O₂ concentrations were monitored by an infrared gas analyzer (Photon II, Madur Electronics, Austria). All measurements were repeated three times.

3. Results and Discussion

3.1. Crystal Structure. Figure 1 shows the XRD patterns of the three catalysts. The authors reported that the TiO₂ crystallites were exfoliated into layered crystalline sheets when the raw P25 was treated in NaOH aqueous [23]. In the meantime, Na–O–Ti bonds were created on the two sides. During the washing process, Na⁺ → H⁺ substitution and imbalance of H⁺ or Na⁺ ion concentration on two different sides of nanosheets occurred, giving rise to excess surface energy and resulting in bending [2]. From the XRD pattern of the Mn/TNTs-AL sample, strong diffraction peaks for NaNO₃

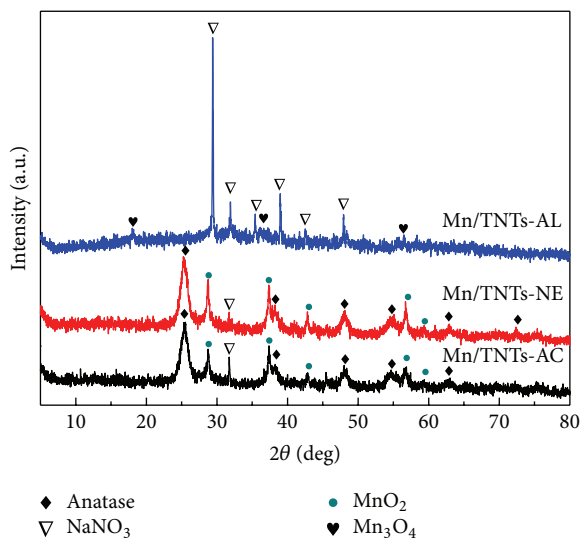


FIGURE 1: XRD patterns of the Mn/TNTs-AL, Mn/TNTs-AC, and Mn/TNTs-NE catalysts.

(PDF#01-070-1518) were observed. This finding indicates that a large number of Na^+ still remained in the Mn/TNTs-AL sample. It is because only a part of Na^+ was substituted by H^+ if the precipitate was washed with 0.1 mol/L HCl solution to pH value just near 12. The residual Na^+ in titanate structure combined with NO_3^- groups from manganese nitrate solution. With respect to the manganese oxides, diffraction peaks for Mn_3O_4 were observed, whereas those for MnO_2 were absent.

Compared with the Mn/TNTs-AL sample, the crystal phase of Mn/TNTs-AC had two obvious changes. Firstly, strong diffraction peaks for anatase (PDF#01-083-2243) appeared, but most of the diffraction peaks for NaNO_3 disappeared (only the peak situated at 31.90° still remains). These findings indicate that the number of residual Na^+ in titanate structure was greatly reduced by washing the precipitates with HCl solution from pH value near 12 to pH value near 2. In this substitution process, the sodium titanate transformed to anatase [20]. Secondly, diffraction peaks for Mn_3O_4 were hardly observed, but diffraction peaks for MnO_2 were clearly observed. This phenomenon suggests the different metal-support interaction occurring in Mn/TNTs-AL and Mn/TNTs-AC.

The crystal phase of Mn/TNTs-NE was very similar to that of Mn/TNTs-AC; only small differences on peak intensity could be observed. The diffraction peak situated at 31.90° for NaNO_3 became weaker, but the diffraction peaks for MnO_2 got enhanced, which means the residual Na^+ in the structure of TNTs-AC was further removed by washing with distilled water to pH value near 7, and stronger metal-support interaction occurred in the Mn/TNTs-NE sample.

3.2. Morphology and Microstructure. TEM micrographs shown in Figure 2 expressed visual impressions of the morphologies of the catalysts. From Figure 2(a), it can be seen that sodium titanate of the Mn/TNTs-AL sample mainly existed

TABLE 1: Surface area, total pore volume, and mean pore diameter of the Mn/TNTs-AL, Mn/TNTs-AC, and Mn/TNTs-NE samples.

Sample	BET surface area (m^2/g)	Pore volume (cm^3/g)	Pore size (nm)
Mn/TNTs-AC	97.1	0.35	11.74
Mn/TNTs-NE	122.4	0.53	16.45
Mn/TNTs-AL	8.3	0.06	19.46

in the form of nanosheets. Nanotubes were hardly observed. This finding indicates that $\text{Na}^+ \rightarrow \text{H}^+$ substitution was inadequate, and perhaps the driving force for bending was insufficient. It is reported that almost all the sodium titanate nanosheets will bend to form nanotubes after washing with dilute acid to pH value reaching 7 [19]. However, most of titanate structure will transform to anatase TiO_2 by further washing with dilute acid to pH value reaching 0–2, and part of the nanotubular morphology was lost [24, 25]. In addition, calcination treatment will accelerate the speed of transforming into anatase TiO_2 [26]. This is the reason why the assumed nanotubular morphology of the Mn/TNTs-AC sample was absent (Figure 2(b)). Notably, the transformation between titanate nanotube and anatase TiO_2 was reversible [24, 25]. So it is reasonable that the Mn/TNTs-NE sample, which was obtained after washing TNTs-AC with distilled water to pH value near 7, impregnating with manganese nitrate and annealing at 400°C for 3 h, still maintained nanotube-dominating morphology (Figure 2(c)).

3.3. Physical Characteristics and Chemical Composition. The surface area, total pore volume, and mean pore diameter of the three catalysts are given in Table 1. The surface areas of Mn/TNTs-AC and Mn/TNTs-NE are large, but that of Mn/TNTs-AL is especially low due to the smooth surface of nanosheets. Large-surface-area feature for titanate materials is advantageous for dispersion of active species [16]. So the dispersion of manganese oxides might be the best in Mn/TNTs-NE and the worst in Mn/TNTs-AL. The pore volume of nanosheets or nanorods is mainly contributed by the interstices between the nanocomposites. The pore volume of nanotubes, on the other hand, is contributed by the internal volume inside the tubes as well as the interstices between the tubes. The Mn/TNTs-NE sample showed the largest pore volume among the three catalysts. The pore volume of Mn/TNTs-AL was negligibly low, indicating the serious agglomeration of the nanosheets. The pore size, which corresponds to the interstice width, would increase with the size of the constituting nanocomposites. The pore sizes of the three catalysts follow the order Mn/TNTs-AC < Mn/TNTs-NE < Mn/TNTs-AL, in line with the size of their constituting nanocomposites (see Figure 2).

As shown in Figure 3(a), typical pore distribution of mesoporous materials could be confirmed in the three catalysts, with most pores concentrating in 2–50 nm. N_2 adsorption/desorption isotherms demonstrated in Figure 3(b) gave further information for the pore composition. The hysteretic

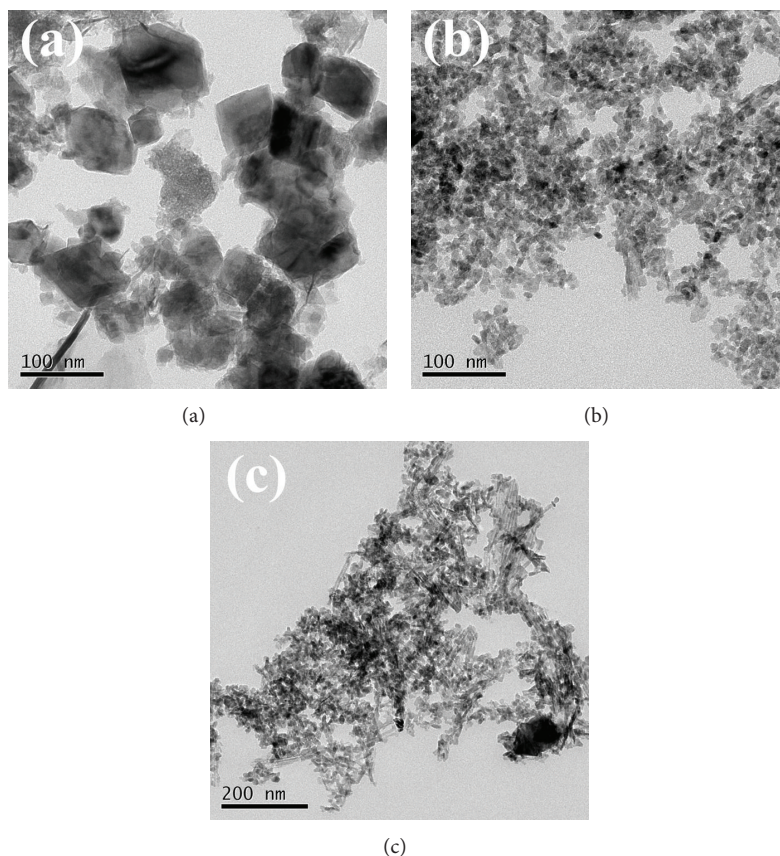


FIGURE 2: TEM micrographs of (a) Mn/TNTs-AL, (b) Mn/TNTs-AC, and (c) Mn/TNTs-NE.

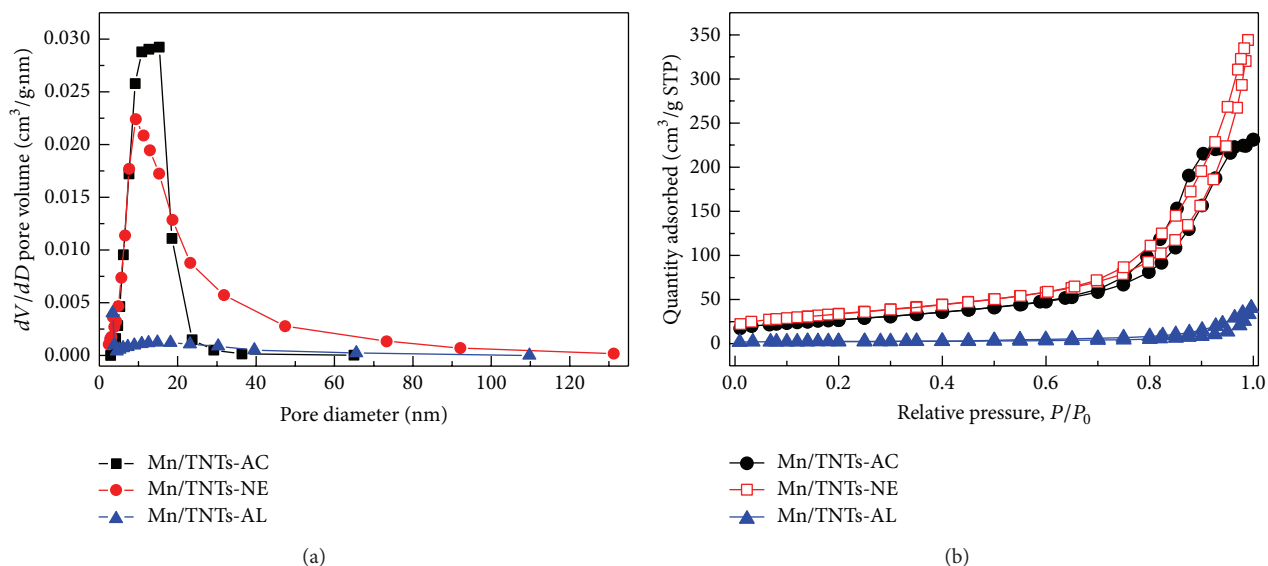


FIGURE 3: Pore size distribution (a) and N_2 adsorption/desorption isotherms (b) of the three catalysts.

loops of Mn/TNTs-AC could be recognized as type H1, whereas those of Mn/TNTs-NE and Mn/TNTs-AL could be recognized as type H3. Type H1 was always associated with porous materials with uniform shapes and pore size distributions [27, 28]. By contrast, type H3 was always associated

with porous materials with nonuniform shapes and pore size distributions [28]. In fact, these findings accord well with the TEM results. According to the TEM images, Mn/TNTs-AC showed nanorod-dominating morphology. The accumulation of nanorods resulted in uniform mesoporous pores.

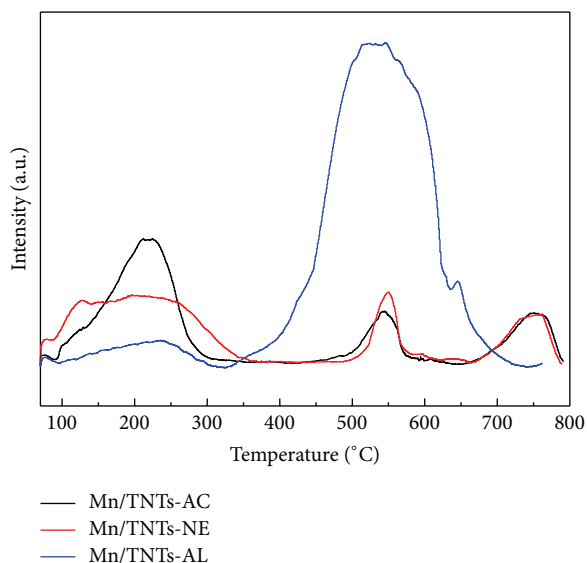


FIGURE 4: NH_3 -TPD of the Mn/TNTs-AL, Mn/TNTs-AC, and Mn/TNTs-NE samples.

Mn/TNTs-NE showed nanotube-dominating morphology. The nanotubes were arranged randomly, giving rise to the hollow channels in the tubes and the interstices between the tubes. The inner diameter of TNTs was *ca.* 2 nm, but the size of the interstices was tens of nanometers [14, 15]. Mn/TNTs-AL showed nanosheet-dominating morphology. These comparatively large nanosheets accumulated to form slits with different sizes.

XPS was utilized to identify the surface nature and atomic concentration of the three catalysts. The atomic concentration of each element was obtained by peak area integral of its narrow spectrum. Previous reports have revealed that the surface atomic concentration of the doped metal obtained with XPS was lower once the metallic species entered the nanotubes [15, 29]. Since the thickness of the wall of titanate nanotubes was 2–3 nm, which was close to the penetration depth of XPS analysis, manganese located in the tubular channels could only be partially detected. In this paper, the loading amount of manganese for all the three catalysts was designed as the same weight percentage to support, which is equal to Mn/Ti molar ratio between 0.28 and 0.39. However, their atomic concentration shown in Table 2 differed greatly. Mn/Ti molar ratio for Mn/TNTs-NE was observed at 0.20, indicating that lots of manganese in Mn/TNTs-NE entered the tubular channel of titanate nanotubes. By contrast, Mn/Ti molar ratios for Mn/TNTs-AC and Mn/TNTs-AL were observed at 0.97 and 1.96, respectively, far exceeding the design value. This is an evidence for the bad dispersion and agglomeration of manganese oxides in Mn/TNTs-AC and Mn/TNTs-AL (especially bad in the latter sample). It is also worth noting that the Na/Ti molar ratio of Mn/TNTs-AL reached up to 3.57, exceeding the other two catalysts by 5–8 times. This finding that indicates the quantity of residual Na^+ in the Mn/TNTs-AL catalyst was much larger than the other two samples. This result accords well with the XRD results revealing the formation of NaNO_3 crystal in Mn/TNTs-AL.

TABLE 2: Atomic concentration obtained with XPS.

Sample	Ti (%)	O (%)	Mn (%)	Na (%)	Mn/Ti	Na/Ti
Mn/TNTs-AC	9.92	73.57	9.59	6.92	0.97	0.70
Mn/TNTs-NE	21.36	64.14	4.24	10.26	0.20	0.48
Mn/TNTs-AL	5.58	63.56	10.94	19.92	1.96	3.57

3.4. NH_3 Adsorption. As shown in Figure 4, the NH_3 -TPD profiles of the three catalysts have a common peak situated from 100°C to 300°C. This peak always appeared in the profiles of titanate compounds, belonging to the desorption of ammonia adsorbed at weak acid sites [14]. The intensity of this peak for Mn/TNTs-AL was much weaker than Mn/TNTs-AC and Mn/TNTs-NE. The Mn/TNTs-AC and Mn/TNTs-NE samples also have another two common peaks centered at *ca.* 550°C and 750°C, respectively. The former peak could be ascribed to the desorption of chemisorbed ammonia at strong acid sites, and the later peak was generated by the decomposition of residual NaNO_3 and Mn-nitrate [30]. As to the NH_3 -TPD profile of the Mn/TNTs-AL sample, a strong peak ranging within 350–710°C was observed. The decomposition of Mn-nitrate and the desorption of chemisorbed ammonia at strong acid sites might contribute to this peak. Considering the large quantity of residual NaNO_3 , the continued decomposition of NaNO_3 also contributed to this peak greatly.

3.5. Redox Property. The H_2 -TPR profiles of the three catalysts are shown in Figure 5. According to the previous reports, MnO_2 and Mn_2O_3 always reduced firstly to Mn_3O_4 in the lower temperature range, and secondly to MnO at higher temperature range [30, 31]. With respect to the H_2 -TPR profiles of the Mn/TNTs-AC and Mn/TNTs-NE catalysts, the two-step reduction was obviously observed. The two reduction peaks for Mn/TNTs-NE centered at 462°C and 528°C appeared earlier than those for Mn/TNTs-AC centered at 507°C and 566°C. This result suggests that manganese oxides of Mn/TNTs-NE were more active than those of Mn/TNTs-AC. Indeed, according to the physical characteristics, a better dispersion of manganese oxides was expected in the surface of Mn/TNTs-NE, leading to the easier reduction at lower temperatures.

Unlike the other two samples, the H_2 -TPR profile of Mn/TNTs-AL only showed a strong and broad reduction peak. Due to the small surface area of Mn/TNTs-AL, a bad dispersion of manganese oxides tended to occur, giving rise to formation of bulk MnO_x . So the reduction peak which appeared in the H_2 -TPR profile of the Mn/TNTs-AL was in all probability ascribed to the reduction of bulk MnO_x .

3.6. SCR Activity. The NO conversion as a function of reaction temperature over the Mn/TNTs-AC, Mn/TNTs-NE, and Mn/TNTs-AL catalysts is shown in Figure 6. It can be seen that these three catalysts showed entirely different activity for the SCR of NO. Mn/TNTs-NE showed a good SCR activity even though the activity tests were conducted with a high GHSV at about 100,000 h^{-1} . The NO conversion

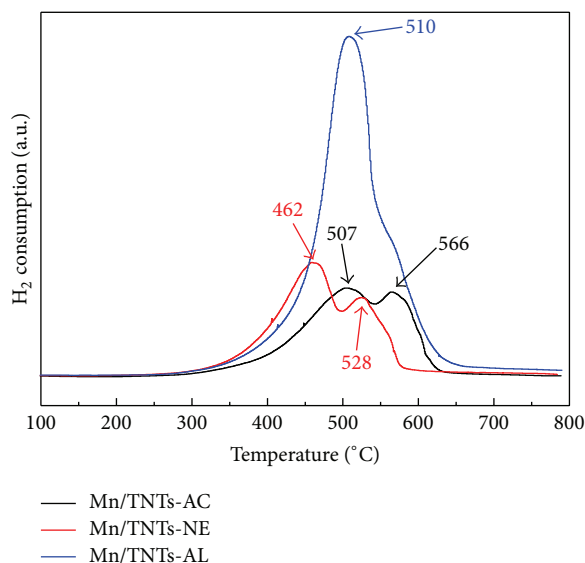


FIGURE 5: H_2 -TPR of the Mn/TNTs-AL, Mn/TNTs-AC, and Mn/TNTs-NE samples.

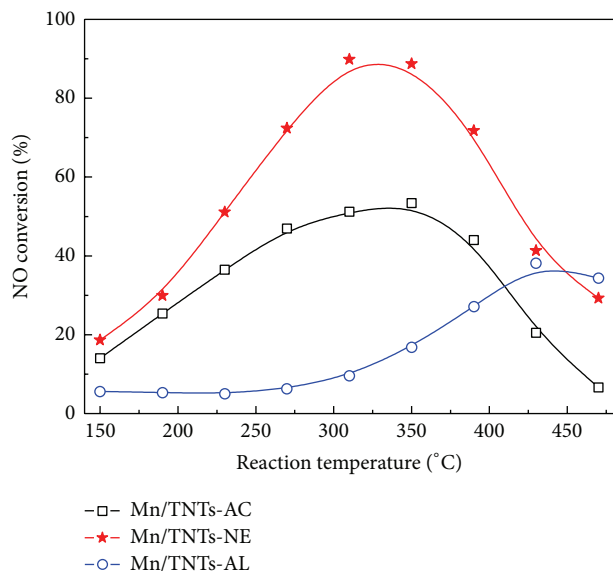


FIGURE 6: Effect of reaction temperature on NO conversion of the Mn/TNTs-AC, Mn/TNTs-NE, and Mn/TNTs-AL catalysts. Reaction conditions: $[NO] = [NH_3] = 600$ ppm, $[O_2] = 3.5\%$, balanced N_2 , catalyst 0.5 g, and GHSV about $100,000$ h^{-1} .

for Mn/TNTs-NE at $300^\circ C$ to $350^\circ C$ reached 90%. The SCR activity of Mn/TNTs-AC is worse in comparison. Even worse, the NO conversion of Mn/TNTs-AL was negligibly low in the main reaction temperature range of $200^\circ C$ to $400^\circ C$.

Based on the above discussions, the composition, dispersion, and redox property of manganese oxides might have affected the SCR activity. Two types of crystal phase for manganese oxides were formed due to different metal-support interaction. MnO_2 was observed in Mn/TNTs-AC and Mn/TNTs-NE, whereas Mn_3O_4 was observed in

Mn/TNTs-AL. It was reported that the SCR activity of MnO_2 was better than Mn_3O_4 [32]. Mn/TNTs-NE possessed the maximum surface area, resulting in the best dispersion of manganese oxides. In addition, partial manganese oxides of Mn/TNTs-NE entered into the tubular channels; thus the redox property of manganese oxides might be tuned and a unique metal-support interaction might occur [5–7], leading to the enhancement of activity. By contrast, Mn/TNTs-AL showed especially low surface area, thus giving rise to the worse dispersion of manganese oxides.

4. Conclusion

Alkaline TNTs, acidic TNTs, and neutral TNTs were synthesized by hydrothermal method with controlled postwashing treatment. Manganese oxides were loaded on these TNTs and used for the SCR of NO with ammonia. TEM images revealed that titanate nanosheets, titanate nanorods, and titanate nanotubes were dominated in Mn/TNTs-AL, Mn/TNTs-AC and Mn/TNTs-NE, respectively. MnO_2 crystal was observed in Mn/TNTs-AC, and Mn/TNTs-NE. Mn_3O_4 and $NaNO_3$, on the other hand, were observed in Mn/TNTs-AL. Among the three catalysts, Mn/TNTs-NE showed the largest surface area, the best dispersion of active species, and the most active redox property of manganese oxides, and thus had the best SCR activity. By contrast, Mn/TNTs-AL showed especially low surface area, Mn_3O_4 -dominating crystal structure, and bad dispersion of manganese oxides and unsurprisingly showed negligible SCR activity.

Acknowledgments

This research was financially supported by the National Natural Science Foundation of China (NSFC-51306068), the Key Laboratory for Water and Air Pollution Control, Guangdong Province (no. 2011A060901002), the Central-Level Nonprofit Scientific Institutes for Basic R&D Operations (PM-zx021-201211-106), and the National High Technology Research and Development Program (863) of China (2012AA062505).

References

- [1] X. Pan and X. Bao, "Reactions over catalysts confined in carbon nanotubes," *Chemical Communications*, no. 47, pp. 6271–6281, 2008.
- [2] D. V. Bavykin, J. M. Friedrich, and F. C. Walsh, "Protonated titanates and TiO_2 nanostructured materials: synthesis, properties, and applications," *Advanced Materials*, vol. 18, no. 21, pp. 2807–2824, 2006.
- [3] X. Pan, Z. Fan, W. Chen, Y. Ding, H. Luo, and X. Bao, "Enhanced ethanol production inside carbon-nanotube reactors containing catalytic particles," *Nature Materials*, vol. 6, no. 7, pp. 507–511, 2007.
- [4] Q. Fu, W.-X. Li, Y. Yao et al., "Interface-confined ferrous centers for catalytic oxidation," *Science*, vol. 328, no. 5982, pp. 1141–1144, 2010.
- [5] W. Chen, X. Pan, M.-G. Willinger, D. S. Su, and X. Bao, "Facile autoreduction of iron oxide/carbon nanotube encapsulates,"

- Journal of the American Chemical Society*, vol. 128, no. 10, pp. 3136–3137, 2006.
- [6] W. Chen, X. Pan, and X. Bao, “Tuning of redox properties of iron and iron oxides via encapsulation within carbon nanotubes,” *Journal of the American Chemical Society*, vol. 129, no. 23, pp. 7421–7426, 2007.
- [7] W. Chen, Z. Fan, X. Pan, and X. Bao, “Effect of confinement in carbon nanotubes on the activity of Fischer-Tropsch iron catalyst,” *Journal of the American Chemical Society*, vol. 130, no. 29, pp. 9414–9419, 2008.
- [8] H. G. Yang, C. H. Sun, S. Z. Qiao et al., “Anatase TiO₂ single crystals with a large percentage of reactive facets,” *Nature*, vol. 453, no. 7195, pp. 638–641, 2008.
- [9] G. Busca, L. Lietti, G. Ramis, and F. Berti, “Chemical and mechanistic aspects of the selective catalytic reduction of NO_x by ammonia over oxide catalysts: a review,” *Applied Catalysis B*, vol. 18, no. 1-2, pp. 1–36, 1998.
- [10] W. Shan, F. Liu, H. He, X. Shi, and C. Zhang, “Novel cerium-tungsten mixed oxide catalyst for the selective catalytic reduction of NO_x with NH₃,” *Chemical Communications*, vol. 47, no. 28, pp. 8046–8048, 2011.
- [11] F. Liu, H. He, and C. Zhang, “Novel iron titanate catalyst for the selective catalytic reduction of NO with NH₃ in the medium temperature range,” *Chemical Communications*, no. 17, pp. 2043–2045, 2008.
- [12] G. Qi and R. T. Yang, “A superior catalyst for low-temperature NO reduction with NH₃,” *Chemical Communications*, no. 7, pp. 848–849, 2003.
- [13] T. Kasuga, M. Hiramatsu, A. Hoson, T. Sekino, and K. Niihara, “Formation of titanium oxide nanotube,” *Langmuir*, vol. 14, no. 12, pp. 3160–3163, 1998.
- [14] H. Wang, X. Chen, X. Weng, Y. Liu, S. Gao, and Z. Wu, “Enhanced catalytic activity for selective catalytic reduction of NO over titanium nanotube-confined CeO₂ catalyst,” *Catalysis Communications*, vol. 12, no. 11, pp. 1042–1045, 2011.
- [15] X. Chen, H. Wang, Z. Wu, Y. Liu, and X. Weng, “Novel H₂Ti₁₂O₂₅-confined CeO₂ catalyst with remarkable resistance to alkali poisoning based on the ‘shell protection effect,’” *The Journal of Physical Chemistry C*, vol. 115, no. 35, pp. 17479–17484, 2011.
- [16] J.-N. Nian, S.-A. Chen, C.-C. Tsai, and H. Teng, “Structural feature and catalytic performance of Cu species distributed over TiO₂ nanotubes,” *The Journal of Physical Chemistry B*, vol. 110, no. 51, pp. 25817–25824, 2006.
- [17] Y. Yao, S.-L. Zhang, Q. Zhong, and X.-X. Liu, “Low temperature selective catalytic reduction of NO over manganese supported on TiO₂ nanotubes,” *Journal of Fuel Chemistry and Technology*, vol. 39, no. 9, pp. 694–701, 2011.
- [18] P. Forzatti, “Present status and perspectives in de-NO_x SCR catalysis,” *Applied Catalysis A*, vol. 222, no. 1-2, pp. 221–236, 2001.
- [19] X. Sun and Y. Li, “Synthesis and characterization of ion-exchangeable titanate nanotubes,” *Chemistry*, vol. 9, no. 10, pp. 2229–2238, 2003.
- [20] C.-C. Tsai and H. Teng, “Structural features of nanotubes synthesized from NaOH treatment on TiO₂ with different post-treatments,” *Chemistry of Materials*, vol. 18, no. 2, pp. 367–373, 2006.
- [21] C.-C. Tsai and H. Teng, “Regulation of the physical characteristics of titania nanotube aggregates synthesized from hydrothermal treatment,” *Chemistry of Materials*, vol. 16, no. 22, pp. 4352–4358, 2004.
- [22] J. Yang, Z. Jin, X. Wang et al., “Study on composition, structure and formation process of nanotube Na₂Ti₂O₄(OH)₂,” *Dalton Transactions*, no. 20, pp. 3898–3901, 2003.
- [23] B. D. Yao, Y. F. Chan, X. Y. Zhang, W. F. Zhang, Z. Y. Yang, and N. Wang, “Formation mechanism of TiO₂ nanotubes,” *Applied Physics Letters*, vol. 82, no. 2, pp. 281–283, 2003.
- [24] H. Y. Zhu, Y. Lan, X. P. Gao et al., “Phase transition between nanostructures of titanate and titanium dioxides via simple wet-chemical reactions,” *Journal of the American Chemical Society*, vol. 127, no. 18, pp. 6730–6736, 2005.
- [25] H. Zhu, X. Gao, Y. Lan, D. Song, Y. Xi, and J. Zhao, “Hydrogen titanate nanofibers covered with anatase nanocrystals: a delicate structure achieved by the wet chemistry reaction of the titanate nanofibers,” *Journal of the American Chemical Society*, vol. 126, no. 27, pp. 8380–8381, 2004.
- [26] D. V. Bavykin, M. Carravetta, A. N. Kulak, and F. C. Walsh, “Application of magic-angle spinning NMR to examine the nature of protons in titanate nanotubes,” *Chemistry of Materials*, vol. 22, no. 8, pp. 2458–2465, 2010.
- [27] J. Liu, Y. Liu, Z. Wu, X. Chen, H. Wang, and X. Weng, “Polyethyleneimine functionalized protonated titanate nanotubes as superior carbon dioxide adsorbents,” *Journal of Colloid and Interface Science*, vol. 386, no. 1, pp. 392–397, 2012.
- [28] K. S. W. Sing, “Reporting physisorption data for gas/solid systems with special reference to the determination of surface-area and porosity,” *Pure and Applied Chemistry*, vol. 54, no. 11, pp. 2201–2218, 1982.
- [29] X. Chen, S. Cao, X. Weng, H. Wang, and Z. Wu, “Effects of morphology and structure of titanate supports on the performance of ceria in selective catalytic reduction of NO,” *Catalysis Communications*, vol. 26, pp. 178–182, 2012.
- [30] M. Pourkhalil, A. Z. Moghaddam, A. Rashidi, J. Towfighi, and Y. Mortazavi, “Preparation of highly active manganese oxides supported on functionalized MWNTs for low temperature NO_x reduction with NH₃,” *Applied Surface Science*, vol. 279, pp. 250–259, 2013.
- [31] K. Zhuang, J. Qiu, F. Tang, B. Xu, and Y. Fan, “The structure and catalytic activity of anatase and rutile titania supported manganese oxide catalysts for selective catalytic reduction of NO by NH₃,” *Physical Chemistry Chemical Physics*, vol. 13, no. 10, pp. 4463–4469, 2011.
- [32] L. Wang, B. Huang, Y. Su et al., “Manganese oxides supported on multi-walled carbon nanotubes for selective catalytic reduction of NO with NH₃: catalytic activity and characterization,” *Chemical Engineering Journal*, vol. 192, pp. 232–241, 2012.

Research Article

Mechanical and Morphological Properties of Poly-3-hydroxybutyrate/Poly(butyleneadipate-co-terephthalate)/Layered Double Hydroxide Nanocomposites

Yen Leng Pak,¹ Mansor Bin Ahmad,¹ Kamyar Shameli,^{1,2} Wan Md Zin Wan Yunus,³ Nor Azowa Ibrahim,¹ and Norhazlin Zainuddin¹

¹ Department of Chemistry, Faculty of Science, Universiti Putra Malaysia, 43400 Serdang, Selangor, Malaysia

² Nanotechnology and Advance Department, Materials and Energy Research Center, Meshkin-Dasht Road, Karaj 3177983634, Iran

³ Faculty of Defence Science and Technology, National Defence University of Malaysia, Sungai Besi Camp, 57000 Kuala Lumpur, Malaysia

Correspondence should be addressed to Mansor Bin Ahmad; mansorahmad@gmail.com and Kamyar Shameli; kamyarshameli@gmail.com

Received 1 September 2013; Revised 1 November 2013; Accepted 5 November 2013

Academic Editor: Haiqiang Wang

Copyright © 2013 Yen Leng Pak et al. This is an open access article distributed under the Creative Commons Attribution License, which permits unrestricted use, distribution, and reproduction in any medium, provided the original work is properly cited.

Nanocomposites of poly-3-hydroxybutyrate/poly(butyleneadipate-co-terephthalate)/layered double hydroxide (PHB/PBAT/LDH) were prepared from a binary blend of PHB/PBAT and stearate-Zn₃Al LDH via a solution casting method using chloroform as solvent in this study. The pristine Zn₃Al LDH was synthesized from nitrate salts solution at pH 7 by using coprecipitation technique and then was modified by stearate anions surfactant via ion exchange reaction. As a result, the basal spacing of the LDH was increased from 8.77 to 24.94 Å after the modification. Intercalated nanocomposites were formed due to the presence of diffraction peak in XRD diffractograms. The infrared spectrum of stearate-Zn₃Al LDH exhibited the existence of stearate anions in the synthesized Zn₃Al LDH. Mechanical properties with 2 wt% stearate-Zn₃Al LDH loading nanocomposites showed 56 wt% improvements in elongation at break compared to those of the blend.

1. Introduction

Great contributions have been made by introducing polymers into the market to enhance the grade of living and lifestyle. Plastics are being used throughout the world. Plastics are extremely important to the job market especially packaging field. Production of ecofriendly plastics that are more compatible with the environment is needed since plastics created ecological concern due to the lack of deprivation. Therefore, biodegradable plastics began being of sparking interest. Creating of biodegradable materials draw high attention as oil prices increased and they are considered to assist in reducing the waste issue.

Poly-3-hydroxybutyrate (PHB) is produced by controlled bacterial fermentation [1]. It is a high melting temperature and a high degree of crystallinity of semicrystalline polymer. It is not soluble in water and 100% biodegraded. PHB has a few points of weakness that limited its applications such as inefficient and high cost of the fermentation and extraction process, poor mechanical properties, and poor formability. Cracking and brittleness properties of PHB are because of the large spherulites in its structure. Efforts have been made by worldwide researchers to overcome those problems and to improve different properties. The most cost effective and generally used method is blending of PHB with another kind of polymers, [2–5] such as starch, polycaprolactone (PCL),

poly (vinyl acetate) (PVAc), and cellulose derivatives which have been studied to modify the properties and expand its practical application [6–8].

Poly (butylene adipate-co-terephthalate) (PBAT) is eco-friendly polymers which totally biodegraded with the assist of naturally occurring enzymes in a few weeks. It has the same properties as low density polyethylene (LDPE), but with superior mechanical properties. Its excellent physical properties give high flexibility when blended with other biodegradable resins. As a result, PBAT is an excellent candidate for toughening polymers such as poly (lactic acid) and PHBV [9].

Inorganic-organic nanocomposite materials with functional organic compounds immobilized into a layered inorganic matrix have a potential to offer scientific and technological advantages since the organized two-dimensional arrays of organic species between the interlayers can result in novel functions that are different from the typical functions of the individual organic species [10–17].

An electrostatic layer-by-layer assembly technique that employs inorganic nanocomposites as building blocks is a possible means of forming a well-ordered multilayered architecture containing the arrays because the nanocomposites have ultimate two-dimensional anisotropy with nanoscale thickness and microscale length in the plane of sheet [18]. It is known that some smectite clay minerals like montmorillonite, metal phosphates, and layered oxides can be exfoliated into negatively charged nanosheets [19]. In contrast, positively charged nanosheets are a minority among exfoliated nanosheets. Recently, the exfoliation of layered double hydroxides (LDHs) has been studied as a method of preparing such positively charged nanosheets [20]. LDH nanosheets have high potential for being used as building blocks to integrate negatively charged organic molecules into restricted arrays, due to their high stability and compatibility with many functional molecules [21–24].

Layered double hydroxide (LDH) is one of the attractive choices as nanofiller which have significantly improved the physicochemical properties of polymer matrix. In contrast to either neat polymer or the conventional composites, polymer nanocomposites are characterized by improved mechanical, thermal, and barrier properties, reduced gas permeability, and flame retardancy [25–28]. Improvement in properties of the nanocomposites is related to their unique phase morphology that maximizes the interfacial interaction between the well-dispersed nanometer size domains and the matrices. LDH has received world-wide attention because they are useful to be incorporated in many applications, such as catalysis, stabilizer, flame retardant materials, medical materials, adsorbents, ion exchangers, and in environmental chemistry [29].

In this research, our aims are to investigate the influences of stearate- Zn_3Al LDH nanolayers on the tensile properties and morphology of PHB/PBAT blends.

2. Experimental Section

2.1. Materials. Poly [(r)-3-hydroxybutyric acid] was purchased from Sigma-aldrich, Germany, in powder form.

Poly (butylenes adipate-co-terephthalate), PBAT, trade name ECOFLEX, F BX 7011, was supplied by BASF Plastic Technologies, USA. Zinc nitrate ($Zn(NO_3)_2 \cdot 6H_2O$) was supplied by Bendosen Laboratory Chemicals, Norway. Aluminium nitrate ($Al(NO_3)_3 \cdot 9H_2O$) was supplied by Hmbg Chemicals, Germany. All the chemicals were used as received without further purification process.

2.2. Synthesis of Zn_3Al LDH. The Zn_3Al LDH was synthesized via coprecipitation by adding dropwise a solution of NaOH (1M) into a 250 mL solution of 22.30 g $Zn(NO_3)_2 \cdot 6H_2O$ and 9.38 g $Al(NO_3)_3 \cdot 9H_2O$ with the mole ratio of 3 : 1 until pH 7 was obtained. The solution was stirred vigorously under nitrogen atmosphere in order to minimize any contamination of carbonate from the air. At 100 rpm and 70°C, the resulting suspension was shaken for 16 hours. The slurry was filtered and washed several times with deionized water. The Zn_3Al LDH was obtained after being dried at 60°C for 24 hours.

2.3. Preparation of Stearate- Zn_3Al LDH. The stearate- Zn_3Al LDH was prepared by replacing nitrate ions in the LDH layers with stearate ions using the following method. One gram of dry Zn_3Al LDH was dispersed into 1L of 0.003 M sodium stearate solution. The solution was stirred for 24 hours and aged at 70°C in water bath. The slurry was filtered and washed several times with deionized water and dried at 60°C. The dried sample was ground and sieved into particles which were less than 100 micrometer. This chemical modification method already reported by Costantino et al. [30].

2.4. Preparation of PHB/PBAT/Stearate- Zn_3Al LDH Nanocomposites. The nanocomposites of PHB/PBAT blend and stearate- Zn_3Al LDH were prepared by a solution casting method. The blend composition was kept constant (PHB 90 wt% + PBAT 30 wt%) whereas the stearate- Zn_3Al LDH content was varied between 0 wt% and 5 wt%. Desired amount of stearate- Zn_3Al LDH and blend were measured and transferred into 50 mL of chloroform. Both mixtures were stirred for 1 h, mixed, and stirred for another 1 h. The mixture was casted in a petri dish and left in fume cupboard for few days to obtain the sample sheets.

2.5. Characterization Techniques. X-ray diffraction (XRD) measurement for LDHs and nanocomposites were carried out by using Shimadzu XRD 6000 diffractometer at 30 kV and 30 mA with Cu-K α radiation of the wavelength of 1.5405 nm in 2θ range from 2 to 30°. Fourier-transform infrared (FTIR) spectra of the materials were recorded using a Perkin Elmer Spectrum 1000 series Spectrophotometer equipped with attenuated total reflectance (ATR). The infrared spectra of the samples were recorded in the range of frequency of 400–4,000 cm^{-1} . Scanning electron microscopy (SEM) images were obtained using a Philips XL30 ESEM scanning electron microscope operated at 20 kV. The samples were coated with gold by a Bio-Rad coating system before viewing. Tensile tests were carried out by a Universal Testing Machine, Instron 4302, according to ASTM D638-5. The samples were cut into

dumbbell shape and the average of thickness and width were measured. The average of at least 5 measurements of tensile test was used in calculation.

3. Results and Discussion

3.1. Characterization of Zn_3Al LDH and Stearate- Zn_3Al LDH.

Figure 1 illustrates the XRD patterns for the pristine and stearate- Zn_3Al LDH in the range of 2θ from 2 to 30° . Both LDHs were crystalline in nature with definite and distinct of layered structure. By using Bragg's equation, $n\lambda = 2d \times \sin \theta$, the first diffraction peak from both pristine and stearate- Zn_3Al LDH was used to calculate the basal spacing (d). The clay interlayer spacing was increased from 8.77 Å in pristine LDH (corresponding 2θ value of $\langle 003 \rangle$ peak is 10.08°) to 24.94 Å in stearate- Zn_3Al LDH ($2\theta = 3.54^\circ$) after the modification of pristine LDH with stearate ions. The increase of the basal spacing indicates that the stearate anions were intercalated into the interlayers of LDH successfully [25].

FTIR spectra of the pristine Zn_3Al LDH and stearate- Zn_3Al LDH are exposed in Figure 2. The broad absorption peak observed was at around 3398 cm^{-1} in pristine LDH for O–H stretching of both hydroxide layers and interlayer water molecules [26]. An intense peak observed at 1340 cm^{-1} is due to the asymmetric and symmetric vibration of the nitrate anions in Figure 2(a) [27]. At about 1639 cm^{-1} , the interlayer water of stretching vibration (H–OH) can be obtained. The lattice vibration bands of the M–O and O–M–O (M = Mg or Al) bonding are present at below 800 cm^{-1} region.

At the same time, the stearate- Zn_3Al LDH spectrum (Figure 2(b)) shows the peak at around 2850 and 2917 cm^{-1} which exhibits the C–H stretching vibration due to appearance of the $-\text{CH}_3$ and $-\text{CH}_2$ group in the chain of stearate anions [29]. Carboxylate asymmetric and symmetric stretching is represented by two intense absorption peaks at 1546 cm^{-1} and 1409 cm^{-1} , respectively [31]. It can be concluded that spectrum of the stearate- Zn_3Al LDH and pristine Zn_3Al LDH contains many similar major peaks. Surface morphology of the pristine Zn_3Al LDH and modified stearate- Zn_3Al LDH particles are shown in Figure 3. As shown in Figure 3, the clay is received as porous particles in the existence of the organic anions [26].

3.2. Characterization of PHB/PBAT/Stearate- Zn_3Al LDH.

XRD patterns for pure PHB, pure PBAT, PHB/PBAT blend, and PHB/PBAT/LDH nanocomposites are shown in Figure 4. The peaks obtained in the diffraction patterns of the pure films of PHB and PBAT also appeared in PHB/PBAT blends. The diffraction pattern of polymer blend displayed distinct peaks (2θ) at 13.18° , 16.48° , 19.76° , 21.96° , 25.36° , and 26.90° , which correspond to the (020), (110), (101), (111), (121), and (002) reflections of the orthorhombic crystalline lattice, respectively. The diffraction peaks remain practically unchanged in PHB/PBAT nanocomposites diffractograms can be observed. This observation suggested that the polymer blend crystalline lattice is not modified appreciably in the existence of LDH [32].

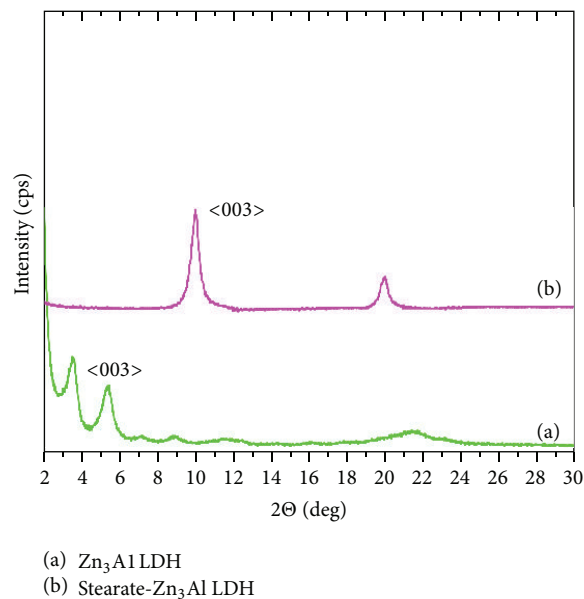


FIGURE 1: XRD pattern of (a) pristine Zn_3Al LDH and (b) stearate- Zn_3Al LDH.

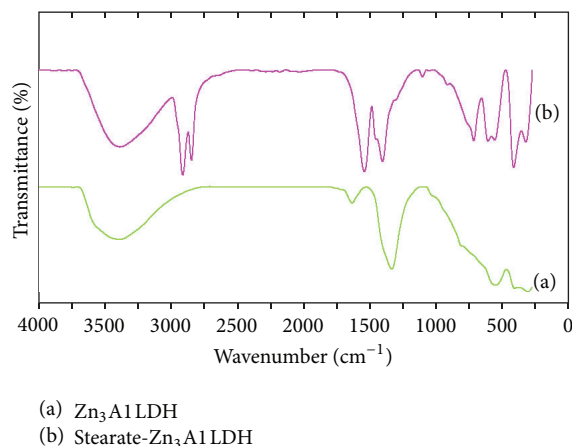


FIGURE 2: FTIR spectra for (a) pristine Zn_3Al LDH and (b) stearate- Zn_3Al LDH.

The presence of the diffraction peak in the PHB/PBAT/LDH nanocomposites with 1.0, 2.0, 3.0, 4.0, or 5.0 wt% of the LDH indicated that the stearate- Zn_3Al LDH layers were completely intercalated in the blend matrix. The interlayer spacings for 1.0, 2.0, 3.0, 4.0, or 5.0 wt% of the LDH in polymer blend were 41.25 Å, 43.70 Å, 40.87 Å, and 40.49 Å, respectively.

The FTIR spectra of PHB, PBAT, PHB/PBAT blend, and PHB/PBAT/stearate- Zn_3Al LDH nanocomposites are shown in Figure 5. The C=O stretching bands of PHB are located at 1719 cm^{-1} , with shoulders at about 1740 cm^{-1} , which are representative of PHB crystalline and amorphous

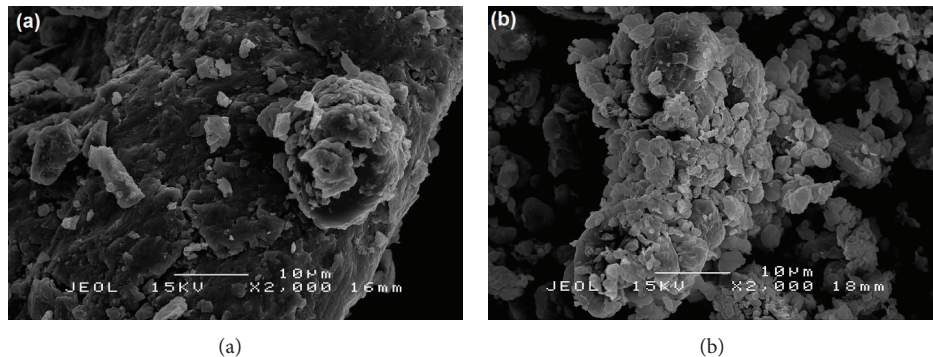


FIGURE 3: Scanning electron micrographs of (a) pristine Zn_3Al LDH and (b) stearate- Zn_3Al LDH.

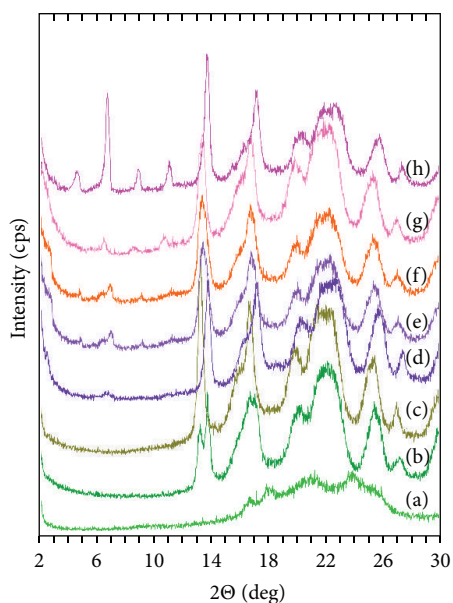


FIGURE 4: XRD pattern for (a) pure PBAT, (b) pure PHB, (c) PHB/PBAT blend, and nanocomposites of 1.0, 2.0, 3.0, 4.0, and 5 wt% of stearate- Zn_3Al LDH (d-h).

zone. Meanwhile, the major peak observed was at 1712 cm^{-1} for C=O stretching and 1475 cm^{-1} for aromatic C=C stretching in PBAT chains. The spectra of PHB/PBAT blend and PHB/PBAT/stearate- Zn_3Al LDH are consistent with the combination of PHB and PBAT. No major peak shifting and no new peak formation in the blend and nanocomposites spectra indicate that there is no strong interaction among PHB, PBAT, and stearate- Zn_3Al LDH.

The tensile properties of PHB, PHB/PBAT blend, and PHB/PBAT/LDH nanocomposites were shown in Figures 6 and 7. The tensile strength of neat PHB was 25.54 MPa and decreased to 23.10 MPa with the addition of 10 wt% of PBAT. The tensile strength decreased again as the PBAT contents increase up to 50 wt%. This observation was shown

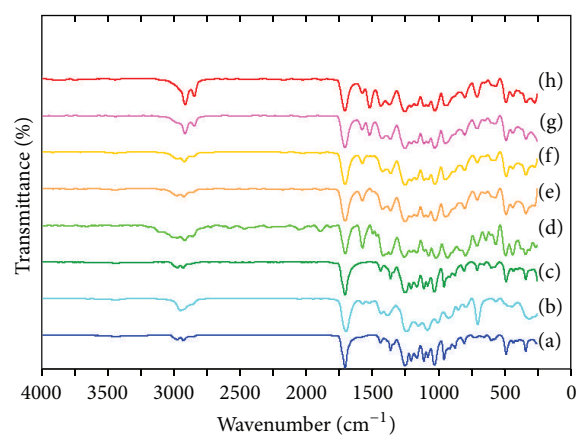


FIGURE 5: FTIR spectra for (a) pure PHB, (b) pure PBAT, (c) PHB/PBAT blend, and nanocomposites of PHB/PBAT with 1.0, 2.0, 3.0, 4.0, and 5 wt% of stearate- Zn_3Al LDH (d-h).

in Figure 6(a). The effect of the amount of PBAT on tensile modulus and elongation at break for PHB/PBAT composites were shown in Figures 6(b)-6(c), respectively. The tensile modulus and elongation at break increased with the loading of 10 wt% of PBAT content as compared to neat PHB. However, they were decreased thereafter as shown in Figures 6(b)-6(c). It was indicated that PBAT is able to enhance the elasticity of PHB. However, incorporation of more than 20 wt% PBAT content deteriorates the properties of the final products. As a result, PHB/PBAT blend with 90/10 ratio was chosen as the best ratio among others.

Figure 7(a) shows that addition of 1 wt% of stearate- Zn_3Al LDH into PHB/PBAT blend decreased the tensile strength to 19.62 MPa. Further increase in the stearate- Zn_3Al LDH decreased the tensile strength too as compared to that blend. The tensile strength for 2.0, 3.0, 4.0, and 5.0 wt% of the LDH in polymer blend was 18.17, 18.13, 18.70, and 19.60 MPa, respectively. It may be due to the extended aggregation of LDH layer into the blend matrix [31]. Figure 7(b) shows

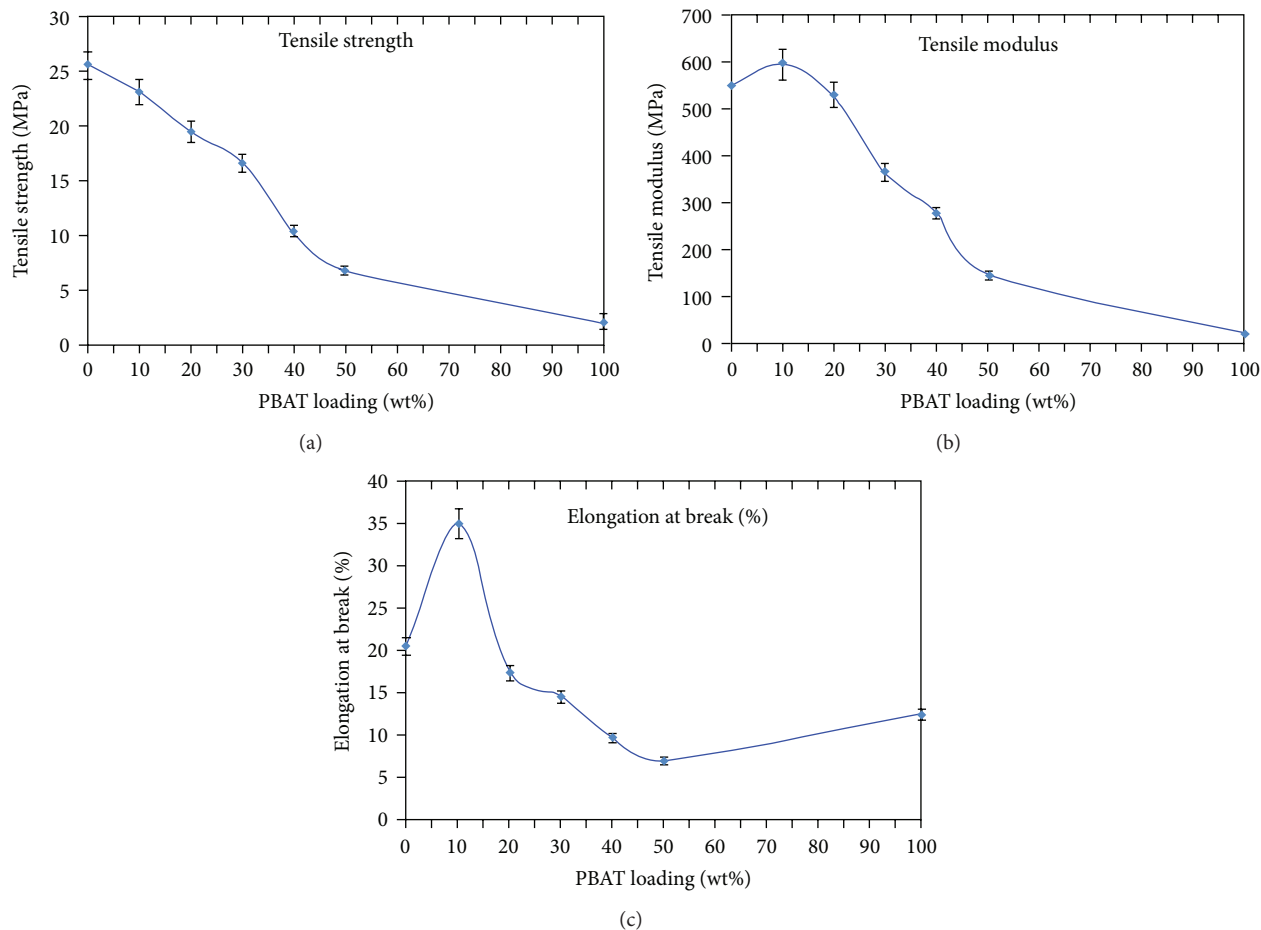


FIGURE 6: Tensile strength, tensile modulus, and elongation at break for PHB/PBAT blends (a-c).

that tensile modulus for nanocomposites also decreased as compared to the blend.

Adding 2.0 wt% LDH into the polymer blend increased the elongation at break from 35.03% up to 54.58%, with an improvement of 56% compared to that of the unfilled PHB/PBAT blend in Figure 7(c). The significant increase in the flexibility of the nanocomposites may be due to the presence of the long chain hydrocarbon parts of stearate anions in the modified LDH that act as a plasticizer. The elongations at break for 1.0, 3.0, 4.0, and 5.0 wt% nanocomposites were 38.55, 25.15, 10.10, and 9.53%, respectively. Decreasing trend of elongation at break can be observed after further addition of 3.0 to 5.0 wt% of LDH. It may be due to the presence of large agglomerates which make the nanocomposites more brittle, decrease of elongation at break consequently.

Figure 8 shows SEM micrographs obtained from the tensile fracture surfaces of PHB/PBAT blend and its nanocomposites containing 2.0 wt% of stearate- Zn_3Al LDH. The image of the fractured surface of the PHB/PBAT blend sample (Figure 8(a)) shows a relatively compact solid surface indicating that the sample is brittle while the images of the 2.0 wt% nanocomposites (Figure 8(b)) show the rough and stretched surfaces which support the reduction of the rigidity of the samples.

The dispersion of stearate- Zn_3Al LDH in the composites was observed by TEM as shown in Figure 9 which presented PHB/PBAT nanocomposites with 2.0 wt% loading of stearate- Zn_3Al LDH. The dark parts of the micrograph were the stearate- Zn_3Al LDH while PHB/PBAT matrix was represented by the clear parts. The TEM images of 2.0 wt% of LDH/PHB/PBAT nanocomposites confirmed that the intercalated silicate layers that were well distributed can be observed in PHB/PBAT as suggested by XRD diffractogram. The figures clearly show that the stack consists of several silicates layers, which indicated the formation of intercalated nanocomposites. The result supported by basal reflection in XRD diffractogram which confirmed the intercalated type of nanocomposites was formed. The TEM image revealed that the LDH layers are in intercalated but not well-ordered structure form and dominantly distributed in the PHB/PBAT matrix.

4. Conclusions

Stearate- Zn_3Al LDH was successfully prepared via ion exchange reaction. The presence of alkyl group in FTIR spectrum indicated that the stearate anions were

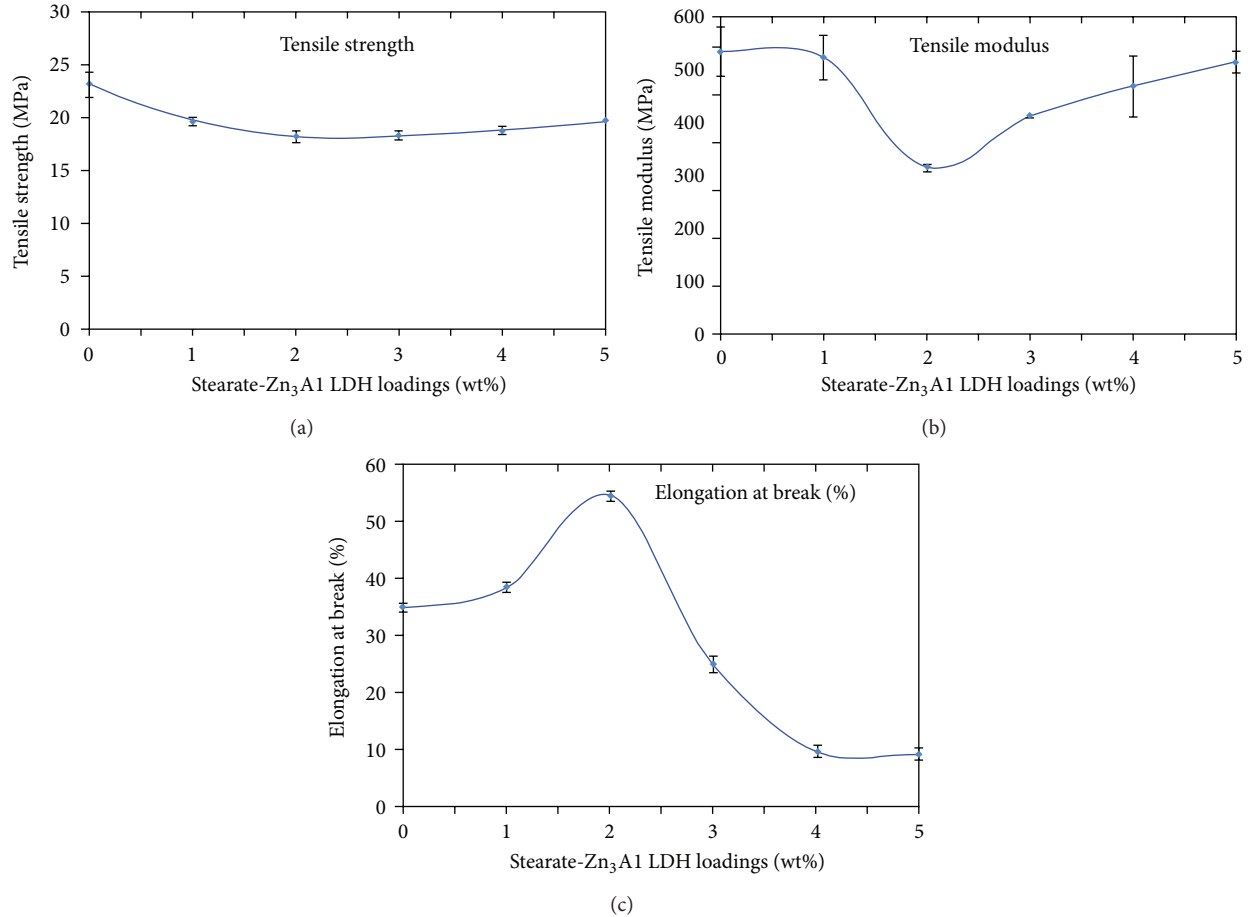


FIGURE 7: Tensile strength, tensile modulus, and elongation at break of PHB/PBAT blends with different stearate-Zn₃Al LDH content (a–c).

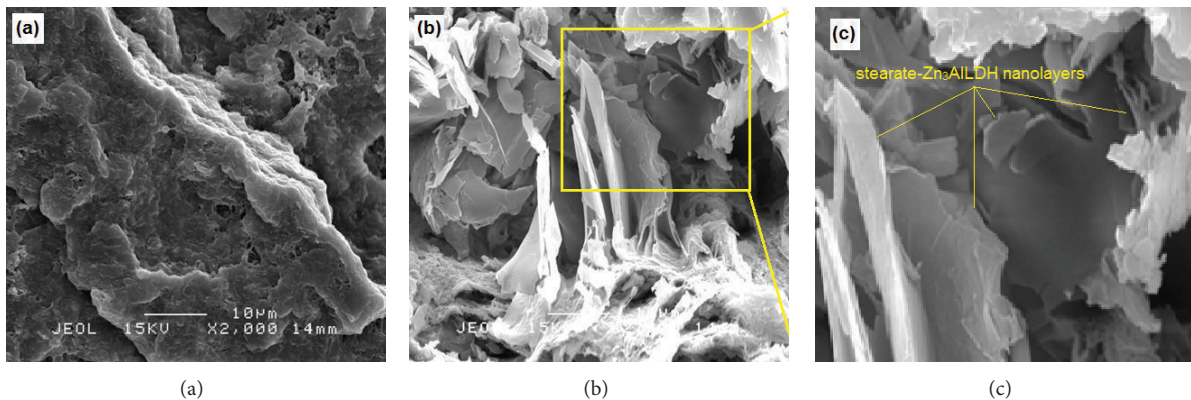


FIGURE 8: Scanning electron micrograph of (a) PHB/PBAT blend and (b, c) 2.0 wt% nanocomposites with low and high resolutions.

successfully intercalated into pristine LDH. The X-ray diffraction (XRD) patterns showed that the basal spacing of stearate-Zn₃Al LDH was higher than that of the pristine LDH. PHB/PBAT nanocomposites were successfully prepared with modified stearate-Zn₃Al LDH through solution casting method. The XRD and TEM showed that the PHB/PBAT/stearate-Zn₃Al LDH formed intercalated

structure as the modified stearate-Zn₃Al LDH content increased thus facilitating better compatibility of PHB/PBAT between the galleries of LDH. Mechanical analyses of nanocomposites showed that adding 2.0 wt% SLDH into the polymer blend increases the elongation at break from 35.03% up to 54.58%, with an improvement of 56% compared to that of the neat PHB/PBAT blend.

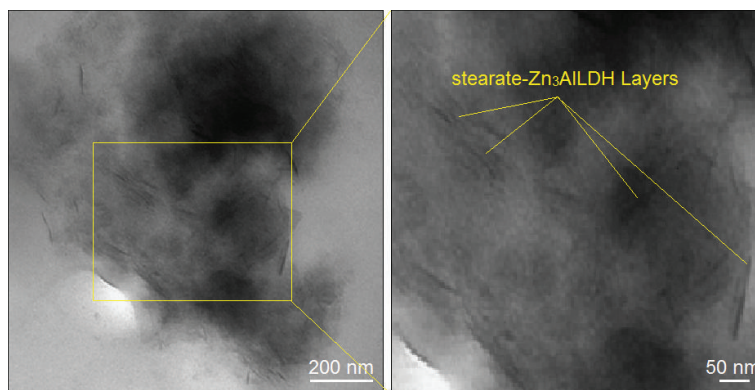


FIGURE 9: TEM micrographs of PHB/PBAT/2.0 wt% stearate- Zn_3Al LDH.

Conflict of Interests

The authors declare that there is no conflict of interests.

Acknowledgments

The authors would like to acknowledge the financial support from the Universiti Putra Malaysia (UPM) (RUGS Project no. 9199840). The authors are also grateful to the staff of the Department of Chemistry UPM and the Institute of Bioscience UPM for the technical assistance.

References

- [1] W. S. Ahn, S. J. Park, and S. Y. Lee, "Production of poly(3-hydroxybutyrate) by fed-batch culture of recombinant escherichia coli with a highly concentrated whey solution," *Applied and Environmental Microbiology*, vol. 66, no. 8, pp. 3624–3627, 2000.
- [2] S. Godbole, S. Gote, M. Latkar, and T. Chakrabarti, "Preparation and characterization of biodegradable poly-3-hydroxybutyrate-starch blend films," *Bioresource Technology*, vol. 86, no. 1, pp. 33–37, 2003.
- [3] L. H. Innocentini-Mei, J. R. Bartoli, and R. C. Baltieri, "Mechanical and thermal properties of poly(3-hydroxybutyrate) blends with starch and starch derivatives," *Macromolecular Symposia*, vol. 197, pp. 77–87, 2003.
- [4] F. Gassner and A. J. Owen, "Physical properties of poly(β -hydroxybutyrate)-poly(ϵ -caprolactone) blends," *Polymer*, vol. 35, no. 10, pp. 2233–2236, 1994.
- [5] D. Lovera, L. Márquez, V. Balsamo, A. Taddei, C. Castelli, and A. J. Müller, "Crystallization, morphology, and enzymatic degradation of polyhydroxybutyrate/polycaprolactone (PHB/PCL) blends," *Macromolecular Chemistry and Physics*, vol. 208, no. 9, pp. 924–937, 2007.
- [6] K. Fukushima, C. Abbate, D. Tabuani, M. Gennari, and G. Camino, "Biodegradation of poly(lactic acid) and its nanocomposites," *Polymer Degradation and Stability*, vol. 94, no. 10, pp. 1646–1655, 2009.
- [7] A. El-Hadi, R. Schnabel, E. Straube, G. Muller, and M. Riemschneider, "Effect of melt processing on crystallization behavior and rheology of poly (3-hydroxybutyrate) (PHB) and its blends," *Macromolecular Materials and Engineering*, vol. 287, pp. 363–372, 2002.
- [8] M. Eili, K. Shameli, N. A. Ibrahim, and W. M. Z. Wan Yunus, "Degradability enhancement of poly(lactic acid) by stearate- Zn_3Al LDH nanolayers," *International Journal of Molecular Sciences*, vol. 13, pp. 7938–7951, 2012.
- [9] M. Yamaguchi and K. Arakawa, "Control of structure and mechanical properties for binary blends of poly(3-hydroxybutyrate) and cellulose derivative," *Journal of Applied Polymer Science*, vol. 103, no. 5, pp. 3447–3452, 2007.
- [10] M. B. Ahmad, K. Shameli, W. M. Z. W. Yunus, N. A. Ibrahim, and M. Darroudi, "Synthesis and characterization of Silver/Clay/Starch bionanocomposites by green method," *Australian Journal of Basic and Applied Sciences*, vol. 4, no. 7, pp. 2158–2165, 2010.
- [11] M. B. Ahmad, K. Shameli, M. Darroudi, W. M. Z. W. Yunus, and N. A. Ibrahim, "Synthesis and characterization of silver/clay nanocomposites by chemical reduction method," *American Journal of Applied Sciences*, vol. 6, no. 11, pp. 1909–1914, 2009.
- [12] M. B. Ahmad, M. Y. Tay, K. Shameli, M. Z. Hussein, and J. J. Lim, "Green synthesis and characterization of silver/chitosan/polyethylene glycol nanocomposites without any reducing agent," *International Journal of Molecular Sciences*, vol. 12, no. 8, pp. 4872–4884, 2011.
- [13] K. Shameli, M. B. Ahmad, S. D. Jazayeri, P. Shabanzadeh, P. Sangpour, and H. Jahangirian, "Investigation of antibacterial properties silver nanoparticles prepared via green method," *Chemistry Central Journal*, vol. 6, no. 1, pp. 1–10, 2012.
- [14] K. Shameli, M. B. Ahmad, E. A. Jaffar Al-Mulla, N. A. Ibrahim, and P. Shabanzadeh, "Green biosynthesis of silver nanoparticles using *Callicarpa maingayi* stem bark extraction," *Molecules*, vol. 17, no. 7, pp. 8506–8517, 2012.
- [15] K. Shameli, M. B. Ahmad, S. D. Jazayeri, and P. Shabanzadeh, "Synthesis and characterization of polyethylene glycol mediated silver nanoparticles by the green method," *International Journal of Molecular Sciences*, vol. 13, no. 6, pp. 6639–6650, 2012.
- [16] K. Shameli, M. B. Ahmad, A. Zamanian et al., "Green biosynthesis of silver nanoparticles using *Curcuma longa* tuber powder," *International Journal of Nanomedicine*, vol. 7, pp. 5603–5610, 2012.
- [17] M. B. Ahmad, J. J. Lim, K. Shameli, N. A. Ibrahim, and M. Y. Tay, "Synthesis of silver nanoparticles in chitosan, gelatin and chitosan/gelatin bionanocomposites by a chemical reducing agent and their characterization," *Molecules*, vol. 16, no. 9, pp. 7237–7248, 2011.

- [18] S. Srivastava and N. A. Kotov, "Composite Layer-by-Layer (LBL) assembly with inorganic nanoparticles and nanowires," *Accounts of Chemical Research*, vol. 41, no. 12, pp. 1831–1841, 2008.
- [19] S. J. Ahmadi, Y. D. Huang, and W. Li, "Synthetic routes, properties and future applications of polymer-layered silicate nanocomposites," *Journal of Materials Science*, vol. 39, no. 6, pp. 1919–1925, 2004.
- [20] T. Hibino and W. Jones, "New approach to the delamination of layered double hydroxides," *Journal of Materials Chemistry*, vol. 11, no. 5, pp. 1321–1323, 2001.
- [21] S. H. Cypes, W. M. Saltzman, and E. P. Giannelis, "Organo-silicate-polymer drug delivery systems: controlled release and enhanced mechanical properties," *Journal of Controlled Release*, vol. 90, no. 2, pp. 163–169, 2003.
- [22] J. Zhu, F. M. Uhl, A. B. Morgan, and C. A. Wilkie, "Studies on the mechanism by which the formation of nanocomposites enhances thermal stability," *Chemistry of Materials*, vol. 13, no. 12, pp. 4649–4654, 2001.
- [23] V. Bugatti, U. Costantino, G. Gorrasi, M. Nocchetti, L. Tamaro, and V. Vittoria, "Nano-hybrids incorporation into poly(ϵ -caprolactone) for multifunctional applications: mechanical and barrier properties," *European Polymer Journal*, vol. 46, no. 3, pp. 418–427, 2010.
- [24] A. Szép, A. Szabó, N. Tóth, P. Anna, and G. Marosi, "Role of montmorillonite in flame retardancy of ethylene-vinyl acetate copolymer," *Polymer Degradation and Stability*, vol. 91, no. 3, pp. 593–599, 2006.
- [25] F. R. Costa, A. Leuteritz, U. Wagenknecht, D. Jehnichen, L. Häußler, and G. Heinrich, "Intercalation of Mg-Al layered double hydroxide by anionic surfactants: preparation and characterization," *Applied Clay Science*, vol. 38, no. 3-4, pp. 153–164, 2008.
- [26] E. Mahboobeh, W. M. Z. W. Yunus, Z. Hussein, M. Ahmad, and N. A. Ibrahim, "Flexibility improvement of poly(lactic acid) by stearate-modified layered double hydroxide," *Journal of Applied Polymer Science*, vol. 118, no. 2, pp. 1077–1083, 2010.
- [27] Y. Ding, Z. Gui, J. Zhu, Y. Hu, and Z. Wang, "Exfoliated poly(methyl methacrylate)/MgFe-layered double hydroxide nanocomposites with small inorganic loading and enhanced properties," *Materials Research Bulletin*, vol. 43, no. 12, pp. 3212–3220, 2008.
- [28] F. Leroux and J. Besse, "Polymer interleaved layered double hydroxide: a new emerging class of nanocomposites," *Chemistry of Materials*, vol. 13, no. 10, pp. 3507–3515, 2001.
- [29] J. Liu, G. Chen, and J. Yang, "Preparation and characterization of poly(vinyl chloride)/layered double hydroxide nanocomposites with enhanced thermal stability," *Polymer*, vol. 49, no. 18, pp. 3923–3927, 2008.
- [30] U. Costantino, F. Marmottini, M. Nocchetti, and R. Vivani, "New synthetic routes to hydrotalcite-like compounds—characterisation and properties of the obtained materials," *European Journal of Inorganic Chemistry*, no. 10, pp. 1439–1446, 1998.
- [31] H.-B. Hsueh and C.-Y. Chen, "Preparation and properties of LDHs/polyimide nanocomposites," *Polymer*, vol. 44, no. 4, pp. 1151–1161, 2003.
- [32] R. M. Da Silva Moreira Thiré, L. C. Arruda, and L. S. Barreto, "Morphology and thermal properties of poly(3-hydroxybutyrate-co-3-hydroxyvalerate)/attapulgite nanocomposites," *Materials Research*, vol. 14, no. 3, pp. 340–344, 2011.

Research Article

A Novel Synthesis Method of Porous Calcium Silicate Hydrate Based on the Calcium Oxide/Polyethylene Glycol Composites

Wei Guan, Fangying Ji, Yong Cheng, Zhuoyao Fang, Dexin Fang, Peng Yan, and Qingkong Chen

Key Laboratory of Three Gorges Reservoir Region's Eco-Environment, Ministry of Education, Chongqing University, Chongqing 400045, China

Correspondence should be addressed to Fangying Ji; jfytougao@163.com

Received 9 August 2013; Revised 1 September 2013; Accepted 2 September 2013

Academic Editor: Fan Dong

Copyright © 2013 Wei Guan et al. This is an open access article distributed under the Creative Commons Attribution License, which permits unrestricted use, distribution, and reproduction in any medium, provided the original work is properly cited.

This paper proposed a novel method to prepare porous calcium silicate hydrate (CSH) based on the calcium oxide/polyethylene glycol (CaO/PEG₂₀₀₀) composites as the calcium materials. The porosity formation mechanism was revealed via X-ray diffraction (XRD), field-emission scanning electron microscopy (FESEM), Brunauer-Emmett-Teller (BET), and Fourier transformed infrared spectroscopy (FT-IR). The reactivity of silica materials (SiO₂) enhanced by increasing pH value. Ca²⁺ could not sustain release from CaO/PEG₂₀₀₀ and reacted with SiO₃²⁻ caused by silica to form CSH until the hydrothermal temperature reached to 170°C, avoiding the hardly dissolved intermediates formation efficiently. The as-prepared CSH, due to the large specific surface areas, exhibited excellent release capability of Ca²⁺ and OH⁻. This porous CSH has potential application in reducing the negative environmental effects of continual natural phosphate resource depletion.

1. Introduction

Phosphate, as an irreplaceable and nonrenewable resource, has an important contribution to industry and agriculture [1–4]. But this precious resource will be exhausted as a result of increased consumption in the near future [5–8]. The sustainable utilization of phosphate has become a severe challenge for human beings. Calcium silicate hydrate, due to the unique release capability of Ca²⁺ and OH⁻, has caused international extensive concern in the field of “recovery of phosphate from wastewater” [9–14]. This is because the released Ca²⁺ and OH⁻ can react with the phosphate ions to form hydroxyapatite (HAP) on the surface of CSH when the concentration of these ions reached to the supersaturated conditions [15–17]. Therefore, the release capability of Ca²⁺ and OH⁻ of CSH plays a key role in the field of phosphate recovery.

It is worthy to notice that the release capability is related to the specific surface area (S_{BET}) and pore structure. Large S_{BET} and porous structures are beneficial to enhance the solubility of CSH [18, 19]. The current CSH samples were prepared by dynamic hydrothermal synthesis using CaO materials and SiO₂ materials [20–23]. However, there two critical problems

that affect the solubility of CSH. On the one hand, the reactivity of SiO₂ was too poor to participate in the formation of CSH. The residual SiO₂ precipitated on the surface of CSH is easy to block the pore structure and decrease the solubility of CSH. According to the previous study, the proper temperature to synthesize CSH was 170°C [18, 19]. However, there were abundant hard dissolve intermediates such as calcium silicate, formed during the heating process. These intermediates coated on the surface of CSH and affected the solubility of CSH [24, 25]. Therefore, enhancing the reactivity of SiO₂ materials and avoiding the formation of intermediates are the critical factors for the formation of CSH with porous structure.

A synthesis strategy based on calcium oxide/polyethylene glycol (CaO/PEG₂₀₀₀) composites was developed for the formation of porous CSH. Under the dynamic hydrothermal condition, massive SiO₃²⁻ (released from the SiO₂ materials due to the increased pH values) reacted with Ca²⁺ (sustained released from CaO/PEG₂₀₀₀ composites) at a proper temperature to form CSH efficiently. Compared with previously reported synthesis methods, this new synthesis method

TABLE 1: Chemical components of carbide residue.

	Chemical composition (%)									
	CaO	SiO ₂	Al ₂ O ₃	SO ₂	MgO	Fe ₂ O ₃	SrO	NaOH	CuO	H ₂ O
Carbide residue	79.34	3.57	2.14	1.22	0.62	0.21	0.26	—	—	12.64
Silica	0.08	97.46	0.16	1.82	—	0.03	—	0.29	0.02	0.14

herein avoided the formation of the hardly dissolved intermediates. Thus, the as-prepared CSH with porous structure exhibited excellent release capabilities of Ca²⁺ and OH⁻. In addition, a novel porosity formation mechanism was revealed in the present paper.

2. Materials and Methods

2.1. Raw Materials. The CaO material (carbide residue, content of CaO > 75%) and SiO₂ material (Silica, content of SiO₂ > 98%) were obtained from Chongqing Changshou Chemical Co. Ltd. PEG₂₀₀₀ (the chemical formula is HO(CH₂CH₂O)_nH) and NaOH were obtained from Chengdu Kelong chemical Co. Ltd. The Chemical composition of the carbide residue and silica is presented in Table 1. The above materials and chemicals were placed into sealed bottles for storage.

2.2. Dynamic Hydrothermal Synthesis of Porous CSH. Prior to CSH synthesis, PEG₂₀₀₀ was put into 300 mL deionized water with strong stirring to obtain the PEG solution, and the mass fraction of PEG₂₀₀₀ was 2% w/v. Subsequently, 6 mg of carbide residue was added into the PEG solution with strong stirring and reacted 60 min at 80°C. Then, the solid segments were centrifugal separated from the PEG solution and were dried at 105°C for 2 h to obtain the CaO/PEG₂₀₀₀ composites.

Subsequently, CaO/PEG₂₀₀₀ composites and CaO materials were mixed with SiO₂ material to form a 300 mL slurry (liquid/solid mass ratio is 30/1; Ca/Si molar ratio is 1.75/1), respectively. 1 mol/L of NaOH was used to maintain the pH values of the slurry at 13.0. Mixtures were agitated at 90 rpm, and the resulting slurry was put into a high-pressure kettle for hydrothermal synthesis at 170°C for 6 h. The as-prepared CSH samples obtained from CaO/PEG₂₀₀₀ composites and CaO materials were labeled as CSH (CaO/PEG₂₀₀₀) and CSH (CaO), respectively.

2.3. Dissolution Experiment. The release of Ca²⁺ and OH⁻ from CSH was investigated via a series of batch experiments. For each experiment, 1 g of CSH was poured into 1 L of deionized water in glass bottles, thus leading to a sample to solution ratio of 1 g/L. The bottles were then placed on an agitation table and mixed at 40 rpm at 20°C for 5, 10, 15, 20, 40, 60, 80, and 100 min. The resulting Ca²⁺ concentration was determined using the EDTA coordination titration method (the relative derivation of data is 0.05%). Solution pH value was measured (±0.1) using precise pH paper (pH 7.0–10.0, Sana-i-si reagent Co., Ltd., Shanghai, China). The accuracy of pH measurement is 0.1.

2.4. Experiments on Phosphate Recovery from Synthetic Solutions. Phosphate recovery property of the as-synthesized samples were investigated in a series of batch experiments. The pH values of phosphate-content solution were in the range of 7.0–7.5 before the CSH samples were added into this solution. For each one, one glass bottle containing 1 L of a synthetic solution with initial phosphate concentration (100 mg/L) was prepared. Then 1 g of synthesized sample was put into this bottle, thus leading to a sample-to-solution ratio of 1 g/L. The bottle was placed on an agitation table and shaken at 40 r/min under given temperature conditions (20°C) for 60 min. The solid samples after reaction were then separated from the removed synthetic solution, and were added again to synthetic solution with initial phosphate concentration of 100 mg/L. This experiment was repeated for six times until the phosphate concentration was kept unchanged with the addition of samples. The content of phosphate in the recovered products was identified with atomic absorption spectrophotometry (Atomic Absorption Spectrometer, AA800, USA).

2.5. Characterization Instruments. The phase component and crystal structure of CSH are determined using X-ray diffraction with Cu K_α radiation (XRD, model XD-2 instrument, China). The morphology was observed by field-emission scanning electron microscopy (FESEM, IUE, Hitachi, Japan) and transmission electron microscope (TEM, JEOL JEM-2010, Japan). The S_{BET} and pore structure was investigated using adsorption-desorption measurements. Nitrogen adsorption-desorption isotherms were obtained on a nitrogen adsorption apparatus (ASAP-2010, USA). The microstructures are evaluated by Fourier transformed infrared spectroscopy (FT-IR, IR Prestige-21FT-infrared spectrometer, Shimadzu, Japan).

3. Results and Discussion

3.1. The Effect of pH on the Reactivity of SiO₂. In the water solution, the main existence forms of silicon are different with the changes of pH values. Silicon exists in the form of SiO₃²⁻ when the pH value is over 13.0 [26–28]. This result can be verified according to the fraction formula of H₂SiO₃, HSiO₃⁻ and SiO₃²⁻ under the given pH value as follows:

$$\delta_{\text{H}_2\text{SiO}_3} = \frac{[\text{H}^+]^2}{[\text{H}^+] + K_{\alpha 1} [\text{H}^+] + K_{\alpha 1} K_{\alpha 2}},$$

$$\delta_{\text{HSiO}_3^-} = \frac{K_{\alpha 1} [\text{H}^+]}{[\text{H}^+]^2 + K_{\alpha 1} [\text{H}^+] + K_{\alpha 1} K_{\alpha 2}},$$

$$\delta_{\text{SiO}_3^{2-}} = \frac{K_{\alpha 1} K_{\alpha 2}}{[\text{H}^+]^2 + K_{\alpha 1} [\text{H}^+] + K_{\alpha 1} K_{\alpha 2}}, \quad (1)$$

where $[\text{H}^+]$ is the concentration of hydrogen ions and $K_{\alpha 1}$ and $K_{\alpha 2}$ are the first and second dissociation constants, respectively. When $\text{pH} = 12.0$, the distribution coefficients of H_2SiO_3 , HSiO_3^- , and SiO_3^{2-} are 0%, 39%, and 61%, respectively. When $\text{pH} = 13.0$, these coefficients are 0%, 6%, and 94%, respectively, [29]. This trend indicated that silicon exists only in the form of SiO_3^{2-} that is beneficial to the formation of CSH.

3.2. Complexation between CaO and PEG₂₀₀₀. The reaction mechanism between CaO and PEG₂₀₀₀ was revealed via FT-IR analysis. Figures 1(a) and 1(b) show the FT-IR spectra of neat CaO and CaO/PEG₂₀₀₀ composites, respectively. As shown in Figure 1(a), a broad and sharp peak at 1402~1546 cm^{-1} and 870 cm^{-1} can be attributed to the characteristic peak of CaO. The stretching vibration band of C–O–C at 1090 cm^{-1} and the characteristic absorption band occurred at about 2270 cm^{-1} due to a bent oscillation peak of C–H bond in Figure 1(b) can be assigned to bands of PEG₂₀₀₀, and the absorption peak of C–O–C moves to a low band. This phenomenon indicated that the asymmetric stretching vibration frequency of C–O–C group of PEG₂₀₀₀ decreased due to the effect of Ca^{2+} . Furthermore, this result demonstrated that Ca^{2+} reacted with oxygen atom in PEG molecule to form complexation structure; that is, CaO and PEG₂₀₀₀ existed together in the form of complex.

3.3. The Porosity Formation Mechanism of CSH

3.3.1. Morphological Structure. The surface morphology of CSH (CaO) and CSH (CaO/PEG₂₀₀₀) was examined by FESEM, as shown in Figures 2(a) and 2(b). It can be seen that CSH (CaO) possessed a dense surface and compact structure (Figure 2(a)). In contrast, pore size of CSH (CaO/PEG₂₀₀₀) tended to be larger (Figure 2(b)). The morphological structure of CSH (CaO) and CSH (CaO/PEG₂₀₀₀) was further examined by TEM, as shown in Figures 2(c) and 2(d). The TEM image shows that the surface of CSH (CaO) was compact (Figure 2(c)) consistent with the FESEM observation. In contrast, CSH (CaO/PEG₂₀₀₀) possesses hollow microspheres due to the absence of the hardly dissolved intermediates (Figure 2(d)).

3.3.2. Specific Surface Area and Pore Structure. The S_{BET} and pore structure of the as-prepared samples were investigated by adsorption-desorption measurements. As shown in Table 2, the S_{BET} of CSH (CaO/PEG₂₀₀₀) increased to 133 m^2/g compared to CSH (CaO) (62 m^2/g). In comparison to CSH (CaO) (0.16 cm^3/g), the pore volume of CSH (CaO/PEG₂₀₀₀) increased to 0.36 cm^3/g .

Figure 3(a) shows the N_2 adsorption-desorption isotherms of the CSH samples. According to the Brunauer-Deming-Deming-Teller (BDDT) classification, the majority

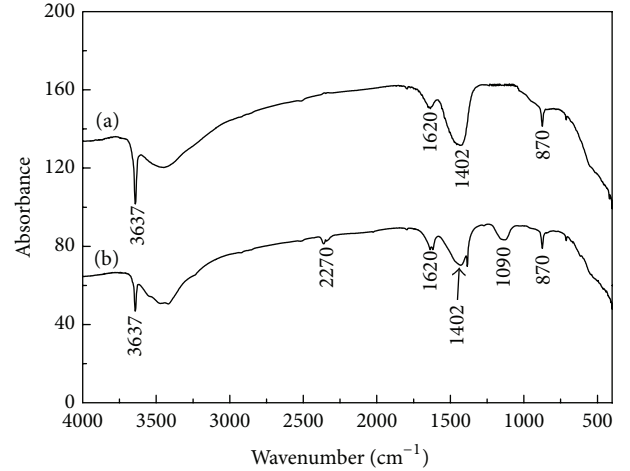


FIGURE 1: FT-IR spectra of CaO (a) and CaO/PEG₂₀₀₀ composites (b).

TABLE 2: Specific BET surface areas and pore parameters of CSH samples.

CSH samples	Total volume (cm^3/g)	Peak pore diameter (nm)	S_{BET} (m^2/g)
CSH (CaO)	0.16	13.57	62
CSH (CaO/PEG ₂₀₀₀)	0.36	5.8	133

of physisorption isotherms can be grouped into six types. The isotherms of all the samples belonged to type IV, including the pore-size distributions in the mesoporous regions [30]. The shapes of hysteresis loops were of the type H3, which was associated with mesopores formed due to aggregation of plates-like particles [31].

Figure 3(b) shows the corresponding PSD of the samples. For the CSH (CaO), the PSD curve is bimodal with smaller (~2.54 nm) and larger (~45.42 nm) mesopores. For CSH (CaO/PEG₂₀₀₀), the PSD curve exhibits small (~6.52 nm) mesopores. The small mesopores and larger ones came from the aggregation of primary particles and secondary particles, respectively. This result was consistent with the result of N_2 adsorption-desorption isotherms. A large number of small mesopores contribute to the large S_{BET} .

3.3.3. Phase Structure. Figure 4 shows the XRD patterns of CSH (CaO) and CSH (CaO/PEG₂₀₀₀). Multiple phases, such as Jennite (PDF card 18-1206, chemical formula $\text{Ca}_9\text{Si}_6\text{O}_{18}(\text{OH})_6 \cdot 8\text{H}_2\text{O}$), xonotlite (PDF card 23-0125, chemical formula $\text{Ca}_6\text{Si}_6\text{O}_{17}(\text{OH})_2$), and $\text{Ca}_3\text{Si}_2\text{O}_7$ (PDF card 11-0317), appear in the XRD pattern of Figure 4(a). By comparison, the phase of CSH (CaO/PEG₂₀₀₀) was only Jennite (Figure 4(b)). Combined with the above analysis, the as-prepared CSH (CaO/PEG₂₀₀₀) (i.e., Jennite), without intermediates, exhibited large S_{BET} and porous structure.

The porosity formation mechanism can be revealed as follows: (1) during the heating process, SiO_3^{2-} was released from SiO_2 materials due to the increased pH value (13.0), and Ca^{2+} cannot be released from CaO/PEG₂₀₀₀ composites due to

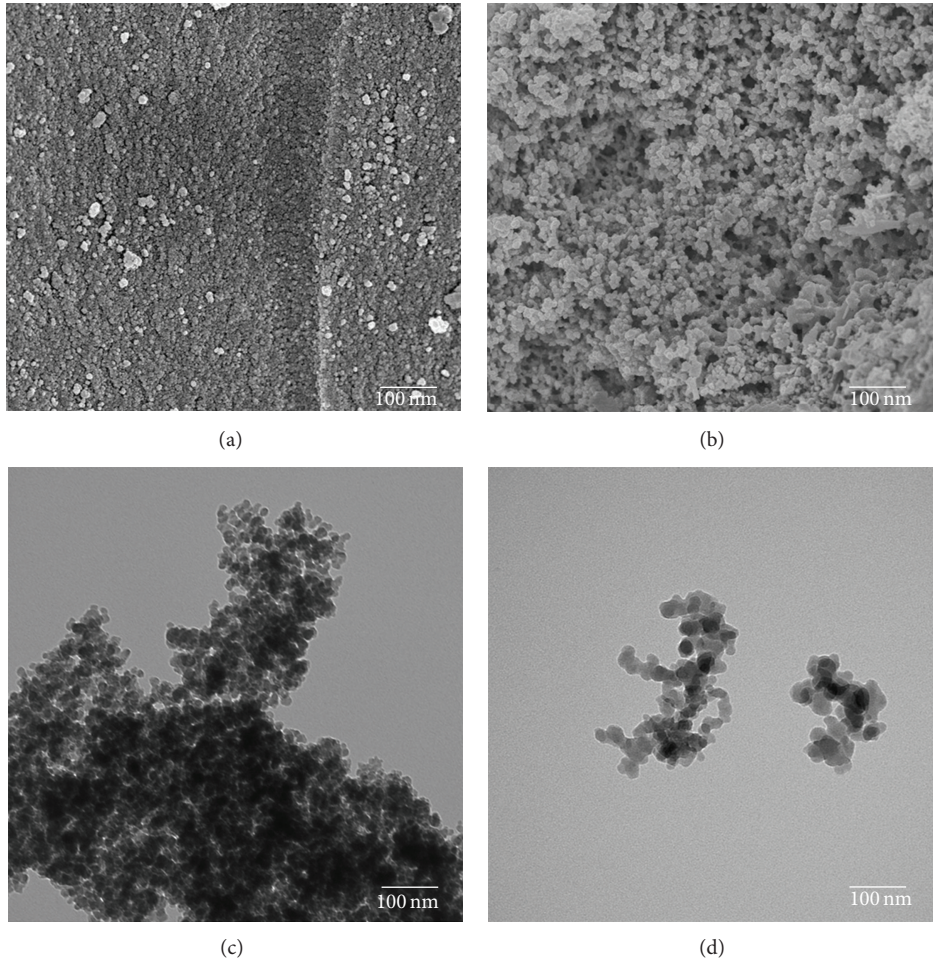


FIGURE 2: FESEM photographs of CSH (CaO) (a) and CSH (CaO/PEG₂₀₀₀) (b); TEM images of CSH (CaO) (c) and CSH (CaO/PEG₂₀₀₀) (d).

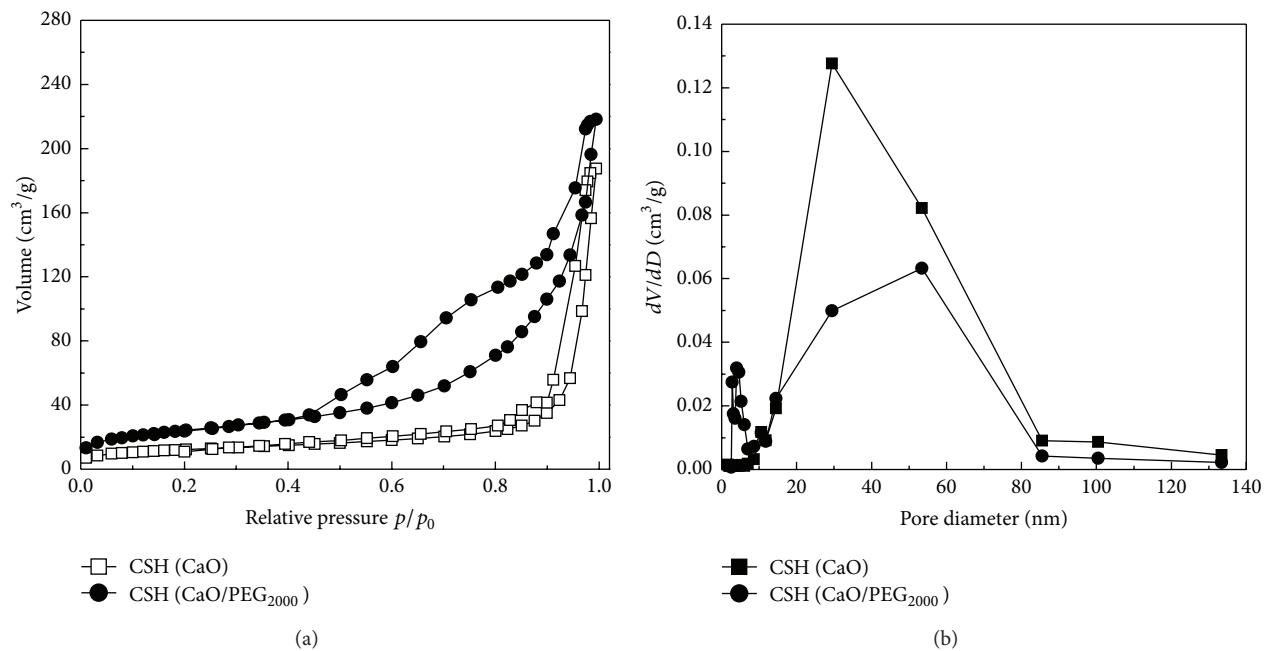


FIGURE 3: N_2 adsorption-desorption isotherms (a) and pore-size distribution curves (b) of the as-prepared CSH samples.

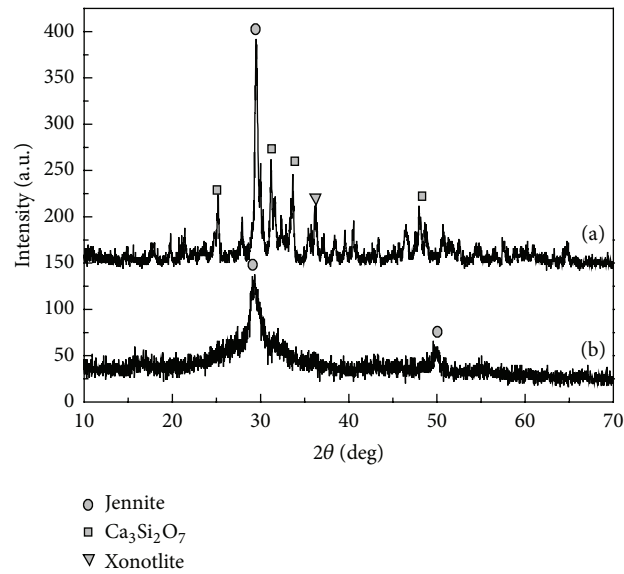


FIGURE 4: XRD patterns of CSH (CaO) (a) and CSH (CaO/PEG₂₀₀₀) (b).

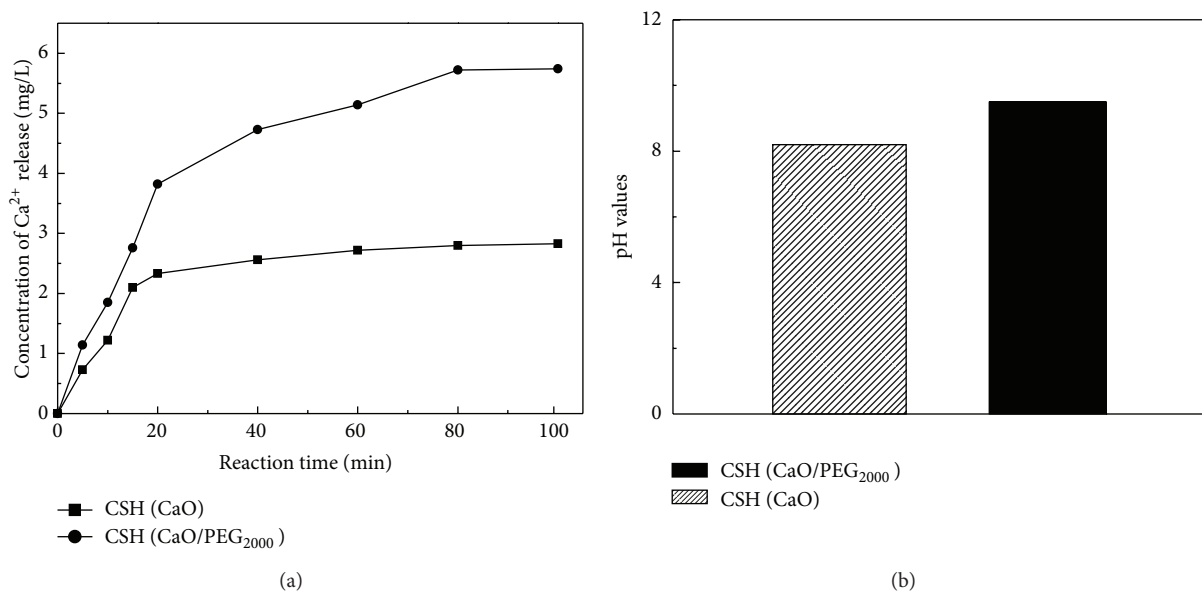


FIGURE 5: Concentration of Ca²⁺ released from CSH samples (a) and pH in deionized water kept by CSH samples (b).

the coating of PEG₂₀₀₀ below the hydrothermal temperature (170°C); (2) when the hydrothermal temperature reached to a proper condition (170°C), the molecular chain broke between CaO and PEG₂₀₀₀. At this time, Ca²⁺ released from CaO/PEG₂₀₀₀ composites and reacted with SiO₃²⁻ quickly to form CSH (CaO/PEG₂₀₀₀). To the synthesis of CSH (CaO), massive Ca²⁺ was released from neat CaO materials during the heating process before the hydrothermal temperature reached to 170°C, leading to formation of abundant hardly dissolved intermediates. By comparison, the new synthesis method herein avoided the formation of the hard dissolve intermediates.

3.4. The Enhanced Solubility of CSH. Figure 5 shows the variations of concentration of Ca²⁺ and OH⁻ released from the as-synthesized CSH samples and pH-values in deionized water. According to Figure 5(a), CSH (CaO/PEG₂₀₀₀) releases more Ca²⁺ than CSH (CaO). Compared with the CSH (CaO) (2.83 mg/L), the concentration of Ca²⁺ was released from CSH (CaO/PEG₂₀₀₀) and increased to 5.74 mg/L. Figure 5(b) shows that the pH value of the solution can be kept at 9.5 by CSH (CaO/PEG₂₀₀₀); however, CSH (CaO) can only maintain the pH value at 8.2. The as-prepared CSH (CaO/PEG₂₀₀₀) with porous structure exhibited enhanced release capability of Ca²⁺ and OH⁻.

3.5. *The Enhanced Phosphate Recovery Property of CSH.* The phosphate content of the product recovered by CSH (CaO/PEG₂₀₀₀) increased to 117.6 mg/g, compared with CSH (CaO) (84.5 mg/g). This result indicated that the as-prepared porous CSH, without the hardly dissolved intermediates, exhibited highly enhanced phosphate recovery property. Meanwhile, the recovered phosphate products, due to their abundant phosphate content, can be reused as phosphate rock or phosphate fertilizer.

4. Conclusion

Porous CSH was prepared based on the CaO/PEG₂₀₀₀ composites as the calcium materials; Ca²⁺ could not sustain release from CaO/PEG₂₀₀₀ and reacted with SiO₃²⁻ caused by silica to form CSH until the hydrothermal temperature reached to 170°C, avoiding the formation of hardly dissolved intermediates compared with previously reported synthesis methods. The as-prepared CSH, due to the large specific surface areas, exhibited excellent release capability of Ca²⁺ and OH⁻. Thus, the phosphate recovery property of CSH enhanced. The recovered phosphate products, due to their abundant phosphate content, can be reused in industry and agriculture instead of phosphate rock. Therefore, the as-prepared porous material has potential application value in recovering phosphate from wastewater to solve the environmental problems caused by the shortage of phosphate resource.

Conflict of Interests

The authors declare that there is no conflict of interests regarding the publication of this paper.

References

- [1] W. Cai, B. G. Zhang, Y. X. Jin et al., "Behavior of total phosphorus removal in an intelligent controlled sequencing batch biofilm reactor for municipal wastewater treatment," *Biore-source Technology*, vol. 132, pp. 190–196, 2013.
- [2] B. M. Spears, S. Meis, A. Anderson, and M. Kellou, "Comparison of phosphorus (P) removal properties of materials proposed for the control of sediment p release in UK lakes," *Science of the Total Environment*, vol. 442, pp. 103–110, 2013.
- [3] D. Seyhan, "Country-scale phosphorus balancing as a base for resources conservation," *Resources, Conservation and Recycling*, vol. 53, no. 12, pp. 698–709, 2009.
- [4] D. Cordell, J.-O. Drangert, and S. White, "The story of phosphorus: global food security and food for thought," *Global Environmental Change*, vol. 19, no. 2, pp. 292–305, 2009.
- [5] C. J. Dawson and J. Hilton, "Fertiliser availability in a resource-limited world: production and recycling of nitrogen and phosphorus," *Food Policy*, vol. 36, supplement 1, pp. S14–S22, 2011.
- [6] S. Petzet, B. Peplinski, and P. Cornel, "On wet chemical phosphorus recovery from sewage sludge ash by acidic or alkaline leaching and an optimized combination of both," *Water Research*, vol. 46, no. 12, pp. 3769–3780, 2012.
- [7] H. Kodera, M. Hatamoto, K. Abe, T. Kindaichi, N. Ozaki, and A. Ohashi, "Phosphate recovery as concentrated solution from treated wastewater by a PAO-enriched biofilm reactor," *Water Research*, vol. 47, no. 6, pp. 2025–2032, 2013.
- [8] Z. Bradford-Hartke, P. Lant, and G. Leslie, "Phosphorus recovery from centralised municipal water recycling plants," *Chemical Engineering Research and Design*, vol. 90, no. 1, pp. 78–85, 2012.
- [9] K. Okano, M. Uemoto, J. Kagami et al., "Novel technique for phosphorus recovery from aqueous solutions using amorphous calcium silicate hydrates (A-CSHs)," *Water Research*, vol. 47, no. 7, pp. 2251–2259, 2013.
- [10] X. Cong and R. J. Kirkpatrick, "²⁹Si and ¹⁷O NMR investigation of the structure of some crystalline calcium silica hydrates," *Advanced Cement Based Materials*, vol. 3, no. 3-4, pp. 133–143, 1996.
- [11] H. Maeda and E. H. Ishida, "Hydrothermal preparation of diatomaceous earth combined with calcium silicate hydrate gels," *Journal of Hazardous Materials*, vol. 185, no. 2-3, pp. 858–861, 2011.
- [12] Z.-L. Ye, S.-H. Chen, S.-M. Wang et al., "Phosphorus recovery from synthetic swine wastewater by chemical precipitation using response surface methodology," *Journal of Hazardous Materials*, vol. 176, no. 1-3, pp. 1083–1088, 2010.
- [13] J. J. Chen, J. J. Thomas, H. F. W. Taylor, and H. M. Jennings, "Solubility and structure of calcium silicate hydrate," *Cement and Concrete Research*, vol. 34, no. 9, pp. 1499–1519, 2004.
- [14] C. Barca, C. Gérente, D. Meyer, F. Chazarenc, and Y. Andrès, "Phosphate removal from synthetic and real wastewater using steel slags produced in Europe," *Water Research*, vol. 46, no. 7, pp. 2376–2384, 2012.
- [15] P. Q. Franco, C. F. C. João, J. C. Silva, and J. P. Borges, "Electrospun hydroxyapatite fibers from a simple sol-gel system," *Materials Letters*, vol. 67, no. 1, pp. 233–236, 2012.
- [16] E. Vasile, L. M. Popescu, R. M. Piticescu, A. Burlacu, and T. Buruiana, "Physico-chemical and biocompatible properties of hydroxyapatite based composites prepared by an innovative synthesis route," *Materials Letters*, vol. 79, pp. 85–88, 2012.
- [17] S. Santhosh and S. B. Prabu, "Thermal stability of nano hydroxyapatite synthesized from sea shells through wet chemical synthesis," *Materials Letters*, vol. 97, pp. 121–124, 2013.
- [18] W. Guan, F. Y. Ji, Q. K. Chen, P. Yan, and W. W. Zhou, "Influence of hydrothermal temperature on phosphorus recovery efficiency of porous calcium silicate hydrate," *Journal of Nanomaterials*, vol. 2013, Article ID 451984, 6 pages, 2013.
- [19] W. Guan, F. Y. Ji, Q. K. Chen, P. Yan, and Q. Zhang, "Preparation and phosphorus recovery performance of porous calcium-silicate-hydrate," *Ceramics International*, vol. 39, no. 2, pp. 1385–1391, 2013.
- [20] X.-L. Zhao and M. Saigusa, "Fractionation and solubility of cadmium in paddy soils amended with porous hydrated calcium silicate," *Journal of Environmental Sciences*, vol. 19, no. 3, pp. 343–347, 2007.
- [21] L. Nicoleau, "Accelerated growth of calcium silicate hydrates: experiments and simulations," *Cement and Concrete Research*, vol. 41, no. 12, pp. 1339–1348, 2011.
- [22] S. Shaw, S. M. Clark, and C. M. B. Henderson, "Hydrothermal formation of the calcium silicate hydrates, tobermorite (Ca₅Si₆O₁₆(OH)₂·4H₂O) and xonotlite (Ca₆Si₆O₁₇(OH)₂): an in situ synchrotron study," *Chemical Geology*, vol. 167, no. 1-2, pp. 129–140, 2000.
- [23] D. Sugiyama and T. Fujita, "A thermodynamic model of dissolution and precipitation of calcium silicate hydrates," *Cement and Concrete Research*, vol. 36, no. 2, pp. 227–237, 2006.

- [24] A. A. P. Mansur and H. S. Mansur, "Preparation, characterization and cytocompatibility of bioactive coatings on porous calcium-silicate-hydrate scaffolds," *Materials Science and Engineering C*, vol. 30, no. 2, pp. 288–294, 2010.
- [25] C. Noiriel, L. Luquot, B. Madé, L. Raimbault, P. Gouze, and J. van der Lee, "Changes in reactive surface area during limestone dissolution: an experimental and modelling study," *Chemical Geology*, vol. 265, no. 1-2, pp. 160–170, 2009.
- [26] H. Yang, L. Feng, C. Wang, W. Zhao, and X. Li, "Confinement effect of SiO₂ framework on phase change of PEG in shape-stabilized PEG/SiO₂ composites," *European Polymer Journal*, vol. 48, no. 4, pp. 803–810, 2012.
- [27] Q. Guo and T. Wang, "Influence of SiO₂ pore structure on phase change enthalpy of shape-stabilized polyethylene glycol/silica composites," *Journal of Material Science*, vol. 48, no. 10, pp. 3716–3721, 2013.
- [28] I. Y. Kim, G. Kawachi, K. Kikuta, S. B. Cho, M. Kamitakahara, and C. Ohtsuki, "Preparation of bioactive spherical particles in the CaO-SiO₂ system through sol-gel processing under coexistence of poly(ethylene glycol)," *Journal of the European Ceramic Society*, vol. 28, no. 8, pp. 1595–1602, 2008.
- [29] X. Huang, D. L. Jiang, and S. H. Tan, "Hydrothermal synthesis of tobermorite fibers through calcium chelated complex," *Journal of Inorganic Materials*, vol. 18, no. 1, pp. 143–148, 2003 (Chinese).
- [30] F. Dong, S. C. Lee, Z. Wu et al., "Rose-like monodisperse bismuth subcarbonate hierarchical hollow microspheres: one-pot template-free fabrication and excellent visible light photocatalytic activity and photochemical stability for NO removal in indoor air," *Journal of Hazardous Materials*, vol. 195, pp. 346–354, 2011.
- [31] F. Dong, H. T. Liu, W. K. Ho, M. Fu, and Z. B. Wu, "(NH₄)₂CO₃ mediated hydrothermal synthesis of N-doped (BiO)₂CO₃ hollow nanoplates microspheres as high-performance and durable visible light photocatalyst for air cleaning," *Chemical Engineering Journal*, vol. 214, pp. 198–207, 2013.